DECEMBER 2017

AJNR

VOLUME 38 • PP 2219–2405

AJNR

AMERICAN JOURNAL OF NEURORADIOLOGY

DECEMBER 2017
VOLUME 38
NUMBER 12
WWW.AJNR.ORG

THE JOURNAL OF DIAGNOSTIC AND INTERVENTIONAL NEURORADIOLOGY

MRI and cardiac implantable electronic devices
Head and neck cancer staging
Photon-counting CT of the brain

Official Journal ASNR • ASFNR • ASHNR • ASPNR • ASSR

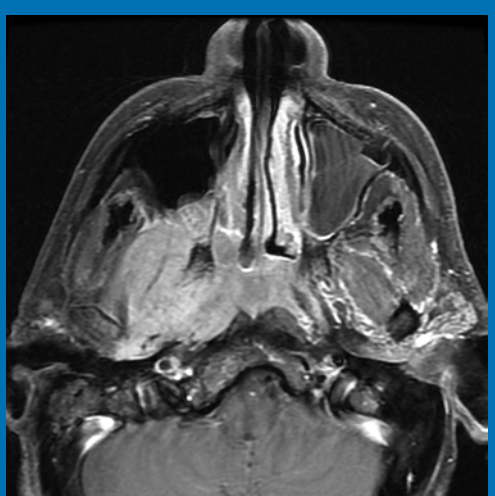
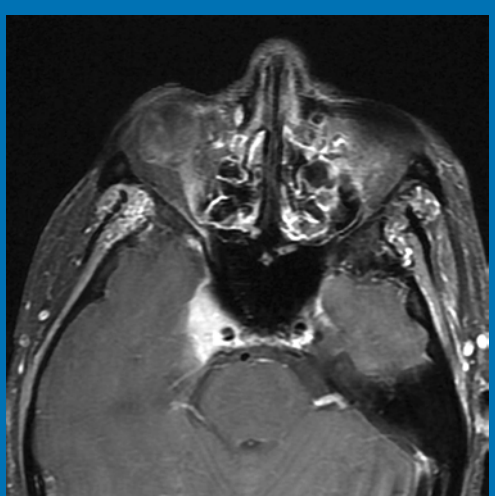
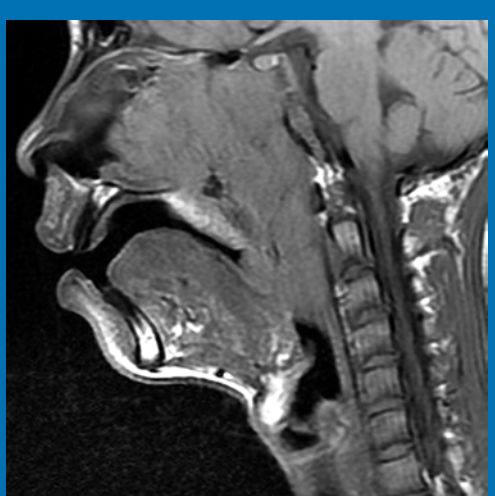
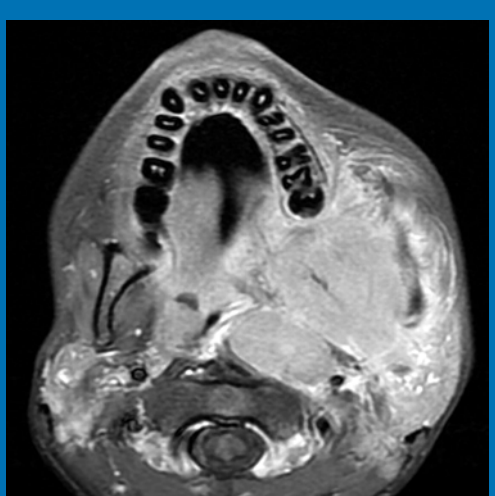

A 360-Degree Approach to Neuroendovascular Therapy

Aneurysm Therapy Solutions

LVIS® | LVIS® Jr.
Intraluminal Support Device

Braided Coil Assist Stents with High Neck Coverage, Excellent Opening, and Improved Radial Force*

**Humanitarian Device: Authorized by Federal Law for use with bare platinum embolic coils for the treatment of unruptured, wide neck (neck ≥ 4 mm or dome to neck ratio < 2), intracranial, saccular aneurysms arising from a parent vessel with a diameter ≥ 2.5 mm and ≤ 4.5 mm. The effectiveness of this device for this use has not been demonstrated.*

Access Product Solutions

Headway® DUO
Microcatheter

Innovative Catheter Technology and Construction in a Complete Range of Sizes and Softness

For more information or a product demonstration, contact your local MicroVention representative:

MicroVention® TERUMO

MicroVention, Inc.
Worldwide Headquarters PH +1.714.247.8000
35 Enterprise
Aliso Viejo, CA 92656 USA
MicroVention UK Limited PH +44 (0) 191 258 6777
MicroVention Europe, S.A.R.L. PH +33 (1) 39 21 77 46
MicroVention Deutschland GmbH PH +49 211 210 798-0
microvention.com

stryker®
Neurovascular

Purposeful innovation in mind.

Smooth and stable.

Target Detachable Coils deliver consistently smooth deployment and exceptional microcatheter stability. Designed to work seamlessly together for framing, filling and finishing. Target Coils deliver the high performance you demand.

For more information, please visit www.strykerneurovascular.com/Target or contact your local Stryker Neurovascular sales representative.

Target®
DETACHABLE COILS

NV00018669.AA

Magic®

balt

FLOW-DEPENDENT MICROCATHETER SERIES

Now available through Balt USA

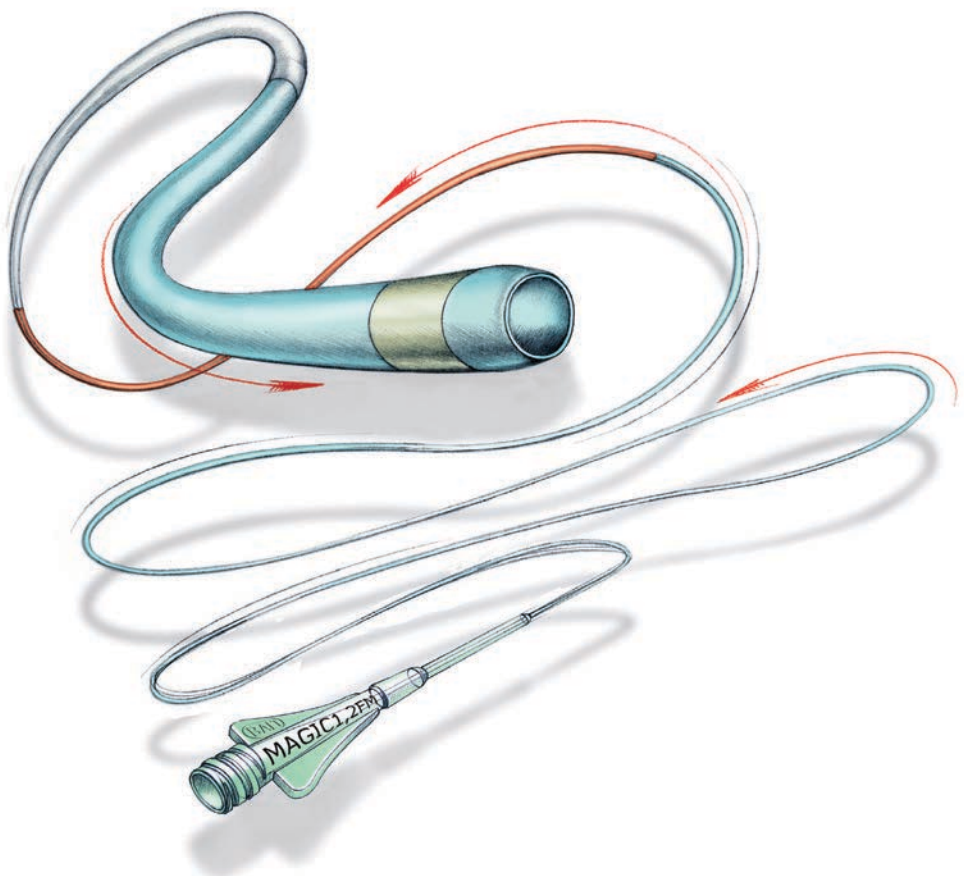

ordermagics@balt-usa.com

MAGIC catheters are designed for general intravascular use. They may be used for the controlled, selective regional infusion of therapeutic agents or embolic materials into vessels.[1]

Federal (USA) law restricts this device to sale, distribution by or on the order of a physician. Indications, contraindications, warnings and instructions for use can be found in the product labeling supplied with each device.

1. Magic Catheters IFU – Ind 19

balt
inspiring innovation

BALT USA
18 Technology Drive #169, Irvine, CA 92618
P 949.788.1443 **F** 949.788.1444


Happy Holidays
RAPIDMEDICAL

ASNR 56th Annual Meeting & The Foundation of the ASNR Symposium 2018

June 2 - 7, 2018 | Vancouver, B.C., CANADA

The Vancouver Convention Centre East

Welcome and Greetings

Please join us in Vancouver, CANADA for the **56th Annual Meeting of the American Society of Neuroradiology** on June 2–7, 2018 at the Vancouver Convention Centre East. Surrounded by the coastal mountains and located on the waterfront, you can enjoy these spectacular views in the heart of downtown Vancouver. With its undeniable charm and friendly atmosphere, Vancouver is known around the world as both a popular tourist attraction and one of the best places to live.

ASNR enthusiastically presents **Neuroradiology: Adding Value and Improving Healthcare** at the Symposium of the Foundation of the ASNR, as well as the common thread throughout the Annual Meeting. Implementing a value-based strategy in imaging has grasped the attention of nearly every healthcare provider; in particular with Radiologists understanding that the future will demand their imaging practices deliver better value. Value in healthcare is typically defined as those imaging strategies that yield improved outcomes, lower costs, or both. As payment transitions from a fee-for-service to a value-based system, thus creating a fundamentally different marketplace dynamic, measuring good outcomes are at the center of this changeover. At this time of uncertainty what little remains clear is that without a well-defined knowledge of their outcomes, no medical specialty will be able to succeed in the future value-based system. The Symposium will feature how Neuroradiology, in its many subspecialty areas, adds value to clinical care pathways by directing healthcare practice towards better outcomes. The annual meeting programming will continue on this theme emphasizing imaging that improves health outcomes, while considering costs, thus adding value. Our discussions will incorporate many innovative approaches to how neuroimaging currently does and will continue to improve overall healthcare performance.

As the Program Chair for ASNR 2018, it is my pleasure and honor to welcome you to Vancouver, CANADA for our annual meeting! Vancouver is known for being a very walkable city with a compact downtown core hosting many places to enjoy. So pack your comfortable walking shoes and let's tour together with our colleagues and friends!

Pina Sanelli

Pina C. Sanelli, MD, MPH, FACR
ASNR 2018 Program Chair/President-Elect

NEURORADIOLOGY
Adding Value & Improving Healthcare

ASNR 2018 ▪ VANCOUVER

ASFNR ASHNR ASPNR ASSR SNIS

THE FOUNDATION OF THE ASNR

Pina C. Sanelli, MD, MPH, FACR
ASNR 2018 Program Chair/President-Elect

Programming developed in cooperation with the…

American Society of Functional Neuroradiology (ASFNR)
Max Wintermark, MD

American Society of Head and Neck Radiology (ASHNR)
Deborah R. Shatzkes, MD

American Society of Pediatric Neuroradiology (ASPNR)
Ashok Panigrahy, MD

American Society of Spine Radiology (ASSR)
John D. Barr, MD, FACR, FSIR, FAHA

Society of NeuroInterventional Surgery (SNIS)
Mahesh V. Jayaraman, MD

ASNR Health Policy (HPC) Committee
William D. Donovan, MD, MPH, FACR,
Gregory N. Nicola, MD, FACR

ASNR Computer Sciences & Informatics (CSI) Committee
John L. Go, MD, FACR

ASNR Research Scientist Programming Committee
Dikoma C. Shungu, PhD, Timothy P.L. Roberts, PhD

The International Hydrocephalus Imaging Working Group (IHIWG) / CSF Flow Group
William G. Bradley, Jr., MD, PhD, FACR, Harold L. Rekate, MD and Bryn A. Martin, PhD

Meeting Registration Opening SOON!
Please visit 2018.asnr.org for more information

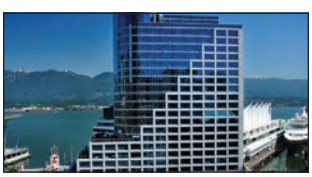

Fairmont Waterfront

Pan Pacific Vancouver

ASNR 56th Annual Meeting
c/o American Society of Neuroradiology
800 Enterprise Drive, Suite 205
Oak Brook, Illinois 60523-4216
Phone: 630-574-0220 + Fax: 630 574-0661
2018.asnr.org

AJNR

CALL FOR AJNR EDITORIAL FELLOWSHIP CANDIDATES

ASNR and AJNR are pleased once again to join efforts with other imaging-related journals that have training programs on editorial aspects of publishing for trainees or junior staff (3–5 years after training), including Radiology (Olmsted fellowship), AJR (Figley and Rogers fellowships), JACR (Bruce J. Hillman fellowship), and Radiologia.

2018 Candidate Information and Requirements

GOALS

- Increase interest in "editorial" and publication-related activities in younger individuals.
- Increase understanding and participation in the AJNR review process.
- Incorporate into AJNR's Editorial Board younger individuals who have previous experience in the review and publication process.
- Fill a specific need in neuroradiology not offered by other similar fellowships.
- Increase the relationship between "new" generation of neuroradiologists and more established individuals.
- Increase visibility of AJNR among younger neuroradiologists.

ACTIVITIES OF THE FELLOWSHIP

- Serve as Editorial Fellow for one year. This individual will be listed on the masthead as such.
- Review at least one manuscript per month for 12 months. Evaluate all review articles submitted to AJNR.
- Learn how electronic manuscript review systems work.
- Be involved in the final decision of selected manuscripts together with the Editor-in-Chief.
- Participate in all monthly Senior Editor telephone conference calls.
- Participate in all meetings of the Editors and Publications Committee during the annual meetings of ASNR and RSNA as per candidate's availability. The Foundation of the ASNR will provide $2000 funding for this activity.
- Evaluate progress and adjust program to specific needs in annual meeting or telephone conference with the Editor-in-Chief.
- Embark on an editorial scientific or bibliometric project that will lead to the submission of an article to AJNR or another appropriate journal as determined by the Editor-in-Chief. This project will be presented by the Editorial Fellow at the ASNR annual meeting.
- Serve as liaison between AJNR and ASNR's Young Professionals Network and the 3 YPs appointed to AJNR as special consultants. Participate in meetings and telephone calls with this group. Design one electronic survey/year, polling the group regarding readership attitudes and wishes.
- Recruit trainees as reviewers as determined by the Editor-in-Chief.
- Organize and host a Fellows' Journal Club podcast.
- Serve as Guest Editor for an issue of AJNR's News Digest with a timely topic.

QUALIFICATIONS

- Be a fellow in neuroradiology from North America, including Canada (this may be extended to include other countries).
- Be a junior faculty neuroradiology member (< 3 years) in either an academic or private environment.
- Be an "in-training" or member of ASNR in any other category.

APPLICATION

- Include a short letter of intent with statement of goals and desired research project. CV must be included.
- Include a letter of recommendation from the Division Chief or fellowship program director. A statement of protected time to perform the functions outlined is desirable.
- Applications will be evaluated by AJNR's Senior Editors and the Chair of the Publications Committee prior to the ASNR meeting. The name of the selected individual will be announced at the meeting.
- Applications should be received by March 1, 2018 and sent to Ms. Karen Halm, AJNR Managing Editor, electronically at khalm@asnr.org.

We're Inside Every Great Neuroradiologist!

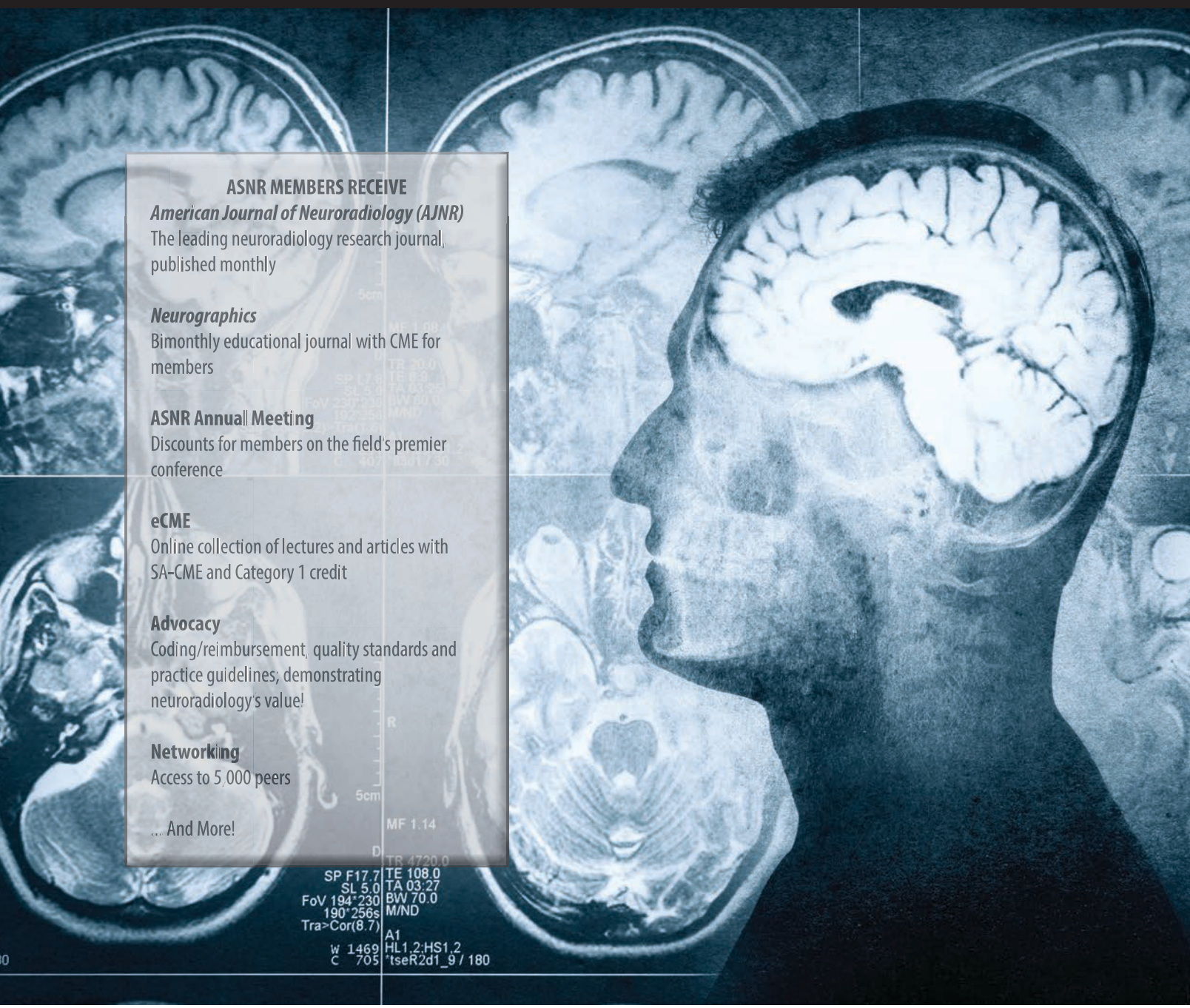

Join the leaders in neuroradiology today!
Learn more at www.asnr.org/join

ASNR
American Society of Neuroradiology

800 Enterprise Dr., Suite 205, Oak Brook, IL 60523 • (630)574-0220 • membership@asnr.org • www.asnr.org

ASHNR
American Society of
Head & Neck Radiology

52nd Annual Meeting | **American Society of**

Head & Neck Radiology

The Westin Savannah Harbor Golf Resort & Spa
Savannah, GA

September 26 - 30, 2018

Please contact Educational Symposia at 813-806-1000 or ASHNR@edusymp.com or visit www.ASHNR.org for additional information.

Neuroform Atlas™ Stent System

See package insert for complete indications, contraindications, warnings and instructions for use.

Humanitarian Device. Authorized by Federal law for use with neurovascular embolic coils in patients who are ≥ 18 years of age for the treatment of wide neck, intracranial, saccular aneurysms arising from a parent vessel with a diameter of ≥ 2 mm and ≤ 4.5 mm that are not amenable to treatment with surgical clipping. Wide neck aneurysms are defined as having a neck ≥ 4 mm or a dome-to-neck ratio < 2. The effectiveness of this device for this use has not been demonstrated.

INDICATIONS FOR USE

The Neuroform Atlas™ Stent System is indicated for use with neurovascular embolic coils in patients who are ≥ 18 years of age for the treatment of wide neck, intracranial, saccular aneurysms arising from a parent vessel with a diameter of ≥ 2 mm and ≤ 4.5 mm that are not amenable to treatment with surgical clipping. Wide neck aneurysms are defined as having a neck ≥ 4 mm or a dome-to-neck ratio of < 2.

CONTRAINDICATIONS

Patients in whom antiplatelet and/or anticoagulation therapy is contraindicated.

POTENTIAL ADVERSE EVENTS

The potential adverse events listed below, as well as others, may be associated with the use of the Neuroform Atlas™ Stent System or with the procedure:

Allergic reaction to nitinol metal and medications, Aneurysm perforation or rupture, Coil herniation through stent into parent vessel, Death, Embolus, Headache, Hemorrhage, In-stent stenosis, Infection, Ischemia, Neurological deficit/intracranial sequelae, Pseudoaneurysm, Stent fracture, Stent migration/embolization, Stent misplacement, Stent thrombosis, Stroke, Transient ischemic attack, Vasospasm, Vessel occlusion or closure, Vessel perforation/rupture, Vessel dissection, Vessel trauma or damage, Vessel thrombosis, Visual impairment, and other procedural complications including but not limited to anesthetic and contrast media risks, hypotension, hypertension, access site complications.

WARNINGS

- Contents supplied STERILE using an ethylene oxide (EO) process. Do not use if sterile barrier is damaged. If damage is found, call your Stryker Neurovascular representative.
- For single use only. Do not reuse, reprocess or resterilize. Reuse, reprocessing or resterilization may compromise the structural integrity of the device and/or lead to device failure which, in turn, may result in patient injury, illness or death. Reuse, reprocessing or resterilization may also create a risk of contamination of the device and/or cause patient infection or cross-infection, including, but not limited to, the transmission of infectious disease(s) from one patient to another. Contamination of the device may lead to injury, illness or death of the patient.
- After use, dispose of product and packaging in accordance with hospital, administrative and/or local government policy.
- This device should only be used by physicians who have received appropriate training in interventional neuroradiology or interventional radiology and preclinical training on the use of this device as established by Stryker Neurovascular.
- Select a stent size (length) to maintain a minimum of 4 mm on each side of the aneurysm neck along the parent vessel. An incorrectly sized stent may result in damage to the vessel or stent migration. Therefore, the stent is not designed to treat an aneurysm with a neck greater than 22 mm in length.
- If excessive resistance is encountered during the use of the Neuroform Atlas™ Stent System or any of its components at any time during the procedure, discontinue use of the stent system. Continuing to move the stent system against resistance may result in damage to the vessel or a system component.
- Persons allergic to nickel titanium (Nitinol) may suffer an allergic response to this stent implant.
- Purge the system carefully to avoid the accidental introduction of air into the stent system.
- Confirm there are no air bubbles trapped anywhere in the stent system.

CAUTIONS / PRECAUTIONS

- Federal Law (USA) restricts this device to sale by or on the order of a physician.
- Use the Neuroform Atlas Stent System prior to the "Use By" date printed on the package
- Carefully inspect the sterile package and Neuroform Atlas Stent System prior to use to verify that neither has been damaged during shipment. Do not use kinked or damaged components; contact your Stryker Neurovascular representative.
- The stent delivery microcatheter and the Neuroform Atlas Stent delivery wire should not be used to recapture the stent.
- Exercise caution when crossing the deployed stent with adjunctive devices.
- After deployment, the stent may foreshorten from up to 6.3%.
- The max OD of the coiling microcatheter should not exceed the max OD of the stent delivery microcatheter.
- Standard interventional devices with distal tips > 1.8 F may not be able to pass through the interstices of the stent.
- Safety of the Neuroform Atlas Stent System in patients below the age of 18 has not been established.
- In cases where multiple aneurysms are to be treated, start at the most distal aneurysm first.

MAGNETIC RESONANCE IMAGING (MRI)

Safety Information Magnetic Resonance Conditional

Non-clinical testing and analysis have demonstrated that the Neuroform Atlas Stent is MR Conditional alone, or when overlapped with a second stent, and adjacent to a Stryker Neurovascular coil mass. A patient with the Neuroform Atlas Stent can be safely scanned immediately after placement of this implant, under the following conditions:

- Static magnetic field of 1.5 and 3.0 Tesla
- Maximum spatial gradient field up to 2500 Gauss/cm (25 Tesla/m)
- Maximum MR system reported whole body averaged specific absorption rate of 2 W/kg (Normal Operating Mode) and head averaged specific absorption rate of 3.2 W/kg.

Under the scan conditions defined above, the Neuroform Atlas Stent is expected to produce a maximum temperature rise of 4°C after 15 minutes of continuous scanning. The Neuroform Atlas Stent should not migrate in this MRI environment.

In non-clinical testing, the image artifact caused by the device extends approximately 2 mm from the Neuroform Atlas Stent when imaged with a spin echo pulse sequence and 3 Tesla MRI System. The artifact may obscure the device lumen. It may be necessary to optimize MR imaging parameters for the presence of this implant.

Excelsior® XT-17™ Microcatheter

See package insert for complete indications, contraindications, warnings and instructions for use.

INTENDED USE / INDICATIONS FOR USE

Stryker Neurovascular's Excelsior XT-17 Microcatheters are intended to assist in the delivery of diagnostic agents, such as contrast media, and therapeutic agents, such as occlusion coils, into the peripheral, coronary and neuro vasculature.

CONTRAINDICATIONS

None known.

POTENTIAL ADVERSE EVENTS

Potential adverse events associated with the use of microcatheters or with the endovascular procedures include, but are not limited to: access site complications, allergic reaction, aneurysm perforation, aneurysm rupture, death, embolism (air, foreign body, plaque, thrombus), hematoma, hemorrhage, infection, ischemia, neurological deficits, pseudoaneurysm, stroke, transient ischemic attack, vasospasm, vessel dissection, vessel occlusion, vessel perforation, vessel rupture, vessel thrombosis

WARNINGS

- The accessories are not intended for use inside the human body.
- Limited testing has been performed with solutions such as contrast media, saline and suspended embolic particles. The use of these microcatheters for delivery of solutions other than the types that have been tested for compatibility is not recommended. Do not use with glue or glue mixtures.
- Carefully inspect all devices prior to use. Verify shape, size and condition are suitable for the specific procedure.
- Exchange microcatheters frequently during lengthy procedures that require extensive guidewire manipulation or multiple guidewire exchanges.
- Never advance or withdraw an intravascular device against resistance until the cause of the resistance is determined by fluoroscopy. Movement of the microcatheter or guidewire against resistance could dislodge a clot, perforate a vessel wall, or damage microcatheter and guidewire. In severe cases, tip separation of the microcatheter or guidewire may occur.
- Contents supplied STERILE using an ethylene oxide (EO) process. Do not use if sterile barrier is damaged. If damage is found, call your Stryker Neurovascular representative.
- For single use only. Do not reuse, reprocess or resterilize. Reuse, reprocessing or resterilization may compromise the structural integrity of the device and/or lead to device failure which, in turn, may result in patient injury, illness or death. Reuse, reprocessing or resterilization may also create a risk of contamination of the device and/or cause patient infection or cross-infection, including, but not limited to, the transmission of infectious disease(s) from one patient to another. Contamination of the device may lead to injury, illness or death of the patient.
- After use, dispose of product and packaging in accordance with hospital, administrative and/or local government policy.
- These devices are intended for use only by physicians trained in performing endovascular procedures.
- Inspect product before use for any bends, kinks or damage. Do not use a microcatheter that has been damaged. Damaged microcatheters may rupture causing vessel trauma or tip detachment during steering maneuvers.
- The shaping mandrel is not intended for use inside the human body.
- Discontinue use of microcatheter for infusion if increased resistance is noted. Resistance indicates possible blockage. Remove and replace blocked microcatheter immediately. DO NOT attempt to clear blockage by over-pressurization. Doing so may cause the microcatheter to rupture, resulting in vascular damage or patient injury.
- Do not exceed 2,070 kPa (300 psi) infusion pressure. Excessive pressure could dislodge a clot, causing thromboemboli, or could result in a ruptured microcatheter or severed tip, causing vessel injury.

CAUTIONS / PRECAUTIONS

- To reduce the probability of coating damage in tortuous vasculature, use a guide catheter with a minimum internal diameter as specified in Table 1 above, and is recommended for use with Stryker Neurovascular hydrophilically coated microcatheters.
- To control the proper introduction, movement, positioning and removal of the microcatheter within the vascular system, users should employ standard clinical angiographic and fluoroscopic practices and techniques throughout the interventional procedure.
- Exercise care in handling of the microcatheter during a procedure to reduce the possibility of accidental breakage, bending or kinking.
- Use the product prior to the "Use By" date printed on the label.
- Limited testing indicates that Excelsior XT-17 Microcatheter is compatible with Dimethyl Sulfoxide (DMSO). The compatibility of Excelsior XT-17 Microcatheter with individual agents suspended in DMSO has not been established.
- Federal Law (USA) restricts this device to sale by or on the order of a physician.
- Wet dispenser coil or packaging tray and hydrophilically coated outer shaft of microcatheters prior to removal from packaging tray. Once the microcatheter has been wetted, do not allow to dry.
- The packaging mandrel is not intended for reuse. The packaging mandrel is not intended for use inside the human body.
- Check that all fittings are secure so that air is not introduced into guide catheter or microcatheter during continuous flush.
- In order to achieve optimal performance of Stryker Neurovascular Microcatheters and to maintain the lubricity of the Hydrolene® Coating surface, it is critical that a continuous flow of appropriate flush solution be maintained between the Stryker Neurovascular Microcatheter and guide catheter, and the microcatheter and any intraluminal device. In addition, flushing aids in preventing contrast crystal formation and/or clotting on both the intraluminal device and inside the guide catheter and/or the microcatheter lumen.
- Do not position microcatheter closer than 2.54 cm (1 in) from the steam source. Damage to the microcatheter may result.
- Excessive tightening of a hemostatic valve onto the microcatheter shaft may result in damage to the microcatheter. Removing the peel away introducer without a guidewire inserted in the microcatheter lumen might result in damage to the microcatheter shaft.
- To facilitate microcatheter handling, the proximal portion of the microcatheter does not have the hydrophilic surface. Greater resistance may be encountered when this section of the microcatheter is advanced into the RHV.

Excelsior® SL-10® Microcatheter

See package insert for complete indications, contraindications, warnings and instructions for use.

INTENDED USE / INDICATIONS FOR USE

Stryker Neurovascular Excelsior SL-10 Microcatheter is intended to assist in the delivery of diagnostic agents, such as contrast media, and therapeutic agents, such as occlusion coils, into the peripheral, coronary, and neurovasculature.

CONTRAINDICATIONS

None known.

POTENTIAL ADVERSE EVENTS

Potential adverse events associated with the use of microcatheters or with the endovascular procedures include, but are not limited to: access site complications, allergic reaction, aneurysm perforation, aneurysm rupture, death, embolism (air, foreign body, plaque, thrombus), hematoma, hemorrhage, infection, ischemia, neurological deficits, pseudoaneurysm, stroke, transient ischemic attack, vessel dissection, vessel occlusion, vessel perforation, vessel rupture, vessel thrombosis.

WARNINGS

- Contents supplied STERILE using an ethylene oxide (EO) process. Do not use if sterile barrier is damaged. If damage is found, call your Stryker Neurovascular representative.
- For single patient use only. Do not reuse, reprocess or resterilize. Reuse, reprocessing or resterilization may compromise the structural integrity of the device and/or lead to device failure which, in turn, may result in patient injury, illness or death. Reuse, reprocessing or resterilization may also create a risk of contamination of the device and/or cause patient infection or cross-infection, including, but not limited to, the transmission of infectious disease(s) from one patient to another. Contamination of the device may lead to injury, illness or death of the patient.
- After use, dispose of product and packaging in accordance with hospital, administrative and/or local government policy.
- **These devices are intended for use only by physicians trained in performing endovascular procedures.**
- Limited testing has been performed with solutions such as contrast media, saline and suspended embolic particles. The use of these catheters for delivery of solutions other than the types that have been tested for compatibility is not recommended. Do not use with glue or glue mixtures.
- The accessories are not intended for use inside the human body.
- Carefully inspect all devices prior to use. Verify shape, size and condition are suitable for the specific procedure.
- Exchange microcatheters frequently during lengthy procedures that require extensive guidewire manipulation or multiple guidewire exchanges.
- Never advance or withdraw an intravascular device against resistance until the cause of the resistance is determined by fluoroscopy. Movement of the microcatheter or guidewire against resistance could dislodge a clot, perforate a vessel wall, or damage microcatheter and guidewire. In severe cases, tip separation of the microcatheter or guidewire may occur.
- Inspect product before use for any bends, kinks or damage. Do not use a microcatheter that has been damaged. Damaged microcatheters may rupture causing vessel trauma or tip detachment during steering maneuvers.
- Shaping mandrel is not intended for use inside the human body.
- Discontinue use of microcatheter for infusion if increased resistance is noted. Resistance indicates possible blockage. Remove and replace blocked microcatheter immediately. DO NOT attempt to clear blockage by over-pressurization. Doing so may cause the microcatheter to rupture, resulting in vascular damage or patient injury.
- Do not exceed 2,070 kPa (300 psi) infusion pressure. Excessive pressure could dislodge a clot, causing thromboemboli, or could result in a ruptured microcatheter or severed tip, causing vessel injury.

CAUTIONS / PRECAUTIONS

- Federal Law (USA) restricts this device to sale by or on the order of a physician.
- To facilitate microcatheter handling, the proximal portion of the microcatheter does not have the hydrophilic surface. Greater resistance may be encountered when this section of the microcatheter is advanced into the RHV.
- Exercise care in handling of the microcatheter during a procedure to reduce the possibility of accidental breakage, bending or kinking.
- To reduce the probability of coating damage in tortuous vasculature, use a guide catheter with a minimum internal diameter that is ≥ 1.00 mm (0.038 in) and is recommended for use with Stryker Neurovascular hydrophilically coated microcatheters.
- To control the proper introduction, movement, positioning and removal of the microcatheter within the vascular system, users should employ standard clinical angiographic and fluoroscopic practices and techniques throughout the interventional procedure.
- Flush dispenser coil of hydrophilically coated microcatheters prior to removal from dispenser coil. Once the microcatheter has been wetted, do not allow to dry. Do not reinsert the microcatheter into dispenser coil.
- Do not position microcatheter closer than 2.54 cm (1 in) from the steam source. Damage to the microcatheter may result.
- Check that all fittings are secure so that air is not introduced into guide catheter or microcatheter during continuous flush.
- In order to achieve optimal performance of Stryker Neurovascular Microcatheters and to maintain the lubricity of the Hydrolene® Coating surface, it is critical that a continuous flow of appropriate flush solution be maintained between the Stryker Neurovascular Microcatheter and guide catheter, and the microcatheter and any intraluminal device. In addition, flushing aids in preventing contrast crystal formation and/or clotting on both the intraluminal device and inside the guide catheter and/or the microcatheter lumen.
- Excessive tightening of a hemostatic valve onto the microcatheter shaft may result in damage to the microcatheter.

Stryker Neurovascular
47900 Bayside Parkway
Fremont, CA 94538

strykerneurovascular.com

Date of Release: NOV/2017

EX_EN_US

Target® Detachable Coil

See package insert for complete indications, contraindications, warnings and instructions for use.

INTENDED USE / INDICATIONS FOR USE

Target Detachable Coils are intended to endovascularly obstruct or occlude blood flow in vascular abnormalities of the neurovascular and peripheral vessels.

Target Detachable Coils are indicated for endovascular embolization of:

- Intracranial aneurysms
- Other neurovascular abnormalities such as arteriovenous malformations and arteriovenous fistulae
- Arterial and venous embolizations in the peripheral vasculature

CONTRAINDICATIONS

None known.

POTENTIAL ADVERSE EVENTS

Potential complications include, but are not limited to: allergic reaction, aneurysm perforation and rupture, arrhythmia, death, edema, embolus, headache, hemorrhage, infection, ischemia, neurological/intracranial sequelae, post-embolization syndrome (fever, increased white blood cell count, discomfort), TIA/stroke, vasospasm, vessel occlusion or closure, vessel perforation, dissection, trauma or damage, vessel rupture, vessel thrombosis. Other procedural complications including but not limited to: anesthetic and contrast media risks, hypotension, hypertension, access site complications.

WARNINGS

- Contents supplied STERILE using an ethylene oxide (EO) process. Do not use if sterile barrier is damaged. If damage is found, call your Stryker Neurovascular representative.
- For single use only. Do not reuse, reprocess or resterilize. Reuse, reprocessing or resterilization may compromise the structural integrity of the device and/or lead to device failure which, in turn, may result in patient injury, illness or death. Reuse, reprocessing or resterilization may also create a risk of contamination of the device and/or cause patient infection or cross-infection, including, but not limited to, the transmission of infectious disease(s) from one patient to another. Contamination of the device may lead to injury, illness or death of the patient.
- After use, dispose of product and packaging in accordance with hospital, administrative and/or local government policy.
- **This device should only be used by physicians who have received appropriate training in interventional neuroradiology or interventional radiology and preclinical training on the use of this device as established by Stryker Neurovascular.**
- Patients with hypersensitivity to 316LVM stainless steel may suffer an allergic reaction to this implant.
- MR temperature testing was not conducted in arteriovenous malformations or fistulae models.
- The safety and performance characteristics of the Target Detachable Coil System (Target Detachable Coils, InZone Detachment Systems, delivery systems and accessories) have not been demonstrated with other manufacturer's devices (whether coils, coil delivery devices, coil detachment systems, catheters, guidewires, and/or other accessories). Due to the potential incompatibility of non Stryker Neurovascular devices with the Target Detachable Coil System, the use of other manufacturer's device(s) with the Target Detachable Coil System is not recommended.
- To reduce risk of coil migration, the diameter of the first and second coil should never be less than the width of the ostium.
- In order to achieve optimal performance of the Target Detachable Coil System and to reduce the risk of thromboembolic complications, it is critical that a continuous infusion of appropriate flush solution be maintained between a) the femoral sheath and guiding catheter, b) the 2-tip microcatheter and guiding catheter, and c) the 2-tip microcatheter and Stryker Neurovascular guidewire and delivery wire. Continuous flush also reduces the potential for thrombus formation on, and crystallization of infusate around, the detachment zone of the Target Detachable Coil.
- Do not use the product after the "Use By" date specified on the package.
- Reuse of the packaging hoop or use with any coil other than the original coil may result in contamination of, or damage to, the coil.

Damaged delivery wires may cause detachment failures, vessel injury or unpredictable distal tip response during coil deployment. If a delivery wire is damaged at any point during the procedure, do not attempt to straighten or otherwise repair it. Do not proceed with deployment or detachment. Remove the entire coil and replace with undamaged product.

- Utilization of damaged coils may affect coil delivery to, and stability inside, the vessel or aneurysm, possibly resulting in coil migration and/or stretching.
- The fluoro-saver marker is designed for use with a Rotating Hemostatic Valve (RHV). If used without an RHV, the distal end of the coil may be beyond the alignment marker when the fluoro-saver marker reaches the microcatheter hub.
- If the fluoro-saver marker is not visible, do not advance the coil without fluoroscopy.
- Do not rotate delivery wire during or after delivery of the coil. Rotating the Target Detachable Coil delivery wire may result in a stretched coil or premature detachment of the coil from the delivery wire, which could result in coil migration.
- Verify there is no coil loop protrusion into the parent vessel after coil placement and prior to coil detachment. Coil loop protrusion after coil placement may result in thromboembolic events if the coil is detached.
- Verify there is no movement of the coil after coil placement and prior to coil detachment. Movement of the coil after coil placement may indicate that the coil could migrate once it is detached.
- Failure to properly close the RHV compression fitting over the delivery wire before attaching the InZone® Detachment System could result in coil movement, aneurysm rupture or vessel perforation.
- Verify repeatedly that the distal shaft of the catheter is not under stress before detaching the Target Detachable Coil. Axial compression or tension forces could be stored in the 2-tip microcatheter causing the tip to move during coil delivery. Microcatheter tip movement could cause the aneurysm or vessel to rupture.
- Advancing the delivery wire beyond the microcatheter tip once the coil has been detached involves risk of aneurysm or vessel perforation.
- The long term effect of this product on extravascular tissues has not been established so care should be taken to retain this device in the intravascular space.

CAUTIONS / PRECAUTIONS

- Federal Law (USA) restricts this device to sale by or on the order of a physician.
- Besides the number of InZone Detachment System units needed to complete the case, there must be an extra InZone Detachment System unit as back up.
- Removing the delivery wire without grasping the introducer sheath and delivery wire together may result in the detachable coil sliding out of the introducer sheath.
- Failure to remove the introducer sheath after inserting the delivery wire into the RHV of the microcatheter will interrupt normal infusion of flush solution and allow back flow of blood into the microcatheter.
- Some low level overhead light near or adjacent to the patient is required to visualize the fluoro-saver marker; monitor light alone will not allow sufficient visualization of the fluoro-saver marker.
- Advance and retract the Target Detachable Coil carefully and smoothly without excessive force. If unusual friction is noticed, slowly withdraw the Target Detachable Coil and examine for damage. If damage is present, remove and use a new Target Detachable Coil. If friction or resistance is still noted, carefully remove the Target Detachable Coil and microcatheter and examine the microcatheter for damage.
- If it is necessary to reposition the Target Detachable Coil, verify under fluoroscopy that the coil moves with a one-to-one motion. If the coil does not move with a one-to-one motion or movement is difficult, the coil may have stretched and could possibly migrate or break. Gently remove both the coil and microcatheter and replace with new devices.
- Increased detachment times may occur when:
  - Other embolic agents are present.
  - Delivery wire and microcatheter markers are not properly aligned.
  - Thrombus is present on the coil detachment zone.
- Do not use detachment systems other than the InZone Detachment System.

Stryker Neurovascular
47900 Bayside Parkway
Fremont, CA 94538

strykerneurovascular.com

Date of Release: NOV/2017

EX_EN_US

MicroVention®
TERUMO

Access Product Solutions

Sofia® Plus

Distal Access Catheter

Soft Torqueable Catheter Optimized for Intracranial Access with Excellent Navigation and Trackability

Neurovascular Malformation Solutions

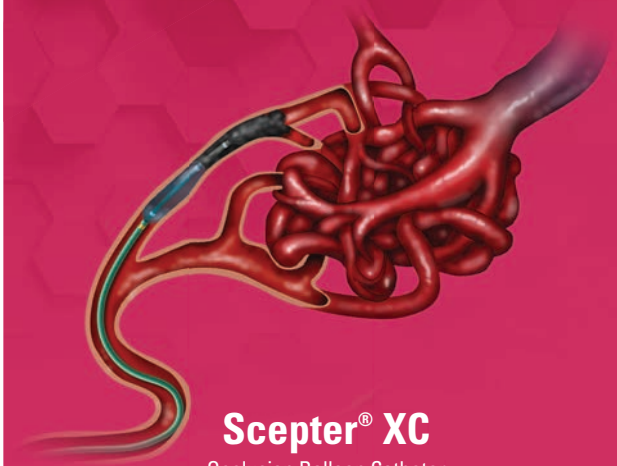

Scepter® XC

Occlusion Balloon Catheter

Clinical Applications in Four Key Areas: Balloon Remodeling, Stent Delivery, Liquid Embolic Injection, and Balloon-Test Occlusion

INDICATIONS FOR USE:

The SOFIA® Catheter is indicated for general intravascular use, including the neuro and peripheral vasculature. The SOFIA® Catheter can be used to facilitate introduction of diagnostic or therapeutic agents. The SOFIA® Catheter is not intended for use in coronary arteries.

The Scepter C® and Scepter XC® Occlusion Balloon Catheters are intended for use in the peripheral and neuro vasculature where temporary occlusion is desired. The balloon catheters provide temporary vascular occlusion which is useful in selectively stopping or controlling blood flow. The balloon catheters also offer balloon assisted embolization of intracranial aneurysms. For use in the peripheral vasculature for the infusion of diagnostic agents, such as contrast media, and therapeutic agents such as embolization materials. For neurovascular use for the infusion of diagnostic agents such as contrast media, and therapeutic agents, such as embolization materials, that have been approved or cleared for use in the neurovasculature and are compatible with the inner diameter of the Scepter C/XC Balloon Catheter.

The LVIS® Device is intended for use with bare platinum embolic coils for the treatment of unruptured, wide neck (neck ≥ 4 mm or dome to neck ratio < 2), intracranial, saccular aneurysms arising from a parent vessel with a diameter ≥ 2.5 mm and ≤ 4.5 mm.

The Headway® Duo Microcatheter is intended for general intravascular use, including the peripheral and coronary vasculature for the infusion of diagnostic agents, such as contrast media, and therapeutic agents, such as embolization materials. The Headway® Duo Microcatheter is intended for neurovascular use, for the infusion of diagnostic agents, such as contrast media, and therapeutic agents that have been cleared or approved for use in the neurovasculature and are compatible with the inner diameter of the Headway® Duo Microcatheter.

stryker

Bending expectations of conformability and stability.

Enhanced conformability – The hybrid cell structure is designed to enhance stent opening and conformability in bifurcations and tight curves.

Ease of use – All sizes of the Neuroform Atlas Stent are deliverable through Excelsior® SL-10® and Excelsior XT-17™ Microcatheters.

Higher deployment accuracy – The Neuroform Atlas Stent is designed to have very low foreshortening, which enables very high deployment accuracy.

Neuroform Atlas™
STENT SYSTEM

The Neuroform Atlas Stent System is authorized under a Humanitarian Device Exemption (HDE). IRB approval is required prior to use.

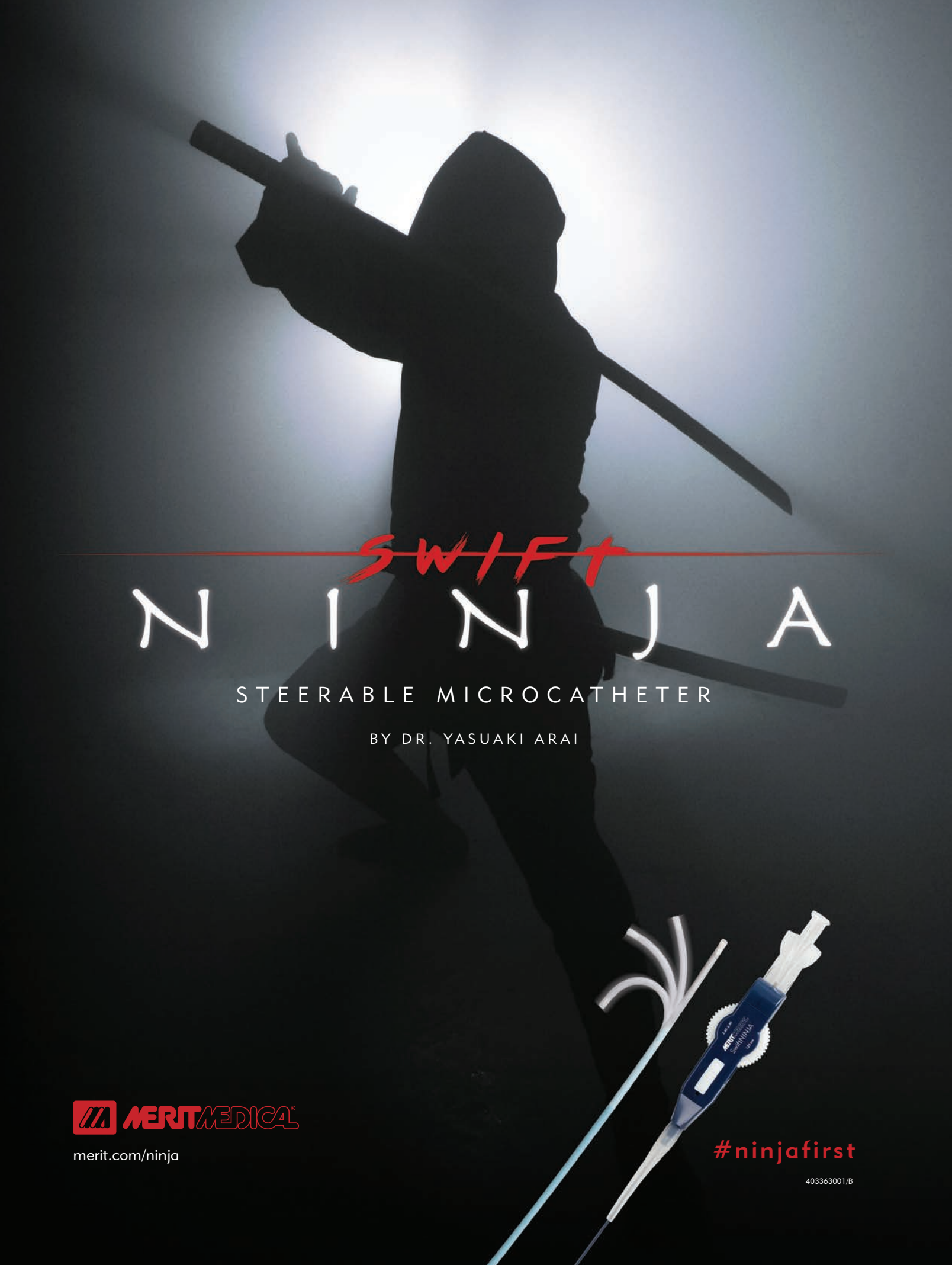
SWIFT
NINJA
STEERABLE MICROCATHETER
BY DR. YASUAKI ARAI
MERITMEDICAL®
merit.com/ninja
#ninjafirst
403363001/B

AJNR

AMERICAN JOURNAL OF NEURORADIOLOGY

Publication Preview at www.ajnr.org features articles released in advance of print. Visit www.ajnrblog.org to comment on AJNR content and chat with colleagues and AJNR's News Digest at http://ajnrdigest.org to read the stories behind the latest research in neuroimaging.

DECEMBER 2017 • VOLUME 38 • NUMBER 12 • WWW.AJNR.ORG

AJNR

AMERICAN JOURNAL OF NEURORADIOLOGY

DECEMBER 2017
VOLUME 38
NUMBER 12
WWW.AJNR.ORG

Publication Preview at www.ajnr.org features articles released in advance of print. Visit www.ajnrblog.org to comment on AJNR content and chat with colleagues and AJNR's News Digest at http://ajnrdigest.org to read the stories behind the latest research in neuroimaging.

AJNR (Am J Neuroradiol ISSN 0195–6108) is a journal published monthly, owned and published by the American Society of Neuroradiology (ASNR), 800 Enterprise Drive, Suite 205, Oak Brook, IL 60523. Annual dues for the ASNR include $170.00 for journal subscription. The journal is printed by Cadmus Journal Services, 5457 Twin Knolls Road, Suite 200, Columbia, MD 21045; Periodicals postage paid at Oak Brook, IL and additional mailing offices. Printed in the U.S.A. POSTMASTER: Please send address changes to American Journal of Neuroradiology, P.O. Box 3000, Denville, NJ 07834, U.S.A. Subscription rates: nonmember $400 ($470 foreign) print and online, $320 online only; institutions $460 ($530 foreign) print and basic online, $915 ($980 foreign) print and extended online, $380 online only (basic), extended online $825; single copies are $35 each ($40 foreign). Indexed by PubMed/Medline, BIOSIS Previews, Current Contents (Clinical Medicine and Life Sciences), EMBASE, Google Scholar, HighWire Press, Q-Sensei, RefSeek, Science Citation Index, and SCI Expanded.

ONLINE FEATURES

LETTERS

BOOK REVIEWS *R.M. Quencer, Section Editor*

Please visit www.ajnrblog.org to read and comment on Book Reviews.

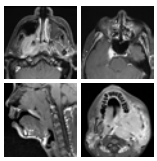

Top row: A 64-year-old man with EBV(+) undifferentiated nonkeratinizing carcinoma. Axial T1 C+ fat-saturated images demonstrate lateral extension to the right masticator space lateral pterygoid muscle. In the 7th edition of the *AJCC Cancer Staging Manual*, this is T4 disease; however, in the 8th edition, this is only T2 disease. Note the superior extension to the right cavernous sinus (top right), which is T4 disease in both seventh and eighth editions. Bottom row: A 15-year-old boy with EBV(+) undifferentiated nonkeratinizing carcinoma. Sagittal T1 (left) shows the mass filling the nasopharynx while the T1 C+ with fat saturation (right) shows lateral extension of the mass into the left parotid gland. In the 8th edition, involvement of the parotid gland or extension of tumor beyond the lateral surface of the lateral pterygoid muscle determines T4 status.

Title: Pagoda and Oriental Garden, Norfolk, Virginia. This image was shot with an infrared-converted Nikon D40 camera. Conventional digital cameras possess a filter designed to block the infrared spectrum of light while passing through visible light. Infrared-converted cameras have this filter either removed or replaced with one that only allows a small portion of the infrared spectrum.

Efstathios Spinos, MD, Peripheral & Neurovascular Interventional Radiology, Johnston-Willis Medical Center, Richmond, Virginia

Bring Back the Joy in Neuroradiology

D.M. Yousem, K.P. Yousem, and K.A. Skarupski

In School of Medicine leadership forums, affinity group meetings of the Association of American Medical Colleges, and at the American Medical Association, everyone is talking about "resilience," "burnout," and "attrition."[1-4] Medical practitioners struggle with the demands of serving their patients, finding meaning in their work in the face of increased emphasis on revenue generation and regulatory demands, and maintaining some semblance of a home life. In our field of neuroradiology, recognized by the readership of the *American Journal of Neuroradiology* as the best profession ever, we too have experienced anxiety when we hear about the future changes in health care that dampen our positive attitudes.

However, if we focus only on how to build resilience, prevent burnout, handle disappointments, or prevent attrition, we have already lost the battle. What we want instead is to be delighted to be at work! Fun! Pleasure! In this short editorial, we hope to provide you with some tips on returning joy to neuroradiology.

Mission Centric

Believing in the principles of the mission of your work is the first step to joyfulness in that work. If you believe in the vision and values of your practice and the worthiness of committing energy to its success, you will have a sense of purpose that enables a sense of satisfaction.[1,5] We advocate strongly for a thoughtful intermittent full staff review of the mission statement of the practice and a commitment to dedicating necessary resources to achieving the goals in that statement. When you believe in your work, you are happy performing it.[2,5]

Empowerment

Physicians are often, by virtue of their profession, considered leaders in their community. Part of enhancing job satisfaction resides in finding the individual niches in which all members of the team are empowered and eager to lead, grow, and excel.[6] Centralization of power under 1 Director/CEO/President/Chairman with autocratic governance should be weighed against providing colleagues responsibility and encouragement to determine that part of the practice where they have jurisdiction/sovereignty/growth to be creative.[2] That may mean considering assigning directors of spine imaging, brain imaging, head and neck imaging, fellowship training, residency training, medical student training, outpatient clinics, hospital services, and so forth, within neuroradiology. When people do what they love, their work excels, and data show that physicians spending at least 20% of their professional effort doing the work they find most meaningful are at much lower risk of burnout.[3] Give people an opportunity to shine and then shine the spotlight on their good work, which leads to. . .

http://dx.doi.org/10.3174/ajnr.A5392

Gratitude

People want to be appreciated. One of the best ways to foster a happy workplace is to have an attitude of gratitude, in which finding someone doing something right is the norm.[7] Having people feel comfortable complimenting each other in an open fashion takes practice to sound sincere and not forced. Consider "Thankful Thursdays," when people are encouraged to acknowledge the exceptionally positive interactions in their work life in a public way. Build an atmosphere of beneficence.

Mindfulness

While we all must be planful about addressing the challenges of the future, mindfulness training brings one back to present conditions. When mindful, one focuses awareness on the present moment, channeling the inner harmony of body and mind, yet being available to others. Being able to engage fully in the moment (and put away our social media/electronic distracting devices) allows one to set the mind at peace and connect fully with patients, colleagues, and loved ones.[8-10] Setting aside several minutes each day for refocusing, be it meditation or introspection or self-reflective exercises, has long-term joy-inspiring consequences.

Play

Nothing has inspired greater joy in our workplace than the playfulness we bring to our jobs in neuroradiology. Whether it is dressing up in kooky outfits for Halloween or showering faculty with candy/games/shaving cream/jokes, cultivating an atmosphere of light-heartedness is good. Having leadership dress up in self-deprecating costumes for Halloween or Santa outfits for the winter holidays are examples of transforming the dreariness of the mundane into a super-special delightful day. The suspense about how the boss will be dressed this year in September and October lends a cheerfulness to the workplace that far exceeds the cost of an Ironman costume. Daily 15- to 20-minute competitions for a month devoted to Sudoku/finding the missing words/puzzlers/scavenger hunts also can lighten the mood during the heavy-volume periods at work. A 5-minute dance party elevates the mood and energizes an often-sluggish midafternoon (the introverts here get to pick the music, clap on the side, and take the embarrassing videos to post to social media). Share joy.

Decorations

Why do people ride around sundry neighborhoods during the winter/Christmas festival times? Why have some Jewish families adopted Hanukkah bushes? Why are the Kwanza lights and Diwali fireworks so popular? For whatever reason, seeing decorations and holiday cheer (on the walls of your office/workplace/building and so forth) in a tasteful and diversity-respectful manner brings joy to the workplace.[11] After an initial investment, being able to pull out wall decorations for the New Year, Valentine's Day, St Patrick's Day, Springtime, Memorial Day, Independence Day, Thanksgiving, Halloween, Winterfest, and Elvis Presley commemorations has a dramatic impact on those coming to

work. You create a party atmosphere based on the environment. Working here is fun.

Celebrations

Festivities that acknowledge group and individual successes or milestones help to create a positive mental outlook at work. Have you installed that new magnet in the department? Party! Junior faculty member got her first RO1? Celebrate at work! Instead of going to the corner bar for champagne, let the workplace become associated with the successes and the happy place where those successes are recognized. Combine the partying with acknowledgment of the diversity within your work group by selecting ethnic food for the revelry with nation-specific music selections, and you can multiply the good will that such celebrations inspire. Take the opportunity to acknowledge success and have the work environment be the place for celebrations.[4,12]

Group Exercise and Nutrition

In healthy people, being joyful is easier. Exercise, movement releases, and healthy meals and snacks at work will inspire better spirit and more energy.[13] In 1 such initiative, we spent 20 minutes a day doing staff-led dance instruction with the goal of being the best dancing division at the winter holiday departmental party. Doing line dances led by experienced talented members of the team not only showed what people are capable of outside of work but also allowed moving in a fun fashion that built enthusiasm throughout the day…before and after the lessons. Some team members even felt an improved self-image because they were finally, with practice, able to move more rhythmically on the dance floor (yes, we mean you Dave Yousem!). Make sure you are offering heart-healthy whole foods and plant-based treats at these breaks.

These are just some ideas that can be implemented at a low cost of time, energy, and finances yet yield great gains for building happiness at work. Each of these categories of interventions can be discussed more fully with the leadership team, but often the initiatives are best implemented from rank and file ideas that are part of an explicit program to bring the joy back to the workplace.

Disclosures: David M. Yousem—*UNRELATED: Expert Testimony*: self, medicolegal expert witness; *Payment for Lectures Including Service on Speakers Bureaus*: American College of Radiology Education Center; *Royalties:* Elsevier for 5 books.

REFERENCES

1. Shanafelt TD, Noseworthy JH. **Executive leadership and physician well-being: nine organizational strategies to promote engagement and reduce burnout.** *Mayo Clin Proc* 2017;92:129–46 CrossRef Medline
2. Shanafelt TD, Gorringe G, Menaker R, et al. **Impact of organizational leadership on physician burnout and satisfaction.** *Mayo Clin Proc* 2015;90:432–40 CrossRef Medline
3. Shanafelt TD, West CP, Sloan JA, et al. **Career fit and burnout among academic faculty.** *Arch Intern Med* 2009;169:990–95 CrossRef Medline
4. Sklar DP. **Fostering student, resident, and faculty wellness to produce healthy doctors and a healthy population.** *Acad Med* 2016;9:1185–88 CrossRef Medline
5. Michel JB, Sangha DM, Erwin JP 3rd. **Burnout among cardiologists.** *Am J Cardiol* 2017;119:938–40 CrossRef Medline
6. Swensen S, Kabcenell A, Shanafelt T. **Physician-organization collaboration reduces physician burnout and promotes engagement: the Mayo Clinic experience.** *J Healthc Manag* 2016;61:105–27 Medline
7. Kelly JD 4th. **Your best life: breaking the cycle: the power of gratitude.** *Orthop Relat Res* 2016;474:2594–97 CrossRef Medline
8. Beach MC, Roter D, Korthuis PT, et al. **A multicenter study of physician mindfulness and health care quality.** *Ann Fam Med* 2013;11:421–28 CrossRef Medline
9. Goyal M, Singh S, Sibinga EM, et al. **Meditation programs for psychological stress and well-being: a systematic review and meta-analysis.** *JAMA Intern Med* 2014;174:357–68 CrossRef Medline
10. Gotink RA, Chu P, Busschbach JJ, et al. **Standardised mindfulness-based interventions in healthcare: an overview of systematic reviews and meta-analyses of RCTs.** *PLoS One* 2015;10:e0124344 CrossRef Medline
11. Smith L. 9 Things Science Says Your Home Needs If You Want to Be Happy. Good Housekeeping. November 7, 2016. http://www.goodhousekeeping.com/home/decorating-ideas/g3164/scientific-reasons-household-items-make-you-happy/. Accessed July 7, 2017
12. Hu YY, Fix ML, Hevelone ND, et al. **Physicians' needs in coping with emotional stressors: the case for peer support.** *Arch Surg* 2012;147:212–17 CrossRef Medline
13. McClafferty H, Brown OW. **Physician health and wellness.** *Pediatrics* 2014;134:830–35 CrossRef Medline

Pacemakers in MRI for the Neuroradiologist

A.W. Korutz, A. Obajuluwa, M.S. Lester, E.N. McComb, T.A. Hijaz, J.D. Collins, S. Dandamudi, B.P. Knight, and A.J. Nemeth

ABSTRACT

SUMMARY: Cardiac implantable electronic devices are frequently encountered in clinical practice in patients being screened for MR imaging examinations. Traditionally, the presence of these devices has been considered a contraindication to undergoing MR imaging. Growing evidence suggests that most of these patients can safely undergo an MR imaging examination if certain conditions are met. This document will review the relevant cardiac implantable electronic devices encountered in practice today, the background physics/technical factors related to scanning these devices, the multidisciplinary screening protocol used at our institution for scanning patients with implantable cardiac devices, and our experience in safely performing these examinations since 2010.

ABBREVIATIONS: CIED = cardiac implantable electronic device; EP = electrophysiologist; ICD = implantable cardioverter-defibrillator; RF = radiofrequency; SAR = specific absorption rate

MR imaging examinations are being performed with increasing frequency worldwide, with nearly 35 million scans performed annually in the United States alone.[1] More than 1.8 million individuals in the United States have a cardiac pacemaker or implantable cardioverter-defibrillator (ICD), both of which fall under the larger umbrella term of cardiac implantable electronic devices (CIEDs). Traditionally, these devices have precluded patients from undergoing MR imaging examinations.[2-5] More recently, "MR imaging–conditional" CIEDs have been developed, which contain components that can be safely placed in an MR imaging scanner.[6] Despite the development of these devices, many patients with a CIED that is not MR imaging–conditional remain and would benefit clinically from an MR imaging examination.

To date, a growing body of research suggests that CIEDs that were traditionally considered MR imaging incompatible can be scanned safely when certain precautions are taken.[2,7-10] Despite these published reports, many institutions still do not have protocols in place to scan patients with CIEDs.

In this article, we will begin by providing an overview of the types of CIEDs encountered in practice today as well as some of the relevant physics and technical factors related to scanning these devices. Then we will discuss the multidisciplinary protocol used at our institution for scanning patients with CIEDs, including initial cardiac evaluation/cardiac clearance, cardiac monitoring during scanning, and the relevant postscan evaluation and clinical follow-up. Finally, we will outline the number and types of procedures performed at our institution since 2010 and any complications encountered during this period.

Cardiac Implantable Electronic Devices

A pacemaker is an implantable device that senses cardiac activity and delivers the required electrical stimuli to the heart to regulate slow heart rates or erratic cardiac rhythms. An ICD is a device that contains both pacemaker and defibrillator components, the latter of which can provide a high-energy shock for treating life-threatening arrhythmias, most commonly ventricular tachyarrhythmias. These devices are currently classified under the more general term "cardiac implantable electronic devices," and they consist of a pulse generator and leads that extend into ≥1 of the chambers of the heart. The pulse generator contains the relevant circuitry for the device and the device battery. The CIED leads are bidirectional wires that function to sense intrinsic cardiac activity and deliver electrical impulses to the heart.[11-13]

As described above, a CIED may have ≥1 cardiac lead. If only a single lead is present, it is usually implanted into either the right ventricle or right atrium. When a 2-lead CIED is present, the leads are typically implanted into both the right atrium and right ventricle, with the latter lead performing both pacemaker and defibrillator functions. Biventricular pacing, also called "cardiac resynchronization therapy," uses a third lead, which is usually implanted in a ventricular branch of the coronary sinus to capture

From the Departments of Radiology (A.W.K., A.O., M.S.L., E.N.M., T.A.H., J.D.C., A.J.N.), Medicine, Division of Cardiology (S.D., B.P.K.), and Neurology (A.J.N.), Northwestern University Feinberg School of Medicine, Chicago, Illinois.

Please address correspondence to Alexander W. Korutz, MD, 676 N St Clair St, Suite 800, Chicago, IL 60611; e-mail: Alexander.Korutz@nm.org

Indicates open access to non-subscribers at www.ajnr.org

http://dx.doi.org/10.3174/ajnr.A5314

Table 1: Pacing modes

Chamber Paced	Chamber Sensed	Pacer Response to Sensed Beat
V = ventricle	V = ventricle	I = inhibited
A = atrium	A = atrium	T = triggered
D = both (dual)	D = both (dual)	D = inhibited or triggered depending on chamber (dual)
O = none	O = none	O = none

the left ventricular epicardium at the same time as right ventricular activation to improve synchronization between right and left ventricular contractions.[11-13] Regardless of whether the patient has a pacemaker device or a combined pacemaker/defibrillator and irrespective of the number of device leads, a CIED is programmed to operate in a specific pacing mode chosen to provide the greatest benefit to the patient.

In the simplest terms, the pacing mode is denoted with a 3-letter code (eg, DDD or VOO), with both the letter position and letter type describing specific pacemaker functions. Fourth and fifth letters can be added to this code; however, discussion of these is beyond the scope of this article. The first letter describes which chamber is being paced, the second describes which chamber is being sensed, and the third describes how the pacemaker responds when a beat is sensed (Table 1). While the first 2 letters in this code are self-explanatory, the third letter requires a brief discussion. During "inhibition" mode, a pacemaker will inhibit ventricular pacing when a heartbeat is sensed. "Trigger" mode indicates that the device will trigger a ventricular pacing stimulus every time an atrial beat is sensed. Finally, "dual" mode indicates a more complex situation in which the device responds to a sensed beat in the atrium or ventricle by inhibiting pacing output to that chamber and simultaneously delivering a stimulus to the ventricle after the atrial beat is sensed. This scenario only arises if there is no inhibition of the pacemaker by an intrinsic beat originating in the ventricle. For example, when a patient's device is programmed in DDD mode, the device may operate in 4 possible ways: pace both chambers, sense only in both chambers without pacing, pace the atrium with natural conduction to the ventricle, or pace the ventricle following an intrinsic atrial beat. Finally, asynchronous (also known as "fixed") pacing can be used as a more general term to describe any scenario in which cardiac pacing is not inhibited by intrinsic cardiac activity.[13] For instance, in VOO pacing, the ventricle is paced at a fixed rate with no device sensing, so there is no capacity to inhibit/trigger based on sensed activity.

Current Experience of CIEDs with MR Imaging

Traditional CIEDs are currently referred to as non-MR imaging–conditional devices, given the advent of newer, MR imaging–conditional devices. The presence of a non-MR imaging–conditional CIED was conventionally thought to be a contraindication for undergoing MR imaging.[14-16] As will be discussed shortly, this is no longer the case. Multiple risks have been associated with these nonconditional devices, primarily related to interactions between the ferromagnetic components of these devices and the static magnetic field, gradient magnetic fields, and the transmitted radiofrequency (RF) field.[17]

The static magnetic field can affect a CIED in multiple ways. For instance, the field can reset/reprogram the device or deplete its battery.[4,18-20] It can also affect the magnetically activated reed switch within the device, spontaneously switching the CIED into an asynchronous pacing mode.[21,22] The potential for some of these scenarios to occur can be limited by switching the device into asynchronous mode before placing the patient in the scanner and switching off the ability of an ICD to provide a therapeutic shock.[4,21,23] The static magnetic field can also interact with charged ions in moving blood, producing small local voltages that, when superimposed on the patient's electrocardiogram, can falsely mimic arrhythmias or other electrocardiogram changes. In some instances, this phenomenon may inhibit pacemaker function or falsely simulate the presence of a cardiac arrhythmia, which requires administration of a shock.[4,21] Last, the static field can cause a mechanical torque on the device, which can move the pulse generator within the chest wall or dislodge the device leads within the myocardium.[21,24,25]

Complications associated with the rapidly alternating gradient magnetic fields mainly involve the induction of currents within the device leads themselves. Similar to local currents produced by moving blood within the static field, currents within the cardiac leads can also mimic cardiac electrical activity, thereby inhibiting the need for pacing, pacing the heart at inappropriately high rates, or administering electronic shocks, depending on the scenario in which the above occurs.[21,24,25] Alternatively, induced current at the lead tip could surpass the activation threshold needed to stimulate cardiac myocytes, thereby having the potential to generate life-threatening arrhythmias such as ventricular fibrillation and ventricular tachycardia.[21,24]

Finally, the RF pulse used during an MR imaging examination can also induce currents within device leads. Due to the high frequency of these RF pulses and the high conductivity of the device leads relative to the adjacent soft tissues, energy can be lost in the form of heat or so-called ohmic (also known as "resistive") heating. This heating is concentrated at the tip of a device lead or at a point where a lead is fractured. Resultant focal heating may cause adjacent tissue damage and, subsequently, the need for a higher pacing threshold or loss of pacing capture entirely.[4,7,15,24,26,27]

Despite these hypothetic risks when scanning a patient with a non-MR imaging–conditional CIED, recent statements from the American Heart Association and the European Society of Cardiology have suggested that MR imaging may be performed at a 1.5T field strength when using specific protocols for programming and monitoring.[4,5] These statements are based on results from a growing number of trials that have investigated this issue, focusing specifically on the potential risks and overall safety of MR imaging in patients with non-MR imaging–conditional devices.[2,7-10] For instance, Martin et al[9] examined 54 non-pacer-dependent patients with non-MR imaging–conditional pacemaker devices who underwent 62 MR imaging examinations that included both thoracic and nonthoracic studies. This study found a change in the pacing threshold in 37% of device leads, of which most threshold changes were judged to be unimportant and no threshold changes were noted to have any clinical impact.[9]

In 2011, Nazarian et al[2] reported their prospective experience following 438 patients with pacemakers and ICDs who underwent 555 MR imaging examinations. This study included thoracic ex-

aminations but excluded pacer-dependent patients with ICDs. The authors reported power-on resets in 3 of 438 patients, none of which were associated with long-term device dysfunction. With regard to lead parameters such as sensing, impedance, and capture thresholds, no device in this study required device revision or reprogramming due to any parameter changes. However, right ventricular lead–sensed amplitude was lower and right ventricular capture thresholds tended to be higher both immediately following MR imaging examinations and at long-term device follow-up. These lead parameter changes were most strongly associated with thoracic MR imaging examinations, though they were not clinically important.[2] Dandamudi et al[10] evaluated 58 patients with non-MR imaging–conditional CIEDs who underwent only cardiac and thoracic spine MR imaging examinations. No clinically important parameter changes, arrhythmias, device mode changes/electrical resets, or battery depletions were found following the MR imaging examinations in this study.

More recently, the largest study to date, The MagnaSafe Registry (http://magnasafe.org/), examined 1500 nonthoracic MR imaging scans in patients with non-MR imaging–conditional CIEDs.[8] In this study, device interrogation following the MR imaging examinations assessed parameter changes such as a decrease in battery voltage, an increase in pacing threshold, pacing or shock lead impedance change, and a decrease in P- and R-wave amplitudes. This study found that no patient who was appropriately screened and reprogrammed following the procedure had device or lead failure. The authors also noted that changes in device settings were uncommon and not clinically important. Of note, 1 case of the 1500 (in the subgroup of 500 patients with ICDs) did require device replacement due to device failure from inappropriate programming during the MR imaging examination. Additionally, there were 6 cases of partial electrical reset, which was corrected following the MR imaging examination during standard device reprogramming. Finally, 6 patients developed atrial fibrillation/flutter, though 5 of these patients had a history of paroxysmal atrial fibrillation and the sixth patient had resolution by 48 hours.

To date, an overwhelming body of evidence suggests that patients with intact CIEDs can be scanned safely when using proper MR imaging protocols and if the risk to the patient is well-managed. A few absolute contraindications remain for performing MR imaging in a patient with a CIED. The first is a device that was implanted $<$6 weeks before the MR imaging examination. These leads have not fully healed and are susceptible to dislodgement.[2] The second is the presence of an abandoned or fractured lead. When the lead is not connected to a CIED generator, then, there is no heat sink in place for the lead. The third is the presence of surgically placed permanent epicardial pacing leads. The lead design for these devices is different from that in the more common transvenous leads, and there are insufficient data to recommend MR imaging in these patients at this time.[4]

A few additional pacing devices can be encountered in clinical practice, the 2 most common of which are temporary epicardial pacing devices and temporary intracardiac pacing devices. Both devices comprise an external pulse generator paired with $\geq$1 cardiac lead. In all instances, the patient should not undergo an MR imaging examination when the external pulse generator is present, regardless of its type. External pulse generators for temporary pacing devices use less sophisticated designs, which make them more prone to electromagnetic interference. In addition, no studies of the safety of these devices in an MR imaging environment have been performed, to our knowledge. Retained (also known as "abandoned") temporary epicardial pacing leads are not believed to present a risk of injury during an MR imaging examination, given that these leads are relatively short and usually do not form large "antennalike" loops. Nevertheless, there is still a theoretic risk with these devices of cardiac excitation and thermal injury, though at our institution, this risk is not considered high enough to prevent scanning these patients. On the other hand, retained leads for temporary intracardiac (ie, transvenous) pacing devices are considered a contraindication for undergoing an MR imaging examination. These devices tend to have unfixed leads, which are more susceptible to movement, and longer leads, which are more prone to current induction.[4]

Given the traditional thinking that the presence of a non-MR imaging–conditional device was a contraindication for performing an MR imaging examination, there was a time when an unmet need existed for a CIED that could be safely placed in an MR imaging environment. In 2008, the first MR imaging–conditional device was released in the European market with subsequent release of a similar pacemaker in the United States in 2011.[24] Multiple design changes were used to produce CIEDs that were safe for an MR imaging environment. These include constructing the device from materials that are less magnetosensitive (ie, nickel, cobalt, or chromium) or entirely nonferromagnetic, using a solid-state Hall-effect sensor rather than the somewhat unpredictable reed switch, protecting/desensitizing the electronic circuits within the CIED from energy deposition during the MR imaging examination, modifying the construction of the device leads, and using MR imaging–specific programing algorithms (ie, a specific "MR imaging mode").[21,25]

For a CIED in a specific patient to be correctly labeled as MR imaging–conditional, the entire device, including the pulse generator, pulse generator software, and cardiac leads, must all be constructed from MR imaging–conditional components produced by the same manufacturer. In addition, each manufacturer requires that other specific conditions be met. These are related to magnet field strength (1.5T magnet only), time when the CIED was implanted ($>$6 weeks before the MR examination), body part to be scanned, specific absorption rate (SAR; maximum of 2 W/kg), and so forth.[21,24,25] Please see Table 2 for a list of currently approved MR imaging–conditional CIEDs.

Despite the wide availability of MR imaging–conditional CIEDs, non-MR imaging–conditional devices are still implanted in clinical practice today. In certain instances, non-MR imaging–conditional devices are implanted for cost reasons. Non-MR imaging–conditional generators also continue to be installed in patients who have non-MR imaging–conditional devices, in which the leads are intact and the device generator must be replaced due to battery depletion.

MR Imaging Physics and Technical Considerations Relevant to Pacemakers

When an object is placed in an MR imaging scanner, hydrogen atoms tend to align either with or against the static magnetic field,

Table 2: Currently approved MRI-conditional CIEDs

Device Manufacturer	Device Model	Device Type
Boston Scientific[a]	Accolade	Pacemaker
Boston Scientific	Essentio	Pacemaker
Boston Scientific	Emblem	Subcutaneous ICD
BIOTRONIK[b]	Entovis	Pacemaker
BIOTRONIK	Eluna	Pacemaker
BIOTRONIK	Edora	Pacemaker
BIOTRONIK	Iperia 7 DRT-T/VR-T	ICD
BIOTRONIK	Iperia 7 HF-T	CRT
Medtronic[c]	Advisa MRI	Pacemaker
Medtronic	Revo MRI	Pacemaker
Medtronic	Visia AF MRI	ICD
Medtronic	Evera MRI	ICD
Medtronic	Claria MRI	CRT
Medtronic	Amplia MRI	CRT
Medtronic	Compia MRI	CRT
St. Jude Medical[d]	Assurity MRI	Pacemaker

Note:—CRT indicates cardiac resynchronization therapy.
[a] Natick, Massachusetts.
[b] Lake Oswego, Oregon.
[c] Minneapolis, Minnesota.
[d] Minnetonka, Minnesota.

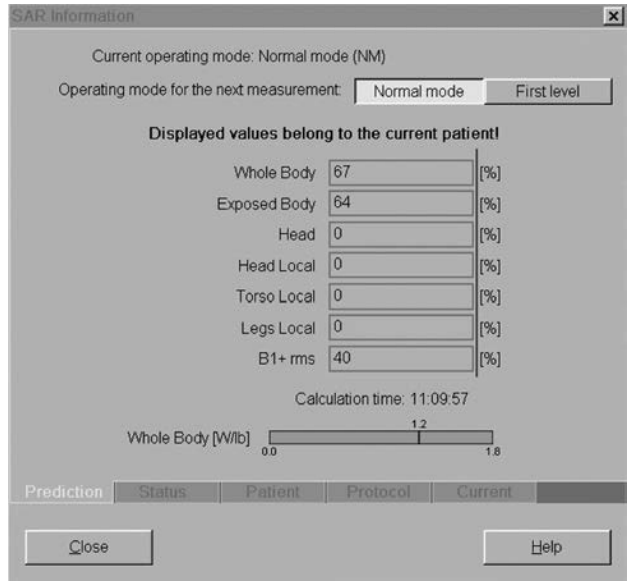

FIG 1. Normal versus first-level mode: normal level only for neuroradiology. SAR information panel at the scanner console for a sagittal STIR TSE acquisition of the lumbar spine. Any neurologic imaging study that can be run on a 1.5T magnet, including echo-planar imaging, can be performed in a patient with a CIED, as long as the examination is performed in normal operating mode. Image courtesy of Charles Fasanati.

B_0. A rotating radiofrequency pulse can then be applied that contains 2 orthogonally oriented components, the magnetic field (B-field or B_1) and the electric field (E-field). The positive component of the B-field tilts the hydrogen atoms into the transverse plane, where the atoms rotate and produce a signal detected in the receiver coil. As described previously, this RF pulse deposits energy in the tissue and results in tissue heating.[4,21,28,29] The term that has been traditionally used to describe the RF power that is absorbed per unit mass of an object is the "specific absorption rate." SAR is expressed in watts per kilogram and is related to the square of the main magnetic field, square of the flip angle, square of the patient radius, patient conductivity, and the RF duty cycle.[29] "Duty cycle" refers to the percentage of time that the RF pulse is "on" and can be shortened by lengthening the TR.

Because the SAR calculation relies on estimates of patient size and composition, each scanner manufacturer uses proprietary models for calculating this value. Therefore, SAR values calculated for a patient may vary among scanner vendors.[30] Thus, the term B_{1+RMS} has been proposed as a replacement for SAR. Briefly, B_{1+RMS} refers to the time-averaged RF magnetic field, which is generated by the RF coil. This term is independent of patient factors and is solely determined by MR imaging scanner parameters, such as flip angle, RF pulse duration, echo-train length, choice of a gradient-echo rather than a spin-echo sequence, and so forth.[30,31]

Per the Faraday law, a changing magnetic field will produce a voltage in an exposed electrical conductor. The resulting current depends on the speed with which the magnetic field changes (dB/dt), the conductivity of the object, and the cross-sectional area of the conducting loop. Therefore, both the transmitted RF magnetic field and the time-alternating gradient magnetic fields are capable of producing currents within conductors, albeit to different degrees.[17,32] The RF fields used in MR imaging are high-frequency pulses capable of producing high-frequency oscillating currents (64 MHz at 1.5T), which can deposit relatively large amounts of energy in tissue. On the other hand, the alternating gradient magnetic fields produce relatively low-frequency currents (ie, <1000 Hz), which deposit very low levels of energy in tissue.[17,28,29] Therefore, a CIED generator and leads could serve as an antenna with which to generate and concentrate a current, a current concentrated at the lead tip or any site of lead fracture, if present.[4,15,23,26,27,32,33]

The quantity of energy deposited in a patient with a CIED also depends, in part, on the patient's location within the magnet and the configuration of the generator and device leads within the patient. In general, the greatest RF energy is deposited when the generator and leads are positioned entirely within the RF coil isocenter.[7,9,26,32,34] In addition, the amount of energy deposited in the patient also increases as the length of the exposed device lead increases. The "exposed" lead refers to the length of wire that extends from the device generator to the insertion site in the myocardial tissue. A longer exposed lead creates a longer loop with which to interact with the RF field.[32,33] Last, pacemaker generators placed within the right chest wall have also been shown to lead to greater tissue heating, even at times when a smaller lead area is present. This has been attributed to nonuniform RF generated E-fields within the scanner bore.[32,34-37]

While the focused examinations performed in clinical practice (ie, MR imaging of the brain) produce a local SAR value in the region being scanned, SAR is typically averaged over the entire body, generating a single whole-body SAR value. When performing an MR imaging examination, the operator (ie, technologist) can choose between scanning in normal and first-level modes. In normal mode, the whole-body SAR is limited to 2 W/kg. In first-level mode, there is an allowed maximum SAR of 4 W/kg. The scanning mode is selected at the MR imaging scanner console (Fig 1). B_{1+RMS} values are also displayed in this region.

At our institution, all MR imaging in patients with pacemakers is performed at 1.5T, and the pacemaker must have been in place

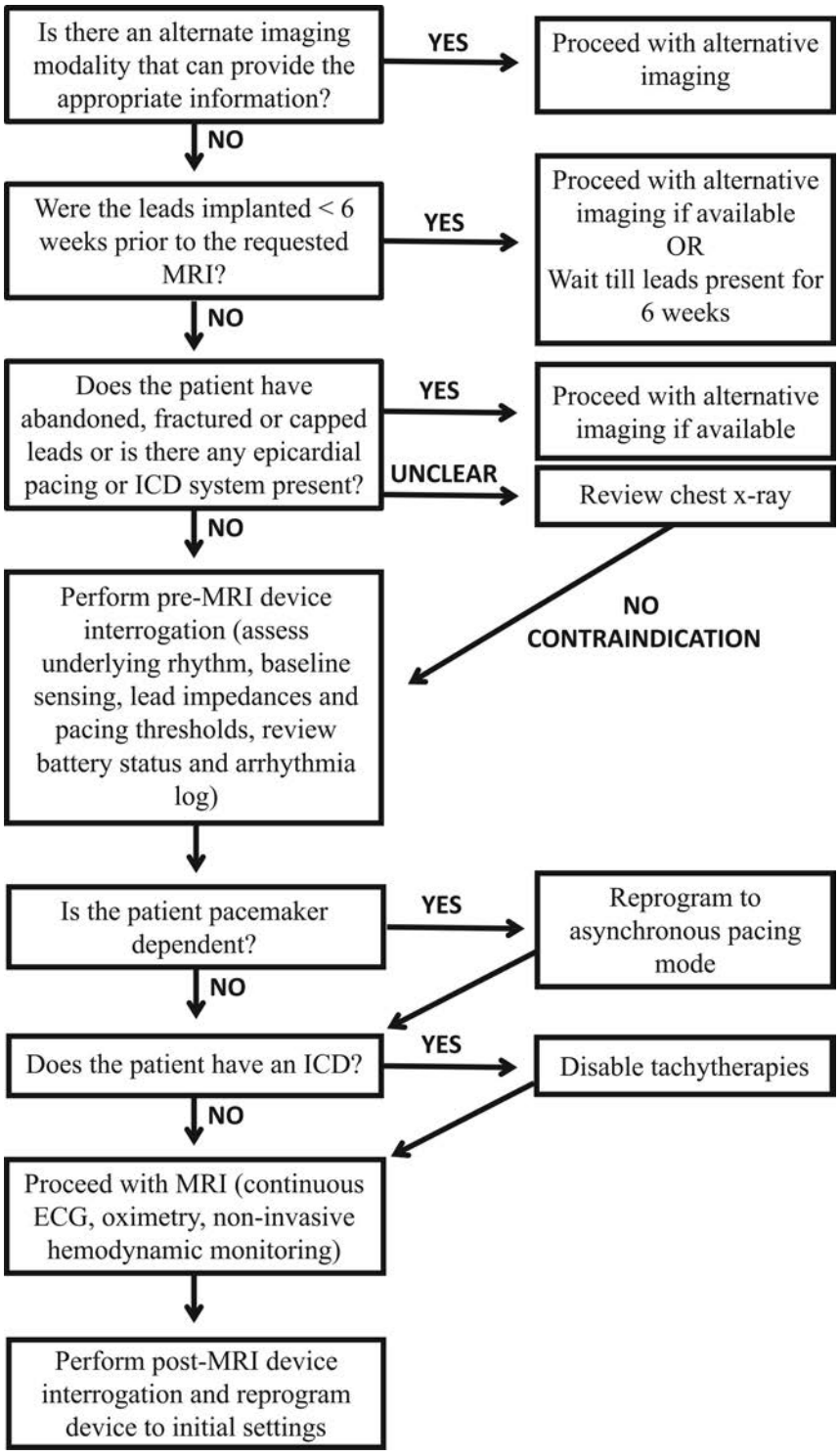

FIG 2. Comprehensive safety protocol: collaboration between neuroradiology and cardiology.

for >6 weeks. Examinations are typically performed with receive-only coils. Although we have used head transmit/receive coils in the past to minimize patient RF exposure, we are not currently using head transmit/receive coils because these coils do not allow the use of parallel imaging in patients with non-MR imaging–conditional CIEDs. Not using parallel imaging would lengthen and thus may degrade the examination. Many patients are also undergoing concurrent MR imaging of the spine for which we use the body transmit coil because there is no body transmit/receive coil available. We believe that it would be contradictory and overly complicated to use a head transmit/receive coil followed by the body transmit coil and spine receive coil for imaging of the thoracic spine, which is the portion of the examination in which the CIED is positioned entirely within the coil.

In general, no alterations are made to our MR imaging protocols when a patient with a non-MR imaging–conditional CIED undergoes an MR imaging examination of the neural axis. In fact, any neurologic imaging study that can be run on a 1.5T magnet, including sequences using echo-planar imaging, can be performed in a patient with a CIED, as long as the examination is performed in normal operating mode. This includes diffusion-weighted imaging, perfusion imaging, and diffusion tensor imaging. These factors are independent of the pacemaker device. In contrast to artifacts encountered due to the device generator and leads when performing cardiac or breast MR imaging examinations, no alterations to our scanning protocols were necessary to combat artifacts when scanning the neural axis in patients with a CIED. However, the longer acquisition times used for some sequences when scanning in the normal operating mode (eg, due to longer scan TRs) make some sequences more susceptible to motion artifacts.

Cardiac Evaluation

A comprehensive protocol was established through the collaboration between the department of radiology and the division of cardiology (Fig 2) to ensure patient safety when performing MR imaging in patients with a CIED. The comprehensive safety protocol is similar to that initially described by Nazarian et al.[38,39] Understanding the potential interactions between MR imaging and CIED systems is imperative to the preimaging patient evaluation as well as the risk and benefit discussion. The main risk categorizations include the following: 1) ferromagnetic interaction, leading to induced electrical currents, arrhythmia induction, device-sensing malfunction, or electrical resets; 2) lead thermal conduction causing loss of capture ("capture" refers to the excitation of heart tissue by a pacing stimulus, assuming that the strength of stimulus is sufficient and tissue is not in a refractory

period) due to local myocardial edema and scar formation with subsequent increased pacing thresholds; 3) change in the pacing mode to asynchronous or inhibition of pacing; 4) inappropriate arrhythmia sensing, which may lead to ICD therapy or antitachycardia therapy (Fig 3); and 5) saturation of device storage for diagnostic and event data.[23]

All patients scheduled for an MR imaging examination are screened by the department of radiology at the time of scheduling for the presence of a CIED. If a non-MR imaging–conditional CIED is present, the patient's case is reviewed by a radiologist and alternative imaging is recommended when the radiologist or ordering physician determines that the clinical information needed could be obtained from a non-MR imaging technique. In patients for whom MR imaging is judged to be the most appropriate test, the radiologist makes this documentation in the patient's electronic medical record. Before imaging, the patient is then evaluated by an electrophysiologist (EP) in the same way that patients scheduled to undergo an operation are evaluated preoperatively. If scheduled as an outpatient, a patient with a non-MR imaging–conditional CIED is referred to the cardiac EP clinic, where a physician performs a history, physical, electrocardiogram, and device interrogation. A chest radiograph is performed when there is uncertainty as to the presence of a fractured or retained transvenous pacing lead or a permanent epicardial pacing lead, each of which is an absolute contraindication to undergoing an MR imaging examination (Fig 4). Please refer to Table 3 for a complete list of absolute contraindications for undergoing MR imaging in patients with nonconditional CIEDs. If the patient has no absolute contraindication to MR imaging, the cardiologist discusses the potential risks and benefits with the patient, and the study is scheduled. If scheduled as an inpatient, a patient with a non-MR imaging–conditional CIED is evaluated by the EP consult service in a fashion similar to that in an outpatient. An important point of clarification is for patients who are not awake and alert for the MR imaging examination, such as those who are intubated or heavily sedated. These patients are unable to report pain or discomfort during the examination and are only imaged in circumstances in which the benefits of the procedure greatly outweigh the risk of a complication, which could potentially go unnoticed.

On the day of the examination, a staff radiologist obtains informed consent from the patient following a discussion of the risks and benefits of the procedure. A physician or appropriately credentialed EP nurse then performs a complete device interrogation to determine the underlying rhythm and measures baseline sensing, lead impedances, and pacing thresholds. All devices are programmed to an asynchronous pacing mode (DOO/VOO) (Table 1) during imaging in patients who are pacemaker-dependent; this mode is defined as the absence of a spontaneous underlying rhythm of >40 beats per minute. In those who are not pacemaker-dependent, devices may be placed in a mode in which backup pacing is possible (AAI/VVI/DDI) or they may be placed in a mode in which pacing is disabled entirely (OVO/ODO). All ICD therapies to treat ventricular tachycardia or ventricular fibrillation are disabled before MR imaging.

Continuous electrocardiogram, pulse oximetry, and noninvasive blood pressure monitoring are performed, in addition to patient symptom assessment throughout imaging. Imaging was per-

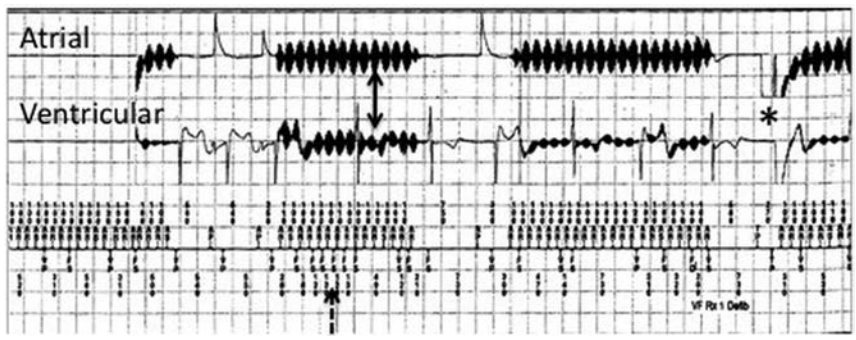

FIG 3. Risk categorization: inappropriate device sensing during MR imaging. Intracardiac electrograms from a patient with a dual-chamber ICD. Electromagnetic interference is seen on both atrial and ventricular channels (*solid arrows*), resulting in oversensing (*dashed arrow*) and an inappropriate ICD shock (*asterisk*).

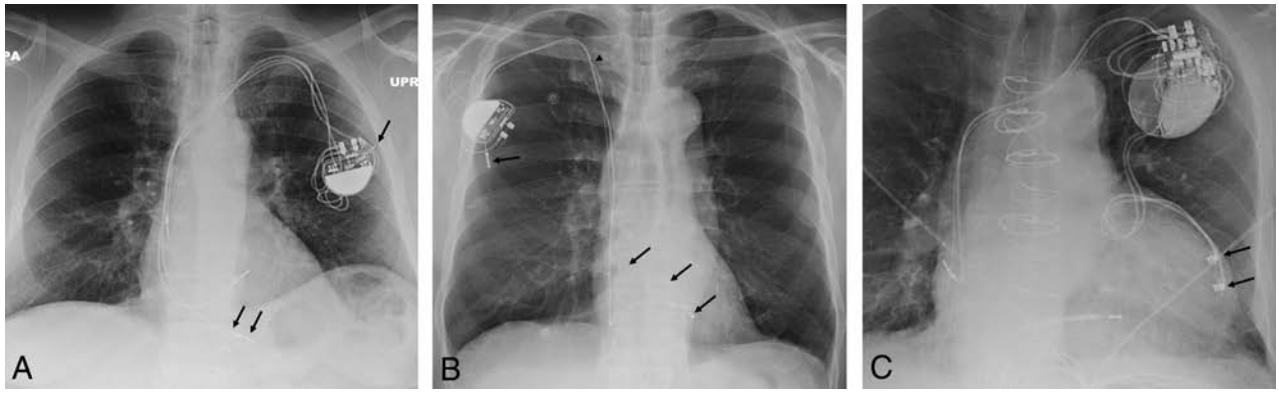

FIG 4. Absolute contraindications: chest x-ray examinations with abandoned and epicardial leads. Posteroanterior view of the chest (*A*) demonstrates an abandoned lead (*black arrows*) in a patient with a dual-chamber pacemaker device. *B*, An abandoned right ventricular lead (*black arrows*) in a patient with a single-lead pacemaker device. The *black arrowhead* denotes a fracture of the abandoned lead. *C*, A patient with a biventricular ICD pacing system, which includes transvenous atrial and right ventricular leads and 2 permanent epicardial pacing leads (*black arrows*). None of these 3 patients would be cleared to undergo MR imaging examination at our institution.

Table 3: Contraindications for undergoing MRI with a non-MRI–conditional CIED

Contraindications
A device implanted <6 weeks prior to the MRI examination
Abandoned or fractured permanent intracardiac pacing leads
Permanent epicardial pacing leads
Temporary epicardial pacing leads when the device generator is attached
Temporary intracardiac pacing leads (with or without attached generator)
Intubated, obtunded, or heavily sedated patients (relative contraindication)

formed under the continuous supervision of a member of the EP consult team until 2011, when it was determined that the risks in patients who were not pacemaker-dependent were low. Since that time, only patients who are pacemaker-dependent require continuous supervision by a member of the EP consult team during imaging. Patients who are not pacemaker-dependent are currently supervised by a radiology MR imaging technician and a radiology nurse, neither of whom routinely undergo additional training for this procedure. Resuscitation equipment and an external defibrillator with the capability of delivering transcutaneous pacing are immediately available. Imaging is terminated for any adverse events or if the safety of the patient is thought to be compromised.

On completion of the examination, a physician or appropriately credentialed EP nurse performs a repeat device interrogation with measurements, noting any changes in device settings, arrhythmias, therapies delivered, or battery depletion. Device settings are reprogrammed to the initial settings if any adjustments have been made previously or modified on the basis of postimaging observations. Patients are then followed routinely in their outpatient cardiac device clinics.

Our Experience

Using the electronic medical record of the hospital, we retrospectively identified 292 MR imaging examinations of the neural axis that were performed in 121 patients with non-MR imaging–conditional pacemakers between June 2010 and November 2016. All examinations were performed at 1.5T following appropriate cardiac clearance per the multidisciplinary protocol outlined in the "Cardiac Evaluation" section. Of the 292 MR imaging examinations, there were 162 MRIs of the brain (55%), 26 MRAs of the head (9%), 16 MRAs of the neck (5%), 28 MRIs of the cervical spine (10%), 26 MRIs of the thoracic spine (9%), 32 MRIs of the lumbar spine (11%), 1 MRI of the face/neck, and 1 MRI of the orbits. In patients requiring >1 MR imaging examination, multiple studies were grouped into single patient encounters when possible. In total, 204 discrete MR imaging encounters occurred in this group of 121 patients.

Seven of 121 patients (6% of patients with a total of 17 MR imaging encounters) were pacemaker-dependent, 111 of 121 patients (92%) were non-pacemaker-dependent, and in 3 of 121 patients (2%), it was unclear whether the patient was pacemaker-dependent or not. As described in the "Cardiac Evaluation" section, pacemakers were set to an asynchronous pacing mode in patients who were pacemaker-dependent.

All MR imaging examinations were completed safely with no clinically important complications reported. No examinations were terminated prematurely due to pacemaker-related problems. There were 8 episodes in 204 total encounters (4%), in which minor, unexpected programming changes occurred with no immediate or delayed adverse outcomes. In 2 patients, MR imaging electromagnetic interference artifacts were noted in the ventricular fibrillation zone; however, no therapy was administered (as noted in the "Cardiac Evaluation" section, all ICD therapies to treat ventricular tachycardia or ventricular fibrillation are disabled before MR imaging). In these 2 patients, no subsequent change in device settings or postprocedural complication was noted following the MR imaging examination. In 1 patient with a dual-chamber pacemaker, there was a minor change in the right ventricular lead impedance, though the impedance remained within normal limits. In another patient with a dual-chamber pacemaker, a slight increase in the right atrial lead capture threshold was managed by a slight increase in the right atrial lead pacing output amplitude.

Variations in lead impedance and pacing capture thresholds have been noted previously but are generally deemed to be not clinically important and occur, to some degree, in the general CIED population.[40,41] There were noise reversion episodes in 3 patients (multiple episodes in 2 of those patients). In all 3 patients, there were no immediate adverse outcomes, and the device was reprogrammed to the original settings after the MR imaging examination. In 1 patient with a single-lead pacemaker who experienced 6 MR imaging encounters, the pacemaker mode converted to asynchronous pacing with a rate of 100 beats per minute during 1 of the 6 MR imaging examinations. This patient had atrial fibrillation with an underlying ventricular rate ranging from the 40s to the 50s and required pacing 88% of the time. No subsequent adverse outcomes were reported in this patient. No programming changes or other unexpected events were recorded during the patient's other 5 encounters.

Our cohort of patients who were safely scanned with MR imaging included those who were pacer-dependent and others who underwent examinations of the thorax. Limitations of this study include the relatively low number of pacer-dependent patients (17/292 confirmed MR imaging encounters) and the general heterogeneity of specific CIED manufacturer generator/lead combinations. In addition, no pediatric patients were scanned at our institution, and no patients were scanned at field strengths of >1.5T.

CONCLUSIONS

On the basis of our experience during the past 6 years performing MR imaging examinations in patients with non-MR imaging–conditional CIEDs, including those who are pacemaker dependent or are undergoing an MR imaging of the thorax, as well as the growing body of supportive evidence in the literature, it is our opinion that these examinations can be performed safely when risks to the patient are well-managed. Before proceeding with an MR imaging examination, it is important to confirm that doing so is judged appropriate following a thorough review of the patient's chart and a discussion with the ordering physician by the supervising radiologist. Strict adherence to basic screening and scan protocols is also required. Patient populations that should con-

tinue to be excluded from MR imaging include those with devices implanted <6 weeks prior, those with retained or fractured device leads, those with surgically placed permanent epicardial pacing leads, and those with temporary intracardiac/epicardial pacer devices with the external generator still attached.

ACKNOWLEDGMENTS

The authors thank Charles Fasanati for his help in preparing this article.

Disclosures: Jeremy D. Collins—*UNRELATED*: *Consultancy*: Guerbet, *Comments*: advisory board meeting; *Grants/Grants Pending*: Siemens, *Comments*: Conebeam CT grant for hepatocellular carcinoma. Bradley P. Knight—*UNRELATED*: *Grant*: Medtronic, Boston Scientific, St. Jude Medical, BIOTRONIK*; *Consulting Fee or Honorarium*: Medtronic, Boston Scientific, St. Jude Medical, BIOTRONIK. Alexander J. Nemeth—*UNRELATED*: *Grants/Grants Pending*: National Institutes of Health, *Comments*: RO1HL092259, SP0039078, coinvestigator 5% effort salary support for Cerebral Autoregulation Monitoring to Reduce Brain Injury from Cardiac Surgery. *Money paid to the institution.

REFERENCES

1. OECD. **Magnetic resonance imaging (MRI) exams, total.** Health: Key Tables. OECD 2014. https://data.oecd.org/healthcare/magnetic-resonance-imaging-mri-exams.htm. Accessed December 24, 2016
2. Nazarian S, Hansford R, Roguin A, et al. **A prospective evaluation of a protocol for magnetic resonance imaging of patients with implanted cardiac devices.** *Ann Intern Med* 2011;155:415–24 CrossRef Medline
3. Kanal E, Barkovich AJ, Bell C, et al; ACR Blue Ribbon Panel on MR Safety. **ACR guidance document for safe MR practices: 2007.** *AJR Am J Roentgenol* 2007;188:1447–74 CrossRef Medline
4. Levine GN, Gomes AS, Arai AE, et al; American Heart Association Committee on Diagnostic and Interventional Cardiac Catheterization, American Heart Association Council on Clinical Cardiology, American Heart Association Council on Cardiovascular Radiology and Intervention. **Safety of magnetic resonance imaging in patients with cardiovascular devices: an American Heart Association scientific statement from the Committee on Diagnostic and Interventional Cardiac Catheterization, Council on Clinical Cardiology, and the Council on Cardiovascular Radiology and Intervention: endorsed by the American College of Cardiology Foundation, the North American Society for Cardiac Imaging, and the Society for Cardiovascular Magnetic Resonance.** *Circulation* 2007;116:2878–91 CrossRef Medline
5. Roguin A, Schwitter J, Vahlhaus C, et al. **Magnetic resonance imaging in individuals with cardiovascular implantable electronic devices.** *Europace* 2008;10:336–46 CrossRef Medline
6. Wilkoff BL, Bello D, Taborsky M, et al; EnRhythm MRI SureScan Pacing System Study Investigators. **Magnetic resonance imaging in patients with a pacemaker system designed for the magnetic resonance environment.** *Heart Rhythm* 2011;8:65–73 CrossRef Medline
7. Sommer T, Naehle CP, Yang A, et al. **Strategy for safe performance of extrathoracic magnetic resonance imaging at 1.5 Tesla in the presence of cardiac pacemakers in non-pacemaker-dependent patients: a prospective study with 115 examinations.** *Circulation* 2006;114:1285–92 CrossRef Medline
8. Russo RJ, Costa HS, Silva PD, et al. **Assessing the risks associated with MRI in patients with a pacemaker or defibrillator.** *N Engl J Med* 2017;376:755–64 CrossRef Medline
9. Martin ET, Coman JA, Shellock FG, et al. **Magnetic resonance imaging and cardiac pacemaker safety at 1.5-Tesla.** *J Am Coll Cardiol* 2004;43:1315–24 CrossRef Medline
10. Dandamudi S, Collins JD, Carr JC, et al. **The safety of cardiac and thoracic magnetic resonance imaging in patients with cardiac implantable electronic devices.** *Acad Radiol* 2016;23:1498–505 CrossRef Medline
11. Aguilera AL, Volokhina YV, Fisher KL. **Radiography of cardiac conduction devices: a comprehensive review.** *Radiographics* 2011;31:1669–82 CrossRef Medline
12. Hunter TB, Taljanovic MS, Tsau PH, et al. **Medical devices of the chest.** *Radiographics* 2004;24:1725–46 CrossRef Medline
13. Kirk M. **Basic principles of pacing**. In: Chow AW, Buxton AE, eds. *Implantable Cardiac Pacemakers and Defibrillators*: *All You Wanted to Know*. Oxford, UK: Blackwell Publishing; 2006:1–28 CrossRef
14. Kalin R, Stanton MS. **Current clinical issues for MRI scanning of pacemaker and defibrillator patients.** *Pacing Clin Electrophysiol* 2005;28:326–28 CrossRef Medline
15. Langman DA, Goldberg IB, Finn JP, et al. **Pacemaker lead tip heating in abandoned and pacemaker-attached leads at 1.5 Tesla MRI.** *J Magn Reson Imaging* 2011;33:426–31 CrossRef Medline
16. Pavlicek W, Geisinger M, Castle L, et al. **The effects of nuclear magnetic resonance on patients with cardiac pacemakers.** *Radiology* 1983;147:149–53 CrossRef Medline
17. Kanal E, Shellock FG, Talagala L. **Safety considerations in MR imaging.** *Radiology* 1990;176:593–606 CrossRef Medline
18. Horwood L, Attili A, Luba F, et al. **Magnetic resonance imaging in patients with cardiac implanted electronic devices: focus on contraindications to magnetic resonance imaging protocols.** *Europace* 2017;19:812–17 CrossRef Medline
19. Naehle CP, Strach K, Thomas D, et al. **Magnetic resonance imaging at 1.5-T in patients with implantable cardioverter-defibrillators.** *J Am Coll Cardiol* 2009;54:549–55 CrossRef Medline
20. Higgins JV, Sheldon SH, Watson RE Jr, et al. **"Power-on resets" in cardiac implantable electronic devices during magnetic resonance imaging.** *Heart Rhythm* 2015;12:540–44 CrossRef Medline
21. Ferreira AM, Costa F, Tralhao A, et al. **MRI-conditional pacemakers: current perspectives.** *Med Devices (Auckl)* 2014;7:115–24 CrossRef Medline
22. Luechinger R, Duru F, Zeijlemaker VA, et al. **Pacemaker reed switch behavior in 0.5, 1.5, and 3.0 Tesla magnetic resonance imaging units: are reed switches always closed in strong magnetic fields?** *Pacing Clin Electrophysiol* 2002;25:1419–23 CrossRef Medline
23. van der Graaf AW, Bhagirath P, Götte MJ. **MRI and cardiac implantable electronic devices; current status and required safety conditions.** *Neth Heart J* 2014;22:269–76 CrossRef Medline
24. Ahmed FZ, Morris GM, Allen S, et al. **Not all pacemakers are created equal: MRI conditional pacemaker and lead technology.** *J Cardiovasc Electrophysiol* 2013;24:1059–65 CrossRef Medline
25. Boutet C, Mansourati J, Ben Salem D. **How to manage central nervous system MRI with a cardiac implantable electronic device?** *J Neuroradiol* 2016;43:307–08 CrossRef Medline
26. Luechinger R, Zeijlemaker VA, Pedersen EM, et al. **In vivo heating of pacemaker leads during magnetic resonance imaging.** *Eur Heart J* 2005;26:376–83; discussion 325–27 CrossRef Medline
27. Mollerus M, Albin G, Lipinski M, et al. **Cardiac biomarkers in patients with permanent pacemakers and implantable cardioverter-defibrillators undergoing an MRI scan.** *Pacing Clin Electrophysiol* 2008;31:1241–45 CrossRef Medline
28. Sommer T, Naehle CP, Schild H. **Magnetic resonance imaging in patients with cardiac pacemakers.** *J Am Coll Cardiol* 2005;46:561–62; author reply 562 Medline
29. Collins CM, Wang Z. **Calculation of radiofrequency electromagnetic fields and their effects in MRI of human subjects.** *Magn Reson Med* 2011;65:1470–82 CrossRef Medline
30. Baker KB, Tkach JA, Nyenhuis JA, et al. **Evaluation of specific absorption rate as a dosimeter of MRI-related implant heating.** *J Magn Reson Imaging* 2004;20:315–20 CrossRef Medline
31. International Electrotechnical Commision. Medical electrical equipment – Part 2-33: Particular requirements for the basic safety and essential performance of magnetic resonance equipment for medical diagnosis. IEC 60601-2-33 2010
32. Calcagnini G, Triventi M, Censi F, et al. **In vitro investigation of pacemaker lead heating induced by magnetic resonance imaging: role of implant geometry.** *J Magn Reson Imaging* 2008;28:879–86 CrossRef Medline

33. Nitz WR, Oppelt A, Renz W, et al. **On the heating of linear conductive structures as guide wires and catheters in interventional MRI.** *J Magn Reson Imaging* 2001;13:105–14 Medline
34. Nordbeck P, Ritter O, Weiss I, et al. **Impact of imaging landmark on the risk of MRI-related heating near implanted medical devices like cardiac pacemaker leads.** *Magn Reson Med* 2011;65:44–50 CrossRef Medline
35. Mattei E, Triventi M, Calcagnini G, et al. **Complexity of MRI induced heating on metallic leads: experimental measurements of 374 configurations.** *Biomed Eng Online* 2008;7:11 CrossRef Medline
36. Nordbeck P, Fidler F, Weiss I, et al. **Spatial distribution of RF-induced E-fields and implant heating in MRI.** *Magn Reson Med* 2008; 60:312–19 CrossRef Medline
37. Nordbeck P, Weiss I, Ehses P, et al. **Measuring RF-induced currents inside implants: impact of device configuration on MRI safety of cardiac pacemaker leads.** *Magn Reson Med* 2009;61:570–78 CrossRef Medline
38. Nazarian S, Halperin HR. **How to perform magnetic resonance imaging on patients with implantable cardiac arrhythmia devices.** *Heart Rhythm* 2009;6:138–43 CrossRef Medline
39. Nazarian S, Roguin A, Zviman MM, et al. **Clinical utility and safety of a protocol for noncardiac and cardiac magnetic resonance imaging of patients with permanent pacemakers and implantable-cardioverter defibrillators at 1.5 Tesla.** *Circulation* 2006;114:1277–84 CrossRef Medline
40. Gimbel JR, Bello D, Schmitt M, et al; Advisa MRI System Study Investigators. **Randomized trial of pacemaker and lead system for safe scanning at 1.5 Tesla.** *Heart Rhythm* 2013;10:685–91 CrossRef Medline
41. Mollerus M, Albin G, Lipinski M, et al. **Magnetic resonance imaging of pacemakers and implantable cardioverter-defibrillators without specific absorption rate restrictions.** *Europace* 2010;12:947–51 CrossRef Medline

Setting the Stage for 2018: How the Changes in the American Joint Committee on Cancer/Union for International Cancer Control *Cancer Staging Manual* Eighth Edition Impact Radiologists

C.M. Glastonbury, S.K. Mukherji, B. O'Sullivan, and W.M. Lydiatt

ABSTRACT

SUMMARY: The updated eighth edition of the *Cancer Staging Manual* of the American Joint Committee on Cancer will be implemented in January 2018. There are multiple changes to the head and neck section of the manual, which will be relevant to radiologists participating in multidisciplinary head and neck tumor boards and reading pretreatment head and neck cancer scans. Human papillomavirus–related/p16(+) oropharyngeal squamous cell carcinoma will now be staged separately; this change reflects the markedly better prognosis of these tumors compared with non-human papillomavirus/p16(−) oropharyngeal squamous cell carcinoma. Nodal staging has dramatically changed so that there are different tables for human papillomavirus/p16(+) oropharyngeal squamous cell carcinoma, Epstein-Barr virus–related nasopharyngeal carcinoma, and all other head and neck squamous cell carcinomas. Extranodal extension of tumor is a new clinical feature for this third staging group. In the oral cavity, the pathologically determined depth of tumor invasion is a new staging criterion, while extrinsic tongue muscle invasion is no longer part of staging. This review serves to educate radiologists on the eighth edition changes and their rationale.

ABBREVIATIONS: AJCC = American Joint Committee on Cancer; cN = clinical nodal staging; DOI = depth of invasion; EBV = Epstein-Barr virus; ENE = extranodal extension; HN = head and neck; HPV = human papillomavirus; NPC = nasopharyngeal carcinoma; OPSCC = oropharyngeal squamous cell carcinoma; pN = pathologic nodal staging; SCC = squamous cell carcinoma; TNM = tumor, node, metastasis; UICC = Union for International Cancer Control

The tumor, node, metastasis (TNM) cancer staging system is a collaborative effort between the American Joint Committee on Cancer (AJCC) and the Union for International Cancer Control (UICC) to systematically record, analyze, and better understand cancer and cancer treatment worldwide.[1,2] For the clinical team, this staging system allows a common, consistent nomenclature and provides a framework for managing patient care. For the individual patient, this system allows classification of the extent of disease so that prognostic information can be provided and treatment options determined.

Received July 5, 2017; accepted after revision August 17.

From the Department of Radiology and Biomedical Imaging (C.M.G.), University of California, San Francisco, California; Department of Radiology (S.K.M.), Michigan State University, East Lansing, Michigan; Department of Radiation Oncology (B.O.), Princess Margaret Cancer Center, University of Toronto, Toronto, Ontario, Canada; Department of Surgery, Head and Neck Oncology (W.M.L.), Estabrook Cancer Center, Nebraska Methodist Hospital, Omaha, Nebraska; Creighton University (W.M.L.), Omaha, Nebraska; and Naval Medical Center (W.M.L.), Portsmouth, Virginia.

All authors are members of the Head and Neck Expert Panel for the eighth edition of the American Joint Committee on Cancer *Cancer Staging Manual*. W.M. Lydiatt is the Panel Vice-Chair. B. O'Sullivan is the UICC representative and the chair of the UICC HN subcommittee.

Please address correspondence to Christine M. Glastonbury, MBBS, Department of Radiology, Box 0628, Room L-358, 505 Parnassus Ave, San Francisco, CA 94143-0628; e-mail: christine.glastonbury@ucsf.edu; @CMGlastonbury

http://dx.doi.org/10.3174/ajnr.A5409

Periodically, the TNM system is revised to reflect changes in our understanding of tumor pathology and pathophysiology. The AJCC *Cancer Staging Manual* seventh edition was implemented in 2010, with the most recent eighth edition completed and published this year and implemented for staging of all patients with cancer as of January 1, 2018.[3] There are many important changes to the head and neck (HN) section, which again forms Part II of the AJCC eighth edition and has expanded to 11 chapters. Two new chapter titles have been added to the head and neck section, one on cervical nodes and unknown primary tumors and one on HN-specific cutaneous malignancy. Pharynx cancer has been divided into 3 separate chapters: "Nasopharynx," "Human Papillomavirus (HPV)-Mediated p16+ Oropharyngeal Cancer," and "p16− plus Hypopharynx." Thyroid cancer staging has been moved from the HN section to the "Endocrine System" (Part XVII), and orbital and eyelid tumors remain in "Ophthalmic Sites" (Part XV). Within the HN chapters, there are important changes related to extranodal extension (ENE) of tumor and some key changes to T-categories, some of which relate to pathology staging and others to imaging. Changes to the eighth edition of the AJCC *Cancer Staging Manual* head and neck section require knowing specific clinical and/or pathologic information in order to use the correct staging table. Specifically, it is important to know the p16 status of oropharynx primary tumors because

Table 1: Clinical N staging for all non-HPV, non-EBV SCCs[a]

N Category	N Criteria
Nx	Regional lymph nodes cannot be assessed
N0	No regional lymph node metastasis
N1	Metastasis in a single ipsilateral lymph node ≤3 cm in greatest dimension and ENE−
N2a	Metastasis in a single ipsilateral lymph node >3 cm but ≤6 cm in greatest dimension and ENE−
N2b	Metastasis in multiple ipsilateral nodes, none >6 cm in greatest dimension and ENE−
N2c	Metastasis in bilateral or contralateral lymph node(s), none >6 cm in greatest dimension and ENE−
N3a	Metastasis in a lymph node >6 cm in greatest dimension and ENE−
N3b	Metastasis in any node(s) with clinically overt ENE+ (ENEc)

Note:—ENEc indicates invasion of skin, infiltration of musculature, dense tethering or fixation to adjacent structures, or cranial nerve, brachial plexus, sympathetic trunk, or phrenic nerve invasion with dysfunction.

[a] Note the addition of ENE to the staging system, creating a new N3b designation in the eighth edition of the *AJCC Cancer Staging Manual*. Table used with the permission of the American Joint Committee on Cancer (AJCC), Chicago, Illinois. The original source for this material is the *AJCC Cancer Staging Manual*.[1]

Table 2: Clinical nodal staging for HPV-related OPSCC[a]

N Category	N Criteria
Nx	Regional lymph nodes cannot be assessed
N0	No regional lymph node metastasis
N1	One or more ipsilateral lymph nodes, none larger than 6 cm
N2	Contralateral or bilateral lymph nodes, none >6 cm
N3	Lymph node(s) >6 cm

[a] The HPV-related OPSCC nodal staging shows a dramatic change compared with the eighth edition non-HPV OPSCC staging. Table adapted with permission of the American Joint Committee on Cancer, Chicago, Illinois. The original source for this material is the *AJCC Cancer Staging Manual*.[1]

p16(+) and p16(−) oropharynx tumors are staged differently. Also, when evaluating cases of nodal disease, one must know whether an HN primary tumor is known and whether that tumor is a skin or mucosal primary. This review serves to summarize the critical changes relevant to all imagers reading HN CT, MR imaging, or PET/CT scans, particularly those participating in tumor board clinical staging.

AJCC Changes with Impact for the Radiology Report

Cervical Nodes and Extranodal Extension. The changes made to nodal staging might be perceived by radiologists as the most confusing part of the HN section in the eighth edition, and while many areas elsewhere in the HN section are about simplification from the seventh edition, nodal definition shows increasing complexity. This reflects the key changes resulting from a better understanding of both HPV-related oropharyngeal squamous cell carcinoma (OPSCC) and the significance of extranodal extension of tumor in non-HPV and non-Epstein-Barr virus (EBV) nodal disease.[4-11]

There are now 5 different staging tables for nodes, 2 of which are purely pathologic staging (pN) following cervical lymph node dissection (of ≥15 nodes) (Tables 1–3):

- HPV-related OPSCC: clinical (cN) and separate pathologic (pN) nodal staging
- EBV-related nasopharyngeal carcinoma (NPC): clinical staging very similar to that in the seventh edition with changes to N3 designation only
- All other HN squamous cell carcinomas (SCCs): clinical and separate pathologic nodal staging.

Particularly given this increasing complexity, referring to the published charts is the best way to avoid confusion and errors in staging. For radiologists reading scans who are unsure of the HPV or EBV tumor status, it will not be possible to know which clinical nodal category (cN) table to use. In the first instance, radiologists should, if possible, search the pathology report in the electronic medical record for this information. When EBV/HPV/p16 information is not available, it is important that the nodal level system be used to describe the location of ipsilateral and/or contralateral abnormal nodes to enable the clinician to assign a cN. When one determines the presence of concerning adenopathy, all morphologic characteristics of a node should be assessed, particularly in the expected drainage pattern of the known primary tumor: size (>10-mm short axis), shape (rounded), loss of fatty hilus, focal nodal inhomogeneity (focal necrosis), and cystic change. Additionally, for all tumors except nasopharyngeal carcinoma and HPV/p16(+) oropharyngeal tumors, radiologists should evaluate evidence of extranodal extension of the tumor. Currently, the clinical designation of ENE+ requires overt clinical examination evidence of ENE, such as skin invasion, infiltration of muscle with tethering or fixation to adjacent structures, or large-nerve invasion with dysfunction such as the brachial plexus, sympathetic trunk, phrenic, or cranial nerves. While indistinct nodal margins and an irregular nodal capsular enhancement suggest ENE, the strongest imaging feature supporting the clinical diagnosis of ENE is clear infiltration of perinodal tumor into adjacent fat or muscle.[12-14] It will be most useful for radiologists to describe features suspicious for ENE so that the clinician can re-evaluate the clinical nodal status. Improving the imaging specificity for ENE is clearly an area of focus for radiologists and therefore potentially contributing to future revisions of the *AJCC Cancer Staging Manual*.

HPV-Related (p16+) Oropharyngeal Squamous Cell Carcinoma. Probably the most significant change to HN tumor staging is the separation of tumors related to human papilloma virus infection and/or determined to be p16+ on immunohistochemistry. This separate staging designation reflects the novelty of this disease, which exhibits an overall markedly better prognosis compared with p16− and largely tobacco- and alcohol-related OPSCC.[4-7,11]

Metastatic nodes with HPV-related OPSCC are frequently large, multiple, and/or bilateral, yet the disease will overall have a much better survival than non-HPV OPSCC with similar extent of nodal involvement. Thus, there have been significant changes made to the nodal staging, which will result in quite dramatic changes to overall prognostic grouping compared with the staging used for all OPSCC in the seventh edition (Figs 1 and 2 and Tables 2, 4, and 5). For clinical N categories of HPV/p16+ OPSCC, any ipsilateral node or nodes that are ≤6 cm are designated N1 disease. Bilateral or contralateral nodes of ≤6 cm are designated N2 disease, and N3 disease is determined when a nodal mass is >6

Table 3: Clinical nodal staging for NPC[a]

N Category	N Criteria
Nx	Regional lymph nodes cannot be assessed
N0	No regional lymph node metastasis
N1	Unilateral metastasis in cervical lymph node(s) and/or unilateral or bilateral metastasis in retropharyngeal lymph node(s) ≤6 cm in greatest dimension, above the caudal border of cricoid cartilage
N2	Bilateral metastasis in cervical lymph nodes ≤6 cm in greatest dimension, above the caudal border of cricoid cartilage
N3	Unilateral or bilateral metastasis in cervical lymph node(s) >6 cm in greatest dimension, and/or extension below the caudal border of cricoid cartilage

[a] Changes in the eighth edition reflect the designation of level IV or VB nodes as N3 disease with no distinct a or b status. Table adapted with permission of the American Joint Committee on Cancer, Chicago, Illinois. The original source for this material is the *AJCC Cancer Staging Manual*.[1]

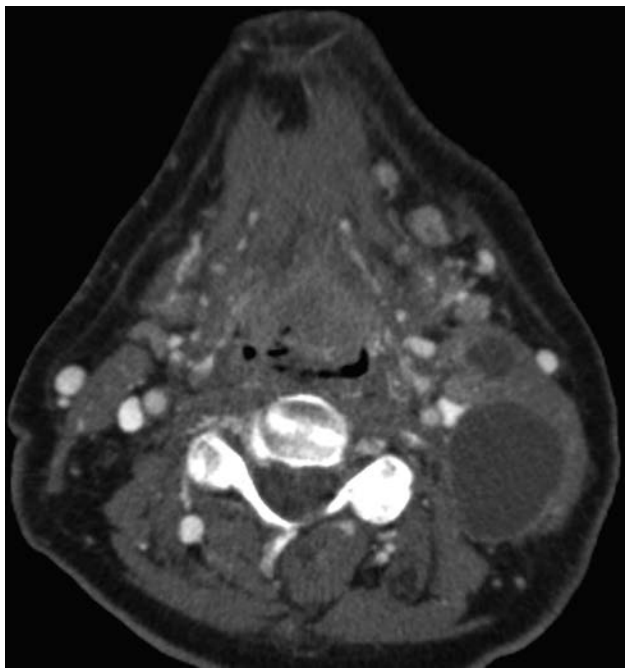

FIG 1. Axial contrast-enhanced CT in a 69-year-old man demonstrates a heterogeneously enlarged lingual tonsil filling the valleculae and at least 2 left cystic cervical nodes. No right neck adenopathy was evident. Biopsy of the primary site revealed p16(+) OPSCC. This was staged as cT2N2b, stage IVA OPSCC. In the eighth edition of the AJCC, the T-category does not change; however, multiple ipsilateral nodes are now assigned N1 category if <6 cm in greatest diameter. In the eighth edition, T2N1 p16(+) OPSCC is designated stage I disease.

cm. For prognostic staging of tumors with T0–2, N1 disease is stage I, N2 is stage II, and N3 is stage III. For T3 tumors, stage II is a minimum stage regardless of N, and for T4 or N3, stage III is the minimum as seen in Table 5. Stage IV will now be reserved for M1 disease, regardless of T and N. There are no changes to the primary tumor size criteria, which separate T1, T2, and T3 disease; and extension of base of tongue tumor onto the lingual surface of the epiglottis is still T3 disease, but T4a and T4b are combined into one as T4.

Nasopharyngeal Carcinoma. Nasopharyngeal carcinoma is most often nonkeratinizing differentiated or undifferentiated carcinoma, which is EBV-related and, in the United States, most often found in Asian populations, particularly those of southern Chinese migration or descent. HPV-related NPC and tobacco-/alcohol-related EBV are less common worldwide. Staging is not currently altered by EBV status of the tumor; however, if EBV-positive nodal disease is found in the neck without a primary source determined, then the nodal metastases are presumed to be from the nasopharynx and they are designated T0 NPC and staged accordingly.

The most significant change to the T-assignment for NPC is the clarification of involvement of specific bony and masticator structures. Involvement of any bony structures such as cervical vertebrae, pterygoid plates, skull base, or paranasal sinuses is T3 disease. In the AJCC *Cancer Staging Manual* seventh edition, involvement of any masticator space structure was designated T4 disease. This has now been subdivided so that involvement of the medial or lateral pterygoid muscle or of the prevertebral muscles is T2 disease, but if there is extension of tumor beyond the lateral surface of the pterygoid muscle or involvement of the parotid gland, this is T4 disease (Fig 3 and Tables 3 and 6). This reflects study evidence of a relatively good prognosis for lateral pterygoid muscle infiltration compared with more extensive lateral tumor spread.[15]

For NPC nodal disease, the clinical designation of N3 disease has been modified. In the seventh edition staging system, N3b disease was determined by the presence of ≥1 supraclavicular node in the triangle of Ho, with N3a indicating any nodal mass measuring >6 cm that lies above the supraclavicular fossa. From a radiologic perspective, a supraclavicular node was determined by the presence of a clavicle on the same axial imaging section; however, variable patient positioning in the scanner makes this designation unreliable, and for many radiologists, supraclavicular nodal status was left to the physical examination. N3 disease is now designated as any nodal mass of >6 cm or any nodal mass below the inferior aspect of the cricoid—that is, any node that is level IV or Vb. There is no longer subdivision into N3a and N3b.

"Non-HPV OPSCC and Hypopharynx." This is an entirely new chapter after creation of distinct nasopharyngeal and HPV-related/p16+ oropharyngeal SCC chapters from a previous pharynx chapter that encompassed all pharyngeal tumors. There are, however, no changes to the T-staging described in the seventh edition for oropharyngeal and hypopharyngeal tumors. The nodal staging of these tumors will follow the non-HPV, non-EBV HN clinical (cN) and pathologic (pN) nodal staging definitions, with special attention to the new inclusion of ENE (Table 1).

Oral Cavity SCC. The chapter, historically entitled "Lip and Oral Cavity," will now be called "Oral Cavity," with the lip tumors now staged in the new chapter entitled "Cutaneous Carcinoma of HN."

In the seventh edition, one of the defining features requiring careful imaging evaluation of oral tongue tumors was the presence of invasion of the extrinsic tongue muscles. This feature has been difficult for pathologists to determine because it is typically not possible for them to distinguish intrinsic and extrinsic skeletal

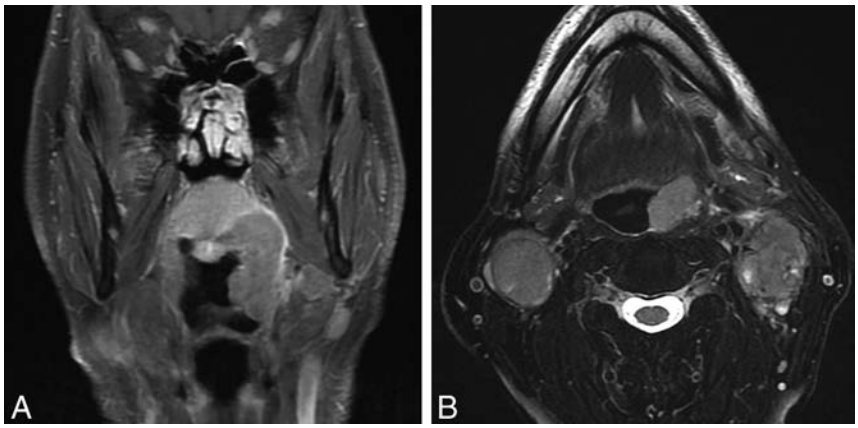

FIG 2. HPV-related p16(+) OPSCC in a 62-year-old man presenting with bilateral neck masses determined to be p16+ squamous cell carcinoma. Coronal T1 postcontrast fat-saturated MR image (*A*) demonstrates a left tonsillar tumor extending superiorly to the soft palate. Because this tumor measured >4 cm in longest dimension, it is assigned T3 with no change in the primary tumor staging from the seventh-to-eighth edition of the *AJCC Cancer Staging Manual*. Axial T2 fat-saturated image (*B*) shows bilateral heterogeneous nodal masses with a high degree of suspicion of extranodal extension bilaterally. In the seventh edition, bilateral adenopathy of <6 cm in greatest dimension for all OPSCCs is designated T2c disease, with prognostic grouping of T3N2c as stage IVA. In the new eighth edition, bilateral adenopathy of <6 cm is N2 disease and the new prognostic grouping for p16+ OPSCC T3N2 is stage II. Extranodal extension does not affect the N designation for HPV/p16(+) OPSCC or NPC.

Table 4: Tumor staging for HPV-related OPSCC[a]

T Category	T Criteria
T0	No primary identified
T1	Tumor ≤2 cm in greatest dimension
T2	Tumor >2 but ≤4 cm in greatest dimension
T3	Tumor >4 cm in greatest dimension or extension to lingual surface of epiglottis
T4	Moderately advanced local disease; tumor invades the larynx, extrinsic muscles of tongue, medial pterygoid, hard palate or mandible, or beyond

[a] The T4a and T4b features from OPSCC staging in the seventh edition are now combined as T4 in the new eighth edition. Table adapted with permission of the American Joint Committee on Cancer, Chicago, Illinois. The original source for this material is the *AJCC Cancer Staging Manual*.[1]

Table 5: AJCC clinical prognostic groupings for HPV-related OPSCC[a]

When T Is...	And N Is...	And M Is...	Then the Stage Group Is...
T0, T1, or T2	N0 or N1	M0	I
T0, T1, or T2	N2	M0	II
T3	N0, N1, or N2	M0	II
Any T	N3	M0	III
T4	Any N	M0	III
Any T	Any N	M1	IV

[a] Table adapted with permission of the American Joint Committee on Cancer, Chicago, Illinois. The original source for this material is the *AJCC Cancer Staging Manual*.[1]

muscles on sections. The eighth edition sees the removal of extrinsic muscle invasion as a T4 feature and the introduction of the depth of invasion (DOI) as a critical determinant of T-staging (Table 7). Depth of invasion is a pathology measurement and is the deep or endophytic invasive growth below a horizontal line drawn at the level of the basement membrane relative to the closest intact squamous mucosa. This is distinct from tumor thickness, which includes both the endophytic component and the exophytic tumor. Tumor infiltration below the basement membrane is the critical factor for DOI and is very difficult to accurately assess by imaging. Measurement by the radiologist of tumor thickness may help guide the clinician in preoperative planning, but DOI is a pathologic assessment. It is still useful to comment on infiltration into the tongue or soft tissues of the oral cavity, particularly when evaluating the presence of bone invasion.

Nodal staging again follows the nodal groupings above, with separate nodal staging for HPV− and HPV+ tumors and both clinical and pathologic nodal staging (Table 1). Radiologists should report nodal disease ipsilateral and contralateral to the primary site. Midline nodes in level IA, which are not uncommon with anterior oral cavity tumors, are considered ipsilateral to the primary tumor. Imaging should also evaluate ENE, though again this is ultimately a clinical examination or pathologic designation. Because neck dissections are frequently performed for oral cavity SCC, the pN tables for non-HPV SCC will be used for final staging designation.

"Cutaneous Carcinoma of HN." This entirely new chapter reorganizes all HN skin cancers other than eyelid SCC, melanoma, and Merkel cell carcinoma into a distinct chapter. Notably, lip SCC, which has traditionally been included with oral cavity tumor staging, is now included here. While tumor size constitutes much of the T-staging and is likely better determined by direct clinical examination, there are important features such as bone erosion, perineural tumor, and skull base invasion that should be sought by the radiologist when reading staging scans (Table 8). The nodal staging follows the cN and pN for all non-HPV, non-EBV SCCs elsewhere in the HN (Table 1).

Key AJCC Changes without Specific Radiologic Impact

Unknown Primary Carcinomas. Unknown primary carcinomas are characterized by the presentation of metastatic nodal disease in the absence of a defined primary tumor (T0). More than 90% of these tumors are HPV-related SCCs, and the occult primary is considered of oropharyngeal origin.[16] When a primary tumor cannot be found by clinical examination or cross-sectional imaging, p16 mmunohistochemistry and HPV-ISH are performed. P16+ nodal disease should be further evaluated with HPV-ISH because p16+ (non-HPV-related) tumors can be found elsewhere in the HN. HPV and p16+ disease are likely of oropharyngeal origin and will therefore be categorized as T0. A positive EBV-ISH of nodal disease favors the unknown primary being of nasopharyngeal origin, T0.

SCC nodal disease that is p16-negative, HPV-negative, and EBV-negative is not assigned to any primary site unless there is a known or suspected prior skin malignancy with the expected pattern of nodal disease. This metastatic nodal disease is staged using the HN clinical and pathologic nodal definitions for all non-HPV,

non-EBV SCCs found in Chapter 6 of the *AJCC Cancer Staging Manual* (Fig 4 and Table 1).

Larynx. There are no changes to laryngeal T-staging, and again nodal staging follows the changes outlined previously for non-EBV, non-HPV SCCs for the entire HN (Table 1). Unknown primary tumors that are EBV and HPV negative are not assigned to the larynx as outlined above. When one evaluates primary laryngeal tumors, imaging offers utility for evidence of invasion of the paraglottic space (T3) and inner lamina of the thyroid cartilage (T3) or invasion through the outer thyroid cortex or of the cricoid (T4a). Arytenoid and epiglottic cartilage involvement does not change the laryngeal tumor stage.

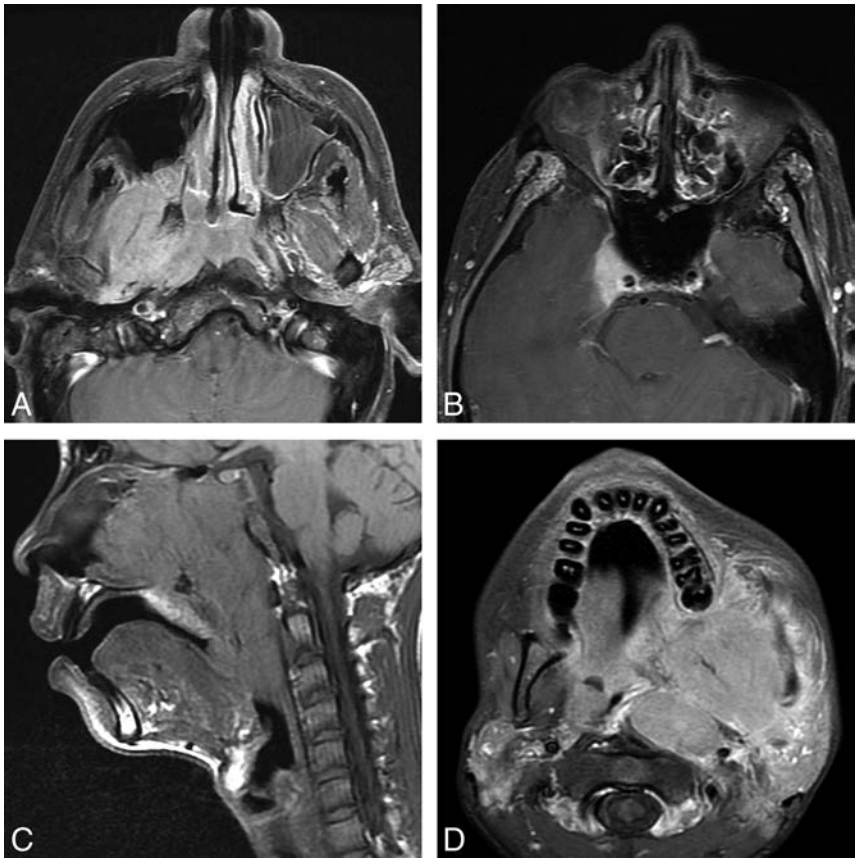

FIG 3. Two patients with nasopharyngeal carcinoma. *A* and *B*, A 64-year-old man with a nasopharyngeal mass found incidentally on PET/CT and determined to be EBV(+) undifferentiated nonkeratinizing carcinoma. Axial T1 postcontrast fat-saturated images (*A* and *B*) demonstrate an asymmetric nasopharyngeal mass with lateral extension to the right masticator space lateral pterygoid muscle. In the seventh edition, this would be T4 disease; however, in the eighth edition, this is only T2 disease. Note however that in this patient, there is also involvement of the pterygoid plates, which is now clarified as T3 disease, and superior extension to the right cavernous sinus, which is T4 disease in both AJCC *Cancer Staging Manual* seventh and eighth editions. *C* and *D*, A 15-year-old boy presenting with epistaxis and a large mass arising from the nasopharynx determined to be EBV(+) undifferentiated nonkeratinizing carcinoma. Sagittal T1 (*C*) shows the large mass filling the nasopharynx, extending inferiorly to the oropharynx and anteriorly to the nasal cavity. Axial postcontrast T1 with fat saturation (*D*) shows lateral extension of the mass into the masticator space but also to the left parotid gland. In the eighth edition, involvement of the parotid gland or extension of tumor beyond the lateral surface of the lateral pterygoid muscle determines T4 status.

Major Salivary Gland Tumors. There have been no changes to the T-staging tables for salivary masses. The N nodal staging table changes reflect those described above for all p16−, EBV− HN nodal disease (Table 1). Again, SCC masses in the parotid gland may reflect metastatic nodal disease, particularly from cutaneous facial and scalp malignancies.

Nasal Cavity and Paranasal Sinuses. There have been no significant changes to the T-staging for nasal cavity and paranasal sinuses, and the N nodal staging tables reflect those described above for the HN (Table 1). Both CT and MR imaging offer advantages for complete pretreatment evaluation of sinonasal malignancies and are often both used. CT offers superior detail for hard palate invasion, while MR imaging allows better discrimination of tumor from obstructed sinus secretions. MR imaging offers a more detailed evaluation for dural or brain parenchymal involvement as well as perineural tumor spread. Both allow nodal evaluation with the caveat that retropharyngeal nodal tumor may be more conspicuous on MR imaging when isodense to prevertebral muscles on contrast-enhanced CT.

Mucosal Melanoma of the HN. There are no changes to this staging system for mucosal melanoma of the HN com-

Table 6: Tumor definitions for nasopharyngeal carcinoma[a]

T Category	T Criteria
Tx	Primary tumor cannot be assessed
T0	No tumor identified, but EBV+ cervical lymph node(s) involvement
Tis	In situ carcinoma
T1	Tumor confined to nasopharynx, or extension to oropharynx and/or nasal cavity without parapharyngeal involvement
T2	Tumor with extension to parapharyngeal space, and/or adjacent soft-tissue involvement (medial pterygoid, lateral pterygoid, prevertebral muscles)
T3	Tumor with infiltration of bony structures at skull base, cervical vertebrae, pterygoid structures, and/or paranasal sinuses
T4	Tumor with intracranial extension, involvement of cranial nerves, hypopharynx, orbit, parotid gland, and/or extensive soft-tissue infiltration beyond the lateral surface of the lateral pterygoid muscle

[a] The eighth edition shows critical changes from the prior edition with downstaging of masticator space involvement from T4 to T2 and clarification of the T-staging for invasion of bony structures. Table adapted with permission of the American Joint Committee on Cancer, Chicago, Illinois. The original source for this material is the *AJCC Cancer Staging Manual*.[1]

Table 7: Oral cavity primary tumor definitions[a]

T Category	T Criteria
Tx	Primary tumor cannot be assessed
Tis	Carcinoma in situ
T1	Tumor ≤2 cm, ≤5-mm DOI; DOI is depth of invasion and not tumor thickness
T2	Tumor ≤2 cm, DOI >5 mm and ≤10 mm or tumor >2 but ≤4-cm and ≤10-mm DOI
T3	Tumor >4 cm or any tumor >10-mm DOI
T4a	Moderately advanced local disease; tumor invades adjacent structures only (eg, through cortical bone of the mandible or maxilla or involves the maxillary sinus or skin of the face); note that superficial erosion of bone/tooth socket (alone) by a gingival primary is not sufficient to classify a tumor as T4
T4b	Very advanced local disease; tumor invades masticator space, pterygoid plates, or skull base and/or encases the internal carotid artery

[a] Note that the greatest diameter of the primary tumor is still measured, but primary tumor depth of invasion is also a critical determinant of T-staging. This is the deep extent of tumor invasion below the surface and is distinct from tumor thickness. Lip tumors are no longer staged along with oral cavity SCC, but using the tables from "Cutaneous Carcinoma of HN." Table adapted with permission of the American Joint Committee on Cancer, Chicago, Illinois. The original source for this material is the *AJCC Cancer Staging Manual*.[1]

Table 8: Tumor definitions for cutaneous carcinoma of the HN[a]

T Category	T Criteria
Tx	Primary tumor cannot be identified
Tis	Carcinoma in situ
T1	Tumor ≤2 cm in greatest dimension
T2	Tumor >2 but ≤4 cm in greatest dimension
T3	Tumor >4 cm in maximum dimension or minor bone erosion or perineural invasion, or deep invasion[b]
T4a	Tumor with gross cortical bone/marrow invasion
T4b	Tumor with skull base invasion and/or skull base foramen involvement

[a] This new chapter in the eighth edition should be used for all HN cutaneous malignancies except the eyelid and cutaneous melanoma and Merkel cell carcinoma. Lip tumors are now staged using this table. Table adapted with permission of the American Joint Committee on Cancer, Chicago, Illinois. The original source for this material is the *AJCC Cancer Staging Manual*.[1]

[b] Deep invasion is defined as invasion beyond the subcutaneous fat or >6 mm (as measured from the granular layer of adjacent normal epidermis to the base of the tumor). Perineural invasion for the T3 classification is defined as tumor cells within the nerve sheath of a nerve lying deeper than the dermis or measuring ≥0.1 mm in caliber or presenting with clinical or radiographic involvement of named nerves without skull base invasion or transgression.

pared with the seventh edition. As a reminder for radiologists when evaluating these aggressive tumors, there is only T3 or T4a/b disease (there is no T1 or T2). There is also a tumor-specific mucosal melanoma nodal staging in which N0 is the absence of nodal metastasis and N1 is the presence of regional nodal disease. Nx is used when regional nodes cannot be assessed. Extranodal extension has not been added to this nodal staging. There is not yet a prognostic stage grouping for mucosal melanoma.

Final Reminders about Staging

1) For all sites in the head and neck, M0 is used when there is a negative metastatic work-up or there are no known metastases. M1 is the presence of metastatic disease. There is no Mx designation.

2) When in doubt, the general rules of AJCC staging are to assign the lower of the two T, N, or M categories—that is, to downstage rather than upstage.[17]

3) Tumor staging is a team effort. The radiologist can add significant value to tumor boards by attending them, explaining the radiologic subtleties, and being aware of the critical features that distinguish different T and N categories.

Summary

Perhaps the most dramatic changes noticeable to radiologists who are participating in tumor boards or who have been making it a practice to include TNM categories in the radiology report are those relating to HPV-related p16+ OPSCC and nodal staging. There is a dramatic downstaging of HPV-related p16(+) OPSCC disease with the new staging system, reflecting the overall markedly better prognosis of these tumors compared with p16(−) OPSCC. Because p16/HPV status may be unavailable to the radiologist at the time of reporting, it remains important, as with all reports for tumor staging, to include all the relevant imaging information of tumor size and extent of invasion. This information can then be combined with immunohistochemistry to determine the accurate p16(+) or p16(−) OPSCC clinical stage.

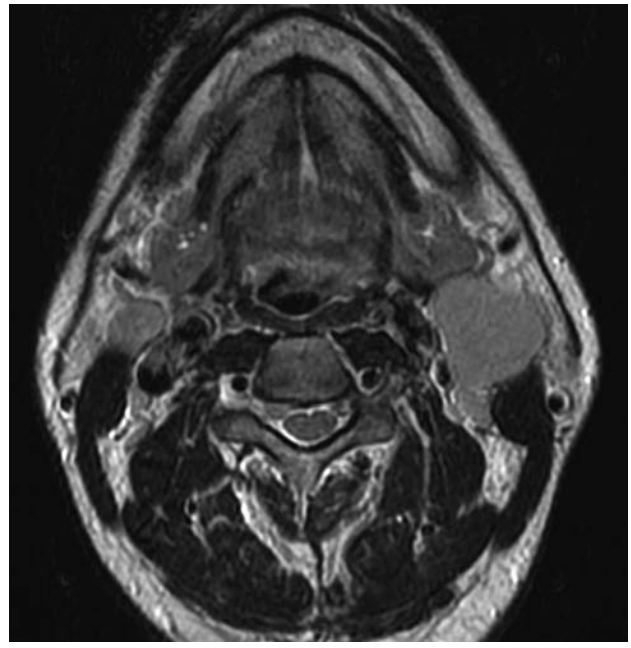

FIG 4. Axial T2-weighted MR image through the neck in a 45-year-old man presenting with neck masses. The enlarged solid left level 2A node measured 3.5 cm in maximal diameter with additional abnormal nodes seen on the right at 2A and bilaterally at levels 3 and 5A. No primary tumor was evident on clinical examination or on this MR imaging. In the absence of a primary tumor, it is difficult to determine which nodal table to use, though most unknown primary tumors are HPV/p16(+) OPSCC. If fine-needle aspiration of the node reveals HPV/p16(+), then an OPSCC primary would be assumed and this would be assigned T0N2. If pathology revealed HPV-negative, p16 negative, and ENB negative, then this would be assigned N2c and no primary site assigned. Fine-needle aspiration revealed this to be undifferentiated, nonkeratinizing carcinoma EBV+, with categories then assigned as T0N2 NPC.

Nodal staging has also expanded so that there are different clinical nodal categories (cN) for HPV/p16(+) OPSCC, EBV(+) NPC, and all other HN SCCs. There are also 2 new pathologic nodal staging systems (pN) for HPV/p16(+) OPSCC and all other HN SCCs when neck dissections are performed. The standard imaging-based classification should be used to describe nodal levels, and it is important that radiologists clarify both ipsilateral and contralateral nodes that appear positive and whether there is perinodal infiltration of adjacent fat or muscles, the strongest imaging features supporting ENE. Currently the staging designation of ENE+ requires gross clinical examination evidence of ENE or pathologic demonstration of ENE, but it will be very useful for radiologists to describe features suspicion for ENE so that the clinician can re-evaluate the clinical nodal status.

Additional, less complex changes have been made to the staging in other HN sections to reflect the changing understanding of tumor biology and pathophysiology and patient outcomes. Radiologists are encouraged to become familiar with the new TNM system when reporting staging scans and to include all relevant imaging information in reports to facilitate cancer care. Regardless of whether an individual radiologist includes TNM categories in their report, it is important that we try to understand the process of tumor staging, the critical role radiologists play in providing staging information, and the value we add to patient care. The AJCC and UICC eighth editions will be implemented for staging new tumors as of January 1, 2018.

Disclosures: Christine M. Glastonbury—*RELATED: Support for Travel to Meetings for the Study or Other Purposes:* all authors reimbursed for travel for a AJCC committee meeting. William M. Lydiatt—*UNRELATED: Royalties:* Up-to-Date and *Cancers of the Mouth and Throat.*

REFERENCES

1. Amin MB, Edge SB, Greene FL, et al, eds. *AJCC Cancer Staging Manual*. 8th ed. New York: *Springer-Verlag*; 2017
2. Brierley JD, Gospodarowicz MK, Wittekind C, eds, *TNM Classification of Malignant Tumours.* Hoboken: Wiley Blackwell; 2017
3. Edge S, Byrd DR, Compton CC, et al, eds. *AJCC Cancer Staging Manual.* 7th ed. New York: Springer-Verlag; 2010
4. Ang KK, Harris J, Wheeler R, et al. **Human papillomavirus and survival of patients with oropharyngeal cancer.** *N Engl J Med* 2010;363: 24–35 CrossRef Medline
5. O'Sullivan B, Huang SH, Su J, et al. **Development and validation of a staging system for HPV-related oropharyngeal cancer by the International Collaboration on Oropharyngeal Cancer Network for Staging (ICON-S): a multicentre cohort study.** *Lancet Oncol* 2016; 17:440–51 CrossRef Medline
6. Huang SH, Xu W, Waldron J, et al. **Refining American Joint Committee on Cancer/Union for International Cancer Control TNM stage and prognostic groups for human papillomavirus-related oropharyngeal carcinomas.** *J Clin Oncol* 2015;33:836–45 CrossRef Medline
7. Haughey BH, Sinha P, Kallogjeri D, et al. **Pathology-based staging for HPV-positive squamous carcinoma of the oropharynx.** *Oral Oncol* 2016;62:11–19 CrossRef Medline
8. Wreesmann VB, Katabi N, Palmer FL, et al. **Influence of extracapsular nodal spread extent on prognosis of oral squamous cell carcinoma.** *Head Neck* 2016;38(suppl 1):E1192–99 CrossRef Medline
9. Myers JN, Greenberg JS, Mo V, et al. **Extracapsular spread: a significant predictor of treatment failure in patients with squamous cell carcinoma of the tongue.** *Cancer* 2001;92:3030–36 Medline
10. Sinha P, Lewis JS Jr, Piccirillo JF, et al. **Extracapsular spread and adjuvant therapy in human papillomavirus-related, p16-positive oropharyngeal carcinoma.** *Cancer* 2012;118:3519–30 CrossRef Medline
11. Lydiatt WM, Patel SG, O'Sullivan B, et al. **Head and neck cancers-major changes in the American Joint Committee on cancer eighth edition cancer staging manual.** *CA Cancer J Clin* 2017;67:122–37 CrossRef Medline
12. King AD, Tse GM, Yuen EH, et al. **Comparison of CT and MR imaging for the detection of extranodal neoplastic spread in metastatic neck nodes.** *Eur J Radiol* 2004;52:264–70 CrossRef Medline
13. Lodder WL, Lange CA, van Velthuysen ML, et al. **Can extranodal spread in head and neck cancer be detected on MR imaging.** *Oral Oncol* 2013;49:626–33 CrossRef Medline
14. Prabhu RS, Magliocca KR, Hanasoge S, et al. **Accuracy of computed tomography for predicting pathologic nodal extracapsular extension in patients with head-and-neck cancer undergoing initial surgical resection.** *Int J Radiat Oncol Biol Phys* 2014;88:122–29 CrossRef Medline
15. Pan JJ, Ng WT, Zong JF, et al. **Prognostic nomogram for refining the prognostication of the proposed 8th edition of the AJCC/UICC staging system for nasopharyngeal cancer in the era of intensity-modulated radiotherapy.** *Cancer* 2016;122:3307–15 CrossRef Medline
16. Motz K, Qualliotine JR, Rettig E, et al. **Changes in unknown primary squamous cell carcinoma of the head and neck at initial presentation in the era of human papillomavirus.** *JAMA Otolaryngol Head Neck Surg* 2016;142:223–28 CrossRef Medline
17. Gress DM, Edge SB, Greene FL, et al. **Principles of cancer staging**. In: Amin MB, Edge SB, Greene FL, et al, eds. *AJCC Cancer Staging Manual.* 8th Ed. New York: Springer-Verlag; 2017:3–30

Wide Variability in Prethrombectomy Workflow Practices in the United States: A Multicenter Survey

A.P. Kansagra, G.C. Meyers, M.S. Kruzich, D.T. Cross III, and C.J. Moran

ABSTRACT

BACKGROUND AND PURPOSE: Clinical outcomes in patients with acute ischemic stroke caused by large vessel occlusion depend on the speed and quality of workflows leading to mechanical thrombectomy. In the absence of universally accepted best practices for workflow, developing stroke hospitals can benefit from improved awareness of real-world workflows in effect at experienced centers. To this end, we surveyed prethrombectomy workflow practices at stroke centers throughout the United States.

MATERIALS AND METHODS: E-mail and phone interviews were conducted with neurointerventional team members at 30 experienced, endovascular-capable stroke centers. Questions were chosen to reflect workflow components of triage, team activation, transport, case setup, and anesthesia.

RESULTS: There is wide variation in prethrombectomy workflows. At 53% of institutions, nonphysician staff respond to stroke alerts alongside physicians. Imaging triage involves noninvasive angiography or perfusion imaging at 97% and 63% of institutions, respectively. Neurointerventional consultation is initiated before the completion of neuroimaging at 86% of institutions, and the team is activated before a final treatment decision at 59%. The neurointerventional team most commonly arrives within 30 minutes. Patients may be transported to the neuroangiography suite before team arrival at 43% of institutions. Procedural trays are set up in advance of team arrival at 13% of centers; additional thrombectomy devices are centrally stored at 54%. A power injector for angiographic runs is consistently used at 43% of institutions. Anesthesiology routinely supports thrombectomies at 67% of institutions.

CONCLUSIONS: Prethrombectomy workflows vary widely between experienced centers. Improved awareness of real-world workflows and their variations may help to guide institutions in designing their own protocols of care.

ABBREVIATIONS: LVO = large vessel occlusion; NI = neurointerventional

Recent clinical trials have conclusively demonstrated the outcome benefit of mechanical thrombectomy in selected patients with acute ischemic stroke caused by large vessel occlusion (LVO).[1-5] For these patients, the likelihood of a good neurologic outcome depends on the time elapsed between symptom onset and revascularization.[6-11] Indeed, the negative results of 3 earlier clinical trials[12-14] may be attributed in part to prolonged treatment delays.[8,15-17]

These developments have sparked considerable interest in designing efficient workflows for diagnosis and treatment that can reduce the time between patient presentation and thrombectomy.[7,18-20] Although many of these efforts have been successful, there is currently no broadly accepted consensus for optimal prethrombectomy workflow. In the absence of such consensus, individual centers have implemented a heterogeneous assortment of workflows that may be influenced by individual physician preference, institution-specific factors, or incomplete awareness of effective solutions at competing institutions.

Given the overall importance of prethrombectomy workflow on time to treatment, improved guidance is needed for hospitals looking to redesign their own systems to care for patients with LVO. Understanding the range of current practice patterns is an important first step toward that goal. In this work, we aimed to attain a broader perspective on prethrombectomy workflow prac-

Received June 13, 2017; accepted after revision July 13.

From the Mallinckrodt Institute of Radiology (A.P.K., D.T.C., C.J.M.) and Departments of Neurosurgery (A.P.K., D.T.C., C.J.M.) and Neurology (A.P.K.), Washington University School of Medicine, St. Louis, Missouri; and Barnes-Jewish Hospital (G.C.M., M.S.K.), St. Louis, Missouri.

Paper previously presented at: Annual Meeting of the Society of NeuroInterventional Surgeons, July 25–29, 2016; Boston, Massachusetts, and Annual Meeting of the Society of Vascular and Interventional Neurology, November 16–29, 2016; Brooklyn, New York.

Please address correspondence to Akash P. Kansagra, MD, MS, Mallinckrodt Institute of Radiology, 510 South Kingshighway Blvd, Campus Box 8131, Saint Louis, MO 63110; e-mail: apkansagra@gmail.com; @AkashKansagra

Indicates article with supplemental on-line table.

http://dx.doi.org/10.3174/ajnr.A5384

FIGURE. Locations of stroke centers responding to the survey.

tices by conducting a nationwide survey of practices in effect at experienced stroke centers, identify highly consistent workflow steps that may indicate general agreement on best practices in real-world conditions, and recognize areas of greater workflow variability that may suggest that such a consensus has yet to emerge.

MATERIALS AND METHODS

Institutional review board approval was obtained for this survey. Target institutions were identified based on American Heart Association certification as an Advanced Comprehensive Stroke Center or endovascular-capable Advanced Primary Stroke Center, or the presence of a fellowship-level neurointerventional (NI) training program. Contact information was obtained from institutional Web sites and/or hospital operators at each of these centers, and an attempt was made to contact NI team members (physicians, technologists, and nurses who are directly involved in thrombectomy procedures) via telephone during normal business hours between August 2015 and November 2015. If this initial attempt was unsuccessful, a second attempt was made between 1 and 3 weeks later.

At centers where contact was successfully established, interviews were conducted by experienced NI technologists with NI team members via telephone or e-mail, depending on the preference of the person being surveyed. Each of these centers reported performing at least 50 thrombectomy cases in the previous 12 months. Survey questions were chosen based on perceived areas of opportunity to reduce time to treatment or workflow complexity at our institution, as suggested by a multidisciplinary group of physicians, technologists, and nurses while streamlining our own protocol for the management of patients with LVO. Questions were categorized into primary workflow components of triage, team activation, transport, case setup, and anesthesia. Respondents were asked to consider a typical patient when providing answers. Responses were stored in an electronic data base. No compensation was offered to study participants. Data are reported as simple proportions.

RESULTS

Responses

The complete list of questions and answers is reported in the Online Table. An attempt was made to contact NI team members at 50 different institutions. Of these, 60% (30/50) responded in whole or in part to the survey (Figure). These institutions included 22 Advanced Comprehensive Stroke Centers, 6 Advanced Primary Stroke Centers, and 2 Massachusetts Designated Primary Stroke Services Hospitals. Of these 30 institutions, 60% (18/30) included a postresidency NI fellowship training program.

Triage

Fifty-three percent (16/30) of institutions reported creating an acute response team of nonphysicians to facilitate triage in the emergency department. CT was the preferred imaging technique and was used as the sole modality at 90% (27/30) of institutions. Noninvasive angiographic imaging was incorporated into routine patient selection at 97% (29/30) of centers, whereas noninvasive perfusion imaging was routinely used at 63% (19/30) of facilities.

Team Activation

At 93% (28/30) of institutions, initial contact with the NI service was directed only to an NI physician—typically the NI fellow at centers with fellowship training programs—rather than the full NI team. Initial contact was made before image acquisition at 86% (25/29) of centers, but activation of the full NI team before reach-

ing a final decision to treat occurred at only 59% (17/29) of institutions.

Activation of the full NI team occurred by direct contact from the NI physician at 63% of institutions (19/30) and through a hospital operator at 23% (7/30). In total, 97% (29/30) of institutions had a defined response time requirement for the NI nurses and technologists, most commonly 30 minutes.

Transport

The emergency department team (including any responding neurologists in the emergency department) took part in transport of the patient to the neuroangiography suite at 87% (26/30) of centers, whereas the NI team was routinely involved in transport at 20% (6/30) of institutions. Patients were permitted to be transported to the neuroangiography suite before NI team arrival at 43% (12/28) of centers.

Case Setup

The procedural tray was opened by the NI team upon arrival at 90% (27/30) of institutions. The procedural tray comprised a basic diagnostic angiography tray at 90% (27/30) of centers, with additional supplies needed for mechanical thrombectomy added as necessary. Additional thrombectomy supplies were stored in a centralized location in the neuroangiography suite at 54% (15/28) of institutions. A power injector was routinely or variably used at 47% (14/30) of centers, but was not kept preloaded with contrast at any institution (0/30).

Anesthesia

Members of the anesthesiology service routinely assisted mechanical thrombectomy at 67% (20/30) of institutions and variably at 7% (2/30). Regardless of anesthesiology service involvement, the preferred type of anesthesia was conscious sedation at 43% (12/28) of centers and general anesthesia at 21% (6/28).

DISCUSSION

With the goal of maximizing the clinical outcome benefit of mechanical thrombectomy, several groups have described efficient workflows or suggested improvements to facilitate timely thrombectomy in patients with LVO.[7,16,18-24] These case studies can serve as important prototypes for other hospitals attempting to redesign their own prethrombectomy workflows. However, these prototypes are likely to be heavily influenced by institution-specific factors. As such, hospitals looking to these examples for guidance may not become aware of workflow variations in effect at other experienced centers. By reviewing in aggregate the workflows at many centers rather than just a single facility, our findings offer a more institution-agnostic view of real-world prethrombectomy workflows. Moreover, the considerable heterogeneity we identified in these workflows suggest areas where consensus on universal best practices is not established or does not exist, while also suggesting opportunities for workflow customization tailored to conditions at individual hospitals.

Mirroring the practices in recent positive thrombectomy trials,[1-5] we found nearly universal use of noninvasive angiography to identify LVO before attempted thrombectomy. However, we also found that nearly two-thirds of institutions routinely used perfusion imaging for patient selection despite the fact that perfusion imaging was not consistently used in the initial trials demonstrating the effectiveness of thrombectomy.[2-5] Overall, only a small minority of institutions made routine use of MR imaging for patient selection, presumably reflecting resource constraints and the greater time typically required for MR imaging.

One common workflow solution was to have an acute response team of nonphysicians able to respond immediately to cases of suspected LVO alongside neurology and emergency department physicians. These teams are fluent in prethrombectomy workflows and can facilitate timely management in the acute care setting. Several respondents expressed frustration at a perceived lack of awareness among nonspecialists of the need for rapid evaluation in patients with LVO and noted that acute response teams can bridge this awareness gap until emergency department teams gain familiarity with modern reperfusion strategies in LVO.

At most institutions, initial contact occurs with a single NI physician who is responsible in turn for notifying the remainder of the NI team. Some hospitals facilitate this notification process by designating specific personnel to identify and contact the full NI team, freeing the physician to focus on medical decision-making. A large majority of facilities initiate NI consultation on clinical grounds even before the acquisition of neuroimaging necessary for patient selection. This approach[25] may confer some time benefit, but comes at the cost of more frequent consultation for patients who later prove to have imaging contraindications to thrombectomy (eg, intracranial hemorrhage, absence of LVO, or a large burden of completed infarction). However, we note that though initial NI consultation precedes neuroimaging at most institutions, it is far less common to activate the full NI team before completing the clinical and imaging evaluation necessary to fully assess the appropriateness of thrombectomy. Once the NI team is activated, most hospitals set a mandatory response time for NI team members.

Transport of patients to the neuroangiography suite is most commonly handled by members of the emergency department team. Furthermore, at many facilities, patients can be transported to the neuroangiography suite by the emergency department team before the arrival of the NI team. Even if the NI team is in house, active ownership of the patient transport process by the emergency department team may allow the NI team to work in parallel to set up the neuroangiography suite. Thus, regardless of NI team location, an emergency department–led transport process may help to minimize the actual time penalty associated with team travel and room setup.

Most commonly, a procedural tray is set up by the NI team upon arrival, as opposed to a "dry tray" set up in advance by the NI team or a conventional tray set up by an in-house designee while the NI team travels to the hospital. Each of these approaches has its virtues; setting up the tray in advance of team arrival likely confers a small time benefit, but sacrifices a clear chain of custody for sterile supplies. Regardless of the approach, most NI teams save time by initially opening a basic diagnostic angiography tray, thereby allowing the NI physician to establish arterial access and perform initial angiographic runs while other NI team members

work in parallel to retrieve additional thrombectomy supplies. Curiously, many centers have not centralized the location of these supplies within the neuroangiography suite—for example, on a supply cart or cabinet dedicated to stroke interventions—which is a simple and straightforward means to facilitate the retrieval of thrombectomy devices and reduce the cognitive burden on NI team members.

The preferred type of anesthesia during thrombectomy procedures is most commonly conscious sedation, possibly reflecting a desire to avoid the time delay of intubation or concern about early data suggesting worsened postthrombectomy outcomes with general anesthesia.[26-28] Regardless of the type of anesthesia used, members of the anesthesiology service routinely assist thrombectomy at two-thirds of the surveyed institutions. Although our and other investigators' experience is that door-to-puncture times are shortest when the number of teams engaged in the prethrombectomy workflow is minimized,[16,22] these data suggest that many NI physicians value having more experienced personnel provide sedation and/or anesthesia, thereby allowing NI physicians to concentrate on the technical aspects of the procedure.

There are 3 principal limitations of this work. First, although we have captured details about the degree of workflow variation between hospitals, we cannot evaluate the validity of these workflow variations without knowledge of door-to-puncture times and clinical outcomes, which many hospitals are unwilling or unable to disclose. Thus, although our data may suggest general agreement on highly consistent workflow steps, we cannot define best practices on the basis of patient impact. Second, although the sample size of 30 institutions is sufficient to extract qualitative insights into practice patterns and the general scale of workflow variation, it is not sufficiently large to permit accurate quantitative assessment. Third, all surveyed institutions are experienced stroke centers, which likely skews demographics toward large, academic institutions that may have different infrastructure and resources than smaller, nonacademic centers.

Our results suggest an opportunity for future work to detail the impact of specific workflow variations on clinical outcomes across multiple institutions. However, it is important to note that not all workflow variations will meaningfully impact time to treatment, though all are likely to impact workflow complexity. The benefits of reduced workflow complexity can be difficult to capture in patient-centered clinical outcome data, but may include increased speed, greater capacity to multitask, fewer errors, and decreased cognitive stress, all of which are likely to be important during critical and time-sensitive procedures.

CONCLUSIONS

Even at experienced stroke centers, there is considerable heterogeneity in real-world workflow processes leading to mechanical thrombectomy. These differences may reflect institution-specific factors or incomplete awareness of workflow variations in effect at other facilities. Knowledge of the range of prethrombectomy workflows seen in actual clinical practice can guide institutions looking to redesign their own systems of care in a manner best suited to their needs.

ACKNOWLEDGMENTS

The authors thank Ashley Whitehead, RN, for suggesting the need for a multicenter survey.

Disclosures: Christopher J. Moran—*UNRELATED*: *Consultancy*: Medtronic, Microvention, Neurana; *Payment for Lectures (Including Service on Speakers Bureaus)*: Medtronic; *Travel/Accommodations/Meeting Expenses Unrelated to Activities Listed*: Medtronic, Microvention, Neurana.

REFERENCES

1. Berkhemer OA, Fransen PS, Beumer D, et al. **A randomized trial of intraarterial treatment for acute ischemic stroke.** *N Engl J Med* 2015; 372:11–20 CrossRef Medline
2. Campbell BC, Mitchell PJ, Kleinig TJ, et al. **Endovascular therapy for ischemic stroke with perfusion-imaging selection.** *N Engl J Med* 2015;372:1009–18 CrossRef Medline
3. Goyal M, Demchuk AM, Menon BK, et al. **Randomized assessment of rapid endovascular treatment of ischemic stroke.** *N Engl J Med* 2015;372:1019–30 CrossRef Medline
4. Jovin TG, Chamorro A, Cobo E, et al. **Thrombectomy within 8 hours after symptom onset in ischemic stroke.** *N Engl J Med* 2015;372: 2296–306 CrossRef Medline
5. Saver JL, Goyal M, Bonafe A, et al. **Stent-retriever thrombectomy after intravenous t-PA vs. t-PA alone in stroke.** *N Engl J Med* 2015; 372:2285–95 CrossRef Medline
6. Fransen PS, Berkhemer OA, Lingsma HF, et al. **Time to reperfusion and treatment effect for acute ischemic stroke: a randomized clinical trial.** *JAMA Neurol* 2016;73:190–96 CrossRef Medline
7. Goyal M, Jadhav AP, Bonafe A, et al. **Analysis of workflow and time to treatment and the effects on outcome in endovascular treatment of acute ischemic stroke: results from the SWIFT PRIME randomized controlled trial.** *Radiology* 2016;279:888–97 CrossRef Medline
8. Khatri P, Yeatts SD, Mazighi M, et al. **Time to angiographic reperfusion and clinical outcome after acute ischaemic stroke: an analysis of data from the Interventional Management of Stroke (IMS III) phase 3 trial.** *Lancet Neurol* 2014;13:567–74 CrossRef Medline
9. Mazighi M, Chaudhry SA, Ribo M, et al. **Impact of onset-to-reperfusion time on stroke mortality: a collaborative pooled analysis.** *Circulation* 2013;127:1980–85 CrossRef Medline
10. Menon BK, Sajobi TT, Zhang Y, et al. **Analysis of workflow and time to treatment on thrombectomy outcome in the endovascular treatment for small core and proximal occlusion ischemic stroke (ESCAPE) randomized, controlled trial.** *Circulation* 2016;133: 2279–86 CrossRef Medline
11. Sheth SA, Jahan R, Gralla J, et al. **Time to endovascular reperfusion and degree of disability in acute stroke.** *Ann Neurol* 2015;78:584–93 CrossRef Medline
12. Broderick JP, Palesch YY, Demchuk AM, et al. **Endovascular therapy after intravenous t-PA versus t-PA alone for stroke.** *N Engl J Med* 2013;368:893–903 CrossRef Medline
13. Ciccone A, Valvassori L, Nichelatti M, et al. **Endovascular treatment for acute ischemic stroke.** *N Engl J Med* 2013;368:904–13 CrossRef Medline
14. Kidwell CS, Jahan R, Gornbein J, et al. **A trial of imaging selection and endovascular treatment for ischemic stroke.** *N Engl J Med* 2013; 368:914–23 CrossRef Medline
15. Goyal M, Almekhlafi M, Menon B, et al. **Challenges of acute endovascular stroke trials.** *Stroke* 2014;45:3116–22 CrossRef Medline
16. Goyal M, Menon BK, Hill MD, et al. **Consistently achieving computed tomography to endovascular recanalization <90 minutes: solutions and innovations.** *Stroke* 2014;45:e252–256 CrossRef Medline
17. Qureshi AI, Abd-Allah F, Aleu A, et al. **Endovascular treatment for acute ischemic stroke patients: implications and interpretation of IMS III, MR RESCUE, and SYNTHESIS EXPANSION trials: a report from the Working Group of International Congress of Interventional Neurology.** *J Vasc Interv Neurol* 2014;7: 56–75 Medline

18. Aghaebrahim A, Streib C, Rangaraju S, et al. **Streamlining door to recanalization processes in endovascular stroke therapy.** *J Neurointerv Surg* 2017;9:340–45 CrossRef Medline
19. Asif KS, Lazzaro MA, Zaidat O. **Identifying delays to mechanical thrombectomy for acute stroke: onset to door and door to clot times.** *J Neurointerv Surg* 2014;6:505–10 CrossRef Medline
20. Mehta BP, Leslie-Mazwi TM, Chandra RV, et al. **Reducing door-to-puncture times for intra-arterial stroke therapy: a pilot quality improvement project.** *J Am Heart Assoc* 2014;3:e000963 CrossRef Medline
21. Eesa M, Menon BK, Hill MD, et al. **Achieving faster recanalization times by IA thrombolysis in acute ischemic stroke: where should we direct our efforts?** *Interv Neuroradiol* 2011;17:228–34 CrossRef Medline
22. Menon BK, Almekhlafi MA, Pereira VM, et al. **Optimal workflow and process-based performance measures for endovascular therapy in acute ischemic stroke: analysis of the Solitaire FR thrombectomy for acute revascularization study.** *Stroke* 2014;45:2024–29 CrossRef Medline
23. Rai AT, Smith MS, Boo S, et al. **The 'pit-crew' model for improving door-to-needle times in endovascular stroke therapy: a Six-Sigma project.** *J Neurointerv Surg* 2016;8:447–52 CrossRef Medline
24. Zerna C, Assis Z, d'Esterre CD, et al. **Imaging, intervention, and workflow in acute ischemic stroke: the Calgary approach.** *AJNR Am J Neuroradiol* 2016;37:978–84 CrossRef Medline
25. van Heerden J, Yan B, Churilov L, et al. **Picture-to-puncture time in acute stroke endovascular intervention: are we getting faster?** *J Neurointerv Surg* 2015;7:564–68 CrossRef Medline
26. Brinjikji W, Murad MH, Rabinstein AA, et al. **Conscious sedation versus general anesthesia during endovascular acute ischemic stroke treatment: a systematic review and meta-analysis.** *AJNR Am J Neuroradiol* 2015;36:525–29 CrossRef Medline
27. Jumaa MA, Zhang F, Ruiz-Ares G, et al. **Comparison of safety and clinical and radiographic outcomes in endovascular acute stroke therapy for proximal middle cerebral artery occlusion with intubation and general anesthesia versus the nonintubated state.** *Stroke* 2010;41:1180–84 CrossRef Medline
28. Takahashi C, Liang CW, Liebeskind DS, et al. **To tube or not to tube? The role of intubation during stroke thrombectomy.** *Front Neurol* 2014;5:170 CrossRef Medline

Comparison between the Prebolus T1 Measurement and the Fixed T1 Value in Dynamic Contrast-Enhanced MR Imaging for the Differentiation of True Progression from Pseudoprogression in Glioblastoma Treated with Concurrent Radiation Therapy and Temozolomide Chemotherapy

J.G. Nam, K.M. Kang, S.H. Choi, W.H. Lim, R.-E. Yoo, J.-H. Kim, T.J. Yun, and C.-H. Sohn

ABSTRACT

BACKGROUND AND PURPOSE: Glioblastoma is the most common primary brain malignancy and differentiation of true progression from pseudoprogression is clinically important. Our purpose was to compare the diagnostic performance of dynamic contrast-enhanced pharmacokinetic parameters using the fixed T1 and measured T1 on differentiating true from pseudoprogression of glioblastoma after chemoradiation with temozolomide.

MATERIALS AND METHODS: This retrospective study included 37 patients with histopathologically confirmed glioblastoma with new enhancing lesions after temozolomide chemoradiation defined as true progression ($n = 15$) or pseudoprogression ($n = 22$). Dynamic contrast-enhanced pharmacokinetic parameters, including the volume transfer constant, the rate transfer constant, the blood plasma volume per unit volume, and the extravascular extracellular space per unit volume, were calculated by using both the fixed T1 of 1000 ms and measured T1 by using the multiple flip-angle method. Intra- and interobserver reproducibility was assessed by using the intraclass correlation coefficient. Dynamic contrast-enhanced pharmacokinetic parameters were compared between the 2 groups by using univariate and multivariate analysis. The diagnostic performance was evaluated by receiver operating characteristic analysis and leave-one-out cross validation.

RESULTS: The intraclass correlation coefficients of all the parameters from both T1 values were fair to excellent (0.689–0.999). The volume transfer constant and rate transfer constant from the fixed T1 were significantly higher in patients with true progression ($P = .048$ and .010, respectively). Multivariate analysis revealed that the rate transfer constant from the fixed T1 was the only independent variable (OR, 1.77×10^5) and showed substantial diagnostic power on receiver operating characteristic analysis (area under the curve, 0.752; $P = .002$). The sensitivity and specificity on leave-one-out cross validation were 73.3% (11/15) and 59.1% (13/20), respectively.

CONCLUSIONS: The dynamic contrast-enhanced parameter of rate transfer constant from the fixed T1 acted as a preferable marker to differentiate true progression from pseudoprogression.

ABBREVIATIONS: DCE = dynamic contrast-enhanced; K_{ep} = rate transfer constant; K^{trans} = volume transfer constant; TMZ = temozolomide; V_p = the blood plasma volume per unit volume of tissue; V_e = the extravascular extracellular space per unit volume of tissue; AUC = area under the curve

Glioblastoma is the most common primary brain malignancy, and concurrent chemoradiation with temozolomide (TMZ) after surgical resection is the standardized treatment known to exhibit the best survival for patients.[1] For the TMZ chemoradiation treatment, the well-known radiologic false progression (so-called "pseudoprogression") has been previously reported to appear in approximately 20% of patients after their first posttreatment MR imaging.[2,3] This phenomenon is most conspicuous at 12 weeks after chemoradiation therapy and is regarded to result from the transient treatment-induced changes of the capillary and cell membrane permeability, distortion of the BBB, and alterations in cell metabolism.[2] Because TMZ is one of the few limited treatment options for patients with glioblastoma, revised Response Assessment in Neuro-Oncology criteria accept the radiologic decision of true progression only when the lesion increases in the follow-up imaging after the completion of 6 cycles of adjuvant chemotherapy.[4] However, in this clinical setting, patients with true progression may suffer from the side effects of ineffective chemotherapy and be deprived of opportunities to pursue alternative treatments such as bevacizumab chemotherapy. Therefore, it is clinically important to distinguish true progres-

Received February 23, 2017; accepted after revision July 24.

From the Department of Radiology (J.G.N., K.M.K., S.H.C., W.H.L., R.-E.Y., J.-H.K., T.J.Y., C.-H.S.), Seoul National University Hospital, Seoul, Korea; and Center for Nanoparticle Research, Institute for Basic Science (S.H.C., C.-H.S.) and School of Chemical and Biological Engineering (S.H.C.), Seoul National University, Seoul, Korea.

Please address correspondence to Koung Mi Kang, MD, Department of Radiology, Seoul National University Hospital, 101 Daehangno, Jongno-gu, Seoul 110-744, Korea; e-mail: we3001@gmail.com

http://dx.doi.org/10.3174/ajnr.A5417

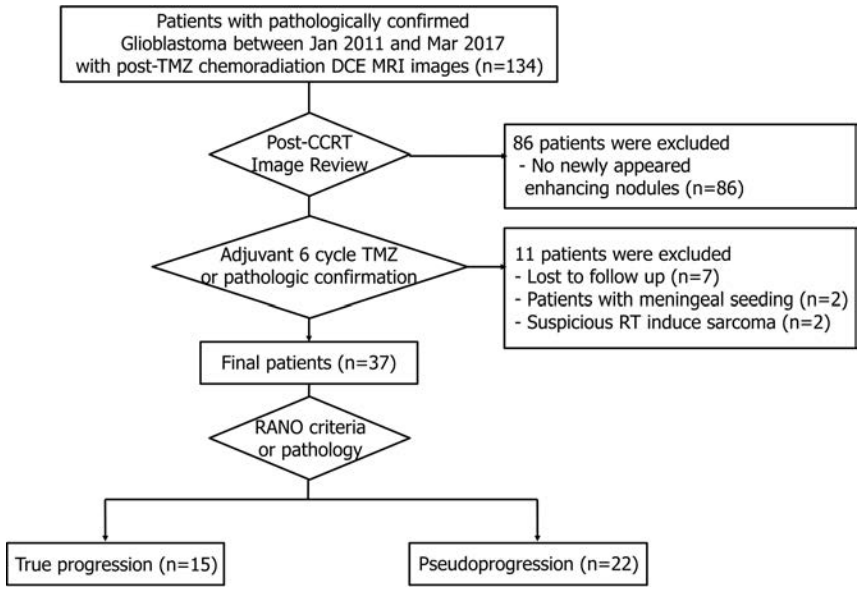

FIG 1. Flowchart of the inclusion and exclusion criteria of our study population.

sion from pseudoprogression after 12 weeks of chemoradiation before the administration of adjuvant chemotherapy.

There have been continuous efforts to differentiate true progression by using conventional MR imaging techniques with contrast enhancement, DWI, or PWI,[5-9] but achieving clinically credible differentiation still remains challenging. Dynamic contrast-enhanced (DCE) MR imaging can noninvasively provide pharmacokinetic parameters representing the microcirculation of the tissue; these parameters include the volume transfer constant (K^{trans}), the rate transfer constant (K_{ep}), the blood plasma volume per unit volume of tissue (V_e), and the extravascular extracellular space per unit volume of tissue (V_p). A few studies reported that some parameters, such as K^{trans} and V_e, showed significant differences between true progression and pseudoprogression[10,11]; however, there has been a lack of studies that meticulously explored the diagnostic performance of all DCE parameters in accordance with the prebolus T1 acquisition methods.

To derive the pharmacokinetic parameters from the DCE MR imaging, a prebolus T1 is required at the initial step to obtain a concentration-time curve.[12] Between 2 options of the precontrast T1 value, the measured and the fixed T1, the baseline T1 measurement is theoretically the more accurate method reflecting the nature of the tissue. However, the fixed T1 method, less prone to systematic errors resulting from scale factor miscalibration and motion susceptibility, has been reported to be more reliable.[12-14] Among T1 measurement methods, because of the long acquisition time, standard inversion recovery is prone to systemic error and also is less applicable in routine clinical practice. The multiple flip-angle method is generally regarded as the clinically more applicable method compared with the inversion-recovery method because of its reduced acquisition time and decreased motion artifacts.[15,16]

Therefore, the purpose of this study was to evaluate the value of the pharmacokinetic parameters from DCE MR imaging in differentiating true progression from pseudoprogression of glioblastoma after TMZ chemoradiation as well as to compare the diagnostic performance of the following 2 methods in calculating the baseline T1: the T1 measurement when using the multiple flip-angle method versus using the fixed T1 of 1000 ms.

MATERIALS AND METHODS

Patients

The institutional review board of Seoul National University Hospital approved this retrospective study, and the requirement for informed consent was waived. Using a computerized search of the pathology records at our institution and reviewing the electronic medical records, we identified 134 consecutive patients pathologically diagnosed with glioblastoma after either surgical resection or biopsy between January 2011 to March 2017 who met the following criteria: 1) available baseline contrast-enhanced MR imaging performed within 2 days after surgery or biopsy and 2) underwent DCE MR imaging with multiple flip-angle imaging within 2 months after TMZ chemoradiation therapy. We excluded 86 patients who did not show a newly manifested measurable enhanced area (larger than 10 mm bidimensionally on MR imaging) in the radiation field on postchemoradiation MR imaging. In addition, 11 patients who were lost to follow-up ($n = 7$), who had a decreased nodule size but developed meningeal seeding during the follow-up ($n = 2$), or whose lesion was suspicious for radiation therapy–induced sarcoma ($n = 2$) were excluded. Finally, 37 patients were included, with a mean age ± SD of 57.0 years ± 12.8 years (Fig 1). Among them, 5 patients were defined to have true progression (ie, the patient's status was not attributable to concurrent medication or the patient's comorbid conditions were apparent to declare progression on current treatment) according to pathologic confirmation ($n = 3$) or obvious clinical deterioration ($n = 2$). The other 32 patients were classified as having either true progression ($n = 10$) or pseudoprogression ($n = 22$) radiologically according to the Response Assessment in Neuro-Oncology criteria in consensus of 3 radiologists (J.G.N., K.M.K., and S.H.C.) with 2, 8, and 15 years of experience, respectively. True progression was decided when either there was new enhancement outside the radiation field or the enhancing lesions showed an increase by ≥25% in the sum of the products of the perpendicular diameters on the postadjuvant TMZ chemotherapy scan; otherwise, pseudoprogression was decided.[4]

DCE MR Imaging Acquisition

All patients underwent follow-up DCE MR imaging studies after the completion of concurrent TMZ chemoradiation with a 3T imaging unit with a 32-channel head coil (Verio; Siemens, Erlangen, Germany [$n = 33$] and Ingenia; Philips Healthcare, Best, the Netherlands [$n = 4$, respectively]). The MR imaging included sagittal T1WI and reconstructed transverse and coronal images acquired before and after contrast enhancement with a 3D rapid

acquisition of gradient-echo sequence and a transverse FLAIR sequence. For the gradient-echo sequence, the following MR parameters were used: TR, 1500 ms; TE, 1.9 ms; flip angle, 9°; and matrix, 256 × 232 with an FOV of 220 × 250, a section thickness of 1 mm, and 1 acquired signal. For the T1 measurement analysis, additional precontrast images were collected with multiple flip angles of 2°, 8°, and 15° from the spoiled gradient-echo T1WI. Afterward, transverse T2WI with TSE was collected with the following MR parameters: TR, 5160 ms; TE, 91 ms; flip angle, 130°; and matrix, 640 × 510–580 with an FOV of 175–199 × 220, section thickness of 5 mm, and 3 NEX. Axial FLAIR imaging was performed with the following MR parameters: TR, 9000 ms; TE, 97 ms; flip angle, 130°; and matrix, 384 × 348 with an FOV of 199 × 220 and a section thickness of 5 mm. Contrast-enhanced imaging was performed after intravenous administration of gadobutrol (Gadovist; Bayer Schering Pharma, Berlin, Germany) at a dose of 0.1 mmol/L per kilogram of body weight.

DCE MR imaging was performed by using 3D gradient-echo T1WI after intravenous administration of gadobutrol (0.1 mmol/L/kg) by using a power injector (Spectris; MedRad, Indianola, Pennsylvania) at a rate of 4 mL/s. A 30-mL bolus injection of saline followed gadobutrol treatment at the same injection rate. For each section, 40 images were acquired at intervals equal to the TR. The following MR parameters were used: TR, 2.8 ms; TE, 1.0 ms; flip angle, 10°; and matrix, 192 × 192 with a section thickness of 3 mm, an FOV of 240 × 240 mm, a voxel size of 1.25 × 1.25 × 3 mm^3, a pixel bandwidth of 789 Hz, and a total acquisition time of 1 minute 30 seconds.

Image Analysis

T1 Measurement from the Multiple Flip-Angle Method. DCE MR images were processed by using the MR imaging perfusion analysis method (nordicICE; NordicNeuroLab, Bergen, Norway), and the 3D gradient-echo T1-weighted images were used. After registering the precontrast acquisitions with the multiple flip-angle images (by using 3 flip angles [2°, 8°, and 15°] from the spoiled gradient-echo T1-weighted images), the T1 measurement was automatically calculated by the following equation by using the software (nordicICE):

$$S = M_0 \times \frac{\sin \propto \times (1 - E_1) \times E_2}{1 - E_1 \times \cos \propto}$$

where $E_1 = \exp(-TR/T_1)$ and $E_2 = \exp(-TE/T_2^*)$, (S = signal intensity; M_0 = the equilibrium magnetization; T1 = longitudinal relaxation; T2* = effective transverse relaxation; and α = flip angle). As E_2 is usually ignored when $TE \ll T_2^*$, the equation can be simplified to the following linear form.[17-19]

$$\frac{S}{\sin \propto} = E_1 \times \frac{S}{\tan \alpha} + M_0 \times (1 - E_1)$$

Then, E_1 and finally T1 maps can be derived by solving multiple equations generated by entering multiple flip angles (2°, 8°, and 15°).[17-19]

DCE Parameter Acquisition. For each patient, the arterial input function was automatically detected from the software (nordicICE) by analyzing all pixel-time curves in the dataset and applying cluster analysis to select the time courses that most resembled the expected arterial input function properties, satisfying large area under the curve (AUC), low first moment, and high peak enhancement.[20] The VOI was plotted section by section by using the semiautomatic segmentation method in the pixel analysis software (nordicICE), including all newly developed enhancing areas and excluding vessels and necrotic or liquefied regions. Then, the overall value for each tumor was obtained automatically by the software by summing up all values from each plane.

The pharmacokinetic DCE parameters, including K^{trans}, K_{ep}, blood plasma volume per unit volume of tissue, and extravascular extracellular space per unit volume of tissue, were calculated based on the 2-compartment pharmacokinetics model proposed by Tofts and Kermode.[21] Each parameter was calculated by using both the measured T1 derived from T1 mapping and the fixed T1 of 1000 ms. Each procedure, including arterial input function selection and VOI plotting, was performed twice for both T1 methods by a radiologist (J.G.N.) at 2-week intervals and once by another radiologist (W.H.L; 3 years of experience). The total image processing for each patient required approximately 4–6 minutes and 8–10 minutes for the fixed T1 and measured T1 methods, respectively, for both observers.

Statistical Analysis

For comparison of clinical and demographic characteristics, the Student t test and χ^2 test were used, as appropriate. The intra- and interobserver reproducibility were assessed by using the intraclass correlation coefficient. We adapted the following guidelines for the intraclass correlation coefficient: excellent, higher than 0.75; fair, 0.40–0.75; and poor, less than 0.40.[22] The Kolmogorov-Smirnov test was used to determine whether any noncategoric data were normally distributed. The means of the variables were compared between the true progression and pseudoprogression groups by using the Student t test when the data were normally distributed, and the median and ranges of the variables were compared by using the Mann-Whitney U test for variables not normally distributed. Significant variables from the univariate analyses were applied to the multivariate logistic regression analysis. The diagnostic performance was evaluated by receiver operating characteristic analysis; the optimal criterion that maximizes sensitivity and specificity corresponding with the Youden Index J was selected by the software (MedCalc; MedCalc Software, Mariakerke, Belgium).[23] To compare the diagnostic power of T1 measurement and fixed T1 methods, a pair-wise comparison receiver operating characteristic curve analysis was used.[24] Leave-one-out cross-validation was also performed to validate the diagnostic performance.

Statistical analyses were performed by using MedCalc software version 15.8 (MedCalc Software). For all tests, values of $P < .05$ were considered statistically significant.

RESULTS

As mentioned previously, among 37 patients, 15 were defined as having true progression according to pathologic confirmation ($n = 3$), apparent clinical deterioration ($n = 2$), or radiologic diagnosis following the Response Assessment in Neuro-

Table 1: Clinical information of the enrolled patients

Variable	True Progression (n = 15)	Pseudoprogression (n = 22)	P Value[a]
Age, yr (mean ± SD)	59.6 ± 11.9	56.7 ± 13.7	.61
Gender			.12
Male	9 (60.0%)	17 (77.3%)	
Female	6 (40.0%)	5 (22.7%)	
Surgery			.24
Biopsy	4 (26.7%)	2 (9.1%)	
Subtotal	6 (40.0%)	9 (40.9%)	
Total	5 (33.3%)	11 (50.0%)	
Time interval of end of TMZ-chemoradiation to DCE MRI, d (mean ± SD [range])	27.0 ± 7.3 [15–44]	28.7 ± 6.0 [17–44]	.39
End of adjuvant TMZ chemotherapy to follow-up MRI, d (mean ± SD [range])	31.2 ± 10.6 [20–53][b]	26.2 ± 8.7 [16–54]	.46
Initial operation to the last follow-up, d (mean ± SD [range])	391.4 ± 156.3 [224–716]	657.3374.7 [274–1774]	.002

[a] P values are from either Student t test or the χ^2 test, as appropriate, for all variables.
[b] Four patients who underwent pathologic confirmation (n = 2) or developed obvious clinical deterioration before the termination of adjuvant TMZ chemotherapy (n = 2) were excluded for this parameter.

Table 2: Comparison of the DCE pharmacokinetic parameters of patients with true progression versus pseudoprogression

Pharmacokinetic Parameter	T1 Method	True Progression (n = 15)		Pseudoprogression (n = 22)		P Value[a]	Intraclass Correlation Coefficient [95% CI]	
		Mean ± SD	Median [range]	Mean ± SD	Median [range]		Intraobserver	Interobserver
K^{trans}, min^{-1}	Fixed	0.138 ± 0.148	0.096 [0.042–0.579]	0.068 ± 0.043	0.064 [0.0005–0.154]	.05[b]	0.893 [0.792–0.945]	0.897 [0.799–0.947]
	Measured	0.126 ± 0.139	0.069 [0.025–0.499]	0.056 ± 0.045	0.058 [0.0001–0.194]	.10	0.923 [0.850–0.960]	0.943 [0.888–0.970]
K_{ep}, min^{-1}	Fixed	0.321 ± 0.244	0.244 [0.135–1.082]	0.179 ± 0.103	0.179 [0.024–0.483]	.01[b]	0.910 [0.825–0.954]	0.929 [0.862–0.963]
	Measured	0.224 ± 0.108	0.202 [0.035–0.396]	0.192 ± 0.148	0.157 [0.009–0.494]	.47	0.861 [0.729–0.928]	0.882 [0.771–0.939]
V_p, %	Fixed	3.309 ± 4.429	1.468 [0.709–18.298]	1.998 ± 1.462	1.705 [0.140–6.723]	.60	0.872 [0.752–0.934]	0.888 [0.784–0.943]
	Measured	2.358 ± 2.701	1.339 [0.478–10.407]	1.521 ± 1.456	1.134 [0.081–6.056]	.27	0.800 [0.605–0.895]	0.688 [0.394–0.839]
V_e	Fixed	0.536 ± 0.330	0.446 [0.168–1.050]	0.506 ± 0.284	0.482 [0.114–1.156]	.77	0.761 [0.537–0.877]	0.718 [0.516–0.844]
	Measured	0.550 ± 0.511	0.377 [0.121–1.192]	0.316 ± 0.265	0.270 [0.041–1.297]	.08	0.937 [0.877–0.968]	0.936 [0.875–0.967]

[a] P values are from Student t test when the variables satisfied normality (K_{ep} from measured T1 and V_e from fixed T1) or from Mann-Whitney U tests otherwise, according to Kolmogorov-Smirnov test.
[b] Significant P value for each test.

Oncology criteria (n = 10).[4] The other 22 patients were defined as having pseudoprogression.

Among the patients, 73.3% (11/15) of the true progression patients and 90.9% (20/22) of the pseudoprogression patients underwent radical surgery, whereas the others underwent stereotactic biopsy. The immediate postoperative MR imaging showed that total resection was achieved for 45.5% (5/11) and 55.0% (11/20) of surgical cases in the true progression and pseudoprogression groups, respectively. Detailed demographics are listed in Table 1.

Intraobserver and Interobserver Reproducibility of DCE Pharmacokinetic Parameters

The intraclass correlation coefficients for intra- and interobserver agreement for each DCE pharmacokinetic parameter were deemed mostly excellent, or at least fair, ranging from 0.689–0.943,[22] for both the fixed T1 and measured T1 methods (Table 2).

Comparison of DCE Pharmacokinetic Parameters: True Progression versus Pseudoprogression

Among the 4 DCE pharmacokinetic parameters calculated from the 2 different precontrast T1 values, the mean value was compared for the 2 parameters that satisfied normality based on the Kolmogorov-Smirnov test: K_{ep} from the measured T1 and V_e from the fixed T1. The median and ranges for the other 6 parameters were compared. Only 2 parameters showed a significant difference between the true progression and pseudoprogression groups: K^{trans} evaluated from the fixed T1 (median [range] value of true progression versus pseudoprogression, 0.096 $minutes^{-1}$ [0.042–0.580] versus 0.064 $minutes^{-1}$ [0.0005–0.154]; P = .048) and K_{ep} calculated from the fixed T1 (median [range], 0.244 $minutes^{-1}$ [0.135–1.082] versus 0.179 $minutes^{-1}$ [0.024–0.483]; P = .010). No parameters obtained from the measured T1 showed significant difference between the 2 groups (Table 2). The representative cases are presented in Figs 2 and 3.

The multivariate logistic regression analysis with the backward method was conducted for 3 variables, including significant variables on the univariate analysis (K^{trans} and K_{ep} evaluated from the fixed T1) and V_e calculated from the fixed T1 method, which was shown to exhibit significant difference in the previous study.[10] As a result, K_{ep} from the fixed T1 method was the only significant parameter (OR [95% CI], 1.77 × 10^5 [4.27–7.32 × 10^9]; P = .007).

Diagnostic Performance of DCE Pharmacokinetic Parameters: Comparison of the Fixed T1 and T1 Measurement Methods

In the receiver operating characteristic analysis, K^{trans} and K_{ep} from the fixed T1 showed significant diagnostic power in distinguishing true progression from pseudoprogression (AUC, 0.694 and 0.752; P = .03 and .002, respectively). The 2 parameters did not demonstrate a significant difference based on a comparison of

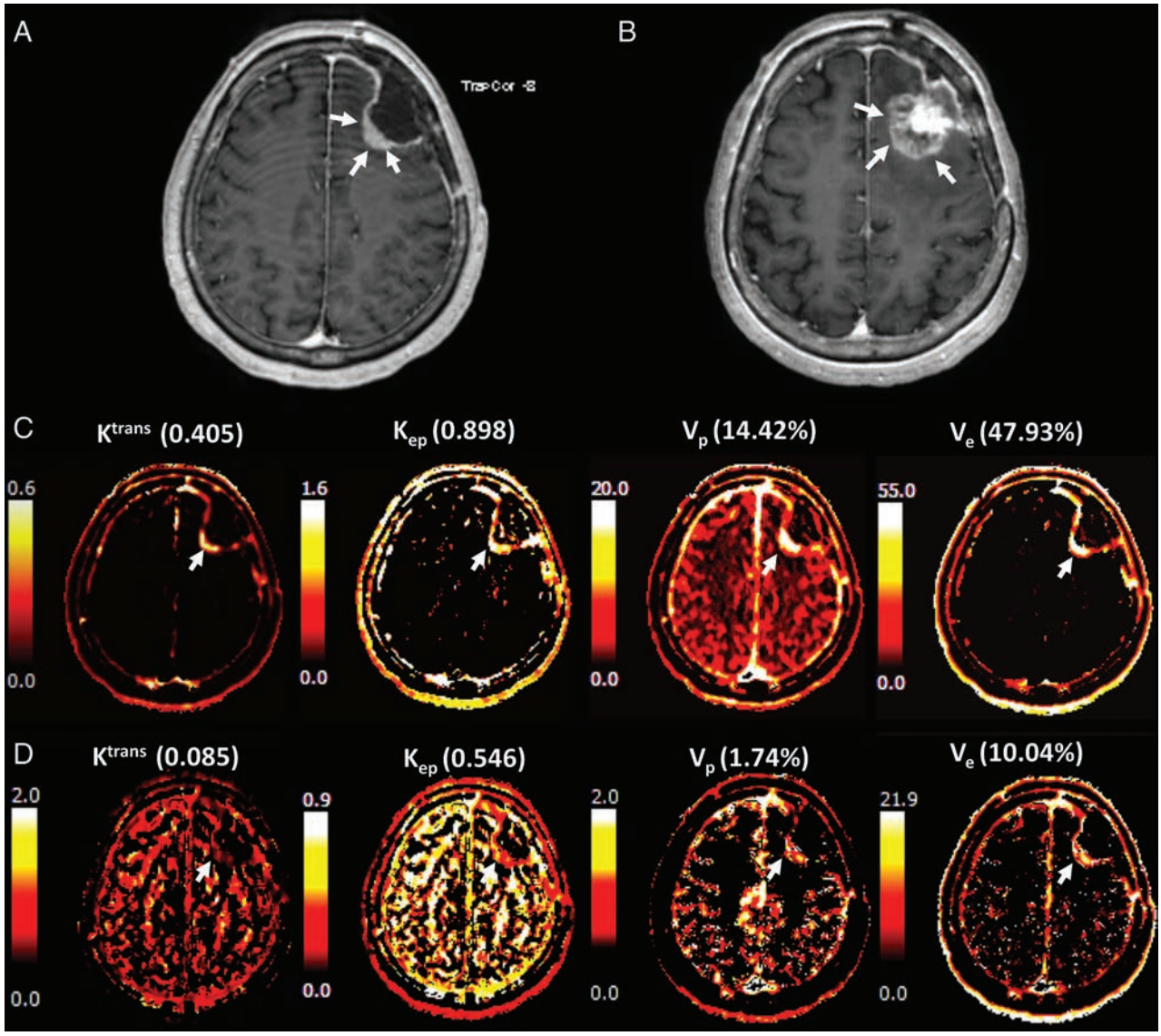

FIG 2. A 68-year-old female patient with surgically proved glioblastoma presented *A*, a newly appeared enhancing nodule on DCE-MR imaging taken 1 month after temozolomide chemoradiation. The lesion was not identified on the postoperative MR imaging. *B*, The lesion was markedly increased after 6 cycles of temozolomide chemotherapy, implying that the lesion was true progression according to the Response Assessment in Neuro-Oncology criteria. The pharmacokinetic DCE maps, especially those for K^{trans} and K_{ep}, showed a bright signal from both the *C*, fixed T1 and *D*, measured T1 methods.

the receiver operating characteristic analysis ($P = .29$). No parameters obtained from the measured T1 method showed a proper diagnostic performance (all $Ps > .05$).

The diagnostic accuracy of K^{trans} and K_{ep} from the fixed T1 was 73.0% (27/37) and 70.3% (26/37), respectively. Whereas K^{trans} from the fixed T1 exhibited high specificity (86.4%; [19/22]) but suboptimal sensitivity (53.3% [8/15]), K_{ep} from the fixed T1 showed relatively reliable sensitivity and specificity (80.0% [12/15] and 63.6% [14/22], respectively), along with fair positive predictive value (60.0%, [12/20]) and reliable negative predictive value (82.4% [14/17]) (Table 3). The leave-one-out cross-validation for K_{ep} from the fixed T1 method demonstrated similar results: sensitivity, specificity, accuracy, and positive and negative predictive values of 73.3% (11/15), 59.1% (13/22), 64.9% (24/37), 55.0% (11/20), and 76.5% (13/17), respectively (Table 4).

DISCUSSION

In our study, some pharmacokinetic parameters of the fixed T1 method derived from post–TMZ chemoradiation DCE MR imaging showed a significant difference between the true progression and pseudoprogression groups: K^{trans} and K_{ep} from the fixed T1 were significantly larger in the true progression group than in the pseudoprogression group. No parameters calculated from the measured T1 method demonstrated a significant difference between the 2 groups. In the multivariate analysis, K_{ep} from the fixed T1 method was the only significant variable. It exhibited a fair diagnostic performance with acceptable intra- and interobserver reproducibility, especially in terms of sensitivity and negative predictive value, in both the AUC analysis and leave-one-out cross-validation.

Although the baseline T1 measurement provides the tissue

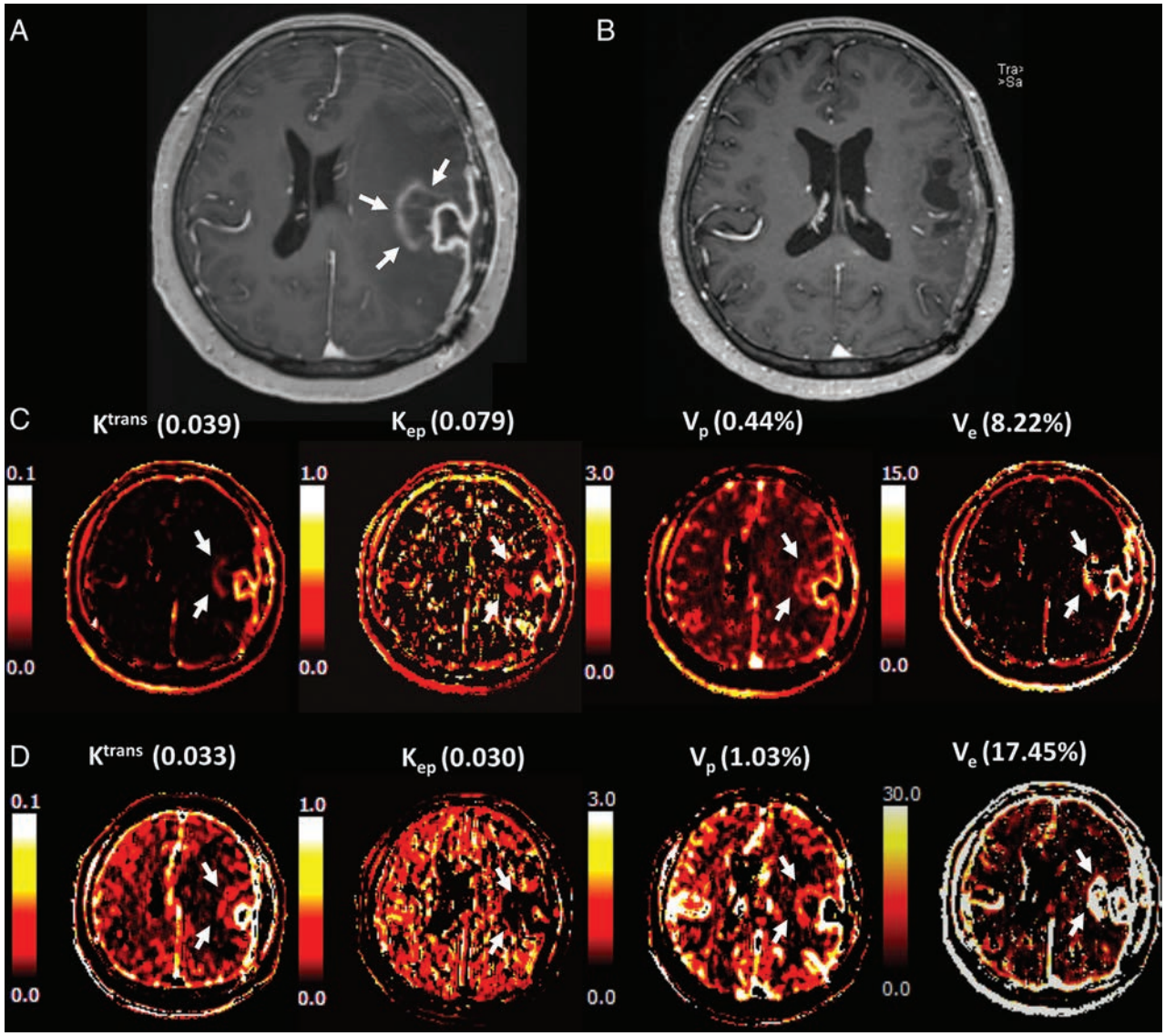

FIG 3. A 57-year-old female patient with surgically proved glioblastoma presented *A*, a newly appeared enhancing nodule on DCE-MR imaging taken 1 month after temozolomide chemoradiation. *B*, The lesion had disappeared after 6 cycles of temozolomide chemotherapy, defining the lesion as a pseudoprogression according to the Response Assessment in Neuro-Oncology criteria. The pharmacokinetic DCE maps, especially those for K^{trans} and K_{ep}, showed less intense signals from both *C*, the fixed T1 and *D*, measured T1 methods.

Table 3: Diagnostic performance of the DCE pharmacokinetic parameters in detecting true progression

Pharmacokinetic Parameter	T1 Method	Median AUC	Optimal Threshold Value	Sensitivity [%]	Specificity [%]	*P* Value[a]
K^{trans}, min^{-1}	Fixed	0.694	0.093	53.3	86.4	.03[b]
	Measured	0.664	0.059			.08
K_{ep}, min^{-1}	Fixed	0.752	0.184	80.0	63.6	.002[b]
	Measured	0.603	0.159			.28
V_p, %	Fixed	0.552	3.423			.62
	Measured	0.609	0.597			.25
V_e	Fixed	0.518	0.349			.86
	Measured	0.606	0.546			.30

Note:—V_e indicates extravascular extracellular space per unit volume; V_p, blood plasma volume per unit volume.

[a] *P* values are from the receiver operating characteristics analysis.

[b] Significant *P* value for each test.

property, it has the problem of weak reliability and reproducibility because of major systematic errors resulting from scale factor miscalibration and susceptibility to motion.[12,25] Because signal artifacts are known to be particularly important in the overall errors of DCE MR imaging among other tissue- or acquisition-related parameters,[13] the fixed T1, simple and reproducible, has

Table 4: Diagnostic performance of K_{ep} from the fixed T1 and results from the leave-one-out cross-validation

Median AUC	Optimal Threshold Value	Sensitivity	Specificity	Accuracy	Positive Predictive Value	Negative Predictive Value
0.752	0.184	80.0% (12/15)	63.6% (14/22)	70.3% (26/37)	60.0% (12/20)	82.4% (14/17)
Leave-one-out cross-validation		73.3% (11/15)	59.1% (13/22)	64.9% (24/37)	55.0% (11/20)	76.5% (13/17)

its strength. In this situation, it is necessary to compare the diagnostic performance of DCE parameters from the fixed T1 with measured T1 methods to verify the better processing method. Our study demonstrated that the fixed T1 method more reliably predicts true progression from pseudoprogression. Clinically, our results can provide evidence to eliminate the T1 measurement process in DCE MR interpretation, possibly resulting in the reduction of both imaging acquisition time and postprocessing time.

The use of DCE MR imaging in differentiating true progression from pseudoprogression is in its infancy, and few studies have been performed. Yun et al[10] reported that the mean K^{trans} from the fixed T1 method is the most convincing parameter in differentiating true progression, but K_{ep} was not evaluated. Our study agrees with a previous study reporting that the mean K^{trans} from the fixed T1 method was significantly different between true progression and pseudoprogression with similar sensitivity and specificity.[10] However, the multivariate analysis in our study revealed that K_{ep} was the only independently differentiable parameter. To the best of our knowledge, there are no studies that have reported the difference of K_{ep} between the 2 groups.

Although both pseudoprogression and true progression appear as new enhancing lesions on the post–TMZ chemoradiation therapy MR imaging, the pathologies are markedly dissimilar. It has been well known that pseudoprogression histopathologically resembles radiation necrosis.[3,26] Radiation-induced endothelial injury is understood to be the major cause of radiation injury, including pseudoprogression, resulting in destruction of the BBB concomitant with vasogenic edema and tissue ischemia.[26,27] Because angiogenesis in addition to breakdown of the BBB occurs for true progression, vascularity-related parameters, including K^{trans} and K_{ep}, are likely to be higher in true progression than in pseudoprogression.[28-30]

The exchange rate constant K_{ep} is a composite parameter of K^{trans}/V_e and represents the transit between the extravascular and the intravascular compartments. K_{ep} is known to reflect the vessel permeability and the surface area,[31] both of which are known to be increased in true progression. There have been other reports in other organs that indicated K_{ep} as a potential parameter for predicting tumor angiogenesis: K_{ep} showed a significant correlation with the microvessel attenuation calculated from immunohistochemistry in prostate cancer,[32,33] whereas other parameters, including K^{trans}, V_p, and V_e, did not demonstrate a significant correlation.[33] A similar study of multiple myeloma also reported that K_{ep} was significantly higher in tumors with a high vessel attenuation.[34] Other reports showed that K_{ep} was the only significant DCE parameter (along with K^{trans} and V_e) that was correlated with the histologic grade in rectal cancer and correlated with poor response in malignant pleural mesothelioma.[35,36] In agreement with the previous explanation,[33] because it is a composite of 2 parameters, the compounding effects of these parameters might subside and allow K_{ep} to present a better correlation with the nature of the lesion.

Our study has some limitations. First, because of its retrospective nature, patients had variable time intervals between treatment and imaging. We selected patients who satisfied Response Assessment in Neuro-Oncology criteria to define the nature of the lesion; thus, some patients with true progression of an aggressive nature might have not been selected because they could not survive 6 cycles of adjuvant chemotherapy. However, because DCE MR imaging was routinely performed at our hospital for patients with glioblastoma with TMZ chemoradiation, our cohort might work as a potentially representative selection. Second, our sample size was small, and the number of tumor types was disproportionate (15 true progression patients and 22 pseudoprogression patients). Third, we did not compare our arterial input function acquisition method with other patient-specific methods or population-based arterial input function, which can reduce both image processing and postprocessing time. Because DCE parameters can also be affected by various arterial input function calculations, further study is recommended for robust arterial input function calculation. In addition, despite previous studies suggesting the reliability of the multiple flip-angle method, further validation of the method compared with the inversion-recovery method should be needed. Finally, we did not compare the diagnostic power of our values with other MR imaging modalities that are reported to be able to differentiate true progression from pseudoprogression, such as ADC or dynamic susceptibility contrast-enhanced MR imaging.[5-9]

CONCLUSIONS

The semiquantitative DCE-derived parameter K_{ep} based on the fixed T1 value is a preferable marker to differentiate true progression from pseudoprogression versus other parameters derived from tissue T1 measurement.

REFERENCES

1. Stupp R, Hegi ME, Gorlia T, et al. **Cilengitide combined with standard treatment for patients with newly diagnosed glioblastoma with methylated MGMT promoter (CENTRIC EORTC 26071–22072 study): a multicentre, randomised, open-label, phase 3 trial.** *Lancet Oncol* 2014;15:1100–08 CrossRef Medline
2. Brandsma D, Stalpers L, Taal W, et al. **Clinical features, mechanisms, and management of pseudoprogression in malignant gliomas.** *Lancet Oncol* 2008;9:453–61 CrossRef Medline
3. Chaskis C, Neyns B, Michotte A, et al. **Pseudoprogression after radiotherapy with concurrent temozolomide for high-grade glioma: clinical observations and working recommendations.** *Surg Neurol* 2009;72:423–28 CrossRef Medline
4. Wen PY, Macdonald DR, Reardon DA, et al. **Updated response assessment criteria for high-grade gliomas: Response Assessment in**

Neuro-Oncology working group. *J Clin Oncol* 2010;28:1963–72 CrossRef Medline
5. Baek HJ, Kim HS, Kim N, et al. **Percent change of perfusion skewness and kurtosis: a potential imaging biomarker for early treatment response in patients with newly diagnosed glioblastomas.** *Radiology* 2012;264:834–43 CrossRef Medline
6. Chen X, Wei X, Zhang Z, et al. **Differentiation of true-progression from pseudoprogression in glioblastoma treated with radiation therapy and concomitant temozolomide by GLCM texture analysis of conventional MRI.** *Clin Imaging* 2015;39:775–80 CrossRef Medline
7. Choi YJ, Kim HS, Jahng GH, et al. **Pseudoprogression in patients with glioblastoma: added value of arterial spin labeling to dynamic susceptibility contrast perfusion MR imaging.** *Acta Radiol* 2013;54:448–54 CrossRef Medline
8. Song YS, Choi SH, Park CK, et al. **True progression versus pseudoprogression in the treatment of glioblastomas: a comparison study of normalized cerebral blood volume and apparent diffusion coefficient by histogram analysis.** *Korean J Radiol* 2013;14:662–72 CrossRef Medline
9. Chu HH, Choi SH, Ryoo I, et al. **Differentiation of true progression from pseudoprogression in glioblastoma treated with radiation therapy and concomitant temozolomide: comparison study of standard and high-b-value diffusion-weighted imaging.** *Radiology* 2013;269:831–40 CrossRef Medline
10. Yun TJ, Park CK, Kim TM, et al. **Glioblastoma treated with concurrent radiation therapy and temozolomide chemotherapy: differentiation of true progression from pseudoprogression with quantitative dynamic contrast-enhanced MR imaging.** *Radiology* 2015;274:830–40 CrossRef Medline
11. Thomas AA, Arevalo-Perez J, Kaley T, et al. **Dynamic contrast enhanced T1 MRI perfusion differentiates pseudoprogression from recurrent glioblastoma.** *J Neurooncol* 2015;125:183–90 CrossRef Medline
12. Tietze A, Mouridsen K, Mikkelsen IK. **The impact of reliable pre-bolus T 1 measurements or a fixed T 1 value in the assessment of glioma patients with dynamic contrast enhancing MRI.** *Neuroradiology* 2015;57:561–72 CrossRef Medline
13. Dale BM, Jesberger JA, Lewin JS, et al. **Determining and optimizing the precision of quantitative measurements of perfusion from dynamic contrast enhanced MRI.** *J Magn Reson Imaging* 2003;18:575–84 CrossRef Medline
14. Walker-Samuel S, Parker CC, Leach MO, et al. **Reproducibility of reference tissue quantification of dynamic contrast-enhanced data: comparison with a fixed vascular input function.** *Phys Med Biol* 2007;52:75–89 CrossRef Medline
15. Mikkelsen IK, Peters DA, Tietze A. **DCE-PWI 3D T1-measurement as function of time or flip angle.** In: *Proceedings of the International Society for Magnetic Resonance in Medicine 20th Annual Meeting and Exhibition*, Melbourne, Australia. May 5–11, 2012
16. Studler U, White LM, Andreisek G, et al. **Impact of motion on T1 mapping acquired with inversion recovery fast spin echo and rapid spoiled gradient recalled-echo pulse sequences for delayed gadolinium-enhanced MRI of cartilage (dGEMRIC) in volunteers.** *J Magn Reson Imaging* 2010;32:394–98 CrossRef Medline
17. Li Z, Sun J, Hu X, et al. **Assessment of liver fibrosis by variable flip angle T1 mapping at 3.0T.** *J Magn Reson Imaging* 2016;43:698–703 CrossRef Medline
18. Deoni SC, Rutt BK, Peters TM. **Rapid combined T1 and T2 mapping using gradient recalled acquisition in the steady state.** *Magn Reson Med* 2003;49:515–26 CrossRef Medline
19. Blüml S, Schad LR, Stepanow B, et al. **Spin-lattice relaxation time measurement by means of a TurboFLASH technique.** *Magn Reson Med* 1993;30:289–95 CrossRef Medline
20. Mouridsen K, Christensen S, Gyldensted L, et al. **Automatic selection of arterial input function using cluster analysis.** *Magn Reson Med* 2006;55:524–31 CrossRef Medline
21. Tofts PS, Kermode AG. **Measurement of the blood-brain barrier permeability and leakage space using dynamic MR imaging. 1. Fundamental concepts.** *Magn Reson Med* 1991;17:357–67 CrossRef Medline
22. Kang KM, Lee JM, Yoon JH, et al. **Intravoxel incoherent motion diffusion-weighted MR imaging for characterization of focal pancreatic lesions.** *Radiology* 2014;270:444–53 CrossRef Medline
23. Youden WJ. **Index for rating diagnostic tests.** *Cancer* 1950;3:32–35 Medline
24. DeLong ER, DeLong DM, Clarke-Pearson DL. **Comparing the areas under two or more correlated receiver operating characteristic curves: a nonparametric approach.** *Biometrics* 1988:837–45 CrossRef Medline
25. Haacke EM, Filleti CL, Gattu R, et al. **New algorithm for quantifying vascular changes in dynamic contrast-enhanced MRI independent of absolute T1 values.** *Magn Reson Med* 2007;58:463–72 CrossRef Medline
26. Motegi H, Kamoshima Y, Terasaka S, et al. **IDH1 mutation as a potential novel biomarker for distinguishing pseudoprogression from true progression in patients with glioblastoma treated with temozolomide and radiotherapy.** *Brain Tumor Pathol* 2013;30:67–72 CrossRef Medline
27. Wong CS, Van der Kogel AJ. **Mechanisms of radiation injury to the central nervous system: implications for neuroprotection.** *Mol Interv* 2004;4:273–84 CrossRef Medline
28. Sugahara T, Korogi Y, Kochi M, et al. **Correlation of MR imaging-determined cerebral blood volume maps with histologic and angiographic determination of vascularity of gliomas.** *AJR Am J Roentgenol* 1998;171:1479–86 CrossRef Medline
29. Oh BC, Pagnini PG, Wang MY, et al. **Stereotactic radiosurgery: adjacent tissue injury and response after high-dose single fraction radiation: Part I–Histology, imaging, and molecular events.** *Neurosurgery* 2007;60:31–44; discussion 44–45 CrossRef Medline
30. Tofts PS. **T1-weighted DCE imaging concepts: modelling, acquisition and analysis.** *MAGNETOM Flash* 2010;3:30–39
31. Heverhagen JT, von Tengg-Kobligk H, Baudendistel KT, et al. **Benign prostate hyperplasia: evaluation of treatment response with DCE MRI.** *MAGMA* 2004;17:5–11 CrossRef Medline
32. Schlemmer HP, Merkle J, Grobholz R, et al. **Can pre-operative contrast-enhanced dynamic MR imaging for prostate cancer predict microvessel density in prostatectomy specimens?** *Eur Radiol* 2004;14:309–17 CrossRef Medline
33. Oto A, Yang C, Kayhan A, et al. **Diffusion-weighted and dynamic contrast-enhanced MRI of prostate cancer: correlation of quantitative MR parameters with Gleason score and tumor angiogenesis.** *AJR Am J Roentgenol* 2011;197:1382–90 CrossRef Medline
34. Nosàs-Garcia S, Moehler T, Wasser K, et al. **Dynamic contrast-enhanced MRI for assessing the disease activity of multiple myeloma: a comparative study with histology and clinical markers.** *J Magn Reson Imaging* 2005;22:154–62 CrossRef Medline
35. Yao WW, Zhang H, Ding B, et al. **Rectal cancer: 3D dynamic contrast-enhanced MRI; correlation with microvascular density and clinicopathological features.** *Radiol Med* 2011;116:366–74 CrossRef Medline
36. Giesel FL, Bischoff H, von Tengg-Kobligk H, et al. **Dynamic contrast-enhanced MRI of malignant pleural mesothelioma: a feasibility study of noninvasive assessment, therapeutic follow-up, and possible predictor of improved outcome.** *Chest* 2006;129:1570–76 CrossRef Medline

Initial Investigation into Microbleeds and White Matter Signal Changes following Radiotherapy for Low-Grade and Benign Brain Tumors Using Ultra-High-Field MRI Techniques

J.-G. Belliveau, G.S. Bauman, K.Y. Tay, D. Ho, and R.S. Menon

ABSTRACT

BACKGROUND AND PURPOSE: External beam radiation therapy is a common treatment for many brain neoplasms. While external beam radiation therapy adheres to dose limits to protect the uninvolved brain, areas of high dose to normal tissue still occur. Patients treated with chemoradiotherapy can have adverse effects such as microbleeds and radiation necrosis, but few studies exist of patients treated without chemotherapy.

MATERIALS AND METHODS: Ten patients were treated for low-grade or benign neoplasms with external beam radiation therapy only and scanned within 12–36 months following treatment with a 7T MR imaging scanner. A multiecho gradient-echo sequence was acquired and postprocessed into SWI, quantitative susceptibility mapping, and apparent transverse relaxation maps. Six patients returned for follow-up imaging approximately 18 months following their first research scan and were imaged with the same techniques.

RESULTS: At the first visit, 7/10 patients had microbleeds evident on SWI, quantitative susceptibility mapping, and apparent transverse relaxation. All microbleeds were within a dose region of >45 Gy. Additionally, 4/10 patients had asymptomatic WM signal changes evident on standard imaging. Further analysis with our technique revealed that these lesions were venocentric, suggestive of a neuroinflammatory process.

CONCLUSIONS: There exists a potential for microbleeds in patients treated with external beam radiation therapy without chemotherapy. This finding is of clinical relevance because it could be a precursor of future neurovascular disease and indicates that additional care should be taken when using therapies such as anticoagulants. Additionally, the appearance of venocentric WM lesions could be suggestive of a neuroinflammatory mechanism that has been suggested in diseases such as MS. Both findings merit further investigation in a larger population set.

ABBREVIATIONS: QSM = quantitative susceptibility mapping; R_2^* = apparent transverse relaxation; RN = radiation necrosis; XRT = external beam radiation therapy

External beam radiation therapy (XRT) is commonly used in the treatment of many brain neoplasms. In benign and low-grade neoplasms (meningiomas, neuromas, low-grade gliomas), safe maximal surgical resection combined with XRT is usually the standard of care. The prescribed dose is typically a course of 54–60 Gy in 30 fractions using conformal delivery with techniques such as intensity-modulated radiation therapy. These dose plans attempt to follow specific guidelines such as Quantitative Analysis of Normal Tissue Effects in the Clinic (http://www.aapm.org/pubs/QUANTEC.asp) to limit the dose to radiosensitive areas, including the uninvolved brain, brain stem, optic nerve, and optic chiasm,[1] as well as the hippocampus, which is known for its role in neurogenesis.[2,3] Due to the infiltrative nature of some neoplasms such as low-grade gliomas or the proximity of tumors to normal brain in other neoplasms, even conformal radiation techniques can result in some volume of healthy tissue receiving radiation. The dose delivered to the normal brain can potentially cause long-term effects later in the patient's life.

Following XRT, there are numerous reports of clinical sequelae that are classified into acute, early-delayed, or late effects.[4]

Received August 12, 2016; accepted after revision July 24, 2017.

From the Departments of Medical Biophysics (J.-G.B., G.S.B., R.S.M.), Oncology (G.S.B.), and Medical Imaging (K.Y.T.), University of Western Ontario, London, Ontario, Canada; Centre for Functional and Metabolic Mapping (J.-G.B., R.S.M.), Robarts Research Institute, London, Ontario, Canada; London Regional Cancer Program (G.S.B.), London, Ontario, Canada; and Department of Radiology (D.H.), Woodstock General Hospital, Woodstock, Ontario, Canada.

This work was supported by the London Regional Cancer Program Catalyst Grant, the Canada Research Chairs Program, and the Canada Foundation for Innovation.

Please address correspondence to Ravi Menon, MD, Robarts Research Institute, Western University, 1151 Richmond St N, London, ON N6A 5B7, Canada; e-mail: rmenon@robarts.ca; @northernthrux

Indicates open access to non-subscribers at www.ajnr.org

Indicates article with supplemental on-line table.

http://dx.doi.org/10.3174/ajnr.A5395

Acute and early-delayed adverse effects are usually temporary and resolve spontaneously with minimal treatment or steroids. Late effects are typically much more severe because they cause permanent changes to the brain parenchyma, including radiation necrosis (RN), cavernous angiomas, and microbleeds,[4] resulting in ongoing neurologic deficits.

RN is an adverse effect that may present a few years following XRT; however, it can occur as early as 6 months and as late as 10 years following XRT. In some patients, regions of RN may be small and do not produce symptoms. In others, progressive RN can be seen with detrimental effects on the patient's quality of life.[5] Symptoms ranging from headaches and drowsiness to memory loss, seizures, and focal deficits have been documented. Treatments of RN vary from observation to steroids or antiangiogenic agents.[6] In some patients, surgical resection is required to debulk necrotic areas to alleviate symptoms.

The exact cause of RN is not entirely understood, but the 2 main hypotheses developed in the past 50 years are related to vascular and glial damage.[4] The vascular hypothesis suggests that radiation necrosis is secondary to an ischemic event due to small-vessel injury, while the glial hypothesis suggests that damage to the white matter precursor cells occurs during XRT. Recently, the potential role of the immune response following XRT has been documented,[7,8] implicating neuroinflammation as another mechanism contributing to the development of RN.

In addition to frank RN, microbleeds detected on imaging following XRT are a recent discovery.[9,10] Generally, microbleeds are thought to be either small deposits of hemosiderin, which can be attributed to damage to the small vessels,[11]; or, following radiation, microbleeds have been shown pathologically to be areas of telangiectasia.[12] Microbleeds may be indicative of future vascular disease such as stroke.[13] Microbleeds indicate not only that more serious disease could occur in the future but also that the patient could be put at risk of serious intracranial bleeding if started on anticoagulants.[14]

Techniques such as SWI are becoming more prominent with higher magnetic field strengths available clinically (3T) or for research (≥7T). These techniques make locating microbleeds increasingly easier due to the increased SNR, which makes increased resolution possible at higher magnetic fields, and the linear-with-field-enhancement of the paramagnetic effect of the hemosiderin deposits. However, the increased resolution can also lead to false-positives in microbleed detection because small venous vasculature that runs parallel to the magnetic field can be misinterpreted as a microbleed. SWI, quantitative susceptibility mapping (QSM), and apparent transverse relaxation (R_2^*) have been previously shown to be extremely sensitive to the vasculature and hemosiderin-rich microbleeds.[15-18] These techniques are also sensitive to white matter lesions, as shown in various multiple sclerosis studies.[19,20] Previous work from Reichenbach et al[21] estimated that these techniques are sensitive to venous vasculature of approximately 100–200 μm in diameter.

Among patients with brain tumors, most studies to date have investigated microbleeds and radiation necrosis among patients who have high-grade neoplasms[22,23]; however, long-term RN studies in this patient population may be less feasible due to the shortened life expectancy of most patients with malignant gliomas and the difficulty in distinguishing treatment effects and tumor progression. Additionally, these studies involve patients treated with chemotherapy, which has been shown potentially to influence the number of microbleeds present in the brain[10,24] and may confound the estimates of microbleeds due to radiation alone.

This initial feasibility study presents results that focus on imaging microbleeds and white matter imaging changes using SWI, QSM, and R_2^* on patients treated for benign or low-grade neoplasms with radiation alone. These patients have a longer overall survival following successful treatment and thus are at higher risk of eventually experiencing delayed adverse XRT effects. It was hypothesized that SWI, QSM, and R_2^* may be useful imaging techniques to detect late radiation changes among this patient population. The ability to detect such changes would then warrant a larger scale investigation for patients who might be at risk of longer term sequelae of their treatment (cognitive effects or focal brain injury).

MATERIALS AND METHODS

Patient Recruitment

The study was approved by the human subjects' research ethics board of the University of Western Ontario. Ten patients (2 men, 8 women) were recruited from our affiliated cancer program at the London Regional Cancer Program and were screened for eligibility by the treating radiation oncologist (G.S.B.). Eligibility requirements included patients who were older than 18 years of age with a Karnofsky Performance Scale score of >60 and were treated for benign or World Health Organization grade I or II brain neoplasms within 12–36 months of their recruitment for the study. Treatments for their neoplasms could have included surgical resection followed by radiation therapy or primary radiation therapy alone. As per protocol, patients underwent an initial imaging session at the time of enrollment and a second session 12–24 months later to detect any evolution in imaging changes.

MR Imaging

Patients were scanned on a 7T MR imaging machine. This scanner underwent an upgrade between visits for some of the patients. Preupgrade, an Agilent/Siemens 7T MR imaging scanner (Agilent, Santa Clara, California) with a 15-channel transmit/31-receive channel coil was used. Postupgrade, a Siemens 7T Magnetom Step 2.3 MR imaging scanner (Siemens, Erlangen, Germany) with an 8-channel transmit/32-receive channel coil was used. All patients had their initial scan performed on the preupgrade scanner. Three patients had their second visit on the preupgrade scanner, while 3 had their second visit on the postupgrade scanner. An anatomic T1WI was obtained (preupgrade: MPRAGE, 1-mm isotropic voxel, scan time of 5 minutes 45 seconds; postupgrade: MP2RAGE, 0.8-mm isotropic voxel, scan time of 8 minutes 26 seconds); and a CSF-attenuated magnetization-prepared FLAIR sequence (preupgrade: 1-mm isotropic resolution, scan time of 12 minutes 42 seconds; postupgrade: not acquired) was acquired for registration to clinical scans. A multiecho gradient-echo (preupgrade: multiecho gradient-echo, 1 mm in-plane resolution,

1.5-mm sections, TR = 40 ms, TE = 2.4 ms, echo spacing = 3.3 ms, echoes = 6, flip angle = 13°, generalized autocalibrating partially parallel acquisition = 2.1; postupgrade: multiecho gradient-echo, 1-mm in-plane resolution, 1.5-mm sections, TR = 40 ms, TE = 4.9 ms, echo spacing = 4.5 ms, echoes = 6, flip angle = 13°, generalized autocalibrating partially parallel acquisition = 2) sequence was acquired. A less sensitive form of imaging had to be used postupgrade due to vendor constraints on the number of transmit coils.

Postprocessing

The multiecho gradient-echo data set was acquired and postprocessed into SWI, R_2^* and QSM maps using in-house software.

QSM

The implementation of QSM used a preconjugate gradient method[25] and was compared with QSM using the MEDI toolbox in Matlab (MathWorks, Natick, Massachusetts)[17]; however, the data from the preupgrade scanner was not optimized for MEDI processing. The algorithm uses the phase information that is temporally unwrapped over each echo with the background field contributions being removed with a Gaussian high-pass filter of 11 mm to produce the local frequency shift. The QSM image was calculated by performing the regularized inversion demonstrated in Reichenbach et al.[21] Postupgrade data were run through both the preconjugate gradient and MEDI toolbox; however, only data from the preconjugate gradient method were analyzed using the postupgrade data.

R_2^*

R_2^* was computed with a nonlinear least-squares monoexponential fit with a voxel spread function for correction.[26]

SWI

An 11-mm Gaussian high-pass filter was used to filter the phase and was fit with respect to TEs using a weighted nonlinear least-squares function to calculate the local frequency-shift map. A frequency mask of 15 Hz was then applied to an average magnitude image from all echoes to create an SWI using in-house software. Finally, Matlab (MathWorks) was used to create a minimum-intensity-projection image through 7 mm (7 sections) of the SWI.

Dose Plan Overlay

Treatment dose plan and planning CT and MRIs were retrieved and were registered to the research MR imaging with the FMRIB Linear Image Registration Tool (FLIRT; http://www.fmrib.ox.ac.uk).[27] It was found beneficial to crop the CT simulator session to include only the head including just a few sections below the cerebellum from the CT and a T1WI without the use of skull-stripping. The matching was determined to be within the error of the 3-mm dose grid. CERR (http://cerr.info/about.php)[28] was used to export the dose plan.

Radiographic Assessment

Images (SWI, MPRAGE, and FLAIR) were reviewed by 2 board-certified neuroradiologists (K.Y.T., D.H.) blinded to the history of the patient. Both radiologists reviewing the images independently and in a group setting established what constituted a microbleed. The microbleeds on all images were counted, and images were further assessed for vasculature and white matter abnormalities.

Once identified, the microbleeds were manually segmented on the SWI with ITK-SNAP 1.6 (www.itksnap.org)[29] for further analysis with R_2^* and QSM.

Microbleeds at visit 1 and visit 2[a]

Patient	Visit 1 Microbleeds	Visit 2 Microbleeds	New Microbleeds	Resolved Microbleeds
1	7	4	2	5
2	5	X	Did not return	Did not return
3	4	X	Did not return	Did not return
4	0	0	0	0
5	2	2	0	0
6	2	0	0	2
7	0	0	0	0
8	0	0	0	0
9	1	X	Did not return	Did not return
10	5	X	Did not return	Did not return

Note:—X indicates patient did not return.
[a] All microbleeds occurred in areas of radiation of >45 Gy.

RESULTS

Clinical Findings

Ten patients consented to imaging and were enrolled in the study. The On-line Table provides a full description of their cases, treatment, and current clinical status. A Mini-Mental State Examination was performed at the first visit, and a mean score of 29/30 ± 0.9 indicated that patients were cognitively intact at assessment. Patients were imaged at a mean of 26.7 ± 7.5 months following their treatment, and 6 of 10 patients returned for a second MR imaging between 12 and 24 months (17.3 ± 7.3 months) following their first MR imaging. Four patients did not return for this second scan. Two patients became ill for unrelated health reasons, 1 patient opted not to return for a second research scan, and 1 patient's low-grade glioma evolved into a malignant glioma, precluding investigational re-imaging.

Radiologic Findings

No gross abnormalities or venous vessel density discrepancies were observed on the SWI. One patient (patient 8) had a cavernous angioma that had been previously detected on conventional MR imaging before enrollment in this study.

Microbleeds

Six of 10 patients had microbleeds on the postradiation imaging. In all except 1 patient (patient 6), microbleeds occurred in areas of high dose (>45 Gy). Some microbleeds resolved between the initial and follow-up scans. The Table reports the full list of microbleeds. In all patients, microbleeds had an R_2^* of >80 seconds^{-1} and QSM values lower than −0.25 ppm. Most microbleeds had halo artifacts on QSM as shown in Fig 1, which aided in their detection.

White Matter Lesions

Three patients had periventricular or lobar lesions on their T1WI and FLAIR images in the mid- (>30 Gy) to high-dose (>45 Gy)

regions, consistent with white matter changes reported after radiation therapy[30,31] as shown in Figs 2–4.

Current Clinical Status

As shown in the On-line Table, most patients who enrolled in this study are clinically stable following treatment for their neoplasms. Aside from patient 10, who developed a glioblastoma, their symptoms are not directly related to their diagnosis or treatment.

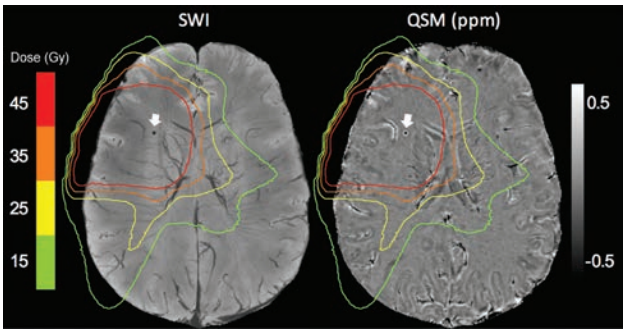

FIG 1. Patient 1 with microbleeds illustrated by the *white arrow* on SWI and QSM. Haloing artifacts can be seen on QSM. Venous vasculature is apparent in the high-dose region on SWI.

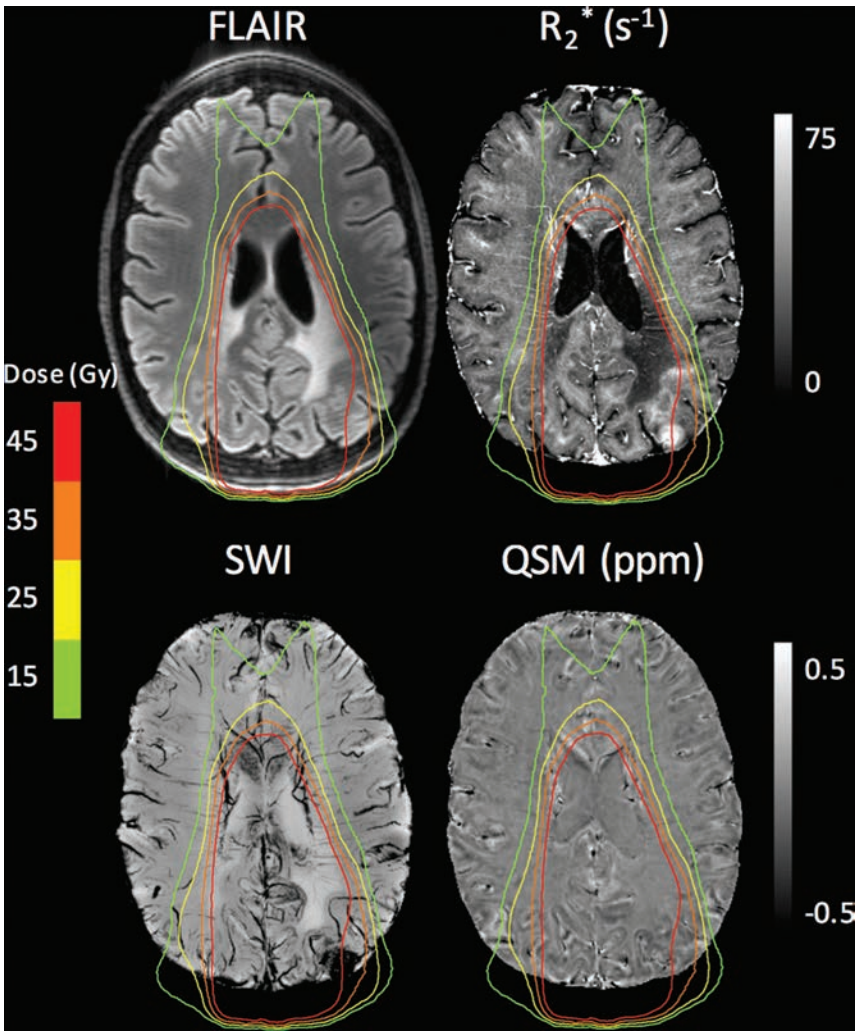

FIG 2. Patient 2 showing white matter abnormalities within the high-dose region as evidenced on FLAIR, R_2^*, and SWI.

DISCUSSION

Searches of prior literature led us to believe that this is the first study that investigated vasculature and white matter changes with 7T MR imaging in patients treated for low-grade or benign neoplasms with radiation and an operation only. The potentially long survival of this patient population posttreatment increases the chance that they may experience late radiation adverse effects compared with patients with higher grade lesions. Imaging biomarkers that could identify patients at risk of delayed radiation sequelae could be useful in this patient population to refine radiation-delivery techniques and to explore mitigating strategies such as pharmacologic interventions.[32]

The focus of this study was to determine the feasibility of this technique being susceptible to late effects of XRT on the normal parenchyma (1–5 years after therapy). Gross abnormalities were not expected because these patients were clinically stable and monitored by conventional imaging, but it was hypothesized that it could be possible to detect subclinical lesions in the brain receiving high doses of radiation therapy. It is known that microbleeds have appeared in patients treated with chemotherapy or radiation therapy for high-grade neoplasms.[10] Additionally, Liu et al[17] demonstrated the ability to distinguish microbleeds from venous vasculature using quantitative methods. Therefore, an investigation into the occurrence of microbleeds and white matter signal changes as a potential imaging biomarker of late radiation effects in patients treated for low-grade brain neoplasms was performed. While some of the imaging indicated potentially demyelinating lesions based on the white matter signal changes, a clinical diagnosis was not possible.

In this cohort, 6 of 10 patients showed microbleeds within the high-dose regions; and in 5 of 6 patients, no microbleeds were observed outside the high-dose region. Long-term follow-up is required to correlate with clinical end points such as future vascular incidents or cognitive adverse effects to determine whether microbleed monitoring could be important in these patients.

Although these patients do not have the frequency of microbleeds as shown in other studies of high-grade neoplasms, the appearance of microbleeds is indicative of endothelial damage within the high-dose region. This suggests the importance of long-term monitoring in this low-grade cohort because these patients could be at a higher potential for symptomatic vascular or cognitive changes later in life.[33,34] The appearance of microbleeds could also indicate that further studies are required

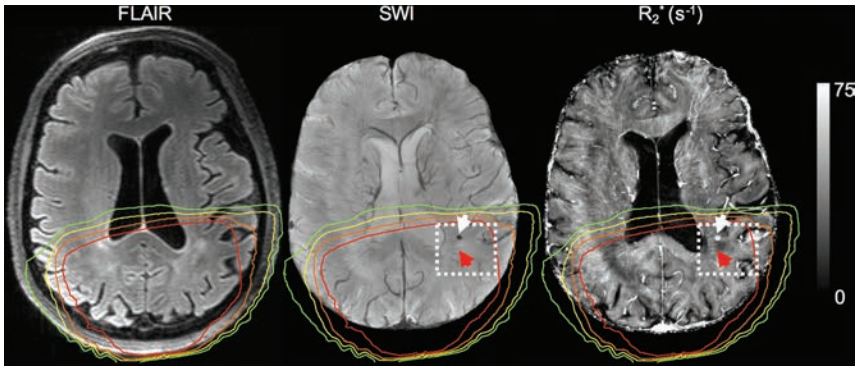

FIG 3. Patient 3 showing microbleeds on SWI and R_2^* (*white arrow*) and the white matter lesion (*red arrow*). *Isodose lines* are same as in Fig 1.

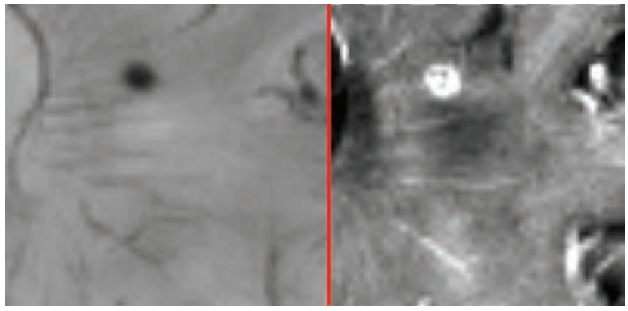

FIG 4. Zoomed-in view of Fig 3 (within the *white box* in Fig 3). Venous vasculature is seen through the suspected white matter lesion.

to look at the effect of anticoagulants. Certain studies have already shown that the appearance of microbleeds in other disease states could be a contraindication for the use of anticoagulants,[35] and these findings suggest strategies attempting to limit radiation injury using antiplatelet agents or anticoagulants in this patient population should be evaluated cautiously. The disappearance of microbleeds between visits could not be considered imaging artifacts or due to true resolution as discussed by Yates et al.[36]

In addition to venous vasculature being present in high-dose regions, veins within the white matter lesions with high doses can be observed as shown in Fig 4. This is a common finding in MS and acute disseminated encephalomyelitis.[37] The white matter lesions have been reported previously,[30,31,38] with reports of cognitive decline. A recent communication has shown that a 43-year-old patient developed similar MS-type lesions following XRT.[39] In MS, these lesions have been shown to have an immune response that could be indicative of neuroinflammation. The ability to show that these lesions have venules running through them suggests that further studies are warranted to test this hypothesis of neuroinflammation as a mediator of late radiation effects. Supporting this finding was the detection of FLAIR hyperintensities coupled with the low R_2^* values, which could indicate demyelination, though the white matter signal changes could not be pathologically confirmed as demyelinating. Neuroinflammation as a mediator of late radiation cerebral effects and as a potential therapeutic target is an area of active investigation,[32] and these findings suggest imaging biomarkers such as SWI and R_2^* might be useful tools for noninvasive monitoring of neuroinflammatory processes.

Additionally, the high R_2^* can help distinguish microbleeds and small venules that have much lower R_2^* values (20–40 seconds^{-1}). The halo effect and large susceptibility value of the microbleeds on QSM as shown in Fig 1 could lead to a reduced burden for neuroradiologists when detecting microbleeds using automated methods.

A limitation of this study is the small number of participants and an inability to acquire follow-up imaging for all patients. This preliminary experience illustrates the feasibility of the technique in this population and suggests that a study of a larger cohort of patients with this imaging technique may be warranted.

Another limitation of SWI techniques, in general, is that titanium clips used following surgery result in blooming artifacts on postprocessed images. The artifacts are due to the magnetic field perturbation due to these clips causing the signal to decay at a much higher rate, resulting in more distortions with lengthened TEs. These artifacts may lead to being unable to identify microbleeds in tissue close to the skull. Finally, SWI is limited in its ability to view the arterioles; however, Bian et al[40] have shown that arteries and veins can be imaged in the same acquisition. This method could also decrease false-positives and improve microbleed detection, and it would also be beneficial in observing damage to the arterioles.

CONCLUSIONS

This work is a preliminary study examining the long-term effects of radiation therapy on patients treated for benign or low-grade neoplasms using ultra-high-field MR imaging. This study presented the potential of microbleeds in patients treated with XRT alone; the increased ability to detect microbleeds with ultra-high-field MR imaging with the use of SWI, R_2^*, and QSM; and the potential for white matter lesions in the high-dose area. The results presented in this study warrant further investigation in a larger patient cohort because these could have wide-ranging consequences in the long-term management of these patients.

Disclosures: Jean-Guy Belliveau—*RELATED*: *Grant*: London Regional Cancer Program Catalyst Grant, *Comments*: also, Canada Research Chairs Program, Canada Foundation for Innovation. Glenn S. Bauman—*UNRELATED*: *Grants/Grants Pending*: Canadian Institutes of Health Research/Ontario Institute for Cancer Research, *Comments*: support prostate cancer research. Keng Yeow Tay—*RELATED*: *Grant*: London Regional Cancer Program Catalyst Grant, *Comments*: London Regional Cancer Program Catalyst Grant, Canada Research Chairs Program, Canada Foundation for Innovation. Ravi S. Menon—*RELATED*: *Grant*: London Regional Cancer Program internal competition; *UNRELATED*: *Payment for Lectures Including Service on Speakers Bureaus*: Siemens; *Patents (Planned, Pending or Issued)*: Siemens, *Comments*: sale of patent to Siemens in 2015.

REFERENCES

1. Lawrence YR, Li XA, el Naqa I, et al. **Radiation dose-volume effects in the brain.** *Int J Radiat Oncol Biol Phys* 2010;76:S20–27 CrossRef Medline
2. Monje ML, Dietrich J. **Cognitive side effects of cancer therapy dem-**

onstrate a functional role for adult neurogenesis. *Behav Brain Res* 2012;227:376–79 CrossRef Medline
3. Monje ML. **Cranial radiation therapy and damage to hippocampal neurogenesis.** *Dev Disabil Res Rev* 2008;14:238–42 CrossRef Medline
4. Fink JR, Born D, Chamberlain MC. **Radiation necrosis: relevance with respect to treatment of primary and secondary brain tumors.** *Curr Neurol Neurosci Rep* 2012;12:276–85 CrossRef Medline
5. Rahmathulla G, Marko NF, Weil RJ. **Cerebral radiation necrosis: a review of the pathobiology, diagnosis and management considerations.** *J Clin Neurosci* 2013;20:485–502 CrossRef Medline
6. Levin VA, Bidaut L, Hou P, et al. **Randomized double-blind placebo-controlled trial of bevacizumab therapy for radiation necrosis of the central nervous system.** *Int J Radiat Oncol Biol Phys* 2011;79:1487–95 CrossRef Medline
7. Moravan MJ, Olschowka JA, Williams JP, et al. **Cranial irradiation leads to acute and persistent neuroinflammation with delayed increases in T-cell infiltration and CD11c expression in C57BL/6 mouse brain.** *Radiat Res* 2011;176:459–73 CrossRef Medline
8. Ballesteros-Zebadúa P, Chavarria A, Celis MA, et al. **Radiation-induced neuroinflammation and radiation somnolence syndrome.** *CNS Neurol Disord Drug Targets* 2012;11:937–49 CrossRef Medline
9. Lupo JM, Chuang CF, Chang SM, et al. **7-Tesla susceptibility-weighted imaging to assess the effects of radiotherapy on normal-appearing brain in patients with glioma.** *Int J Radiat Oncol Biol Phys* 2012;82:e493–500 CrossRef Medline
10. Tanino T, Kanasaki Y, Tahara T, et al. **Radiation induced microbleeds after cranial irradiation: evaluation by phase-sensitive magnetic resonance imaging with 3.0 Tesla.** *Yonago Acta Med* 2013;56:7–12 Medline
11. Warring DJ. *Cerebral Microbleeds: Pathophysiology to Clinical Practice.* Cambridge: Cambridge University Press; 2011
12. Gaensler E, Dillon W, Edwards M, et al. **Radiation-induced telangiectasia in the brain simulates cryptic vascular malformations at MR imaging.** *Radiology* 1994;193:629–36 CrossRef Medline
13. Charidimou A, Werring DJ. **Cerebral microbleeds and cognition in cerebrovascular disease: an update.** *J Neurol Sci* 2012;322:50–55 CrossRef Medline
14. Cordonnier C. **Brain microbleeds.** *Pract Neurol* 2010;10:94–100 CrossRef Medline
15. Bian W, Hess CP, Chang SM, et al. **Susceptibility-weighted MR imaging of radiation therapy-induced cerebral microbleeds in patients with glioma: a comparison between 3T and 7T.** *Neuroradiology* 2014;56:91–96 CrossRef Medline
16. Vernooij MW, Ikram MA, Wielopolski PA, et al. **Cerebral microbleeds: accelerated 3D T2*-weighted GRE MR imaging versus conventional 2D T2*-weighted GRE MR imaging for detection.** *Radiology* 2008;248:272–77 CrossRef Medline
17. Liu J, Liu T, Rochefort L De, et al. **Morphology enabled dipole inversion for quantitative susceptibility mapping using structural consistency between the magnitude image and the susceptibility map.** *Neuroimage* 2012;59:2560–68 CrossRef Medline
18. Liu T, Surapaneni K, Lou M, et al. **Cerebral microbleeds: burden assessment by using quantitative susceptibility mapping.** *Radiology* 2012;262:269–78 CrossRef Medline
19. Langkammer C, Liu T, Khalil M. **Quantitative susceptibility mapping in multiple sclerosis.** *Radiology* 2013;267:551–59 CrossRef Medline
20. Wisnieff C, Ramanan S, Olesik J, et al. **Quantitative susceptibility mapping (QSM) of white matter multiple sclerosis lesions: interpreting positive susceptibility and the presence of iron.** *Magn Reson Med* 2015;74:564–70 CrossRef Medline
21. Reichenbach JR, Barth M, Haacke EM, et al. **High-resolution MR venography at 3.0 Tesla.** *J Comput Assist Tomogr* 2000;24:949–57 CrossRef Medline
22. Lupo JM, Molinaro AM, Essock-Burns E, et al. **The effects of anti-angiogenic therapy on the formation of radiation-induced microbleeds in normal brain tissue of patients with glioma.** *Neuro Oncol* 2016;18:87–95 CrossRef Medline
23. Na A, Haghigi N, Drummond KJ. **Cerebral radiation necrosis.** *Asia Pac J Clin Oncol* 2014;10:11–21 CrossRef Medline
24. Koppelmans V, Vernooij MW, Boogerd W, et al. **Prevalence of cerebral small-vessel disease in long-term breast cancer survivors exposed to both adjuvant radiotherapy and chemotherapy.** *J Clin Oncol* 2015;33:588–93 CrossRef Medline
25. de Rochefort L, Liu T, Kressler B, et al. **Quantitative susceptibility map reconstruction from MR phase data using Bayesian regularization: validation and application to brain imaging.** *Magn Reson Med* 2010;63:194–206 CrossRef Medline
26. Yablonskiy DA, Sukstanskii AL, Luo J, et al. **Voxel spread function method for correction of magnetic field inhomogeneity effects in quantitative gradient-echo-based MRI.** *Magn Reson Med* 2013;70:1283–92 CrossRef Medline
27. Jenkinson M, Smith SM. **A global optimization method for robust affine registration of brain images.** *Med Imaging Anal* 2001;5:143–56 CrossRef Medline
28. Deasy JO, Blanco AI, Clark VH. **CERR: a computational environment for radiotherapy research.** *Med Phys* 2003;30:979–85 CrossRef Medline
29. Ibáñez L, Schroeder W, Ng L, et al; Insight Software Consortium. The ITK Software Guide. August 21, 2003. https://www.sci.utah.edu/publications/ibanez03/ItkSoftwareGuide.pdf. Accessed August 2015
30. Rane N, Quaghebeur G. **CNS effects following the treatment of malignancy.** *Clin Radiol* 2012;67:61–68 CrossRef Medline
31. Szerlip N, Rutter C, Ram N, et al. **Factors impacting volumetric white matter changes following whole brain radiation therapy.** *J Neurooncol* 2011;103:111–19 CrossRef Medline
32. Greene-Schloesser DM, Moore E, Robbins ME. **Molecular pathways: radiation-induced cognitive impairment.** *Clin Cancer Res* 2013;19:2294–300 CrossRef Medline
33. Plummer C, Henderson RD, O'Sullivan JD, et al. **Ischemic stroke and transient ischemic attack after head and neck radiotherapy: a review.** *Stroke* 2011;42:2410–18 CrossRef Medline
34. Martinez-Ramirez S, Greenberg SM, Viswanathan A. **Cerebral microbleeds: overview and implications in cognitive impairment.** *Alzheimers Res Ther* 2014;6:33 CrossRef Medline
35. Haley KE, Greenberg SM, Gurol ME. **Cerebral microbleeds and macrobleeds: should they influence our recommendations for antithrombotic therapies?** *Curr Cardiol Rep* 2013;15:425 CrossRef Medline
36. Yates PA, Villemagne VL, Ellis KA, et al. **Cerebral microbleeds: a review of clinical, genetic, and neuroimaging associations.** *Front Neurol* 2014;4:205 CrossRef Medline
37. Quinn MP, Kremenchutzky M, Menon RS. **Venocentric lesions: an MRI marker of MS?** *Front Neurol* 2013;4:98 CrossRef Medline
38. Armstrong CL, Gyato K, Awadalla AW, et al. **A critical review of the clinical effects of therapeutic irradiation damage to the brain: the roots of controversy.** *Neuropsychol Rev* 2004;14:65–86 CrossRef Medline
39. Shaygannejad V, Zare M, Maghzi H, et al. **Brain radiation and possible presentation of multiple sclerosis.** *J Res Med Sci* 2013;18(suppl 1):S93–95 Medline
40. Bian W, Banerjee S, Kelly DA, et al. **Simultaneous imaging of radiation-induced cerebral microbleeds, arteries and veins, using a multiple gradient echo sequence at 7 Tesla.** *J Magn Reson Imaging* 2015;42:269–79 CrossRef Medline

Photon-Counting CT of the Brain: In Vivo Human Results and Image-Quality Assessment

A. Pourmorteza, R. Symons, D.S. Reich, M. Bagheri, T.E. Cork, S. Kappler, S. Ulzheimer, and D.A. Bluemke

ABSTRACT

BACKGROUND AND PURPOSE: Photon-counting detectors offer the potential for improved image quality for brain CT but have not yet been evaluated in vivo. The purpose of this study was to compare photon-counting detector CT with conventional energy-integrating detector CT for human brains.

MATERIALS AND METHODS: Radiation dose–matched energy-integrating detector and photon-counting detector head CT scans were acquired with standardized protocols (tube voltage/current, 120 kV(peak)/370 mAs) in both an anthropomorphic head phantom and 21 human asymptomatic volunteers (mean age, 58.9 ± 8.5 years). Photon-counting detector thresholds were 22 and 52 keV (low-energy bin, 22–52 keV; high-energy bin, 52–120 keV). Image noise, gray matter, and white matter signal-to-noise ratios and GM–WM contrast and contrast-to-noise ratios were measured. Image quality was scored by 2 neuroradiologists blinded to the CT detector type. Reproducibility was assessed with the intraclass correlation coefficient. Energy-integrating detector and photon-counting detector CT images were compared using a paired *t* test and the Wilcoxon signed rank test.

RESULTS: Photon-counting detector CT images received higher reader scores for GM–WM differentiation with lower image noise (all $P <$ .001). Intrareader and interreader reproducibility was excellent (intraclass correlation coefficient, ≥0.86 and 0.79, respectively). Quantitative analysis showed 12.8%–20.6% less image noise for photon-counting detector CT. The SNR of photon-counting detector CT was 19.0%–20.0% higher than of energy-integrating detector CT for GM and WM. The contrast-to-noise ratio of photon-counting detector CT was 15.7% higher for GM–WM contrast and 33.3% higher for GM–WM contrast-to-noise ratio.

CONCLUSIONS: Photon-counting detector brain CT scans demonstrated greater gray–white matter contrast compared with conventional CT. This was due to both higher soft-tissue contrast and lower image noise for photon-counting CT.

ABBREVIATIONS: CNR = contrast-to-noise ratio; EID = energy-integrating detector; ICC = intraclass correlation coefficient; PCD = photon-counting detector

Brain CT remains the first-line technique of choice for the evaluation of traumatic and nontraumatic brain injury and is the most-often-performed CT examination in many emergency departments.[1,2] However, there is limited gray matter–white matter differentiation with brain CT, decreasing the ability to assess the hypoattenuation and loss of GM–WM differentiation seen in early ischemic brain changes.[3,4] In addition, beam-hardening artifacts due to attenuation by the skull of lower energy photons degrade brain CT diagnostic image quality, potentially mimicking intracranial hemorrhage and reducing GM–WM differentiation.[5]

The energy spectrum of x-ray tubes for CT is usually characterized by the peak kilovoltage, but the applied x-ray spectrum consists of a wide distribution of lower energy photons. Conventional CT uses energy-integrating detectors (EIDs) to combine the effects of x-ray photon number and photon energy into an

Received June 19, 2017; accepted after revision July 20.

From the Department of Radiology and Imaging Sciences (A.P., R.S., D.S.R., M.B., T.E.C., D.A.B.), National Institutes of Health Clinical Center, Bethesda, Maryland; Department of Radiology and Imaging Sciences (A.P.), Emory University School of Medicine, Atlanta, Georgia; Department of Imaging and Pathology (R.S.), Medical Imaging Research Centre, University Hospitals, Leuven, Belgium; Translational Neuroradiology Section (D.S.R.), National Institute of Neurological Disorders and Stroke, Bethesda, Maryland; Departments of Radiological Sciences and Bioengineering (T.E.C.), University of California, Los Angeles, Los Angeles, California; and Siemens (S.K., S.U.), Erlangen, Germany.

A. Pourmorteza and R. Symons contributed equally to this work.

This study was supported by the National Institutes of Health intramural research program (ZIACL090019; ZIAEB000072; ZIANS003119) and a collaborative research agreement with Siemens (Erlangen, Germany).

Data inclusion and analysis were performed by authors, who are not employees of or consultants for Siemens.

Please address correspondence to David A. Bluemke, MD, PhD, Radiology and Imaging Sciences; 10 Center Dr, Bldg 10/Room 1C355, National Institutes of Health/Clinical Center, Bethesda, MD 20892; e-mail: david.bluemke@nih.gov; DBluemke@rsna.org

Indicates open access to non-subscribers at www.ajnr.org

http://dx.doi.org/10.3174/ajnr.A5402

intensity value through conversion of x-rays to light photons to electrical pulses. Consequently, with EID CT, low-energy photons (eg, 40–70 keV) have less contribution to the CT intensity value than high-energy photons (eg, 110–140 keV). For brain imaging however, it is these low-energy photons that have better soft-tissue discrimination for identification of gray–white matter contrast.

Photon-counting detectors (PCDs) are a new technology for CT imaging that directly converts x-ray photons into electrical pulses. PCDs measure the number of detected x-ray photons (ie, photon count) and their photon energy.[6-11] These characteristics allow equal weighting of low- and high-energy photons and may therefore be useful for improving soft-tissue contrast in the brain.[8] In addition, the direct conversion and counting of individual photons provide a better estimate of the underlying photon statistics, which, in turn, may improve image quality by reducing image noise.[8,12-14] We hypothesized that the combined effects of better contrast and reduced noise may lead to better overall GM–WM differentiation in brain PCD CT.

To date, PCD CT scanning of a cadaver head[15] has suggested the feasibility of PCD for brain CT, but in vivo results have not been previously studied, to our knowledge. Thus, the purpose of the current study was to compare the image quality of PCD with that of conventional EID for human brain CT.

MATERIALS AND METHODS

Ex Vivo Human Head Phantom Studies

We used a custom-made anthropomorphic head phantom made of a human skull embedded in plastic (Phantom Laboratory, Salem, New York) to assess image quality (Hounsfield unit accuracy and image noise) and calculate sample size. The phantom was filled with gel made from a mixture of agar and sucrose with attenuation values close to those of WM.

In Vivo Human Studies

This Health Insurance Portability and Accountability Act–compliant, institutional review board–approved study with informed consent prospectively enrolled 21 asymptomatic volunteers (42.9% men) older than 45 years of age at the National Institutes of Health Clinical Center. All study subjects were included in the analysis. Exclusion criteria were age younger than or equal to 45 years, prior CT scan within 12 months, pregnancy, and genetic predisposition to radiation-induced cancer.

Photon-Counting CT System

The whole-body prototype PCD CT system has been previously described.[16] In brief, this hybrid scanner is based on a dual-source CT system (Somatom Definition Flash; Siemens, Erlangen, Germany) with 2 x-ray sources at 95° separation; one of the conventional EIDs was replaced with a cadmium-telluride PCD. The 2 subsystems cannot be operated simultaneously; however, it is possible to perform back-to-back EID and PCD scans with delays as short as 1 second. With identical x-ray sources and spectra and similar scanner geometries, this setup provides a convenient platform for EID versus PCD comparative studies. The EID and PCD have FOVs of 500 and 275 mm, and a collimation × pixel of 64 × 0.6 mm and 32 × 0.5 mm at the isocenter, respectively. Each PCD pixel consists of 4 × 4 subpixels, coupled to fast application–specific integrated circuits that count the number of electrical pulses created by incident photons and measure their energies above 2 set thresholds. The thresholds can be defined at 1-keV increments: low-energy threshold between 20 and 50 keV and high-energy threshold between 50 and 90 keV.

CT Scan Protocol

Spiral noncontrast EID brain CT scans were acquired at clinical routine settings according to the American Association of Physicists in Medicine guidelines (tube voltage/reference tube current-time product, 120 kVp/370 mAs; pitch, 0.55; rotation time, 1 second; volume CT dose index, 56.7 mGy).[17] After a 5-second delay due to table movements, the EID scan was followed by a PCD scan with identical tube voltage, current-time, rotation time, and pitch values. The PCD energy thresholds were defined at 22 and 52 keV, resulting in 2 energy bins (low-energy bin, 22–52 keV; high-energy bin, 52–120 keV). The low threshold was set at 22 keV to capture all detected photons, whereas the high threshold was set at 52 keV to avoid low-energy scatter photons while still maintaining relatively high photon counts. We used the term "PCD images" to refer to images reconstructed from all detected photons with energies of >22 keV; the quality of these PCD images was compared with that of the EID images.

In addition, we investigated the quality of images reconstructed from low- and high-energy photons detected by the PCD. With the same tube voltage and tube current–time product settings, the volume CT dose index estimates for the PCD were approximately 10% higher than those for the EID. This is not a limitation of the PCD technology and can be attributed to the difference in z-axis collimation of the 2 detector systems in the prototype. Identical collimations would result in similar volume CT dose index values for both systems.[18] Therefore, we matched the tube voltage and tube current–time product values to obtain a similar energy spectrum and the number of x-ray photons incident on both detector systems, allowing a fair comparison.[13] The effective dose was calculated by multiplying the dose-length product by 0.0021 mSv/mGy as the constant k-value for brain imaging.

CT Image Reconstruction

Phantom scans were reconstructed using the sinogram-affirmed iterative reconstruction (strength 3 with J40f [medium] kernel) (ReconCT, Version 13.8.6.0; Siemens). Human scans were reconstructed with 2 different kernels: J40f to assess soft tissue and I70f (very sharp) to assess bone. The FOV was 250 mm with section thickness/increment of 2/2 mm and a 512 × 512 matrix size.

Qualitative Image Analysis

Two neuroradiologists (M.B. and D.S.R., with 23 and 14 years of experience, respectively) independently evaluated the image quality of the EID and PCD images on a conventional PACS system. Readers were blinded to CT detector type and study-subject demographics. Images were presented side by side in random order with initial standard window center/width values for brain (45/80 HU) and bone (490/2500 HU). This presentation resulted in 84 blinded image reads (21 subjects × 2 readers × 2 detectors). Image-quality scores were based on the European Guidelines on

Quality Criteria for Computed Tomography.[19] Readers evaluated GM–WM differentiation, the posterior cranial fossa, ventricles, bone, and subjective image noise on a 5-point scale. The images were re-evaluated by 1 reader (M.B.) after 4 weeks to assess intrareader reproducibility.

Quantitative Image Analysis

ROIs were carefully positioned in the center of the head phantom to assess attenuation values and image noise. Image noise was calculated from corrected SDs of the difference of 2 repeated acquisitions for each detector system; the radial noise-power spectrum was estimated for a set of 3.2 × 3.2 cm ROIs centered 5.5 cm away from the isocenter, as explained in detail in Friedman et al.[20] For human datasets, ROIs were placed in the basal ganglia GM, the internal capsule WM, and the lateral ventricle CSF. The average ROI size was 24.7 ± 4.2 mm^2. Image noise was calculated as the SD of each ROI. The signal-to-noise ratio for GM and WM ROIs was calculated as mean attenuation divided by the SD. GM–WM contrast was calculated as the difference of their mean attenuation values. GM–WM contrast-to-noise ratio (CNR) was calculated as the GM-WM contrast divided by the square root of the sum of the variances.

Statistical Analysis

R statistical and computing software, Version 3.3.1 (http://www.r-project.org) was used for statistical analysis. The Shapiro-Wilk test was used for normality testing. Continuous data were expressed as mean ± SD. The Wilcoxon signed rank test (paired) with continuity correction was used to compare reader quality scores. The paired *t* test was used to compare continuous variables. Interreader and intrareader reproducibility was scored with the intraclass correlation coefficient (ICC) as excellent (ICC, >0.75), good (ICC, 0.40–0.75), or poor (ICC, <0.40). Significance was defined as $P < .05$. The improvement ratio of PCD compared with EID was calculated as the difference between EID and PCD quality indices (image noise, SNR, contrast, and CNR) divided by the value for the EID as described by Pomerantz et al.[21] A priori sample size calculation was based on the interstudy SD of image noise difference between EID and PCD in the head phantom as described by Machin et al[22] and Altman[23] with the following formula: $n = f(\alpha, P) \times \sigma^2 \times 2/\delta^2$, where α is the significance level, P is the study power, f is a function of α and P, with σ as the interstudy SD, δ as the desired percentage difference to be detected; and n is the sample size needed. An image noise δ of 10% would correspond to approximately 20% radiation dose reduction without compromising diagnostic image quality.[24] To compensate for increased variability in human subjects compared with phantom experiments, we doubled the σ value of our phantom measurements (9.6%). Under these circumstances, a paired comparison of 21 subjects would be sufficient to reliably detect a 10% image noise difference with $P = 90\%$ and $\alpha = .05$.

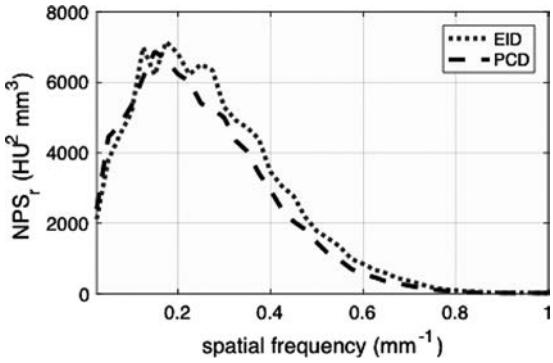

FIG 1. Radial noise-power spectrum (NPS) measured in an anthropomorphic head phantom for energy-integrating detector and photon-counting detector scans at 120 kVp and 370 mAs. The PCD curve was lower than the EID curve. The difference is more prominent at mid-to-high spatial frequencies.

RESULTS

Ex Vivo Human Head Phantom Studies

Attenuation values in the center of the head phantom were similar for EID and PCD scans (25.2 ± 0.3 versus 24.5 ± 1.5 HU, $P = .170$). PCD images showed 8.5% ± 4.8% less image noise than EID images (4.1 ± 0.3 versus 3.8 ± 0.2 HU, $P < .001$). The radial noise-power spectrum at 5.5-cm off-center was estimated for both detectors. The PCD images showed lower noise power in most of the detectable spatial frequencies (Fig 1).

In Vivo Human Head CT Studies

Twenty-one subjects (9 men, 12 women) were evaluated. The mean age for men, women, and all subjects was 61 years (range, 48–79 years), 57 years (range, 45–70 years), and 59 years (range,

Table 1: Interreader and intrareader reproducibility of subjective image-quality analysis

	Interreader		Intrareader	
Parameter	ICC	95% CI	ICC	95% CI
Image quality				
GM–WM differentiation	0.79	0.65–0.88	0.86	0.75–0.92
Posterior fossa	0.87	0.77–0.93	0.86	0.76–0.92
Bone	0.90	0.82–0.94	0.90	0.82–0.94
Image noise	0.93	0.87–0.96	0.95	0.91–0.97

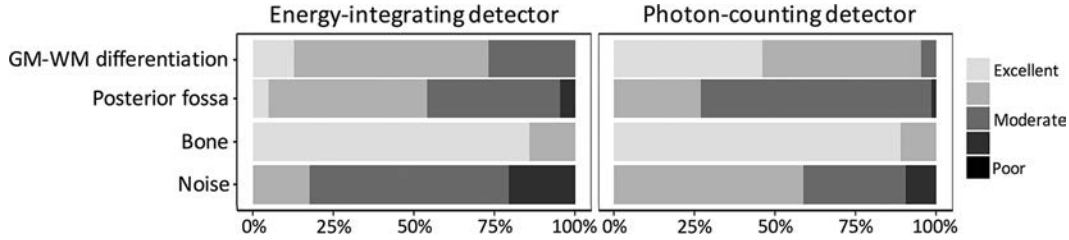

FIG 2. Blinded reader evaluation of image quality for energy-integrating detector and photon-counting detector head images. PCD scores are better for gray matter-versus-white matter differentiation and image noise, whereas EID scores are better for posterior fossa image quality (all $P < .001$, paired Wilcoxon signed rank test). Image quality scores are based on the European Guidelines for Image Quality Criteria for Computed Tomography.[19]

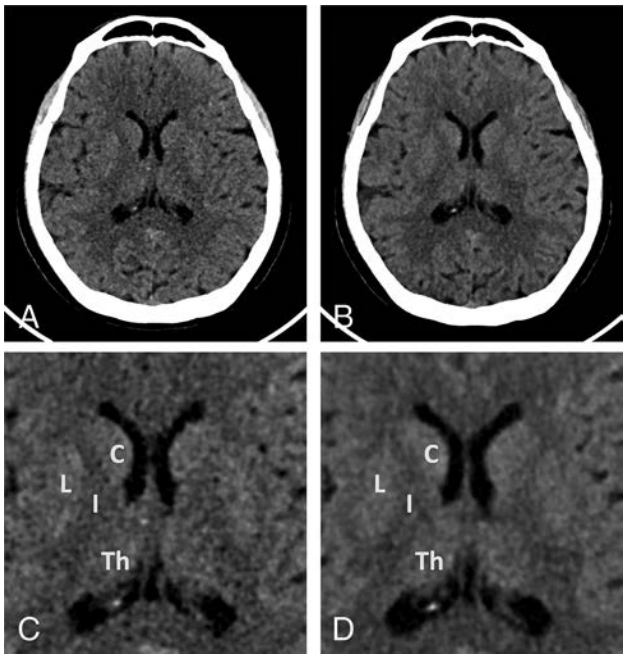

FIG 3. Example energy-integrating detector and photon-counting detector images of a 59-year-old woman (section thickness, 2 mm; increment, 2 mm; window center, 45 HU; window width, 80 HU). *A*, Axial EID reconstruction at the level of the basal ganglia. *B*, Axial PCD reconstruction at the same level as *A*. Lower image noise is shown for the PCD image. Zoomed-in EID (*C*) and PCD (*D*) images at the same level as *A* and *B*. C indicates caudate; I, internal capsule; L, lentiform nucleus; Th, thalamus.

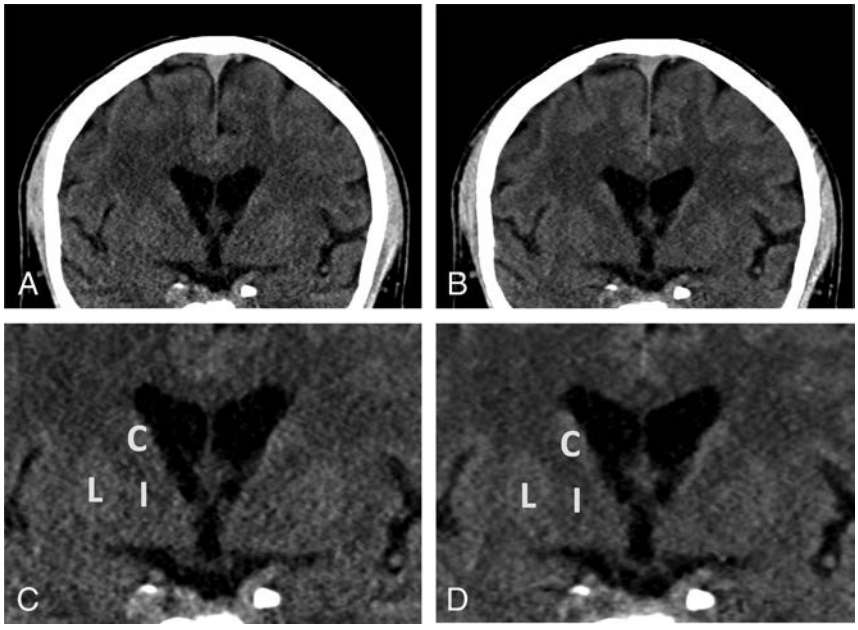

FIG 4. Sample energy-integrating detector and photon-counting detector images of a 67-year-old man (section thickness, 2 mm; increment, 2 mm; window center, 45 HU; window width, 80 HU). *A*, Coronal EID image at the level of the basal ganglia. *B*, Coronal PCD image at the same level as *A* shows lower image noise for the PCD image. Zoomed-in EID (*C*) and PCD (*D*) images at the same level. C indicates caudate; I, internal capsule; L, lentiform nucleus.

Table 2: Mean attenuation value and SD of ROIs in energy-integrating detector and photon-counting detector CT images in human subjects

Attenuation Values (HU)	EID	PCD	*P* Value
Gray matter	39.0 ± 1.6	39.5 ± 1.6	.40
White matter	30.2 ± 1.4	29.2 ± 1.7	.06
Lateral ventricle (CSF)	5.8 ± 1.4	5.2 ± 1.8	.27

45–79 years), respectively. No clinically relevant incidental findings were detected in our study population. The volume CT dose index was approximately 10% higher for the PCD system (63.6 versus 56.7 mGy for PCD and EID, respectively) (see "Materials and Methods"). This resulted in a dose-length product/effective dose of 860.7 ± 43.1 mGy × cm/1.8 ± 0.1 mSv for EID and 957.8 ± 45.2 mGy × cm/2.0 ± 0.1 mSv for PCD.

Qualitative Image Analysis

Each reader scored 21 pairs (42 acquisitions) of EID and PCD CT images in a blinded fashion. PCD image-quality scores were significantly better for GM–WM differentiation and image noise (both $P < .001$) (Fig 2). EID scores were better for the evaluation of the posterior fossa (3.5 ± 0.7 versus 3.3 ± 0.5, $P = .003$). Bone image-quality scores were similar for both detectors. Reader reproducibility was excellent for all scores (ICC, ≥0.86, and ICC, ≥0.79, for intra- and interreader reproducibility, respectively) (Table 1). Sample EID and PCD images are shown in Figs 3 and 4.

Quantitative Image Analysis

Attenuation measurements for basal ganglia GM, internal capsule WM, and lateral ventricle CSF were similar for the EID and PCD CT systems (Table 2). Image noise in GM, WM, and CSF was 12.8%–20.6% lower for PCD than for EID images (GM noise, 3.2 ± 0.5 HU for PCD versus 3.9 ± 1.0 HU for EID; WM, 2.7 ± 0.7 HU for PCD versus 3.4 ± 0.8 HU for EID; lateral ventricle CSF, 3.4 ± 0.7 for PCD versus 3.9 ± 0.8, for EID; all, $P < .01$). GM and WM SNR improvement of PCD CT versus EID CT was 19.0% and 20.0%, respectively. GM–WM contrast was 15.7% higher for PCD CT versus EID CT (10.3 ± 1.9 versus 8.9 ± 1.8 HU, respectively, $P = .02$) and GM–WM CNR was 33.3% higher (2.4 ± 0.8 versus 1.8 ± 0.5, respectively, $P < .001$). Quantitative quality indices are summarized in Table 3.

Spectral Analysis

We compared attenuation values and image-quality metrics between low- and high-energy bin images in the same ROIs (Table 4). The image noise for the low- and high-energy PCD bins for WM was 5.0 ± 1.6 and 3.9 ± 0.7 HU, respectively. Because each bin contained only a portion of the detected photons, the noise for

each bin was higher than that of the PCD image (2.7 ± 0.7 HU) containing all detected photons. However, GM–WM contrast was significantly better for the low-energy bin images versus high-energy bin images (10.6 ± 2.3 versus 8.8 ± 2.5 HU, respectively, $P = .02$). GM and WM SNR and GM–WM CNR between the low- and high-energy bin images were not significantly different (Fig 5).

Table 3: Image-quality comparison between energy-integrating detector and photon-counting detector CT for gray matter, white matter, and CSF

Image-Quality Index	EID[a]	PCD[a]	*P* Value	Improvement Ratio[b] (%)
GM noise (HU)	3.9 ± 1.0	3.2 ± 0.5	<.001	17.9
WM noise (HU)	3.4 ± 0.8	2.7 ± 0.7	.002	20.6
CSF noise (HU)	3.9 ± 0.8	3.4 ± 0.7	<.001	12.8
GM SNR	10.5 ± 2.5	12.6 ± 2.2	<.001	19.0
WM SNR	9.5 ± 2.3	11.4 ± 2.7	.01	20.0
GM–WM contrast (HU)	8.9 ± 1.8	10.3 ± 1.9	.02	15.7
GM–WM CNR	1.8 ± 0.5	2.4 ± 0.8	<.001	33.3

[a] Values are means ± SD.
[b] Improvement ratio was defined as the difference between EID and PCD quality indices (image noise, SNR, GM–WM contrast, and CNR) divided by the EID quality index.

Table 4: Attenuation values and image-quality comparison between photon-counting detector low-energy and high-energy bin images for gray matter, white matter, and CSF

	Low-Energy Bin (22–52 keV)[a]	High-Energy Bin (52–120 keV)[a]	*P* Value
Attenuation values (HU)			
Basal nuclei GM	41.5 ± 2.1	38.3 ± 2.1	<.001
Internal capsule WM	30.9 ± 2.7	29.5 ± 2.0	.03
Lateral ventricle (CSF)	7.2 ± 2.1	4.7 ± 1.9	<.001
Image-quality metrics			
GM noise (HU)	5.4 ± 1.2	4.5 ± 0.9	.004
WM noise (HU)	5.0 ± 1.6	3.9 ± 0.7	.01
CSF noise (HU)	4.9 ± 0.9	4.7 ± 1.2	.36
GM SNR	8.2 ± 2.1	8.9 ± 1.8	.11
WM SNR	6.7 ± 1.9	7.7 ± 1.6	.05
GM–WM contrast (HU)	10.6 ± 2.3	8.8 ± 2.5	.02
GM–WM CNR	1.5 ± 0.5	1.5 ± 0.5	.96

[a] Values are means ± SD.

DISCUSSION

Photon-counting CT is a new development in CT scanning in which fully digital detectors replace crystals that emit light and photodetectors. In this study, objective measures of image quality showed that improvement ratios of PCD CT compared with EID were 12.8%–20.6% for image noise, 19.0%–20.0% for SNR, 15.7% for GM–WM contrast, and 33.3% for GM–WM CNR. These improvements in image quality were detected by experienced neuroradiologists blinded to the type of CT scan (conventional versus photon-counting CT). Neuroradiologists identified better GM–WM differentiation and less image noise on PCD images. These initial, in vivo human results for a prototype photon-counting CT suggest a high potential for PCD CT to improve image quality for brain CT compared with conventional detector CT. Alternatively, the lower image noise of the PCD CT system could translate to reduced radiation dose (approximately 40%) at similar quality levels of current brain CT.[24] Our results show that better GM–WM differentiation (CNR) with PCD versus EID CT is due to both higher GM–WM contrast and lower image noise. The improved contrast can be attributed to the better weighting of low-energy photons, which produce more contrast among soft tissues. The lower image noise in PCD was more visible in the mid-to-high frequencies of the noise-power spectrum.

Improved image quality and better gray–white matter contrast with PCD CT may be very relevant to interpretation of brain CT examinations. For example, early CT recognition of acute (1–3 hours) stroke relies on detection of subtle GM hypoattenuation changes such as obscuration of the lentiform nucleus or the insular ribbon sign due to cytotoxic edema.[25] Detection of subtle attenuation differences also plays an important role in the diagnosis

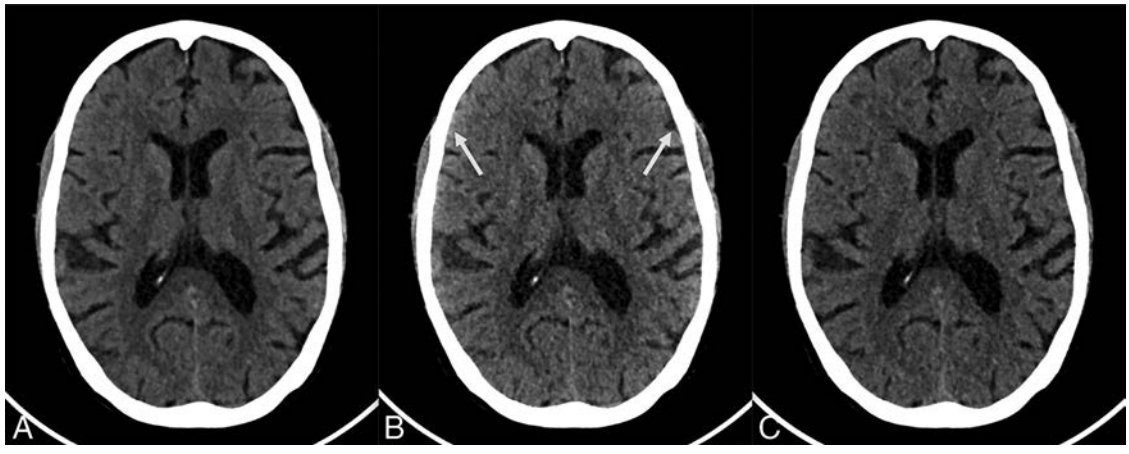

FIG 5. Sample photon-counting detector images of low- and high-energy bins of a 70-year-old woman (section thickness, 2 mm; increment, 2 mm; window center, 45 HU; window width, 80 HU). *A*, Axial PCD image reconstructed from all detected photons (22–120 keV) at the level of the basal ganglia. *B*, Axial PCD image reconstructed from a low-energy bin image (22–52 keV) at the same level as *A*. *C*, Axial PCD image reconstructed from the high-energy bin image (52–120 keV) at the same level as *A*. The image noise for both the low- and high-energy bins is higher than that of the PCD image reconstructed from all detected photons because each bin contains only a subset of all detected photons. The low-energy bins provide good gray matter–white matter differentiation but are susceptible to beam-hardening, best seen as an artifactual increase in attenuation of the cortical GM and the subarachnoid space (*arrows* in *B*). The high-energy photons are less susceptible to beam-hardening but have poorer GM–WM differentiation. The image reconstructed from all photons is a trade-off between the good GM–WM differentiation of the low-energy image and the lower beam-hardening artifacts of the high-energy images.

of other intracranial conditions such as hemorrhage, demyelinating diseases, and masses.[26-28] However, dedicated future studies are warranted to assess the potential impact of PCD technology on the diagnostic accuracy of brain CT.

Besides improved overall image quality for photon-counting CT of the brain, spectral imaging is inherent with this new type of CT detector. Similar to dual-energy CT, PCDs can use the attenuation measurements acquired with different energy spectra to differentiate materials.[29] Material classification has mostly been examined in contrast-enhanced CT but may also play an important role in noncontrast brain CT (eg, differentiation between hemorrhage and calcification).[30] Image analysis of the energy bins confirmed better GM–WM contrast for the low-energy images compared with the high-energy images; however, the low-energy images were more susceptible to beam-hardening artifacts. The PCD images reconstructed from all detected photons combined the good GM–WM differentiation of the low-energy image with the lower beam-hardening artifacts of the high-energy images. Further studies in patients with intracranial pathology are be needed to determine whether PCD CT may result in improved perception of brain abnormalities.

Although PCDs are already being used in nuclear medicine and mammography, the high x-ray photon flux required for body CT imaging has been a major challenge for photon-counting technology until recently. When incident x-ray photons are too close in time to be counted separately by the PCDs at high x-ray photon flux, multiple photons are counted as 1 photon. This phenomenon is known as "pulse pileup" and negatively affects image quality, Hounsfield unit accuracy, and material decomposition.[8] However, recent advances in PCD technology with high-speed application-specific integrated circuits and small pixel sizes have led to the development of PCDs resistant to pulse pileup at clinically routine CT tube currents.[15] Another PCD artifact is charge sharing, which occurs when the energy of an x-ray photon is distributed across multiple adjacent detector pixels, reducing the accuracy of the detected photon energy.[8] Multiple anti-charge-sharing techniques are currently being developed to limit this artifact.[31,32]

There are several limitations of this study. Unlike the EID system, the current implementation of the PCD prototype does not support z-flying focal spot technology. This feature resulted in increased PCD streaking artifacts, especially in the infratentorial region (eg, the posterior fossa). However, these are not a limitation of photon-counting technology but rather of the prototype implementation. Second, radiation dose–saving technologies such as tube-current modulation and model-based iterative reconstruction were not available for the PCD system; therefore, the performance of PCD could not be assessed under these conditions. Finally, experienced neuroradiologists blinded to detector type preferred the PCD image quality to that of EID CT. However, further studies are needed to determine whether this preference would translate to clinically meaningful differences for brain lesion detection. On the other hand, it appears likely that the lower image noise for PCD could be used to reduce the radiation dose while providing "always on" spectral x-ray information.

CONCLUSIONS

Qualitative and quantitative analyses of human brain PCD CT scans demonstrated better GM–WM differentiation than conventional EID CT, due to higher soft-tissue contrast and lower image noise of photon-counting detectors.

ACKNOWLEDGMENTS

The authors wish to thank Drs Bernhard Krauss and Bernhard Schmidt for their insightful discussions regarding the behavior of noise and artifacts in PCDs and Drs. André Henning, Martin Sedlmair, Rainer Raupach, and Friederike Schöck from Siemens for many helpful discussions and for building and maintaining the prototype scanner.

Disclosures: Amir Pourmorteza—*RELATED: Grant*: National Institutes of Health intramural research program, *Comments*: ZIACL090019, ZIAEB000072, ZIANS003119*; *Support for Travel to Meetings for the Study or Other Purposes*: National Institutes of Health–Siemens Collaborative research and development agreement*; *UNRELATED: Payment for Lectures Including Service on Speakers Bureaus*: Delaware Valley Chapter of American Association for Physicists in Medicine, *Comments*: received honorarium for a Continuing Medical Association lecture on photon-counting CT at the Delaware Valley Chapter of the American Association of Physicists in Medicine meeting in 2017*; *Travel/Accommodations/Meeting Expenses Unrelated to Activities Listed*: Delaware Valley Chapter of American Association for Physicists in Medicine. Rolf Symons—*OTHER RELATIONSHIPS*: institutional collaborative research agreement with Siemens. Mohammadhadi Bagheri—*OTHER RELATIONSHIPS*: institutional collaborative research agreement with Siemens. Stefan Ulzheimer—*UNRELATED: Employment*: Siemens. David A. Bluemke—*OTHER RELATIONSHIPS*: research agreement with Siemens, nonfinancial. *Money paid to the institution.

REFERENCES

1. Korley FK, Pham JC, Kirsch TD. **Use of advanced radiology during visits to US emergency departments for injury-related conditions, 1998–2007.** *JAMA* 2010;304:1465–71 CrossRef Medline
2. Larson DB, Johnson LW, Schnell BM, et al. **National trends in CT use in the emergency department: 1995–2007.** *Radiology* 2011;258:164–73 CrossRef Medline
3. Barber PA, Demchuk AM, Zhang J, et al. **Validity and reliability of a quantitative computed tomography score in predicting outcome of hyperacute stroke before thrombolytic therapy: ASPECTS Study Group. Alberta Stroke Programme Early CT Score.** *Lancet* 2000;355:1670–74 CrossRef Medline
4. Kalafut MA, Schriger DL, Saver JL, et al. **Detection of early CT signs of >1/3 middle cerebral artery infarctions: interrater reliability and sensitivity of CT interpretation by physicians involved in acute stroke care.** *Stroke* 2000;31:1667–71 CrossRef Medline
5. Morita S, Ueno E, Masukawa A, et al. **Hyperattenuating signs at unenhanced CT indicating acute vascular disease.** *Radiographics* 2010;30:111–25 CrossRef Medline
6. Schlomka JP, Roessl E, Dorscheid R, et al. **Experimental feasibility of multi-energy photon-counting K-edge imaging in pre-clinical computed tomography.** *Phys Med Biol* 2008;53:4031–57 CrossRef Medline
7. Iwanczyk JS, Nygard E, Meirav O, et al. **Photon counting energy dispersive detector arrays for x-ray imaging.** *IEEE Trans Nucl Sci* 2009;56:535–42 CrossRef Medline
8. Taguchi K, Iwanczyk JS. **Vision 20/20: single photon counting x-ray detectors in medical imaging.** *Med Phys* 2013;40:100901 CrossRef Medline
9. Symons R, Cork TE, Lakshmanan MN, et al. **Dual-contrast agent photon-counting computed tomography of the heart: initial experience.** *Int J Cardiovasc Imaging* 2017;33:1253–61 CrossRef Medline
10. Symons R, Krauss B, Sahbaee P, et al. **Photon-counting CT for simultaneous imaging of multiple contrast agents in the abdomen: an in vivo study.** *Med Phys* 2017 Apr 26. [Epub ahead of print] CrossRef Medline

11. Symons R, Reich DS, Bagheri M, et al. **Photon-counting computed tomography for vascular imaging of the head and neck: first in vivo human results.** *Invest Radiol* 2017 Sep 18. [Epub ahead of print] CrossRef Medline
12. Tanguay J, Kim HK, Cunningham IA. **The role of x-ray Swank factor in energy-resolving photon-counting imaging.** *Med Phys* 2010;37: 6205–11 CrossRef Medline
13. Symons R, Cork TE, Sahbaee P, et al. **Low-dose lung cancer screening with photon-counting CT: a feasibility study.** *Phys Med Biol* 2016;62:202–13 CrossRef Medline
14. Symons R, Pourmorteza A, Sandfort V, et al. **Feasibility of dose-reduced chest CT using photon-counting detectors: initial human results.** *Radiology* 2017 Jul 28. [Epub ahead of print] CrossRef Medline
15. Yu Z, Leng S, Jorgensen SM, et al. **Evaluation of conventional imaging performance in a research whole-body CT system with a photon-counting detector array.** *Phys Med Biol* 2016;61:1572–95 CrossRef Medline
16. Kappler S, Henning A, Kreisler B, et al. **Photon counting CT at elevated X-ray tube currents: contrast stability, image noise and multi-energy performance.** In: *Proceedings of SPIE Medical Imaging Conference*, San Diego, California. February 18–20, 2014
17. AAPM Adult Routine Head CT Protocols. Version 2.0. https://www.aapm.org/pubs/CTProtocols/documents/AdultRoutineHeadCT.pdf. Accessed November 8, 2016
18. Dixon RL. **A new look at CT dose measurement: beyond CTDI.** *Med Phys* 2003;30:1272–80 CrossRef Medline
19. Bongartz G, Golding SJ, Jurik AG, et al. **European Guidelines on Quality Criteria for Computed Tomography.** *EUR(Luxembourg)* 1999. http://www.drs.dk/guidelines/ct/quality/htmlindex.htm. Accessed March 18, 2017
20. Friedman SN, Fung GS, Siewerdsen JH, et al. **A simple approach to measure computed tomography (CT) modulation transfer function (MTF) and noise-power spectrum (NPS) using the American College of Radiology (ACR) accreditation phantom.** *Med Phys* 2013; 40:051907 CrossRef Medline
21. Pomerantz SR, Kamalian S, Zhang D, et al. **Virtual monochromatic reconstruction of dual-energy unenhanced head CT at 65–75 keV maximizes image quality compared with conventional polychromatic CT.** *Radiology* 2013;266:318–25 CrossRef Medline
22. Machin D, Campbell MJ, Tan SB, et al. *Sample Size Tables for Clinical Studies.* Somerset: John Wiley & Sons; 2011
23. Altman DG. *Practical Statistics for Medical Research.* Boca Raton: CRC Press; 1990
24. Primak AN, McCollough CH, Bruesewitz MR, et al. **Relationship between noise, dose, and pitch in cardiac multi-detector row CT.** *Radiographics* 2006;26:1785–94 CrossRef Medline
25. Kucinski T, Väterlein O, Glauche V, et al. **Correlation of apparent diffusion coefficient and computed tomography density in acute ischemic stroke.** *Stroke* 2002;33:1786–91 CrossRef Medline
26. Kidwell CS, Chalela JA, Saver JL, et al. **Comparison of MRI and CT for detection of acute intracerebral hemorrhage.** *JAMA* 2004;292: 1823–30 CrossRef Medline
27. Kim DS, Na DG, Kim KH, et al. **Distinguishing tumefactive demyelinating lesions from glioma or central nervous system lymphoma: added value of unenhanced CT compared with conventional contrast-enhanced MR imaging.** *Radiology* 2009;251:467–75 CrossRef Medline
28. Fink K, Fink J. **Imaging of brain metastases.** *Surg Neurol Int* 2013; 4(suppl 4):S209–19 CrossRef Medline
29. Pourmorteza A, Symons R, Sandfort V, et al. **Abdominal imaging with contrast-enhanced photon-counting CT: first human experience.** *Radiology* 2016;279:239–45 CrossRef Medline
30. Hu R, Daftari Besheli L, Young J, et al. **Dual-energy head CT enables accurate distinction of intraparenchymal hemorrhage from calcification in emergency department patients.** *Radiology* 2016;280: 177–83 CrossRef Medline
31. Ballabriga R, Campbell M, Heijne EH, et al. **The Medipix3 prototype, a pixel readout chip working in single photon counting mode with improved spectrometric performance.** In: *2006 IEEE Nuclear Science Symposium Conference Record. IEEE.* http://www.phys.hawaii.edu/~varner/PHYS476_Spr10/476_RefPapers/IEEEXplore_RB1.pdf. Accessed March 18, 2017
32. Koenig T, Hamann E, Procz S, et al. **Charge summing in spectroscopic x-ray detectors with high-Z sensors.** *IEEE Trans Nucl Sci* 2013;60:4713–18 CrossRef

Redefining the Pulvinar Sign in Fabry Disease

S. Cocozza, C. Russo, A. Pisani, G. Olivo, E. Riccio, A. Cervo, G. Pontillo, S. Feriozzi, M. Veroux, Y. Battaglia, D. Concolino, F. Pieruzzi, R. Mignani, P. Borrelli, M. Imbriaco, A. Brunetti, E. Tedeschi, and G. Palma

ABSTRACT

BACKGROUND AND PURPOSE: The pulvinar sign refers to exclusive T1WI hyperintensity of the lateral pulvinar. Long considered a common sign of Fabry disease, the pulvinar sign has been reported in many pathologic conditions. The exact incidence of the pulvinar sign has never been tested in representative cohorts of patients with Fabry disease. The aim of this study was to assess the prevalence of the pulvinar sign in Fabry disease by analyzing T1WI in a large Fabry disease cohort, determining whether relaxometry changes could be detected in this region independent of the pulvinar sign positivity.

MATERIALS AND METHODS: We retrospectively analyzed brain MR imaging of 133 patients with Fabry disease recruited through specialized care clinics. A subgroup of 26 patients underwent a scan including 2 FLASH sequences for relaxometry that were compared with MRI scans of 34 healthy controls.

RESULTS: The pulvinar sign was detected in 4 of 133 patients with Fabry disease (3.0%). These 4 subjects were all adult men (4 of 53, 7.5% of the entire male population) with renal failure and under enzyme replacement therapy. When we tested for discrepancies between Fabry disease and healthy controls in quantitative susceptibility mapping and relaxometry maps, no significant difference emerged for any of the tested variables.

CONCLUSIONS: The pulvinar sign has a significantly lower incidence in Fabry disease than previously described. This finding, coupled with a lack of significant differences in quantitative MR imaging, allows hypothesizing that selective involvement of the pulvinar is a rare neuroradiologic sign of Fabry disease.

ABBREVIATIONS: ERT = enzyme replacement therapy; FD = Fabry disease; HC = healthy controls; PS = pulvinar sign; qMRI = quantitative MRI; QSM = quantitative susceptibility mapping; R1 = longitudinal relaxation rate; R2 = pure transverse relaxation rate

Fabry disease (FD) is a rare X-linked metabolic disorder caused by insufficient/absent lysosomal α-galactosidase A activity. This enzymatic defect leads to pathologic storage of glycosphingolipids, especially globotriaosylceramide, occurring in all tissues and causing multiorgan progressive dysfunction, in the kidney, heart, and central nervous system.[1,2]

Neurologic involvement is common in FD.[3] Most prominent manifestations include cerebrovascular events, such as transient ischemic attacks and strokes, chronic cerebral vasculopathy, and vessel ectasia, especially in the posterior circulation.[4-7] Such clinical manifestations translate, on brain MR imaging, in the presence of white matter hyperintensities[3] and increased basilar artery diameter,[8,9] both nonspecific for FD.[10,11]

The pulvinar sign (PS), defined as the exclusive involvement of the lateral pulvinar with symmetric hyperintensity on unenhanced T1-weighted brain MR imaging, has long been considered a common neuroradiologic sign of FD.[8,12-16] Originally thought to be pathognomonic of FD,[12,13] the PS has actually been reported in other conditions, such as metabolic disorders (eg, Krabbe or Tay-Sachs disease),[17,18] CNS infections,[19] or after chemoradia-

Received March 30, 2017; accepted after revision July 22.

From the Departments of Advanced Biomedical Sciences (S.C., C.R., G.O., A.C., G.P., M.I., A.B., E.T.) and Public Health (A.P., E.R.), Nephrology Unit, University "Federico II," Naples, Italy; Department of Neuroscience (G.O.), Uppsala University, Uppsala, Sweden; Nephrology and Dialysis Department (S.F.), Belcolle Hospital, Viterbo, Italy; Department of Medical and Surgical Sciences and Advanced Technologies (M.V.), University Hospital of Catania, Catania, Sicily, Italy; Department of Specialized Medicine (Y.B.), Division of Nephrology and Dialysis, St. Anna Hospital-University, Ferrara, Italy; Department of Pediatrics (D.C.), University Magna Graecia, Catanzaro, Italy; Nephrology Unit (F.P.), University of Milano-Bicocca, Milan, Italy; Nephrology and Dialysis Department (R.M.), Infermi Hospital, Rimini, Italy; IRCCS SDN (P.B.), Naples, Italy; and Institute of Biostructure and Bioimaging (G.P.), National Research Council, Naples, Italy.

Sirio Cocozza and Camilla Russo contributed equally to this work.

Enrico Tedeschi and Giuseppe Palma share senior authorship.

Please address correspondence to Camilla Russo, MD, Department of Advanced Biomedical Sciences, Università degli Studi di Napoli "Federico II," Via Pansini, 5, 80131, Naples, Italy; e-mail: camilla_russo@hotmail.it

Indicates article with supplemental on-line table.

http://dx.doi.org/10.3174/ajnr.A5420

tion therapy[15]; therefore, its pathognomonic role has been largely rediscussed.[20,21] In fact, the pulvinar nuclei are sensitive to metabolic disturbances, and their MR imaging appearance can be altered in a variety of conditions, especially in patients in whom an abnormal renal function can be a relevant confounding comorbidity.

Moreover, the prevalence of the PS among the FD population has been reconsidered across the years.[14-15,22] To date, the exact incidence of the PS has never been tested in a large and representative cohort of patients with FD, because all studies conducted so far were limited to small samples[13] or performed only on affected males.[12]

In this respect, quantitative MR imaging (qMRI) and, in particular, relaxometry are likely to provide unique insight into the pathogenetic mechanisms of the PS. Indeed, a variety of microstructural conditions leading to a shorter longitudinal relaxation rate (R1) (thus, to T1WI hyperintensity) are associated with a faster free induction decay (ie, increase in R2*) and a rise of the pure transverse relaxation rate (R2). As a result, competitive roles of the longitudinal and transverse relaxation rates in MR signal generation suggest that standard evaluations of signal intensity are not the best choice for studying the incidence of PS-associated changes. A thorough relaxometry study would disentangle the contributions of several physical quantities to signal equation of conventional sequences, therefore providing a more accurate indication of the actual PS incidence.

This study has dual aims: 1) to assess the prevalence of PS in a large cohort of subjects with FD by retrospectively analyzing T1WI of 133 patients, and 2) to determine, for the first time, whether relaxometry modifications could be detected in the pulvinar, independent of the PS.

MATERIALS AND METHODS

Subjects

For the retrospective analysis, in this multicenter study, we analyzed a group of 133 patients with FD (80 women, 60.1%; mean age, 41 ± 13.8 years; age range, 13–73 years) recruited in the previous 5 years through the FD specialized care clinics of 6 different hospitals. Diagnosis of FD was based on reduced plasma levels of α galactosidase A activity of less than average normal values, then confirmed by genotyping tests. Clinical and radiologic data were obtained in different centers as part of the clinical work-up deemed necessary for each patient, and authorization for transfer of data was formerly obtained from the local ethics committee of the coordinating center. Activity of the α galactosidase A enzyme was absent in 42 patients (31.6%), while it showed a residual activity in 91 patients (68.4%); distinct *GLA* gene mutations were represented, and the clinical manifestations were different, with multiple organ involvement. Finally, 85 patients were treated with enzyme replacement therapy (ERT) (63.9%, with a mean duration of 39.9 ± 61.6 months). Demographic and clinical information of all patients with FD in the retrospective analysis are listed in the On-line Table. For the qMRI analysis, a subgroup of 26 patients with FD (17 women, 65.4%; mean age, 43 ± 12.4 years; age range, 20–68 years) underwent MR imaging at the coordinating center, along with a group of healthy controls (HC) of comparable age and sex, without a history of neurologic, metabolic, or psychiatric disorders. Activity of the α galactosidase A enzyme was absent in 7 patients (26.9%), while it had residual activity in 19 patients (73.1%), with 25 patients treated with ERT (96.2%; mean therapy duration, 43.8 ± 51.2 months). Demographic and clinical information of the qMRI subgroup of patients with FD are also listed in the On-line Table.

This study was performed in accordance with the ethical standards of the Declaration of Helsinki, and written informed consent for the qMRI analysis was preliminarily obtained from the 26 patients with FD and the HC.

Inclusion criteria for patients with FD were the following: genetically proved FD; availability of documentation of brain MR images, including at least 1 spin-echo T1WI sequence independent of the orientations with a section thickness <4 mm; and signed informed consent for participation in the study for subjects undergoing the qMRI analysis. Both adult male and female subjects were approached to participate, without age limitations. Diagnosis of FD was confirmed by biochemical or genetic testing. Indications for brain MR imaging varied between and within centers, including, but not limited to, routine MR imaging, headache, transient neurologic symptoms, and evaluation of an acute cerebrovascular accident. Exclusion criteria for all subjects were evidence of hypo- or hypercalcemia or the presence of any other comorbidity that could have biased the neuroradiologic examination.

From each specialized care center participating in this study, demographic and clinical variables were extracted by a clinician experienced in FD from the medical records or obtained in direct interviews and recorded. These included age recorded at the time of the brain MR imaging, sex, hypertension, diabetes mellitus, cardiac arrhythmia, left ventricular hypertrophy, renal failure (considered present when the estimated glomerular filtration rate of the patient was <90 mL/min), proteinuria (considered present when the patient scored a value >150 mg/24 hours), the presence of neurologic symptoms (including stroke, cephalalgia, acroparesthesia, and so forth), gastrointestinal involvement, renal or cardiac transplant, current use of tobacco or alcohol, as well as treatment with ERT. About 63% of patients with renal failure showed metabolic alterations of parathyroid hormone serum levels attributable to secondary hyperparathyroidism, with no significant derangements of serum calcium levels. Renal function was expressed as the estimated glomerular filtration rate, calculated with the Chronic Kidney Disease Epidemiology Collaboration equation.[23] Other laboratory values were measured using standard hospital laboratory techniques. Activity of the α galactosidase A enzyme was reported as "absent" (when showing <1% of normal values) or "residual" (for enzyme activity ranging from 1% to 5% of normal values) because of the different measurement methods used in the recruiting centers (plasma, leukocytes, and so forth).

Each center received a dedicated case report form in which demographic and clinical information were recorded, and then forms were entered into a central data base at the coordinating center according to Good Clinical Practice guidelines.

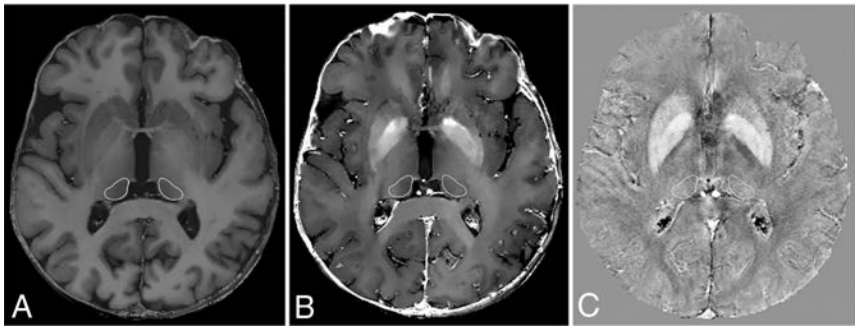

FIG 1. R1 (*A*), R2* (*B*), and QSM (*C*) maps showing the 2 hand-drawn irregular bilateral ROIs placed in consensus by 2 experienced neuroradiologists on the axial section of the gradient recalled-echo images with the best representation of the pulvinar nuclei.

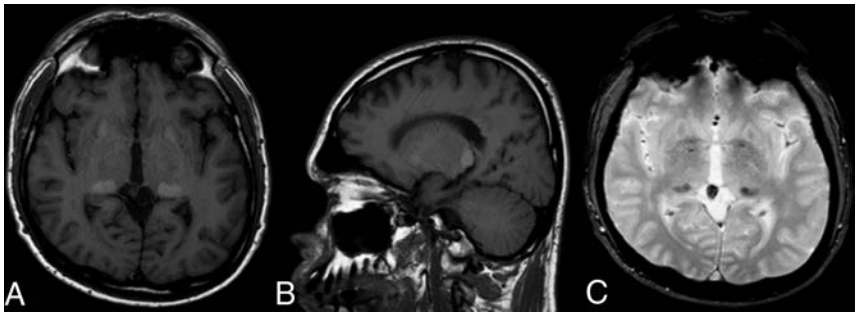

FIG 2. Unenhanced T1WI axial (*A*) and sagittal (*B*) images showing bilateral, symmetric, and well-circumscribed hyperintensity of the pulvinar nuclei in a 47-year-old male patient with FD (*A*). Axial T2* gradient echo image (*C*) shows bilateral and symmetric hypointensity corresponding exactly to the T1 hyperintensity, supporting the current hypothesis of focal calcium deposition in both pulvinar nuclei.

qMRI Data Acquisition

All studies for the qMRI analysis were performed on the same 3T MR imaging scanner (Magnetom Trio; Siemens, Erlangen, Germany). The acquisition protocol included a dual-echo spoiled gradient-echo (FLASH) sequence (TR = 32 ms, TE_1 = 7.38 ms, TE_2 = 22.14 ms, flip angle = 20°) and a single-echo FLASH sequence (TR = 16 ms, TE = 7.38 ms, flip angle = 2°). Both sequences were acquired on an FOV of 230 × 194 × 160 mm^3, with a voxel size of 0.5 × 0.5 × 1.0 mm^3 and a receiver bandwidth of 100 Hz/pixel.

The acquired data were saved as complex datasets reconstructed in magnitude and phase representation for further analyses.

MR Imaging Data Analysis

For the retrospective analysis, MR imaging brain scans were visually assessed by 2 neuroradiologists in consensus, who rated the presence of a clear unilateral or bilateral T1WI hyperintensity at the level of the posterior thalami.

For the qMRI analysis, all magnitude datasets underwent a preliminary multispectral denoising as described in Borrelli et al,[24] using a multi-graphics processing unit implementation of the non-local means algorithm previously introduced.[25] Quantitative susceptibility mapping (QSM) and R2* maps were derived from the dual-echo FLASH.[26] Conversely, given the signal equation of FLASH with FA = θ

$$S = K|\sin\theta|\,\frac{1-E_1}{1-E_1\cos\theta}e^{-T_E R_2^*},$$

$$E_1 = e^{-T_R R_1},$$

it can be shown that assuming a T1 > 3 ms, the actual settings of the acquisition parameters (TR = 16 ms, θ_1 = 2°, θ_2 = 20°) allow R1 computation as

$$R_1 = \frac{1}{T_R}\log\frac{R+\sqrt{R^2+4C(r-k)}}{2C},$$

where

$$r = \frac{S_1}{S_2},$$

$$k = \frac{|\sin\theta_1|}{|\sin\theta_2|},$$

$$R = r(1-\cos\theta_1),$$

and

$$C = r\cos\theta_1 - k\cos\theta_2.$$

For each study, 2 irregular bilateral ROIs were hand-drawn in consensus by 2 experienced neuroradiologists on axial sections of the gradient recalled-echo images with the best representation of pulvinar nuclei (Fig 1), according to a human anatomy atlas.[27] Mean R1, R2*, and QSM values were automatically obtained from the corresponding maps.

Statistical Analysis

Statistical analyses were performed with the Statistical Package for the Social Sciences (Version 17.0; IBM, Armonk, New York). An independent 2-sample *t* test was used for comparing ages and mean values obtained from qMRI analysis, while a χ^2 test was used to determine differences in terms of sex. A $P = .05$ indicated a statistically significant difference. Finally, no Cohen coefficient was needed to evaluate the performance of the evaluation because the 2 neuroradiologists performed the analysis in consensus.

RESULTS

For the retrospective analysis, a clear T1WI hyperintensity of the pulvinar was detected in 4 of 133 patients with FD (3.0%). All 4 patients with positive PSs underwent MR imaging examinations in 2 of the 6 hospitals involved; they all were adult male subjects with an age ranging from 38 to 59 years (mean, 46.5 ± 9.4 years) under ERT and showing signs of renal failure. An example of the PS is shown in Fig 2.

For the qMRI analysis, the FD and HC groups were comparable for age and sex. No subject with a positive PS was found in the qMRI subgroup. When we tested for possible differences between these 2 clusters in relaxometry and QSM maps in the FD and HC groups, no significant differences emerged. A complete list of the results obtained by relaxometry and susceptibility analysis, along with the comparison of *P* values, is shown in the Table.

Results of the relaxometry analysis[a]

	HC	FD	*P* Value
Right pulvinar area	49 ± 7	46 ± 6	.14
Left pulvinar area	53 ± 7	51 ± 10	.41
Right pulvinar R1	1.31 ± 0.11	1.33 ± 0.09	.45
Left pulvinar R1	1.41 ± 0.14	1.44 ± 0.12	.32
Right pulvinar R2*	19.9 ± 1.7	20.6 ± 3.4	.35
Left pulvinar R2*	19.9 ± 1.9	20.3 ± 2.8	.55
Right pulvinar QSM	40 ± 19	41 ± 19	.75
Left pulvinar QSM	38 ± 17	35 ± 18	.56

Note:—R1 indicates the longitudinal relaxation rate (1/T1), expressed in second^{-1}; R2*, transverse relaxation rate (1/T2*), expressed as second^{-1}.

[a] QSM is expressed in parts per billion. Areas are expressed in square millimeters. *P* values refer to an independent 2-sample *t* test, with a significance level of $P = .05$.

DISCUSSION

Our findings support the hypothesis that the true incidence of the PS is considerably lower than previously reported. No significant qMRI differences emerged when testing for possible alterations in subjects without positive PSs, allowing us to speculate that this sign is poorly sensitive for FD.

Exclusive involvement of the lateral pulvinar was first observed by 2 separate groups.[12,13] Since then, this sign has been considered as distinctive of FD. Independent from its diagnostic value, the exact incidence of the PS has changed across time,[14,15] with a clear downward trend going from 70%[13] of earlier studies (though reported in a very small group of patients without any ascertainment data) to complete absence in recent works.[20] However, the real incidence of the PS has never been tested in an ample-sized group of patients with FD. Here we expand this knowledge by performing a retrospective analysis of a large and representative population of patients with FD. We observed a prevalence of the PS in FD of 3.0%, significantly lower than previously reported.[8,12-16] A possible explanation for this discrepancy could reflect the relatively small sample size of some of the previous studies.[15]

Nevertheless, when considering the study by Moore et al,[12] which included a number of subjects comparable with ours, a higher incidence of the PS was observed. However, the above-mentioned study included only male patients with FD,[12] in whom the PS is known to be more frequent,[21] and this could have somehow biased the real prevalence of the PS in the global FD population. Supporting this speculation, we were able to replicate such findings when we selected only males with renal function impairment,[28] showing a PS prevalence similar to the one reported in Moore et al (4/25, 16.0%).

Another explanation of the previously reported high incidence of a positive PS in patients with FD may be related to possible gadolinium deposition in this structure. Indeed, recent evidence suggests that in subjects with normal renal function receiving multiple contrast administrations, the dentate nuclei and other deep gray matter structures, including the globus pallidus and the pulvinar, could accumulate gadolinium, leading to changes detectable on both conventional and quantitative imaging.[29-31] It may, therefore, be hypothesized that the reduced glomerular filtration rate in patients with FD could have influenced the gadolinium clearance, leading to its accumulation in the pulvinar nuclei with subsequent T1WI shortening. However, in patients with FD, T1WI hyperintensity was not observed in the dentate nuclei, which is the preferred site of gadolinium accumulation, and contrast media are rarely administered in these patients, due to their usually impaired renal function. Even though this evidence mitigates the hypothesis of gadolinium accumulation in patients with FD, further properly designed studies may better address the possible relationships between impaired renal function and metal buildup in the pulvinar.

In line with literature data,[21] no affected females with the PS were found, considered a rare event[16] due to partial/residual enzyme activity. The mean age of our PS-positive patients was 46.5 years, confirming the current hypothesis that the PS could be the neuroradiologic epiphenomenon of a long-term accumulation, whose manifestations only appear progressively.[15]

Other literature data indicate the poor prognostic value of the PS. Indeed, it has been demonstrated that the PS is somehow independent of major cerebrovascular events, which may occur at any stage of disease.[21] Furthermore, no changes in the pulvinar nuclei occurred after long-term ERT, and no association between the PS and a specific genotype has been demonstrated.[15]

Aside from the incidence of the PS, we aimed to evaluate whether possible changes in susceptibility maps could occur in the pulvinar of patients with FD.

It is widely accepted that the pulvinar is a sensitive region where alterations could develop, independent from the cause. Selective modifications of pulvinar nuclei have been described in other pathologic conditions, such as Wernicke encephalopathy[32,33] and Creutzfeldt-Jakob [34,35] and Tay-Sachs diseases.[17] In particular, T1WI hyperintensity in the pulvinar has also been described in patients who received chemotherapy/radiation therapy, in patients with neurofibromatosis type 1, and in subjects with Fahr disease or disturbances of the calcium-phosphorus metabolism or even laminar necrosis.[36-38]

To date, the real pathogenesis of the PS in FD is still unclear. The most reliable hypothesis is the development of subtle dystrophic calcification, confirmed by CT brain scans, probably related to chronic hypoperfusion secondary to microvascular alterations.[6,14,39-41] These alterations have been reported not only in the pulvinar but also in other deep gray nuclei such as the globus pallidus, even if in a lower percentage of cases.[12-14]

Quantitative MR imaging can allow early detection of changes not appreciable on conventional MR images,[42] possibly providing additional information in understanding PS physiopathology. However, we found no differences in the pulvinar in any of the examined qMRI maps of patients with FD compared with HC. This absence of significant differences, however, should not lead to the superficial deduction that the PS is not linked to abnormal mineral deposition. Unfortunately, in our qMRI FD subgroup, no subjects with clear PSs were present because of the low incidence of this sign. On the other hand, in patients positive for the PS, a clinical T2*WI FLASH sequence was available and showed clear hypointensity corresponding to T1WI hyperintensity, corroborating the current hypothesis of calcium deposition in the posterior thalami when the PS is present. A possible explanation for the absence of sensitive mineralization in the PS-negative group might be related to the ongoing therapy, since the FD subgroup with available qMRI sequences almost entirely consisted of subjects under ERT (25/26 patients). Indeed, due to the current

pathogenetic assumption that microvascular changes are responsible for PS development, it can be hypothesized that early diagnosis of FD, coupled with the availability of effective treatment options, could have directly or indirectly improved local microvascular homeostasis. Nonetheless, this speculation should be corroborated by further longitudinal evaluations of qMRI, to clarify the relationship between these measures and ERT.

CONCLUSIONS

We showed a significantly lower incidence (only 3%) of the PS in FD compared with what has been previously described, coupled with no significant qMRI differences in these regions between those with FD and HC. Our results, taken together, allow hypothesizing that selective pulvinar involvement with well-circumscribed T1-hyperintensity, though easy to identify, is a rare neuroradiologic sign whose presence is detectable in only a few exceptional cases of FD. Moreover, because this finding has also been reported in other conditions of metabolic dysfunction, it should not be considered specifically related to globotriaosylceramide accumulation and its role as a sensitive sign of this disease should be reconsidered.

Disclosures: Sirio Cocozza—*UNRELATED*: *Payment for Lectures Including Service on Speakers Bureaus*: Genzyme; *Travel/Accommodations/Meeting Expenses unrelated to Activities Listed*: Genzyme. Antoni Pisani—*UNRELATED*: *Consultancy*: Genzyme, Shire, Amicus; *Payment for Lectures Including Service on Speakers Bureaus*: Genzyme, Shire, Amicus; *Travel/Accommodations/Meeting Expenses unrelated to Activities Listed*: Genzyme, Shire, Amicus. Eleonora Riccio—*UNRELATED*: *Payment for Lectures Including Service on Speakers Bureaus*: Genzyme, Shire; *Travel/Accommodations/Meeting Expenses unrelated to Activities Listed*: Genzyme, Shire. Daniela Concolino—*UNRELATED*: *Payment for Lectures Including Service on Speakers Bureaus*: Shire; *Travel/Accommodations/Meeting Expenses unrelated to Activities Listed*: Shire. Federico Pieruzzi—*UNRELATED*: *Payment for Lectures Including Service on Speakers Bureaus*: Genzyme, Shire, Amicus; *Travel/Accommodations/Meeting Expenses unrelated to Activities Listed*: Genzyme, Shire, Amicus. Sandro Feriozzi—*UNRELATED*: *Payment for Lectures Including Service on Speakers Bureaus*: Genzyme, Shire; *Travel/Accommodations/Meeting Expenses unrelated to Activities Listed*: Genzyme, Shire. Renzo Mignani—*UNRELATED*: *Payment for Lectures Including Service on Speakers Bureaus*: Genzyme, Shire; *Travel/Accommodations/Meeting Expenses unrelated to Activities Listed*: Genzyme, Shire. Massimiliano Veroux—*UNRELATED*: *Payment for Lectures Including Service on Speakers Bureaus*: Genzyme, Shire; *Travel/Accommodations/Meeting Expenses unrelated to Activities Listed*: Genzyme, Shire. Yuri Battaglia—*UNRELATED*: *Payment for Lectures Including Service on Speakers Bureaus*: Genzyme; *Travel/Accommodations/Meeting Expenses unrelated to Activities Listed*: Genzyme.

REFERENCES

1. Eng CM, Germain DP, Banikazemi M, et al. **Fabry disease: guidelines for the evaluation and management of multi-organ system involvement.** *Genet Med* 2006;8:539–48 CrossRef Medline
2. Germain DP. **Fabry disease.** *Orphanet J Rare Dis* 2010;5:30 CrossRef Medline
3. Buechner S, Moretti M, Burlina AP, et al. **Central nervous system involvement in Anderson-Fabry disease: a clinical and MRI retrospective study.** *J Neurol Neurosurg Psychiatry* 2008;79:1249–54 CrossRef Medline
4. Kaye EM, Kolodny EH, Logigian EL, et al. **Nervous system involvement in Fabry's disease: clinicopathological and biochemical correlation.** *Ann Neurol* 1988;23:505–09 CrossRef Medline
5. Mitsias P, Levine SR. **Cerebrovascular complications of Fabry's disease.** *Ann Neurol* 1996;40:8–17 CrossRef Medline
6. Moore DF, Kaneski CR, Askari H, et al. **The cerebral vasculopathy of Fabry disease.** *J Neurol Sci* 2007;257:258–63 CrossRef Medline
7. Fellgiebel A, Keller I, Marin D, et al. **Diagnostic utility of different MRI and MR angiography measures in Fabry disease.** *Neurology* 2009;72:63–68 CrossRef Medline
8. Fellgiebel A, Keller I, Martus P, et al. **Basilar artery diameter is a potential screening tool for Fabry disease in young stroke patients.** *Cerebrovasc Dis* 2011;31:294–99 CrossRef Medline
9. Manara R, Carlier RY, Righetto S, et al. **Basilar artery changes in Fabry disease.** *AJNR Am J Neuroradiol* 2017;38:531–36 CrossRef Medline
10. Putaala J, Kurkinen M, Tarvos V, et al. **Silent brain infarcts and leukoaraiosis in young adults with first-ever ischemic stroke.** *Neurology* 2009;72:1823–29 CrossRef Medline
11. Uçeyler N, Homola GA, Guerrero González H, et al. **Increased arterial diameters in the posterior cerebral circulation in men with Fabry disease.** *PLoS One* 2014;9:e87054 CrossRef Medline
12. Moore DF, Ye F, Schiffmann R, et al. **Increased signal intensity in the pulvinar on T1-weighted images: a pathognomonic MR imaging sign of Fabry disease.** *AJNR Am J Neuroradiol* 2003;24:1096–101 Medline
13. Takanashi J, Barkovich AJ, Dillon WP, et al. **T1 hyperintensity in the pulvinar: key imaging feature for diagnosis of Fabry disease.** *AJNR Am J Neuroradiol* 2003;24:916–21 Medline
14. Fellgiebel A, Mazanek M, Whybra C, et al. **Pattern of microstructural brain tissue alterations in Fabry disease: a diffusion-tensor imaging study.** *J Neurol* 2006;253:780–87 CrossRef Medline
15. Burlina AP, Manara R, Caillaud C, et al. **The pulvinar sign: frequency and clinical correlations in Fabry disease.** *J Neurol* 2008;255:738–44 CrossRef Medline
16. Burlina AP, Politei J, Cinque S, et al. **The pulvinar sign in Fabry patients: the first report in female patients.** *J Neurol* 2012;259:1227–28 CrossRef Medline
17. Mugikura S, Takahashi S, Higano S, et al. **MR findings in Tay-Sachs disease.** *J Comput Assist Tomogr* 1996;20:551–55 CrossRef Medline
18. Kendall BE. **Disorders of lysosomes, peroxisomes, and mitochondria.** *AJNR Am J Neuroradiol* 1992;13:621–53 Medline
19. Sahraian MA, Motamedi M, Azimi AR, et al. **Bilateral pulvinar thalamic calcification in a patient with chronic cryptococcal meningitis.** *Eur J Neurol* 2007;14:e1–2 Medline
20. Fazekas F, Enzinger C, Schmidt R, et al; SIFAP 1 Investigators. **Brain magnetic resonance imaging findings fail to suspect Fabry disease in young patients with an acute cerebrovascular event.** *Stroke* 2015;46:1548–53 CrossRef Medline
21. Kolodny E, Fellgiebel A, Hilz MJ, et al. **Cerebrovascular involvement in Fabry disease: current status of knowledge.** *Stroke* 2015;46:302–13 CrossRef Medline
22. Lee HJ, Hsu TR, Hung SC, et al. **A comparison of central nervous system involvement in patients with classical Fabry disease or the later-onset subtype with the IVS4+919G>A mutation.** *BMC Neurol* 2017;17:25 CrossRef Medline
23. Vučić Lovrenčić M, Radišić Biljak V, Božičević S, et al. **Estimating glomerular filtration rate (GFR) in diabetes: the performance of MDRD and CKD-EPI equations in patients with various degrees of albuminuria.** *Clin Biochem* 2012;45:1694–96 CrossRef Medline
24. Borrelli P, Palma G, Tedeschi E, et al. **Improving signal-to-noise ratio in susceptibility weighted imaging: a novel multicomponent non-local approach.** *PLoS One* 2015;10:e0126835 CrossRef Medline
25. Palma G, Comerci M, Alfano B, et al. **3D non-local means denoising via multi-GPU.** *Fed Conf Comput Sci* 2013:495–98
26. Palma G, Tedeschi E, Borrelli P, et al. **A novel multiparametric approach to 3D quantitative MRI of the brain.** *PLoS One* 2015;10:e0134963 CrossRef Medline
27. Schaltenbrand G, Wahren W. *Atlas for Stereotaxy of the Human Brain*. 2nd ed. Stuttgart: Thieme; 1977
28. Branton M, Schiffmann R, Kopp JB. **Natural history and treatment of renal involvement in Fabry disease.** *J Am Soc Nephrol* 2002;13(suppl 2):S139–43 Medline
29. Kanda T, Ishii K, Kawaguchi H, et al. **High signal intensity in the dentate nucleus and globus pallidus on unenhanced T1-weighted MR images: relationship with increasing cumulative dose of a gadolinium-based contrast material.** *Radiology* 2014;270:834–41 CrossRef Medline

30. Ramalho J, Semelka RC, Ramalho M, et al. **Gadolinium-based contrast agent accumulation and toxicity: an update.** *AJNR Am J Neuroradiol* 2016;37:1192–98 CrossRef Medline
31. Tedeschi E, Palma G, Canna A, et al. **In vivo dentate nucleus MRI relaxometry correlates with previous administration of gadolinium-based contrast agents.** *Eur Radiol* 2016;26:4577–84 CrossRef Medline
32. Torvik A, Lindboe CF, Rogde S. **Brain lesions in alcoholics: a neuropathological study with clinical correlations.** *J Neurol Sci* 1982;56:233–48 CrossRef Medline
33. Antunez E, Estruch R, Cardenal C, et al. **Usefulness of CT and MR imaging in the diagnosis of acute Wernicke's encephalopathy.** *AJR Am J Roentgenol* 1998;171:1131–37 CrossRef Medline
34. Zeidler M, Sellar RJ, Collie DA, et al. **The pulvinar sign on magnetic resonance imaging in variant Creutzfeldt-Jakob disease.** *Lancet* 2000;355:1412–18 CrossRef Medline
35. Keohane C. **Pulvinar sign on MRI images in variant Creutzfeldt-Jakob disease.** *Lancet* 2000;355:1384 CrossRef Medline
36. Ginat DT, Meyers SP. **Intracranial lesions with high signal intensity on T1-weighted MR images: differential diagnosis.** *Radiographics* 2012;32:499–516 CrossRef Medline
37. Renard D, Castelnovo G, Campello C, et al. **Thalamic lesions: a radiological review.** *Behav Neurol* 2014;2014:154631 CrossRef Medline
38. Zaitout Z, Romanowski C, Karunasaagarar K, et al. **A review of pathologies associated with high T1W signal intensity in the basal ganglia on magnetic resonance imaging.** *Pol J Radiol* 2014;79:126–30 CrossRef Medline
39. Moore DF, Altarescu G, Barker WC, et al. **White matter lesions in Fabry disease occur in 'prior' selectively hypometabolic and hyperperfused brain regions.** *Brain Res Bull* 2003;62:231–40 CrossRef Medline
40. Igarashi T, Sakuraba H, Suzuki Y. **Activation of platelet function in Fabry's disease.** *Am J Hematol* 1986;22:63–67 CrossRef Medline
41. DeGraba T, Azhar S, Dignat-George F, et al. **Profile of endothelial and leukocyte activation in Fabry patients.** *Ann Neurol* 2000;47:229–33 Medline
42. Deoni SC. **Quantitative relaxometry of the brain.** *Top Magn Reson Imaging* 2010;21:101–13 CrossRef Medline

Correlation between Clinical Outcomes and Baseline CT and CT Angiographic Findings in the SWIFT PRIME Trial

A.P. Jadhav, H.-C. Diener, A. Bonafe, V.M. Pereira, E.I. Levy, B.W. Baxter, T.G. Jovin, R.G. Nogueira, D.R. Yavagal, C. Cognard, D.D. Purcell, B.K. Menon, R. Jahan, J.L. Saver, and M. Goyal, on behalf of the SWIFT PRIME investigators

ABSTRACT

BACKGROUND AND PURPOSE: Patient selection for endovascular therapy remains a great challenge in clinic practice. We sought to determine the effect of baseline CT and angiography on outcomes in the Solitaire With the Intention for Thrombectomy as Primary Endovascular Treatment for Acute Ischemic Stroke (SWIFT PRIME) trial and to identify patients who would benefit from endovascular stroke therapy.

MATERIALS AND METHODS: The primary end point was a 90-day modified Rankin Scale score of 0–2. Subgroup and classification and regression tree analysis was performed on baseline ASPECTS, site of occlusion, clot length, collateral status, and onset-to-treatment time.

RESULTS: Smaller baseline infarct ($n = 145$) (ASPECTS 8–10) was associated with better outcomes in patients treated with thrombectomy versus IV tPA alone (66% versus 41%; rate ratio, 1.62) compared with patients with larger baseline infarcts ($n = 44$) (ASPECTS 6–7) (42% versus 21%; rate ratio, 1.98). The benefit of thrombectomy over IV tPA alone did not differ significantly by ASPECTS. Stratification by occlusion location also showed benefit with thrombectomy across all groups. Improved outcomes after thrombectomy occurred in patients with clot lengths of ≥8 mm (71% versus 43%; rate ratio, 1.67). Outcomes stratified by collateral status had a benefit with thrombectomy across all groups: none–fair collaterals (33% versus 0%), good collaterals (58% versus 44%), and excellent collaterals (82% versus 28%). Using a 3-level classification and regression tree analysis, we observed optimal outcomes in patients with favorable baseline ASPECTS, complete/near-complete recanalization (TICI 2b/3), and early treatment (mean mRS, 1.35 versus 3.73), while univariate and multivariate logistic regression showed significantly better results in patients with higher ASPECTS.

CONCLUSIONS: While benefit was seen with endovascular therapy across multiple subgroups, the greatest response was observed in patients with a small baseline core infarct, excellent collaterals, and early treatment.

Patient selection for mechanical thrombectomy in acute ischemic strokes presents a major challenge in achieving good outcomes. First-generation randomized controlled trials investigating the benefit of intra-arterial therapy failed to demonstrate improved rates of independence in the treatment group. A limitation of these trials was the large baseline core infarcts at the time of enrollment. In the Interventional Management of Stroke III (IMS III) trial, 40% of patients had lower Alberta Stroke Program Early CT Scores on presentation (ASPECTS 0–7).[1] In patients with lower ASPECTS, there was a 2-fold less likelihood of benefit with IV or intra-arterial therapy compared with patients with higher ASPECTS. In the Mechanical Retrieval and Recanalization

Received April 3, 2017; accepted after revision July 19.

From Department of Neurology and Neurological Surgery (A.P.J., T.G.J.), University of Pittsburgh Medical Center, Pittsburgh, Pennsylvania; Department of Neurology (H.-C.D.), University Hospital of University Duisburg-Essen, Essen, Germany; Department of Neuroradiology (A.B.), Hôpital Gui-de-Chauliac, Montpellier, France; Division of Neuroradiology and Division of Neurosurgery (V.M.P.), Toronto Western Hospital, University Health Network, University of Toronto, Ontario, Canada; Department of Neurosurgery (E.I.L.), State University of New York at Buffalo, Buffalo, New York; Department of Radiology (B.W.B.), Erlanger Hospital at University of Tennessee, Chattanooga, Tennessee; Department of Neurology (R.G.N.), Marcus Stroke and Neuroscience Center, Grady Memorial Hospital, Emory University School of Medicine, Atlanta, Georgia; Department of Neurology and Neurosurgery (D.R.Y.), University of Miami Miller School of Medicine/Jackson Memorial Hospital, Miami, Florida; Department of Diagnostic and Therapeutic Neuroradiology (C.C.), University Hospital of Toulouse, Toulouse, France; BioClinica (D.D.P.), Newark, California; Department of Radiology (D.D.P.), California Pacific Medical Center, San Francisco, California; Division of Neuroradiology (D.D.P.), University of California San Francisco, San Francisco, California; Departments of Radiology and Clinical Neurosciences (M.G.) and Neurology and Neurosurgery (B.K.M.), University of Calgary, Calgary, Alberta, Canada; and Division of Interventional Neuroradiology (R.J.) and Department of Neurology and Comprehensive Stroke Center (J.L.S.), David Geffen School of Medicine at the University of California Los Angeles, University of California, Los Angeles, Los Angeles, California.

An academic steering committee supervised the trial design and operations. The sponsor of the study (Covidien) was responsible for site management, data management, and safety reporting. The study data were independently monitored. The statistical analyses were prepared by an independent external statistician (S. Brown; Altair Biostatistics, St. Louis Park, Minnesota).

This work was supported by the SWIFT PRIME study, funded by Covidien.

Please address correspondence to Mayank Goyal, MD, Department of Radiology, University of Calgary, Foothills Hospital, 1403 29th St NW, Calgary, AB, Canada; e-mail: mgoyal@ucalgary.ca

http://dx.doi.org/10.3174/ajnr.A5406

of Stroke Clots Using Embolectomy (MR RESCUE) trial, the core baseline infarct was 36 mL at enrollment with only 21% of patients achieving functional independence at 90 days (modified Rankin Scale score, 0–2).[2] To overcome these constraints, the Solitaire With the Intention for Thrombectomy as Primary Endovascular Treatment for Acute Ischemic Stroke (SWIFT PRIME) trial limited enrollment to patients with small–moderate core infarcts as defined by head CT, CT angiography, and/or CT perfusion. We have previously reported on the primary outcomes of the SWIFT PRIME trial[3] and the secondary prespecified analysis of baseline CT perfusion imaging and follow-up infarct volume and outcomes.[4,5] In this study, we describe the effect of the baseline CT and CTA findings on clinical outcome.

MATERIALS AND METHODS

The study design of the SWIFT PRIME trial has been previously described.[3,6] Primary outcomes for all 196 patients have been previously reported,[3] while a subset of 151 patients has been evaluated and presented for outcomes based specifically on perfusion imaging.[4] In this article, we report, for the first time, the effects of imaging parameters (including ASPECTS and collateral status), substantial reperfusion, and time to treatment on clinical outcomes. An independent core imaging lab evaluated all imaging. Baseline head CT was available for review in 185 patients. CT angiography was available for review in 88% of patients. The ASPECTS is a 10-point semiquantitative topographic score for assessing stroke burden in the middle cerebral artery distribution on CT.[7] Enrollment (after the first 71 patients) was restricted to patients with ASPECTS scores of >5. For the first 71 patients, the inclusion criteria were based on a CT perfusion study as follows: ischemic core lesion volume, ≤50 mL; time-to-maximum, >10 seconds; lesion volume, ≤100 mL; mismatch volume, ≥15 mL; and mismatch ratio, >1.8. Ischemic core was defined as an area with >70% reduction in CBF (relative CBF < 0.3) in comparison with the mean CBF of normally perfused brain parenchyma. An ischemic core lesion defined by CT perfusion corresponds to an ASPECTS of >5.

For subgroup analysis according to ASPECTS, we made 2 comparisons of higher-versus-lower ASPECTS: ASPECTS 8–10 versus ASPECTS 6–7 and ASPECTS 9–10 versus ASPECTS 6–8. The site of occlusion was defined by baseline head CTA: ICA occlusion, proximal M1 occlusion, middle M1 occlusion, and distal M1/M2 occlusion. Clot length was measured on CTA or MRA as the length of a vessel that was nonopacified/nonvisualized using 5-mm multiplanar MIP reformations. Contrast-enhanced MRA was used whenever possible. In a subset of cases in which the distal end of the clot could not be identified, CT perfusion source images allowed visualization and measurement of the clot. The earlier phases of CTP were used to determine the proximal end of the clot, while the later phases were used to determine the distal end of the clot. Prior studies have identified a thrombus length of ≥8 mm in the middle cerebral artery as being refractory to recanalization from intravenous thrombolysis,[8] which can potentially impact clinical outcomes. To understand the impact of clot length on responsiveness to endovascular therapy, clinical outcomes were compared in patients with ≥8 mm of thrombus.

Collateral Scoring on CTA

Collateral assessment was defined on CTA as excellent, good, fair, poor, minimal, or none.[9] Definitions were as follows: excellent, increased or normal prominence and extent of pial vessels beyond the occluded artery within the symptomatic hemisphere; good, slightly reduced prominence and extent of pial vessels beyond the occluded artery within the symptomatic hemisphere; fair, moderately reduced prominence and extent of pial vessels beyond the occluded artery within the symptomatic hemisphere; poor, decreased prominence and extent and regions with no vessels in some part of the occluded territory; minimal, compared with the asymptomatic contralateral hemisphere, just a few vessels visible in the occluded vascular territory; and none, no vessels visible within the occluded vascular territory.[9]

Statistical Analysis

All available data were used for analyses. Statistical tests for binary variables were performed with the Fisher exact test, and for continuous variables, they were performed with the Student *t* test. Univariate and multivariate logistic regressions were used to test relationships between potential predictor variables and outcomes defined by the modified Rankin Scale score of 0–2 at 90 days. Classification and regression tree analysis were used to further investigate relationships among study variables. All statistical tests were 2-sided. with *P* values < .05 considered statistically significant. All analyses were performed in R, Version 3.0 or above (R Foundation for Statistical Computing; Vienna, Austria; http://www.R-project.org).

RESULTS

Baseline CT ASPECTS

A higher baseline ASPECTS of 8–10 was noted in 145 patients (74 in the IV tPA arm; 71 in the endovascular and IV tPA arm), of whom 142 had mRS available at 90 days. Good outcomes (mRS 0–2) at 90 days were observed in 66% of patients in the treatment arm compared with 41% of patients in the control arm ($P = .004$). Lower baseline ASPECTS of 6–7 was noted in 44 patients (24 in the IV tPA arm; 20 in the endovascular and IV tPA arm). Good outcomes were observed in 42% of patients in the treatment arm compared with 21% of patients in the control arm ($P = .2$; Fig 1). In univariate and multivariate logistic regression analyses, a higher baseline ASPECTS was associated with better outcomes, particularly when dichotomized for ASPECTS of 9–10 versus ≤8 (Tables 1 and 2).

Site of Occlusion

Distribution of the site of occlusion was as follows: ICA (20 patients), proximal M1 (39 patients), middle M1 (55 patients), and distal M1/M2 (49 patients). Treatment effect with endovascular therapy was noted across all sites of occlusion (Fig 2), with the greatest treatment effect in patients with a proximal M1 occlusion (88% versus 14%, $P < .0001$). The site of occlusion was not significantly associated with good outcome in the univariate analysis (Table 1).

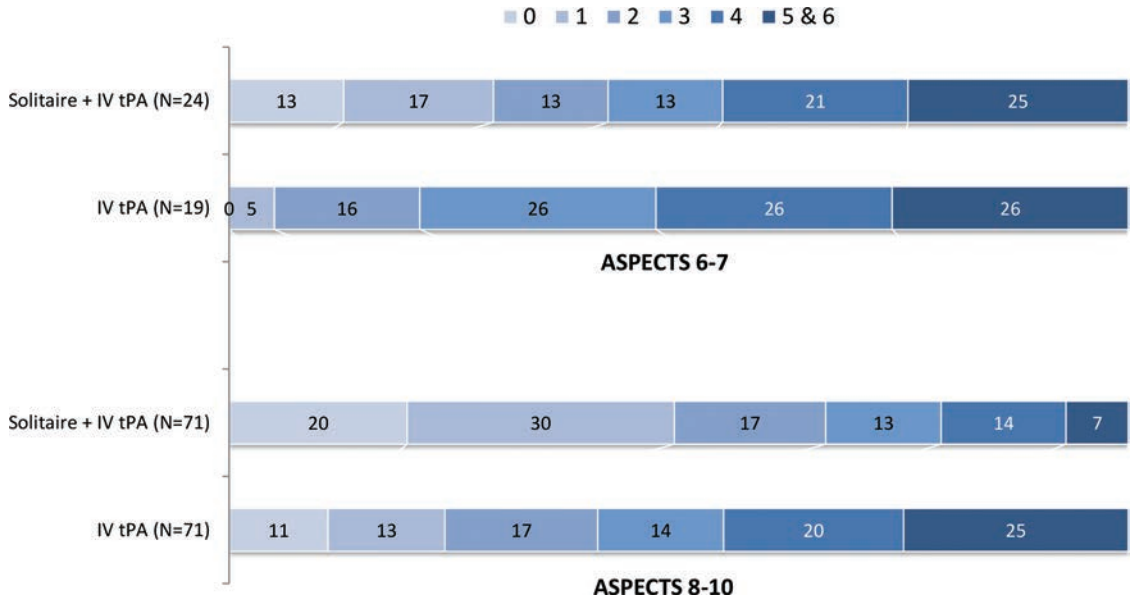

FIG 1. Influence of baseline CT ASPECTS on outcome (90-day mRS), indicating better outcomes with higher ASPECTS and better outcome with endovascular therapy irrespective of ASPECTS.

Table 1: Univariate predictors of functional independence (mRS 0–2) at 90 days, endovascular arm only[a]

Predictor	No. Total	No. Category	Odds Ratio	Lower CI	Upper CI	*P* Value
ASPECTS (per unit)	95	NA	1.53	1.09	2.15	.015
ASPECTS 8–10 (vs 6–7)	95	71/24	2.74	1.06	7.08	.037
ASPECTS 9–10 (vs 6–8)	95	52/43	3.43	1.45	8.09	.005
M1 occlusion (vs non-M1)	95	60/35	2.12	0.90	4.97	.085
Onset-to-groin puncture (per 60 min)	94	NA	0.68	0.48	0.98	.040
TICI 3 postprocedure (vs ≤TICI 2b)	80	56/24	2.11	0.79	5.61	.13
TICI 2b/3 postprocedure (vs ≤TICI 2a)	80	70/10	1.80	0.47	6.82	.39
Collateral grade (per unit)	56	NA	2.77	1.13	6.82	.026
Clot length (per mm)	50	NA	1.12	0.96	1.30	.14
Clot length of ≥8 mm (vs <8 mm)	50	44/6	2.38	0.42	13.40	.32
Clot length of ≥13 mm (vs <13 mm)	50	23/27	2.48	0.71	8.66	.16

Note:—No. reflects the number of data points available for each variable; NA, not applicable.

[a] Univariate logistic regression analysis of patients undergoing endovascular therapy was performed with the following variables: ASPECTS (as scored on preprocedural head CT, 6–7 vs 8–10 and 6–8 vs 9–10), site of occlusion (M1 versus non-M1), onset to groin puncture, quality of recanalization (TICI scale), collateral grade, and clot length (>8 mm versus <8 mm).

Table 2: Multivariate predictors of functional independence (mRS 0–2) at 90 days, endovascular arm only[a]

Predictor	No. Total	No. Category	Odds Ratio	Lower CI	Upper CI	*P* Value
ASPECTS 9–10 (vs 6–8)	48	28/20	4.25	1.06	17.10	.042
Onset-to-groin puncture (per 60 min)	48	NA	0.79	0.44	1.42	.43
TICI 2b/3 postprocedure (vs ≤TICI 2a)	48	43/5	1.03	0.12	8.46	.98
Collateral grade (per unit)	48	NA	2.85	0.90	9.08	.076

Note:—No. reflects the number of data points available for each variable; NA, not applicable.

[a] Multivariate logistic regression analysis of patients undergoing endovascular therapy was performed with the following variables: ASPECTS (as scored on preprocedural head CT), onset to groin puncture, quality of recanalization (TICI scale), and collaterals.

Length of Clot

Clot length was available in 111 patients, of whom 89% had ≥8-mm clot length. In this subgroup, 71% of patients having undergone thrombectomy versus 43% of patients receiving IV tPA alone had good outcomes ($P = .005$, Fig 3). Median clot length was 13 mm. In 59 patients with a clot length greater than the median, 79% of patients having undergone thrombectomy versus 34% of patients with IV tPA alone had good outcomes ($P = .001$). In univariate analysis, clot length was not associated with good outcome in the subgroup of patients treated with endovascular therapy (Table 1).

Quality of Collaterals

Collateral status on baseline head CTA was available for review in 113 patients. Poor collaterals (none-to-fair) were noted in 19% of patients with a median baseline ASPECTS of 8 and a mean core infarct volume of 18.9 mL. High-quality collaterals (good-to-excellent) were associated with a median baseline ASPECTS of 9 and a mean core infarct volume of 7.4 mL. A beneficial effect of endovascular therapy was observed over IV tPA alone across all levels of collateral flow, with the greatest effect in patients with excellent collaterals (82% versus 28%, $P = .008$; Fig 4). In univariate and multivariate analysis, a good collateral grade was associated with good outcome (statistically significant in univariate analysis and a trend toward significance in multivariate analysis) (Tables 1 and 2).

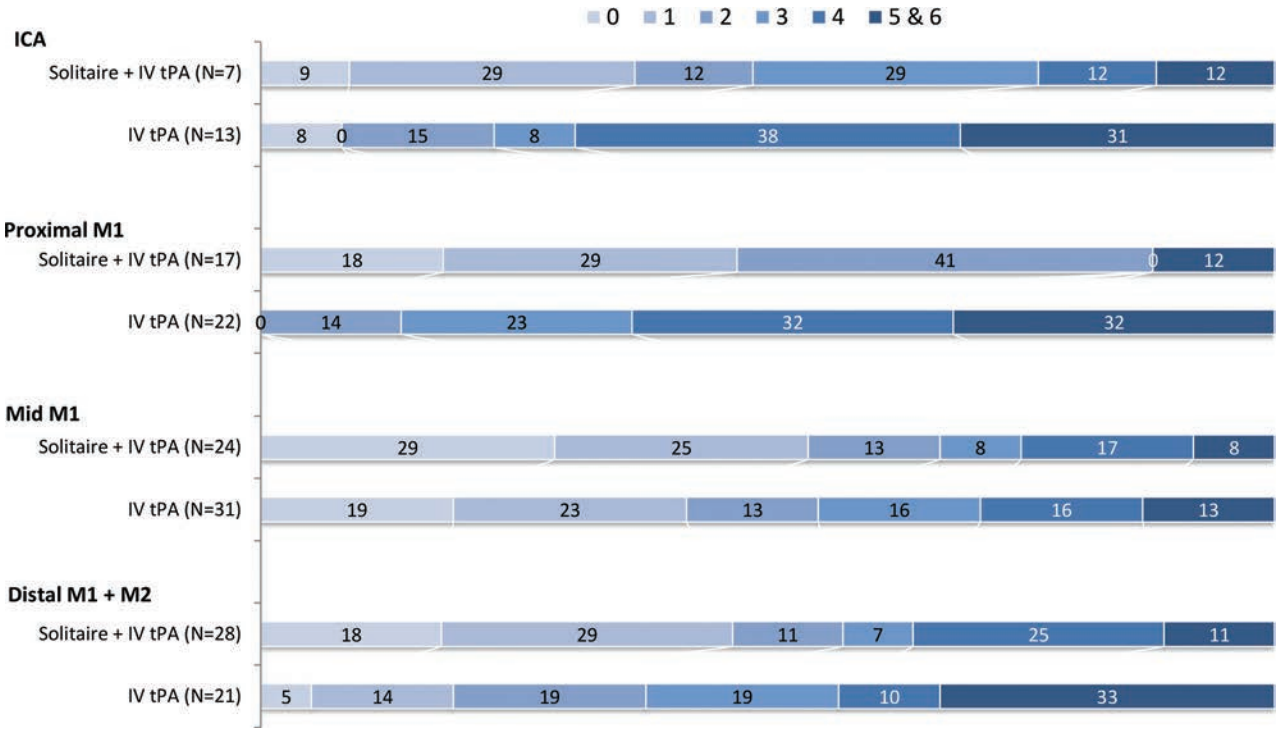

FIG 2. Influence of the site of occlusion on outcome (90-day mRS), indicating better outcome with endovascular therapy irrespective of site and the greatest treatment effect in proximal M1 occlusions.

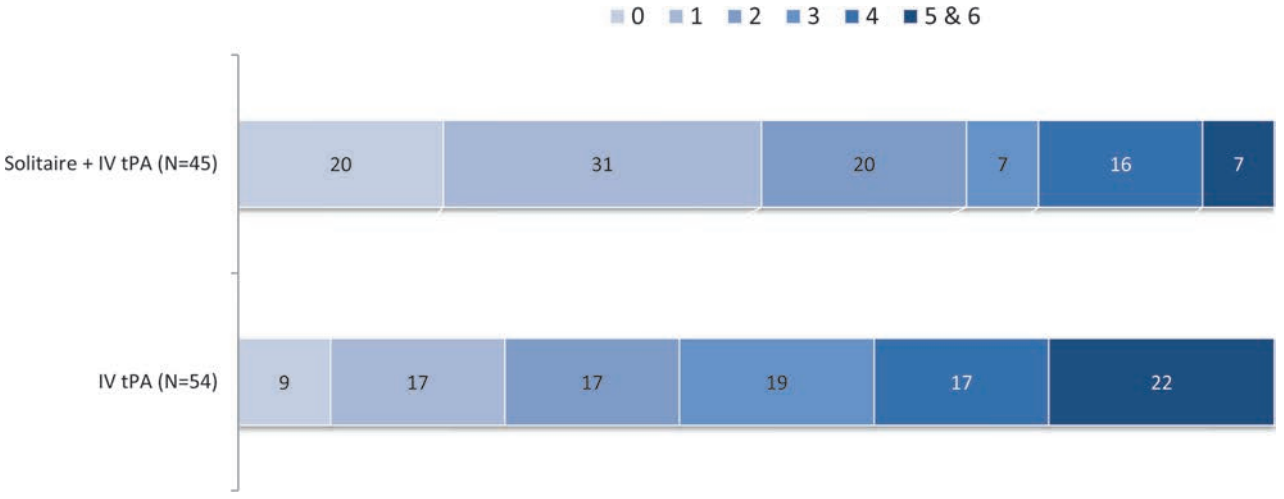

FIG 3. Outcomes (90-day mRS) in patients with a clot length of ≥8 mm, indicating statistically superior outcomes with endovascular therapy in these clots.

Classification and Regression Tree Analysis

Univariate analysis revealed that favorable ASPECTS, earlier treatment, good collaterals, and complete recanalization are associated with better outcomes (Table 1). With the classification and regression tree algorithm, binary cut points affecting outcome were identified as dichotomized ASPECTS (ASPECTS 9–10 versus ASPECTS 6–8), onset-to-puncture time (within 4 hours versus beyond 4 hours), and quality of recanalization (TICI 3 versus TICI 2b or less). Of 98 patients undergoing thrombectomy, better outcomes were observed in patients with favorable ASPECTS, early treatment, and complete recanalization (Fig 5). In the patients undergoing thrombectomy, the average time from symptom onset to recanalization was 260 minutes and the rate of TICI 2b/3 recanalization was 88% (70/80).

DISCUSSION

While the primary results of the SWIFT PRIME study revealed a benefit of endovascular therapy over intravenous thrombolysis alone in patients with acute ischemic stroke, several questions remain about understanding subsets of patients most likely to benefit from intra-arterial therapy. In this report, we found that the benefit of endovascular therapy persisted across multiple subgroups, with the highest likelihood of benefit noted in patients with higher ASPECTS, early treatment, and favorable collaterals.

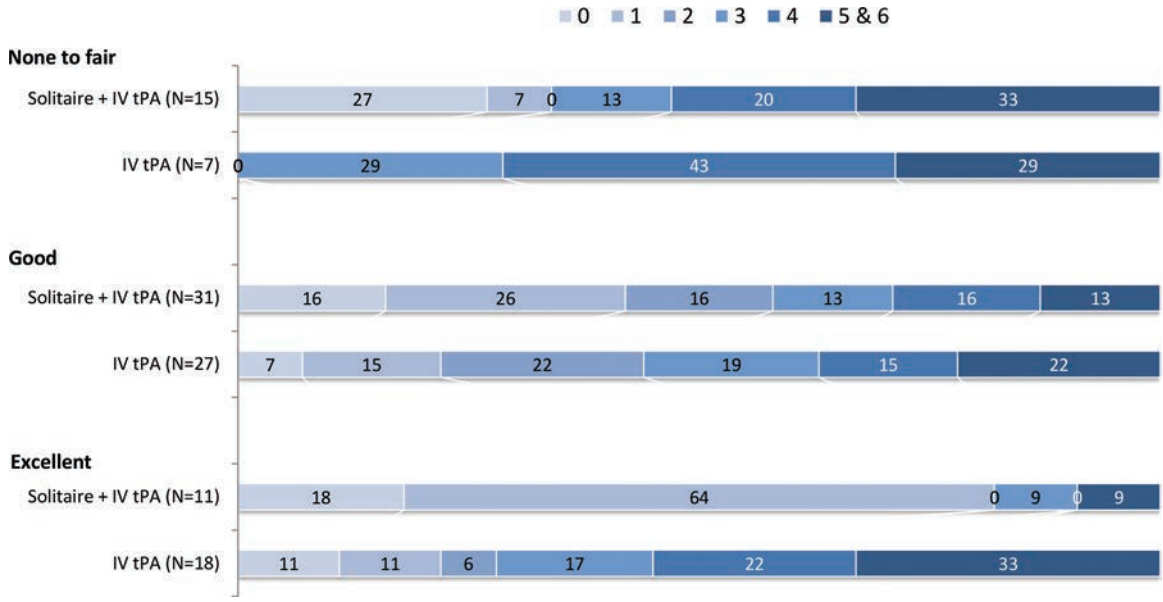

FIG 4. Influence of baseline collateral status on outcome (90-day mRS), indicating better outcomes with better collaterals, better outcomes with endovascular therapy irrespective of collateral quality, and the greatest treatment effect associated with excellent collaterals.

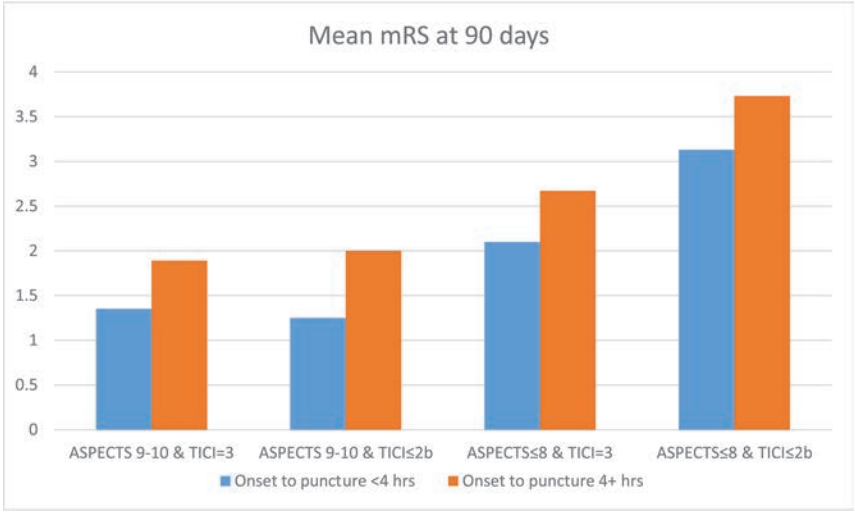

FIG 5. Mean mRS in dichotomized subgroups identified by classification and regression tree analysis indicating time to recanalization, initial ASPECTS, and TICI scores posttreatment as substantial predictors of outcome with the displayed cut-points for dichotomization.

Previous studies of endovascular therapy (Intra-arterial Prourokinase for Acute Ischemic Stroke [PROACT II] and IMSI) demonstrated a strong interaction between favorable ASPECTS (8–10)[10,11] and outcome; however, a similar analysis of IMS III did not confirm this relationship.[1] Failure to appreciate this relationship in IMS III has been attributed to long onset-to-treatment times as well as the low reperfusion rates in the treatment arm. In contrast, the SWIFT PRIME trial had fast treatment times and high rates of reperfusion. Furthermore, the baseline ASPECTSs in SWIFT PRIME were much higher, with 72% of patients having an ASPECTS of 8–10 compared with 58% of patients in IMS III.[1] We found that patients with higher ASPECTS had better clinical outcomes, particularly with endovascular therapy. This finding is in keeping with numerous other studies demonstrating that baseline ASPECTS is an important predictor of final outcome.

In the SWIFT PRIME trial, patients were selected for enrollment on the basis of small core infarcts on presentation. Accordingly, the current analysis is limited to patients with overall favorable ASPECTS. The benefit of complete or near-complete recanalization of patients with poor ASPECTS (<5) remains unclear and may warrant further investigation,[12] particularly in younger patients in whom recanalization may limit further infarct growth. Such a clinical result may not be well-captured in a dichotomized mRS outcome of 0–2 versus 3–6, but it may spare a young patient hemicraniectomy, respiratory compromise, or other stroke-related complications. Furthermore, a population with a poor ASPECTS may be well-suited for bridging neuroprotection therapies in which recanalization along with adjunctive therapy may result in acceptable outcomes.[13]

ASPECTS alone is a single freeze-frame in the evolution of necrosing brain tissue. Additional information about the speed and extent of infarct burden can be inferred by clinical examination (a large deficit suggests large tissue at risk), perfusion imaging, and collateral status. The presence of robust collateral blood circulation indicates brain tissue that is more likely to be reperfused and, when reperfused, more likely to have a favorable response.[14] Additionally, patients with robust collaterals are likely to have smaller core infarcts on presentation. Furthermore, previous studies have indicated that reperfusion therapies in patients with poor baseline collateral circulation do not typically have a favorable response, and this feature eventually results in a higher likelihood of infarct growth.[15] Most interesting, we found trends toward benefit in patients with poor baseline collateral status after

endovascular therapy, though the overall numbers are small and not statistically significant. This population will require further examination because the natural history tends to be quite poor and treatment options are limited. A caveat with collateral assessment is that single-phase CTAs may mislabel patients with moderate-to-good collaterals as poor in CTAs that are mistimed (acquired in the early arterial phase). Collateral assessment with multiphase CTA is a potential solution.[16] Arguably, patients with poor collateral circulation presenting at early time windows may continue to benefit from thrombectomy if achieved in ultrarapid fashion. Given the quickly growing core infarct in this population, there may be a role for additional therapies designed to arrest stroke progression, such as neuroprotective therapy[17] or hypothermia.

The site of occlusion and thrombus burden is associated with failure of IV tPA to recanalize large-vessel occlusion. Distal occlusions such as M2 or distal M1 are particularly responsive to IV tPA, whereas proximal occlusions such as ICA or proximal M1 are more refractory to IV tPA.[18] While benefit was observed with endovascular therapy across groups, the highest benefit was noted in proximal M1 occlusions compared with distal M1 occlusions. Similarly, IV tPA is less effective as thrombus burden increases. In 1 study of patients undergoing intravenous thrombolysis for acute stroke, hardly any patients (<1%) with clot measuring ≥8 mm had successful recanalization.[8] One limitation of measuring clot length on CTA is that it does not accurately define the thrombus extent because the lack of distal contrast opacification may be related to delayed distal filling rather than a true filling defect. In univariate analysis, the site of occlusion and clot length did not predict 90-day mRS 0–2 after endovascular therapy. It is possible that the effectiveness of endovascular therapy to recanalize such clots may mitigate the role of clot length in predicting good clinical outcomes. A priori identification of IV tPA nonresponders may ultimately guide future management strategies in which IV thrombolysis may be bypassed in favor of a direct intra-arterial therapy.[18]

Limitations

There are important limitations to our study. First, the sample size is relatively small, so further validation of our findings will require analysis in a larger cohort of patients. Second, given the nature of the study design and focus on patients re-presenting with small core infarcts, very few patients in our analysis had large core infarcts on initial presentation. The extent of benefit in this larger core population remains unanswered. Additionally, the participating clinical sites in the SWIFT PRIME trial were specifically selected on the basis of clinical volume and expertise. The generalizability of these results across additional centers remains untested. Finally, this study included post hoc analysis, so additional confirmation will require prospective studies of specific subgroups and patient features.

CONCLUSIONS

Overall, this report supports the selection of patients for intra-arterial therapy on the basis of favorable patient characteristics (small core, good collateral circulation) and low likelihood of recanalization with intravenous thrombolysis (large and proximal clot burden). Additional studies will be needed to further understand the continued benefit of intra-arterial treatment for patients with larger infarct burden or distal occlusions.

ACKNOWLEDGMENTS

The authors thank Scott Brown for statistical analysis, Mark Lowerison for help with figure design, and Cynthia Yang and Rachel Castro for project management.

Disclosures: Hans-Christoph Diener—*OTHER RELATIONSHIPS*: H.-C.D. received honoraria for participation in clinical trials, contribution to advisory boards, or oral presentations from the following: Abbott, Allergan, AstraZeneca, Bayer Vital, Bristol-Myers Squibb, Boehringer Ingelheim, CoAxia, Corimmun, Covidien, Daiichi Sankyo, D-Pharm, Fresenius, GlaxoSmithKline, Janssen-Cilag, Johnson & Johnson, Knoll, Eli Lilly, Merck Sharp & Dohme, Medtronic, Mindframe, Neurobiological Technologies, Novartis, Novo Nordisk, Paion, Parke-Davis, Pfizer, Sanofi-Aventis, Schering-Plough, Servier, Solvay, St. Jude, Syngis, Talecris Pharma Resources, Thrombogenics, WebMD Global, Wyeth and Yamanouchi. Financial support for research projects was provided by AstraZeneca, GlaxoSmithKline, Boehringer Ingelheim, Lundbeck, Novartis, Janssen-Cilag, Sanofi-Aventis, Syngis, and Talecris Pharma Resources. The Department of Neurology at the University Duisburg-Essen received research grants from the German Research Council, German Ministry of Education and Research, European Union, National Institutes of Health, the Bertelsmann Foundation, and the Heinz-Nixdorf Foundation. H.-C.D. has no ownership interest and does not own stocks in any pharmaceutical company. Alain Bonafe—*UNRELATED*: *Consultancy*: Medtronic, Stryker. Vitor Mendes Pereira—*RELATED*: *Consulting Fee or Honorarium*: Medtronic/Covidien, *Comments*: as EU Interventional Principal Investigator for the SWIFT PRIME trial*; *UNRELATED*: *Consultancy:* Medtronic, Stryker, Codman Neuro, Penumbra, *Comments*: proctoring and studies Advisory Board. Elad I. Levy—*UNRELATED*: *Board Membership*: Stryker, NeXtGen Biologics, MEDX, Cognition Medical Corp, *Comments*: serves on the Advisory Board; *Consultancy*: Pulsar Vascular; *Expert Testimony*, *Comments*: renders medical/legal opinion as an expert witness; *Payment for Development of Educational Presentations*: Covidien, *Comments*: honorarium for training and lectures; *Stock/Stock Options*: Intratech Medical, NeXtGen Biologics, *Comments:* shareholder/ownership interest; *Other*: Abbott Vascular, *Comments*: carotid training sessions for physicians. Blaise W. Baxter—*UNRELATED*: *Consultancy*: Penumbra, *Comments*: consulting fees for stroke therapy development; *Payment for Lectures Including Service on Speakers Bureaus*: Penumbra, *Comments*: Speakers Bureau expenses paid for talks; *Patents (Planned, Pending or Issued)*: Advanced Catheter Therapies, *Comments*: devices and methods for perfusion therapy; Patent No. US 8622992 B2; *Stock/Stock Options*: Penumbra, *Comments*: hold stock in the company. Tudor G. Jovin—*UNRELATED*: *Consultancy*: Codman Neurovascular, Neuravi; *Stock/Stock Options*: Silk Road, Anaconda, Blockade Medical; *Travel/Accommodations/Meeting Expenses Unrelated to Activities Listed*: Stryker, Fundació Ictus. Raul G. Nogueira—*RELATED*: *Consulting Fee or Honorarium*: Stryker Neurovascular (TREVO-2 Trial, Principal Investigator, modest; DAWN Trial, Principal Investigator, no compensation; TREVO Registry Steering Committee, no compensation); Medtronic (SWIFT Trial Steering Committee, modest; SWIFT-PRIME Trial Steering Committee, no compensation; STAR Trial Angiographic Core Lab, significant), Penumbra (3D Separator Trial Executive Committee, no compensation), Neuravi (ARISE-2 Steering Committee, no compensation), Genentech (Physician Advisory Board, modest), Allm Inc (Physician Advisory Board, no compensation), Editor-In-Chief *Interventional Neurology* (no compensation). Dileep R. Yavagal—*RELATED*: *Grant*: Medtronic, *Comments*: University of Miami was a site for the SWIFT-PRIME study*; *Consulting Fee or Honorarium*: Medtronic, *Comments*: Steering Committee member for this trial; *Support for Travel to Meetings for the Study or Other Purposes:* Medtronic; *UNRELATED*: *Consultancy*: Medtronic; *Payment for Lectures Including Service on Speakers Bureaus*: Penumbra, Medtronic, *Comments*: consultant to Medtronic; *Travel/Accommodations/Meeting Expenses Unrelated to Activities Listed*: Medtronic; *Other*: Medtronic. Christophe Cognard—*UNRELATED*: *Consultancy*: MicroVention, Stryker, Medtronic. Derk D. Purcell—*RELATED*: *Other*: BioClinica, *Comments*: I was a central reader, paid by the imaging clinical research organization (BioClinica); *UNRELATED*: *Consultancy*: BioClinica, *Comments*: central reader for imaging clinical research organization. Reza Jahan—*RELATED*: *Fees for Participation in Review Activities such as Data Monitoring Boards, Statistical Analysis, Endpoint Committees, and the Like*: Medtronic, *Comments*: on Executive Steering Committee of SWIFT PRIME; *UNRELATED*: *Consultancy*: Medtronic. Jeffrey L. Saver—*RELATED*: *Grant*: Medtronic, *Comments*: The University of California Regents received payments on the basis of clinical trial contracts for the number of subjects enrolled*; *Consulting Fee or Honorarium*: Medtronic, *Comments*: Dr Saver received funding for services as a scientific consultant regarding the SWIFT PRIME trial design and conduct to Medtronic; *Support for Travel to Meetings for the Study or Other Purposes*: Medtronic, *Comments*: Dr Saver received funding for travel as a

scientific consultant regarding the SWIFT PRIME trial design and conduct to Medtronic; *UNRELATED*: *Consultancy*: Stryker, Neuravi, BrainsGate, Pfizer, Squibb, Boehringer Ingelheim (prevention only), ZZ Biotech, and St. Jude Medical, *Comments*: Dr Saver has received funding for services as a scientific consultant regarding trial design and conduct to Stryker, Neuravi, BrainsGate, Pfizer, Squibb, Boehringer Ingelheim (prevention only), ZZ Biotech, and St. Jude Medical; *Royalties*: University of California, *Comments*: The University of California has patent rights for retrieval devices for stroke.* Mayank Goyal—*RELATED*: *Grant*: Medtronic, *Comments*: HERMES collaboration, part funding for the ESCAPE trial*; *Consulting Fee or Honorarium:* Medtronic, *Comments*: For the design and conduct of the SWIFT PRIME trial; *Other*: Stryker, MicroVention, Ablynx, *Comments*: For advice and teaching on acute stroke; *UNRELATED: Patents (Planned, Pending or Issued):* GE Healthcare, *Comments*: licensing agreement regarding systems of stroke diagnosis. *Money paid to the institution.

REFERENCES

1. Hill MD, Demchuk AM, Goyal M, et al; IMS3 Investigators. **Alberta Stroke Program Early Computed Tomography Score to select patients for endovascular treatment: Interventional Management of Stroke (IMS)-III trial.** *Stroke* 2014;45:444–49 CrossRef Medline
2. Kidwell CS, Jahan R, Gornbein J, et al; MR RESCUE Investigators. **A trial of imaging selection and endovascular treatment for ischemic stroke.** *N Engl J Med* 2013;368:914–23 CrossRef Medline
3. Saver JL, Goyal M, Bonafe A, et al; SWIFT PRIME Investigators. **Stent-retriever thrombectomy after intravenous t-PA vs. t-PA alone in stroke.** *N Engl J Med* 2015;372:2285–95 CrossRef Medline
4. Albers GW, Goyal M, Jahan R, et al. **Ischemic core and hypoperfusion volumes predict infarct size in SWIFT PRIME.** *Ann Neurol* 2016;79:76–89 CrossRef Medline
5. Albers GW, Goyal M, Jahan R, et al. **Relationships between imaging assessments and outcomes in Solitaire With the Intention For Thrombectomy as Primary Endovascular treatment for acute ischemic stroke.** *Stroke* 2015;46:2786–94 CrossRef Medline
6. Saver JL, Goyal M, Bonafe A, et al; SWIFT PRIME Investigators. **Solitaire with the Intention for Thrombectomy as Primary Endovascular Treatment for Acute Ischemic Stroke (SWIFT PRIME) trial: protocol for a randomized, controlled, multicenter study comparing the Solitaire revascularization device with IV tPA with IV tPA alone in acute ischemic stroke.** *Int J Stroke* 2015;10:439–48 CrossRef Medline
7. Barber PA, Demchuk AM, Zhang J, et al. **Validity and reliability of a quantitative computed tomography score in predicting outcome of hyperacute stroke before thrombolytic therapy: ASPECTS Study Group—Alberta Stroke Programme Early CT Score.** *Lancet* 2000; 355:1670–74 CrossRef Medline
8. Riedel CH, Zimmermann P, Jensen-Kondering U, et al. **The importance of size: successful recanalization by intravenous thrombolysis in acute anterior stroke depends on thrombus length.** *Stroke* 2011;42:1775–77 CrossRef Medline
9. Menon BK, Qazi E, Nambiar V, et al; Interventional Management of Stroke III Investigators. **Differential effect of baseline computed tomographic angiography collaterals on clinical outcome in patients enrolled in the Interventional Management of Stroke III trial.** *Stroke* 2015;46:1239–44 CrossRef Medline
10. Hill MD, Demchuk AM, Tomsick TA, et al. **Using the baseline CT scan to select acute stroke patients for IV-IA therapy.** *AJNR Am J Neuroradiol* 2006;27:1612–16 Medline
11. Hill MD, Rowley HA, Adler F, et al; PROACT-II Investigators. **Selection of acute ischemic stroke patients for intra-arterial thrombolysis with pro-urokinase by using ASPECTS.** *Stroke* 2003;34:1925–31 CrossRef Medline
12. Noorian AR, Rangaraju S, Sun CH, et al. **Endovascular therapy in strokes with ASPECTS 5–7 may result in smaller infarcts and better outcomes as compared to medical treatment alone.** *Interv Neurol* 2015;4:30–37 CrossRef Medline
13. Horn CM, Sun CH, Nogueira RG, et al. **Endovascular Reperfusion and Cooling in Cerebral Acute Ischemia (ReCCLAIM I).** *J Neurointerv Surg* 2014;6:91–95 CrossRef Medline
14. Leng X, Fang H, Leung TW, et al. **Impact of collateral status on successful revascularization in endovascular treatment: a systematic review and meta-analysis.** *Cerebrovasc Dis* 2016;41:27–34 CrossRef Medline
15. Hwang YH, Kang DH, Kim YW, et al. **Impact of time-to-reperfusion on outcome in patients with poor collaterals.** *AJNR Am J Neuroradiol* 2015;36:495–500 CrossRef Medline
16. Menon BK, d'Esterre CD, Qazi EM, et al. **Multiphase CT angiography: a new tool for the imaging triage of patients with acute ischemic stroke.** *Radiology* 2015;275:510–20 CrossRef Medline
17. Hill MD, Martin RH, Mikulis D, et al. **Safety and efficacy of NA-1 in patients with iatrogenic stroke after endovascular aneurysm repair (ENACT): a phase 2, randomised, double-blind, placebo-controlled trial.** *Lancet Neurol* 2012;11:942–50 CrossRef Medline
18. Mishra SM, Dykeman J, Sajobi TT, et al. **Early reperfusion rates with IV tPA are determined by CTA clot characteristics.** *AJNR Am J Neuroradiol* 2014;35:2265–72 CrossRef Medline

Necessary Catheter Diameters for Mechanical Thrombectomy with ADAPT

O. Nikoubashman, A. Nikoubashman, M. Büsen, and M. Wiesmann

ABSTRACT

BACKGROUND AND PURPOSE: Large-bore catheters allow mechanical thrombectomy in ischemic stroke by engaging and retrieving clots without additional devices (direct aspiration first-pass technique [ADAPT]). The purpose of this study was to establish a model for minimal catheter diameters needed for ADAPT.

MATERIALS AND METHODS: We established a theoretic model for the calculation of minimal catheter diameters needed for ADAPT. We then verified its validity in 28 ADAPT maneuvers in a porcine in vivo model. To account for different mechanical thrombectomy techniques, we factored in ADAPT with/without a hypothetic 0.021-inch microcatheter or 0.014-inch microwire inside the lumen of the aspiration catheter and aspiration with a 60-mL syringe versus an aspiration pump.

RESULTS: According to our calculations, catheters with an inner diameter of >0.040 inch and >0.064 inch, respectively, are needed to be effective in the middle cerebral artery (2.5-mm diameter) or in the internal carotid artery (4 mm) in an average patient. There was a significant correlation between predicted and actual thrombectomy results ($P = .010$). Our theoretic model had a positive and negative predictive value of 78% and 79%, respectively. Sensitivity and specificity were 88% and 64%, respectively.

CONCLUSIONS: Our theoretic model allows estimating the minimal catheter diameters needed for successful mechanical thrombectomy with ADAPT, as demonstrated by the good agreement with our animal experiments. Our model will be helpful to interventionalists in avoiding selecting catheters that are likely too small to be effective.

ABBREVIATIONS: ADAPT = direct aspiration first-pass technique; MT = mechanical thrombectomy

Endovascular mechanical thrombectomy (MT) with stent retrievers is the most effective treatment option for acute ischemic stroke caused by large-vessel occlusion.[1] Newly developed large-bore catheters, which can be placed in close proximity to the intracranial occlusion site, allow engagement and retrieval of a clot without additional devices (so-called direct aspiration first-pass technique [ADAPT]).[2] The concept of ADAPT is to engage a clot, clog the catheter tip, and retrieve the catheter and clot together. This simple technique is promising for establishing MT in a wider range of hospitals and may reduce the risk of procedure-related subarachnoid hemorrhage.[3,4] However, the effectiveness of ADAPT is an issue that needs to be resolved; failure rates for ADAPT and the need to change the MT strategy have been reported in 22%–44% of cases.[4-7]

The size and composition of the clot on the one hand and suction force at the catheter tip on the other are supposedly the most crucial factors for successful MT with ADAPT.[8] While the size and composition of a clot cannot be influenced, the force at the catheter tip is the product of applied pressure and cross-sectional area of the catheter. Consequently, the catheter with the largest tip diameter will apply the greatest force. Instinctively, one would think it would be best to follow the principle of "the bigger the better" and use the largest available catheter, but smaller catheters leave more spare lumen in the access catheter for proximal aspiration and have the advantage of better maneuverability and therefore allow easier and less traumatic access to the occlusion site. Hence, the ideal catheter is as small as possible and as large as necessary. However, the force needed to engage a given clot is unknown. The purpose of this study was to develop a theoretic model for calculating the minimal catheter diameters necessary for MT with ADAPT and to validate this model in an in vivo porcine experiment.

Received May 7, 2017; accepted after revision August 7.

From the Department of Diagnostic and Interventional Neuroradiology (O.N., M.W.), University Hospital, RWTH Aachen University, Aachen, Germany; Institute of Physics (A.N.), Johannes Gutenberg University Mainz, Mainz, Germany; and Institute of Applied Medical Engineering (M.B.), RWTH Aachen University, Aachen, Germany.

O. Nikoubashman and A. Nikoubashman contributed equally to this work.

Please address correspondence to Omid Nikoubashman, MD, Klinik für Neuroradiologie, Universitätsklinikum Aachen, Pauwelsstr 30, 52074 Aachen, Germany; e-mail: onikoubashman@ukaachen.de

http://dx.doi.org/10.3174/ajnr.A5401

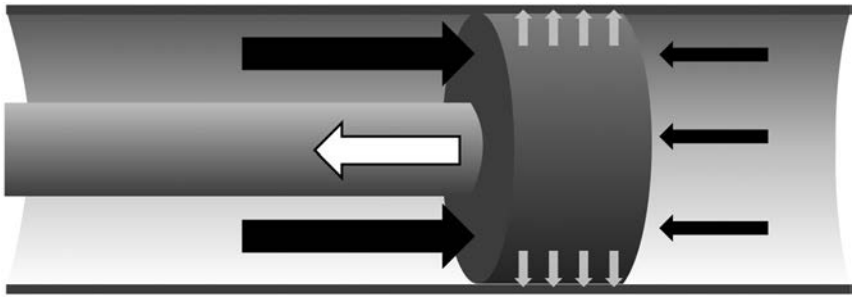

FIG 1. Schematic depicting forces affecting the clot. The suction force at the tip of the catheter (*white arrow*) must exceed the force of the blood pressure (*black arrows*) and the adhesion force that hold the clot in its position (*gray arrows*). *Arrows* represent the direction and idealized amount of force.

MATERIALS AND METHODS

Theoretic Model

For clot retrieval, the force at the catheter tip must exceed the force that keeps the clot in position. In a minimal model, the total force effectively acting on a clot can be expressed as $F_{Total} = F_{Aspiration} + F_{Adhesion}$ (Fig 1). To estimate these forces (see below), we used a simplified model, in which the clot is a fully occlusive impervious rigid body, the vessel is a rigid tube with a constant diameter, and there is no flow in the aspiration catheter and consequent head loss. Furthermore, our model neglects possible contributing factors such as the thickness of the catheter wall and pulsatile blood flow around the clot.

$F_{Aspiration}$ is the suction force at the tip of the aspiration catheter and is defined as $F_{Aspiration} = A_{Catheter}\Delta P_{Catheter}$, with $A_{Catheter}$ being the area at the tip and $\Delta P_{Catheter}$ being the pressure in the tubing system (white arrow in Fig 1). The respective surface is subtracted from the area of the catheter tip to account for variations of the ADAPT technique with a microcatheter or a microwire introduced into the catheter.

$F_{Pressure}$ is determined by the pressure difference before and behind the clot and the surface of the clot exposed to this pressure. Hence $F_{Pressure} = A_{clot}\Delta P_{Vessel}$, with A_{Clot} being the area of the clot minus the area of the catheter tip and ΔP_{Vessel} being the intravascular pressure difference before and behind the clot (black arrows in Fig 1). The effective pressure difference depends on the presence of collaterals that maintain blood pressure behind the clot.[9] In our model, we use a gradient of 60 mm Hg, which Sorimachi et al[10] have assessed on average in occlusions of the internal carotid artery and the M1 segment of the MCA in 36 patients with stroke.

The adhesion force ($F_{Adhesion}$) between the clot and the vessel wall is unknown and may be small when it is determined by mechanical friction alone or very large if the clot is wedged or if there is protein binding between the clot and the vessel wall (gray arrows in Fig 1).[11] Because a clot does not constantly migrate in a vessel, the minimal adhesion force that keeps the clot in position can be estimated as $F_{Adhesion} \geq F_{Pressure}$, which equals $F_{Adhesion} = C\,F_{Pressure}$, with C being a constant that is ≥ 1. Romero et al[11] estimated the adhesion forces between clots and the vessel wall in the MCA with a bond graph model for the aspiration device and found that typical adhesion forces ranged between 0.01 and 0.1 N. Chueh et al[12] experimentally determined adhesion forces in a rabbit model and indicated adhesion forces of 0.7 N after 5 hours of clot/vessel interaction. These values lie in the range of our model, which provides for $C = 1$ adhesion forces between 0.014 and 0.16 N for clotted vessels with diameters between 1.5 and 5 mm, respectively.

Hence, $F_{Total} = \pi(R^2_{Catheter} - R^2_{InnerCatheter})\Delta P_{Catheter} + \pi(R^2_{Vessel} - R^2_{Catheter})\Delta P_{Vessel} + \pi R^2_{Vessel}\Delta P_{Vessel}$, with R representing the respective radii. The minimal catheter radius needed to move the clot, $F_{Total} \leq 0$, can be calculated as follows:

$$R_{Catheter} \geq \sqrt{\frac{R^2_{InnerCatheter}\Delta P_{Catheter} - 2\,R^2_{Vessel}\Delta P_{Vessel}}{\Delta P_{Catheter} - \Delta P_{Vessel}}}.$$

We calculated the catheter diameters needed for ADAPT in vessels with diameters from 1.5 to 5 mm, which are typical for cerebral arteries. To take into account different MT techniques, we compared ADAPT techniques with/without a hypothetic 0.021-inch microcatheter (outer diameter, 0.8 mm) or a 0.014-inch microwire (outer diameter, 0.46 mm) inside the lumen of the aspiration catheter and factored in vacuum pressure generated with a 60-mL syringe (experimentally determined maximal vacuum pressure of −0.89 bar) or generated with an aspiration pump ([Pump MAX; Penumbra, Alameda, California], vacuum pressure of −0.86 bar, which corresponds to the manufacturer's recommended pressure).

Animal Model

To verify our theoretic model, we performed ADAPT maneuvers in an in vivo porcine animal model and compared the predictions with the actual results. All experiments were performed in 2 female Landrace swine (average weight, 58 kg) with peri- and intrainterventional management as reported previously.[13] The experiments were performed in accordance with the German legislation governing animal studies following the *Guide for the Care and Use of Laboratory Animals* (National Research Council, 8th ed, 2011) and the "Directive 2010/63/EU on the Protection of Animals Used for Scientific Purposes" (*Official Journal of the European Union,* 2010). Official permission was granted from the governmental animal care and use office (Landesamt für Natur, Umwelt und Verbraucherschutz Nordrhein-Westfalen, Recklinghausen, Germany).

One week before the procedures, we produced whole-blood clots in a Chandler loop to have radiopaque and solid clots that can be engaged with the aspiration catheter without being aspirated into it.[14,15] We then injected the clots into various branches of the subclavian artery with diameters ranging from 1.5 to 6 mm. Before the ADAPT maneuvers, we measured the diameters of the occluded vessels as well as the pressure before and behind the clot with a Trevo Pro 18 microcatheter (Stryker, Kalamazoo, Michigan) using a PowerLab 16/35 workstation (AdInstruments, Dunedin, New Zealand) and LabChart 8 Software (AdInstruments). Before the ADAPT maneuvers, there was a pause of at least 10

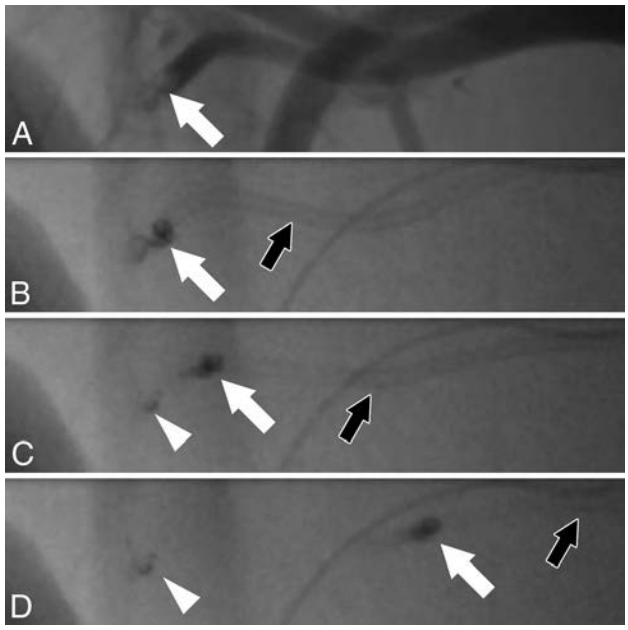

FIG 2. Fluoroscopic angiography of an ADAPT maneuver. Angiography shows a clot (*A*, *white arrow*) in a branch of the axillary artery with a diameter of 1.9 mm. The pressure gradient before and behind the clot is 38 mm Hg, necessitating an aspiration catheter with an inner diameter of at least 1.9F for clot removal, according to our calculations. The clot (*A–D*: *white arrow*), which is partially radiopaque, is engaged with a Sofia 5F catheter (*B*, *black arrow*). When the catheter is pulled back (*C* and *D*, *black arrow*), the larger portion of the clot can be removed (*C* and *D*, *white arrow*). However, there is fragmentation of the clot, with a small portion of the clot remaining in the vessel (*C* and *D*, *arrowhead*).

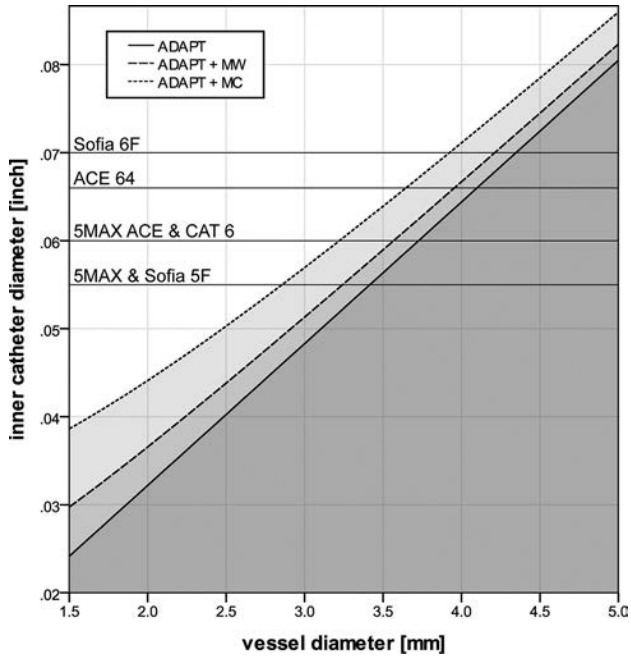

FIG 3. Correlations between minimal catheter size and vessel diameter in an average patient. Graphs represent the minimal inner catheter diameter (y-axis) needed to overcome the force that keeps a clot in its position in a vessel with a given diameter (x-axis), using ADAPT with manual aspiration in an average patient (ie, a pressure gradient of 60 mm Hg before and behind the clot). The *continuous line* represents the ADAPT technique without microcatheters or microwires in the aspiration catheter. *Dotted lines* represent the ADAPT technique with an additional microcatheter (MC) or microwire (MW) in the aspiration catheter. *Gray areas* under the curves correspond to catheter diameters that are not large enough for ADAPT. Given the lower pressure provided by a pump, catheters need to be approximately 1% larger than indicated in the figure when a pump instead of a syringe is used for aspiration. *Black horizontal lines* represent the inner diameters of various commercially available catheters: Sofia (MicroVention); AXS Catalyst 6 (CAT6; Stryker); and 5MAX, 5MAX ACE, and ACE64 (Penumbra).

minutes to allow reocclusion of the channel produced by the microcatheter. ADAPT maneuvers were conducted approximately 20–60 minutes after injection of the clots. We performed ADAPT maneuvers with Sofia 5F and 6F aspiration catheters (MicroVention, Tustin, California), which were introduced through an 8F long sheath (Flexor Shuttle Guiding Sheath; Cook, Bloomington, Indiana). Aspiration was applied with a an aspiration pump (Penumbra Pump MAX), which was connected to the aspiration catheter via a standard 3-way valve (Discofix C; Braun, Melsungen, Germany) and a hemostatic Gateway Adapter (Boston Scientific, Fremont, California) with the standard tubing, on the recommended setting of 25.5 inHg (≈0.86 bar). Because our aim was to verify our ADAPT model, ADAPT was only considered successful if the clot could be engaged (indicated by clogging of the aspiration catheter) and removed with 1 pass (Fig 2), whereas complete ingestion of the clot was not regarded as successful. To prevent ingestion of a clot, the thrombectomy maneuver was performed 5–10 seconds after presumed contact between the catheter and the clot.

Statistical Analysis

Continuous parametric variables are presented as means ± SD; ordinal and nonparametric variables, as medians; and categoric variables, as frequencies. Fisher exact, χ^2, Student *t*, and Mann-Whitney *U* tests were used whenever applicable after testing our data for normal distribution with a Shapiro-Wilk test. *P* values of an α level ≤ .05 were significant. All statistical analyses were performed with SPSS 23 software (IBM, Armonk, New York).

RESULTS

Theoretic Model

Figure 3 depicts the minimum inner diameters needed to overcome the force that keeps a clot in its position in a vessel with a given diameter using ADAPT with manual aspiration in an average patient with stroke. Using an additional microcatheter necessitates a significantly larger aspiration catheter ($P \leq .024$), but introducing a microwire does not ($P \geq .368$). When a pump instead of a syringe is used for aspiration, catheters need to be approximately 1% larger than indicated in Fig 3. However, the use of a pump instead of a syringe has no significant impact on the required catheter diameters ($P = .839$).

Animal Model

We performed 28 ADAPT maneuvers, 19 of which were with the Sofia 5F catheter and 9 with the Sofia 6F catheter. The mean vessel diameter was 3.8 ± 1.1 mm, ranging from 1.9 to 5.9 mm. The median pressure gradient before and behind the clot was 39.5 mm Hg (interquartile range, 34 mm Hg), ranging from 2 to 116 mm Hg. According to our model predictions, our catheters were oversized by 0.11 ± 0.020 inch on average, ranging from largely undersized cases (−0.030 inch) to largely oversized cases (+0.043 inch).

Nine maneuvers were performed with catheters that were sup-

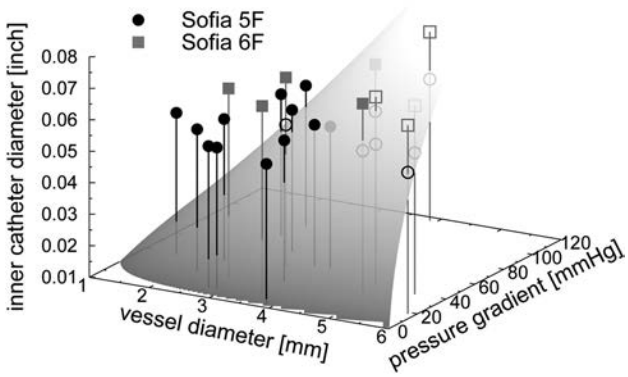

FIG 4. Plot of all 28 ADAPT experiments. The *shaded plane* indicates the minimal inner catheter diameter (z-axis) needed to engage a clot in a vessel with a given diameter (x-axis) when a specific pressure gradient (y-axis) is applied. *Filled* and *open symbols* indicate experiments, in which the removal of the clot was successful or failed, respectively. In case of perfect agreement between theory and experiment, all *filled symbols* lie above the dividing plane, whereas all *open symbols* lie below it. Note that most deviating points (*open symbols* above the *shaded plane* and *filled symbols* below the *shaded plane*) are located so close to the dividing surface that small variations in the measurement of the vessel diameter and/or pressure gradient could lead to a substantially better agreement between theory and experiments.

posedly too small for successful thrombectomy according to our calculations (Sofia 5F, $n = 6$, and Sofia 6F, $n = 3$). In fact, 7 of these 9 maneuvers failed, and 2 were successful (1 case each with a Sofia 5F and 6F). Conversely, 4 of 19 maneuvers that were predicted to be successful failed (2 cases each with a Sofia 5F and 6F). There was a significant correlation between predicted and actual thrombectomy results ($P = .010$). Our theoretic model had a positive and negative predictive value of 78% and 79%, respectively. Sensitivity and specificity were 88% and 64%, respectively.

Figure 4 depicts the correlation among vessel diameter, pressure gradient, catheter diameter, and predicted-versus-actual outcome of all 28 ADAPT maneuvers. Successful ADAPT maneuvers were performed in significantly smaller vessels (3.1 ± 0.8 mm versus 4.7 ± 0.9 mm; $P < .001$) and with significantly oversized catheters ($+0.21 \pm 0.016$ inch versus -0.006 ± 0.013 inch; $P < .001$). Pressure gradients were comparable in successful and unsuccessful cases (median, 38.0 mm Hg, versus 41.0 mm Hg; $P = .378$). The 4 cases in which the ADAPT failed unexpectedly were performed in significantly larger vessels compared with cases with correct predictions (4.9 ± 1.3 mm versus 3.5 ± 1.1 mm; $P = .025$). Catheters in both groups had a comparable marginal oversize ($+0.008 \pm 0.006$ inch versus $+0.012 \pm 0.022$ inch; $P = .437$), and pressure gradients did not differ significantly (median, 29.5 mm Hg, versus 39.0 mm Hg; $P = .607$).

DISCUSSION

The rationale of the ADAPT technique is to engage a clot with a large-bore catheter and establish constant adherence between the clot and the catheter with suction force. This force can be calculated easily, given that it is the product of the cross-sectional area at the catheter tip and the pressure. Because the cross-sectional area increases by the square of the radius, small changes of diameter result in a large change of force. For instance, a 27% increase of the inner diameter of the Sofia 6F catheter compared with the Sofia 5F catheter (0.07 versus 0.055 inch) results in a 62% increase of force. Recently, Nikoubashman et al[16] and Hu and Stiefel[8] have characterized various commercially available catheters and calculated the flow through them and the force at the tip of these catheters. However, knowledge of this force is of little use if the force needed to engage a clot is unknown. We approached this problem with a simplified theoretic model and calculated the minimal catheter diameter necessary for clot retrieval with ADAPT. A significant correlation between our experimental and theoretic models validates the latter and provides a justification for the approximations used (Fig 4).

We estimated a minimal catheter diameter below which MT is unlikely to be successful in an average patient with stroke (Fig 3). The negative predictive value of 78% and the positive predictive value of 79% derived from our in vivo experiment support the hypothesis that there is a minimal catheter size required for ADAPT but that larger catheters do not necessarily result in successful recanalization. We calculated that in an average patient, catheters with an inner diameter of >0.040 and >0.064 inch, respectively, are needed to be effective in an MCA with a diameter of 2.5 mm or in the terminal segment of the internal carotid artery with a diameter of 4 mm (Fig 3). If collaterals are better than in the average patient and there is a pressure gradient of 40 mm Hg instead of 60 mm Hg, catheters with an inner diameter of >0.033 and >0.053 inch, respectively, would be sufficient to be effective in the MCA and terminal segment of the internal carotid artery. Hence, our calculations imply that in most cases, the available aspiration catheters should be sufficient for ADAPT in the MCA and that the aspiration catheters of the newest generation are sufficient to extract most occlusions in the average patient (Fig 3). This finding is in accordance with results by Turk et al,[5] who reported that recanalization (TICI 2b/3a) was achieved often with the 5MAX catheter (Penumbra) (75%) but significantly more often with the larger 5MAX ACE catheter (Penumbra) (82%). Conversely, this result is also in line with our clinical experience that ADAPT with smaller catheters (ie, 5F) is more frequently (but not always) successful in the MCA than in the internal carotid artery. However, conclusive data to support this hypothesis are lacking because no study has specifically addressed the correlation between target vessel and recanalization, to our knowledge.

Turk et al[5] published a series of 100 ADAPT cases with 15% ICA occlusions, which were predominantly treated with 5MAX and 5MAX ACE catheters and reported successful recanalization (TICI 2b/3) in 78% of all cases. Supporting the hypothesis that ADAPT recanalization in the ICA is less likely to be successful, Kowoll et al[7] had a higher proportion of ICA occlusions (26%) and a lower recanalization rate of 56% in their series of 54 patients while exclusively using the larger 5MAX ACE catheter. However, Delgado Almandoz et al,[4] who treated 45 patients with an even higher proportion of ICA occlusions (42%), reported a comparably high recanalization rate of 71%, using the 5MAX ACE in most cases (89%). Also on the contrary, Möhlenbruch et al,[6] who had a comparably low proportion of ICA occlusions (17%) in their series of 85 patients, used the largest available catheter (Sofia 6F) and reported a relatively low recanalization rate of 65%. This lower rate may be partly due to varying study designs, because Möhlenbruch et al performed 1.5 passes on average before chang-

ing the MT strategy, whereas Delgado Almandoz et al performed 2.5 passes. Also, various nonmanipulable factors such as collateral situation (ie, pressure gradient along the clot) and clot composition may have had an impact on recanalization results.

In summary, our theoretic model is a helpful tool to select the most efficient catheters, also for techniques in which a combination of stent-retriever thrombectomy and ADAPT is used.[17,18] The strength of our ADAPT model is that it considers all relevant forces in the system that play a role when the clot is engaged with the catheter. Flows, however, which are altered by resistors such as 3-way valves, hemostatic valves, and additional tubing for the aspiration system, play no considerable role in ADAPT when contact between the catheter and the clot is established and the force at its tip becomes constant. Hence, our model requires only knowledge of the applied vacuum pressure and the diameter of the vessel to estimate the necessary catheter diameter. Thus, our model lends itself to clinical situations in which time is of the essence.

However, even though we made great effort to validate our model, it has several limitations that might affect its accuracy: First, the nature of our experiments did not allow a systematic analysis of all possible settings because we were restricted by the porcine anatomy. Also, our theoretic model does not consider actual collateral status and adhesion force and clot burden; this feature is likely the reason why our model did not correctly predict the failure of clot removal in very large vessels. In addition, our model does not account for wedging of clots, which may occur in bifurcations and make thrombectomy more difficult. Our model also neglects clot composition, which possibly has an impact on clot fragmentation (Fig 2) and thrombectomy by clot aspiration. This is a potentially important mechanism in the context of soft clots and large-bore catheters and may have occurred unnoticed in some of our experiments. Last, vessel access (ie, balloon catheter versus large sheath), which may have an impact on thrombectomy results, was an unstudied factor in our model. Despite these limitations, the good agreement between our theoretic model and our experimental results implies that our theoretic model captures the essential physics of the problem, and our study provides a useful step toward better understanding and controlling clot removal with ADAPT.

CONCLUSIONS

Our theoretic model allows estimating the minimal catheter diameters needed for successful MT with ADAPT, as demonstrated by the good agreement with our animal experiments. Our model may be helpful to interventionalists in avoiding selecting catheters that are too small to be effective.

ACKNOWLEDGMENTS

The authors thank Johanna Sandmann, Franziska Müschenich, and Thorsten Sichtermann for their helpful contributions during data acquisition. Arash Nikoubashman acknowledges support from the German Research Foundation (DFG) under project number NI 1487/2-1.

Disclosures: Martin Wiesmann—*UNRELATED*: *Consultancy*: Stryker Neurovascular; *Payment for Lectures Including Service on Speakers Bureaus*: Bracco, Siemens, Stryker Neurovascular; *Payment for Development of Educational Presentations*: Abbott, abmedica, Acandis, Bayer HealthCare, Bracco, B. Braun Melsungen, Codman Neurovascular, Covidien, Dahlhausen, MicroVention, Penumbra, phenox, Philips Healthcare, Siemens, Silk Road Medical, St. Jude, Stryker Neurovascular.

REFERENCES

1. Goyal M, Menon BK, van Zwam WH, et al; HERMES collaborators. **Endovascular thrombectomy after large-vessel ischaemic stroke: a meta-analysis of individual patient data from five randomised trials.** *Lancet* 2016;387:1723–31 CrossRef Medline
2. Turk AS, Spiotta A, Frei D, et al. **Initial clinical experience with the ADAPT technique: a direct aspiration first pass technique for stroke thrombectomy.** *J Neurointerv Surg* 2014;6:231–37 CrossRef Medline
3. Nikoubashman O, Reich A, Pjontek R, et al. **Postinterventional subarachnoid haemorrhage after endovascular stroke treatment with stent retrievers.** *Neuroradiology* 2014;56:1087–96 CrossRef Medline
4. Delgado Almandoz JE, Kayan Y, Young ML, et al. **Comparison of clinical outcomes in patients with acute ischemic strokes treated with mechanical thrombectomy using either Solumbra or ADAPT techniques.** *J Neurointerv Surg* 2016;8:1123–28 CrossRef Medline
5. Turk AS, Frei D, Fiorella D, et al. **ADAPT FAST study: a direct aspiration first pass technique for acute stroke thrombectomy.** *J Neurointerv Surg* 2014;6:260–64 CrossRef Medline
6. Möhlenbruch MA, Kabbasch C, Kowoll A, et al. **Multicenter experience with the new SOFIA Plus catheter as a primary local aspiration catheter for acute stroke thrombectomy.** *J Neurointerv Surg* 2016 Dec 20. [Epub ahead of print] CrossRef Medline
7. Kowoll A, Weber A, Mpotsaris A, et al. **Direct aspiration first pass technique for the treatment of acute ischemic stroke: initial experience at a European stroke center.** *J Neurointerv Surg* 2016;8:230–34 CrossRef Medline
8. Hu YC, Stiefel MF. **Force and aspiration analysis of the ADAPT technique in acute ischemic stroke treatment.** *J Neurointerv Surg* 2016;8:244–46 CrossRef Medline
9. Sorimachi T, Fujii Y, Tsuchiya N, et al. **Blood pressure in the artery distal to an intraarterial embolus during thrombolytic therapy for occlusion of a major artery: a predictor of cerebral infarction following good recanalization.** *J Neurosurg* 2005;102:870–78 CrossRef Medline
10. Sorimachi T, Morita K, Ito Y, et al. **Blood pressure measurement in the artery proximal and distal to an intra-arterial embolus during thrombolytic therapy.** *J Neurointerv Surg* 2011;3:43–46 CrossRef Medline
11. Romero G, Higuera I, Martinez ML, et al. **Analysis and simulation of the adhesion forces between clot and the artery wall for a novel thrombectomy device applied to the middle cerebral artery**. In: *Proceedings of the 2010 12th International Conference on Computer Modelling and Simulation (UKSim 2010),* Cambridge UK. March 24–26, 2010;195–200
12. Chueh J, Kuhn, AL, Mehra M, et al. **Embolus adhesion to activated endothelium after embolization: a parameter to predict outcomes of mechanical thrombectomy in acute ischemic stroke.** *Stroke* 2012; 43(suppl 1):A3750
13. Nikoubashman O, Pjontek R, Brockmann MA, et al. **Retrieval of migrated coils with stent retrievers: an animal study.** *AJNR Am J Neuroradiol* 2015;36:1162–66 CrossRef Medline
14. Robbie LA, Young SP, Bennett B, et al. **Thrombi formed in a Chandler loop mimic human arterial thrombi in structure and RAI-1 content and distribution.** *Thromb Haemost* 1997;77:510–15 Medline
15. Gralla J, Schroth G, Remonda L, et al. **A dedicated animal model for mechanical thrombectomy in acute stroke.** *AJNR Am J Neuroradiol* 2006;27:1357–61 Medline
16. Nikoubashman O, Alt JP, Nikoubashman A, et al. **Optimizing endovascular stroke treatment: removing the microcatheter before clot retrieval with stent-retrievers increases aspiration flow.** *J Neurointerv Surg* 2017;9:459–62 CrossRef Medline
17. Massari F, Henninger N, Lozano JD, et al. **ARTS (Aspiration-Retriever Technique for Stroke): initial clinical experience.** *Interv Neuroradiol* 2016;22:325–32 CrossRef Medline
18. Maus V, Behme D, Kabbasch C, et al. **Maximizing first-pass complete reperfusion with SAVE.** *Clin Neuroradiol* 2017 Feb 13. [Epub ahead of print] CrossRef Medline

WEB Treatment of Ruptured Intracranial Aneurysms: A Single-Center Cohort of 100 Patients

S.B.T. van Rooij, W.J. van Rooij, J.P. Peluso, M. Sluzewski, R.S. Bechan, H.G. Kortman, G.N. Beute, B. van der Pol, and C.B. Majoie

ABSTRACT

BACKGROUND AND PURPOSE: The Woven EndoBridge device was recently introduced for the intrasaccular treatment of wide-neck aneurysms without the need for adjunctive devices. We present our results of the primary treatment of ruptured aneurysms with the Woven EndoBridge regardless of location or neck size.

MATERIALS AND METHODS: Between February 2015 and April 2017, 100 ruptured aneurysms were selectively treated with the Woven EndoBridge. No supporting stents or balloons were used. There were 71 women treated (mean patient age, 59 years; median age, 60 years; range, 23–82 years).

RESULTS: The mean aneurysm size was 5.6 mm (range, 3–13 mm), and 42 aneurysms were ≤4 mm. Sixty-six aneurysms (66%) had a wide neck, defined as ≥4 mm or a dome-neck ratio ≤1.5. There was 1 procedural rupture without sequelae. In 9 patients (9%), thromboembolic complications occurred. One poor grade patient died; neurologic deficits remained in 3. Overall treatment-related morbidity-mortality was 4% (4 of 100; 95% CI, 1.2%–10.2%).

Two of 100 aneurysms were initially incompletely occluded and were additionally treated early after initial intervention. Of 80 eligible patients, 74 (93%) had 3-month angiographic follow-up. Fifty-four aneurysms (73%) were completely occluded, 17 (23%) had a small neck remnant, and 3 (4%) were incompletely occluded. One patient was additionally treated with a second Woven EndoBridge, and in 2 patients, additional treatment is scheduled. The overall reopening/retreatment rate was 6.8% (5 of 74; 95% CI, 2.6%–15.2%). There were no rebleeds during follow-up.

CONCLUSIONS: Treatment of small ruptured aneurysms with the Woven EndoBridge was safe and effective. The Woven EndoBridge proved to be a valuable alternative to coils without the need for stents or balloons.

ABBREVIATION: WEB = Woven EndoBridge

Endovascular treatment of wide-neck intracranial aneurysms with coils mostly requires the use of a temporary protection balloon or a stent. However, this makes the procedure more complicated with a higher chance of complications.[1-4] With stents, periprocedural dual antiplatelet therapy is required and has to be prolonged for 3–6 months. With this antiaggregation regimen, stent-assisted coiling in ruptured aneurysms has a higher inherent risk for early rebleed or hemorrhage in the postoperative period. Despite antiaggregation, thromboembolic complications still occur.[5]

Recently, the intrasaccular flow disruptor Woven EndoBridge (WEB; Sequent Medical, Aliso Viejo, California) device has been developed, primarily for the treatment of (bifurcation) wide-neck aneurysms without the need for adjunctive devices. The first clinical results of the WEB device show good safety and efficacy profiles. Most of the published series comprised wide-neck, unruptured aneurysms.[6-24]

In a previous publication, we presented our first results of the use of the WEB for all ruptured aneurysms suitable for the device, regardless of location or neck size.[25] Our intention was to avoid stents in the treatment of ruptured aneurysms. Our strategy was to treat ruptured wide-neck aneurysms with the WEB or, when WEB placement was not possible, with coiling or surgery. In this study, we present the results of this treatment strategy with an extended cohort of 100 patients with ruptured aneurysms treated with the WEB.

Received May 9, 2017; accepted after revision July 7.

From the Department of Radiology (S.B.T.v.R.), Noordwest Ziekenhuisgroep, Alkmaar, the Netherlands; Departments of Radiology (W.J.v.R., J.P.P., M.S., R.S.B., H.G.K.), and Neurosurgery (G.N.B., B.v.d.P.), Elisabeth Tweesteden Ziekenhuis, Tilburg, the Netherlands; and Department of Neuroradiology (C.B.M.), Academisch Medisch Centrum, Amsterdam, the Netherlands.

Please address correspondence to W.J. van Rooij, MD, PhD, Department of Radiology, Elisabeth Tweesteden Ziekenhuis, Hilvarenbeekseweg 60, 5022GC Tilburg, the Netherlands; e-mail: wjjvanrooij@gmail.com

http://dx.doi.org/10.3174/ajnr.A5371

MATERIALS AND METHODS

This observational study with prospectively collected data was compliant with our institutional privacy policy. The institutional review board gave exempt status for approval and informed consent. The study was performed in the Elisabeth Tweesteden Ziekenhuis in Tilburg, the Netherlands.

The WEB

The Woven EndoBridge system is a self-expanding, spherical or pumpkin-shaped, braided mesh of platinum-cored nitinol wires that can be deployed in the aneurysm sac. The design of the WEB device has evolved from a dual-layer configuration (WEB-DL) to a single-layer version (WEB-SL) with a higher number of nitinol wires. The WEB-SL device is available in diameters ranging from 4–11 mm and heights ranging from 3–9 mm. The WEB-SLS (Single-Layer Sphere) has a spherical shape and is available in diameters ranging from 4–11 mm, each with a fixed height ranging between 2.6 and 9.6 mm. The WEBs with diameters of 4–7 mm can be delivered through a 0.021-inch internal diameter microcatheter, the WEBs with diameters of 8–9 mm through a 0.027-inch microcatheter, and the WEBs with diameters of 10–11 mm through a 0.033-inch microcatheter (VIA 21, 27, and 33; Sequent Medical). Recently, a lower-profile range of WEBs compliant with a 0.017-inch microcatheter (VIA 17) has become available in clinical practice.

Placed in the aneurysm, the WEB modifies the blood flow at the level of the neck and induces aneurysmal thrombosis. The WEB can be fully retrieved until final detachment by an electrothermal detachment system contained in a hand-held controller.

General Indications in This Study

In our institution, the treatment of patients with ruptured aneurysms is primarily endovascular within 24 hours after admission. Because of previous poor results with stent-assisted coiling in ruptured aneurysms,[5] from January 2015 onwards, we decided not to use stents with inherent antiplatelet medication anymore. Wide-neck aneurysms were treated either with the WEB, with coiling, or by surgery. Surgery was always an option in good grade patients with wide-neck anterior circulation aneurysms. In poor grade patients with wide-neck aneurysms not suitable for endovascular treatment, surgery was generally postponed several days.

The WEB device was initially developed for the treatment of wide-neck intracranial aneurysms as an alternative to balloon- or stent-assisted treatment. After our first encouraging experiences in unruptured wide-neck aneurysms, during the study period, we gradually expanded the indication to all aneurysms suitable for the WEB regardless of neck size, location, or rupture status. Examples of WEB treatment of ruptured aneurysms are provided in Figs 1–3.

Under general anesthesia, a microcatheter was advanced into the aneurysm via a coaxial or triaxial approach. Hence, the aneurysm was occluded with coils or with a WEB. The WEB was slightly oversized according to recommendations of the manufacturer. WEB sizes and shapes were recorded. Apart from heparin in the pressure bags for flushing (1000 IU/L), no anticoagulation was used.

Patient demographics and treatment and aneurysm characteristics were collected. Clinical grading during admission was according to the Hunt and Hess scale, and clinical follow-up was classified in mRS. For surviving patients, angiographic follow-up was scheduled at 3 months and 3T MRA follow-up at 6 months.

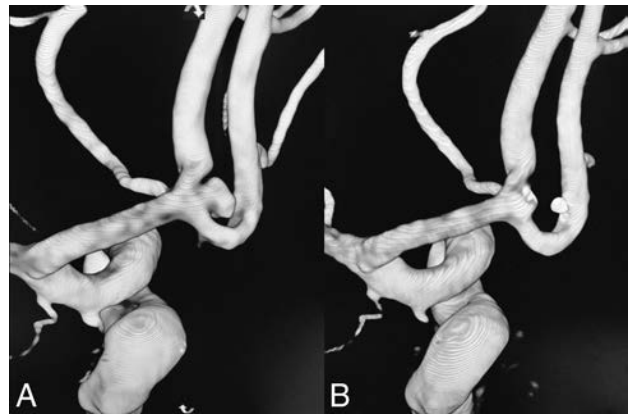

FIG 1. Ruptured anterior communicating artery aneurysm in a 52-year-old man treated with the WEB. *A*, 3-mm aneurysm with a relatively small neck treated with a WEB Single-Layer Sphere (4 mm). *B*, 3-month follow-up angiogram shows complete occlusion.

Quantitative variables were expressed with descriptive statistics, and categoric variables were expressed as frequencies or percentages with 95% CIs.

RESULTS

Patients

Between February 2015 and April 2017, 242 patients with a ruptured aneurysm were treated in our institution (Fig 4). Of 242 aneurysms, 189 (78%) were treated with endovascular techniques, and 104 of those were treated with the WEB device. Four patients with vertebral dissection aneurysms were treated with parent vessel occlusion by using the WEB, and these were excluded from further analysis. The remaining 100 patients with ruptured aneurysms selectively treated with the WEB form the subject of this study.

There were 29 men and 71 women, with a mean age of 59 years (median, 60 years; range, 23–82 years). The clinical condition at the time of treatment was Hunt and Hess 1–2 in 53 patients, 3 in 24 patients, and 4–5 in 23 patients. The timing of treatment after SAH was 0–1 day in 77 patients, 2–4 days in 16 patients, and >4 days in 7 patients. The aneurysm location was the anterior communicating artery in 46 patients, the posterior communicating artery in 22 patients, the MCA in 16 patients, the pericallosal artery in 7 patients, the basilar tip in 5 patients, the superior cerebellar artery in 2 patients, the carotid tip in 1 patient, and the vertebral artery in 1 patient. The mean aneurysm size was 5.6 mm (median, 5 mm; range, 3–13 mm), and 42 aneurysms were ≤4 mm. Of 100 aneurysms, 66 (66%) had a wide neck, defined as ≥4 mm or a dome-neck ratio ≤1.5. Four patients had 1 additional unruptured aneurysm treated in the same session, 1 with WEB and 3 with coils. One patient had 3 additional unruptured aneurysms treated with the WEB in the same session.

Initial Results and Complications

After WEB placement with sealing of the aneurysm neck, the position of the WEB inside the aneurysm was judged as good in 98 of

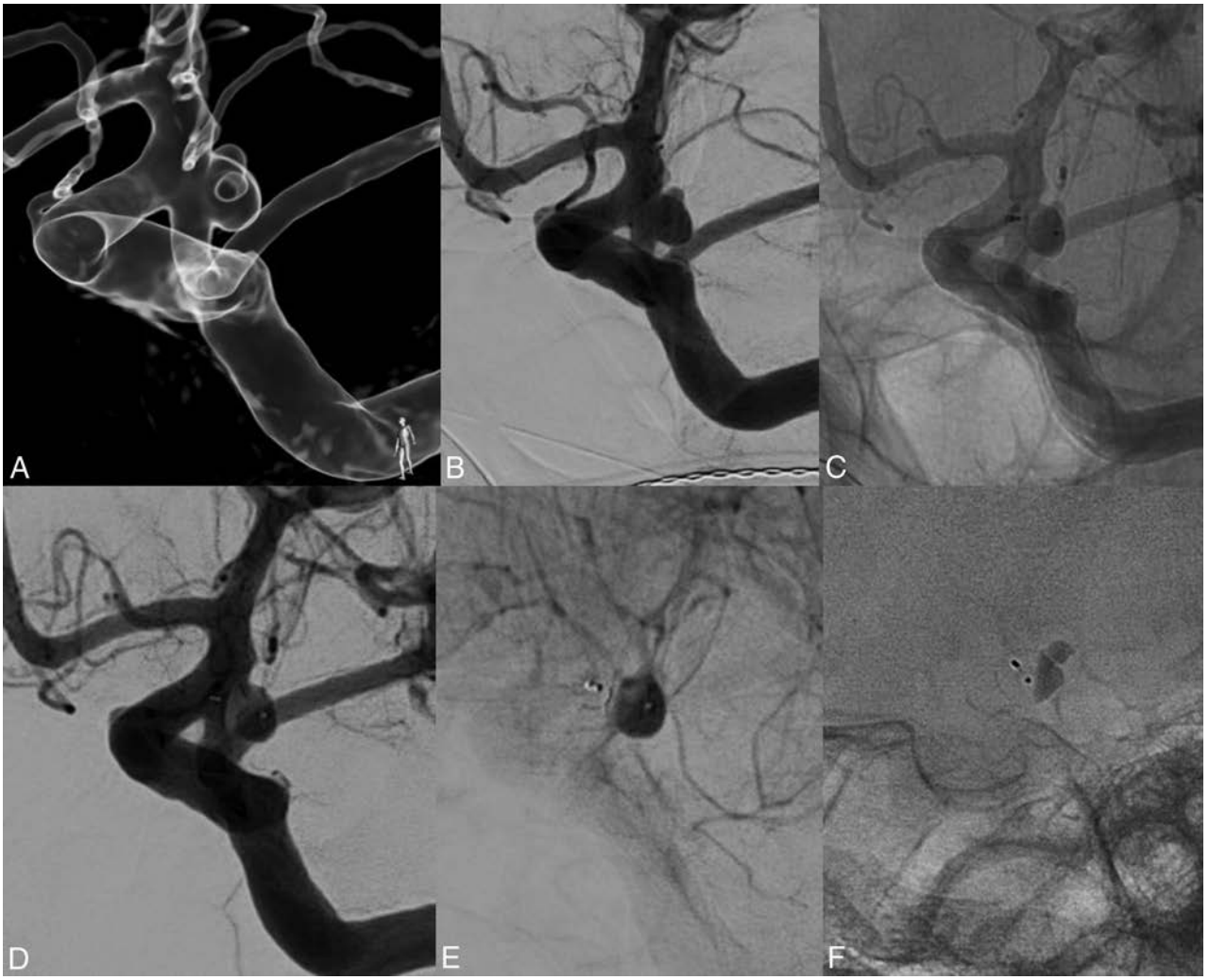

FIG 2. Ruptured wide-neck posterior communicating artery aneurysm in a 62-year-old woman. *A*, 3D and *B*, 2D angiograms of a small wide-neck aneurysm on a fetal posterior cerebral artery. Note 2 blebs on the aneurysm. *C* and *D*, The WEB fills the aneurysm with bridging of the neck. *E* and *F*, Contrast stasis in the aneurysm after WEB placement.

100 aneurysms, without filling of aneurysm remnants. In 1 patient with a 13-mm ruptured pericallosal artery aneurysm, a WEB was placed to protect the dome only. This aneurysm was later additionally clipped. In 1 patient, the WEB was undersized, but this was only noticed after detachment. Follow-up angiography after 1 week showed an aneurysm remnant that was then occluded with coils.

In 2 patients, coils were placed in the aneurysm dome through a jailed second microcatheter before detachment of the WEB.

WEB sizes and shapes used are displayed in Fig 5. Most WEBs used (91 of 100) were in the smaller ranges suitable for the VIA 21 microcatheter, and the most frequently used size was 4 mm (43 of 100).

There was 1 procedural rupture by puncture of the dome of a posterior communicating artery aneurysm with the undeployed WEB. The bleeding stopped after WEB deployment; the patient remained unchanged in good grade. In 9 patients, thromboembolic complications occurred. In 7 of those 9 patients, thrombus was present before WEB placement. Five patients were treated with thrombosuction (followed by tirofiban in 2) and 4 with tirofiban only. One poor grade patient with incomplete result after thrombosuction developed a partial MCA infarction and died (mortality, 1 of 100 [1%]). Neurologic deficits remained in 3 patients with outcomes of mRS 3 in 2 patients and mRS 2 in 1 patient (morbidity, 3 of 100 [3%]). In 1 patient, catheterization caused a dissection of the internal carotid artery, which was successfully treated with a stent. Overall treatment-related permanent morbidity-mortality was 4% (4 of 100; 95% CI, 1.2%–10.2%).

Clinical Follow-Up

Of 100 patients, 17 died during hospital admission of the sequelae of SAH. Of these 17 patients, 15 were admitted in poor grade (Hunt and Hess 4–5) and 2 in Hunt and Hess 3. One other poor grade patient died after a thromboembolic complication in an M2 branch during treatment led to partial right frontal brain infarction. Clinical follow-up in the 82 patients who survived the hospital admission period was mRS 0–2 in 75 patients and mRS 3–5 in 7 patients. There were no rebleeds from the ruptured aneurysm during follow-up.

Angiographic Follow-Up

Two patients had early additional treatment of the WEB-treated ruptured aneurysm. Of the remaining surviving 80 patients, 74 (93%) had 3-month angiographic follow-up. Three patients re-

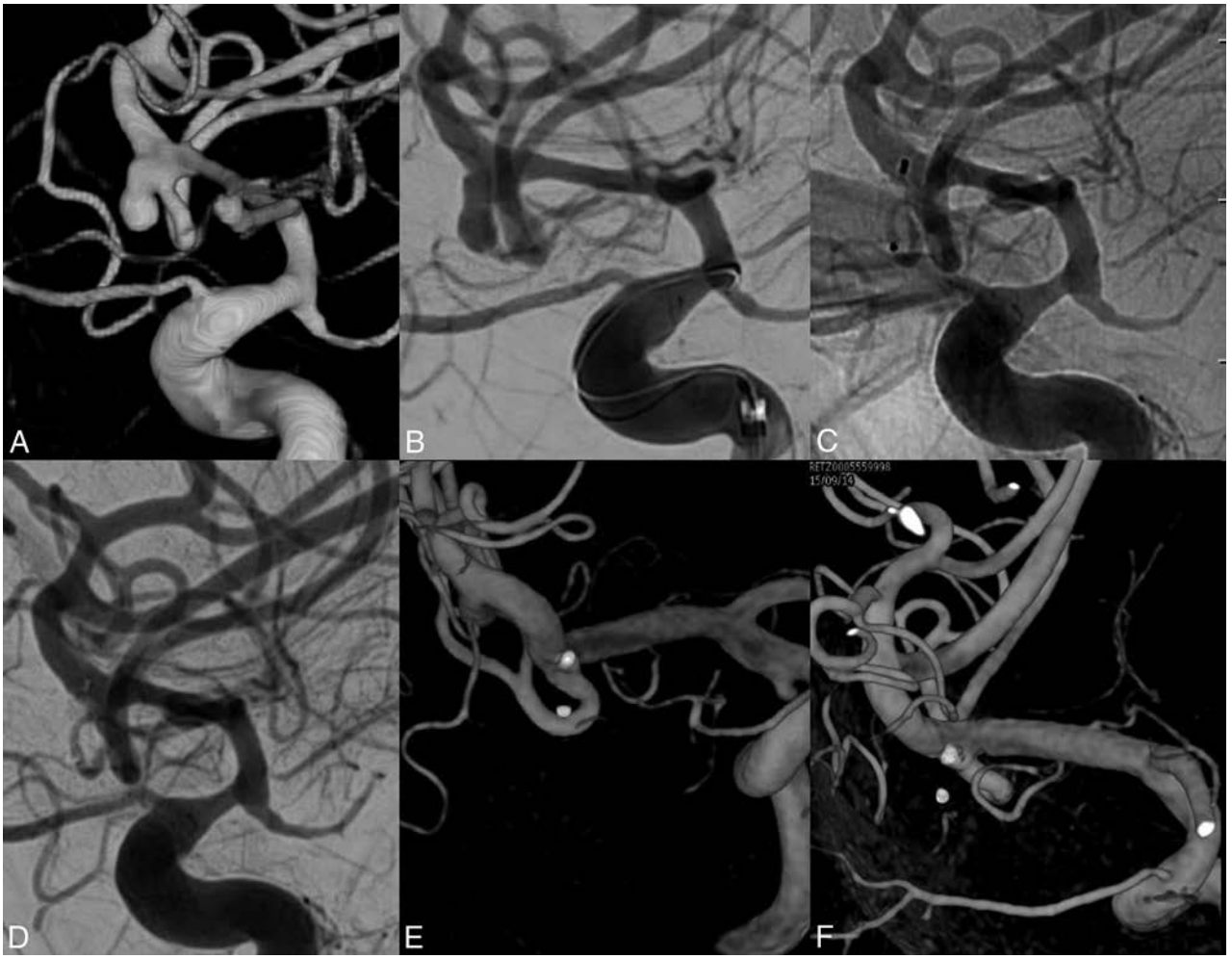

FIG 3. Small ruptured MCA aneurysm in a 58-year-old woman. *A*, 3D and *B*, 2D angiograms show downward-pointing small MCA aneurysm. *A*, Native and *B*, subtracted angiogram after WEB placement. *E* and *F*, 3D angiogram at 3 months shows persistent complete occlusion.

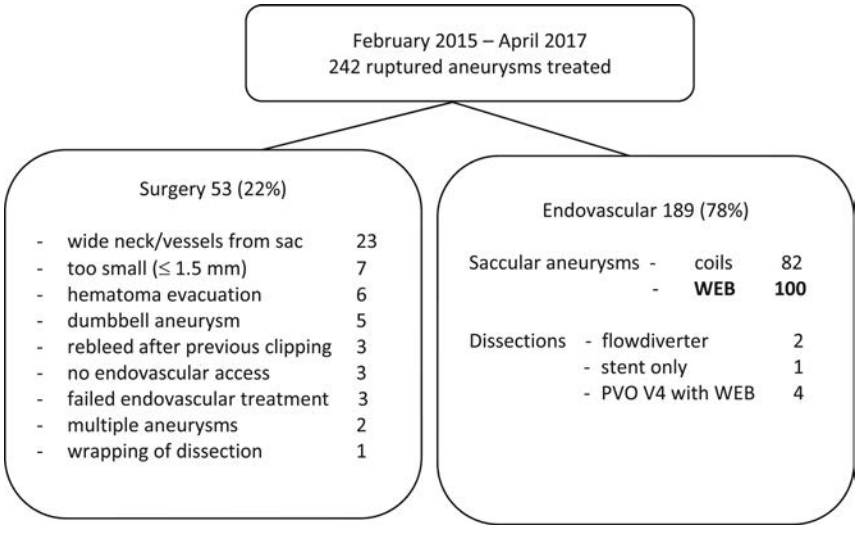

FIG 4. Flow chart of 242 ruptured aneurysms treated between February 2015 and April 2017, including main reasons to proceed to surgery. PVO indicates parent vessel occlusion; V4, vertebral artery segment 4.

fused follow-up angiography. In 3 patients, imaging follow-up is pending. Of the 74 patients with angiographic follow-up, 54 aneurysms (73%) were completely occluded, 6 of those with some proximal WEB recess filling.[26-28] Seventeen aneurysms (23%) had a small neck remnant. In 3 patients (4%), the aneurysm was incompletely occluded. In 1 of those 3 patients, the aneurysm remnant was additionally treated with a second WEB, and in 2 patients, additional treatment is scheduled. The reopening/retreatment rate was 6.8% (5 of 74; 95% CI, 2.6%–15.2%).

DISCUSSION

Our results show that we succeeded in our primary aim to avoid the use of stents in the treatment of acutely ruptured aneurysms by introducing the WEB. No stents were used in the endovascularly treated ruptured aneurysms, and in coiled ruptured aneurysms, even balloon assistance was not used. One might argue that a larger proportion of wide-neck aneurysms were allocated to surgery. However, fewer than 1 in 10 ruptured aneurysms (23 of 242) were referred to surgery for anatomic rea-

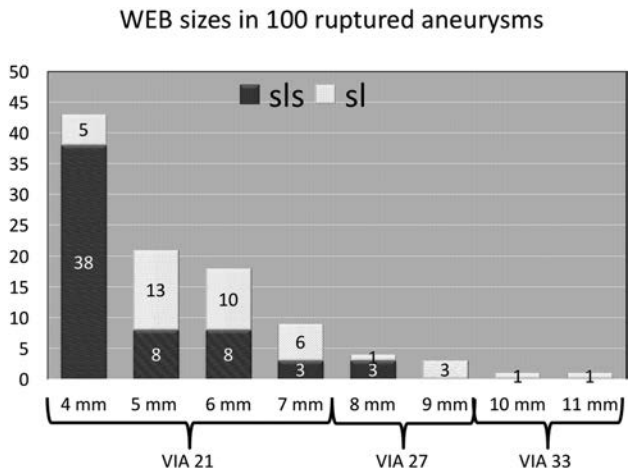

FIG 5. WEB sizes and shapes used in 100 ruptured aneurysms. VIA indicates the microcatheter used.

sons, mostly because of branches coming from the aneurysm sac or aneurysms with limited height (over wide or under tall).[29] In our practice, 78% of ruptured aneurysms were treated endovascularly. This proportion is higher than the 66% from a recent survey in Germany.[30] This indicates that the avoidance of the use of stents by introduction of the WEB was probably not counterweighted by increased referral to surgery.

With the use of stents in ruptured aneurysms, complication rates tend to be higher than with selective coiling because of the thrombogenicity of the devices and the need for dual antiplatelet medication with inherent risk in the postoperative period. Most operators are reluctant to use antiplatelet therapy in the setting of SAH because of the potential need for a ventriculostomy, the potential for infarction secondary to vasospasm, and the high likelihood of future invasive interventions. Therefore, stent placement is better avoided in acutely ruptured aneurysms in favor of endovascular techniques that do not mandate dual antiplatelet therapy or clipping.

With our patient selection for endovascular treatment with the WEB, the complication rate with this device was low, and the anatomic results were good. Complications consisted mainly of thromboembolic events. This may be related to the need for a more distal access with use of the WEB compared with coiling. With use of the WEB, a distal access–guiding catheter is indispensable to achieve a stable position of the microcatheter, and manipulations for distal access may promote thromboembolic events. In addition, the more frequent need of a triaxial approach with long sheets may have attributed as well. Of 9 patients with thromboembolic complications, 6 remained without clinical sequelae. In 5 patients with thrombi in the MCA or posterior communicating artery, thrombosuction was successful. This recent therapeutic achievement thus limited the clinical consequences of thromboembolic complications in our cohort. Procedural rupture with the WEB occurred only once, even though many aneurysms were small or very small. After deployment of the WEB, the bleeding stopped within a minute. Rupture with the WEB can only occur at a point when the undeployed WEB begins to exit the microcatheter. Once the WEB is partially deployed inside the aneurysm, the WEB is soft, and rupture can hardly occur.

An essential aspect of the WEB treatment was the sizing. Oversizing the WEB seems crucial to obtain stable results. With oversizing, the WEB anchors itself against the aneurysm wall while bridging the neck completely. Oversizing causes compression of the WEB width, which in turn results in increased height, and one has to be sure that the aneurysm can accommodate this augmented height. Oversizing protects against displacement and overturning and possibly against compression of the WEB during follow-up. In small aneurysms, oversizing of approximately 1 mm will usually be sufficient, whereas in larger aneurysms, 2-mm oversizing is recommended for stable securing in the neck.

Anatomic and clinical results with the WEB were good; adequate occlusion (defined as complete occlusion or neck remnant) at 3-month angiographic follow-up was obtained in 96% (71 of 74 patients with angiographic follow-up). Only 3 aneurysms had reopened at 3-month follow-up. Most important, during follow-up, no rebleeds occurred.

Our anatomic and clinical results in ruptured aneurysms treated with the WEB are better than in previous WEB series and also better than general results of coiling.[10,22,31] The technique of WEB treatment has improved from the first WEB series by the introduction of lower profile microcatheters and imperative oversizing. Our aneurysm population includes small-neck aneurysms, and most aneurysms were small, with only a few larger than 10 mm. Because reopening over time after coiling occurs more frequently in larger aneurysms, long-term results tend to be better in a population of small aneurysms.

Limitations of this study include self-reporting of angiographic results and the limited number of patients, keeping confidence intervals rather wide. A strong point of the study is the almost complete imaging follow-up with use of angiography.

CONCLUSIONS

WEB treatment of ruptured intracranial aneurysms is in our opinion feasible, effective, and safe. The WEB proved a valuable alternative to coils in many ruptured aneurysms regardless of location or neck size. Introduction of the WEB allowed us to refrain from the use of adjunctive stents and supporting balloons. Anticoagulation in the periprocedural period was not necessary. This was a great advantage in view of surgical procedures that were needed in patients with acutely ruptured aneurysms.

In view of our encouraging experiences with the WEB for ruptured aneurysms, this treatment has become first choice in our practice for ruptured aneurysms in sizes between 2 and 10 mm. In larger aneurysms, coiling is the first option, and in exceptional cases, surgery is performed.

Disclosures: Willem Jan van Rooij—*UNRELATED: Consultancy*: Sequent Medical, Microvention, *Comments*: paid for proctoring and speakers bureau. Jo P. Peluso—*OTHER RELATIONSHIPS*: MicroVention, *Comments*, Proctor. Charles B. Majoie—*UNRELATED*: *Consultancy*: Stryker, *Comments*: Academisch Medisch Centrum received funds from Stryker for consultations by CM*; *Grants/Grants Pending*: TWIN Foundation, CVON/Dutch Heart Foundation*. *Money paid to the institution.

REFERENCES

1. Piotin M, Blanc R, Spelle L, et al. **Stent-assisted coiling of intracranial aneurysms: clinical and angiographic results in 216 consecutive aneurysms.** *Stroke* 2010;41:110–15 CrossRef Medline
2. Bartolini B, Blanc R, Pistocchi S, et al. **"Y" and "X" stent-assisted**

coiling of complex and wide-neck intracranial bifurcation aneurysms. *AJNR Am J Neuroradiol* 2014;35:2153–58 CrossRef Medline
3. Chalouhi N, Jabbour P, Singhal S, et al. **Stent-assisted coiling of intracranial aneurysms: predictors of complications, recanalization, and outcome in 508 cases.** *Stroke* 2013;44:1348–53 CrossRef Medline
4. Chung J, Lim YC, Suh SH, et al. **Stent-assisted coil embolization of ruptured wide-necked aneurysms in the acute period: incidence of and risk factors for periprocedural complications.** *J Neurosurg* 2014; 121:4–11 CrossRef Medline
5. Bechan RS, Sprengers ME, Majoie CB, et al. **Stent-assisted coil embolization of intracranial aneurysms: complications in acutely ruptured versus unruptured aneurysms.** *AJNR Am J Neuroradiol* 2016; 37:502–07 CrossRef Medline
6. Lubicz B, Klisch J, Gauvrit JY, et al. **WEB-DL endovascular treatment of wide-neck bifurcation aneurysms: short- and midterm results in a European study.** *AJNR Am J Neuroradiol* 2014;35:432–38 CrossRef Medline
7. Colla R, Cirillo L, Princiotta C, et al. **Treatment of wide-neck basilar tip aneurysms using the WEB II device.** *Neuroradiol J* 2013;6:669–77 CrossRef Medline
8. Pierot L, Moret J, Turjman F, et al. **WEB treatment of intracranial aneurysms: clinical and anatomic results in the French Observatory.** *AJNR Am J Neuroradiol* 2016;37:655–59 CrossRef Medline
9. Pierot L, Spelle L, Molyneux A, et al. **Clinical and anatomical follow-up in patients with aneurysms treated with the WEB device: 1-year follow-up report in the cumulated population of 2 prospective, multicenter series (WEBCAST and French Observatory).** *Neurosurgery* 2016;78:133–41 CrossRef Medline
10. Pierot L, Gubucz I, Buhk JH, et al. **Safety and efficacy of aneurysm treatment with the WEB: results of the WEBCAST 2 study.** *AJNR Am J Neuroradiol* 2017;38:1151–55 CrossRef Medline
11. Liebig T, Kabbasch C, Strasilla C, et al. **Intrasaccular flow disruption in acutely ruptured aneurysms: a multicenter retrospective review of the use of the WEB.** *AJNR Am J Neuroradiol* 2015;36:1721–27 CrossRef Medline
12. Bozzetto Ambrosi P, Gory B, Sivan-Hoffmann R, et al. **Endovascular treatment of bifurcation intracranial aneurysms with the WEB SL/SLS: 6-month clinical and angiographic results.** *Interv Neuroradiol* 2015;4:462–69 CrossRef Medline
13. Pierot L, Costalat V, Moret J, et al. **Safety and efficacy of aneurysm treatment with WEB: results of the WEBCAST study.** *J Neurosurg* 2016;124:1250–56 CrossRef Medline
14. Sivan-Hoffmann R, Gory B, Riva R, et al. **One-year angiographic follow-up after WEB-SL endovascular treatment of wide-neck bifurcation intracranial aneurysms.** *AJNR Am J Neuroradiol* 2015;36: 2320–24 CrossRef Medline
15. Leyon JJ, Chavda S, Lamin S. **Corking the WEB and coiling through a jailed microcatheter: WEB assisted coiling, a useful technique avoiding the use of stents in treating wide-necked large intracranial aneurysms.** *J Neurointerv Surg* 2016;8:e18 CrossRef Medline
16. Gherasim DN, Gory B, Sivan-Hoffmann R, et al. **Endovascular treatment of wide-neck anterior communicating artery aneurysms using WEB-DL and WEB-SL: short-term results in a multicenter study.** *AJNR Am J Neuroradiol* 2015;36:1150–54 CrossRef Medline
17. Caroff J, Mihalea C, Dargento F, et al. **Woven Endobridge (WEB) Device for endovascular treatment of ruptured intracranial wide-neck aneurysms: a single-center experience.** *Neuroradiology* 2014; 56:755–61 CrossRef Medline
18. Armoiry X, Turjman F, Hartmann DJ, et al. **Endovascular treatment of intracranial aneurysms with the WEB device: a systematic review of clinical outcomes.** *AJNR Am J Neuroradiol* 2016;37:868–72 CrossRef Medline
19. Fiorella D, Molyneux A, Coon A, et al. **Demographic, procedural and 30-day safety results from the WEB Intra-saccular Therapy Study (WEB-IT).** *J Neurointerv Surg* 2017 Jan 17. [Epub ahead of print] CrossRef Medline
20. Muskens IS, Senders JT, Dasenbrock HH, et al. **The Woven Endobridge device for treatment of intracranial aneurysms: a systematic review.** *World Neurosurg* 2017;98:809–17.e1 CrossRef Medline
21. Herbreteau D, Bibi R, Narata AP, et al. **Are anatomic results influenced by WEB shape modification? Analysis in a prospective, single-center series of 39 patients with aneurysms treated with the WEB.** *AJNR Am J Neuroradiol* 2016;37:2280–86 CrossRef Medline
22. Asnafi S, Rouchaud A, Pierot L, et al. **Efficacy and safety of the Woven EndoBrigde (WEB) device for the treatment of intracranial aneurysms: a systemic review and meta-analysis.** *AJNR Am J Neuroradiol* 2016;37:2287–92 CrossRef Medline
23. Lawson A, Goddard T, Ross S, et al. **Endovascular treatment of cerebral aneurysms using the Woven EndoBridge technique in a single center: preliminary results.** *J Neurosurg* 2017;126:17–28 CrossRef Medline
24. Clajus C, Strasilla C, Fiebig T, et al. **Initial and mid-term results from 108 consecutive patients with cerebral aneurysms treated with the WEB device.** *J Neurointerv Surg* 2017;9:411–17 CrossRef Medline
25. van Rooij WJ, Peluso JP, Bechan RS, et al. **WEB treatment of ruptured intracranial aneurysms.** *AJNR Am J Neuroradiol* 2016;37: 1679–83 CrossRef Medline
26. Caroff J, Mihalea C, Tuilier T, et al. **Occlusion assessment of intracranial aneurysms treated with the WEB device.** *Neuroradiology* 2016;58:887–91 CrossRef Medline
27. Pierot L. L**etter: WEB aneurysm treatment: occlusion stability and "compression".** *Neurosurgery* 2015;77:E666–67 CrossRef Medline
28. Cognard C, Januel AC. **Remnants and recurrences after the use of the WEB intrasaccular device in large-neck bifurcation aneurysms.** *Neurosurgery* 2015;76:522–30; discussion 530 CrossRef Medline
29. Brinjikji W, Cloft HJ, Kallmes DF. **Difficult aneurysms for endovascular treatment: overwide or undertall?** *AJNR Am J Neuroradiol* 2009;30:1513–17 CrossRef Medline
30. Janssen H, Berlis A, Lutz J, et al. **State of practice: endovascular treatment of acute aneurysmal SAH in Germany.** *AJNR Am J Neuroradiol* 2017;38:1574–79 CrossRef Medline
31. Ferns SP, Sprengers ME, van Rooij WJ, et al. **Coiling of intracranial aneurysms: a systematic review on initial occlusion and reopening and retreatment rates.** *Stroke* 2009;40:e523–29 CrossRef Medline

WEB Device: Ready for Ruptured Aneurysms?

We read with great interest the article by van Rooij et al entitled "WEB Treatment of Ruptured Intracranial Aneurysms: A Single-Center Cohort of 100 Patients."[1] Following our first report on the use of Woven EndoBridge devices (WEB; Sequent Medical, Aliso Viejo, California) for ruptured aneurysms,[2] this is the fourth publication to emphasize the great interest in using WEB devices to treat intracranial aneurysms in the acute phase of a subarachnoid hemorrhage.[3,4] Indeed, the WEB enables fast procedures and broadens the range of aneurysms suitable for endovascular treatment without the use of material inside the parent artery: 2 points that are essential for optimal management of ruptured cases.

However, although results from these retrospective and uncontrolled cases series are promising, some points still require further investigation. Because thromboembolic complication rates appear high in ruptured WEB cases, standard procedural management of anticoagulation and aggregation should still be defined here. van Rooij et al reported a 9% thrombotic complication rate. In a recent meta-analysis,[5] thrombotic complication rates were 21% in ruptured cases versus 5% in nonruptured cases (when patients are usually premedicated with antiplatelet therapy).

In addition, the major point requiring evaluation before the expansion of this technique is the protection against bleeding offered by the device compared with standard coiling. Some cases of early rebleeding previously have been described following WEB treatment.[6] We believe that rebleeding is very unlikely in cases in which WEB sizing and positioning are properly performed because intra-aneurysmal occlusion is usually very fast in ruptured cases (especially because no antiplatelet medications are used). When coils are used, a complete and compact filling of the aneurysm is required to prevent rebleeding. When one uses the WEB device, we believe that it is essential to ensure complete neck sealing to secure the aneurysm. The best way to do so is to systematically use a C-arm VasoCT (Philips Healthcare, Best, the Netherlands)[7] before device detachment in ruptured cases.

To address these issues, we have initiated a prospective multicenter study that follows good clinical practice guidelines: CLinical Assessment of WEB Device in Ruptured aneurYSms.[8] The primary outcome measure is the rebleed rate at 1 month. The enrollment is almost complete, and the results are expected to be available within 1 year.

REFERENCES

1. van Rooij SBT, van Rooij WJ, Peluso JP, et al. **WEB treatment of ruptured intracranial aneurysms: a single-center cohort of 100 patients.** *AJNR Am J Neuroradiol* 2017 Sep 7. [Epub ahead of print] CrossRef
2. Caroff J, Mihalea C, Dargento F, et al. **Woven Endobridge (WEB) device for endovascular treatment of ruptured intracranial wide-neck aneurysms: a single-center experience.** *Neuroradiology* 2014;56:755–61 CrossRef Medline
3. Liebig T, Kabbasch C, Strasilla C, et al. **Intrasaccular flow disruption in acutely ruptured aneurysms: a multicenter retrospective review of the use of the WEB.** *AJNR Am J Neuroradiol* 2015;36:1721–27 CrossRef Medline
4. van Rooij WJ, Peluso JP, Bechan RS, et al. **WEB treatment of ruptured intracranial aneurysms.** *AJNR Am J Neuroradiol* 2016;37:1679–83 CrossRef Medline
5. Asnafi S, Rouchaud A, Pierot L, et al. **Efficacy and safety of the Woven EndoBridge (WEB) device for the treatment of intracranial aneurysms: a systematic review and meta-analysis.** *AJNR Am J Neuroradiol* 2016;37:2287–92 CrossRef Medline
6. Caroff J, Mihalea C, Klisch J, et al. **Single-layer WEBs: intrasaccular flow disrupters for aneurysm treatment—feasibility results from a European study.** *AJNR Am J Neuroradiol* 2015;36:1942–46 CrossRef Medline
7. Caroff J, Mihalea C, Neki H, et al. **Role of C-arm VasoCT in the use of endovascular WEB flow disruption in intracranial aneurysm treatment.** *AJNR Am J Neuroradiol* 2014;35:1353–57 CrossRef Medline
8. The CLARYS trial. https://clinicaltrials.gov/ct2/show/NCT02687607. Accessed July 11, 2017

J. Caroff
Department of Interventional Neuroradiology
Bicêtre Hospital
Le Kremlin-Bicêtre, France
J. Moret
L. Spelle
Department of Interventional Neuroradiology
Bicêtre Hospital
Le Kremlin-Bicêtre, France
Faculté de Médecine
Université Paris Sud
Le Kremlin-Bicêtre, France

http://dx.doi.org/10.3174/ajnr.A5367

Treatment of Middle Cerebral Artery Aneurysms with Flow-Diverter Stents: A Systematic Review and Meta-Analysis

F. Cagnazzo, D. Mantilla, P.-H. Lefevre, C. Dargazanli, G. Gascou, and V. Costalat

ABSTRACT

BACKGROUND: The safety and efficacy of flow-diversion treatment of MCA aneurysms have not been well-established.

PURPOSE: Our aim was to evaluate angiographic and clinical outcomes after flow diversions for MCA aneurysms.

DATA SOURCES: A systematic search of PubMed, MEDLINE, and Embase was performed for studies published from 2008 to May 2017.

STUDY SELECTION: According to Preferred Reporting Items for Systematic Reviews and Meta-Analyses guidelines, we selected studies with >5 patients describing angiographic and clinical outcomes after flow-diversion treatment of MCA aneurysms.

DATA ANALYSIS: Random-effects meta-analysis was used to pool the following outcomes: aneurysm occlusion rate, procedure-related complications, rupture rate of treated aneurysms, and occlusion of the jailed branches.

DATA SYNTHESIS: Twelve studies evaluating 244 MCA aneurysms were included in this meta-analysis. Complete/near-complete occlusion was obtained in 78.7% (95% CI, 67.8%–89.7%) of aneurysms. The rupture rate of treated aneurysms during follow-up was 0.4% per aneurysm-year. The rate of treatment-related complications was 20.7% (95% CI, 14%–27.5%), and approximately 10% of complications were permanent. The mortality rate was close to 2%. Nearly 10% (95% CI, 4.7%–15.5%) of jailed arteries were occluded during follow-up, whereas 26% (95% CI, 14.4%–37.6%) had slow flow. Rates of symptoms related to occlusion and slow flow were close to 5%.

LIMITATIONS: Small and retrospective series could affect the strength of the reported results.

CONCLUSIONS: Given the not negligible rate of treatment-related complications, flow diversion for MCA aneurysms should be considered an alternative treatment when traditional treatment methods are not feasible. However, when performed in this select treatment group, high rates of aneurysm occlusion and protection against re-rupture can be achieved.

ABBREVIATION: PRISMA = Preferred Reporting Items for Systematic Reviews and Meta-Analyses

Flow-diverter stents have become a feasible and effective treatment for most intracranial aneurysms, and their indications are constantly extended, including distal aneurysm locations.[1-3] Commonly, middle cerebral artery aneurysms present with a particularly complex anatomy because of the frequency of wide-neck configurations with incorporating MCA branches. Endovascular treatment of MCA aneurysms can be technically more challenging, and in many institutions, surgical treatment is considered the first option because of the high rate of long-term occlusion with low surgical morbidity.[4] However, with the improvement of angiographic images, increased operator experience, and the use of more complex techniques, an increasing number of MCA aneurysms are treated with endovascular techniques.[1] Recently, flow diversion has been used as an alternative technique for complex wide-neck MCA aneurysms, incorporating ≥1 side branch or in cases of previous endovascular or surgical failure.[5-14] However, the role of flow diversion in this location is controversial, and the efficacy and safety of this technique remain unclear. We performed a systematic review and meta-analysis of all published series examining flow diversions for the treatment of MCA aneurysms with the aim of clarifying the following: 1) aneurysm occlusion rate, 2) treatment-related complications and clinical outcome, and 3) the fate of the MCA side branch covered with the device.

Received June 16, 2017; accepted after revision July 18.

From the Neuroradiology Department, University Hospital Güi-de-Chauliac, Centre Hospitalier Universitaire de Montpellier, Montpellier, France.

Please address correspondence to Federico Cagnazzo, MD, Neuroradiology Department, CHU Gui De Chauliac, 80 Ave Augustin Fliche, 34000 Montpellier, France; e-mail: f.cagnazzo86@gmail.com

Indicates article with supplemental on-line tables.

Indicates article with supplemental on-line photos.

http://dx.doi.org/10.3174/ajnr.A5388

MATERIALS AND METHODS

Literature Search

A comprehensive literature search of PubMed, Ovid MEDLINE, and Ovid Embase was conducted for studies published from 2008 to May 2017. The Preferred Reporting Items for Systematic Reviews and Meta-Analyses (PRISMA) guidelines were followed.[15] The key words "middle cerebral artery," "flow-diverter," "flow diversion," "anterior circulation," "aneurysms," "pipeline," and "endovascular" were used in both "AND" and "OR" combinations. The detailed search strategy is reported in On-line Table 1. The inclusion criteria were the following: 1) studies reporting series of patients with MCA aneurysms treated with flow diverters. Exclusion criteria were the following: 1) studies with <5 patients, 2) review articles, 3) studies published in languages other than English, 4) in vitro studies, and 5) animal studies. In cases of overlapping patient populations, only the series with the largest number of patients or the most detailed data were included. Two reviewers independently selected the included studies, and a third author solved discrepancies.

Data Collection

From each study, we extracted the following information: 1) characteristics and number of MCA aneurysms, 2) aneurysm occlusion rate and related factors, 3) incidence of aneurysm rupture after treatment, 4) treatment-related complications, and 5) angiographic outcome of covered arteries. The rate of aneurysm occlusion was dichotomized into 2 groups: complete/near-complete occlusion and incomplete occlusion. Accordingly, the influence of 6 parameters (age, mean aneurysm size, type of stent used, first treatment versus retreatment, type of first treatment, and anatomic location of MCA aneurysms) on the occlusion rates was analyzed. MCA aneurysms were divided into 3 categories: saccular, fusiform, and blister. Patients with blister aneurysms ($n = 3$) were considered for only the incidence of arterial occlusion after flow-diverter deployment. On the basis of the location, MCA aneurysms were dichotomized into "prebifurcation" (M1 and early cortical branches) and bifurcation aneurysms (M1–M2 bifurcation and M2 bifurcation branches).[16] Complications related to the treatment were summarized in 4 categories: ischemic/thromboembolic, hemorrhagic, iatrogenic (dissection or perforation), and perianeurysmal inflammation. The rate of occlusion and diminished flow of covered branches was analyzed from only studies that specifically reported the angiographic outcome of covered arteries. Finally, good outcome was defined as a modified Rankin Scale score of 0–2 or a Glasgow Outcome Score of 4–5. In cases in which the mRS and Glasgow Outcome Score were not reported, good neurologic outcome was determined if the study used terms such as "no morbidity," "good recovery," or "no symptoms."

Outcomes

The primary objectives were to define the following: 1) the rate of MCA aneurysm occlusion, 2) the incidence of treatment-related complications, and 3) the rate of MCA branch occlusion covered with flow diverters and the incidence of related symptoms.

Quality Scoring

The Newcastle-Ottawa Scale[17] was used to assess the quality of the included studies (On-line Table 2) evaluating the following: patient selection criteria, comparability of the study groups, and exposure assessment. "High-quality" studies were defined on the basis of the following: 1) the presence of a predefined study protocol, 2) defined inclusion and exclusion criteria, 3) adequate clinical and radiologic follow-up, and 4) detailed information about treatment-related outcomes. Accordingly, a star rating of 0–9 was allocated to each study. The quality assessment was performed by 2 authors independently, and a third author solved discrepancies. Studies receiving ≥6 stars were considered high-quality.

Statistical Analysis

We estimated, from each cohort, the cumulative prevalence and 95% confidence interval for each outcome. Rates of each outcome were pooled in meta-analyses across studies by using the random-effects model.[18] We chose this model a priori because it incorporates both within-study and between-studies variances. This is recommended when data are heterogeneous. Heterogeneity of the treatment effect across studies was evaluated with the I^2 statistic, in which an I^2 value of >50% suggests substantial heterogeneity.[19] We also extracted a 2×2 table for each studied outcome for interaction testing and calculated P values for the comparisons between the previously mentioned clinical and anatomic characteristics. Meta-regression was not used in this study. Statistical analysis was performed by using the software program OpenMeta[Analyst] (http://www.cebm.brown.edu/openmeta/).

RESULTS

Literature Review

The search strategy is summarized in On-line Table 1, and studies included in our meta-analysis are summarized in Table. The search flow diagram is shown in On-line Fig 1.

Twelve studies and 244 MCA aneurysms treated with flow-diverter stents were included in our review.

Quality of Studies

Overall, 8 studies were rated high quality. Seven of the high-quality studies specifically analyzed flow-diversion treatment of MCA aneurysms (On-line Table 2). All the high-quality articles reported detailed information about aneurysm occlusion rates, treatment-related complications, flow modifications of covered arteries, and adequate length of follow-up.

Patient Population and Aneurysm Characteristics

The mean age of patients was 54.5 years (range, 3–76 years), and the male/female ratio was 0.6 (On-line Table 3). Overall, 88.1% (95% CI, 83.4%–91.6%) of treated MCA aneurysms were unruptured, whereas 11.9% (95% CI, 8.3%–16.5%) (median, 1%; IQR, 0.4%–2.5%) were previously ruptured and were treated with coils or clipping in the acute phase. The median time of flow-diversion treatment after rupture was 8.5 months (IQR, 3.2–36 months). Saccular and fusiform aneurysms were 81.1% (95% CI, 75.7%–85.5%) and 17.6% (95% CI, 13.3%–22.9%), respectively. Blister aneurysms represented 1.3% (95% CI, 0.2%–3.7%) of the lesions.

Angiographic outcomes and treatment-related complications

Variables	Raw Numbers[a]	No. of Articles	95% CI	I^2	*P* Value
MCA aneurysm occlusion after flow diversion					
Overall rate of complete/near-complete occlusion	137/171 = 78.7%	10	67.8–89.7	76.24	<.001
Factors related to aneurysm occlusion					
Mean age (yr)					.262
Complete/near-complete occlusion	53.6 yr	4	47.3–59.8	75%	
Incomplete occlusion	61.3 yr		48.9–73.5	95%	
Mean size					.614
Complete/near-complete occlusion	7 mm	6	3.6–10.3	83.6%	
Incomplete occlusion	5.5 mm		0.8–10.1	99%	
Complete/near-complete occlusion					.38
Retreatment	64%	5	33.9–93.4	75.2%	
vs	vs				
First treatment	73%		63–83.5	0%	
Complete/near-complete occlusion					.307
Prebifurcation (M1–early cortical branches)	88.1%	11	79.6–96.7	0%	
vs	vs				
Bifurcation aneurysms	77.7%		64.5–89.5	74.92%	
Complications related to treatment and outcome					
Overall rate of treatment-related complications	46/213 = 20.7%	11	14–27.5	34.03%	.126
Transient or asymptomatic	11.3%		7.6–16.2		
vs	vs	11	6.8–15.2		
Permanent	10.3%				
Type of complications					
Ischemic/thromboembolic	16.3%	11	10.1–22.6	36.65%	.106
Hemorrhagic	2%		0.2–3.9	0%	.958
Iatrogenic (dissection/perforation)	1.8%		0%–1.3.5%	0%	.973
Perianeurysmal inflammation	2.6%		0.5–4.7	0%	.997
Complications related to discontinuation of antiplatelet therapy	4/46 = 8.7%	11	2.9–20.8		
Aneurysm rupture after treatment	1/214 = 0.47%	12	0.1–2.8		
Overall rate of good outcome	125/135 = 92.7%	7	86.4–99.1	42.08%	.11
Mortality rate	4/213 = 2%	11	0.2–3.9%	0%	.929

Note:— vs indicates versus.
[a] Results of meta-analysis.

Overall, 76.3% (95% CI, 70.5%–81.1%) of aneurysms were located at the main bifurcation point (M1–M2) or distally (M2), whereas prebifurcation aneurysms (M1–early cortical branches) were 23.7% (95% CI, 18.8%–29.5%). Mean aneurysm size was 8.2 mm (range, 2–20 mm).

Treatment Characteristics

The most common device used was the Pipeline Embolization Device (PED; Covidien, Irvine, California) (71%; 95% CI, 64.1%–75.3%), followed by the Silk flow diverter (Balt Extrusion, Montmorency, France) device (11.4%; 95% CI, 80.3%–15.9%) (On-line Table 3). Most of the aneurysms were treated with 1 device (number of stents/aneurysm = 1.14). The flow-diversion technique was used as a first treatment technique in 75.5% of patients (95% CI, 69.4%–80.6%).

Digital subtraction angiography was the principal diagnostic technique. In about 90% of the reported patients, DSA was performed during the early and long-term radiologic follow-up. In approximately 10% of patients, MRA or CTA was performed during the long-term radiologic follow-up.

Angiographic Outcomes and Treatment-Related Complications

The overall rate of complete/near-complete occlusion during follow-up was 78.7% (95% CI, 67.8%–89.7%) with a 12-month median duration (IQR, 8.1–16 months) of angiographic follow-up (Table and On-line Fig 2*A*). Differences in occlusion rates were not statistically significant among groups of age, mean aneurysm size, first treatment versus retreatment, type of first treatment (endovascular versus surgical), type of device used (PED versus other stents), and MCA aneurysm location ("prebifurcation" versus bifurcation aneurysms) ($P > .05$).

The rate of treatment-related complications was 20.7% (95% CI, 14%–27.5%) (On-line Fig 2*B*), and approximately 10% of complications were permanent. Ischemic/thromboembolic events were the most common type of complications (16.3%), followed by perianeurysmal inflammation (2.6%), hemorrhage (2%), and dissection/perforation (1.8%). The mortality rate after treatment was 2% (95% CI, 0.2%–3.9%). The rate of complications related to premature discontinuation of the antiplatelet therapy was 8.7% (95% CI, 2.9%–20.8%). During follow-up, the incidence of aneurysm rupture after treatment was 0.47% (95% CI, 0.1%–2.8%), with a rupture rate of 0.4% per aneurysm-year. The overall rate of good neurologic outcome after treatment was 92.7% (95% CI, 86.4%–99.1%) with a 12-month median duration (IQR, 7.5–10.5 months) of clinical follow-up. Considering the group of patients with a history of aneurysm rupture, the rate of good neurologic outcome was close to 87% (95% CI, 60.7%–98%).

Outcome of Covered MCA Side Branches

Overall, 174 MCA side branches jailed with flow diverters were available for the analysis (On-line Table 4). The global rate of

occlusion of covered arteries was 10.1% (95% CI, 4.7%–15.5%), whereas 26% (95% CI, 14.4%–37.6%) of cases showed diminished flow (On-line Fig 3). The mean number of devices across the ostium of the arteries was similar between arteries with occlusion and those with normal flow (1.07 versus 1). The incidence of symptoms (ischemic stroke in the MCA territory) related to MCA branch occlusion and diminished flow was 2.7% (95% CI, 0.4%–5%) and 2.6% (95% CI, 0.1%–5.1%), respectively (On-line Fig 4).

Study Heterogeneity

Significant heterogeneity was noted in the analysis of aneurysm occlusion rates after treatment. In addition, significant heterogeneity was reported in the analysis of diminished flow of covered branches.

DISCUSSION

Our meta-analysis stressed several important findings related to the flow-diversion treatment of MCA aneurysms. The overall rate of complete/near-complete occlusion was approximately 80%. The rupture rate after treatment was low (0.4% per aneurysm-year), demonstrating that the aneurysms were successfully secured after flow diversion. Most of the lesions were small and located at the main bifurcation point (M1–M2). The overall complication rate of 20% is not negligible, resulting in permanent neurologic deficits in approximately 10% of patients and treatment-related mortality in about 2%. Most interesting, most of the unfavorable outcomes were related to ischemic or thromboembolic complications. Our study also found a remarkable incidence of occlusion (10%) and diminished flow (25%) of covered MCA branches, resulting in neurologic symptoms in about 5% of patients. These findings are important and showed that though flow diversion is an effective treatment, MCA aneurysms amenable to flow diversion should be carefully selected, due to the not negligible rates of treatment-related morbidity.

Angiographic Outcomes of MCA Aneurysms after Flow Diversion

Flow-diverter stents have become a suitable tool for complex, wide-neck, and anatomically challenging intracranial aneurysms. However, while large and prospective studies demonstrated the safety and effectiveness of flow diversion for ICA aneurysms, the literature is contradictory about the treatment of distal locations, such as MCA aneurysms. Although surgery still represents an effective treatment for MCA aneurysms, difficult-to-treat lesions with conventional endovascular or surgical approaches have increased the use of flow diversion in this location. Overall, previous series have reported a rate of complete/near-complete occlusion between 60% and 90% after flow-diversion treatment of MCA aneurysms.[5-9,12-14,20] The paucity of large and prospective studies, the heterogeneity of the reported populations, and the relatively short follow-up periods can explain this variation. Our study, the largest to date, demonstrated that the overall rate of complete/near-complete occlusion is roughly 80% during a mean follow-up of 14 months. This result is comparable with the angiographic occlusion rates of ICA aneurysms after flow diversion. In a recent prospective study of nearly 200 aneurysms, Kallmes et al[3] reported 75% complete occlusion after Pipeline treatment. Similarly, in a large meta-analysis of nearly 1700 aneurysms, the complete occlusion rate was close to 76%.[21]

Aneurysms of the MCA often arose from the main division point (bifurcation aneurysms), whereas in nearly 20% of cases, they originated from an early cortical branch (temporal or frontal).[16] Early cortical branch aneurysms have a close relation with perforators, whereas bifurcation aneurysms are close to or incorporate M2 branches, influencing the outcomes after surgical or endovascular treatment.[12] Very few articles analyzed differences in endovascular treatments for different MCA aneurysm locations, and it is possible that in the literature, most of the early cortical branch aneurysms are referred to as bifurcation aneurysms. Topcuoglu et al,[12] in a series of 29 MCA aneurysms treated with flow diversion, reported better angiographic results among lesions located at the prebifurcation point (M1 or early bifurcations), compared with MCA bifurcation aneurysms (85% versus 60% of complete/near-complete occlusion). In addition, unsatisfactory aneurysm occlusion was significantly related to the patency of the arterial branches originating from it. Our study demonstrated that the prevalence of complete/near-complete occlusion was slightly higher for aneurysms located at the prebifurcation point, compared with bifurcation (M1–M2) or more distal aneurysms (M2), though the result did not reach statistical significance (88% versus 77%, $P = .3$). In addition, there were no differences in occlusion rates between aneurysms treated with the PED and other types of stents. Similarly, we found that occlusion rates among younger patients and the first-treatment group versus the retreatment group appeared slightly higher, but without statistical relevance. However, among retreatment groups, complete/near-complete occlusion after flow diversion was slightly higher for aneurysms previously treated with coiling or stent-assisted coiling (89%), compared with aneurysms previously treated with clipping (63%), though the results were not statistically significant. Finally, the rupture rate after treatment of 0.4% per aneurysm-year showed that flow diversion gives an effective protection against aneurysm rupture.[22]

Treatment-Related Complications

In general, treatment-related morbidity after flow diversion is reported to be between 4% and 10%.[3,23-25] Our meta-analysis provides more representative data on complication rates after flow-diverter treatment of MCA aneurysms. This location should be considered separately in terms of technical complexity and treatment-related outcomes. The overall incidence of complications close to 20% is not negligible. Most important, permanent complications were approximately 10%, whereas the mortality rate after treatment was 2%. However, the literature is still contradictory about flow diversion among MCA aneurysms, and despite some authors concluding that it seems a reasonable treatment,[9,13] others reported that it is not a suitable solution for aneurysms in this location.[8] Our study showed that most of the reported complications were related to ischemic or thromboembolic events (16%). Compared with the general rate of ischemic complications related to flow diversion, MCA location appears associated with a higher risk of ischemic injury. In the IntrePED[24] study, as well as in other large studies,[21,26] the rate of acute ischemic stroke was

close to 5%, with most of the reported events occurring in the early postoperative period.

A number of important mechanisms can explain the incidence of postoperative infarction after flow-diversion treatment of MCA aneurysms, such as perioperative catheter-related thromboemboli, acute/subacute in-stent thrombosis, or particle emboli from the devices.[27-29] In our study, nearly 9% of ischemic complications were associated with discontinuation of the antiplatelet therapy, which showed the close relationship between ischemic injury and antiplatelet function.[30] Another important factor is the risk of perforating injury due to coverage of lenticulostriate arteries. Multiple overlapping devices[29] or undersized stents with more condensed pores and higher mesh density[31] can increase the risk of perforator occlusion. In a series of 17 anterior circulation aneurysms, 12 of them arising from the MCA, Gawlitza et al[20] reported 40% ischemic events after coverage of perforator arteries with flow-diverter stents, though most were asymptomatic. Despite the high rate of complications, most of the MCA aneurysms treated with flow diverters were anatomically complex, increasing the risk of procedure-related complications. Accordingly, when more complex endovascular techniques are required, such as X- and Y-stent placement or stent-assisted coiling, a large series and meta-analysis reported permanent complications between 4% and 10%.[32,33]

Angiographic Outcome of Covered Side Branches

Placement of flow-diverter stents at the bifurcation points behind the circle of Willis has a potential risk of arterial occlusion. Due to the mechanical properties of the stent, the pressure gradient across the jailed branch is reduced, and if the "flow competition" from the collateral supply is well-represented, the artery can be occluded.[34] MCA bifurcation presents an anatomic configuration without direct collateral arterial connection, and the anastomotic circulation is only with corticopial branches. Our study found 10% occlusion of covered MCA branches. In addition, remodelling of jailed arteries, such as slow flow or arterial narrowing, was present in about 25% of cases. Among large series of flow diverters covering ICA branches, the rates of side branch occlusion are close to 18% for the posterior communicating artery[35-37] and 5% for the ophthalmic and anterior choroidal arteries, with rates of related symptoms close to 1%.[35,38-42] In our study, approximately 5% of patients with occluded or narrowed MCA branches were symptomatic due to transient ischemic events.

Strengths and Limitations

Our study has several limitations. First, I^2 results were above 50% for many of the estimates, suggesting substantial heterogeneity among the analyzed outcomes. The articles were often small, retrospective, and single-institution series, affecting the strength of the reported results. Factors related to procedural complications were not assessed, due to the scant data available. Details of the management of antiplatelet therapy were variable and infrequently specified. Finally, the small number of cases in some subgroups may not provide sufficient power to demonstrate a statistically significant difference in the rates of occlusion among age groups, different aneurysm sizes, prebifurcation-versus-bifurcation aneurysms, type of stent used, first treatment versus retreatment, and type of first treatment. However, although retrospective data are low in quality, our meta-analysis is the best available evidence to guide neurointerventionalists during flow-diversion treatment of MCA aneurysms.

CONCLUSIONS

Flow diversion for MCA aneurysms should only be considered as salvage therapy when traditional treatment methods are unfeasible, given the 10% rate of permanent neurologic morbidity. However, when performed in this select treatment group, high rates of aneurysm occlusion and protection against re-rupture can be achieved.

ACKNOWLEDGMENTS

We thank Professor Beth De Felici for the English revision.

Disclosures: Vincent Costalat—*UNRELATED: Consultancy:* Sequent Medical, Covidien, Stryker, Balt Extrusion; *Payment for Lectures (including service on Speakers Bureaus):* Covidien, Stryker, Sequent Medical; *Payment for Development of Educational Presentations*: Covidien, Stryker.

REFERENCES

1. Brinjikji W, Lanzino G, Cloft HJ, et al. **Endovascular treatment of middle cerebral artery aneurysms: a systematic review and single-center series.** *Neurosurgery* 2011;68:397–402; discussion 402 CrossRef Medline
2. Pierot L, Spelle L, Vitry F, et al; ATENA Investigators. **Immediate clinical outcome of patients harboring unruptured intracranial aneurysms treated by endovascular approach: results of the ATENA study.** *Stroke* 2008;39:2497–504 CrossRef Medline
3. Kallmes DF, Brinjikji W, Boccardi E, et al. **Aneurysm Study of Pipeline in an Observational Registry (ASPIRe).** *Interv Neurol* 2016;5:89–99 CrossRef Medline
4. Rodriguez-Hernandez A, Sughrue ME, Akhavan S, et al. **Current management of middle cerebral artery aneurysms: surgical results with a "clip first" policy.** *Neurosurgery* 2013;72:415–27 CrossRef Medline
5. Bhogal P, AlMatter M, Bäzner H, et al. **Flow diversion for the treatment of MCA bifurcation aneurysms: a single centre experience.** *Front Neurol* 2017;8:20 CrossRef Medline
6. Bhogal P, Martinez R, Gansladt O, et al. **Management of unruptured saccular aneurysms of the M1 segment with flow diversion: a single centre experience.** *Clin Neuroradiol* 2016 Dec 11. [Epub ahead of print] CrossRef Medline
7. Briganti F, Napoli M, Leone G, et al. **Treatment of intracranial aneurysms by flow diverter devices: long-term results from a single center.** *Eur J Radiol* 2014;83:1683–90 CrossRef Medline
8. Caroff J, Neki H, Mihalea C, et al. **Flow-diverter stents for the treatment of saccular middle cerebral artery bifurcation aneurysms.** *AJNR Am J Neuroradiol* 2016;37:279–84 CrossRef Medline
9. Iosif C, Mounayer C, Yavuz K, et al. **Middle cerebral artery bifurcation aneurysms treated by extrasaccular flow diverters: midterm angiographic evolution and clinical outcome.** *AJNR Am J Neuroradiol* 2017;38:310–16 CrossRef Medline
10. Lin N, Lanzino G, Lopes DK, et al. **Treatment of distal anterior circulation aneurysms with the Pipeline Embolization Device: a US multicenter experience.** *Neurosurgery* 2016;79:14–22 CrossRef Medline
11. Pistocchi S, Blanc R, Bartolini B, et al. **Flow diverters at and beyond the level of the circle of Willis for the treatment of intracranial aneurysms.** *Stroke* 2012;43:1032–38 CrossRef Medline
12. Topcuoglu OM, Akgul E, Daglioglu E, et al. **Flow diversion in middle cerebral artery aneurysms: is it really an all-purpose treatment?** *World Neurosurg* 2016;87:317–27 CrossRef Medline
13. Yavuz K, Geyik S, Saatci I, et al. **Endovascular treatment of middle**

cerebral artery aneurysms with flow modification with the use of the Pipeline embolization device. *AJNR Am J Neuroradiol* 2014;35:529–35 CrossRef Medline
14. Zanaty M, Chalouhi N, Tjoumakaris SI, et al. **Flow diversion for complex middle cerebral artery aneurysms.** *Neuroradiology* 2014;56:381–87 CrossRef Medline
15. Moher D, Liberati A, Tetzlaff J, et al. **Preferred reporting items for systematic reviews and meta-analyses: the PRISMA statement.** *Int J Surg* 2010;8:336–41 CrossRef Medline
16. Elsharkawy A, Lehecka M, Niemela M, et al. **A new, more accurate classification of middle cerebral artery aneurysms: computed tomography angiographic study of 1,009 consecutive cases with 1,309 middle cerebral artery aneurysms.** *Neurosurgery* 2013;73:94–102; discussion 102 CrossRef Medline
17. Wells G, Shea B, O'Connell D, et al. **The Newcastle-Ottawa Scale (NOS) for assessing the quality of nonradomized studies in meta-analyses.** Ottawa, Ontario: Ottawal Hospital Research Institute. 2011 http://www.evidencebasedpublichealth.de/download/Newcastle_Ottowa_Scale_Pope_Bruce.pdf. Accessed May 2, 2017
18. DerSimonian R, Laird N. **Meta-analysis in clinical trials.** *Control Clin Trials* 1986;7:177–88 CrossRef Medline
19. Higgins JP, Thompson SG, Deeks JJ, et al. **Measuring inconsistency in meta-analyses.** *BMJ* 2003;327:557–60 CrossRef Medline
20. Gawlitza M, Januel AC, Tall P, et al. **Flow diversion treatment of complex bifurcation aneurysms beyond the circle of Willis: a single-center series with special emphasis on covered cortical branches and perforating arteries.** *J Neurointerv Surg* 2016;8:481–87 CrossRef Medline
21. Brinjikji W, Murad MH, Lanzino G, et al. **Endovascular treatment of intracranial aneurysms with flow diverters: a meta-analysis.** *Stroke* 2013;44:442–47 CrossRef Medline
22. Rouchaud A, Brinjikji W, Lanzino G, et al. **Delayed hemorrhagic complications after flow diversion for intracranial aneurysms: a literature overview.** *Neuroradiology* 2016;58:171–77 CrossRef Medline
23. Berge J, Biondi A, Machi P, et al. **Flow-diverter Silk stent for the treatment of intracranial aneurysms: 1-year follow-up in a multicenter study.** *AJNR Am J Neuroradiol* 2012;33:1150–55 CrossRef Medline
24. Kallmes DF, Hanel R, Lopes D, et al. **International retrospective study of the Pipeline embolization device: a multicenter aneurysm treatment study.** *AJNR Am J Neuroradiol* 2015;36:108–15 CrossRef Medline
25. Brinjikji W, Cloft H, Cekirge S, et al. **Lack of association between statin use and angiographic and clinical outcomes after Pipeline embolization for intracranial aneurysms.** *AJNR Am J Neuroradiol* 2017;38:753–58 CrossRef Medline
26. Briganti F, Leone G, Marseglia M, et al. **Endovascular treatment of cerebral aneurysms using flow-diverter devices: a systematic review.** *Neuroradiol J* 2015;28:365–75 CrossRef Medline
27. Cruz JP, Marotta T, O'Kelly C, et al. **Enhancing brain lesions after endovascular treatment of aneurysms.** *AJNR Am J Neuroradiol* 2014;35:1954–58 CrossRef Medline
28. Tan LA, Keigher KM, Munich SA, et al. **Thromboembolic complications with Pipeline Embolization Device placement: impact of procedure time, number of stents and pre-procedure P2Y12 reaction unit (PRU) value.** *J Neurointerv Surg* 2015;7:217–21 CrossRef Medline
29. Briganti F, Delehaye L, Leone G, et al. **Flow diverter device for the treatment of small middle cerebral artery aneurysms.** *J Neurointerv Surg* 2016;8:287–94 CrossRef Medline
30. Kim B, Kim K, Jeon P, et al. **Thromboembolic complications in patients with clopidogrel resistance after coil embolization for unruptured intracranial aneurysms.** *AJNR Am J Neuroradiol* 2014;35:1786–92 CrossRef Medline
31. Berg P, Iosif C, Ponsonnard S, et al. **Endothelialization of over- and undersized flow-diverter stents at covered vessel side branches: an in vivo and in silico study.** *J Biomech* 2016;49:4–12 CrossRef Medline
32. Bartolini B, Blanc R, Pistocchi S, et al. **"Y" and "X" stent-assisted coiling of complex and wide-neck intracranial bifurcation aneurysms.** *AJNR Am J Neuroradiol* 2014;35:2153–58 CrossRef Medline
33. Hong Y, Wang YJ, Deng Z, et al. **Stent-assisted coiling versus coiling in treatment of intracranial aneurysm: a systematic review and meta-analysis.** *PLoS One* 2014;9:e82311 CrossRef Medline
34. Saleme S, Iosif C, Ponomarjova S, et al. **Flow-diverting stents for intracranial bifurcation aneurysm treatment.** *Neurosurgery* 2014;75:623–31; quiz 631 CrossRef Medline
35. Brinjikji W, Lanzino G, Cloft HJ, et al. **Patency of the posterior communicating artery after flow diversion treatment of internal carotid artery aneurysms.** *Clin Neurol Neurosurg* 2014;120:84–88 CrossRef Medline
36. Daou B, Valle-Giler EP, Chalouhi N, et al. **Patency of the posterior communicating artery following treatment with the Pipeline Embolization Device.** *J Neurosurg* 2017;126:564–69 CrossRef Medline
37. Vedantam A, Rao VY, Shaltoni HM, et al. **Incidence and clinical implications of carotid branch occlusion following treatment of internal carotid artery aneurysms with the Pipeline embolization device.** *Neurosurgery* 2015;76:173–78; discussion 178 CrossRef Medline
38. Rangel-Castilla L, Munich SA, Jaleel N, et al. **Patency of anterior circulation branch vessels after Pipeline embolization: longer-term results from 82 aneurysm cases.** *J Neurosurg* 2017;126:1064–69 CrossRef Medline
39. Neki H, Caroff J, Jittapiromsak P, et al. **Patency of the anterior choroidal artery covered with a flow-diverter stent.** *J Neurosurg* 2015;123:1540–45 CrossRef Medline
40. Rouchaud A, Leclerc O, Benayoun Y, et al. **Visual outcomes with flow-diverter stents covering the ophthalmic artery for treatment of internal carotid artery aneurysms.** *AJNR Am J Neuroradiol* 2015;36:330–36 CrossRef Medline
41. Griessenauer CJ, Ogilvy CS, Foreman PM, et al. **Pipeline Embolization Device for small paraophthalmic artery aneurysms with an emphasis on the anatomical relationship of ophthalmic artery origin and aneurysm.** *J Neurosurg* 2016;125:1352–59 CrossRef Medline
42. Chalouhi N, Daou B, Kung D, et al. **Fate of the ophthalmic artery after treatment with the Pipeline Embolization Device.** *Neurosurgery* 2015;77:581–84; discussion 584 CrossRef Medline

Predictors of Incomplete Occlusion following Pipeline Embolization of Intracranial Aneurysms: Is It Less Effective in Older Patients?

N. Adeeb, J.M. Moore, M. Wirtz, C.J. Griessenauer, P.M. Foreman, H. Shallwani, R. Gupta, A.A. Dmytriw, R. Motiei-Langroudi, A. Alturki, M.R. Harrigan, A.H. Siddiqui, E.I. Levy, A.J. Thomas, and C.S. Ogilvy

ABSTRACT

BACKGROUND AND PURPOSE: Flow diversion with the Pipeline Embolization Device (PED) for the treatment of intracranial aneurysms is associated with a high rate of aneurysm occlusion. However, clinical and radiographic predictors of incomplete aneurysm occlusion are poorly defined. In this study, predictors of incomplete occlusion at last angiographic follow-up after PED treatment were assessed.

MATERIALS AND METHODS: A retrospective analysis of consecutive aneurysms treated with the PED between 2009 and 2016, at 3 academic institutions in the United States, was performed. Cases with angiographic follow-up were selected to evaluate factors predictive of incomplete aneurysm occlusion at last follow-up.

RESULTS: We identified 465 aneurysms treated with the PED; 380 (81.7%) aneurysms (329 procedures; median age, 58 years; female/male ratio, 4.8:1) had angiographic follow-up, and were included. Complete occlusion (100%) was achieved in 78.2% of aneurysms. Near-complete (90%–99%) and partial (<90%) occlusion were collectively achieved in 21.8% of aneurysms and defined as incomplete occlusion. Of aneurysms followed for at least 12 months (211 of 380), complete occlusion was achieved in 83.9%. Older age (older than 70 years), nonsmoking status, aneurysm location within the posterior communicating artery or posterior circulation, greater aneurysm maximal diameter (≥21 mm), and shorter follow-up time (<12 months) were significantly associated with incomplete aneurysm occlusion at last angiographic follow-up on univariable analysis. However, on multivariable logistic regression, only age, smoking status, and duration of follow-up were independently associated with occlusion status.

CONCLUSIONS: Complete occlusion following PED treatment of intracranial aneurysms can be influenced by several factors related to the patient, aneurysm, and treatment. Of these factors, older age (older than 70 years) and nonsmoking status were independent predictors of incomplete occlusion. While the physiologic explanation for these findings remains unknown, identification of factors predictive of incomplete aneurysm occlusion following PED placement can assist in patient selection and counseling and might provide insight into the biologic factors affecting endothelialization.

ABBREVIATION: PED = Pipeline Embolization Device

The flow-diverting Pipeline Embolization Device (PED; Covidien, Irvine, California) has become a mainstay for the treatment of intracranial aneurysms.[1] The device was approved by the US Food and Drug Administration in 2011 for the treatment of large or giant, wide-neck brain aneurysms along the internal carotid artery in adults.[2] Numerous studies have since demonstrated the safety and efficacy of the PED in treating aneurysms with varying morphologies in different anatomic locations.[3-8] As the clinical indications for PED placement expand, predictors of radiographic outcomes have become a topic of ongoing investigation. Although 1 study found that fusiform aneurysm morphology and shorter follow-up length were independent predictors of incomplete occlusion, this study was limited by a small sample size and a mean follow-up of 6.1 months.[9] The expanding use of PEDs for treating intracranial aneurysms necessitates an evaluation of predictors of incomplete occlusion.

MATERIALS AND METHODS

A retrospective analysis of consecutive aneurysms treated with PED placement between 2009 and 2016 at 3 academic institutions

Received February 3, 2017; accepted after revision July 8.

From the Neurosurgical Service (N.A., J.M.M., M.W., C.J.G., R.G., A.A.D., R.M.-L., A.A., A.J.T., C.S.O.), Beth Israel Deaconess Medical Center, Harvard Medical School, Boston, Massachusetts; Department of Neurosurgery (P.M.F., M.R.H.), University of Alabama at Birmingham, Birmingham, Alabama; Department of Neurosurgery (H.S., A.H.S., E.I.L.), State University of New York at Buffalo, Buffalo, New York; and Department of Neurosurgery (N.A.), Louisiana State University, Shreveport, Louisiana.

Nimer Adeeb and Justin M. Moore contributed equally to this work.

Please address correspondence to Christopher S. Ogilvy, MD, Neurosurgical Service, Beth Israel Deaconess Medical Center, Harvard Medical School, 110 Francis St, Suite 3B, Boston, MA 02215-5501; e-mail: cogilvy@bidmc.harvard.edu

Indicates article with supplemental on-line table.

http://dx.doi.org/10.3174/ajnr.A5375

(Beth Israel Deaconess Medical Center; Department of Neurosurgery, University of Alabama at Birmingham; and State University of New York at Buffalo) in United States was performed. Inclusion criteria consisted of all adult patients with intracranial aneurysms treated with the PED who had undergone angiographic follow-up. Both ruptured and unruptured aneurysms were included; all aneurysm morphologies (ie, saccular, blister, fusiform, dissecting) and intracranial locations were included. Institutional review board approval was obtained at all 3 centers before the commencement of the study. We collected the following information: patient demographics, aneurysm and PED characteristics, procedural complications, and angiographic and functional outcomes.

Procedural Details

Patients received aspirin, 325 mg, and clopidogrel, 75 mg daily, for 3–14 days before the intervention. Platelet function testing was routinely performed with a whole-blood Lumi-Aggregometer (Chrono-Log, Havertown, Pennsylvania), light transmission aggregometry, or the VerifyNow P2Y12 assay (Accumetrics, San Diego, California). Clopidogrel nonresponders were identified on the basis of established cutoff values at the individual institutions, and manufacturers' recommendations were used for guidance. If a patient was identified as a clopidogrel responder, the clopidogrel was continued. If a patient was identified as a clopidogrel nonresponder, the choice to continue the same dose of clopidogrel, administer a 1-time 600-mg clopidogrel boost within the 24 hours before the procedure, or switch to ticagrelor was at the discretion of the interventionalist performing the procedure. Patients undergoing treatment of a ruptured aneurysm received a loading dose of aspirin, 650 mg, and clopidogrel, 600 mg, before the intervention.

Patients underwent local anesthesia with sedation or general anesthesia at the discretion of the individual institutions, and all patients were anticoagulated with heparin throughout the procedure. The type of guide catheter and microcatheter used for PED deployment was at the discretion of the individual institutions. The deployment and apposition of the PED to the ICA wall was documented by fluoroscopy. Dual-antiplatelet therapy was continued for at least 3 months after the procedure, and aspirin was continued indefinitely thereafter.

Angiographic Outcome

Angiographic outcome was assessed with digital subtracted angiography or MR angiography[10,11] on the basis of the follow-up protocols at the discretion of each individual institution. In 1 institution, patients were imaged and reviewed at 6 months postprocedure with DSA, then at 2 and 5 years with DSA or MRA. In the second institution, patients were reviewed at 6 and 12 months postprocedure with MRA, then annually until 5 years with MRA. In the third institution, patients were followed at 3 and 6 months postprocedure with MRA, at 12 months with DSA, and then annually until 5 years with MRA. Aneurysm occlusion on follow-up DSA was assessed by the treating interventionalist. Follow-up MRAs were assessed by a radiologist blinded to the clinical history and an interventionalist. Occlusion was categorized as complete occlusion (100%), near-complete occlusion (90%–100%), and partial occlusion (<90%). Both near-complete and partial occlusion were collectively defined as incomplete occlusion.

Outcome

Functional outcome was assessed with the modified Rankin Scale at last follow-up by the interventionalist at each institution.

Statistical Analysis

Statistical analysis was performed with SPSS 21.0 (IBM, Armonk, New York). In univariable analysis, variables were compared among groups with the nonparametric test for continuous variables and the χ^2 test for categoric variables, to identify predictors of incomplete occlusion. Statistical significance was defined as $P < .05$. Multivariable logistic regression was performed on candidate predictor variables to identify variables independently associated with incomplete occlusion at last angiographic follow-up after controlling for potential confounders.

RESULTS

Baseline and Aneurysm Characteristics

A total of 465 aneurysms treated with PED placement at the 3 institutions were identified. Of these, 380 (81.7%) aneurysms treated by 329 PED procedures (median age, 58 years; female/male ratio, 4.8:1) had angiographic follow-up and were included in this study. Current smoking and multiple aneurysms were present in 25.8% and 45% of procedures, respectively. The pretreatment mRS was 0–2 in 95.4% of procedures and 3–5 in 4.6%. Treatment in the setting of immediate aneurysmal subarachnoid hemorrhage occurred in 3% of procedures. Aneurysms were mostly located along the ICA (83.2%), followed by the posterior circulation (13.4%). Most aneurysms were saccular (67.6%) or fusiform (26.9%). The median maximal diameter and neck size were 7.7 and 4 mm, respectively. A daughter sac was present in 24.7% of aneurysms (Table 1).

Treatment Outcome

A single PED was used in the treatment of 77.5% of procedures, while ≥2 PEDs were placed in 22.5%. The median length of angiographic follow-up was 13.5 months (mean, 19.2 months). At last follow-up, complete occlusion (100%) was achieved in 78.2% of aneurysms, while near-complete occlusion (90%–99%) was achieved in 7.6%, and partial occlusion (< 90%), in 14.2%. Of aneurysms followed for at least 12 months (211 of 380), complete occlusion was achieved in 83.9%. Retreatment was performed in 6.3% of aneurysms and was exclusively endovascular. At last follow-up, the mRS scores improved in 33.4% and worsened in 8.8%; this percentage included patients presenting with aneurysmal SAH. Symptomatic thromboembolic complications were encountered in 5.2% of procedures, and symptomatic hemorrhagic complications, in 1.8%. The mortality rate was 1.2% (4 cases); this was due to either ischemic stroke (2 cases), early postprocedure hemorrhage (1 case), or pretreatment aneurysmal SAH (1 case) (Table 2).

Predictors of Incomplete Occlusion

On univariable analysis, older age (older than 70 years, $P = .002$), nonsmoking status ($P = .005$), aneurysm location within the posterior communicating artery or posterior circulation ($P = .01$),

Table 1: Baseline characteristics

Parameter	No.
No. of procedures	329
No. of aneurysms	380
Sex	
Female	272 (82.7%)
Male	57 (17.3%)
Median age (range) (yr)	58 (18–82)
Smoking	85 (25.8%)
Multiple aneurysms	148 (45%)
Pretreatment mRS	
0–2	314 (95.4%)
3–5	15 (4.6%)
Aneurysm location	
ICA	
Petrous	7 (1.8%)
Cavernous	63 (16.6%)
Paraophthalmic	212 (55.8%)
PcomA	34 (9%)
ACA/AcomA	5 (1.3%)
MCA	8 (2.1%)
Posterior circulation	51 (13.4%)
Aneurysm shape	
Saccular	257 (67.6%)
Blister	11 (2.9%)
Fusiform	102 (26.9%)
Dissecting	10 (2.6%)
Aneurysm measurements (median) (range) (mm)	
Maximal diameter[a]	7.7 (1–44.5)
Neck size (for saccular aneurysms)[b]	4 (1–15.6)
Dome-to-neck ratio (for saccular aneurysms)[b]	1.3 (0.4–3.5)
Daughter sac	94 (24.7%)
Subarachnoid hemorrhage	
Acute (<2 wk)	10 (3%)
Remote (>2 wk)	32 (9.7%)
Prior treatment	
Endovascular	33 (8.7%)
Operation	6 (1.6%)
Both	4 (1.1%)

Note:—ACA indicates anterior cerebral artery; PcomA, posterior communicating artery; AcomA, anterior communicating artery.
[a] Data are missing for 11 aneurysms.
[b] Data are missing for 41 aneurysms.

Table 2: Outcome measures

Parameter	No.
No. of Pipelines	
1	255 (77.5%)
2	52 (15.8%)
≥3	22 (6.7%)
Platelet function test	
Yes	316 (96%)
No	13 (4%)
Clopidogrel responder	
Yes	228 (72.2%)
No	88 (27.8%)
Nonresponders' treatment	
Switch to ticagrelor	27 (30.7%)
Clopidogrel boost	39 (44.3%)
Same dose of clopidogrel	22 (25%)
Last angiographic follow-up (median) (range) (mo)	13.5 (1–83)
Follow-up occlusion rate	
Complete (100%)	297 (78.2%)
Near-complete (90%–99%)	29 (7.6%)
Partial (<90%)	54 (14.2%)
Retreatment	
Endovascular	24 (6.3%)
Posttreatment mRS	
0–2	314 (95.6%)
3–5	11 (3.3%)
6 (Death)	4 (1.2%)
Follow-up mRS	
Improved	110 (33.4%)
No change	190 (57.8%)
Worsened	29 (8.8%)
Neurologic complications	
Thromboembolic	31 (9.4%)
Symptomatic	17 (5.2%)
Hemorrhagic	11 (3.3%)
Symptomatic	6 (1.8%)

larger aneurysm maximal diameter (≥21 mm, $P = .03$), and shorter follow-up time (<12 months, $P = .001$) were associated with significantly higher rates of incomplete occlusion at last follow-up (On-line Table).

Significant predictors of incomplete occlusion at last follow-up in univariable analysis were further analyzed in multivariable logistic regression. Older age (older than 70 years; OR, 2; 95% CI, 1.1–3.8; $P = .03$; Figure), nonsmoking status (OR, 2; 95% CI, 1.1–3.9, $P = .03$), and shorter follow-up time (<12 months; OR, 2; 95% CI, 1.2–3.5; $P = .007$) were independently associated with a higher rate of incomplete occlusion at last follow-up (Table 3).

DISCUSSION

In this study, we report a multicenter experience with PED placement for the treatment of intracranial aneurysms, with a focus on identifying predictors of incomplete occlusion at last angiographic follow-up. Complete occlusion was achieved in 79.7% of cases. Although several patient- and aneurysm-related factors were significantly associated with a higher rate of incomplete aneurysm occlusion on univariable analysis, only age, smoking status, and length of follow-up were independently associated with occlusion status.

Predictors of Aneurysm Occlusion

Predictors of complete occlusion and recanalization following endovascular treatment of intracranial aneurysms have been recently studied.[12-14] Ruptured aneurysms, smaller maximal diameter, smaller neck size, and regular shape were independently associated with complete occlusion.[12] Ogilvy et al[13] developed a scoring system to predict aneurysm recanalization following coil embolization. Larger maximal diameter (>10 mm), ruptured aneurysm status, the presence of an intra-aneurysmal thrombus, and incomplete obliteration immediately after aneurysm treatment were each associated with a higher risk of recurrence. The presence of assist devices (stents or flow diverters), meanwhile, was associated with a lower risk of recanalization.[13,14]

Jabbour et al[9] reported predictors of incomplete aneurysm occlusion at last follow-up after treatment with PED placement. In their study, fusiform shape ($P = .05$) and, unsurprisingly, shorter follow-up time ($P = .03$) were independent predictors of incomplete occlusion. However, only 73 aneurysms had angiographic follow-up, with a mean length of 6.1 months. In our study, with a mean follow-up of 19.2 months, the morphology of the aneurysm had no significant effect on occlusion status. However, shorter follow-up length (<12 months) was significantly

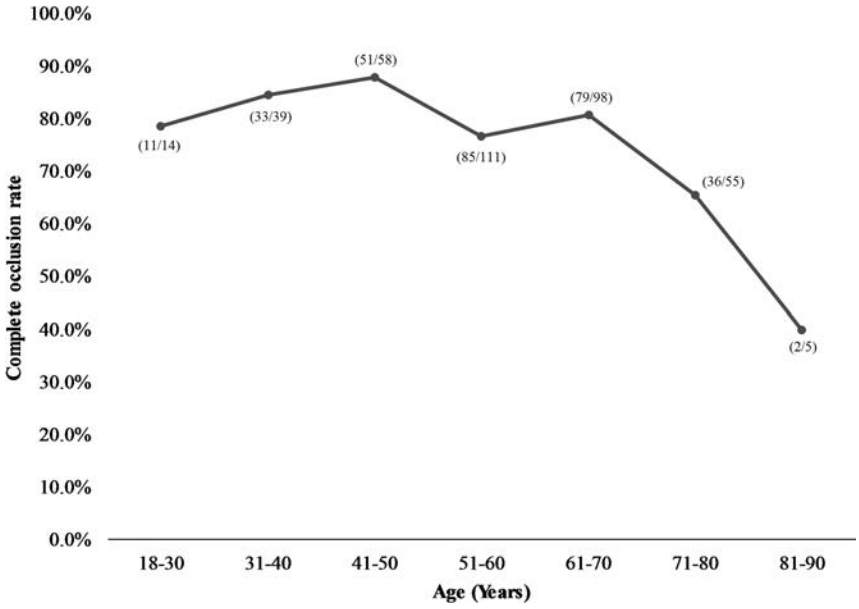

FIGURE. Age-related variation in the rate of complete occlusion following intracranial aneurysm treatment with PEDs.

Table 3: Multivariable logistic regression for predictors of incomplete occlusion at last follow-up

Parameter	OR	95% CI	*P* Value
Age (older than 70 yr)	2.0	1.1–3.8	.03
Nonsmokers	2.0	1.1–3.9	.03
PcomA/posterior circulation	1.6	0.9–2.9	.13
Maximal diameter (≥21 mm)	2.1	0.9–4.7	.08
Length of follow-up (<12 months)	2.1	1.2–3.5	.007

Note:—PcomA indicates posterior communicating artery.

associated with a lower occlusion rate, which is consistent with previous reports.[9,15,16]

Age-Related Variation in Occlusion Rates

A meta-analysis of endovascular coiling of intracranial aneurysms in elderly patients (older than 65 years) reported a 66% complete or near-complete occlusion rate immediately after the procedure, which improved to 74% at 6- to 12-month follow-up and 86% at >12 months.[17] This compares poorly with a 90% complete or near-complete immediate occlusion rate following coil embolization of intracranial aneurysms, when all age groups are considered.[18,19]

In this study, we found that older age (older than 70 years) was a significant predictor of incomplete occlusion at last follow-up. This is the first study to specifically evaluate age and its impact on aneurysm occlusion rates following flow diversion, to our knowledge. There was a tendency for aneurysms to be located within the posterior circulation in this age group compared with younger patients (25% versus 10.9%, $P = .001$), which may influence this finding. Nevertheless, the difference in occlusion rates remained significant after controlling for aneurysm location, which further supported the independent correlation between older age (older than 70 years) and incomplete occlusion. There was no significant difference in the duration of follow-up in older patients compared with younger patients.

As one might expect, as patients age, the risk of complications appears to increase. Brinjikji et al,[20] in a large multicenter study on complications associated with PED placement, found that complication rates rise as the patient age increases. Patients older than 70 years of age had significantly higher rates of neurologic mortality. Increased age was also associated with higher odds of neurologic morbidity.[20] Our data found a nonsignificant trend toward increased complications in patients older than 70 years of age.

While the explanation for the lower occlusion rates in the elderly is currently unknown, it is tempting to speculate that this may be due to a deficiency in the endothelial repair pathway. Rouchaud et al[21] found that the genes involved in cellular migration and the inflammatory response were upregulated in aneurysms successfully treated with flow diverters in rabbits. Other studies have identified an upregulation of metalloproteinases (critical for endothelial wall remodeling), inflammatory modulators, and growth factors.[22] In animal models, complete or near-complete endothelialization, which can occur as rapidly as within the first 7 days, is necessary to ensure complete obliteration of the aneurysm.[23] In a histologic study of giant aneurysms that had undergone flow-diversion treatment and had failed to occlude, lack of endothelialization was predominantly found in patients in their 60s.[24] It may be that the endothelial cells in the cerebral vasculature have a diminished capacity for regeneration and migration across the flow-diverter surface, similar to the reduction in neural stem cell proliferation and differentiation potential in the aging brain.[25,26] While this hypothesis requires further investigation, it raises the tantalizing possibility of coating flow diverters with factors that may enhance endothelialization and may be absent in the cellular milieu of the elderly.

Length of Follow-Up

As was previously discussed, an important physiologic mechanism for aneurysm occlusion following PED treatment is endothelialization along the length of the device, which results in diversion of blood flow away from the aneurysm sac.[27] This process is gradual and varies in duration from months to years. Accordingly, longer angiographic follow-ups for aneurysms treated with the PED may be necessary to demonstrate aneurysm occlusion. Prior studies have supported this hypothesis and have found that shorter angiographic follow-up is associated with a decreased aneurysm occlusion rate, with longer duration having the opposite effect.[9,15,16]

Effect of Cigarette Smoking

Smoking is one of the significant modifiable risk factors for aneurysm formation and increased risk of aneurysm rupture.[28-30] Ortiz et al[31] have previously reported a correlation between current smoking status and an increased risk of aneurysm recurrence. However, in that study, the authors stratified smoking status into never/nonsmokers and former/current smokers, despite smoking secession decreasing the risk of vascular inflammation and related malformations.[32] Therefore, with appropriate stratification of

current smoking as a separate category, there was no significant effect on aneurysm recurrence or retreatment after endovascular treatment.[12,29] Similarly, Rouchaud et al[33] found no significant correlation between smoking status and aneurysm occlusion following PED placement. In our study, smoking was associated with a higher rate of aneurysm occlusion. Although this finding can be attributed to the relatively small sample size, it might also be related to an increased rate of intra-aneurysmal thrombosis. Smoking is a well-known risk factor for thrombus formation in other pathologies, including cancer, cardiac stent thrombosis, and ischemic stroke. It may be that its prothrombotic effects amplify those of the PED.[34-36] These findings support an earlier statement by Rouchaud et al[33] that smoking status should not be a factor for excluding patients from PED embolization of intracranial aneurysms.

Limitations

We acknowledge that our study is limited by its retrospective nature with all the inherent biases associated with such a study design. Although the inclusion of multiple institutions improves the generalizability of the findings, it introduces variability in patient management, follow-up protocols, imaging studies used, and evaluation of aneurysm occlusion. Moreover, some aneurysm measurements were missing.

CONCLUSIONS

Complete occlusion following PED treatment of intracranial aneurysms is influenced by patient characteristics and technical factors. Older age (older than 70 years) and nonsmoking status were independent predictors of incomplete occlusion. While the physiologic explanation for these findings remains unknown, the identification of factors predictive of incomplete aneurysm occlusion following PED placement can help in directing further research on the appropriate clinical use of flow-diversion devices.

Disclosures: Adnan H. Siddiqui—*UNRELATED*: *Board Membership*: Intersocietal Accreditation Commission; *Consultancy*: Codman, Medtronic, Guidepoint Global Consulting, Penumbra, Stryker Neurovascular, MicroVention, W.L. Gore and Associates, Three Rivers Medical, Corindus, Amnis Therapeutics, CereVasc, Pulsar Vascular, The Stroke Project, Cerebrotech Medical Systems, Rapid Medical, Neuravi, Silk Road Medical, Rebound Therapeutics Corp, Claret Medical, *Comments*: also Principal Investigator/National Steering Committees: Penumbra: 3D Separator Trial, COMPASS Trial, INVEST Trial; Covidien (now Medtronic): SWIFT PRIME and SWIFT DIRECT Trials; MicroVention: FRED Trial, CONFIDENCE Study; Codman & Shurtleff: LARGE Trial; MUSC: POSITIVE Trial; *Stock/Stock Options*: StimMed, Valor Medical, Neuro Technology Investors, Cardinal Health, Medina Medical Systems, Buffalo Technology Partners, International Medical Distribution Partners. Elad I. Levy—*UNRELATED*: *Board Membership*: Stryker Neurovascular, NeXtGen Biologics, MEDX, *Comments*: served on acute ischemic stroke Clinical Advisory Board for Stryker Neurovascular, serve on Advisory Board for NeXtGen Biologics and MEDX; no money; *Consultancy*: Pulsar Vascular; *Payment for Development of Educational Presentations*: Covidien, *Comments*: honorarium for training and lectures; *Stock/Stock Options*: Intratech Medical, NeXtGEn Biologics, *Comments*: shareholder/ownership interest; *Other*: Abbott Vascular, *Comments*: carotid training sessions for physicians. Ajith J. Thomas—*UNRELATED*: *Consultancy*: Stryker Neurovascular, *Comments*: data safety monitoring board*; Expert Testimony: CRICO, Comments: expert witness, neurovascular. *Money paid to the institution.

REFERENCES

1. McDowell MM, Feroze RA, Ducruet AF. **Pipeline Embolization Device: long-term outcome data flows in.** *World Neurosurg* 2016;85:6–7 CrossRef Medline
2. Health C for D and R: Recently-Approved Devices: Pipeline™ Embolization Device, P100018. https://www.fda.gov/downloads/AdvisoryCommittees/CommitteesMeetingMaterials/MedicalDevices/MedicalDevicesAdvisoryCommittee/NeurologicalDevicesPanel/UCM442242.pdf. Accessed August 9, 2016
3. Adeeb N, Griessenauer CJ, Moore J, et al. **Pipeline embolization device for recurrent cerebral aneurysms after microsurgical clipping.** *World Neurosurg* 2016;93:341–45 CrossRef Medline
4. Becske T, Kallmes DF, Saatci I, et al. **Pipeline for uncoilable or failed aneurysms: results from a multicenter clinical trial.** *Radiology* 2013;267:858–68 CrossRef Medline
5. Griessenauer CJ, Ogilvy CS, Foreman PM, et al. **Pipeline Embolization Device for small intracranial aneurysms: evaluation of safety and efficacy in a multicenter cohort.** *Neurosurgery* 2017;80:579–87 CrossRef Medline
6. Kühn AL, Hou SY, Perras M, et al. **Flow diverter stents for unruptured saccular anterior circulation perforating artery aneurysms: safety, efficacy, and short-term follow-up.** *J Neurointerv Surg* 2015;7:634–40 CrossRef Medline
7. Lin N, Brouillard AM, Keigher KM, et al. **Utilization of Pipeline embolization device for treatment of ruptured intracranial aneurysms: US multicenter experience.** *J Neurointerv Surg* 2015;7:808–15 CrossRef
8. Nelson PK, Lylyk P, Szikora I, et al. **The Pipeline embolization device for the intracranial treatment of aneurysms trial.** *AJNR Am J Neuroradiol* 2011;32:34–40 CrossRef Medline
9. Jabbour P, Chalouhi N, Tjoumakaris S, et al. **The Pipeline Embolization Device: learning curve and predictors of complications and aneurysm obliteration.** *Neurosurgery* 2013;73:113–20; discussion 120 CrossRef Medline
10. Attali J, Benaissa A, Soize S, et al. **Follow-up of intracranial aneurysms treated by flow diverter: comparison of three-dimensional time-of-flight MR angiography (3D-TOF-MRA) and contrast-enhanced MR angiography (CE-MRA) sequences with digital subtraction angiography as the gold standard.** *J Neurointervl Surg* 2016;8:81–86 CrossRef Medline
11. Boddu SR, Tong FC, Dehkharghani S, et al. **Contrast-enhanced time-resolved MRA for follow-up of intracranial aneurysms treated with the Pipeline embolization device.** *AJNR Am J Neuroradiol* 2014;35:2112–18 CrossRef Medline
12. Chen JX, Lai LF, Zheng K, et al. **Influencing factors of immediate angiographic results in intracranial aneurysms patients after endovascular treatment.** *J Neurol* 2015;262:2115–23 CrossRef Medline
13. Ogilvy CS, Chua MH, Fusco MR, et al. **Validation of a system to predict recanalization after endovascular treatment of intracranial aneurysms.** *Neurosurgery* 2015;77:168–73; discussion 173–74 CrossRef Medline
14. Ogilvy CS, Chua MH, Fusco MR, et al. **Stratification of recanalization for patients with endovascular treatment of intracranial aneurysms.** *Neurosurgery* 2015;76:390–95; discussion 395 CrossRef Medline
15. O'Kelly CJ, Spears J, Chow M, et al. **Canadian experience with the Pipeline embolization device for repair of unruptured intracranial aneurysms.** *AJNR Am J Neuroradiol* 2013;34:381–87 CrossRef Medline
16. Yu SC, Kwok CK, Cheng PW, et al. **Intracranial aneurysms: midterm outcome of Pipeline embolization device—a prospective study in 143 patients with 178 aneurysms.** *Radiology* 2012;265:893–901 CrossRef Medline
17. Sturiale CL, Brinjikji W, Murad MH, et al. **Endovascular treatment of intracranial aneurysms in elderly patients a systematic review and meta-analysis.** *Stroke* 2013;44:1897–902 CrossRef Medline
18. Ferns SP, Sprengers ME, Rooij WJ van, et al. **Coiling of intracranial aneurysms: a systematic review on initial occlusion and reopening and retreatment rates.** *Stroke* 2009;40:e523–29 CrossRef Medline
19. Pouratian N, Oskouian RJ Jr, Jensen ME, et al. **Endovascular management of unruptured intracranial aneurysms.** *J Neurol Neurosurg Psychiatry* 2006;77:572–78 CrossRef Medline
20. Brinjikji W, Kallmes DF, Cloft HJ, et al. **Age-related outcomes following intracranial aneurysm treatment with the Pipeline Emboli-**

zation Device: a subgroup analysis of the IntrePED registry. *J Neurosurg* 2016;124:1726–30 CrossRef Medline
21. Rouchaud A, Johnson C, Thielen E, et al. **Differential gene expression in coiled versus flow-diverter-treated aneurysms: RNA sequencing analysis in a rabbit aneurysm model.** *AJNR Am J Neuroradiol* 2016;37:1114–21 CrossRef Medline
22. Puffer C, Dai D, Ding YH, et al. **Gene expression comparison of flow diversion and coiling in an experimental aneurysm model.** *J Neurointerv Surg* 2015;7:926–30 CrossRef Medline
23. Kadirvel R, Ding YH, Dai D, et al. **Cellular mechanisms of aneurysm occlusion after treatment with a flow diverter.** *Radiology* 2014;270:394–99 CrossRef Medline
24. Szikora I, Turányi E, Marosfoi M. **Evolution of flow-diverter endothelialization and thrombus organization in giant fusiform aneurysms after flow diversion: a histopathologic study.** *AJNR Am J Neuroradiol* 2015;36:1716–20 CrossRef Medline
25. Madonna R, Novo G, Balistreri CR. **Cellular and molecular basis of the imbalance between vascular damage and repair in ageing and age-related diseases: as biomarkers and targets for new treatments.** *Mech Ageing Dev* 2016;159:22–30 CrossRef Medline
26. Yousef H, Morgenthaler A, Schlesinger C, et al. **Age-associated increase in BMP signaling inhibits hippocampal neurogenesis.** *Stem Cells* 2015;33:1577–88 CrossRef Medline
27. Griessenauer CJ, Gupta R, Shi S, et al. **Collar sign in incompletely occluded aneurysms after Pipeline embolization: evaluation with angiography and optical coherence tomography.** *AJNR Am J Neuroradiol* 2017;38:323–26 CrossRef Medline
28. Andreasen TH, Bartek J Jr, Andresen M, et al. **Modifiable risk factors for aneurysmal subarachnoid hemorrhage.** *Stroke* 2013;44:3607–12 CrossRef Medline
29. Brinjikji W, Lingineni RK, Gu CN, et al. **Smoking is not associated with recurrence and retreatment of intracranial aneurysms after endovascular coiling.** *J Neurosurg* 2015;122:95–100 CrossRef Medline
30. Juvela S, Hillbom M, Numminen H, et al. **Cigarette smoking and alcohol consumption as risk factors for aneurysmal subarachnoid hemorrhage.** *Stroke* 1993;24:639–46 CrossRef Medline
31. Ortiz R, Stefanski M, Rosenwasser R, et al. **Cigarette smoking as a risk factor for recurrence of aneurysms treated by endosaccular occlusion.** *J Neurosurg* 2008;108:672–75 CrossRef Medline
32. Athyros VG, Katsiki N, Doumas M, et al. **Effect of tobacco smoking and smoking cessation on plasma lipoproteins and associated major cardiovascular risk factors: a narrative review.** *Curr Med Res Opin* 2013;29:1263–74 CrossRef Medline
33. Rouchaud A, Brinjikji W, Cloft HJ, et al. **Smoking does not affect occlusion rates and morbidity-mortality after Pipeline embolization for intracranial aneurysms.** *AJNR Am J Neuroradiol* 2016;37:1122–26 CrossRef Medline
34. Aigner A, Grittner U, Rolfs A, et al. **Contribution of established stroke risk factors to the burden of stroke in young adults.** *Stroke* 2017;48:1744–51 CrossRef Medline
35. Lemesle G, Tricot O, Meurice T, et al. **Incident myocardial infarction and very late stent thrombosis in outpatients with stable coronary artery disease.** *J Am Coll Cardiol* 2017;69:2149–56 CrossRef Medline
36. Salazar Adum JP, Fuentes HE, Lind BB, et al. **Predictors of active cancer thromboembolic outcomes: mortality associated with calf deep vein thrombosis.** *Int Angiol* 2017 May 24. [Epub ahead of print] CrossRef Medline

Hemodynamic Characteristics of Ruptured and Unruptured Multiple Aneurysms at Mirror and Ipsilateral Locations

R. Doddasomayajula, B.J. Chung, F. Mut, C.M. Jimenez, F. Hamzei-Sichani, C.M. Putman, and J.R. Cebral

ABSTRACT

BACKGROUND AND PURPOSE: Different hemodynamic patterns have been associated with aneurysm rupture. The objective was to test whether hemodynamic characteristics of the ruptured aneurysm in patients with multiple aneurysms were different from those in unruptured aneurysms in the same patient.

MATERIALS AND METHODS: Twenty-four mirror and 58 ipsilateral multiple aneurysms with 1 ruptured and the others unruptured were studied. Computational fluid dynamics models were created from 3D angiographies. Case-control studies of mirror and ipsilateral aneurysms were performed with paired Wilcoxon tests.

RESULTS: In mirror pairs, the ruptured aneurysm had more oscillatory wall shear stress ($P = .007$) than the unruptured one and tended to be more elongated (higher aspect ratio), though this trend achieved only marginal significance ($P = .03$, 1-sided test). In ipsilateral aneurysms, ruptured aneurysms had larger maximum wall shear ($P = .05$), more concentrated ($P < .001$) and oscillatory wall shear stress ($P < .001$), stronger ($P < .001$) and more concentrated inflow jets ($P < .001$), larger maximum velocity ($P < .001$), and more complex flow patterns ($P < .001$) compared with unruptured aneurysms. Additionally, ruptured aneurysms were larger ($P < .001$) and more elongated ($P < .001$) and had wider necks ($P < .001$) and lower minimum wall shear stress ($P < .001$) than unruptured aneurysms.

CONCLUSIONS: High wall shear stress oscillations and larger aspect ratios are associated with rupture in mirror aneurysms. Adverse flow conditions characterized by high and concentrated inflow jets; high, concentrated, and oscillatory wall shear stress; and strong, complex and unstable flow patterns are associated with rupture in ipsilateral multiple aneurysms. In multiple ipsilateral aneurysms, these unfavorable flow conditions are more likely to develop in larger, more elongated, more wide-necked, and more distal aneurysms.

ABBREVIATIONS: CORELEN = vortex core-line length; max = maximum; min = minimum; OSI = oscillatory shear index; PODENT = proper orthogonal decomposition entropy; WSS = wall shear stress

Unruptured cerebral aneurysms are diagnosed with increasing frequency, but despite the relatively low risk of rupture (estimated at 0.3%–3%[1]) and because of high mortality and disability rates (estimated at 45% mortality in the first year[2] and 64% disability of survivors[3]), patients often undergo preventive intervention, which is not without risk of complications (estimated at 10%–14% combining perioperative morbidity and mortality[4]). Therefore, it is imperative to properly select patients, avoiding unnecessary and relatively risky procedures. Selection is particularly important in patients with multiple aneurysms (about 15%–35% of all patients with cerebral aneurysms[5,6]) because in these cases, clinicians need to decide whether to treat each of the lesions, which may require multiple interventions, depending on accessibility and treatment technique (surgical or endovascular).[7]

The process underlying the rupture of a cerebral aneurysm is highly complex, and the principal factors leading to this event are largely unknown.[1,4,8] Numerous features have been investigated as possible rupture risk factors: location, size, sex, age, family history, smoking, alcohol, and hypertension.[9] Size and location have been identified as the most important aneurysm-specific predictors of rupture in both single and multiple aneurysms.[10] However, it is well-known that small aneurysms do rupture, including in cases of multiple aneurysms.[6] Therefore, it is important to identify additional

Received April 3, 2017; accepted after revision August 1.

From the Bioengineering Department (R.D., B.J.C., F.M., J.R.C.), George Mason University, Fairfax, Virginia; Neurosurgery Department (C.M.J.), University of Antioquia, Medellin, Colombia; Department of Neurosurgery (F.H.-S.), Mt. Sinai Medical Center, New York, New York; and Interventional Neuroradiology (C.M.P.), Inova Fairfax Hospital, Falls Church, Virginia.

This work was partially supported by the National Institutes of Health/National Institute of Neurological Disorders and Stroke grant No. R21NS094780.

Please address correspondence to Juan R. Cebral, PhD, Bioengineering Department, Volgenau School of Engineering, George Mason University, 4400 University Dr, MSN 2A1, Fairfax, VA 22030; e-mail: jcebral@gmu.edu

Indicates open access to non-subscribers at www.ajnr.org

Indicates article with supplemental on-line appendix and tables.

http://dx.doi.org/10.3174/ajnr.A5397

independent characteristics to improve the risk assessment of patients with multiple aneurysms. Among all the factors involved, the hemodynamics of the lesion are thought to be one of the fundamental players,[11] interacting with the wall biology, which, in turn, drives the degradation of the wall structure and its mechanical strength.

Multiple aneurysms, in addition to being clinically very important and challenging, offer the unique opportunity for comparing ruptured (cases) and unruptured (controls) aneurysms while perfectly controlling for patient-related confounding factors such as sex, age, family history, previous hemorrhage, smoking, alcohol, drugs, and hypertension. Thus, the objective of this study was to test whether hemodynamic characteristics of the ruptured aneurysm in patients with multiple aneurysms were different from those of unruptured aneurysms in the same patient. This information is important not only to identify hemodynamic factors that could be used to assess which aneurysms are at higher risk of progressing toward rupture but also to better understand the mechanisms that drive the progressive degradation of the wall and ultimately result in aneurysm rupture.

MATERIALS AND METHODS

Image and Patient Data

We have developed a data base of cerebral aneurysms imaged with 3D rotational angiography, mainly from Inova Fairfax Hospital (Northern Virginia), Mt. Sinai Medical Center (New York), and the Mayo Clinic (Rochester, Minnesota). This data base contains 3D rotational angiography images along with basic information, including aneurysm rupture status and location and size of >2000 cerebral aneurysms. The data have been anonymized; and the study was approved by the George Mason University institutional review board. For this study, 2 subsets of multiple aneurysms were considered, as detailed below.

Mirror Aneurysms

The first subset included mirror aneurysm pairs—that is, 2 aneurysms at the same anatomic location on each side. Furthermore, only mirror pairs with 1 ruptured and the other unruptured were considered. Forty-eight mirror aneurysms (24 ruptured and 24 corresponding contralateral unruptured ones) in 24 patients (21 [87.5%] women, 3 [12.5%] men; mean age, 52.9 ± 13.3 years; age range, 23–81 years) were included in the study. Of the 24 pairs, 7 (29%) were middle cerebral artery bifurcation aneurysms, while the remainder (17, 71%) were sidewall or lateral aneurysm pairs.

Ipsilateral Multiple Aneurysms

The second subset included multiple ipsilateral aneurysms—that is, multiple aneurysms along the same arterial tree. Again, only cases with 1 ruptured and ≥1 unruptured aneurysm on the same arterial tree were considered. There were 58 patients (44 [76%] women, 13 men [22.4%], and 1 unknown; mean age, 58 ±14.7 years; age range, 28–88 years). This subset included 144 aneurysms, including 58 ruptured and 86 unruptured ones. There were 97 bifurcation (67%), and 47 lateral (33%) aneurysms.

Vascular and Blood Flow Modeling

Image-based computational fluid dynamics models of all 192 aneurysms (48 mirror and 144 ipsilateral aneurysms) were constructed from the corresponding 3D rotational angiography images using previously described methods.[12,13] For mirror pairs, 2 vascular models were independently constructed for the left and right sides; while for the ipsilateral cases, a single model, including all ipsilateral aneurysms, was created. Numeric simulations were performed under pulsatile flow for 2 cardiac cycles using a solver developed in-house.[14] Blood was assumed to have Newtonian viscosity, and vessel wall compliance was neglected. The inflow conditions were derived from a phase-contrast MR imaging scan of a healthy subject that was scaled with the inflow vessel cross-sectional area.[15] Fully developed velocity profiles were prescribed at the inlets, while outflow boundary conditions were selected to produce flow divisions consistent with the Murray principle of minimal work. Results from the second simulated cardiac cycle were analyzed. Different aspects of the aneurysmal hemodynamic environment, including the wall shear stress distribution, the inflow jet, and the intra-aneurysmal flow pattern, were studied. Different variables or metrics were defined to capture different characteristics of the flow.[16,17] A few additional geometric variables were computed from the reconstructed vascular models. The variables considered (On-line Appendix) are listed in On-line Tables 1–4. For ipsilateral aneurysms, an extra variable that assigns an increasing value for more distal aneurysms (thus called the "distality coordinate") was introduced (On-line Table 5).

Data Analysis

Matched case-control studies were performed for both mirror and ipsilateral aneurysms.

Mirror Aneurysms

The hemodynamic (and geometric) characteristics of ruptured (cases) and unruptured (controls) aneurysms in mirror pairs were compared with a 2-sided paired Wilcoxon test. Differences were considered significant if $P < .05$. By considering case-control pairs of the same patient, all patient-specific characteristics (eg, sex, age, comorbidities, habits, genetics, and so forth) were matched. Furthermore, in mirror pairs, aneurysm location was also matched by definition. The flow rate in the parent artery was not matched because 1 aneurysm is fed from 1 internal carotid artery, while the other is fed from the contralateral ICA.

Ipsilateral Multiple Aneurysms

Similarly, hemodynamic (and geometric) characteristics of ruptured (cases) and unruptured (controls) ipsilateral aneurysms were compared using a 2-sided paired Wilcoxon test. However, some patients had 1 ruptured aneurysm and >1 unruptured aneurysm (multiple controls). Therefore, in these cases, the ruptured aneurysm was paired with a randomly selected unruptured aneurysm of the same patient, thus making all aneurysm pairs independent. The process was repeated 100 times, and the mean and maximum P values were calculated. If the maximum P value of all 100 tests was <.05, the difference between ruptured and unruptured groups was considered statistically significant. If the mean P value was <.05 but the maximum was not, the difference was considered marginally significant. Repeating the random selections 100 or 200 times did not show noticeable differences. Therefore, 100 repetitions were deemed sufficient.

Hemodynamic and geometric characteristics of ruptured and unruptured mirror and multiple ipsilateral aneurysms[a]

Variable	Mirror Aneurysms			Ipsilateral Aneurysms			
	Unruptured	Ruptured	*P* Value	Unruptured	Ruptured	*P*mean	*P*max
WSSmin	0.6 ± 0.9	0.4 ± 0.6	.24	1.3 ± 2.0	0.4 ± 0.8	<.001[b]	<.001[b]
WSSmax	285.3 ± 216.1	269.5 ± 183.1	1.00	269.6 ± 324.5	784.9 ± 2730.4	.006[b]	.05[b]
WSSmean	28.1 ± 26.8	22.3 ± 18.6	.49	29.3 ± 35.5	27.1 ± 36.8	.28	.81
WSSnorm	0.53 ± 0.40	0.44 ± 0.26	.30	0.60 ± 0.39	0.50 ± 0.32	.12	.43
SCI	5.48 ± 10.87	5.54 ± 4.53	.21	3.30 ± 3.95	6.74 ± 7.20	<.001[b]	<.001[b]
LSA	51.6 ± 33.0	50.9 ± 33.4	.81	48.7 ± 32.4	49.6 ± 32.0	.72	1.00
OSImax	0.243 ± 0.123	0.334 ± 0.115	.008[b]	0.181 ± 0.134	0.332 ± 0.103	<.001[b]	<.001[b]
OSImean	0.012 ± 0.010	0.014 ± 0.010	.55	0.009 ± 0.011	0.014 ± 0.010	.005[b]	.06
Q	0.80 ± 1.15	0.72 ± 0.85	.79	0.23 ± 0.29	0.70 ± 0.62	<.001[b]	<.001[b]
ICI	0.72 ± 0.89	0.82 ± 0.80	.66	0.24 ± 0.43	0.68 ± 0.57	<.001[b]	<.001[b]
Vmax	82.3 ± 62.5	80.8 ± 44.4	.88	61.9 ± 63.1	98.2 ± 81.0	<.001[b]	<.001[b]
VE	11.8 ± 10.1	10.1 ± 6.8	.77	9.1 ± 8.9	10.9 ± 9.4	.29	.70
SR	259.6 ± 192.3	229.2 ± 159.8	.68	339.6 ± 305.0	246.1 ± 236.4	.03[b]	.18
VO	363.1 ± 284.9	319.1 ± 225.8	.70	445.7 ± 421.7	346.1 ± 345.6	.09	.38
CORELEN	1.481 ± 2.014	2.501 ± 3.159	.17	0.376 ± 0.557	2.226 ± 2.144	<.001[b]	<.001[b]
PODENT	0.167 ± 0.136	0.175 ± 0.074	.33	0.137 ± 0.121	0.192 ± 0.127	.009[b]	.08
Asize	0.594 ± 0.331	0.713 ± 0.361	.14	0.365 ± 0.185	0.726 ± 0.282	<.001[b]	<.001[b]
Nsize	0.412 ± 0.185	0.422 ± 0.147	.75	0.306 ± 0.127	0.423 ± 0.136	<.001[b]	<.001[b]
AR	0.956 ± 0.755	1.176 ± 0.551	.06	0.669 ± 0.408	1.198 ± 0.609	<.001[b]	<.001[b]
Distality	–	–	–	0.444 ± 0.345	0.612 ± 0.321	<.008[b]	.04[b]

Note:—LSA indicates percentage area under low WSS; SCI, shear concentration index; Vmax, maximum flow velocity; Q, aneurysm flow rate; ICI, inflow concentration index; norm, normalized; Asize, aneurysm maximum size; Nsize, neck maximum size; AR, aspect ratio (≤depth/neck size); VO, mean aneurysm vorticity; SR, shear rates; VE, mean aneurysm velocity; Distality, coordinate of vessel segment along the arterial tree.

[a] Values are given as mean ± SD. *P* values correspond to univariate paired Wilcoxon rank sum tests. For ipsilateral aneurysms, mean and maximum *P* values of 100 randomly selected ruptured–unruptured pairs are given.

[b] Significant difference ($P < .05$).

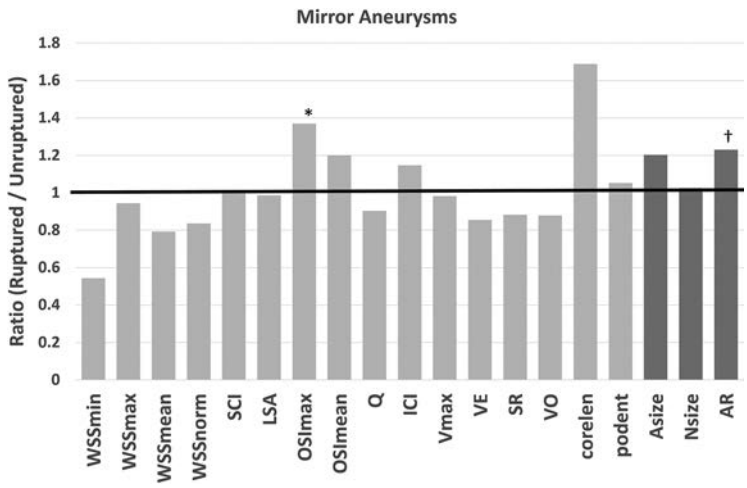

FIG 1. Ratios of mean values of hemodynamic and geometric variables of ruptured over unruptured mirror aneurysms. Statistically significant differences ($P < .05$) are indicated with an *asterisk*, and marginally significant differences ($P < .05$ on 1-sided test), with a *dagger*. LSA indicates percentage area under low WSS; SCI, shear concentration index; Vmax, maximum flow velocity; Q, aneurysm flow rate; ICI, inflow concentration index; norm, normal; Asize, aneurysm maximum size; Nsize, neck maximum size; AR, aspect ratio (≤ depth/neck size); VO, mean aneurysm vorticity; SR, shear rates; VE, mean aneurysm velocity.

RESULTS

Comparisons of the mean values of hemodynamic (and geometric) variables between ruptured and unruptured aneurysms in both mirror pairs and ipsilateral multiple aneurysms are presented in the Table. This Table lists the mean value ± the SD of each variable over the corresponding matched ruptured and unruptured groups. In the mirror cases, the *P* value corresponds to the paired Wilcoxon test. In ipsilateral aneurysms, the mean and maximum (*P*max) *P* values over 100 random pairings are given. Statistically significant differences ($P < .05$) are indicated with a superscript *b*.

The findings for mirror aneurysms are summarized in Fig 1. This figure presents the ratio of the mean values of hemodynamic (and geometric) variables of ruptured over unruptured aneurysms. In mirror aneurysms, the ruptured aneurysms had more oscillatory wall shear stress distributions (higher oscillatory shear index maximum [OSImax], $P = .007$) than unruptured aneurysms. Additionally, ruptured aneurysms were more elongated (ie, higher aspect ratio, $P = .06$), though this trend achieved only marginal significance ($P = .03$ for a 1-sided test, $P = .06$ for a 2-sided test). The inflow rate imposed as boundary conditions based on the parent artery diameter was not significantly different between ruptured and unruptured aneurysms ($P = .12$).

The results for ipsilateral aneurysms are summarized in Fig 2. The error bars indicate the variability of the ratio of the mean values of ruptured over unruptured aneurysms for 100 random pairings. In multiple ipsilateral aneurysms, ruptured aneurysms had larger maximum WSS (WSSmax, *P*max = .05), more concentrated and oscillatory WSS distributions (shear concentration index, *P*max < .001; OSImax, *P*max < .001; OSImean, mean $P = .005$), stronger and more concentrated inflow jets (aneurysm flow rate, *P*max < .001; inflow concentration index, *P*max < .001), a larger maximum flow velocity (*P*max < .001), and more complex and unstable flow

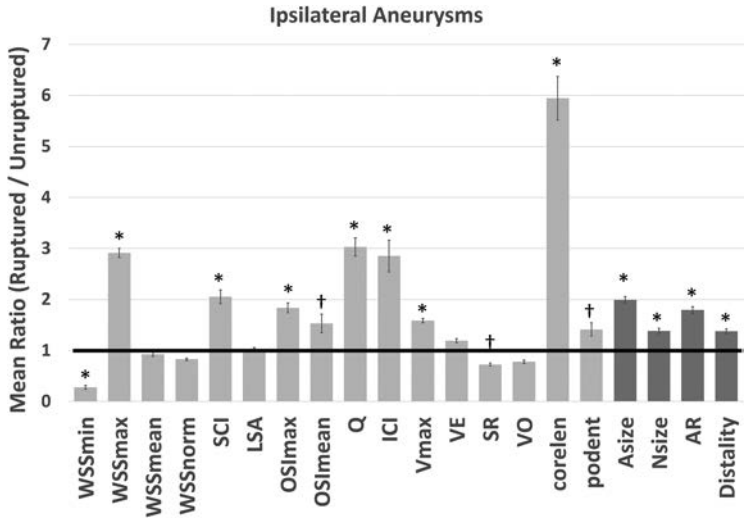

FIG 2. Ratios of mean values of hemodynamic and geometric variables of ruptured over unruptured ipsilateral aneurysms. *Error bars* indicate variability of the mean ratios over 100 random selections of ruptured–unruptured multiple aneurysm pairs. Statistically significant differences (*P*max $<$ .05) are indicated with an *asterisk*, and marginally significant differences (mean $P = .05$ but *P*max $>$ .05), with a *dagger*. LSA indicates percentage area under low WSS; SCI, shear concentration index; Vmax, maximum flow velocity; Q, aneurysm flow rate; ICI, inflow concentration index; norm, normal; Asize, aneurysm maximum size; Nsize, neck maximum size; AR, aspect ratio (≤depth/neck size); VO, mean aneurysm vorticity; SR, shear rates; VE, mean aneurysm velocity.

patterns (vortex core-line length [CORELEN], *P*max $<$ .001; proper orthogonal decomposition entropy [PODENT], mean $P = .009$) compared with unruptured aneurysms. Additionally, ruptured aneurysms had lower minimum WSS (WSSmin, *P*max $<$ .001) and shear rates (mean $P = .03$) than unruptured aneurysms. Geometrically, ruptured ipsilateral aneurysms were larger (aneurysm maximum size, *P*max $<$ .001), had wider necks (neck maximum size, *P*max $<$ .001), were more elongated (aspect ratio, *P*max $<$ .001), and were located more distally (*P*max = .04) than unruptured aneurysms.

DISCUSSION

Between 10% and 33% of patients with subarachnoid hemorrhage have multiple aneurysms, and the approach to these patients becomes complex considering that it is difficult to unequivocally identify the ruptured aneurysm when angiography reveals multiple aneurysms.[18] On the other hand, whether the intervention of patients with multiple aneurysms should be directed to only the ones that bled or to all the lesions found on angiography has been long debated.[19] If none have ruptured, the one at greatest risk of rupture should be identified. Localization and size have traditionally been the 2 variables that have defined the risk of rupture in multiple cerebral aneurysms; however, some other geometric and hemodynamic variables have emerged.[20]

The current study took advantage of multiple aneurysms (1 ruptured and ≥1 unruptured in the same patient) offering a unique opportunity to compare ruptured and unruptured aneurysms while controlling for all patient-specific characteristics, eliminating confounding factors when each patient functions as his or her own internal control because all paired aneurysms are in the same patient. Some authors have argued that otherwise, patient-related confounding variables such as history of smoking, history of hypertension, or even genetic predisposition are difficult or even almost impossible to control for or eliminate.[20] Furthermore, the study was subdivided into the analysis of mirror pairs, in which aneurysm location but not inflow conditions were controlled; and ipsilateral multiple aneurysms, in which inflow conditions but not location were controlled. The objective of these comparisons was to identify aneurysm-specific characteristics that are independent of patient-specific characteristics and can discriminate ruptured and unruptured aneurysms. These aneurysm-specific characteristics could complement patient-specific risk factors in identifying aneurysms at higher risk of rupture. The study focused on aneurysm hemodynamic characteristics because it is thought that adverse hemodynamic conditions could predispose aneurysm walls to further degradation and eventual rupture.[21,22]

In our study, ruptured aneurysms in mirror pairs had more oscillatory WSS distributions (characterized by larger maximum OSI) and were more elongated (ie, having a marginally larger aspect ratio) than the corresponding unruptured aneurysms. An example of a mirror pair is presented in Fig 3. In a previous study, Fan et al[23] analyzed 16 mirror bifurcation aneurysm pairs and found that ruptured aneurysms were larger (larger size and size ratio), were more elongated (larger aspect ratio and height-to-width ratio), and had lower mean WSS and larger area under low WSS. They also observed that ruptured aneurysms tended to have more complex and unstable flow patterns, but these results were not statistically significant. They also noted that the OSI might not be different in their sample because they excluded sidewall aneurysms. Likewise, in our sample, ruptured aneurysms tended to have lower mean WSS and more complex (larger CORELEN) flow patterns, but these results did not achieve statistical significance. However, the area under low WSS was not different in our study. In another study, Huang et al[24] analyzed 63 mirror pairs imaged with CTA and found that ruptured aneurysms were larger (larger size, size ratio, area ratio), were more elongated (larger aspect ratio), and had more irregular walls than unruptured aneurysms. In our study, ruptured aneurysms were also more elongated than unruptured aneurysms, but they were not larger than the unruptured ones.

Our results indicate that in ipsilateral multiple aneurysms, the ruptured aneurysm tends to have hostile flow conditions characterized by higher and more concentrated inflow jets (larger aneurysm inflow rate and inflow concentration index); and higher, more concentrated, and more oscillatory WSS distributions (larger WSSmax, shear concentration index, and OSImax), with lower minimum WSS and stronger, more complex and unstable flow patterns (larger maximum flow velocity, CORELEN, and PODENT) with a lower shear rate, compared with unruptured aneurysms of the same patient. Because the aneurysms considered

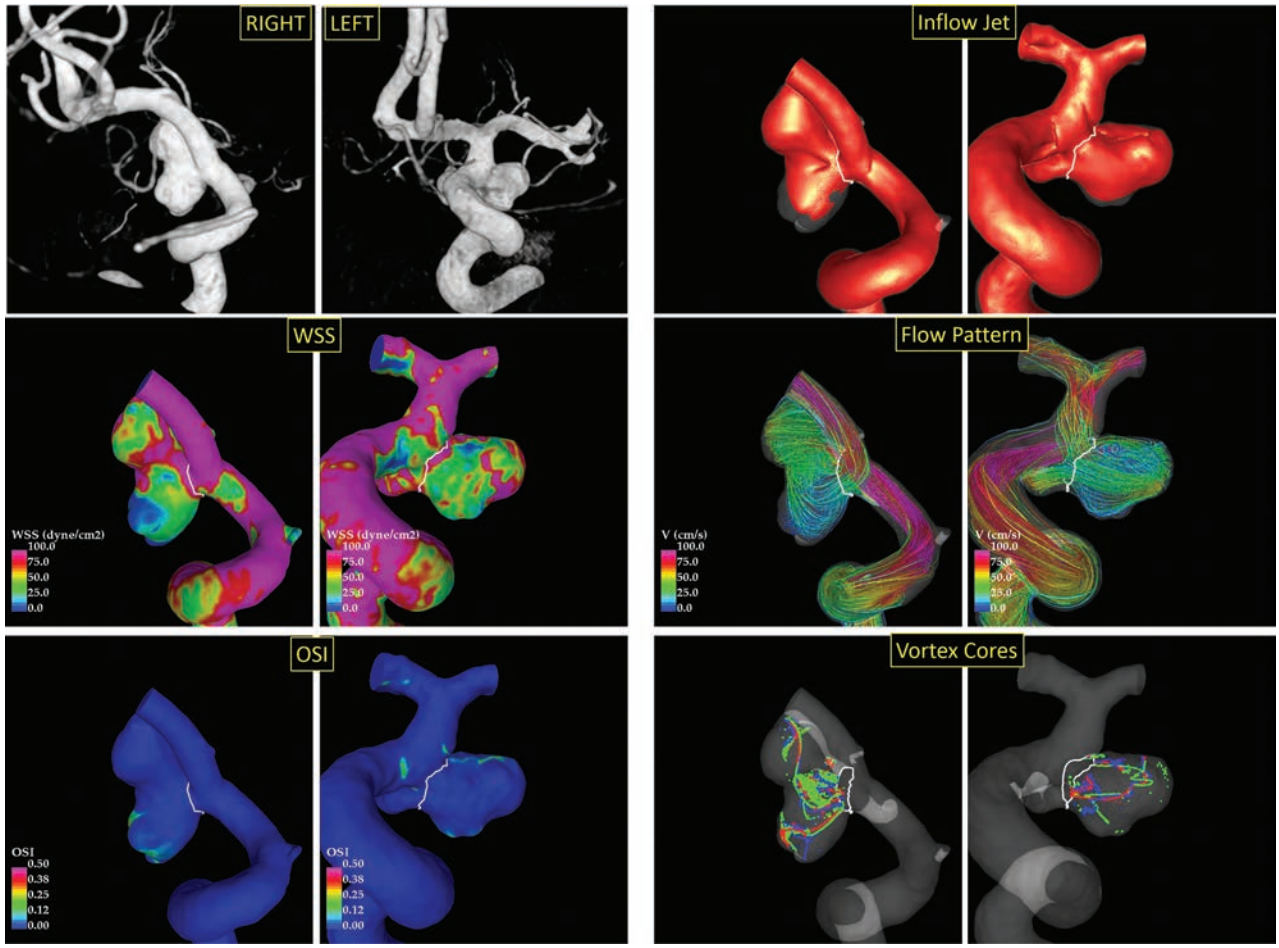

FIG 3. Example of ruptured (right posterior communicating artery aneurysm, *left column*) and unruptured (right posterior communicating artery aneurysm, *right column*) mirror aneurysm pairs. The *Left panel* shows from top to bottom: 3D rotational angiography images, WSS distributions, and OSI distributions. The *right panel* shows from top to bottom: inflow jets, flow patterns, and vortex core lines at 4 times during the cardiac cycle.

here occur on the same arterial tree in the same patient, these findings are independent of the patient-specific flow conditions. Additionally, it was found that ruptured aneurysms tended to be larger, with wider necks, and more elongated than unruptured ipsilateral aneurysms. Most interesting, in general, the ruptured aneurysms tended to be more distal than unruptured aneurysms. Examples of ipsilateral multiple aneurysms illustrating these flow conditions are presented in Fig 4. In a previous study, Zhang et al[25] analyzed 20 ipsilateral aneurysm pairs and found that ruptured aneurysms were more irregular and elongated and had lower minimum WSS and larger areas under low WSS than unruptured aneurysms. Most interesting, in our study, the minimum WSS was also lower in ruptured than in unruptured aneurysms, but the area under low WSS was not different. Zhang et al reported no difference in bleeding sites of ipsilateral aneurysms, while Jou et al[26] speculated that the proximal aneurysm in tandem serial ipsilateral aneurysms may have a higher rupture risk based on their analysis of 4 serial pairs. In contrast, our data suggest that ruptured aneurysms tended to be more distal than the unruptured aneurysms in the same patient.

The adverse flow conditions described above have been previously shown to be associated with aneurysm wall inflammation, which itself is associated with aneurysm rupture,[27] wall weakening and stiffening characteristic of vulnerable walls,[28,29] and damaged collagen architectures.[30] Additionally, these flow conditions have been associated with aneurysm rupture.[31] Our results do not contradict reports that have associated low normalized WSS and large area under low WSS with rupture,[32] though in our sample, normalized WSS and area under low WSS were not significantly different between ruptured and unruptured aneurysms in the same patients. What may constitute a hostile flow environment is a heterogeneous, oscillatory WSS distribution with focal elevations of WSS and large regions of low WSS produced by strong concentrated inflow jets that create complex unstable intrasaccular flow structures. The exact mechanisms that cause wall inflammation and rupture under high-flow conditions are still uncertain. However, this study provides valuable information to consider in future studies to understand the connection between the local flow conditions and the structure and strength of the wall.

Location has been previously identified as a risk factor and has been proposed, along with size and the presence of blebs, as the main aneurysm-specific characteristics to score aneurysm rupture risk.[9] Our study suggests that location may be important because it may be associated with different local flow conditions—that is, adverse flow conditions may be more likely to de-

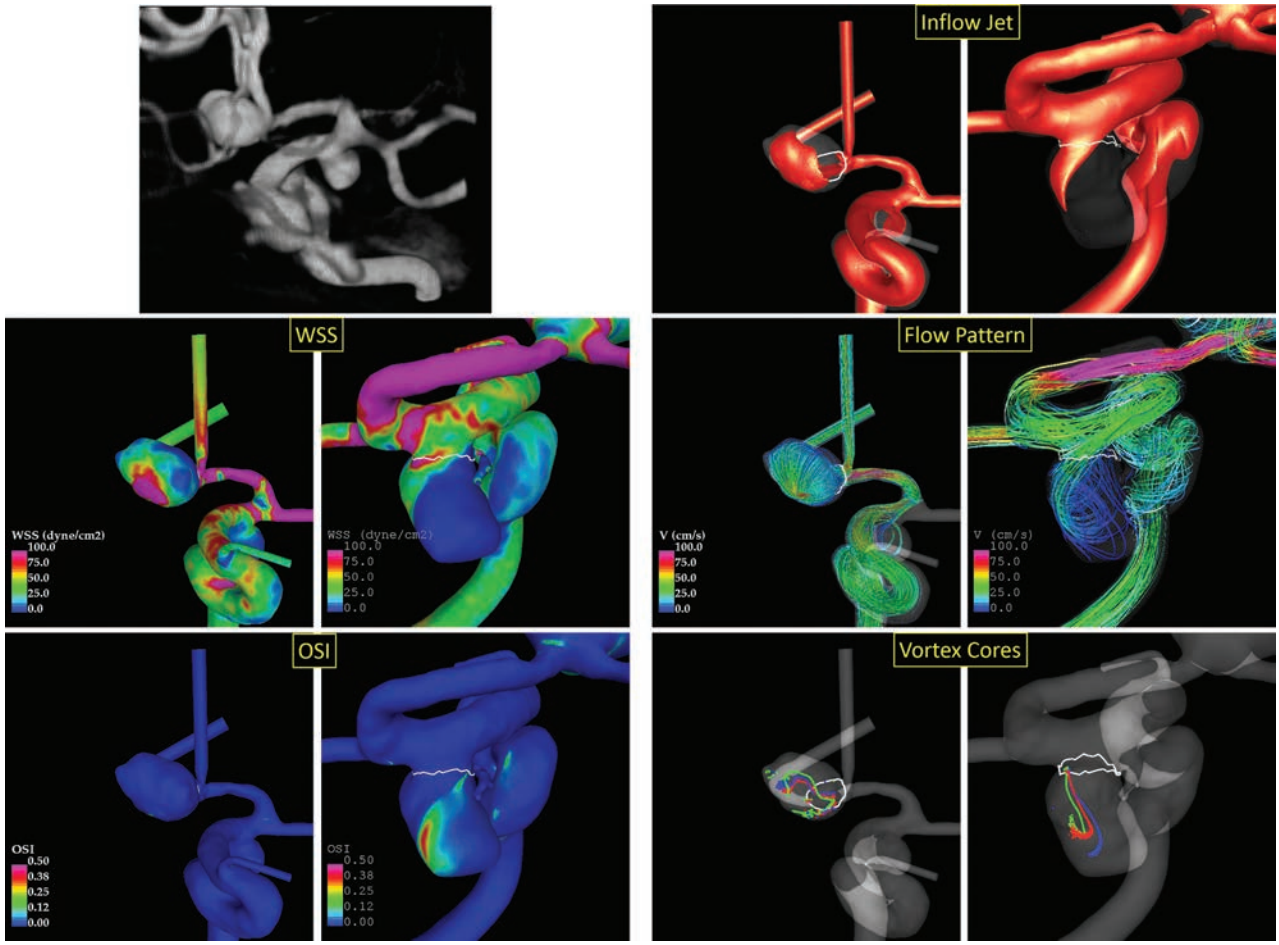

FIG 4. Example of ruptured (anterior communicating artery aneurysm fed from the left A1) and unruptured (left posterior communicating artery aneurysm) multiple ipsilateral aneurysms. The *left panel* shows from top to bottom: 3D rotational angiography image, WSS distributions, and OSI distributions. The *right panel* shows from top to bottom: inflow jets, flow patterns, and vortex core lines at 4 time instances during the cardiac cycle.

velop at certain locations (for example more distally) and are less likely at other locations, independent of the flow rate in the feeding vessel. Furthermore, when we controlled for location as in the mirror-aneurysm analysis, fewer hemodynamic differences were observed.

Our study has some limitations. Although the sample size was large enough to achieve statistically significant results, it did not allow us to subdivide the sample to study bifurcation and sidewall aneurysms separately as has been suggested.[33] Selection bias related to patient referral patterns and indications for treatment may have led to exclusion of important aneurysm subsets. The study was based on cross-sectional data; thus, it is not possible to determine whether the unruptured aneurysms had high or low rupture risk. Furthermore, the relative "ages" of the aneurysms in a single patient (ie, the time since they were formed) are not known, so it is not possible to determine their relative speed of progression. Finally, certain assumptions and approximations were made when constructing the computational fluid dynamics models, including assumptions of flow conditions, rigid walls, and Newtonian viscosity. Thus, the results should be confirmed with additional data from other populations, as well as with longitudinal data.

CONCLUSIONS

High wall shear stress oscillations and larger aspect ratios are associated with aneurysm rupture in mirror bilateral aneurysms. Hostile flow conditions characterized by high and concentrated inflow jets; high, concentrated, and oscillatory wall shear stress distributions; and strong, complex, and unstable flow patterns are associated with rupture in ipsilateral multiple aneurysms. These adverse flow conditions are more likely to develop in aneurysms that are more distal and larger and more elongated and have wider necks in multiple ipsilateral aneurysms.

Disclosures: Fernando Mut—*RELATED*: *Grant*: National Institutes of Health.* Christopher M. Putman—*UNRELATED*: *Payment for Lectures Including Service on Speakers Bureaus*: Penumbra. Juan R. Cebral—*RELATED*: *Grant*: National Institutes of Health, *Comments*: research grant*; *UNRELATED*: *Grants/Grants Pending*: National Institutes of Health and Philips Healthcare, *Comments*: research grants. *Money paid to the institution.

REFERENCES

1. Juvela S, Porras M, Poussa K. **Natural history of unruptured intracranial aneurysms: probability of and risk factors for aneurysm rupture.** *J Neurosurg* 2008;108:1052–60 CrossRef Medline
2. Wiebers DO, Torner JC, Meissner I. **Impact of unruptured intracra-**

nial aneurysms on public health in the United States. *Stroke* 1992; 23:1416–19 CrossRef Medline
3. Kelly PJ, Stein J, Shafqat S, et al. **Functional recovery after rehabilitation for cerebellar stroke.** *Stroke* 2001;32:530–34 Medline
4. Amenta PS, Yadla S, Campbell PG, et al. **Analysis of nonmodifiable risk factors for intracranial aneurysm rupture in a large, retrospective cohort.** *Neurosurgery* 2012;70:693–99; discussion 699–701 CrossRef Medline
5. Kaminogo M, Yonekura M, Shibata S. **Incidence and outcome of multiple intracranial aneurysms in a defined population.** *Stroke* 2003;34:16–21 CrossRef Medline
6. Baumann F, Khan N, Yonekawa Y. **Patient and aneurysm characteristics in multiple intracranial aneurysms.** *Acta Neurchir Suppl* 2008; 103:19–28 CrossRef Medline
7. Wang R, Zhang D, Zhao J, et al. **A comparative study of 43 patients with mirror-like intracranial aneurysms: risk factors, treatment, and prognosis.** *Neuropsychiatr Dis Treat* 2014;10:2231–27 CrossRef Medline
8. Ferguson GG. **Physical factors in the initiation, growth, and rupture of human intracranial saccular aneurysms.** *J Neurosurg* 1972;37: 666–77 CrossRef Medline
9. Greving JP, Wermer MJ, Brown RD Jr, et al. **Development of the PHASES score for prediction of risk of rupture of intracranial aneurysms: a pooled analysis of six prospective cohort studies.** *Lancet Neurol* 2014;13:59–66 CrossRef Medline
10. Lu HT, Tan HQ, Gu BX, et al. **Risk factors for multiple intracranial aneurysms rupture: a retrospective study.** *Clin Neurol Neurosurg* 2013;115:690–94 CrossRef Medline
11. Frösen J, Tulamo R, Paetau A, et al. **Saccular intracranial aneurysm: pathology and mechanisms.** *Acta Neuropathol* 2012;123:773–86 CrossRef Medline
12. Cebral JR, Castro MA, Appanaboyina S, et al. **Efficient pipeline for image-based patient-specific analysis of cerebral aneurysm hemodynamics: technique and sensitivity.** *IEEE Trans Med Imag* 2005;24:457–67 CrossRef Medline
13. Castro MA, Putman CM, Cebral JR. **Patient-specific computational modeling of cerebral aneurysms with multiple avenues of flow from 3D rotational angiography images.** *Acad Radiol* 2006;13: 811–21 CrossRef Medline
14. Mut F, Aubry R, Löhner R, et al. **Fast numerical solutions of patient-specific blood flows in 3D arterial systems.** *Int J Num Meth Biomed Eng* 2010;26:73–85 CrossRef Medline
15. Cebral JR, Castro MA, Putman CM, et al. **Flow-area relationship in internal carotid and vertebral arteries.** *Physiol Meas* 2008;29:585–94 CrossRef Medline
16. Mut F, Löhner R, Chien A, et al. **Computational hemodynamics framework for the analysis of cerebral aneurysms.** *Int J Num Meth Biomed Eng* 2011;27:822–39 CrossRef Medline
17. Byrne G, Mut F, Cebral JR. **Quantifying the large-scale hemodynamics of intracanial aneurysms.** *AJNR Am J Neuroradiol* 2014;35: 333–38 CrossRef Medline
18. Wachter D, Kreitschmann-Andermahr I, Gilsbach JM, et al. **Early surgery of multiple versus single aneurysms after subarachnoid hemorrhage: an increased risk for cerebral vasospasm?** *J Neurosurg* 2011;114:935–41 CrossRef Medline
19. Overgaard J, Riishede J. **Multiple cerebral saccular aneurysms.** *Acta Neurol Scand* 1966;41:363–71 Medline
20. Hoh BL, Sistrom CL, Firment CS, et al. **Bottleneck factor and height-width ratio: association with ruptured aneurysms in patients with multiple cerebral aneurysms.** *Neurosurgery* 2007;61:716–22; discussion 722–33 CrossRef Medline
21. Humphrey JD, Canham PB. **Structure, mechanical properties, and mechanics of intracranial saccular aneurysms.** *Journal of Elasticity and the Physical Science of Solids* 2000;61:49–81
22. Sforza DM, Putman CM, Cebral JR. **Hemodynamics of cerebral aneurysms.** *Annu Rev Fluid Mech* 2009;41:91–107 CrossRef Medline
23. Fan J, Wang Y, Liu J, et al. **Morphological-hemodynamic characteristics of intracranial bifurcation mirror aneurysms.** *World Neurosurg* 2015;84:114–20.e112 CrossRef Medline
24. Huang ZQ, Meng ZH, Hou ZJ, et al. **Geometric parameter analysis of ruptured and unruptured aneurysms in patients with symmetric bilateral intracranial aneurysms: a multicenter CT angiography study.** *AJNR Am J Neuroradiol* 2016;37:1413–17 CrossRef Medline
25. Zhang Y, Yang X, Wang Y, et al. **Influence of morphology and hemodynamic factors on rupture of multiple intracranial aneurysms: matched-pairs of ruptured-unruptured aneurysms located unilaterally on the anterior circulation.** *BMC Neurol* 2014;14:253 CrossRef Medline
26. Jou LD, Morsi H, Shaltoni HM, et al. **Hemodynamics of small aneurysm pairs at the internal carotid artery.** *Med Eng Phys* 2012;34: 1454–61 CrossRef Medline
27. Cebral J, Ollikainen E, Chung BJ, et al. **Flow conditions in the intracranial aneurysm lumen are associated with inflammation and degenerative changes of the aneurysm wall.** *AJNR Am J Neuroradiol* 2017;38:119–26 CrossRef Medline
28. Robertson AM, Duan X, Hill MR, et al. **Diversity in the strength and structure of unruptured cerebral aneurysms.** *Ann Biomed Eng* 2014; 43:1502–15 CrossRef Medline
29. Cebral JR, Duan X, Chung BJ, et al. **Wall mechanical properties and hemodynamics of unruptured intracranial aneurysms.** *AJNR Am J Neuroradiol* 2015;36:1695–703 CrossRef Medline
30. Cebral JR, Duan X, Gade PS, et al. **Regional mapping of flow and wall characteristics of intracranial aneurysms.** *Ann Biomed Eng* 2016;44: 3553–67 CrossRef Medline
31. Cebral JR, Mut F, Weir J, et al. **Quantitative characterization of the hemodynamic environment in ruptured and unruptured brain aneurysms.** *AJNR Am J Neuroradiol* 2011;32:145–51 CrossRef Medline
32. Xiang J, Natarajan SK, Tremmel M, et al. **Hemodynamic-morphologic discriminants for intracranial aneurysm rupture.** *Stroke* 2011; 42:144–52 CrossRef Medline
33. Baharoglu MI, Lauric A, Gao BL, et al. **Identification of a dichotomy in morphological predictors of rupture status between sidewall- and bifurcation-type intracranial aneurysms.** *J Neurosurg* 2012;116: 871–81 CrossRef Medline

Endovascular Treatment of Vein of Galen Malformations: A Systematic Review and Meta-Analysis

W. Brinjikji, T. Krings, M.H. Murad, A. Rouchaud, and D. Meila

ABSTRACT

BACKGROUND: Outcomes after endovascular embolization of vein of Galen malformations remain relatively poorly described.

PURPOSE: We performed a systematic review of the literature to determine outcomes and predictors of good outcomes following endovascular treatment of vein of Galen malformations.

DATA SOURCES: We used Ovid MEDLINE, Ovid Embase, and the Web of Science.

STUDY SELECTION: Our study consisted of all case series with ≥4 patients receiving endovascular treatment of vein of Galen malformations published through January 2017.

DATA ANALYSIS: We studied the following outcomes: complete/near-complete occlusion rates, technical complications, perioperative stroke, perioperative hemorrhage, technical mortality, all-cause mortality, poor neurologic outcomes, and good neurologic outcomes. Outcomes were stratified by age-group (neonate, infant, child). A random-effects meta-analysis was performed.

DATA SYNTHESIS: A total of 27 series with 578 patients were included; 41.9% of patients were neonates, 45.0% of patients were infants, and 13.1% of patients were children. All-cause mortality was 14.0% (95% CI, 8.0%–22.0%). Overall good neurologic outcome rates were 62.0% (95% CI, 57.0%–67.0%). Overall poor neurologic outcome rates were 21.0% (95% CI, 17.0%–26.0%). Neonates were significantly less likely to have good neurologic outcomes than infants (48.0%; 95% CI, 35.0%–62.0% versus 77.0%; 95% CI, 70.0%–84.0%; $P < .01$). Treatment indications following the Bicêtre neonatal evaluation score resulted in significantly higher rates of good neurologic outcome ($P = .04$). Patients with congestive heart failure had significantly lower rates of good neurologic outcome (OR, 0.50; 95% CI, 0.28–0.88; $P = .01$).

LIMITATIONS: Limitations were selection and publication biases.

CONCLUSIONS: Patients receiving endovascular embolization of vein of Galen malformations experienced good long-term clinical outcomes in >60% of cases. Appropriate patient selection is key as treatment guided by the Bicêtre neonatal evaluation score was associated with improved neurologic outcomes.

ABBREVIATIONS: BNES = Bicêtre neonatal evaluation score; CHF = congestive heart failure; PRISMA = Preferred Reporting Items for Systematic Reviews and Meta-Analyses; VOGM = vein of Galen arteriovenous malformation

Vein of Galen arteriovenous malformations (VOGMs) are shunts that form in utero between the choroidal arteries and the precursor of the vein of Galen, the median prosencephalic vein of Markowski.[1-3] Current prevalence estimates of VOGM are quite low, often cited at <1 of 25,000 deliveries.[4,5] A number of studies have shown that the natural history of VOGMs is very poor, with many patients succumbing to complications related to congestive heart failure (CHF), hydrocephalus, and brain parenchymal injury.

Endovascular embolization of VOGMs has emerged as a standard of care in this patient population; however, long-term outcomes after endovascular embolization, as well as predictors of good neurologic outcomes, are still poorly understood.[2-4,6-47]

Received June 14, 2017; accepted after revision August 7.

From the Departments of Radiology (W.B.), Neurosurgery, (W.B.) and Center for the Science of Healthcare Delivery (M.H.M.), Mayo Clinic, Rochester, Minnesota; Division of Neuroradiology and Neurosurgery (W.B., T.K.), University of Toronto, Toronto Western Hospital and University Health Network, Toronto, Ontario, Canada; Neuroradiology Service (A.R.), Centre Hospitalier Universitaire Bicêtre, Le Kremlin Bicêtre, France; Department of Radiology and Neuroradiology (D.M.), Klinikum Duisburg, Duisburg, Germany; and Department of Diagnostic and Interventional Neuroradiology (D.M.), Medical School Hannover, Hannover, Germany.

Please address correspondence to Waleed Brinjikji, MD, Mayo Clinic, 200 First St SW, Rochester, MN 55905; e-mail: brinjikji.waleed@mayo.edu; brinjikji.waleed@gmail.com; @wbrinjikji

Indicates article with supplemental on-line tables.

http://dx.doi.org/10.3174/ajnr.A5403

Thus, to assess the status of endovascular treatment for VOGMs, we performed a systematic review and meta-analysis with an emphasis on determining factors associated with good neurologic outcome in this patient population.

MATERIALS AND METHODS

Literature Search

Our study adheres to Preferred Reporting Items for Systematic Reviews and Meta-Analyses (PRISMA; http://prisma-statement.org/) guidelines. To identify studies on outcomes of endovascular treatment of VOGMs, we performed a computerized MEDLINE search of the literature from January 1980 to January 2017. Three data bases were searched from January 1980 to April 2017: Ovid MEDLINE, Ovid Embase, and the Web of Science as described in On-line Table 1. Initial search terms included "Vein of Galen," "malformation," "aneurysm," "endovascular," "coil," "embolization," and "occlusion." Identified studies from the search were then further evaluated for inclusion in the systematic review. Inclusion criteria were the following: 1) studies reporting a consecutive series of endovascular treatment of VOGMs (≥4 patients), including case series and clinical trials; and 2) studies reporting angiographic and/or clinical outcomes following treatment. Case reports were excluded from this study. Two independent reviewers selected studies for this analysis.

Data Extraction and Outcomes

Each study was analyzed by 2 independent reviewers to collect the following data: 1) patient presentation (congestive heart failure, hydrocephalus, seizure); 2) patient demographics (age, sex); 3) treatment type (transarterial versus transvenous); 4) number of treatments/stages; 5) perioperative complications (technical mortality, perioperative ischemia, and perioperative hemorrhage); 6) complete/near-complete embolization rate; 7) long-term clinical outcomes, including good clinical outcome (defined as no or minor developmental delay and no permanent disability), poor clinical outcome, and all-cause mortality; and 8) angioarchitecture of the lesion (mural versus choroidal). The primary outcome of this study was good neurologic outcome rates. Good neurologic outcome was defined as a child with normal development.

In addition to determining overall rates of the outcomes listed above, we performed subgroup analyses dividing patients by age group. The 3 age groups studied were neonates (younger than 1 month of age), infants (1 month to 2 years of age), and children (2 years of age and older). We also performed subgroup analyses to determine whether the following variables were associated with rates of good neurologic outcome: 1) use of the Bicêtre neonatal evaluation score (BNES) for patient selection, 2) the presence of CHF, 3) a prenatal diagnosis of VOGM, 4) hydrocephalus, and 5) type of VOGM (mural versus choroidal). A subgroup analysis by follow-up time (≤2 years versus >2 years) was also performed.

Risk of Bias Assessment

Risk of bias assessment of the studies was performed with a modified Newcastle-Ottawa Scale. This tool is used for assessing the quality of nonrandomized studies included in systematic reviews and/or meta-analyses. Each study is judged on 8 items categorized into 3 groups: 1) selection of the study groups, 2) comparability of the study groups, and 3) ascertainment of the outcome of interest.[48] Factors that would make a study at low risk of bias would include the following: 1) well-defined selection criteria, 2) well-defined treatment regimen, 3) rates of long-term follow-up of >90% for surviving patients, and 4) age-based stratification of outcomes.

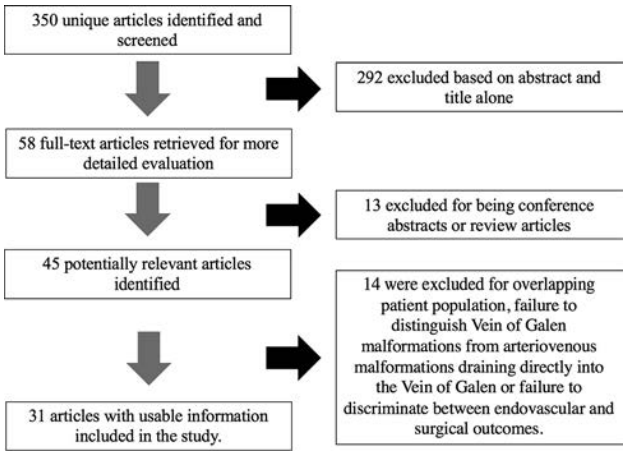

FIG 1. PRISMA flow diagram.

Statistical Analysis

We estimated, from each study, the cumulative incidence (event rate) and 95% confidence interval for each outcome. Event rates were pooled across studies with a random-effects meta-analysis.[49] Heterogeneity across studies was evaluated with the I^2 statistic.[50] Analysis of outcomes for children older than 2 years of age could not be performed due to the lack of sufficient studies. Analysis was conducted with STATA Statistical Software, Release 14 (StataCorp, College Station, Texas).

RESULTS

Literature Search, Study Characteristics, and Risk of Bias

The initial literature searched yielded 350 unique articles. On review of the abstracts and titles, 292 articles were immediately excluded. Fifty-eight articles were retrieved for full-text evaluation. Of these, 13 were excluded because they were review articles or conference abstracts with insufficent information. Forty-five articles were then evaluated. Of these, 14 were excluded for overlapping patient populations, failure to distinguish vein of Galen malformations from arteriovenous malformations draining directly into the vein of Galen, or failure to discriminate between endovascular and surgical outcomes. In total, 31 articles reflective of the experiences of 27 centers were included. There were 4 articles that had overlapping patient populations, but these were included because they provided additional data not available in other articles from the institution. In total, 578 unique patients were included. These findings are summarized in Fig 1.

Six institution experiences were found to have a low risk of bias, 7 institution experiences had a moderate risk of bias, and 14 studies had a high risk of bias. Eight institution experiences used the BNES in determining patient eligibility for treatment. The number of patients ranged from 4 to 216. Mean follow-up ranged from 0.5 to 6.8 years with a median of 2 years. These data are summarized in On-line Table 2.

Baseline Characteristics and Patient Presentation

The median age of patients included in this study was 0.1 month. Age data were available for 547 patients; 229 patients were neonates (41.9%), 246 patients were infants (45.0%), and 72 patients were children (13.2%). Sex data were available for 252 patients, and 173 patients (68.7%) were male. Patient presentation data were available for 318 patients. The most common presentation was CHF (201 patients, 63.2%), followed by hydrocephalus (86 patients, 27.0%) and seizure (37 patients, 11.6%). Intracranial hemorrhage was present in 26 patients (8.2%). An age-related breakdown of patient presentation is provided in Fig 2. Briefly, the most common presentation in neonates was CHF (88.2%). The most common presentation in infants and children was increased head circumference (53.3% and 37.5%, respectively). Angioarchitectural characteristics were available for 276 patients, with 103 being mural (37.3%) and 173 being choroidal (62.7%).

Angiographic Outcomes

Twelve studies primarily used transarterial embolization for treatment of VOGMs. The median number of treatments ranged from 1.5 to 4.1, with the overall median of included studies being 2.25; 27.9% of patients received 1 treatment, 29.1% received 2 treatments, and 43.0% received ≥3 treatments. The overall complete occlusion rate was 56.0% (95% CI, 46.0%–66.0%), with no difference between neonates and infants.

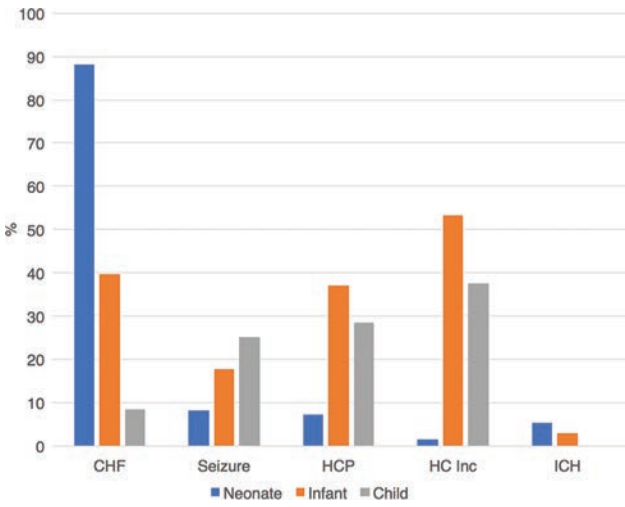

FIG 2. Presentation by age group. HCP indicates hydrocephalus; HC, head circumference; ICH, intracranial hemorrhage; inc, increase.

Perioperative Complications

The overall technical complication rate was 19.0% (95% CI, 12.0%–27.0%), with a trend toward a significantly higher rate of technical complications among neonates (29.0%; 95% CI, 17.0%–41.0%) compared with infants (10.0%; 95% CI, 0.0%–27.0%; $P = .07$). Overall perioperative hemorrhage rates were 9.0% (95% CI, 4.0%–15.0%), with no difference between age groups ($P = .25$). Overall perioperative ischemia rates were 1.0% (95% CI, 0.0%–2.0%), with a higher rate among neonates (3.0%; 95% CI, 0.0%–10.0%) compared with infants (0.0%; 95% CI, 0.0%–2.0%; $P = .03$). Non-neurologic complicate rates were 2.0% (95% CI, 0.0%–4.0%), with no difference among groups ($P = 1.0$). The overall technical mortality rate was 1.0% (95% CI, 0.0%–5.0%), with higher rates in neonates (2.0%; 95% CI, 0.0%–8.0%) than in infants (0.0%; 95% CI, 0.0%–2.0%; $P = .03$). These data are summarized in the Table.

Long-Term Outcomes

The overall rate of good neurologic outcome was 62.0% (95% CI, 57.0%–67.0%). Neonates had significantly lower rates of good neurologic outcomes (48.0%; 95% CI, 35.0%–62.0%) compared with infants (77.0%; 95% CI, 70.0%–84.0%; $P < .0001$). Overall rates of poor neurologic outcome were 21.0% (95% CI, 17.0%–26.0%), with higher rates among neonates (22.0%; 95% CI, 15.0%–31.0%) compared with infants (16.0%; 95% CI, 10.0%–23.0%; $P = .01$). The all-cause mortality rate was 14.0% (95% CI, 8.0%–20.0%), with significantly higher rates among neonates (27.0%; 95% CI, 15.0%–41.0%) compared with infants (1.0%; 95% CI, 0.0%–4.0%; $P < .0001$). These data are summarized in the Table. The forest plot for good neurologic outcomes is provided in Fig 3.

Follow-Up Time, Patient Selection, and Baseline Characteristics and Outcomes

Seven studies reported the use of the BNES in selecting patients for treatment of VOGMs. Studies that reported the use of the BNES had significantly higher rates of good neurologic outcome than those that did not (62%; 95% CI, 50.0%–72.0% versus 57%; 95% CI, 51.0%–65.0%; $P = .04$).

Patients with CHF were significantly less likely to experience good neurologic outcomes than those without CHF (49.4%; 95% CI, 21.7%–57.1% versus 66.2%; 95% CI, 55.1%–75.8%; $P = .01$). Patients with hydrocephalus (61.0%; 95% CI, 45.7%–74.4%) had similar rates of good neurologic outcome as those without it (62.0%; 95% CI, 53.4%–70.0%; $P = .92$). Patients with mural-

Systematic review outcomes

	Overall Rate (95% CI)	I^2 (%)	Neonate Rate (95% CI)	I^2 (%)	Infant Rate (95% CI)	I^2 (%)	*P* Value, Neonate vs Infant
Technical complications	19.0 (12.0–27.0)	48.9	29.0 (17.0–41.0)	7	10.0 (0.0–27.0)	45	.07
Perioperative hemorrhage	9.0 (4.0–15.0)	52	12.0 (3.0–23.0)	21	4.0 (0.0–16.0)	21	.25
Perioperative ischemia	1.0 (0.0–2.0)	0	3.0 (0.0–10.0)	0	0.0 (0.0–2.0)	0	.03
Non-neurologic complications	2.0 (0.0–4.0)	0	1.0 (0.0–7.0)	0	1.0 (0.0–8.0)	0	1
Technical mortality	1.0 (0.0–5.0)	37	2.0 (0.0–8.0)	0	0.0 (0.0–2.0)	10	.03
Complete occlusion	56.0 (46.0–66.0)	49	59.0 (45.0–73.0)	0	56.0 (17.0–91.0)	74	1
All-cause mortality	14.0 (8.0–20.0)	47	27.0 (15.0–41.0)	57	1.0 (0.0–4.0)	0	<.0001
Poor neurologic outcome	21.0 (17.0–26.0)	0	22.0 (15.0–31.0)	0	16.0 (10.0–23.0)	0	.01
Good neurologic outcome	62.0 (57.0–67.0)	3	48.0 (35.0–62.0)	50	77.0 (70.0–84.0)	0	<.0001

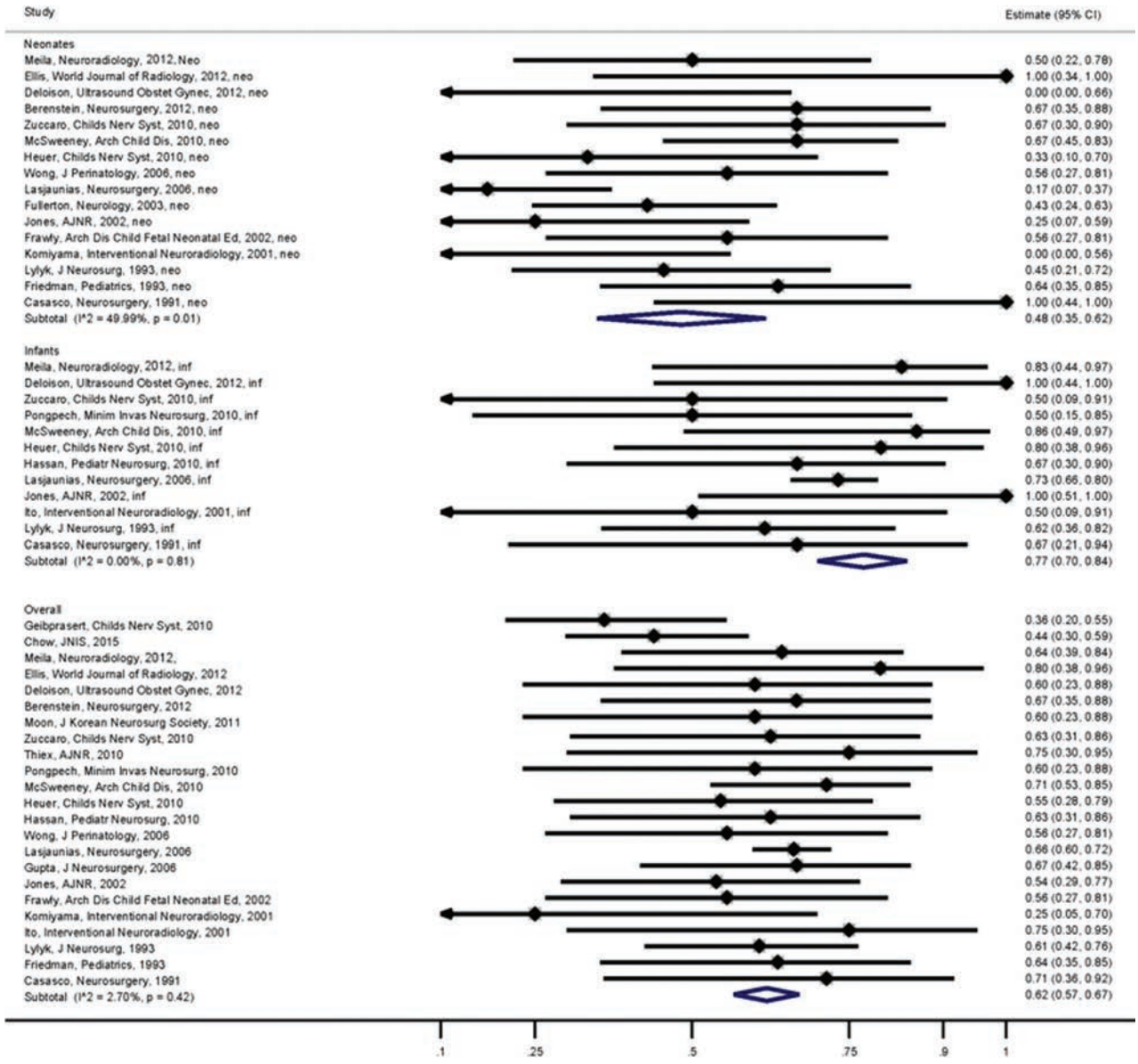

FIG 3. Forest plot for good neurologic outcome.

type VOGMs had a good neurologic outcome rate of 73.8% (95% CI, 59.0%–84.7%) compared with 58.0% (95% CI, 47.2%–68.2%) for choroidal VOGMs ($P = .11$). There was no association between a prenatal diagnosis and good neurologic outcome (66.7%; 95% CI, 53.7%–77.5% versus 63.1%; 95% CI, 50.9%–73.8%; $P = .68$).

There was a wide range in the follow-up times across studies, from 6 months to 6.8 years. The median follow-up time was 2 years, and the median age at which follow-up was performed was 2 years. Studies that reported a follow-up of >2 years had a good neurologic outcome rate of 60.3% (95% CI, 55.1%–65.3%), while studies reporting a follow-up of ≤2 years reported a good neurologic outcome rate of 64.6% (95% CI, 54.6%–73.4%) ($P = .45$).

Study Heterogeneity

When we considered all patients, I^2 values were >50%, indicating substantial heterogeneity for perioperative hemorrhage. I^2 values were <50% for all other outcomes, indicating lack of substantial heterogeneity. When we considered neonates, I^2 values were >50%, indicating substantial heterogeneity for all-cause mortality. I^2 values were <50% for all other outcomes, indicating a lack of substantial heterogeneity. When we considered infants, I^2 values were >50%, indicating substantial heterogeneity for complete occlusion. I^2 values were <50% for all other outcomes, indicating a lack of substantial heterogeneity. These data are summarized in the Table.

DISCUSSION

Our study of >500 patients receiving endovascular treatment for VOGMs demonstrated many interesting findings. First, the most common presentation varied substantially by age of presentation as neonates were more likely to present with symptoms related to CHF, while infants were more likely to present with head circumference increases or hydrocephalus. Given the poor natural history of VOGMs and the poor functional status of many patients

who require treatment for these lesions, rates of good long-term neurologic outcomes were satisfactory at >60%. Patients who underwent treatment during the neonatal period were less likely to have a good neurologic outcome than those who were treated later in life, likely due to poorer cardiologic status at presentation and increased severity of disease. Perioperative complications were not negligible and were more frequent in neonates than in infants. However, procedure-related mortality rates were low. We found that patients who were treated according to the Bicêtre guidelines were more likely to experience good outcomes than those who were not; this finding highlights the importance of patient selection. Overall, our results suggest that endovascular treatment of VOGMs is generally safe and effective and can result in good long-term outcomes for patients in experienced centers. However, an emphasis on patient selection and timing is key.

As demonstrated in our study, the principal clinical manifestations of VOGMs are related to high-output cardiac failure or neurologic symptoms secondary to venous congestion and abnormal CSF flow.[4,23,35,36] CHF is the most common clinical presentation for neonates and is rarely the presenting symptom in infants or children because these patients often have fewer severe cardiac symptoms. In our study, approximately 90% of patients treated in the neonatal stage had CHF compared with 40% of patients treated in the infant stage. Many of the treated infants with CHF had medical stabilization of CHF during neonatal life with delay of treatment later in the first or second year of life. CHF can manifest itself on prenatal sonography or soon after birth, with symptoms ranging from mild overload to multisystem organ failure secondary to cardiogenic shock. On the contrary, patients with mild cardiac dysfunction may not have their VOGMs recognized until later in life when cerebral venous hypertension results in intracranial hypertension and subsequent macrocrania and hydrocephalus. As demonstrated in our study, >50% of infants presented with macrocrania and nearly 40% presented with hydrocephalus. Other neurologic presentations, including seizure and intracranial hemorrhage, are present in roughly 20% and 10% of patients, respectively, with increased prevalence as age increases.

One of the important findings from our study was that studies that used a predefined selection criteria, the BNES, demonstrated higher rates of good neurologic outcome than those that did not.[23] These findings highlight the importance of appropriate patient selection to ensure good neurologic outcomes. The BNES is a 21-point score that assesses a combination of cardiac, neurologic, respiratory, hepatic, and renal functions.[51] Patients with a score of ≤8 are thought to be poor candidates for endovascular treatment, and typically the recommendation is to withhold therapy from these patients. In the series of Lasjaunias et al, 30% of all neonates and 17% of all infants had treatment withheld due to such low scores. A score between 8 and 12 indicates normal neurologic function but cardiac function that is refractory to medical management and, thus, emergency embolization, regardless of patient age. In the Lasjaunias series, only 25% of neonates met these criteria and underwent emergent embolization.[51] However, in these patients, all-cause mortality was high and rates of good neurologic outcome were relatively low. Patients with a neonatal score of 13–21 could have embolization delayed until 3–5 months of age with stabilization of their cardiac function. This population comprised about two-thirds of patients in the series of Lasjaunias et al.[51] Our study found that close to 50% of treated patients were treated in the neonatal stage, while only 5% of treated patients in the series of Lasjaunias et al[23] were neonates.

The high proportion of neonates treated in our study implies that there may be a reflexive instinct to treat neonates presenting with VOGM at some centers without allowing a trial of medical stabilization. Such practice patterns may be detrimental to patients because treatment of neonates is associated with higher rates of technical complications and lower rates of good neurologic outcomes; and in select cases in which the neonate can be stabilized, delaying treatment for a few months may confer a benefit on the patient.[23] Ultimately, due to the complex medical needs of this patient population, an argument can be made for centralization of medical and endovascular treatment for these patients.

Due to substantial heterogeneity and lack of specifics in reporting technical details of embolization procedures, we were unable to perform an extensive evaluation of the safety and efficacy of various techniques in the treatment of VOGMs.[23] However, there are a few important implications from our study. First, as mentioned above, technical complications are more common in neonates than infants, likely due to a combination of smaller size, vascular fragility, and a more tenuous hemodynamic state. While most of the included studies predominantly treated patients transarterially, several series reported the exclusive use of transvenous or transtorcular techniques.[27,37,45] Earlier series were more likely to report exclusive transvenous treatment or transtorcular embolization than more modern series however. In general, isolated transvenous treatment is thought to result in higher rates of technical complications due to higher rates of postoperative venous infarction, hemorrhage, and consumptive coagulopathy.[19,23] Transtorcular embolization has become less and less common during the past decade due to extraordinarily high rates of such complications. Ultimately, treatment should be tailored to the angioarchitecture of the lesion and available routes for embolization.[9] When we considered all patients, complete occlusion rates were approximately 60%. Complete occlusion should not necessarily be the goal of VOGM embolization; rather, improvement in the physiologic and neurologic status of the patient should be the primary treatment goal.

Limitations

Our study has limitations. Ecologic bias (ie, comparisons are made across studies and not within studies), the presence of publication bias, and statistical heterogeneity are limitations that affect all meta-analyses. Our study also had limitations due to the methodologic limitations of included studies. All included studies were retrospective case series, which are prone to substantial selection bias. The use of the BNES in selecting patients also introduced selection bias because patients in whom treatment was thought to be futile were excluded in those studies. Little is known regarding the outcomes of patients who were untreated. It is also conceivable that with advancements in techniques and experience, many of the patients who were excluded on the basis of the BNES could now be treated. Many of the included studies had a small sample size and incomplete follow-up data. In some cases,

definitions of outcomes (ie, good neurologic outcome, complete occlusion, technical versus all-cause mortality, and so forth) were not well-defined. In addition, many of the series in our analysis included cases collected during several years. It is possible that complication rates have improved because of increased operator experience and skill, improved patient selection, and improved devices and technology. We do not have enough data to determine clinical and angiographic outcomes by type of embolic agent used. Last, it is difficult to sort out short- and long-term morbidity and mortality related to the pathology of the underlying VOGM itself and of endovascular treatment.

CONCLUSIONS

Endovascular embolization of VOGMs can be successfully performed; however, complications are not negligible. Patient selection and timing of treatment are key to achieving good clinical outcomes. Further work is needed to provide improved outcomes associated with endovascular treatment of VOGMs. Large multiinstitutional registries may be helpful for collecting data in a standardized manner on the presentation and outcomes of these patients. Ultimately, these treatments are extremely challenging and should probably be reserved for centers with expertise in pediatric critical care and neurointervention.

REFERENCES

1. Raybaud CA, Strother CM, Hald JK. **Aneurysms of the vein of Galen: embryonic considerations and anatomical features relating to the pathogenesis of the malformation.** *Neuroradiology* 1989;31:109–28 CrossRef Medline
2. Moon JH, Cho WS, Kang HS, et al. **Vein of Galen aneurysmal malformation: endovascular management of 6 cases in a single institute.** *J Korean Neurosurg Soc* 2011;50:191–94 CrossRef Medline
3. Berenstein A, Fifi JT, Niimi Y, et al. **Vein of Galen malformations in neonates: new management paradigms for improving outcomes.** *Neurosurgery* 2012;70:1207–13; discussion 13–14 CrossRef Medline
4. Lasjaunias P, Hui F, Zerah M, et al. **Cerebral arteriovenous malformations in children: management of 179 consecutive cases and review of the literature.** *Childs Nerv Syst* 1995;11:66–79; discussion 79 CrossRef Medline
5. Frawley GP, Dargaville PA, Mitchell PJ, et al. **Clinical course and medical management of neonates with severe cardiac failure related to vein of Galen malformation.** *Arch Dis Child Fetal Neonatal Ed* 2002;87:F144–49 CrossRef Medline
6. Lin N, Smith ER, Scott RM, et al. **Safety of neuroangiography and embolization in children: complication analysis of 697 consecutive procedures in 394 patients.** *J Neurosurg Pediatr* 2015;16:432–38 CrossRef Medline
7. Kim DJ, Kim BM, Park KY, et al. **Adjuvant coil assisted glue embolization of high flow vein of Galen aneurysmal shunt lesions in pediatric patients.** *Interv Neuroradiol* 2015;21:315
8. Chow ML, Cooke DL, Fullerton HJ, et al. **Radiological and clinical features of vein of Galen malformations.** *J Neurointerv Surg* 2015;7:443–48 CrossRef Medline
9. Meila D, Hannak R, Feldkamp A, et al. **Vein of Galen aneurysmal malformation: combined transvenous and transarterial method using a "kissing microcatheter technique."** *Neuroradiology* 2012;54:51–59 CrossRef Medline
10. Ellis JA, Orr L, Ii PC, et al. **Cognitive and functional status after vein of Galen aneurysmal malformation endovascular occlusion.** *World J Radiol* 2012;4:83–89 CrossRef Medline
11. Deloison B, Chalouhi GE, Sonigo P, et al. **Hidden mortality of prenatally diagnosed vein of Galen aneurysmal malformation: retrospective study and review of the literature.** *Ultrasound Obstet Gynecol* 2012;40:652–58 CrossRef Medline
12. Li AH, Armstrong D, terBrugge KG. **Endovascular treatment of vein of Galen aneurysmal malformation: management strategy and 21-year experience in Toronto.** *J Neurosurg Pediatr* 2011;7:3–10 CrossRef Medline
13. Zuccaro G, Argañaraz R, Villasante F, et al. **Neurosurgical vascular malformations in children under 1 year of age.** *Childs Nerv Syst* 2010;26:1381–94 CrossRef Medline
14. Thiex R, Williams A, Smith E, et al. **The use of Onyx for embolization of central nervous system arteriovenous lesions in pediatric patients.** *AJNR Am J Neuroradiol* 2010;31:112–20 CrossRef Medline
15. Pongpech S, Aurboonyawat T, Visudibhan A, et al. **Endovascular management in children with vein of Galen aneurysmal malformation.** *Minim Invasive Neurosurg* 2010;53:169–74 CrossRef Medline
16. McSweeney N, Brew S, Bhate S, et al. **Management and outcome of vein of Galen malformation.** *Arch Dis Child* 2010;95:903–09 CrossRef Medline
17. Heuer GG, Gabel B, Beslow LA, et al. **Diagnosis and treatment of vein of Galen aneurysmal malformations.** *Childs Nerv Syst* 2010;26:879–87 CrossRef Medline
18. Hassan T, Nassar M, Elghandour M. **Vein of Galen aneurysms: presentation and endovascular management.** *Pediatr Neurosurg* 2010;46:427–34 CrossRef Medline
19. Geibprasert S, Krings T, Armstrong D, et al. **Predicting factors for the follow-up outcome and management decisions in vein of Galen aneurysmal malformations.** *Childs Nerv Syst* 2010;26:35–46 CrossRef Medline
20. Berenstein A, Ortiz R, Niimi Y, et al. **Endovascular management of arteriovenous malformations and other intracranial arteriovenous shunts in neonates, infants, and children.** *Childs Nerv Syst* 2010;26:1345–58 CrossRef Medline
21. Staberg M, Jonsbo F. **Vein of Galen aneurysm (VGA) diagnosed in the perinatal period: a retrospective assessment** [in Danish]. *Ugeskr Laeger* 2007;169:3190–93 Medline
22. Wong FY, Mitchell PJ, Tress BM, et al. **Hemodynamic disturbances associated with endovascular embolization in newborn infants with vein of Galen malformation.** *J Perinatol* 2006;26:273–78 CrossRef Medline
23. Lasjaunias PL, Chng SM, Sachet M, et al. **The management of vein of Galen aneurysmal malformations.** *Neurosurgery* 2006;59(5 suppl 3):S184–94; discussion S3–13 Medline
24. Gupta AK, Rao VR, Varma DR, et al. **Evaluation, management, and long-term follow up of vein of Galen malformations.** *J Neurosurg* 2006;105:26–33 CrossRef Medline
25. Fullerton HJ, Aminoff AR, Ferriero DM, et al. **Neurodevelopmental outcome after endovascular treatment of vein of Galen malformations.** *Neurology* 2003;61:1386–90 CrossRef Medline
26. Jones BV, Ball WS, Tomsick TA, et al. **Vein of Galen aneurysmal malformation: diagnosis and treatment of 13 children with extended clinical follow-up.** *AJNR Am J Neuroradiol* 2002;23:1717–24 Medline
27. Frawley GP, Dargaville PA, Mitchell PJ, et al. **Clinical course and medical management of neonates with severe cardiac failure related to vein of Galen malformation.** *Arch Dis Child Fetal Neonatal Ed* 2002;87:F144–49 CrossRef Medline
28. Chevret L, Durand P, Alvarez H, et al. **Severe cardiac failure in newborns with VGAM: prognosis significance of hemodynamic parameters in neonates presenting with severe heart failure owing to vein of Galen arteriovenous malformation.** *J Intensive Care Med* 2002;28:1126–30 CrossRef Medline
29. Mitchell PJ, Rosenfeld JV, Dargaville P, et al. **Endovascular management of vein of Galen aneurysmal malformations presenting in the neonatal period.** *AJNR Am J Neuroradiol* 2001;22:1403–09 Medline
30. Komiyama M, Nakajima H, Nishikawa M, et al. **Vein of Galen aneurysms: experience with eleven cases.** *Interv Neuroradiol* 2001;7(suppl 1):99–103 CrossRef Medline
31. Ito O, Goto K, Ogata N, et al. **Selection of endovascular approach of**

vein of Galen aneurysmal malformation. *Interv Neuroradiol* 2001; 7(suppl 1):187–92 CrossRef Medline
32. Meyers PM, Halbach VV, Phatouros CP, et al. **Hemorrhagic complications in vein of Galen malformations.** *Ann Neurol* 2000;47:748–55 Medline
33. Halbach VV, Dowd CF, Higashida RT, et al. **Endovascular treatment of mural-type vein of Galen malformations.** *J Neurosurg* 1998;89: 74–80 CrossRef Medline
34. Borthne A, Carteret M, Baraton J, et al. **Vein of Galen vascular malformations in infants: clinical, radiological and therapeutic aspect.** *Eur Radiol* 1997;7:1252–58 CrossRef Medline
35. Lasjaunias PL, Alvarez H, Rodesch G, et al. **Aneurysmal malformations of the vein of Galen: follow-up of 120 children treated between 1984 and 1994.** *Interv Neuroradiol* 1996;2:15–26 CrossRef Medline
36. Rodesch G, Hui F, Alvarez H, et al. **Prognosis of antenatally diagnosed vein of Galen aneurysmal malformations.** *Childs Nerv Syst* 1994;10:79–83 CrossRef Medline
37. Lylyk P, Viñuela F, Dion JE, et al. **Therapeutic alternatives for vein of Galen vascular malformations.** *J Neurosurg* 1993;78: 438–45 CrossRef Medline
38. Friedman DM, Verma R, Madrid M, et al. **Recent improvement in outcome using transcatheter embolization techniques for neonatal aneurysmal malformations of the vein of Galen.** *Pediatrics* 1993;91: 583–86 Medline
39. Lasjaunias P, Garcia-Monaco R, Rodesch G, et al. **Vein of Galen malformation: endovascular management of 43 cases.** *Childs Nerv Syst* 1991;7:360–67 CrossRef Medline
40. Garcia-Monaco R, De Victor D, Mann C, et al. **Congestive cardiac manifestations from cerebrocranial arteriovenous shunts: endovascular management in 30 children.** *Childs Nerv Syst* 1991;7:48–52 CrossRef Medline
41. Friedman DM, Madrid M, Berenstein A, et al. **Neonatal vein of Galen malformations: experience in developing a multidisciplinary approach using an embolization treatment protocol.** *Clin Pediatr (Phila)* 1991;30:621–29 CrossRef Medline
42. Casasco A, Lylyk P, Hodes JE, et al. **Percutaneous transvenous catheterization and embolization of vein of Galen aneurysms.** *Neurosurgery* 1991;28:260–66 CrossRef Medline
43. Ciricillo SF, Edwards MS, Schmidt KG, et al. **Interventional neuroradiological management of vein of Galen malformations in the neonate.** *Neurosurgery* 1990;27:22–27; discussion 27–28 CrossRef Medline
44. Lasjaunias P, Rodesch G, Terbrugge K, et al. **Vein of Galen aneurysmal malformations: report of 36 cases managed between 1982 and 1988.** *Acta Neurochir (Wien)* 1989;99:26–37 CrossRef Medline
45. Hanner JS, Quisling RG, Mickle JP, et al. **Gianturco coil embolization of vein of Galen aneurysms: technical aspects.** *Radiographics* 1988;8:935–46 CrossRef Medline
46. Johnston IH, Whittle IR, Besser M, et al. **Vein of Galen malformation: diagnosis and management.** *Neurosurgery* 1987; 20:747–58 CrossRef Medline
47. Burrows PE, Lasjaunias PL, Ter Brugge KG, et al. **Urgent and emergent embolization of lesions of the head and neck in children: indications and results.** *Pediatrics* 1987;80:386–94 Medline
48. Deeks JJ, Dinnes J, D'Amico R, et al; International Stroke Trial Collaborative Group; European Carotid Surgery Trial Collaborative Group. **Evaluating non-randomised intervention studies.** *Health Technol Asses* 2003;7:iii–x, 1–173 Medline
49. DerSimonian R, Laird N. **Meta-analysis in clinical trials.** *Control Clin Trials* 1986;7:177–88 CrossRef Medline
50. Higgins JP, Thompson SG, Deeks JJ, et al. **Measuring inconsistency in meta-analyses.** *BMJ* 2003;327:557–60 CrossRef Medline
51. Alvarez H, Garcia Monaco R, Rodesch G, et al. **Vein of Galen aneurysmal malformations.** *Neuroimaging Clin N Am* 2007;17:189–206 CrossRef Medline

Pial Artery Supply as an Anatomic Risk Factor for Ischemic Stroke in the Treatment of Intracranial Dural Arteriovenous Fistulas

S.W. Hetts, A. Yen, D.L. Cooke, J. Nelson, P. Jolivalt, J. Banaga, M.R. Amans, C.F. Dowd, R.T. Higashida, M.T. Lawton, H. Kim, and V.V. Halbach

ABSTRACT

BACKGROUND AND PURPOSE: Although intracranial dural arteriovenous fistulas are principally supplied by dural branches of the external carotid, internal carotid, and vertebral arteries, they can also be fed by pial arteries that supply the brain. We sought to determine the frequency of neurologic deficits following treatment of intracranial dural arteriovenous fistulas with and without pial artery supply.

MATERIALS AND METHODS: One hundred twenty-two consecutive patients who underwent treatment for intracranial dural arteriovenous fistulas at our hospital from 2008 to 2015 were retrospectively reviewed. Patient data were examined for posttreatment neurologic deficits; patients with such deficits were evaluated for imaging evidence of cerebral infarction. Data were analyzed with multivariable logistic regression.

RESULTS: Of 122 treated patients, 29 (23.8%) had dural arteriovenous fistulas with pial artery supply and 93 (76.2%) had dural arteriovenous fistulas without pial arterial supply. Of patients with pial artery supply, 4 (13.8%) had posttreatment neurologic deficits, compared with 2 patients (2.2%) without pial artery supply ($P = .04$). Imaging confirmed that 3 patients with pial artery supply (10.3%) had cerebral infarcts, compared with only 1 patient without pial artery supply (1.1%, $P = .03$). Increasing patient age was also positively associated with pial supply and treatment-related complications.

CONCLUSIONS: Patients with dural arteriovenous fistulas supplied by the pial arteries were more likely to experience posttreatment complications, including ischemic strokes, than patients with no pial artery supply. The approach to dural arteriovenous fistula treatment should be made on a case-by-case basis so that the risk of complications can be minimized.

ABBREVIATION: DAVF = dural arteriovenous fistula

Intracranial dural arteriovenous fistulas (DAVFs) are vascular malformations that connect meningeal arteries to dural venous sinuses or cortical veins. DAVFs account for 10%–15% of all intracranial arteriovenous shunting lesions.[1-14] DAVFs are often thought to be acquired, sometimes in the setting of hypercoagulability.[15] DAVF venous drainage determines the natural history risk of spontaneous intracranial hemorrhage. Thus, venous drainage is incorporated into the most commonly used grading systems of DAVF natural history risk: the Borden-Shucart and Cognard grading scales.[2,3] Drainage to cortical veins is the highest risk category because pressurization of these thin-walled venous structures frequently leads to rupture. Although venous angioarchitecture is a key determinant of natural history risk, the risk of endovascular and/or surgical treatment of DAVFs in the modern era related to underlying lesion angioarchitecture is not well-known.

Although DAVFs are most commonly fed by dural branches of the internal carotid, external carotid, and vertebral arteries, they can also have pial artery supply. Pial arteries lie on the surface of the brain. They then branch into penetrating arteries and parenchymal arterioles that lie within and supply the brain parenchyma. The mechanism of pial feeder formation is not well-understood but is believed to be like that of dural feeders, with increased vascular endothelial growth factor secretion from the venous sinus and abnormal angiogenesis.[16-24] Embolization of pial AVFs has been suggested to lead to the development of subsequent DAVFs in up to 25% of cases.[25,26] The inflammatory reaction within the DAVF vessel wall after embolization may also lead to angiogenesis.[27]

Received February 28, 2017; accepted after revision August 3.

From the Department of Radiology and Biomedical Imaging (S.W.H., D.L.C., P.J., M.R.A., C.F.D., R.T.H., V.V.H.), School of Medicine (A.Y., J.B.), Departments of Anesthesia and Perioperative Care (J.N., P.J., C.F.D., R.T.H., H.K., V.V.H.), Neurological Surgery (C.F.D., R.T.H., M.T.L., V.V.H.), and Neurology (C.F.D., R.T.H., V.V.H.), University of California, San Francisco, San Francisco, California.

Paper previously presented, in part, at: Annual Meeting of the American Society of Neuroradiology, May 21–26, 2016; Washington, DC.

Please address correspondence to Steven W. Hetts, MD, 505 Parnassus Ave, L-352, San Francisco, CA 94143; e-mail: steven.hetts@ucsf.edu

Indicates article with supplemental on-line tables.

http://dx.doi.org/10.3174/ajnr.A5396

Transarterial embolization of DAVFs with pial artery supply with agents that can migrate retrograde (ie, from the dural arteries to the pial arteries) could thus block blood supply to the associated brain parenchyma and cause ischemia. Surgical or endovascular point occlusion of DAVFs with pial artery supply at the fistula site might also result in retrograde thrombosis of feeding pial arteries due to decreased flow. We hypothesized that patients with DAVFs with pial artery supply have a higher risk of postoperative stroke than those who do not have pial supply.

MATERIALS AND METHODS

Patient Population

All patients undergoing neurointerventional procedures at the University of California, San Francisco hospitals are prospectively enrolled in an institutional review board–approved research data base. Patients in this study were treated at the University of California, San Francisco Medical Center or San Francisco General Hospital between 2008 and 2015. We compiled a cohort of 122 consecutive patients with intracranial DAVFs.

Data Collection

Retrospective analysis was conducted on 122 patients with DAVFs examined with digital subtraction angiography and treated with embolization and/or an operation at the University of California, San Francisco. Clinical information was extracted from electronic medical records and radiologic imaging reports. Pretreatment presentations, neurointerventional treatments, surgical treatments, and posttreatment outcomes were abstracted from the electronic medical records. Of note, all patients in our series were anticoagulated with intravenous heparin during our embolization procedures. All patients' initial and posttreatment DSA examinations were interpreted by an experienced interventional neuroradiologist and scored according to a structured angiographic case report form originally developed for brain AVMs by Atkinson et al[7] and subsequently modified for intracranial DAVFs, including the Borden-Shucart and Cognard venous drainage scales.[1-3,6] We have used this form in our prior studies of intracranial dural and pial arteriovenous fistulas[8,26] and have chosen to use it again for consistency and comparability among studies. Radiologic studies (including MR imaging and CT) at each phase in the patients' treatments were assessed for imaging complications and correlation with clinical complications. Neurologic outcomes were individually tabulated and scored with the modified Rankin Scale of disability.

Patient data were examined for postembolization and postsurgical neurologic complications that resulted in strokelike symptoms, including cranial nerve palsies, altered mental status, focal weakness, decreased sensation, and speech or hearing difficulties. From this subset of patients with strokelike symptoms, imaging data were further examined for evidence of cerebral infarction. For analysis, strokes were considered a subset of neurologic deficits, which were, in turn, considered a subset of major complications.

Statistical Analysis

Patient characteristics, DAVF classifications, treatment modalities, and treatment-related outcomes were summarized for all patients, patients with DAVF with pial supply, and patients with DAVF without pial supply. We tested whether patient characteristics were associated with pial supply using a 2-sample t test for continuous variables. The Fisher exact test was used for nominal categoric variables; and logistic regression, for ordinal categoric variables. We treated the Borden-Shucart (grades I, II, and III) and Cognard (grades I, IIa, IIb, IIa+b, III, IV, V) venous drainage natural history scales as ordinal variables, because they increase numerically as the angioarchitectural complexity of the fistula increases; Cognard grades IIa, IIb, and IIa+b were grouped together during analysis. The modified Rankin Scale was also analyzed as an ordinal variable. We performed multivariable logistic regression analysis with any major complication as the outcome and with pial supply, age, and an operation as predictors. Given the small number of stroke and neurologic deficit events, they were not analyzed as separate outcomes in multivariable analysis. We considered P values $\leq .05$ statistically significant. Data analysis was conducted with STATA 13.1 (StataCorp, College Station, Texas).

RESULTS

Patient Population

Summary statistics are presented in On-line Table 1. Of 122 patients, 29 (24%) had DAVFs with pial supply. The average age at treatment of the study population was 59 years, and about half were women. Patients with pial-supply DAVFs were slightly older (63 versus 58 years of age, $P = .049$). There was an association of Borden-Shucart and Cognard grades with the presence of pial artery supply: the higher the Borden-Shucart score, the more likely it was that the DAVF had a pial supply (OR = 1.72, $P = .035$). For the Cognard grading system, higher grade DAVFs were more likely to have pial supply, but this finding was not significant (OR = 1.31, $P = .135$). Patients with DAVFs with pial supply also tended to have poorer pretreatment mRS assessment outcomes, but not significantly so (OR = 1.22, $P = .131$).

Modes and Outcomes of Treatment

Most patients (70%) were treated with embolization exclusively. Pial supply was not associated with the type of treatment (embolization versus an operation versus a combination of embolization and an operation) received ($P = .267$). When we compared an operation versus no operation (irrespective of embolization), patients with DAVFs with pial supply were more likely to have undergone an operation (41%, 12/29 patients) than those without pial supply (26%, 24/93 patients), but this difference was not statistically significant ($P = .160$). However, DAVFs with pial supply were significantly more likely to receive transarterial embolization than those without a pial supply (92% [24/26 patients] versus 59% [51/86 patients], $P = .002$). DAVFs with pial supply were less likely to be fully cured on the basis of posttreatment angiography (55% [16/29 patients] versus 76% [71/93 patients], $P = .035$).

Major Complications, Neurologic Deficits, and Strokes

As outlined above, strokes were considered a subset of neurologic deficits, which were, in turn, considered a subset of major complications. Four treatment-related strokes, 6 neurologic deficits, and 15 major complications were observed. Specific characteris-

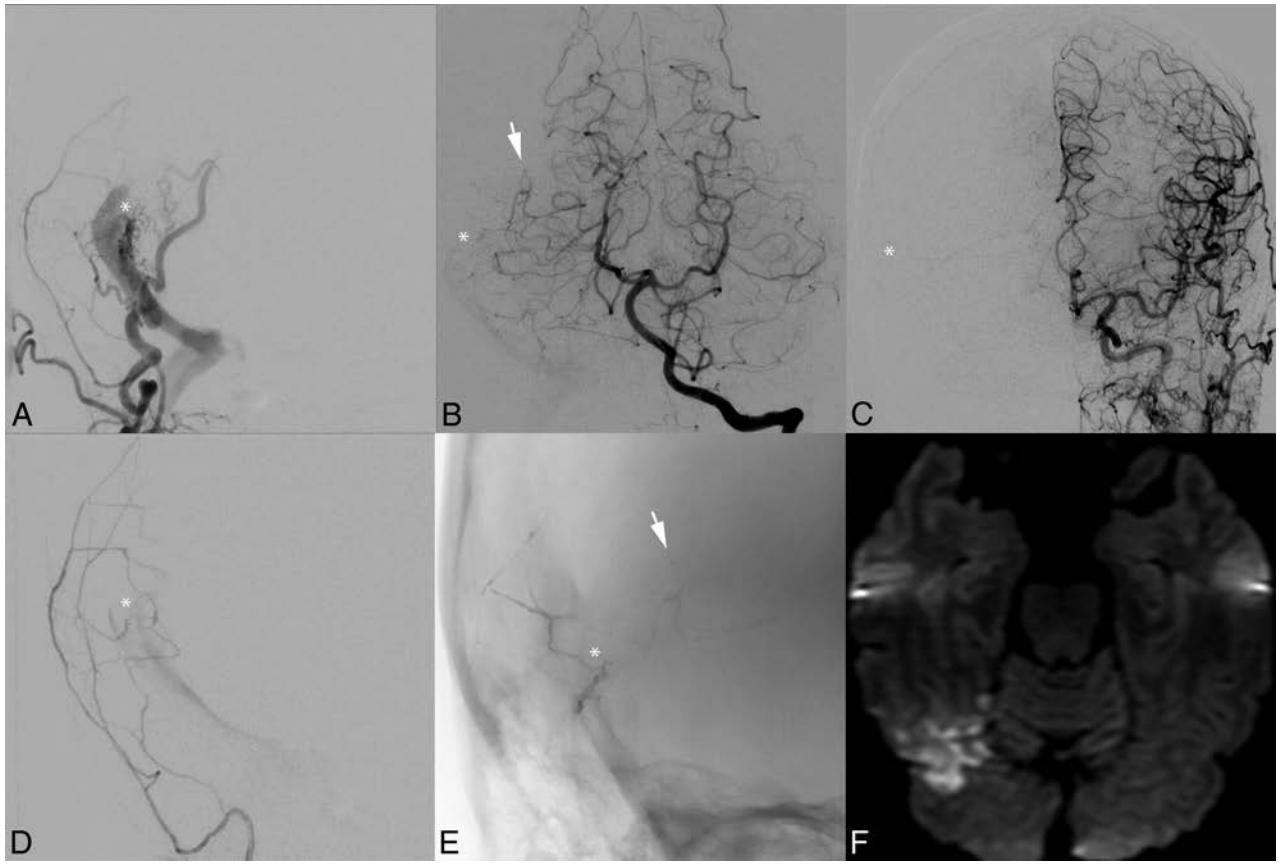

FIG 1. Postembolization infarction due to Onyx migration into a pial artery. A middle-aged woman with severe pulsatile tinnitus underwent endovascular therapy for a right transverse-sigmoid sinus junction Borden-Shucart grade I DAVF supplied principally by the middle meningeal and occipital arteries (*A*) and secondarily by the ipsilateral middle temporal artery (*B*) and tentorial branches from the contralateral middle meningeal artery (*C*). The fistula site is designated by a *white asterisk*. The fusiform gyrus branch of the middle temporal artery is indicated by a *white arrow*. Superselective injection of the right middle meningeal artery demonstrates the fistula site before embolization (*D*). Midembolization x-ray (*E*) demonstrates Onyx in the middle meningeal artery, fistula site, and refluxed into the pial fusiform gyrus branch of the middle temporal artery. The extent of reflux had not been evident on real-time intraprocedural blank roadmap imaging. DWI later the same day (*F*) demonstrates a fusiform gyrus infarction.

tics of patients who had symptomatic ischemic strokes are detailed in On-line Tables 2 and 3, and details regarding all patients with major complications are included in On-line Table 4. DAVFs with pial supply were associated with more strokes (10% versus 1%, $P = .041$), neurologic deficits (14% versus 2%, $P = .028$), and major complications (28% versus 8%, $P = .008$). Pial supply remained associated with major complications in multivariable analysis (OR = 3.66, $P = .030$), when adjusting for age (OR = 1.45 per decade increase, $P = .166$) and an operation (OR = 3.36, $P = .044$).

DISCUSSION

Intracranial DAVFs are rare, and a small subset are supplied by not only dural arteries but also pial arteries. Because pial arteries also supply the brain parenchyma, blockage of blood flow through pial arteries can potentially cause an ischemic stroke. Indeed, we found that DAVFs supplied by pial arteries are associated with a higher risk of developing neurologic deficits, stroke, and major complications after treatment. Furthermore, patients with pial supply tended to be slightly older than patients without pial supply, and increasing age was significantly associated with posttreatment complications. Pial supply to the DAVFs appears to be a marker for greater complexity and the potential for complications, possibly due to several mechanisms, including retrograde reflux of liquid embolics to pial vessels (Fig 1), periprocedural hypercoagulability (Fig 2), retrograde thrombosis of pial arteries (Fig 3), and venous infarction with hemorrhage (Fig 4). To date, DAVF grading scales (eg, Borden-Shucart and Cognard) have focused on natural history risk for venous rupture, not on the risk of treatment. Identifying consistent risk factors for adverse outcomes following treatment is the first step in establishing a grading scale for treatment risk of DAVFs in the modern endovascular and surgical era, akin to what has been done with great success for brain AVMs with the Spetzler-Martin and Lawton-Young supplementary grading scales for surgical treatment risk.[9,16]

The criterion standard for identifying and treating DAVFs is conventional angiography, followed by embolization of the fistula when possible and an operation when embolization is not possible or is incomplete, particularly with lesions with a high natural history risk for rupture. In the past, DAVFs were treated with a combination of multiple embolic agents, including detachable coils, ethanol, *n*-BCA glue, silk sutures, and polyvinyl alcohol particles.[7,10,11,14] The recent emergence of ethylene-vinyl alcohol copolymer (Onyx; Covidien, Irvine, California) has allowed the use

of a single transarterial embolic agent in many cases.[13] A large series of DAVF treatments from the Barrow Neurological Institute[5] recently demonstrated a higher initial occlusion rate via embolization from a single arterial pedicle in the Onyx era compared with the pre-Onyx era, with a similar permanent neurologic complication rate (2% pre-Onyx versus 3% post-Onyx). If initial embolization is unsuccessful or incomplete, subsequent embolizations or craniotomy with surgical clipping or resection can be performed. Although rare, some DAVFs have a very aggressive clinical course and can progress or recur.[6]

Onyx is a liquid embolic agent that has been used more frequently for embolization of DAVFs and AVMs in recent years. Its emergence has allowed the use of a single agent and has caused the use of ethanol, detachable coils, and *n*-BCA glue to decline. Because Onyx is a liquid agent, its path throughout the vasculature cannot always be perfectly controlled, particularly if the Onyx is poorly seen against the bones of the skull base on real-time road-mapping (Fig 1). We believe that the mechanism by which at least some of the strokes reported above occur involves retrograde reflux of Onyx from pial artery feeders to the DAVF into segments of pial arteries that do not supply the DAVF but instead supply the brain parenchyma. This subsequently blocks blood flow to portions of the brain parenchyma and causes infarction. A potential technique to prevent dural-to-pial reflux of Onyx is prophylactically sealing the distal pial arteries supplying a DAVF, for example, by navigating a flow catheter as distal as possible and using *n*-BCA glue to seal off the pial connections into the DAVF. This technique has been advocated to lower hemorrhage risk in a DAVF operation.[17] Such an approach, however, poses a risk for retrograde thrombosis of the pial feeding artery. Thus, if the pial feeding artery supplies an eloquent region of the brain, this technique may pose a risk of stroke in and of itself. Given the long track record of safe transvenous coil embolization of intracranial DAVFs, our practice is to use this technique when possible, particularly if the pial artery supply to a fistula is identified.

Reflux of Onyx does not explain infarctions that occurred after the operation. Instead, precise surgical ligation of

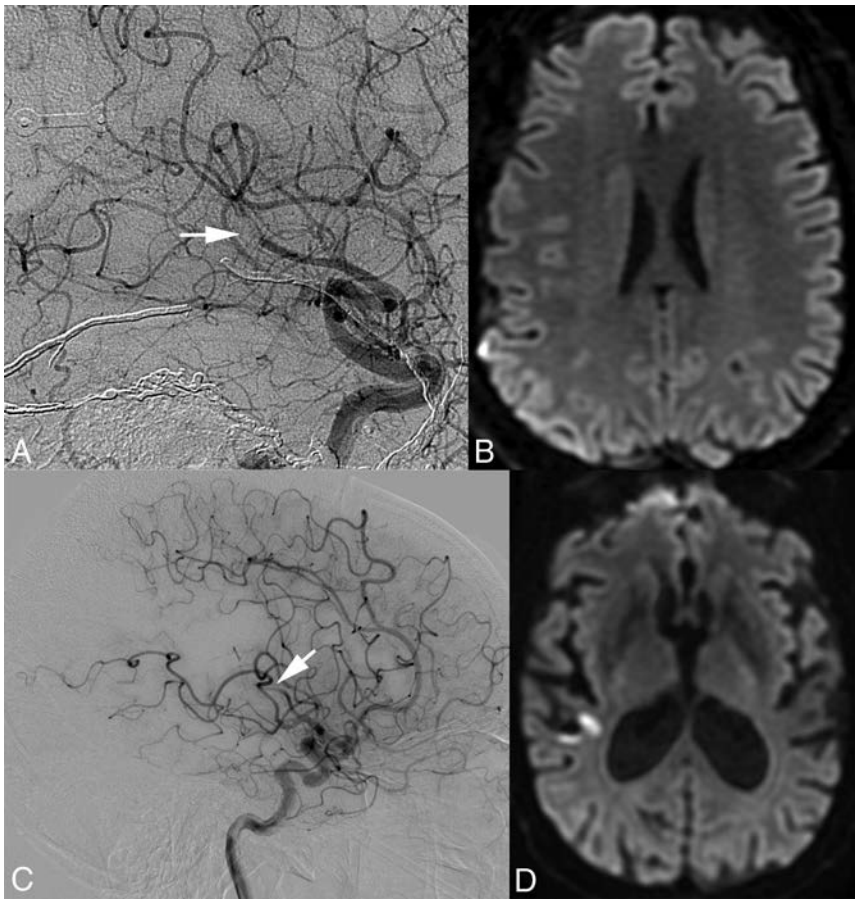

FIG 2. Arterial emboli following endovascular and surgical treatments of DAVFs in 2 patients. Two middle-aged male patients undergoing posttreatment angiography were identified as having middle cerebral artery emboli (*A* and *C*, *white arrows*). Both patients were heparinized, and the second patient underwent superselective intra-arterial tPA treatment with minimal clot lysis. Postangiographic DWIs (*B* and *D*) demonstrate small cortical infarctions in territories associated with the MCA emboli. Although the first patient's MCA thrombus (*A* and *B*) is adjacent to the original DAVF, the second patient's is not (*C* and *D*).

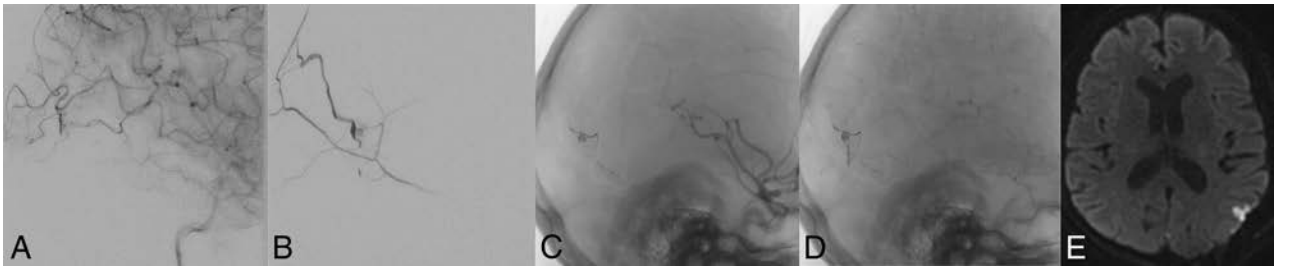

FIG 3. Postsurgical seizure and small cortical infarction after surgical ligation of a residual DAVF. A middle-aged woman status 1 year post temporal lobe hemorrhage underwent endovascular therapy for a Borden-Shucart grade III DAVF supplied principally by the left middle meningeal artery (*B*) and secondarily by pial branches of the left MCA (*A*), with drainage directly to a cortical vein. Onyx embolization eliminated the middle meningeal artery dural supply (*C*), but late-phase angiographic images demonstrated persistent MCA pial supply (*D*). Three days following a craniotomy for successful ligation of the residual DAVF, the patient had a seizure. MR imaging at that time demonstrates a small cortical infarction (*E*).

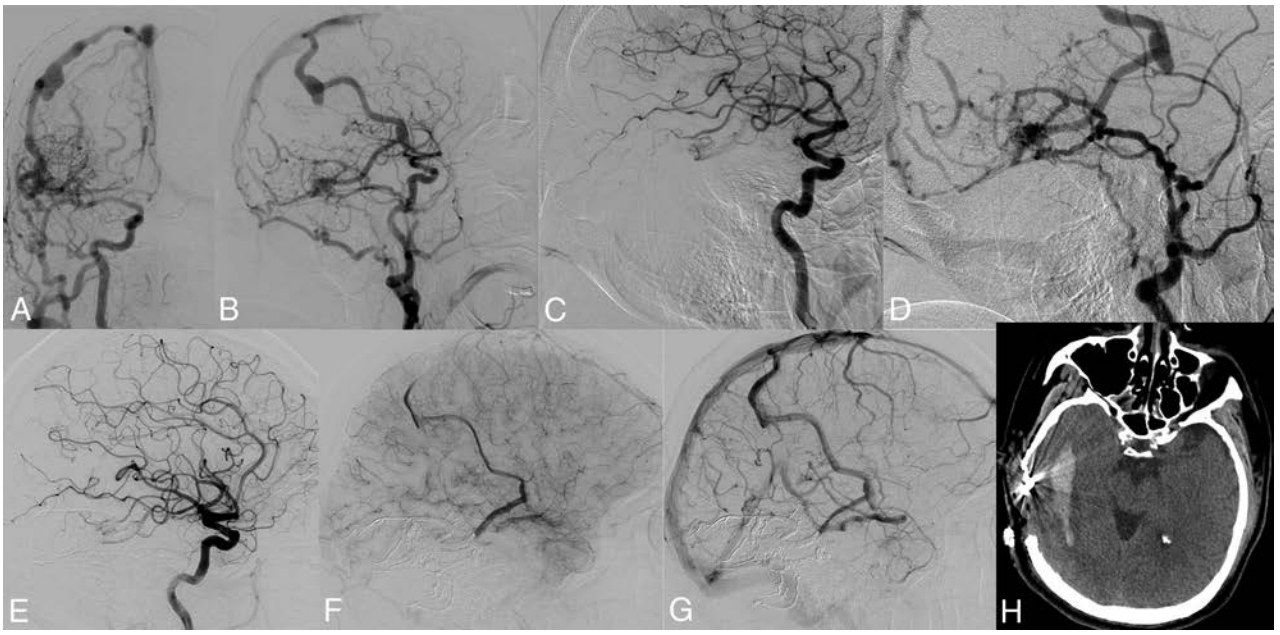

FIG 4. Postoperative parenchymal hemorrhage and possible venous infarction following surgical ligation of a residual DAVF. A middle-aged man had intermittent speech arrest and multiple headaches for several years. Anteroposterior (*A*) and lateral (*B*) angiograms demonstrate a variant-type right transverse-sigmoid sinus junction Borden-Shucart grade III DAVF supplied by dural branches of the external carotid artery and pial branches of the MCA (*C*) with retrograde drainage to the vein of Labbé (*D*), that anastomotically drains to the vein of Trolard. Following Onyx embolization of the dural external carotid artery branches, only the pial MCA supply to the fistula continued to drain to the cortical vein as demonstrated on early (*E*), mid (*F*), and late (*G*) images from a lateral ICA angiogram. During surgical ligation of the residual DAVF, extensive intraoperative bleeding was noted. A CT performed immediately postoperatively (*H*) demonstrates right temporal intraparenchymal hemorrhage. The patient did not have a new neurologic deficit postoperatively.

a fistula site with significant pial supply will interrupt flow in the distal pial artery just proximal to the fistula site. This flow arrest in the pial feeder to the DAVF may result in retrograde thrombosis of the pial artery feeder to the next most proximal arterial branch-point. In our experience, this has led to a few small cortical infarctions. Underlying patient hypercoagulability (a risk factor for DAVF formation in the first place) might also play a role in postoperative retrograde feeding artery thrombosis (Fig 3) as well as parent artery emboli (Fig 2); thus, pial supply may also be an indirect marker for a higher risk of thromboembolic complications separate from those seen intraprocedurally.

Recently, DAVFs with pial artery supply were shown to result in intraoperative hemorrhage in 33% of patients[17]—significantly more than in patients with DAVFs without pial artery supply. Although symptomatic intraoperative hemorrhage was not seen in any of our cases (though an asymptomatic hemorrhage is shown in Fig 4), it helps support our assertion that DAVFs with pial artery supply carry a higher operative risk, and treatment should be approached with appropriate caution.

There were several limitations to this study. It was a retrospective review conducted at a single institution during an 8-year time span. Although the patient population consisted of 122 subjects, the low rate of clinical complications may affect the reliability of inferring statistical significance. Certain comparisons that are not statistically significant, given the small sample size, may, in fact, prove to be clinically significant. If a patient had a radiographic abnormality (eg, focal reduced diffusion on an MR imaging after DAVF) but not a neurologic deficit on clinical examination, the patient would not have been captured in our initial screen for complications, potentially reducing the number of complications identified. However, given that clinical complications are the focus of our analysis, we deemed this approach to be appropriate. Because our institution receives many outside referrals, our patient population may consist of higher risk cases, more complex lesions, and lesions that require staged multimodal treatments tailored to the natural history risk of each unique fistula. In some cases, we choose to stop short of lesion cure to avoid potential complications. Finally, follow-up was highly variable, and subsequent delayed complications may not have been available to us.

CONCLUSIONS

A small subset of intracranial DAVFs is supplied not only by dural arteries but also by pial arteries, raising the potential for increased risk of stroke or major complications during embolization or an operation. Special attention must be paid to the treatment of DAVFs with pial artery supply to minimize the potential for complications. Preprocedural counseling of patients and their families about the elevated treatment risk of DAVFs found to have a pial supply (often evident only on DSA) is prudent and may influence treatment decisions.

Disclosures: Steven W. Hetts—*UNRELATED*: *Grants/Grants Pending*: Siemens, Stryker, MicroVention Terumo, *Comments*: research contracts*; *Royalties*: Penumbra, *Comments*: royalty agreement for a device.* Matthew R. Amans—*UNRELATED*: *Consultancy*: Medtronic. Christopher F. Dowd—*UNRELATED*: *Other*: MicroVention, *Comments*: I serve as Chief Adjudicator for the FRED Trial*. *Money paid to the institution.

REFERENCES

1. Newton TH, Cronqvist S. **Involvement of the dural arteries in intracranial arteriovenous malformations.** *Radiology* 1969;93:1071–78 CrossRef Medline

2. Cordonnier C, Al-Shahi Salman R, Bhattacharya JJ, et al; IVMS Collaborators. **Differences between intracranial vascular malformation types in the characteristics of their presenting haemorrhages: prospective, population-based study.** *J Neurol Neurosurg Psychiatry* 2008;79:47–51 CrossRef Medline
3. Lasjaunias P, Manelfe C, Chiu M. **Angiographic architecture of intracranial vascular malformations and fistulas: pretherapeutic aspects.** *Neurosurg Rev* 1986;9:253–63 CrossRef Medline
4. Singh V, Smith WS, Lawton MT, et al. **Risk factors for hemorrhagic presentation in patients with dural arteriovenous fistulae.** *Neurosurgery* 2008;62:628–35; discussion 628–35 CrossRef Medline
5. Borden JA, Wu JK, Shucart WA. **A proposed classification for spinal and cranial dural arteriovenous fistulous malformations and implications for treatment.** *J Neurosurg* 1995;82:166–79 CrossRef Medline
6. Cognard C, Gobin YP, Pierot L, et al. **Cerebral dural arteriovenous fistulas: clinical and angiographic correlation with a revised classification of venous drainage.** *Neuroradiology* 1995;194:671–80 CrossRef Medline
7. Atkinson RP, Awad IA, Batjer HH, et al; Joint Writing Group of the Technology Assessment Committee American Society of Interventional and Therapeutic Neuroradiology; Joint Section on Cerebrovascular Neurosurgery a Section of the American Association of Neurological Surgeons and Congress of Neurological Surgeons; Section of Stroke and the Section of Interventional Neurology of the American Academy of Neurology. **Reporting terminology for brain arteriovenous malformation clinical and radiographic features for use in clinical trials.** *Stroke* 2001;32:1430–42 CrossRef Medline
8. Hetts SW, Tsai T, Cooke DL, et al. **Progressive versus nonprogressive intracranial dural arteriovenous fistulas: characteristics and outcomes.** *AJNR Am J Neuroradiol* 2015;36:1912–19 CrossRef Medline
9. Lawton MT, Kim H, McCullouch CE, et al. **A supplementary grading scale for selecting patients with brain arteriovenous malformations for surgery.** *Neurosurgery* 2010;66:702–13; discussion 713 CrossRef Medline
10. Spetzler RF, Martin NA. **A proposed grading system for arteriovenous malformations.** *J Neurosurg* 1986;65:476–83 CrossRef Medline
11. Hu YC, Newman CB, Dashti SR, et al. **Cranial dural arteriovenous fistula: transarterial Onyx embolization experience and technical nuances.** *J Neurointerv Surg* 2011;3:5–13 CrossRef Medline
12. Loh Y, Duckwiler GR; Onyx Trial Investigators. **A prospective, multicenter, randomized trial of the Onyx liquid embolic system and N-butyl cyanoacrylate embolization of cerebral arteriovenous malformations: clinical article.** *J Neurosurg* 2010;113:733–41 CrossRef Medline
13. McConnell K, Tjoumakaris S, Allen J, et al. **Neuroendovascular management of dural arteriovenous malformations.** *Neurosurg Clin N Am* 2009;20:431–39 CrossRef Medline
14. Signorelli F, Gory B, Maduri R, et al. **Intracranial dural arteriovenous fistulas: a review of current management based on emerging knowledge.** *J Neurosurg Sci* 2017;61:193–206 CrossRef Medline
15. Saraf R, Shrivastava M, Kumar N, et al. **Embolization of cranial dural arteriovenous fistulae with ONYX: indications, techniques, and outcomes.** *Indian J Radiol Imaging* 2010;20:26–33 CrossRef Medline
16. Gross BA, Albuquerque FC, Moon K, et al. **Evolution of treatment and a detailed analysis of occlusion, recurrence, and clinical outcomes in an endovascular library of 260 dural arteriovenous fistulas.** *J Neurosurg* 2017;126:1884–93 CrossRef Medline
17. Wu Q, Zhang XS, Wang HD, et al. **Onyx embolization for tentorial dural arteriovenous fistula with pial arterial supply: case series and analysis of complications.** *World Neurosurg* 2016;92:58–64 CrossRef Medline
18. Uranishi R, Nakase H, Sakaki T. **Expression of angiogenic growth factors in dural arteriovenous fistula.** *J Neurosurg* 1999;91:781–86 CrossRef Medline
19. Gupta A, Periakaruppan A. **Intracranial dural arteriovenous fistulas: a review.** *Indian J Radiol Imaging* 2009;19:43–48 CrossRef Medline
20. Shin Y, Nakase H, Nakamura M, et al. **Expression of angiogenic growth factor in the rat DAVF model.** *Neurol Res* 2007;29:727–33 CrossRef Medline
21. Tirakotai W, Bertalanffy H, Liu-Guan B, et al. **Immunohistochemical study in dural arteriovenous fistulas and possible role of local hypoxia for the de novo formation of dural arteriovenous fistulas.** *Clin Neurol Neurosurg* 2005;107:455–60 CrossRef Medline
22. Wang SS, Li CH, Zhang XJ, et al. **Investigation of the mechanism of dural arteriovenous fistula formation induced by high intracranial venous pressure in a rabbit model.** *BMC Neurosci* 2014;15:101 CrossRef Medline
23. Li Q, Zhang Q, Huang QH, et al. **A pivotal role of the vascular endothelial growth factor signaling pathway in the formation of venous hypertension-induced dural arteriovenous fistulas.** *Mol Med Rep* 2014;9:1551–58 CrossRef Medline
24. Lee JY, Son YJ, Kim KE. **Intracranial pial arteriovenous fistulas.** *J Korean Neurosurg Soc* 2008;44:101–04 CrossRef Medline
25. Paramasivam S, Toma N, Niimi Y, et al. **De novo development of dural arteriovenous fistula after endovascular embolization of pial arteriovenous fistula.** *J Neurointerv Surg* 2013;5:321–26 CrossRef Medline
26. Hetts SW, Keenan K, Fullterton HJ, et al. **Pediatric intracranial nongalenic pial arteriovenous fistulas: clinical features, angioarchitecture, and outcomes.** *AJNR Am J Neuroradiol* 2012;33:1710–19 CrossRef Medline
27. Buell TJ, Ding D, Starke RM, et al. **Embolization-induced angiogenesis in cerebral arteriovenous malformations.** *J Clin Neurosci* 2014;21:1866–71 CrossRef Medline

Association between Carotid Plaque Features on CTA and Cerebrovascular Ischemia: A Systematic Review and Meta-Analysis

H. Baradaran, K. Al-Dasuqi, A. Knight-Greenfield, A. Giambrone, D. Delgado, E.J. Ebani, H. Kamel, and A. Gupta

ABSTRACT

BACKGROUND: CTA is a widely available imaging examination that may allow the evaluation of high-risk carotid plaque features.

PURPOSE: Our aim was to evaluate the association between specific carotid plaque features on CTA and ipsilateral cerebrovascular ischemia.

DATA SOURCES: We performed a systematic review of Ovid MEDLINE, Ovid Embase, Scopus, and the Cochrane Library from inception to March 2016 for articles that evaluated the relationship between CTA-detected carotid plaque features and ischemic events, defined as ipsilateral ischemic stroke or transient ischemic attack.

STUDY SELECTION: Sixteen studies were ultimately included after screening 12,557.

DATA ANALYSIS: Two readers recorded data from each study and assessed the study quality with all disagreements resolved by a third reader. A random-effects OR was used to evaluate the association between cerebrovascular ischemia and each of the evaluated plaque features.

DATA SYNTHESIS: We found significant positive relationships with cerebrovascular ischemia for the presence of soft plaque (OR, 2.9; 95% CI, 1.4–6.0), plaque ulceration (OR, 2.2; 95% CI, 1.4–3.4), and increased common carotid artery wall thickness (OR, 6.2; 95% CI, 2.5–15.6). We found a significant negative relationship between calcified plaque and ipsilateral ischemia (OR, 0.5; 95% CI, 0.4–0.7).

LIMITATIONS: We found heterogeneity in the existing literature secondary to lack of standardized plaque features and clinical definitions.

CONCLUSIONS: Soft plaque, plaque ulceration, and increased common carotid artery wall thickness on CTA are associated with ipsilateral cerebrovascular ischemia, while calcified plaque is negatively associated with downstream ischemic events.

ABBREVIATION: US = ultrasound

Given recent improvement in medical treatment, patients with asymptomatic carotid artery stenosis receiving modern intensive medical therapy now face an annual risk of stroke of ~1%.[1] Given the limitations of stenosis measurements alone in identifying patients at highest risk of ischemic stroke, recent investigations using vessel wall imaging techniques have attempted to provide more detailed characterization of vulnerable plaque features. Specific plaque features, such as intraplaque hemorrhage on MR imaging and echolucent plaque on ultrasound (US), have been identified as risk factors for future ischemic stroke, which, when considered along with stenosis severity and other factors, may help to identify those patients most likely to benefit from surgical revascularization procedures.[2,3]

CTA is a potentially attractive tool for plaque imaging because it is less operator-dependent than US and is more quickly performed and more widely available than MR imaging.[4] Easily identifiable plaque

Received January 17, 2017; accepted after revision June 30.

From the Department of Radiology (H.B., K.A.-D., A.K.-G., E.J.E., A.G.); Clinical and Translational Neuroscience Unit (H.B., H.K., A.G.), Feil Family Brain and Mind Research Institute (H.K., A.G.); Department of Healthcare Policy and Research (A.G.); Samuel J. Wood Library and C.V. Starr Biomedical Information Center (D.D.); and Department of Neurology (H.K.), Weill Cornell Medicine, New York, New York.

Dr Ajay Gupta is supported by the National Institutes of Health/National Center for Advancing Translational Sciences grant No. KL2TR000458, and Dr Hooman Kamel is supported by the National Institutes of Health/National Institute of Neurological Disorders and Stroke grant No. K23NS082367.

Please address correspondence to Ajay Gupta, MD, 525 East 68th St, Box 141, Starr 8A, New York, NY; e-mail: ajg9004@med.cornell.edu

Indicates open access to non-subscribers at www.ajnr.org
Indicates article with supplemental on-line appendix and tables.
Indicates article with supplemental on-line photos.
http://dx.doi.org/10.3174/ajnr.A5436

features on CTA such as the presence of low attenuation, calcification, and plaque ulceration have been histopathologically validated as markers of high-risk plaque features.[4-6] Although CTA has significant potential to evaluate plaque features, small studies have not reached a consensus regarding plaque features, and high-resolution 3T MR imaging techniques have been favored. We aimed to perform a systematic review and meta-analysis to evaluate the association between multiple specific carotid artery plaque features seen on CTA and cerebrovascular ischemic events.

MATERIALS AND METHODS

We performed this systematic review and meta-analysis according to the guidelines from the Meta-Analysis of Observational Studies in Epidemiology group[7] and the Preferred Reporting Items for Systematic Reviews and Meta-Analyses (PRISMA) statement.[8]

Data Searches

A medical librarian performed a comprehensive literature search in multiple electronic databases, including Ovid MEDLINE, Ovid Embase, Scopus, and the Cochrane Library from inception to March 9, 2016. We searched first in Ovid MEDLINE and then adapted subject headings and key words for other databases and identified additional records using the "Cited by" and "View references" features in Scopus (see On-line Appendix for search methodology details).

Study Selection and Eligibility

We included studies evaluating the association between various plaque features on CTA and symptomatic cerebrovascular ischemic events, defined as either prior or future transient ischemic attack or stroke in the vascular territory supplied by the index carotid artery. Specific inclusion criteria were the following: 1) studies that evaluated patients with plaque in the extracranial internal carotid artery; 2) studies using CTA of the common and cervical internal carotid arteries to assess specific plaque features; 3) studies that correlated the questioned plaque features with symptomatic status, defined as either stroke or transient ischemic attack in the vascular territory supplied by the index carotid artery; 4) studies that included asymptomatic control carotid arteries, either by comparing with the asymptomatic contralateral carotid artery (within-subject controls) or asymptomatic subjects (between-subject controls). If it appeared that authors published data from a single cohort or medical center more than once, the article with the largest sample size was included to minimize duplicate or overlapping samples. We attempted to contact the corresponding authors for additional details when necessary.

Data Extraction

All potentially eligible titles and abstracts were reviewed by a single reader. Two independent readers screened articles in their entirety to determine eligibility for inclusion. Data were extracted by 2 independent readers using a prespecified data-collection template. A third reader resolved any disagreements about data extraction. The readers extracted the following data: study design; basic study demographics for included patients, including risk factors for stroke; definitions of ischemic stroke; specific CTA imaging techniques; and definitions of plaque features.

We also answered specific questions to evaluate potential selection, detection, reporting, or confounding bias using a risk-of-bias assessment like that in previously published meta-analyses.[2,9] The risk of bias was assessed by consensus among 3 readers.

Data Analysis

Meta-analyses of the individual study odds ratios were conducted with StatsDirect statistical software (Version 2.7.9; July 9, 2012; http://www.statsdirect.com). Each pooled OR was calculated with a random-effects (DerSimonian and Laird) model, and forest plots were generated to display the individual study odds ratios and the pooled OR. Random-effects models were used to combine the studies because of the potential of variability in the outcome of interest among the studies. To assess the combinability of the OR, we calculated the P value from the Cochrane Q and I^2 statistical heterogeneity tests. The results of each study were expressed as an OR with a 95% confidence interval. For each meta-analysis with >3 studies, the presence of publication bias was evaluated through a funnel plot. The Begg and Mazumdar rank-correlation test was used to statistically assess the presence of publication bias. All P values $< .05$ were considered significant.

RESULTS

Study Characteristics

After screening 12,557 titles and abstracts, we identified 20 studies that were ultimately included in the systematic review (On-line Fig 1).[6,10-28] Of the 20 articles meeting the inclusion criteria for systematic review, 13 were retrospective, cross-sectional studies[6,10-12,14-18,20,21,24,28] and 7 were prospective, cross-sectional studies.[13,19,22,23,25-27] The time interval between the onset of ischemic symptoms and CTA ranged from 2 weeks to 6 months for those studies that provided these data (On-line Table 1).[14,20,22,23] We found no studies evaluating the association between CTA plaque features and future ischemic events. Seven studies were performed in the United States[6,10,11,18,20,24,28]; 3, in Japan[14,22,23]; 3, in Italy[15-17]; 2, in the Netherlands[19,27]; and 1 each, in Canada,[21] France,[13] China,[26] Germany,[25] and Spain.[12] The mean age of patients in the included studies ranged from 62 to 75.1 years. All studies had a preponderance of male subjects with a percentage range of men from 53.7% to 92.3%. There was a range of degree of ICA stenosis, with 6 studies requiring patients to have at least 50% stenosis,[11,13,14,16,23,25] 2 studies requiring patients to have at least 60% stenosis,[10,12] and 2 studies requiring patients to have at least 70% stenosis.[20,29] Six studies evaluated all patients with CTA examinations regardless of their degree of stenosis,[15,18,19,21,24,26] while 2 studies focused only on patients with mild-to-moderate (30%–69%) stenosis,[22,27] and 1 study focused only on patients with moderate (50%–69%) stenosis.[28] An additional study included those patients with at least 70% stenosis, symptomatic patients with at least 50% stenosis, and all symptomatic patients with evidence of plaque ulceration regardless of the degree of stenosis (On-line Table 2).[11]

Twelve studies were performed on at least a 16–detector row helical CT scanner,[11,14,18-20,22-24,26-29] while only 7 studies included patients who may have been scanned on a 4– or 8–detector row CT scanner.[10,12,13,15-17,21] One study did not provide the relevant number of rows (On-line Table 3).[25]

Of those 20 studies included for systematic review, 16 studies were eligible for meta-analysis in which 2624 patients with 3933 unique carotid arteries were analyzed. The 4 studies excluded from the meta-analysis were not amenable to calculating pooled standardized mean differences because of methodologic differences in calculating volumes, variability in plaque-feature definitions, and small sample sizes for each calculation and included studies that quantitatively evaluated the volume of soft/noncalcified plaque, the volume of calcified plaque, and Hounsfield units (On-line Table 4).

Although specific definitions varied, patients were symptomatic if they had a prior ischemic stroke or TIA in the vascular territory supplied by the carotid artery in question (On-line Table 1). Strokes were generally defined as the patient having had a persistent episode of neurologic dysfunction with confirmatory imaging in the distribution of the carotid artery, while TIAs were defined as brief episodes (<24 hours) of neurologic dysfunction, also within the carotid artery distribution.

Definitions of Plaque Features

From the included studies, we were able to collect the actual number of cerebrovascular events for patients with each plaque feature to calculate pooled odds ratios expressing the strength of association between recent ischemic events and the following 4 plaque features: 1) the presence of low attenuation or "soft" plaque, 2) the presence of calcified plaque, 3) plaque ulceration, and 4) common carotid artery wall thickness (On-line Table 5). Soft plaques were defined as having low density or lipid-rich cores, with 4 studies using a specific threshold of Hounsfield units of <50 or 60.[10,17,25,26] The presence of calcified plaque was defined as extensively calcified plaque with Hounsfield units of >120 or 130.[10,17,25,26] Specific definitions for plaque ulceration varied among studies, but it was generally defined as extension of contrast material beyond the vascular lumen into the plaque. Last, common carotid artery wall thickness was defined as thickening of the common carotid artery wall and was dichotomized by the authors of the included studies using various thresholds.

Meta-Analysis Results

We performed 4 separate meta-analyses. For the meta-analyses evaluating the association between low-attenuation plaque, plaque ulceration, and increased common carotid artery wall thickness, we included 1801, 2883, and 307 arteries in each meta-analysis, respectively (On-line Table 6). We found a significant positive association between soft or low-attenuation plaque, plaque ulceration, and increased common carotid artery wall thickness and the presence of recent ipsilateral stroke or TIA, with pooled ORs of 2.92 (95% CI, 1.41–6.04; $P = .004$), 2.20 (95% CI, 1.43–3.40; $P < .001$), and 6.19 (95% CI, 2.47–15.55; $P < .001$), respectively (Fig 1). We also analyzed 2004 arteries to determine the association of the presence of a calcified plaque and downstream cerebrovascular ischemic symptoms and found a negative association with a pooled OR of 0.536 (95% CI, 0.384–0.749; $P <. 001$) (Fig 1). Measures of study heterogeneity and publication bias for the included meta-analyses (Table) demonstrated moderate heterogeneity. Publication bias (On-line Fig 2) was only statistically significant for plaque ulceration studies.

Assessment of the Quality and Bias of the Included Studies

Our quality and bias assessment questionnaire (On-line Table 7) demonstrated that the inclusion and exclusion criteria were adequately described in all the included studies. All except 1 study included in the meta-analysis had investigators blinded to the symptomatic status of the artery in question, with that single study failing to describe the blinded status of the investigators.[19] Thirteen of the included studies had >1 investigator evaluating the questioned plaque feature, while 3 studies were aided by computer algorithms to assess plaque features.[18,22,24] Half of the studies reported measures of interreader reproducibility with κ values ranging from 0.46 to 1, depending on the specific plaque feature.[11,13,15-17,19,20,27-29] Twelve studies evaluated the degree of stenosis in addition to evaluating specific plaque features.[6,11,13,14,17-22,24,28]

DISCUSSION

In this systematic review and meta-analysis, we found that patients with carotid artery atherosclerotic disease demonstrating CTA evidence of low-attenuation plaque, increased common carotid artery wall thickness, or plaque ulceration are highly associated with the presence of recent ipsilateral ischemic events, while those patients with calcified plaques are associated with fewer ipsilateral ischemic events. Our findings are compatible with studies performed on histopathologic carotid endarterectomy specimens. Low-attenuation or soft plaque on CTA is thought to correspond to the histologically described lipid-rich necrotic core and intraplaque hemorrhage[4] and has been shown to be associated with increased risk of future stroke on both MR imaging and US.[2,3] Additionally, plaque ulceration on histopathologic samples and on high-resolution MR imaging has also been associated with symptomatic plaque.[2,30,31] Increased common carotid artery wall thickness, traditionally measured as intima-media thickness on US, is thought to reflect arterial inflammation and is a predictor of cerebrovascular events in prospective studies.[32] Conversely, histopathologic studies evaluating echogenic calcified plaque on US have found that densely calcified plaques are less frequently associated with ischemic events and may be a protective plaque feature, perhaps by preventing thrombus aggregation or by affording additional mechanical stability to a plaque surface.[3,33] Additionally, a previously published systematic review has shown that symptomatic plaques have less calcification than asymptomatic plaques.[34]

Using CTA to evaluate high-risk carotid plaque features has several strengths: First, CTA can be rapidly performed and is commonly available. Unlike high-resolution plaque imaging with MR imaging, CTA plaque imaging does not require lengthy sequences or dedicated equipment such as carotid coils to evaluate plaque features. Additionally, evaluating the presence of soft or calcified plaque, plaque ulceration, or increased common carotid artery wall thickness can be easily performed with high reproducibility without requiring lengthy interpretive time or postprocessing software.

Our study illustrates some methodologic limitations of the existing literature on CTA evaluation of carotid plaque. Our analysis revealed moderate levels of heterogeneity in the meta-analy-

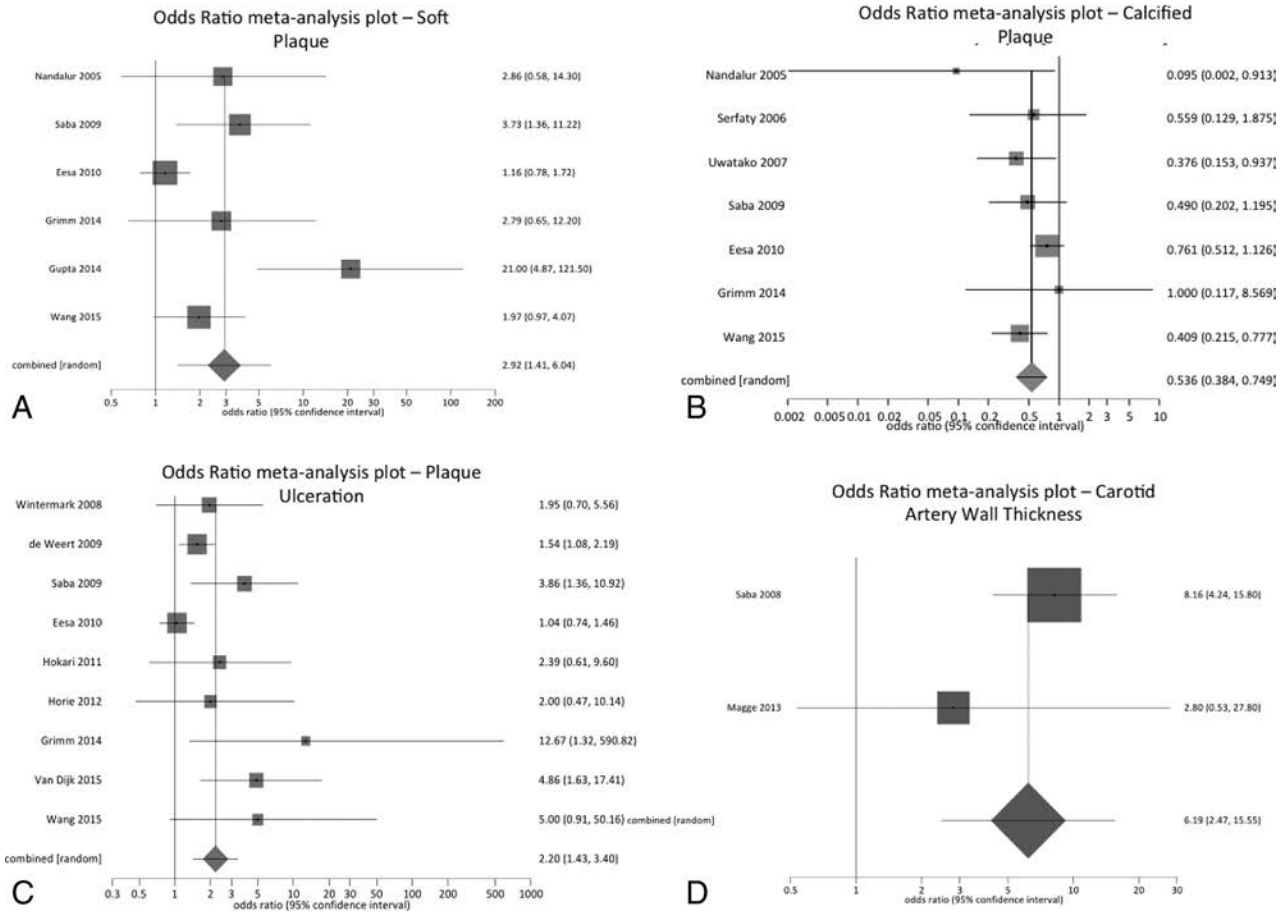

FIG 1. Four separate forest plots of the association between CT angiography–determined plaque characteristics and recent prior ipsilateral ischemic events. Each meta-analysis was calculated with a random-effects model with pooled ORs shown for each forest plot. Each *square* represents the point estimate of the effect size of the study with the square size being proportional to the inverse of the variance of the estimate and the horizontal lines representing each the 95% CI of each study. The *diamond* represents the pooled estimate with the width of the diamond representing the pooled 95% CI.

Heterogeneity and publication bias measures

	Measures of Heterogeneity			Publication Bias	
	I^2	Cochran *Q*	*P* Value	Kendall *T*	*P* Value
Soft-plaque studies	76.3%	21.13	.001	0.47	.27
Calcified-plaque studies	19.8%	7.49	.28	0.14	.56
Plaque ulceration studies	61.1%	20.56	.008	0.389	.018
Carotid artery wall thickness studies	34.6%	1.52	.22	NA	NA

Note:—NA indicates not applicable.

ses evaluating soft plaque and plaque ulceration, which may have been secondary to between-study variability in the definitions of CTA plaque features and differences in how studies adjudicated and defined stroke or TIA. Using a random-effects rather than a fixed-effects model, we could statistically account for this heterogeneity and still show strong associations between each plaque feature and cerebrovascular ischemia. We believe that increased standardization of plaque feature definitions and more consistently applied, uniform definitions of ischemic events are warranted for future studies. Additionally, risk of bias for each article was determined subjectively by consensus among 3 readers. The subjectivity involved in assessing the risk of bias is inherent to systematic reviews and meta-analyses. We also detected the possibility of publication bias in our meta-analysis of plaque ulceration, which raises the possibility that negative studies were not published. However, the evaluation of publication bias is limited, given the small number of studies published on the CTA characterization of plaque ulceration, and future studies are warranted to examine whether such a bias exists.

Our systematic review and meta-analyses also revealed knowledge gaps that future studies should seek to clarify. First, we found that investigators have, to date, evaluated only the relationship between specific plaque features and recent prior ischemic symptoms, rather than future stroke. Although longitudinal MR imaging studies have shown that high-risk carotid plaque features such as intraplaque hemorrhage do not change significantly during a 1-year period in symptomatic patients,[35] prospective studies evaluating future stroke risk are needed if CTA plaque analysis is to play a greater role in primary stroke prevention. It is possible that a more directly applicable use of the results of our study may allow

clinicians to improve their confidence in identifying a culprit lesion after a stroke of uncertain etiology has occurred so that optimal secondary stroke prevention measures can be initiated.[36,37] Second, we found that the time interval between the onset of ischemic symptoms and CTA for the evaluation of plaque features was relatively inconsistent among included studies. Third, many studies did not include precise descriptions of how causation of ischemic stroke was attributed to a given ICA. Prospective studies with standardized protocols and definitions evaluating the predictive value of these plaque features for ischemic symptoms are warranted to improve the clinical usefulness of carotid plaque CTA.

CONCLUSIONS

Our systematic review and meta-analyses suggest that plaque features such as the presence of soft plaque, plaque ulceration, or increased common carotid artery wall thickness seen on CTA are strongly positively associated with cerebrovascular ischemic events and that the presence of calcified plaque is negatively associated with prior ischemic events. Routine assessment of these plaque features on CTA may be complementary to measuring degree of luminal stenosis and aid in identifying high-risk plaque features.

Disclosures: Ajay Gupta—*RELATED*: *Grant*: National Institutes of Health*. *Money paid to the institution.

REFERENCES

1. Raman G, Moorthy D, Hadar N, et al. **Management strategies for asymptomatic carotid stenosis: a systematic review and meta-analysis.** *Ann Intern Med* 2013;158:676–85 CrossRef Medline
2. Gupta A, Baradaran H, Schweitzer AD, et al. **Carotid plaque MRI and stroke risk: a systematic review and meta-analysis.** *Stroke* 2013;44:3071–77 CrossRef Medline
3. Gupta A, Kesavabhotla K, Baradaran H, et al. **Plaque echolucency and stroke risk in asymptomatic carotid stenosis a systematic review and meta-analysis.** *Stroke* 2015;46:91–97 CrossRef Medline
4. Wintermark M, Jawadi SS, Rapp JH, et al. **High-resolution CT imaging of carotid artery atherosclerotic plaques.** *AJNR Am J Neuroradiol* 2008;29:875–82 CrossRef Medline
5. Trelles M, Eberhardt K, Buchholz M, et al. **CTA for screening of complicated atherosclerotic carotid plaque: American Heart Association type VI lesions as defined by MRI.** *AJNR Am J Neuroradiol* 2013;34:2331–37 CrossRef Medline
6. Gupta A, Baradaran H, Mtui EE, et al. **Detection of symptomatic carotid plaque using source data from MR and CT angiography: a correlative study.** *Cerebrovasc Dis* 2015;39:151–61 CrossRef Medline
7. Stroup DF, Berlin JA, Morton SC, et al. **Meta-analysis of observational studies in epidemiology: a proposal for reporting; Meta-Analysis Of Observational Studies in Epidemiology (MOOSE) group.** *JAMA* 2000;283:2008–12 CrossRef Medline
8. Liberati A, Altman DG, Tetzlaff J, et al. **The PRISMA statement for reporting systematic reviews and meta-analyses of studies that evaluate health care interventions: explanation and elaboration.** *PLoS Med* 2009;6:e1000100 CrossRef Medline
9. Gupta A, Giambrone AE, Gialdini G, et al. **Silent brain infarction and risk of future stroke: a systematic review and meta-analysis.** *Stroke* 2016;47:719–25 CrossRef Medline
10. Nandalur KR, Baskurt E, Hagspiel KD, et al. **Calcified carotid atherosclerotic plaque is associated less with ischemic symptoms than is noncalcified plaque on MDCT.** *AJR Am J Roentgenol* 2005;184:295–98 CrossRef Medline
11. Nandalur KR, Hardie AD, Raghavan P, et al. **Composition of the stable carotid plaque: insights from a multidetector computed tomography study of plaque volume.** *Stroke* 2007;38:935–40 CrossRef Medline
12. Miralles M, Merino J, Busto M, et al. **Quantification and characterization of carotid calcium with multi-detector CT-angiography.** *Eur J Vasc Endovasc Surg* 2006;32:561–67 CrossRef Medline
13. Serfaty JM, Nonent M, Nighoghossian N, et al; CARMEDAS Study Group. **Plaque density on CT, a potential marker of ischemic stroke.** *Neurology* 2006;66:118–20 CrossRef Medline
14. Uwatoko T, Toyoda K, Inoue T, et al. **Carotid artery calcification on multislice detector-row computed tomography.** *Cerebrovasc Dis* 2007;24:20–26 CrossRef Medline
15. Saba L, Sanfilippo R, Pascalis L, et al. **Carotid artery wall thickness and ischemic symptoms: evaluation using multi-detector-row CT angiography.** *Eur Radiol* 2008;18:1962–71 CrossRef Medline
16. Saba L, Mallarini G. **Fissured fibrous cap of vulnerable carotid plaques and symptomaticity: are they correlated? Preliminary results by using multi-detector-row CT angiography.** *Cerebrovasc Dis* 2009;27:322–27 CrossRef Medline
17. Saba L, Montisci R, Sanfilippo R, et al. **Multidetector row CT of the brain and carotid artery: a correlative analysis.** *Clin Radiol* 2009;64:767–78 CrossRef Medline
18. Wintermark M, Arora S, Tong E, et al. **Carotid plaque computed tomography imaging in stroke and nonstroke patients.** *Ann Neurol* 2008;64:149–57 CrossRef Medline
19. de Weert TT, Cretier S, Groen HC, et al. **Atherosclerotic plaque surface morphology in the carotid bifurcation assessed with multidetector computed tomography angiography.** *Stroke* 2009;40:1334–40 CrossRef Medline
20. Romero JM, Babiarz LS, Forero NP, et al. **Arterial wall enhancement overlying carotid plaque on CT angiography correlates with symptoms in patients with high grade stenosis.** *Stroke* 2009;40:1894–96 CrossRef Medline
21. Eesa M, Hill MD, Al-Khathaami A, et al. **Role of CT angiographic plaque morphologic characteristics in addition to stenosis in predicting the symptomatic side in carotid artery disease.** *AJNR Am J Neuroradiol* 2010;31:1254–60 CrossRef Medline
22. Hokari M, Kuroda S, Yasuda H, et al. **Lumen morphology in mild-to-moderate internal carotid artery stenosis correlates with neurological symptoms.** *J Neuroimaging* 2011;21:348–54 CrossRef Medline
23. Horie N, Morikawa M, Ishizaka S, et al. **Assessment of carotid plaque stability based on the dynamic enhancement pattern in plaque components with multidetector CT angiography.** *Stroke* 2012;43:393–98 CrossRef Medline
24. Magge R, Lau BC, Soares BP, et al. **Clinical risk factors and CT imaging features of carotid atherosclerotic plaques as predictors of new incident carotid ischemic stroke: a retrospective cohort study.** *AJNR Am J Neuroradiol* 2013;34:402–09 CrossRef Medline
25. Grimm JM, Schindler A, Schwarz F, et al. **Computed tomography angiography vs 3 T black-blood cardiovascular magnetic resonance for identification of symptomatic carotid plaques.** *J Cardiovasc Magn Reson* 2014;16:84 CrossRef Medline
26. Wang P, Wang Y, Zhang G, et al. **Study on the carotid atherosclerotic plaque of patients suffering from ischemic cerebrovascular disease by 64 slices CT.** *Eur Rev Med Pharmacol Sci* 2015;19:3480–85 Medline
27. van Dijk A, Truijman M, Hussain B, et al. **Intraplaque hemorrhage and the plaque surface in carotid atherosclerosis: the Plaque at RISK study (PARISK).** *AJNR Am J Neuroradiol* 2015;36:2127–33 CrossRef Medline
28. Gupta A, Mtui E, Baradaran H, et al. **CT angiographic features of symptom-producing plaque in moderate-grade carotid artery stenosis.** *AJNR Am J Neuroradiol* 2015;36:349–54 CrossRef Medline
29. Gupta A, Baradaran H, Kamel H, et al. **Evaluation of computed tomography angiography plaque thickness measurements in high-grade carotid artery stenosis.** *Stroke* 2014;45:740–45 CrossRef Medline

30. Golledge J, Greenhalgh RM, Davies AH. **The symptomatic carotid plaque.** *Stroke* 2000;31:774–81 CrossRef Medline
31. Fisher M, Paganini-Hill A, Martin A, et al. **Carotid plaque pathology: thrombosis, ulceration, and stroke pathogenesis.** *Stroke* 2005;36: 253–57 CrossRef Medline
32. Simon A, Gariepy J, Chironi G, et al. **Intima–media thickness: a new tool for diagnosis and treatment of cardiovascular risk.** *J Hypertens* 2002;20:159–69 CrossRef Medline
33. Shaalan WE, Cheng H, Gewertz B, et al. **Degree of carotid plaque calcification in relation to symptomatic outcome and plaque inflammation.** *J Vasc Surg* 2004;40:262–69 CrossRef Medline
34. Kwee RM. **Systematic review on the association between calcification in carotid plaques and clinical ischemic symptoms.** *J Vasc Surg* 2010;51:1015–25 CrossRef Medline
35. Kwee RM, Truijman MT, van Oostenbrugge RJ, et al. **Longitudinal MRI study on the natural history of carotid artery plaques in symptomatic patients.** *PLoS One* 2012;7:e42472 CrossRef Medline
36. Gupta A, Gialdini G, Lerario MP, et al. **Magnetic resonance angiography detection of abnormal carotid artery plaque in patients with cryptogenic stroke.** *J Am Heart Assoc* 2015;4:e002012 CrossRef Medline
37. Freilinger TM, Schindler A, Schmidt C, et al. **Prevalence of nonstenosing, complicated atherosclerotic plaques in cryptogenic stroke.** *JACC Cardiovasc Imaging* 2012;5:397–405 CrossRef Medline

Preoperative Cerebral Oxygen Extraction Fraction Imaging Generated from 7T MR Quantitative Susceptibility Mapping Predicts Development of Cerebral Hyperperfusion following Carotid Endarterectomy

J.-i. Nomura, I. Uwano, M. Sasaki, K. Kudo, F. Yamashita, K. Ito, S. Fujiwara, M. Kobayashi, and K. Ogasawara

ABSTRACT

BACKGROUND AND PURPOSE: Preoperative hemodynamic impairment in the affected cerebral hemisphere is associated with the development of cerebral hyperperfusion following carotid endarterectomy. Cerebral oxygen extraction fraction images generated from 7T MR quantitative susceptibility mapping correlate with oxygen extraction fraction images on positron-emission tomography. The present study aimed to determine whether preoperative oxygen extraction fraction imaging generated from 7T MR quantitative susceptibility mapping could identify patients at risk for cerebral hyperperfusion following carotid endarterectomy.

MATERIALS AND METHODS: Seventy-seven patients with unilateral internal carotid artery stenosis (≥70%) underwent preoperative 3D T2*-weighted imaging using a multiple dipole-inversion algorithm with a 7T MR imager. Quantitative susceptibility mapping images were then obtained, and oxygen extraction fraction maps were generated. Quantitative brain perfusion single-photon emission CT was also performed before and immediately after carotid endarterectomy. ROIs were automatically placed in the bilateral middle cerebral artery territories in all images using a 3D stereotactic ROI template, and affected-to-contralateral ratios in the ROIs were calculated on quantitative susceptibility mapping–oxygen extraction fraction images.

RESULTS: Ten patients (13%) showed post-carotid endarterectomy hyperperfusion (cerebral blood flow increases of ≥100% compared with preoperative values in the ROIs on brain perfusion SPECT). Multivariate analysis showed that a high quantitative susceptibility mapping–oxygen extraction fraction ratio was significantly associated with the development of post-carotid endarterectomy hyperperfusion (95% confidence interval, 33.5–249.7; $P = .002$). Sensitivity, specificity, and positive- and negative-predictive values of the quantitative susceptibility mapping–oxygen extraction fraction ratio for the prediction of the development of post-carotid endarterectomy hyperperfusion were 90%, 84%, 45%, and 98%, respectively.

CONCLUSIONS: Preoperative oxygen extraction fraction imaging generated from 7T MR quantitative susceptibility mapping identifies patients at risk for cerebral hyperperfusion following carotid endarterectomy.

ABBREVIATIONS: CEA = carotid endarterectomy; OEF = oxygen extraction fraction; QSM = quantitative susceptibility mapping; ROC = receiver operating characteristic

Cerebral hyperperfusion following carotid endarterectomy (CEA) has been defined as a substantial increase in ipsilateral cerebral blood flow well above the metabolic demands of brain tissue following surgical repair of carotid stenosis.[1,2] Cerebral hyperperfusion syndrome after CEA is a complication of cerebral hyperperfusion;[3] its characteristic features include unilateral headache, pain in the face or eyes, seizures, and focal symptoms secondary to intracerebral hemorrhage or cerebral edema.[1-4] Intracerebral hemorrhage has a low incidence (1%), but patients with this condition have a poor prognosis.[5] Moreover, several studies have found that post-CEA hyperperfusion, even when asymptomatic, causes slight but diffuse damage to the ipsilateral cerebral cortex and white matter.[3,6,7] This damage that occurs after CEA hyperperfusion is a principal cause of the postoperative cognitive impairment observed in 10% of patients following CEA.[3,6,7]

Cerebrovascular autoregulatory mechanisms operate through dilation of precapillary resistance vessels that maintain CBF when

Received June 3, 2017; accepted after revision July 18.

From the Department of Neurosurgery (J.-i.N., S.F., M.K., K.O.) and Division of Ultrahigh Field MRI (I.U., M.S., F.Y., K.I), Institute for Biomedical Sciences, Iwate Medical University School of Medicine, Morioka, Japan; and Department of Diagnostic and Interventional Radiology (K.K.), Hokkaido University School of Medicine, Sappro, Japan.

This work supported, in part, by Grants-in-Aid for Strategic Medical Science Research (S1491001, 2014–2018) from the Ministry of Education, Culture, Sports, Science and Technology of Japan and a Grant-in-Aid for Scientific Research (15K10313) from the Japan Society for the Promotion of Science.

Please address correspondence to Kuniaki Ogasawara, MD, Department of Neurosurgery, Iwate Medical University, Uchimaru 19-1, Morioka 020-8505, Japan; e-mail: kuogasa@iwate-med.ac.jp

http://dx.doi.org/10.3174/ajnr.A5390

reductions in cerebral perfusion pressure occur, and this is referred to as stage 1 ischemia.[3,8-10] However, the autoregulatory mechanism provides insufficient compensation for severe decreases in cerebral perfusion pressure, which then leads to decreased CBF, referred to as misery perfusion or stage 2 ischemia.[3,8-10] Thus, misery perfusion, which is defined as marginally sufficient cerebral blood supply relative to cerebral metabolic demand, is a situation with severely impaired cerebral hemodynamics.[8] This condition occurs in patients with chronic steno-occlusive diseases of the internal carotid artery.[8]

The risk factors for cerebral hyperperfusion include high-grade stenosis, poor collateral blood flow, contralateral carotid occlusion, and long-standing hypertension, and they often result in impaired cerebral hemodynamics.[11-14] When normal perfusion pressure is rapidly restored after CEA, hyperperfusion may occur in regions of the brain with impaired autoregulation due to chronic ischemia. This hypothesis is like the "normal perfusion pressure breakthrough" theory of Spetzler et al.[13,15] Indeed, preoperative misery perfusion in the affected cerebral hemisphere is reportedly associated with the development of cerebral hyperperfusion following CEA or carotid stent placement for cervical ICA stenosis.[16,17]

Misery perfusion is principally detected as an increased oxygen extraction fraction (OEF) on positron-emission tomography.[8] Several approaches have been attempted to measure OEF by using MR imaging techniques.[18] In general, these techniques use blood oxygen level–dependent effects induced by differences in magnetic susceptibility between oxy- and deoxyhemoglobin to quantify oxygenation in venous structures and/or brain parenchyma.[19-21] Quantitative susceptibility mapping (QSM) is a post-processing technique for quantifying the magnetic susceptibility of venous structures and brain parenchyma from T2*-weighted magnitude/phase images, which can be easily obtained by commercial scanners.[22] Indeed, a recent study has introduced an OEF measurement method based on the QSM technique and has demonstrated that cerebral OEF images generated from QSM at 7T MR imaging correlate with OEF images on PET and provide high sensitivity and high specificity for detecting misery perfusion in the middle cerebral artery territory in patients with unilateral chronic ICA or MCA steno-occlusive disease.[23]

The purpose of the present study was to determine whether preoperative OEF imaging generated from 7T MR QSM could identify patients at risk for cerebral hyperperfusion following CEA.

MATERIALS AND METHODS

Study Design

The present study was a prospective observational study. The protocol of this study was reviewed and approved by the institutional ethics committee at Iwate Medical University, and written, informed consent was obtained from all patients or their next of kin before the patient's participation.

Patient Selection

Patients with the following conditions who underwent CEA of the carotid bifurcation in our institution were included in the present study: 1) unilateral ICA stenosis of ≥70% as per the North American Symptomatic Carotid Endarterectomy Trial[24] on angiography/arterial catheterization without occlusion or severe (≥70%) stenosis in the contralateral ICA; 2) useful preoperative residual function (modified Rankin Scale score, 0–2); and 3) no ipsilateral carotid territory ischemic symptoms or ipsilateral carotid territory ischemic symptoms for >6 months before presentation (defined as asymptomatic),[3] or ipsilateral carotid territory ischemic symptoms between 2 weeks and 6 months before presentation (defined as symptomatic).[3] Patients who did not undergo 7T MR imaging preoperatively were excluded.

Preoperative OEF Imaging Generated from MR QSM

A 7T MR imaging scanner (Discovery MR950; GE Healthcare, Milwaukee, Wisconsin) with quadrature transmission and 32-channel receive head coils was used. Source data of QSM were obtained with a 3D spoiled gradient-recalled acquisition technique with the following scanning parameters: TR, 30 ms; TE, 15 ms; flip angle, 20°; FOV, 256 mm; acquisition matrix size, 512 × 256; section thickness, 2 mm; number of sections, 160; reconstruction voxel size after zero-fill interpolation, 0.5 mm^3; and scan time, 3 minutes 25 seconds.[23] Magnitude and real/imaginary phase images were regenerated from this acquisition.

QSM images were generated from the source images with an in-house program with a multiple dipole-inversion combination with *k*-space segmentation[25] and regularization-enabled sophisticated harmonic artifact reduction for phase data methods,[26] as described previously.[23] A 2D Gaussian low-pass filter with a kernel size of 60% of the total image power in each section was applied to extract iron deposition in deep nuclei, hemosiderin deposition, dural sinuses, and large venous structures; and a 2D Gaussian high-pass filter of 2% was applied to extract small venous structures.[23] Subsequently, small venous structures were determined by multiplying the Gaussian high-pass-filter–processed binary images and the logical negations of Gaussian low-pass-filter–processed binary images under the threshold for binarization of ≥2 SDs.[23]

The OEF maps with voxels of interest of 25 mm^3 were generated from the processed QSM images according to a previous study.[22,23] In brief, the susceptibility difference between venous structures and surrounding brain tissues, $\Delta\chi$, is expressed by the following equation:

$$\Delta\chi = \Delta\chi_{do} \times Hct \times (1 - Y_v) \times \frac{1}{p_v},$$

where $\Delta\chi_{do}$ is the difference in the susceptibility per unit hematocrit between fully deoxygenated and fully oxygenated blood [0.18 ppm (cgs) was used],[27] *Hct* is hematocrit (0.45 was used), Y_v is venous oxygen saturation, and *Pv* is a correction factor for partial volume effects that was defined as approximately 7.0 according to the previous study.[23] On the other hand, OEF is defined as $(Y_a - Y_v)/Y_a$, where Y_a is arterial oxygen saturation and can be estimated as $1 - Y_v$ under usual conditions in which Y_a is nearly 100%.[28] Hence, the OEF can be calculated with the following equation:

$$\mathrm{OEF} = \frac{\Delta\chi \times P_v}{\Delta\chi_{do} \times Hct}.$$

FIG 1. Diagrams showing some ROIs of a 3D stereotactic ROI template on MR quantitative susceptibility mapping–oxygen extraction fraction images and brain perfusion single-photon emission CT images. The *white ROIs* indicate the bilateral cortical territories perfused by the bilateral middle cerebral arteries.

Detection of Cerebral Hyperperfusion following CEA

To detect cerebral hyperperfusion following CEA, quantitative brain perfusion SPECT was performed with iodine 123 *N*-isopropyl-p-iodoamphetamine (^{123}I-IMP) within 14 days before and immediately after CEA. The ^{123}I-IMP SPECT study was performed as described previously.[29] Patients with post-CEA hyperperfusion also underwent a third ^{123}I-IMP SPECT in the same manner 3 days after CEA. The quantitative CBF images were calculated according to the ^{123}I-IMP-autoradiography method.[29]

Imaging Data Analysis

All QSM-OEF and brain perfusion SPECT images were transformed into the standard brain size and shape by linear and nonlinear transformation using Statistical Parametric Mapping 12 (http://www.fil.ion.ucl.ac.uk/spm/software/spm12) for anatomic standardization.[3,30] Thus, all the subjects' brain images had the same anatomic format. Then, a 3D stereotactic ROI template was used to automatically place 318 constant ROIs in both the cerebral and cerebellar hemispheres.[3,31] The ROIs were grouped into 10 segments (callosomarginal, pericallosal, precentral, central, parietal, angular, temporal, posterior, hippocampus, and cerebellum) in each hemisphere by arterial supply. Of these 10 segments, 5 (precentral, central, parietal, angular, and temporal) were combined to define an ROI perfused by the MCA (Fig 1).[3]

For QSM-OEF images, the mean value of all pixels was calculated in the bilateral MCA ROIs. For each patient, the asymmetry ratio in the MCA ROI (QSM-OEF ratio) was calculated as the value in the cerebral hemisphere ipsilateral to the side of surgery divided by the value in the contralateral cerebral hemisphere.

For brain perfusion SPECT images, the mean value of all pixels in the MCA ROI in the cerebral hemisphere ipsilateral to the CEA was calculated before and after the operation. For each patient, post-CEA hyperperfusion was defined as a quantitative CBF increase of ≥100% (ie, doubling) compared with preoperative values in an MCA ROI ipsilateral to the side of surgery.[3,13]

Pre-, Intra-, and Postoperative Management

Antiplatelet therapy was given to all patients until the morning of the day of CEA, and surgery was performed with the patient under general anesthesia.[3] A heparin bolus (5000 IU) was administered before ICA clamping.[3] An intraluminal shunt was placed on the basis of the findings of intraoperative electroencephalography with a 12-channel montage.[3,32]

In all patients with post-CEA hyperperfusion on brain perfusion SPECT performed immediately after the operation, arterial blood pressure was intensively controlled between 100 and 140 mm Hg by intravenous antihypertensive drugs.[3] If the CBF decreased and the hyperperfusion had resolved on brain perfusion SPECT performed on the third postoperative day, pharmacologic blood pressure control was stopped.[3] However, if the hyperperfusion continued, the systolic arterial blood pressure was controlled to <140 mm Hg.[3] If a patient developed hyperperfusion syndrome, a propofol coma was induced.[3] Hyperperfusion syndrome was diagnosed with the following criteria: 1) seizure, alteration in consciousness level, and/or focal neurologic signs such as motor weakness that newly developed or worsened between 24 hours and 30 days after the operation; and 2) the presence of hyperperfusion on brain perfusion SPECT.[3]

Statistical Analysis

Data are expressed as means ± SD. The relationship between each variable including the QSM-OEF ratio and the development of cerebral hyperperfusion defined by brain perfusion SPECT was evaluated by univariate analysis with the Mann-Whitney *U* test or the χ^2 test. Multivariate statistical analysis of factors related to the development of cerebral hyperperfusion was also performed with a logistic regression model. Variables with $P < .2$ on univariate analyses were included in the final model. Differences were considered significant with $P < .05$. The accuracy of the QSM-OEF ratio for predicting the development of cerebral hyperperfusion was evaluated by receiver operating characteristic (ROC) curve analyses when the relationship between the 2 parameters was significant. Exact 95% confidence intervals of sensitivity, specificity, and positive and negative predictive values were computed with binomial distributions.

RESULTS

During the 33-month period of the study, 111 patients satisfied the inclusion criteria and were scheduled to undergo 7T MR imaging preoperatively. However, 25 patients did not undergo 7T MR imaging because they had implantable electronic devices or implantable metals such as coronary artery stents, pacemakers, or broken bone fixtures, which are contraindications for 7T MR imaging. In another 5 patients, 7T MR imaging was canceled half-way through scanning due to the development of headache, vertigo, or claustrophobia. The remaining 81 patients successfully underwent 7T MR imaging. However, data that were sufficient to generate OEF maps were not obtained in 7T MR imaging of 4 patients due to motion artifacts, and these 4 patients were excluded from the analysis. Seventy-seven patients were thus enrolled in the present study.

The mean age of the 77 patients (70 men, 7 women) was 70 ±

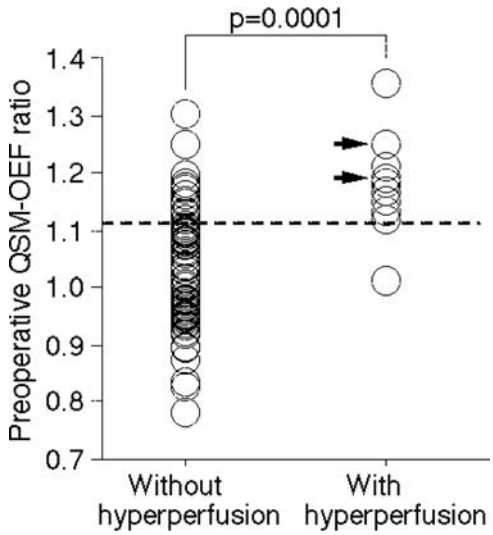

FIG 2. Relationship between the preoperative QSM-OEF ratio and the presence or absence of postoperative hyperperfusion. *Arrows* indicate patients with cerebral hyperperfusion syndrome. The *dashed horizontal line* denotes the cutoff point lying closest to the left upper corner of the ROC characteristic curve for predicting the development of postoperative hyperperfusion.

7 years (range, 52–86 years). There were 73 patients with hypertension, 37 patients with diabetes mellitus, and 64 patients with dyslipidemia. Fifty-one patients had ipsilateral carotid territory symptoms, and 26 patients showed asymptomatic ICA stenosis. The overall average degree of ICA stenosis was 87% ± 9% (range, 70%–99%). The mean duration of ICA clamping was 36 minutes (range, 25–56 minutes). An intraluminal shunt was placed in 3 patients.

Ten patients (13%) fulfilled the CBF criteria for post-CEA hyperperfusion on the quantitative brain perfusion SPECT images obtained immediately after surgery; 8 of these patients showed no hyperperfusion on the SPECT performed on the third postoperative day, and they all had uneventful postoperative courses. However, in the remaining 2 patients with cerebral hyperperfusion immediately after CEA, a progressive increase in CBF was seen on the third postoperative day; they developed cerebral hyperperfusion syndrome with hemiparesis on the side contralateral to the side of surgery or aphasia with onset 5 and 8 days after the operation, respectively. Propofol coma was induced in these 2 patients, and they eventually showed full neurologic recovery after termination of the propofol coma.

Fig 2 shows the relationship between the QSM-OEF ratio and the development of cerebral hyperperfusion defined by brain perfusion SPECT. The QSM-OEF ratio was significantly greater in patients with cerebral hyperperfusion (1.176 ± 0.090) than in those without it (1.027 ± 0.102, $P = .0001$). The Table shows the results of univariate analyses of other factors related to the development of post-CEA hyperperfusion. None of the variables were significantly associated with the development of post-CEA hyperperfusion. After closely related variables were eliminated in univariate analyses, the following variables ($P < .2$), the QSM-OEF ratio and the degree of ICA stenosis, were included in the logistic regression model for multivariate analysis. On multivariate analysis, a high QSM-OEF ratio was significantly associated with the development of post-CEA hyperperfusion (95% CI, 33.5–249.7; $P = .002$).

Risk factors for the development of post-CEA hyperperfusion

Risk Factor	Post-CEA Hyperperfusion		
	Yes ($n = 10$)	No ($n = 67$)	*P* Value
Age (mean) (yr)	71.2 ± 9.2	70.3 ± 6.7	.3623
Male sex	9 (90%)	61 (91%)	>.9999
Hypertension	10 (100%)	63 (94%)	>.9999
Diabetes mellitus	4 (40%)	33 (35%)	.7256
Dyslipidemia	7 (70%)	57 (85%)	.3589
Symptomatic lesion	8 (80%)	43 (64%)	.4802
Degree of ICA stenosis (mean) (%)	91.4 ± 7.0	87.0 ± 9.6	.1112
Duration of ICA clamping (mean) (min)	38.3 ± 4.0	36.4 ± 6.1	.2048
Use of intraluminal shunt	0 (0%)	3 (4%)	>.9999

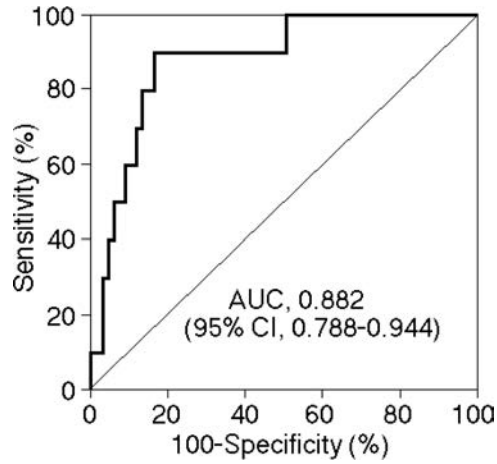

FIG 3. ROC curve used to assess the accuracy of the QSM-OEF ratio for predicting the development of postoperative hyperperfusion. AUC indicates area under the ROC curve.

Fig 3 shows the ROC curve of the QSM-OEF ratio, which can be used to assess its ability to predict the development of post-CEA hyperperfusion. The area under the ROC curve was 0.882 (95% CI, 0.788–0.944). Sensitivity, specificity, and positive and negative predictive values for the QSM-OEF ratio at the cutoff point (1.116) lying closest to the left upper corner of the ROC curve for the prediction of the development of post-CEA hyperperfusion were 90% (95% CI, 71–100), 84% (95% CI, 75–92), 45% (95% CI, 23–67), and 98% (95% CI, 95–100), respectively (Figs 2 and 3).

Representative images of the preoperative QSM-OEF maps and the pre- and postoperative quantitative brain perfusion SPECT from a patient with post-CEA hyperperfusion are shown in Fig 4.

DISCUSSION

The present study demonstrated that preoperative OEF imaging generated from 7T MR QSM could identify patients at risk for cerebral hyperperfusion following CEA.

The benefits and drawbacks of the method used in the present study for OEF estimation have already been discussed in the literature.[23] Briefly, the present QSM-based method has several advantages, such as use of a conventional sequence; short acquisition time; no need for any challenge, contrast agent, or other invasive procedures; sufficient spatial resolution with whole-brain coverage; and robustness to low perfusion status, suggesting

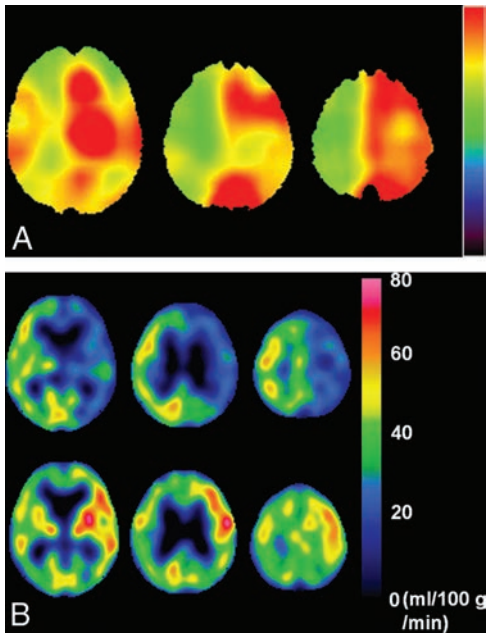

FIG 4. A 77-year-old man with symptomatic left internal carotid artery stenosis (85%) who developed cerebral hyperperfusion syndrome with right-sided hemiparesis and aphasia with onset 5 days after the operation. *A*, Preoperative QSM-OEF images show elevation of the values in the left cerebral cortex compared with those in the right cerebral cortex. *B*, Brain perfusion single-photon emission CT images before the operation show hypoperfusion in the left cerebral hemisphere (*upper row*) where hyperperfusion developed immediately after the operation (*lower row*).

high ease of use in clinical practice and clinical studies for patients with cerebrovascular and other neurologic disorders.[23] Zhang et al[19] have recently demonstrated that QSM can be used with perfusion measurements of pre- and post-caffeine vasoconstriction to map the cerebral metabolic rate of oxygen and OEF. However, this method needs a caffeine challenge and 2 MR images. It also uses arterial spin-labeling MR perfusion imaging to obtain CBF data. This perfusion imaging depends on the arterial transit time.[33] With the postlabeling delay of 1.5 seconds used in the study by Zhang et al, slow flow through collateral vessels in the cerebral hemisphere with ICA steno-occlusive disease is often underestimated, resulting in overestimation of OEF.[33]

On the other hand, as drawbacks, the present method is highly dependent on the algorithms for generating QSM images and for estimating OEF values.[23] Several algorithms for QSM generation have been proposed, and they vary in terms of preservation of small venous structures, which appears crucial to obtain accurate OEF values.[23] The software for estimating OEF values from QSM images are in-house programs that need further revisions to distribute as free software programs.[23] Further optimization of the algorithm and parameters, as well as publication of the program, is needed for wide adoption of the QSM-OEF method.[23]

Various mechanisms to explain the development of post-CEA hyperperfusion have been proposed.[4,13] When there is severe ICA stenosis and deficient collateral circulation, hemispheric perfusion pressure is severely decreased distal to the ICA stenosis, which may reduce perfusion pressure below the compensatory capacity of autoregulatory mechanisms, causing maximal dilation of resistance vessels and misery perfusion. When normal perfusion pressure is restored following CEA, it may take several days for chronically impaired autoregulatory mechanisms to adjust to the new steady-state, resulting in temporary ongoing hyperperfusion. In the present study, a high QSM-OEF ratio was found to be the only independent predictor of post-CEA hyperperfusion, which supports the theory that hyperperfusion occurs due to loss of normal vasoconstriction secondary to chronic cerebral ischemia and dysfunctional autoregulatory mechanisms.

In the present study, the optimal cutoff point of the QSM-OEF ratio on the ROC curve to predict the development of post-CEA hyperperfusion was 1.116. According to a previous study comparing QSM-OEF with PET-OEF,[23] this value corresponded to the mean + 2.9 SD of the QSM-OEF ratio obtained from healthy subjects. With this cutoff point, the QSM-OEF ratio provided a sensitivity of 90% and a negative-predictive value of 98% for predicting the development of post-CEA hyperperfusion. This high sensitivity and high negative predictive value suggest that the QSM-OEF ratio is suitable as a screening test for preoperative prediction of post-CEA hyperperfusion. On the other hand, among the present results, there was a patient with false-negative findings with post-CEA hyperperfusion despite the absence of preoperatively increased QSM-OEF in the affected hemisphere (QSM-OEF ratio of 1.009). These findings in this patient suggest that loss of normal vasoconstriction and maladaptive autoregulatory mechanisms causing post-CEA hyperperfusion rarely develop in cerebral hemodynamic conditions other than with misery perfusion. A previous study demonstrated that post-CEA hyperperfusion can occur even in patients with stage 1 ischemia, in which precapillary resistance vessels are dilated to maintain CBF in the context of reductions in cerebral perfusion pressure, though the OEF was not yet elevated.[3] Because QSM-OEF imaging theoretically does not detect stage 1 ischemia, this imaging can provide false-negative results.

In this study, the QSM-OEF ratio showed a relatively low positive predictive value (45%) for the development of post-CEA hyperperfusion. It has been reported that most patients with preoperatively impaired cerebral hemodynamics and significantly decreased perfusion in the ipsilateral cerebral hemisphere during ICA clamping in CEA developed post-CEA hyperperfusion; this finding suggests that in addition to the impaired cerebrovascular autoregulation due to chronic ischemia, intraoperative acute global ischemia is involved in the pathogenesis of post-CEA hyperperfusion.[34] This may explain the low positive predictive value for the prediction of post-CEA hyperperfusion when only preoperative measurements of cerebral hemodynamics, such as the QSM-OEF ratio, are used.[34]

Regarding management for cerebral hyperperfusion after CEA, several investigators have noted the following: 1) Two-thirds of patients with cerebral hyperperfusion on brain perfusion imaging performed immediately after surgery develop intracerebral hemorrhage within 15 days after the operation if intensive blood pressure control is not started immediately afterwards,[5] and this intensive blood pressure control prevents the development of intracerebral hemorrhage due to cerebral hyperperfusion;[5,13] 2) carotid artery stenosis and other vascular atherosclerotic diseases, including coronary artery disease or lower extremity atherosclerotic occlusive disease, often coexist, and the

intensive blood pressure control (eg, intentional hypotension) for such patients induces ischemic events involving the other atherosclerotic steno-occlusive lesions, suggesting that only patients who are preoperatively determined to have a high risk of cerebral hyperperfusion or are identified as having cerebral hyperperfusion on brain perfusion imaging done immediately after surgery should undergo intensive blood pressure control to minimize the risk of hypotension-induced ischemic events;[13] and 3) an intraoperative administration of a free radical scavenger, edaravone, significantly prevents the development of cerebral hyperperfusion itself,[35] thus reducing the incidence of postoperative cognitive impairment, as well as postoperative intracerebral hemorrhage.[36]

On the basis of these previous findings and the present data, we propose a practical clinical algorithm to manage cerebral hyperperfusion: A patient scheduled to undergo CEA first undergoes preoperative OEF imaging generated from MR QSM. If the QSM-OEF ratio is high (>1.116), the patient is determined to have a high risk for cerebral hyperperfusion and undergoes an intraoperative administration of edaravone, brain perfusion imaging immediately after the operation, and/or postoperative intensive blood pressure control, because patients without a high QSM-OEF ratio rarely experience postoperative cerebral hyperperfusion.

In the present study, a 7T scanner that yields profound susceptibility effects was used to improve the accuracy for estimating misery perfusion. Against our expectations, however, a recent study has demonstrated that QSM-OEF at 7T MR imaging achieved only a slight improvement in the correlation coefficient, and the sensitivity/specificity of OEF obtained with ^{15}O-PET included substantial systematic biases in terms of the agreements compared with that at 3T MR imaging.[22,23] This issue can be mainly attributed to the relatively low spatial resolution of the source images at 7T MR imaging, which was comparable with that at 3T MR imaging.[22,23] Although the blood oxygen level–dependent effect is much stronger at 7T MR imaging than at 3T MR imaging, susceptibility information of minute venous structures at 7T MR imaging was presumably overlooked due to the low resolution of the images.[23] Thus, whereas the use of a 7T scanner in the present study is a significant limitation on the availability of QSM-OEF, the same results as in the present study could probably be obtained with QSM-OEF at 3T MR.

CONCLUSIONS

The present study demonstrated that preoperative OEF imaging generated from 7T MR QSM could identify patients at risk for cerebral hyperperfusion following CEA. Use of 7T MR imaging for humans is currently limited. However, 7T MR imagers will be applied to patients in clinical practice soon, as has occurred for 3T MR imaging. The present results suggest that imaging of cerebral hemodynamics on 7T MR imaging may be useful for predicting the development of brain adverse events following surgical interventions.

Disclosures: Ikuko Uwano—*UNRELATED: Grants/Grants Pending*: SENSHIN Medical Research Foundation. Makoto Sasaki—*UNRELATED: Consultancy*: Actelion Pharmaceuticals; *Grants/Grants Pending*: Hitachi, Japan Agency for Medical Research and Development, Japanese Ministries, Japanese Cabinet Office*; *Payment for Lectures Including Service on Speakers Bureaus*: Hitachi, Tanabe, Mediphysics, Eizai, FUJIFILM Pharmaceuticals, Daiichi Sankyo, Boehringer, Bayer AG, Otsuka Pharmaceutical, Chugai Pharma. Kohsuke Kudo—*UNRELATED*: *Grants/Grants Pending*: Japan Agency for Medical Research Development, Hitachi, Bayer, J-MAC SYSTEM, PSP Corporation*; *Payment for Lectures Including Service on Speakers Bureaus*: Hitachi, Bayer AG, Eizai, Daiichi Sankyo, FUJIFILM Pharmaceuticals. Kuniaki Ogasawara—*RELATED*: *Grant*: Grants-in-Aid for Strategic Medical Science Research (S1491001, 2014–2018) from the Ministry of Education, Culture, Sports, Science and Technology of Japan and a Grant-in-Aid for Scientific Research (15K10313) from the Japan Society for the Promotion of Science. *Money paid to the institution.

REFERENCES

1. Piepgras DG, Morgan MK, Sundt TM Jr, et al. **Intracerebral hemorrhage after carotid endarterectomy.** *J Neurosurg* 1988;68:532–36 CrossRef Medline
2. Sundt TM Jr, Sharbrough FW, Piepgras DG, et al. **Correlation of cerebral blood flow and electroencephalographic changes during carotid endarterectomy: with results of surgery and hemodynamics of cerebral ischemia.** *Mayo Clin Proc* 1981;56:533–43 Medline
3. Oshida S, Ogasawara K, Saura H, et al. **Does preoperative measurement of cerebral blood flow with acetazolamide challenge in addition to preoperative measurement of cerebral blood flow at the resting state increase the predictive accuracy of development of cerebral hyperperfusion after carotid endarterectomy? Results from 500 cases with brain perfusion single-photon emission computed tomography study.** *Neurol Med Chir (Tokyo)* 2015;55:141–48 CrossRef Medline
4. Bernstein M, Fleming JF, Deck JH. **Cerebral hyperperfusion after carotid endarterectomy: a cause of cerebral hemorrhage.** *Neurosurgery* 1984;15:50–56 CrossRef Medline
5. Ogasawara K, Sakai N, Kuroiwa T, et al; Japanese Society for Treatment at Neck in Cerebrovascular Disease Study Group. **Intracranial hemorrhage associated with cerebral hyperperfusion syndrome following carotid endarterectomy and carotid artery stenting: retrospective review of 4494 patients.** *J Neurosurg* 2007;107:1130–36 CrossRef Medline
6. Chida K, Ogasawara K, Suga Y, et al. **Postoperative cortical neural loss associated with cerebral hyperperfusion and cognitive impairment after carotid endarterectomy: 123I-iomazenil SPECT study.** *Stroke* 2009;40:448–53 CrossRef Medline
7. Nanba T, Ogasawara K, Nishimoto H, et al. **Postoperative cerebral white matter damage associated with cerebral hyperperfusion and cognitive impairment after carotid endarterectomy: a diffusion tensor magnetic resonance imaging study.** *Cerebrovasc Dis* 2012;34:358–67 CrossRef Medline
8. Baron JC, Bousser MG, Rey A, et al. **Reversal of focal "misery-perfusion syndrome" by extra-intracranial arterial bypass in hemodynamic cerebral ischemia: a case study with ^{15}O positron emission tomography.** *Stroke* 1981;12:454–59 CrossRef Medline
9. Gibbs JM, Leenders KL, Wise RJ, et al. **Evaluation of cerebral perfusion reserve in patients with carotid-artery occlusion.** *Lancet* 1984;1:182–86 Medline
10. Powers WJ, Raichle ME. **Positron emission tomography and its application to the study of cerebrovascular disease in man.** *Stroke* 1985;16:361–76 CrossRef Medline
11. Reigel MM, Hollier LH, Sundt TM, et al. **Cerebral hyperperfusion syndrome: a cause of neurologic dysfunction after carotid endarterectomy.** *J Vasc Surg* 1987;5:628–34 Medline
12. Hosoda K, Kawaguchi T, Shibata Y, et al. **Cerebral vasoreactivity and internal carotid artery flow help to identify patients at risk for hyperperfusion after carotid endarterectomy.** *Stroke* 2001;32:1567–73 CrossRef Medline
13. Ogasawara K, Yukawa H, Kobayashi M, et al. **Prediction and monitoring of cerebral hyperperfusion after carotid endarterectomy by using single-photon emission computerized tomography scanning.** *J Neurosurg* 2003;99:504–10 CrossRef Medline
14. Yoshimoto T, Houkin K, Kuroda S, et al. **Low cerebral blood flow and perfusion reserve induce hyperperfusion after surgical revascularization: case reports and analysis of cerebral hemody-**

namics. *Surg Neurol* 1997;48:132–38; discussion 138–39 CrossRef Medline
15. Spetzler RF, Wilson CB, Weinstein P, et al. **Normal perfusion pressure breakthrough theory.** *Clin Neurosurg* 1978;25:651–72 Medline
16. Sato Y, Ogasawara K, Kuroda H, et al. **Preoperative central benzodiazepine receptor binding potential and cerebral blood flow images on SPECT predict development of new cerebral ischemic events and cerebral hyperperfusion after carotid endarterectomy.** *J Nucl Med* 2011;52:1400–07 CrossRef Medline
17. Kawai N, Hatakeyama T, Okauchi M, et al. **Cerebral blood flow and oxygen metabolism measurements using positron emission tomography on the first day after carotid artery stenting.** *J Stroke Cerebrovasc Dis* 2014;23:e55–64 CrossRef Medline
18. Christen T, Bolar DS, Zaharchuk G. **Imaging brain oxygenation with MRI using blood oxygenation approaches: methods, validation, and clinical applications.** *AJNR Am J Neuroradiol* 2013;34:1113–23 CrossRef Medline
19. Zhang J, Liu T, Gupta A, et al. **Quantitative mapping of cerebral metabolic rate of oxygen ($CMRO_2$) using quantitative susceptibility mapping (QSM).** *Magn Reson Med* 2015;74:945–52 CrossRef Medline
20. De Vis JB, Petersen ET, Bhogal A, et al. **Calibrated MRI to evaluate cerebral hemodynamics in patients with an internal carotid artery occlusion.** *J Cereb Blood Flow Metab* 2015;35:1015–23 CrossRef Medline
21. Liu Z, Li Y. **Cortical cerebral blood flow, oxygen extraction fraction, and metabolic rate in patients with middle cerebral artery stenosis or acute stroke.** *AJNR Am J Neuroradiol* 2016;37:607–14 CrossRef Medline
22. Kudo K, Liu T, Murakami T, et al. **Oxygen extraction fraction measurement using quantitative susceptibility mapping: comparison with positron emission tomography.** *J Cereb Blood Flow Metab* 2016;36:1424–33 CrossRef Medline
23. Uwano I, Kudo K, Sato R, et al. **Noninvasive assessment of oxygen extraction fraction in chronic ischemia using quantitative susceptibility mapping at 7 Tesla.** *Stroke* 2017;48:2136–41 CrossRef Medline
24. North American Symptomatic Carotid Endarterectomy Trial Collaborators. **Beneficial effect of carotid endarterectomy in symptomatic patients with high-grade carotid stenosis.** *N Engl J Med* 1991;325:445–53 CrossRef Medline
25. Sato R, Shirai T, Taniguchi Y, et al. **Quantitative susceptibility mapping using the multiple dipole-inversion combination with k-space segmentation method.** *Magn Reson Med Sci* 2017 Mar 27. [Epub ahead of print] CrossRef Medline
26. Sun H, Wilman AH. **Background field removal using spherical mean value filtering and Tikhonov regularization.** *Magn Reson Med* 2014;71:1151–57 CrossRef Medline
27. Weisskoff RM, Kiihne S. **MRI susceptometry: image-based measurement of absolute susceptibility of MR contrast agents and human blood.** *Magn Reson Med* 1992;24:375–83 CrossRef Medline
28. van Zijl PC, Eleff SM, Ulatowski JA, et al. **Quantitative assessment of blood flow, blood volume and blood oxygenation effects in functional magnetic resonance imaging.** *Nat Med* 1998;4:159–67 CrossRef Medline
29. Ogasawara K, Ito H, Sasoh M, et al. **Quantitative measurement of regional cerebrovascular reactivity to acetazolamide using 123I-N-isopropyl-p-iodoamphetamine autoradiography with SPECT: validation study using H2 15O with PET.** *J Nucl Med* 2003;44:520–25 Medline
30. Ashburner J. **SPM: a history.** *Neuroimage* 2012;62:791–800 CrossRef Medline
31. Takeuchi R, Matsuda H, Yoshioka K, et al. **Cerebral blood flow SPET in transient global amnesia with automated ROI analysis by 3DSRT.** *Eur J Nucl Med Mol Imaging* 2004;31:578–89 CrossRef Medline
32. Rutgers DR, Blankensteijn JD, van der Grond J. **Preoperative MRA flow quantification in CEA patients: flow differences between patients who develop cerebral ischemia and patients who do not develop cerebral ischemia during cross-clamping of the carotid artery.** *Stroke* 2000;31:3021–28 CrossRef Medline
33. Akiyama T, Morioka T, Shimogawa T, et al. **Arterial spin-labeling magnetic resonance perfusion imaging with dual postlabeling delay in internal carotid artery steno-occlusion: validation with digital subtraction angiography.** *J Stroke Cerebrovasc Dis* 2016;25:2099–108 CrossRef Medline
34. Suga Y, Ogasawara K, Saito H, et al. **Preoperative cerebral hemodynamic impairment and reactive oxygen species produced during carotid endarterectomy correlate with development of postoperative cerebral hyperperfusion.** *Stroke* 2007;38:2712–17 CrossRef Medline
35. Ogasawara K, Inoue T, Kobayashi M, et al. **Pretreatment with the free radical scavenger edaravone prevents cerebral hyperperfusion after carotid endarterectomy.** *Neurosurgery* 2004;55:1060–67 CrossRef Medline
36. Ogasawara K, Yamadate K, Kobayashi M, et al. **Effects of the free radical scavenger, edaravone, on the development of postoperative cognitive impairment in patients undergoing carotid endarterectomy.** *Surg Neurol* 2005;64:309–13; discussion 313–14 Medline

CT Texture Analysis Potentially Predicts Local Failure in Head and Neck Squamous Cell Carcinoma Treated with Chemoradiotherapy

H. Kuno, M.M. Qureshi, M.N. Chapman, B. Li, V.C. Andreu-Arasa, K. Onoue, M.T. Truong, and O. Sakai

ABSTRACT

BACKGROUND AND PURPOSE: The accurate prediction of prognosis and failure is crucial for optimizing treatment strategies for patients with cancer. The purpose of this study was to assess the performance of pretreatment CT texture analysis for the prediction of treatment failure in primary head and neck squamous cell carcinoma treated with chemoradiotherapy.

MATERIALS AND METHODS: This retrospective study included 62 patients diagnosed with primary head and neck squamous cell carcinoma who underwent contrast-enhanced CT examinations for staging, followed by chemoradiotherapy. CT texture features of the whole primary tumor were measured using an in-house developed Matlab-based texture analysis program. Histogram, gray-level co-occurrence matrix, gray-level run-length, gray-level gradient matrix, and Laws features were used for texture feature extraction. Receiver operating characteristic analysis was used to identify the optimal threshold of any significant texture parameter. We used multivariate Cox proportional hazards models to examine the association between the CT texture parameter and local failure, adjusting for age, sex, smoking, primary tumor stage, primary tumor volume, and human papillomavirus status.

RESULTS: Twenty-two patients (35.5%) developed local failure, and the remaining 40 (64.5%) showed local control. Multivariate analysis revealed that 3 histogram features (geometric mean [hazard ratio = 4.68, $P = .026$], harmonic mean [hazard ratio = 8.61, $P = .004$], and fourth moment [hazard ratio = 4.56, $P = .048$]) and 4 gray-level run-length features (short-run emphasis [hazard ratio = 3.75, $P = .044$], gray-level nonuniformity [hazard ratio = 5.72, $P = .004$], run-length nonuniformity [hazard ratio = 4.15, $P = .043$], and short-run low gray-level emphasis [hazard ratio = 5.94, $P = .035$]) were significant predictors of outcome after adjusting for clinical variables.

CONCLUSIONS: Independent primary tumor CT texture analysis parameters are associated with local failure in patients with head and neck squamous cell carcinoma treated with chemoradiotherapy.

ABBREVIATIONS: CRT = chemoradiotherapy; GLCM = gray-level co-occurrence matrix; GLN = gray-level nonuniformity; GLRL = gray-level run-length; HNSCC = head and neck squamous cell carcinoma; HPV = human papillomavirus; HR = hazard ratio; RLN = run-length nonuniformity; SRE = short-run emphasis; SRLGE = short-run low gray-level emphasis

Chemoradiotherapy (CRT) is the mainstay of treatment for early and locally advanced head and neck squamous cell carcinoma (HNSCC). The accurate prediction of prognosis and failure is crucial for optimizing treatment strategies for patients with cancer; however, it remains an area of ongoing controversy. Currently, the American Joint Committee on Cancer staging system, which uses unidimensional tumor size, local anatomic invasion, nodal involvement, and the presence of metastatic disease, is the most widely accepted and applied prognostic system in cancer management. Yet this classification is mainly based on surgical criteria rather than predictors of radiation or chemotherapy response, and this tumor node metastasis information sometimes fails to predict the response to nonsurgical therapy. Several studies have demonstrated a significant impact of primary tumor volume on treatment outcome in patients with HNSCC treated with radiation therapy.[1-5] More recent studies have also shown that patients with human papillomavirus (HPV)-positive HNSCCs have a better response to CRT than patients with HPV-negative tumors.[6-9] However, treatment failure still occurs in patients with HNSCC with small tumor volume and/or HPV-positive status.[10]

Received March 6, 2017; accepted after revision July 16.

From the Departments of Radiology (H.K., M.M.Q., M.N.C., B.L., V.C.A.A., K.O., M.T.T., O.S.), Radiation Oncology (M.M.Q., M.T.T., O.S.), and Otolaryngology–Head and Neck Surgery (O.S.), Boston Medical Center, Boston University School of Medicine, Boston, Massachusetts; and Department of Diagnostic Radiology (H.K.), National Cancer Center Hospital East, Kashiwa, Chiba, Japan.

Please address correspondence to Osamu Sakai, MD, PhD, Department of Radiology, Boston Medical Center, Boston University School of Medicine, FGH Building, 3rd Floor, 820 Harrison Ave, Boston, MA 02118; e-mail: osamu.sakai@bmc.org

Indicates article with supplemental on-line table and appendix.

Indicates article with supplemental on-line photo.

http://dx.doi.org/10.3174/ajnr.A5407

Image texture is defined as a complex visual pattern within an image, consisting of simpler subpatterns with characteristic features, and texture analysis allows the mathematic detection of the subtle spatial arrangement of the gray level among image pixels.[11,12] Texture analysis is a postprocessing technique and a new addition to the image-analysis armamentarium that extracts information native to image data that is not apparent on visual inspection of images. These techniques ultimately provide a quantitative means of extracting image features that are useful for comparative analyses. In the past several years, CT texture analysis has been investigated in oncology imaging for its ability to predict treatment outcome in patients with non-small cell lung cancer, esophageal cancer, and metastatic renal cell carcinoma.[13-18] One study showed that CT texture and histogram analysis parameters of the primary mass were associated with overall survival in patients with HNSCC who were treated with induction chemotherapy followed by chemotherapy, radiation, and/or an operation.[19] However, it is still unclear whether CT texture analysis can predict local failure to radiation therapy in patients with HNSCC, including with important clinical factors such as smoking history, tumor volume, and HPV status. Considering that texture analysis may detect subtle pathologic changes in an image,[20,21] we herein hypothesized that texture analysis on CT would enable assessment of radiosensitivity in a patient with HNSCC.

The purpose of this study was to assess the utility of texture analysis for the prediction of treatment failure in primary HNSCC treated with CRT.

MATERIALS AND METHODS

Patients

The institutional review board at Boston Medical Center approved this study. The requirement to obtain written informed consent was waived for this retrospective analysis.

Between February 2008 and February 2015, one hundred sixty-five consecutive newly diagnosed patients with histologically proved HNSCCs (oropharynx, larynx, hypopharynx, and oral cavity) underwent contrast-enhanced CT before treatment. Eighty-six of the 165 patients (52%) were excluded because they were treated surgically. We excluded an additional 13 patients: 3 patients due to significant artifacts from motion or dental hardware on CT that may have influenced the texture analysis, 5 patients with very small primary tumors (tumor volume <0.4 cm^3) that were difficult to contour, and 5 patients due to an inability to complete treatment. Three patients showing local control were excluded because follow-up periods were <12 months due to other causes of death (2 patients) or transfer to hospice care for distant metastatic disease. One patient who developed metachronous multiple HNSCC was also excluded due to additional treatment with CyberKnife stereotactic radiosurgery (Accuray, Sunnyvale, California) in the same region for a secondary squamous cell carcinoma. The remaining 62 patients (53 men, 9 women; age 31–80 years; median age, 58 years) diagnosed with primary HNSCC were enrolled in this study. Of 62 patients, 31 (50%) had oropharyngeal squamous cell carcinomas, 9 (15%) had hypopharyngeal squamous cell carcinomas, 19 (31%) had laryngeal squamous cell carcinomas, and 3 (5%) had oral cavity squamous cell carcinomas.

Treatment and Follow-Up

All patients were treated with definitive intensity-modulated radiation therapy. The primary gross tumor volume was treated to a median dose of 69.96 Gy (range, 60.0–69.96 Gy), over a median of 33 fractions (range, 30–33 fractions) and a median of 47 days (range, 40–102 days). Concurrent chemotherapy was given to 60 (96.8%) patients, but 1 patient was changed to radiation therapy alone due to stomatitis. Of these 60 patients, 33 also received induction chemotherapy. The remaining 2 patients underwent radiation therapy alone.

Patients were followed after the conclusion of treatment to evaluate local control. All patients were followed clinically for at least 12 months after completion of radiation therapy. The follow-up evaluation included physical and endoscopic examinations. In addition to the clinical examination, CT, MR imaging, and [^{18}F] FDG PET/CT were used to assess the clinical response as part of standard treatment care. Local failures were confirmed by biopsy except in cases of significant progressive disease by clinical examination and imaging assessment with [^{18}F] FDG PET/CT or MR imaging. The follow-up period was designated as the total time of follow-up, starting at treatment initiation and ending either at histologically confirmed local failure or at last patient contact without local failure.

CT Imaging Protocol

Contrast-enhanced CT examinations were performed either independently or combined with [^{18}F] FDG PET examination, acquired by 64- or 16-detector row CT scanners (LightSpeed VCT or Discovery STE-16 PET/CT; GE Healthcare, Milwaukee, Wisconsin). Dedicated neck CT studies were helically acquired (120 kV[peak], gantry rotation time = 0.5 second, automatic tube current modulation on with 10% adaptive statistical iterative reconstruction, helical pitch factor = 0.937:1, scan FOV = 300 mm, reconstructed section thickness = 1.25 or 3.75 mm, image matrix = 512 × 512) extending from the skull base to the thoracic inlet following a 60-second delay after intravenous contrast injection (80–160 mL; ioversol, Optiray 350, Mallinckrodt, St. Louis, Missouri; or iopamidol, Isovue 370, Bracco, Princeton, New Jersey). The images were reviewed in soft-tissue algorithms.

Image Segmentation

The primary tumor was manually contoured by a neuroradiologist with 9 years of experience who was blinded to patient history. Segmentation of the whole primary lesion for each section was performed with a dedicated AW workstation (GE Healthcare) with a semiautomated graphic user interface. We used axial images for the segmentation. If the tumor border was unclear on the axial images, coronal or sagittal reformatted sections were used to guide segmentation. We manually excluded obvious necrotic and cystic areas, regions of ulceration of the tumor, calcification, and areas of artifacts from the contoured tumor volume (On-line Figure). The most solid component of the tumor was contoured. When severe streak artifacts within the tumor were seen, we excluded the artifact section and used only artifact-free sections for texture analysis. The full processing time of image segmentation and texture analysis per subject was approximately 10 minutes.

Table 1: Demographics and tumor characteristics of patients with head and neck cancer[a]

Characteristic	Overall Subjects (*n* = 62)	Local Failure (*n* = 22)	Local Control (*n* = 40)	*P* Value
Age (yr)				.205
Median (range)	58 (31–80)	60 (31–79)	57 (32–80)	
Sex				.098
Male	53 (85)	21 (95)	32 (80)	
Female	9 (15)	1 (5)	8 (20)	
Primary site				.515
Oropharynx	31 (50)	11 (50)	20 (50)	
Hypopharynx	9 (15)	4 (18)	5 (13)	
Larynx	19 (31)	5 (23)	14 (35)	
Oral cavity	3 (5)	2 (9)	1 (2)	
T-Stage				.037[b]
T1	1 (2)	0 (0)	1 (2)	
T2	14 (23)	2 (9)	12 (30)	
T3	18 (29)	8 (36)	10 (25)	
T4	29 (47)	12 (55)	17 (43)	
N-stage				.914
N0	9 (15)	3 (14)	6 (15)	
N1	10 (16)	3 (14)	7 (18)	
N2	39 (63)	14 (64)	25 (63)	
N3	4 (6)	2 (9)	2 (5)	
Histopathologic grade				
Well diff.	9 (15)	3 (14)	6 (14)	.927
Moderately diff.	33 (53)	13 (59)	20 (50)	
Poorly diff.	17 (27)	6 (27)	11 (28)	
Unknown	3 (5)	0	3 (8)	
Smoking (pack-year)				.947
Median (range)	20 (0–100)	30 (0–100)	20 (0–60)	
Tumor volume (mL)				.007[b]
Median (range)	6.28 (0.45–69.47)	15.07 (0.95–51.89)	4.56 (0.45–69.47)	
HPV (p16)				.917
Positive	24 (39)	8 (36)	16 (40)	
Negative	23 (37)	8 (36)	15 (38)	
Unknown	15 (24)	6 (27)	9 (23)	
CT scanner				.618
64–detector row MDCT	12 (19)	5 (23)	7 (18)	
16–detector MDCT	50 (81)	17 (77)	33 (82)	
Section thickness				.689
1.25 cm	50 (81)	18 (82)	31 (78)	
3.75 cm	12 (19)	4 (18)	9 (22)	
ASIR				.655
On	22 (35)	7 (32)	15 (38)	
Off	40 (65)	15 (68)	25 (63)	

Note:—MDCT indicates multidetector row CT; ASIR, adaptive statistical iterative reconstruction; diff., differentiated squamous cell carcinoma.

[a] Data are presented as the number of patients with percentages in parentheses, unless otherwise noted.

[b] Indicates a significant difference by the Pearson χ^2 or Mann-Whitney *U* test ($P < .05$).

Texture Analysis

In this work, we measured 42 features from each segmented tissue volume using an in-house-developed Matlab (MathWorks, Natick, Massachusetts) texture analysis software.[20,22] The mean value of the textural features on an ROI basis was estimated. The volume of each primary tumor was also calculated. The 42 features included the following:

1) Thirteen histogram features
2) Five gray-level co-occurrence matrix (GLCM) features
3) Eleven gray-level run-length (GLRL) features
4) Four gray-level gradient matrix features
5) Nine Laws features.

We discuss the extraneous math behind each texture feature in detail in a subsequent On-line Appendix.[11,12,20,22-25]

Statistical Analysis

First, associations of demographic and clinical characteristics with local control status were tested with the Pearson χ^2 test or Mann-Whitney *U* test. Texture parameters were then compared in patients with local control against patients who developed local failure using the Mann-Whitney *U* test to select significant texture parameters. Second, receiver operating characteristic analysis was used to identify the optimal threshold of any significant texture parameter. The point on the receiver operating characteristic curve farthest from the 45-degree reference line with the best combination of sensitivity and specificity was considered the optimum threshold. The area under the receiver operating characteristic curve was also measured for the selected parameters. Third, Cox proportional hazards models were used to examine the association between each selected CT texture parameter and local failure. The local control time was defined as the time between the start of treatment and the date on which local recurrence was found or the last follow-up. Furthermore, we used multivariate Cox proportional hazards models to examine the association between CT texture parameters and local failure, adjusting for age, sex, smoking (pack-year), primary tumor stage, primary tumor volume, and HPV status. Because 15 of 62 subjects had unknown HPV status, we used 47 subjects with HPV data for multivariate models.

All statistical analyses were performed by using STATA (Version 12.1; StataCorp, College Station, Texas). A *P* value $< .05$ was considered statistically significant.

RESULTS

At a median follow-up of 29 months (range, 7–88 months) for included subjects, 22 patients (35.5%) developed local failure and the remaining 40 patients (64.5%) showed local control. The follow-up time of patients with local failure ranged from 3.7 to 14.4 months (median, 4.6 months), and the follow-up time of patients with local control ranged from 16.8 to 88.4 months (median, 35 months). Among 24 patients positive for HPV, 8 patients (33.3%; 5 oropharynx, 2 larynx, and 1 oral tongue carcinoma) developed local failure. Complete patient demographics and tumor characteristics are described in Table 1. Primary tumor volume of the local control group was significantly smaller than that in the failure group (median, 4.56 versus 15.07 mL, $P = .007$). The primary T-stage was also significantly different between the local control and failure groups ($P =$

Table 2: Optimal thresholds obtained from ROC curves and sensitivity/specificity to predict local failure[a]

Texture Parameter	AUC	Cutoff Point	Sensitivity (%)	Specificity (%)	PPV (%)	NPV (%)	Accuracy (%)
Histogram							
Mean	0.67 (0.54–0.81)	>1102	50.2 (28.2–71.7)	82.5 (67.2–92.6)	64.7	73.3	71.0
SD	0.70 (0.56–0.84)	<252.9	40.9 (20.7–63.7)	92.5 (79.6–98.4)	74.0	75.0	74.2
Geometric mean	0.71 (0.57–0.85)	>920.6	36.4 (17.2–59.3)	92.5 (79.6–98.4)	72.7	72.7	72.6
Harmonic mean	0.71 (0.58–0.85)	>243.4	36.4 (17.2–59.3)	95.0 (83.1–99.4)	80.0	73.1	74.2
Fourth moment	0.69 (0.55–0.83)	<4.65e10	40.9 (20.7–63.6)	92.5 (79.6–98.4)	74.0	75.0	74.2
GLRL							
SRE	0.79 (0.68–0.91)	<0.0341	36.4 (17.2–59.3)	95.0 (83.1–99.4)	80.0	73.1	74.2
LRE	0.80 (0.69–0.91)	<0.0332	63.6 (40.7–82.8)	80.0 (64.4–90.9)	63.6	80.0	74.2
GLN	0.80 (0.69–0.92)	<0.0408	68.2 (45.1–86.1)	80.0 (64.4–90.9)	65.2	82.1	75.8
RLN[b]	0.82 (0.72–0.92)	<0.0329	77.3 (58.8–87.3)	77.5 (54.6–92.2)	65.4	86.1	77.4
RP	0.71 (0.57–0.84)	>433.3	72.7 (49.8–89.3)	65.0 (48.3–79.4)	53.3	81.3	67.7
LGRE	0.73 (0.60–0.85)	>440	81.8 (59.7–94.8)	62.5 (45.8–77.3)	54.6	86.2	69.4
HGRE	0.74 (0.61–0.87)	>433.9	54.6 (32.2–75.6)	85.0 (70.2–94.3)	66.7	77.3	74.2
SRLGE	0.72 (0.59–0.86)	>444.2	77.3 (54.6–92.2)	37.5 (50.9–81.4)	56.7	84.4	71.0

Note:—LRE indicates long-run emphasis; RP, run percentage; LGRE, low gray-level run emphasis; HGRE, high gray-level run emphasis; PPV, positive predictive value; NPV, negative predictive value; AUC, area under the receiver operating characteristic curve; ROC, receiver operating characteristic.

[a] Numbers in parentheses are 95% confidence intervals.

[b] AUC of the RLN was significantly better than that of mean ($P = .022$). The differences with other selected texture features were not significant ($P > .05$).

Table 3: Cox proportional hazards model of selected CT texture parameters for predicting local failure

	Univariate Analysis ($n = 62$)			Multivariate Analysis[a] ($n = 47$)		
Texture Parameter	HR	95% CI	*P* Value	HR	95% CI	*P* Value
Histogram						
Mean	2.79	1.21–6.46	.019[b]	1.74	0.62–4.88	.295
SD	5.69	2.39–13.53	<.001[b]	2.56	0.66–10.00	.176
Geometric mean	4.08	1.50–11.07	.002[b]	4.68	1.21–18.11	.026[b]
Harmonic mean	3.47	1.17–10.26	.012[b]	8.61	2.00–37.19	.004[b]
Fourth moment	5.69	2.40–13.53	<.001[b]	4.56	1.01–20.48	.048[b]
GLRL						
SRE	4.58	2.24–13.48	<.001[b]	3.75	1.23–13.61	.044[b]
LRE	3.63	1.55–8.54	.003[b]	2.68	0.67–10.66	.163
GLN	5.61	2.06–15.28	<.001[b]	5.72	1.74–18.82	.004[b]
RLN	5.69	2.22–14.59	<.001[b]	4.16	1.25–16.48	.043[b]
RP	3.39	1.32–8.67	.007[b]	3.70	0.85–16.21	.082
LGRE	5.06	1.71–14.99	<.001[b]	4.84	0.99–24.34	.055
HGRE	3.74	1.61–8.69	.003[b]	2.39	0.53–10.83	.260
SRLGE	4.53	1.67–12.32	.001[b]	5.94	1.14–24.97	.035[b]

Note:—LRE indicates long-run emphasis; RP, run percentage; LGRE, low gray-level run emphasis; HGRE, high gray-level run emphasis.

[a] Models were adjusted for age, sex, smoking, primary tumor stage, primary tumor volume, and HPV status.

[b] Indicates a significant difference ($P < .05$).

.037). There was no significant difference in the age ($P = .205$), sex ($P = .098$), primary site ($P = .515$), N-stage ($P = .914$), histopathologic grade ($P = .927$), smoking pack-years ($P = .947$), and HPV status ($P = .917$) between the 2 groups. The distributions of the CT scanner, section thickness, and the use of adaptive statistical iterative reconstruction of these study subjects were not different between local control and failure groups ($P = .618$ for CT scanner, $P = .689$ for section thickness, and $P = .655$ for adaptive statistical iterative reconstruction).

Results of 42 texture parameters differentiating local control and local failure are shown in the On-line Table. The Mann-Whitney *U* test revealed that 13 parameters, including 5 histogram features (mean, SD, geometric mean, harmonic mean, fourth moment) and 8 GLRL features (short-run emphasis [SRE], long-run emphasis, gray-level nonuniformity [GLN], run-length nonuniformity [RLN], run percentage, low gray-level run emphasis, high gray-level run emphasis, and short-run low gray-level emphasis [SRLGE]) showed significant differences between the local failure and local control groups.

The results of optimal thresholds for selected texture features obtained from receiver operating characteristic curves and sensitivity/specificity with area under the receiver operating characteristic curve to predict local failure are shown in Table 2. The highest area under the receiver operating characteristic curve was 0.82, with a sensitivity of 77.3% and a specificity of 77.5% in RLN (one of the GLRL features). In subgroup analysis based on the HPV status, the area under the receiver operating characteristic curve was 0.80, with a sensitivity of 87.5% and a specificity of 68.8% for the HPV-positive group and the area under the receiver operating characteristic curve was 0.75 with a sensitivity of 75.0% and a specificity of 73.3% for the HPV-negative group in RLN.

The results of Cox proportional hazards model of selected CT texture parameters and clinical factors for predicting local failure are shown in Table 3. The multivariate Cox proportional hazards model revealed that 3 histogram features [geometric mean (hazard ratio [HR] = 4.68, $P = .026$), harmonic mean (HR = 8.61, $P = .004$), fourth moment (HR = 4.56, $P = .048$)], and 4 GLRL features [SRE (HR = 3.75, $P = .044$), GLN (HR = 5.72, $P = .004$), RLN (HR = 4.15; $P = .043$), and SRLGE (HR = 5.94, $P = .035$)] remained significant predictors of outcome after adjusting for clinical variables. Representative examples of patients positive for HPV with oropharyngeal squamous cell carcinomas with local failure and local control are shown in the Figure.

DISCUSSION

In our study, we measured volumetric texture features of the whole primary HNSCC tumor using pretreatment contrast-enhanced CT. Three histogram features and 4 GLRL features have been associated with local failure in patients treated with CRT

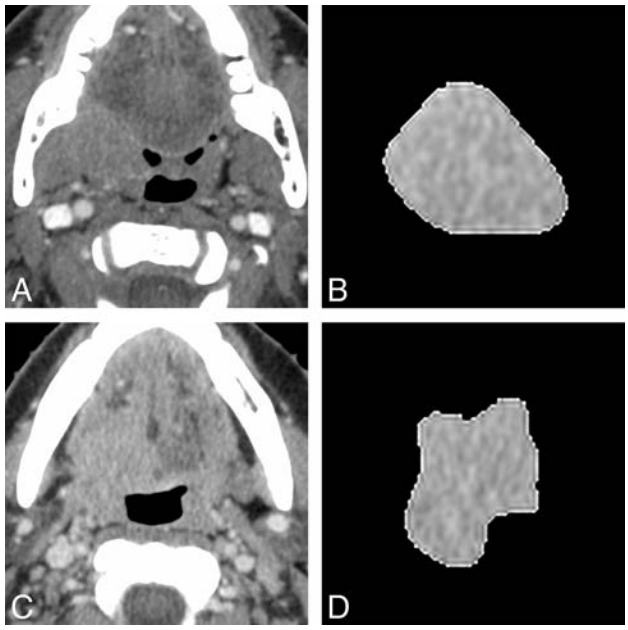

FIGURE. Representative axial contrast-enhanced CT images (*A* and *C*) and corresponding axial section ROI mask-segmented primary tumor (*B* and *D*) for 2 different patients with oropharyngeal squamous cell carcinoma. Segmented tumor is from a 75-year-old man (*B*) with right tonsil squamous cell carcinoma (HPV-positive; smoking, 0 pack-year; tumor volume, 16.4 mL; clinical T-stage, T4) who developed local failure and a 43-year-old woman (*D*) with squamous cell carcinoma of the right base of tongue (HPV- positive; smoking, 0 pack-year; tumor volume, 20.6 mL; clinical T-stage, T4) who showed local control. Representative texture features of each patients are as follows; for geometric mean, 973.2 (local failure, *B*) and 906.6 (local control, *D*); for harmonic mean, 285.1 (local failure, *B*) and 210.3 (local control, *D*); for SRE, 0.026 (local failure, *B*) and 0.043 (local control, *D*); for GLN, 0.026 (local failure, *B*) and 0.042 (local control, *D*); for RLN, 0.019 (local failure, *B*) and 0.032 (local control, *D*); and for SRLGE, 479.1 (local failure, *B*) and 459.1 (local control, *D*).

after adjusting for clinical variables, including smoking history, HPV status, T-stage, and tumor volume. The results suggest that CT texture analysis may serve as an independent indicator of local failure regardless of tumor status, including HPV infection.

In recent years, the measurement of spatial heterogeneity by CT textural analysis has gained acceptance as a means to extract information from imaging of primary tumors to predict treatment outcome in oncology patients.[13-18] In the head and neck, Zhang et al[19] analyzed the predictive value of texture and histogram features in 72 patients with HNSCC treated with induction chemotherapy (TPF; docetaxel, cisplatin, and fluouracil) and found that in addition to expected factors such as tumor volume and N stage, primary mass entropy (HR = 2.10 for each 0.5-unit increase; $P = .036$) and histogram skewness (HR = 3.67 for each 1.0-unit increase; $P = .009$) were independent predictors of overall survival in multivariate Cox regression analysis. However, their study included patients treated with an operation followed by chemotherapy, and HPV status was not provided in their analysis. In our study, we focused on the chemoradiosensitivity of the primary tumor using whole-tumor primary HNSCC volume texture analysis, and the results demonstrated that CT texture analysis parameters such as histogram and GLRL features are associated with local failure in patients with HNSCC treated with CRT.

The GLRL features are one of the categories of spatially dependent texture features based on the length and quantity of runs of adjacent pixels with similar intensity values.[11,12,20] The significant difference in the texture features between local control and local failure groups suggests a different degree of uniformity within the tumors along both long and short matrix runs. Increased heterogeneity of the primary mass on contrast-enhanced CT images indicates that the tumor blood supply is heterogeneous, with some areas having increased vascular supply and others having hypoxic voids.[26-29] Although there is no direct comparison between the underlying tumor histopathology and correlation to the mathematic significance of these features on texture analysis, the texture features may potentially reflect increased heterogeneity or hypoxic voids of the primary mass on contrast-enhanced CT images.[19,30]

Other pretreatment predictive imaging biomarkers of local control for HNSCC have been investigated using advanced imaging techniques, albeit with variable results. CT perfusion has been reported to obtain measures of tumor vascular physiology and hemodynamics, and some investigators demonstrated that CT-determined tumor perfusion was an independent predictor of local control in HNSCC treated by definitive radiation therapy with or without chemotherapy.[29,31-33] Diffusion-weighted imaging[34-37] and dynamic contrast-enhanced MR imaging[38-41] have also been used as functional imaging techniques as predictive biomarkers of radiation therapy. One recently published study showed preliminary results exploring the value of assessing texture features with intratreatment dynamic contrast-enhanced MR imaging for patients with HNSCC.[42] Functional imaging studies including perfusion are useful tools for mapping the vascularity of the tumor environment at baseline. However, these techniques are not routinely used in the clinical protocol for staging of HNSCC, and recently, there are increasing concerns for additional exposure to radiation or gadolinium-based contrast agents.[43,44] [^{18}F] FDG PET/CT is another imaging technique widely used in the evaluation of patients with HNSCC, and its clinical utility for predicting treatment outcome of HNSCC has been previously investigated.[5,45-47] However, [^{18}F] FDG PET/CT examinations are used only in advanced-stage HNSCC when management may be altered due to detection of distant metastases. Contrast-enhanced CT is widely used to stage HNSCC before treatment; therefore, CT texture analysis could be potentially useful for predicting local failure without additional exposure to radiation or contrast material.

There are several limitations to this study. First, CT protocols including the types of CT scanners, section thickness, and adaptive statistical iterative reconstruction were not identical in this population, which may potentially affect the texture analysis.[48] These problems remain to be solved in future validation studies using identical CT parameters. However, the distribution of subjects between local control and failure groups was almost the same for both types of CT scanners, different section thicknesses, and the use of adaptive statistical iterative reconstruction. Additionally, CT texture analysis parameters have been shown to be highly reproducible in multiple kilovolt peaks and milliampere-second settings in a water phantom.[19] We therefore believe that the differences in scanners have little, if any, influence on our presented

results. Second, a single user performed the semiautomated segmentation and workflow for this CT texture analysis. The generalizability of our results to other institutions and users is unknown, though the semiautomated nature of the software has the potential to reduce interobserver variation. Third, we contoured areas of obvious necrotic and cystic changes as well as ulceration out of the final contours that were imported into the texture analysis program, because including foci of air would not accurately reflect the underlying texture features within the solid portion of the tumors. However, the necrosis or ulceration within the tumor has a potential impact on hypoxia/radiosensitivity. This issue needs to be further evaluated in a future study assessing whether the region of necrosis should be included or excluded for texture analysis. Finally, the study subjects included heterogeneous groups of patients with HNSCC of different primary sites. Further studies with a larger number of patients are needed to validate the performance of the predictive model for each subsite.

CONCLUSIONS

Independent primary tumor CT texture analysis parameters are associated with local failure in patients with HNSCC treated with CRT. CT is noninvasive, widely available, and frequently used to stage early and locally advanced HNSCC before treatment. Therefore, CT texture analysis could serve as a widely applicable pretreatment noninvasive biomarker for predicting local failure with the potential to assist in treatment decisions in patients with HNSCC. Further testing using a larger sample size is needed to validate the performance of the predictive model.

Disclosures: Hirofumi Kuno—*UNRELATED*: *Grants/Grants Pending*: Grant-in-Aid for Young Scientists (B) KAKEN (No. 26861033), 2014–2015; *Payment for Lectures Including Service on Speakers Bureaus*: Toshiba Medical Systems, 2014. Osamu Sakai—*UNRELATED*: *Consultancy*: Guerbet; *Payment for Lectures Including Service on Speakers Bureaus*: Bracco Diagnostics, Eisai.

REFERENCES

1. Studer G, Lütolf U, El-Bassiouni M, et al. **Volumetric staging (VS) is superior to TNM and AJCC staging in predicting outcome of head and neck cancer treated with IMRT.** *Acta Oncol* 2007;46:386–94 CrossRef Medline
2. Knegjens JL, Hauptmann M, Pameijer FA, et al. **Tumor volume as prognostic factor in chemoradiation for advanced head and neck cancer.** *Head Neck* 2011;33:375–82 CrossRef Medline
3. Strongin A, Yovino S, Taylor R, et al. **Primary tumor volume is an important predictor of clinical outcomes among patients with locally advanced squamous cell cancer of the head and neck treated with definitive chemoradiotherapy.** *Int J Radiat Oncol Biol Phys* 2012; 82:1823–30 CrossRef Medline
4. Doweck I, Denys D, Robbins KT. **Tumor volume predicts outcome for advanced head and neck cancer treated with targeted chemoradiotherapy.** *Laryngoscope* 2002;112:1742–49 CrossRef Medline
5. Romesser PB, Qureshi MM, Shah BA, et al. **Superior prognostic utility of gross and metabolic tumor volume compared to standardized uptake value using PET/CT in head and neck squamous cell carcinoma patients treated with intensity-modulated radiotherapy.** *Ann Nucl Med* 2012;26:527–34 CrossRef Medline
6. Lassen P, Eriksen JG, Hamilton-Dutoit S, et al; Danish Head and Neck Cancer Group (DAHANCA). **HPV-associated p16-expression and response to hypoxic modification of radiotherapy in head and neck cancer.** *Radiother Oncol* 2010;94:30–35 CrossRef Medline
7. Chung CH, Zhang Q, Kong CS, et al. **p16 protein expression and human papillomavirus status as prognostic biomarkers of nonoropharyngeal head and neck squamous cell carcinoma.** *J Clin Oncol* 2014;32:3930–38 CrossRef Medline
8. Lassen P, Primdahl H, Johansen J, et al Danish Head and Neck Cancer Group (DAHANCA). **Impact of HPV-associated p16-expression on radiotherapy outcome in advanced oropharynx and non-oropharynx cancer.** *Radiother Oncol* 2014;113:310–16 CrossRef Medline
9. Huang SH, Xu W, Waldron J, et al. **Refining American Joint Committee on Cancer/Union for International Cancer Control TNM stage and prognostic groups for human papillomavirus-related oropharyngeal carcinomas.** *J Clin Oncol* 2015;33:836–45 CrossRef Medline
10. Vainshtein JM, Spector ME, McHugh JB, et al. **Refining risk stratification for locoregional failure after chemoradiotherapy in human papillomavirus-associated oropharyngeal cancer.** *Oral Oncol* 2014; 50:513–19 CrossRef Medline
11. Tang X. **Texture information in run-length matrices.** *IEEE Trans Image Process* 1998;7:1602–09 CrossRef Medline
12. Haralick RM, Shanmugam K, Dinstein IH. **Textural features for image classification.** *IEEE Transactions on Systems, Man and Cybernetics* 1973;3:610–21
13. Miles KA, Ganeshan B, Griffiths MR, et al. **Colorectal cancer: texture analysis of portal phase hepatic CT images as a potential marker of survival.** *Radiology* 2009;250:444–52 CrossRef Medline
14. Goh V, Ganeshan B, Nathan P, et al. **Assessment of response to tyrosine kinase inhibitors in metastatic renal cell cancer: CT texture as a predictive biomarker.** *Radiology* 2011;261:165–71 CrossRef Medline
15. Ganeshan B, Goh V, Mandeville HC, et al. **Non-small cell lung cancer: histopathologic correlates for texture parameters at CT.** *Radiology* 2013;266:326–36 CrossRef Medline
16. Ng F, Ganeshan B, Kozarski R, et al. **Assessment of primary colorectal cancer heterogeneity by using whole-tumor texture analysis: contrast-enhanced CT texture as a biomarker of 5-year survival.** *Radiology* 2013;266:177–84 CrossRef Medline
17. Yip C, Landau D, Kozarski R, et al. **Primary esophageal cancer: heterogeneity as potential prognostic biomarker in patients treated with definitive chemotherapy and radiation therapy.** *Radiology* 2014;270:141–48 CrossRef Medline
18. Ganeshan B, Panayiotou E, Burnand K, et al. **Tumour heterogeneity in non-small cell lung carcinoma assessed by CT texture analysis: a potential marker of survival.** *Eur Radiol* 2012;22:796–802 CrossRef Medline
19. Zhang H, Graham CM, Elci O, et al. **Locally advanced squamous cell carcinoma of the head and neck: CT texture and histogram analysis allow independent prediction of overall survival in patients treated with induction chemotherapy.** *Radiology* 2013;269:801–09 CrossRef Medline
20. Buch K, Fujita A, Li B, et al. **Using texture analysis to determine human papillomavirus status of oropharyngeal squamous cell carcinomas on CT.** *AJNR Am J Neuroradiol* 2015;36:1343–48 CrossRef Medline
21. Fujita A, Buch K, Li B, et al. **Difference between HPV-positive and HPV-negative non-oropharyngeal head and neck cancer: texture analysis features on CT.** *J Comput Assist Tomogr* 2016;40:43–47 CrossRef Medline
22. Yu H, Buch K, Li B, et al. **Utility of texture analysis for quantifying hepatic fibrosis on proton density MRI.** *J Magn Reson Imaging* 2015; 42:1259–65 CrossRef Medline
23. Laws KI. *Textured Image Segmentation* [dissertation]. Los Angeles: University of Southern California; 1980
24. Castellano G, Bonilha L, Li LM, et al. **Texture analysis of medical images.** *Clin Radiol* 2004;59:1061–69 CrossRef Medline
25. Li B, Jara H, Yu H, et al. **Enhanced Laws textures: a potential MRI surrogate marker of hepatic fibrosis in a murine model.** *Magn Reson Imaging* 2017;37:33–40 CrossRef Medline
26. Nordsmark M, Overgaard M, Overgaard J. **Pretreatment oxygenation predicts radiation response in advanced squamous cell carcinoma of the head and neck.** *Radiother Oncol* 1996;41:31–39 Medline

27. Janssen H, Haustermans K, Balm A, et al. **Hypoxia in head and neck cancer: how much, how important?** *Head Neck* 2005;27:622–38 CrossRef Medline
28. Nordsmark M, Bentzen SM, Rudat V, et al. **Prognostic value of tumor oxygenation in 397 head and neck tumors after primary radiation therapy: an international multi-center study.** *Radiother Oncol* 2005;77:18–24 CrossRef Medline
29. Hermans R, Meijerink M, Van den Bogaert W, et al. **Tumor perfusion rate determined noninvasively by dynamic computed tomography predicts outcome in head-and-neck cancer after radiotherapy.** *Int J Radiat Oncol Biol Phys* 2003;57:1351–56 CrossRef Medline
30. Kassner A, Thornhill RE. **Texture analysis: a review of neurologic MR imaging applications.** *AJNR Am J Neuroradiol* 2010;31:809–16 CrossRef Medline
31. Zima A, Carlos R, Gandhi D, et al. **Can pretreatment CT perfusion predict response of advanced squamous cell carcinoma of the upper aerodigestive tract treated with induction chemotherapy?** *AJNR Am J Neuroradiol* 2007;28:328–34 Medline
32. Bisdas S, Nguyen SA, Anand SK, et al. **Outcome prediction after surgery and chemoradiation of squamous cell carcinoma in the oral cavity, oropharynx, and hypopharynx: use of baseline perfusion CT microcirculatory parameters vs. tumor volume.** *Int J Radiat Oncol Biol Phys* 2009;73:1313–18 CrossRef Medline
33. Truong MT, Saito N, Ozonoff A, et al. **Prediction of locoregional control in head and neck squamous cell carcinoma with serial CT perfusion during radiotherapy.** *AJNR Am J Neuroradiol* 2011;32:1195–201 CrossRef Medline
34. Hatakenaka M, Nakamura K, Yabuuchi H, et al. **Apparent diffusion coefficient is a prognostic factor of head and neck squamous cell carcinoma treated with radiotherapy.** *Jpn J Radiol* 2014;32:80–89 CrossRef Medline
35. King AD, Chow KK, Yu KH, et al. **Head and neck squamous cell carcinoma: diagnostic performance of diffusion-weighted MR imaging for the prediction of treatment response.** *Radiology* 2013;266:531–38 CrossRef Medline
36. Ohnishi K, Shioyama Y, Hatakenaka M, et al. **Prediction of local failures with a combination of pretreatment tumor volume and apparent diffusion coefficient in patients treated with definitive radiotherapy for hypopharyngeal or oropharyngeal squamous cell carcinoma.** *J Radiat Res* 2011;52:522–30 CrossRef Medline
37. Ng SH, Liao CT, Lin CY, et al. **Dynamic contrast-enhanced MRI, diffusion-weighted MRI and (18)F-FDG PET/CT for the prediction of survival in oropharyngeal or hypopharyngeal squamous cell carcinoma treated with chemoradiation.** *Eur Radiol* 2016;26:4162–72 CrossRef Medline
38. Ng SH, Lin CY, Chan SC, et al. **Dynamic contrast-enhanced MR imaging predicts local control in oropharyngeal or hypopharyngeal squamous cell carcinoma treated with chemoradiotherapy.** *PLoS One* 2013;8:e72230 CrossRef Medline
39. Chawla S, Kim S, Dougherty L, et al. **Pretreatment diffusion-weighted and dynamic contrast-enhanced MRI for prediction of local treatment response in squamous cell carcinomas of the head and neck.** *AJR Am J Roentgenol* 2013;200:35–43 CrossRef Medline
40. Jansen JF, Schöder H, Lee NY, et al. **Tumor metabolism and perfusion in head and neck squamous cell carcinoma: pretreatment multimodality imaging with 1H magnetic resonance spectroscopy, dynamic contrast-enhanced MRI, and [18 F]FDG-PET.** *Int J Radiat Oncol Biol Phys* 2012;82:299–307 CrossRef Medline
41. Kim S, Loevner L, Quon H, et al. **Prediction of response to chemoradiation therapy in squamous cell carcinomas of the head and neck using dynamic contrast-enhanced MR imaging.** *AJNR Am J Neuroradiol* 2010;31:262–68 CrossRef Medline
42. Jansen JF, Lu Y, Gupta G, et al. **Texture analysis on parametric maps derived from dynamic contrast-enhanced magnetic resonance imaging in head and neck cancer.** *World J Radiol* 2016;8:90–97 CrossRef Medline
43. Kanda T, Ishii K, Kawaguchi H, et al. **High signal intensity in the dentate nucleus and globus pallidus on unenhanced T1-weighted MR images: relationship with increasing cumulative dose of a gadolinium-based contrast material.** *Radiology* 2014;270:834–41 CrossRef Medline
44. Kuno H, Jara H, Buch K, et al. **Global and regional brain assessment with quantitative MR imaging in patients with prior exposure to linear gadolinium-based contrast agents.** *Radiology* 2017;283:195–204 CrossRef Medline
45. Chung MK, Jeong HS, Park SG, et al. **Metabolic tumor volume of [18F]-fluorodeoxyglucose positron emission tomography/computed tomography predicts short-term outcome to radiotherapy with or without chemotherapy in pharyngeal cancer.** *Clin Cancer Res* 2009;15:5861–68 CrossRef Medline
46. Kao CH, Lin SC, Hsieh TC, et al. **Use of pretreatment metabolic tumour volumes to predict the outcome of pharyngeal cancer treated by definitive radiotherapy.** *Eur J Nucl Med Mol Imaging* 2012;39:1297–305 CrossRef Medline
47. Hanamoto A, Tatsumi M, Takenaka Y, et al. **Volumetric PET/CT parameters predict local response of head and neck squamous cell carcinoma to chemoradiotherapy.** *Cancer Med* 2014;3:1368–76 CrossRef Medline
48. Buch K, Li B, Qureshi MM, et al. **Quantitative assessment of variation in CT parameters on texture features: pilot study using a nonanatomic phantom.** *AJNR Am J Neuroradiol* 2017;38:981–85 CrossRef Medline

CT Texture Analysis: Defining and Integrating New Biomarkers for Advanced Oncologic Imaging in Precision Medicine: A Comment on "CT Texture Analysis Potentially Predicts Local Failure in Head and Neck Squamous Cell Carcinoma Treated with Chemoradiotherapy"

The remarkable article by Kuno et al[1] in this issue of the *American Journal of Neuroradiology* raises several questions: Can texture analysis provide reliable biomarkers to predict treatment success in head and neck squamous cell carcinoma (HNSCC)? If so, will the role of the expert clinical radiologist who visually recognizes and interprets image patterns in combination with the clinical impression soon be obsolete and replaced by an increasingly ubiquitous and cheap computing infrastructure for mathematic image analysis, or will radiologists play an even more important role in the future by integrating these new biomarkers for treatment response with their expert knowledge?

In their well-designed study, Kuno et al[1] evaluated the performance of pretreatment contrast-enhanced CT texture analysis for the prediction of treatment failure in primary HNSCC treated with chemoradiotherapy. An experienced neuroradiologist, who was blinded to patient history/outcome, contoured the primary tumors manually. An in-house-developed Matlab-based (MathWorks, Natick, Massachusetts) texture analysis program was then used to measure 42 features from each segmented tumor volume. The authors found that 3 histogram features (geometric mean, harmonic mean, and fourth moment) and 4 gray-level run-length features (short-run emphasis, gray-level nonuniformity, run-length nonuniformity, and short-run low gray-level emphasis) were significant predictors of outcome after adjusting for clinical variables, including smoking history, human papillomavirus (HPV) status, T-stage, and tumor volume.[1]

The concept of predicting treatment response based on pretreatment imaging features of HNSCC emerged about 2 decades ago and may be seen as one of the first steps in the development of personalized medicine. During past years, this concept has undergone continuous evolution. The first publications focused on the impact of gross tumor volume on radiation therapy response. In supraglottic HNSCC, preradiotherapy CT-based tumor volume obtained by manual contouring allowed stratification of patients into groups with likely and less likely local control.[2] Although volume-based prediction of tumor response may be considered an important landmark, radiosensitivity may be influenced by not only volume but also heterogeneity of tumor tissue. Further studies found that glottic HNSCC was better controlled with radiation therapy when cartilage showed a normal or high T2 signal than an intermediate T2 signal.[3] These observations were later explained by studies correlating preoperative MR imaging with histology, which revealed that a high T2 signal intensity corresponded to inflammation, whereas intermediate T2 signal corresponded to neoplastic cartilage invasion.[4]

Additional imaging biomarkers emerged, such as apparent diffusion coefficient, dynamic contrast-enhanced MR imaging/CT-derived perfusion parameters, as well as standardized uptake value (SUV) and metabolic tumor volume based on PET. In parallel, researchers evaluated the histologic underpinning of these markers, demonstrating a direct correlation between increased ADC values and high stromal content in HNSCC.[5] Because high stromal content, low cellularity, and micronecrosis are associated with radioresistance, we now have a possible explanation for the observed poor outcome of patients with high pretreatment ADCs.

As a next step, combined multiparametric approaches then emerged as the new tools for predicting treatment response. In oropharyngeal/hypopharyngeal HNSCC, the combination of large tumor volume and high ADC predicted a higher likelihood of postradiotherapy local recurrence.[6] Likewise, the combination of ADC and perfusion maps could separate HNSCC responders from nonresponders to chemoradiation,[7] and more recently, in patients with high maximum SUV, high minimum ADC could identify the patients with the worst prognosis.[8] The complementary information provided by multiparametric imaging is now increasingly allowing us to reveal the complexity of intra- and intertumor heterogeneity in vivo, and slowly the pieces of a great puzzle are beginning to come together.

Although hailed as a revolution, texture analysis to assess tumor heterogeneity is only the next logical step for predicting treatment response. Image texture can be defined as the spatial variation in pixel intensity levels or patterns, some of which are not perceived by the human eye. The great advantage of this postprocessing tool is that it can be retrospectively applied to data acquired during routine imaging. Assessment of image texture can be done with statistical methods, model-based methods, or transform-based models.[9] Most publications on texture analysis in oncology are based on statistical methods, which include first-order

textural features (histograms of pixel-intensity levels based on average pixel value), second-order textural features (gray-level co-occurrence matrices based on the relationship between 2 pixels), and higher-order features based on the relationship between >2 pixels. Higher order textural parameters include neighborhood gray tone difference matrices and run-length matrices. While first-order statistical methods do not convey spatial information, second-order and higher-order statistical methods do. Nevertheless, histogram analysis is more intuitive and thus more easily understood by radiologists, whereas second-order and higher-order textural features are more abstract concepts.

Due to its versatility, texture analysis of CT/MR imaging has been recently investigated in several oncologic fields, including assessment of the HPV status in HNSCC[10,11] or survival of patients with advanced HNSCC treated with induction chemotherapy.[12] The article by Kuno et al[1] fits in this timely area of research and demonstrates some remarkable findings. CT, which is readily available in many institutions, can be used to extract meaningful texture information, allowing prediction of treatment outcome irrespective of scanner type and section thickness or the use of iterative reconstruction.

From a general scientific point of view, several methodologic challenges must still be overcome before texture analysis will be ready for routine clinical use in head and neck (HN) oncology. First, the technical platforms for texture analysis are not yet standardized, and even minor differences in equipment, acquisition protocols, or the presence of artifacts may significantly affect texture features, thus questioning whether the obtained results can be reproduced by another technical platform. Ideally, scientific studies correlating texture-based biomarkers with treatment outcome should, therefore, be conducted on the same scanner, with the same protocol, and in a well-defined homogeneous subgroup of patients. This problem is generally inherent in quantitative image analysis and is currently being addressed by international research alliances such as the Quantitative Imaging Biomarker Alliance and the European Imaging Biomarker Alliance. Second, segmentation of HN tumors, a key ingredient for any meaningful texture analysis, remains a time-consuming procedure, which must be done manually and based on visual assessment by an experienced radiologist. In view of the complex morphology of HN tumors, reliable digital automatic segmentation tools based on artificial intelligence may be difficult to develop for this particular purpose. Third, we must agree on a standard method for manual segmentation to make data comparable and reproducible. Should we contour only the most representative tumor section or rather include the entire tumor volume in the analysis? Should we include or exclude necrotic portions or ulcerated tumor parts from our analysis? Such questions need to be answered to avoid noise due to inconsistent data analysis and allow a meaningful correlation of texture features with treatment outcome. Fourth, the scarcity of histopathologic, functional, or metabolic correlates often implies that statistical power cannot be obtained unless data can be shared among institutions.

Finally, the question remains about how far we must go to understand the underlying biologic mechanisms influencing texture analysis, such as cellularity, hypoxia, or angiogenesis. Some may argue that it is sufficient to provide biomarkers with proved correlation between treatment and outcome, whereas others may insist that true scientific progress will not be possible without a real understanding of the biologic correlates of surrogate imaging biomarkers.

Texture analysis is now entering the area of personalized medicine, accompanied by sensationalistic comments in the lay press and a media hype announcing a new revolution in oncologic research. There is, indeed, little doubt that the possibility of developing biomarker-based texture analysis is promising for the progress of oncologic imaging, though many scientific questions still need to be answered. The work of Kuno et al[1] is a significant contribution and takes us a step ahead. From a clinical point of view, there is still some way to go before texture analysis can be effectively implemented for the benefit of our patients. Those of us who are actively taking part in multidisciplinary HN tumor boards are fully aware that the not-so-well-quantifiable clinical-radiologic impression will continue to play an important role in multidisciplinary therapeutic decision-making.

The upcoming challenge will consist of integrating the information of biomarkers derived from multiparametric texture analysis with the more pragmatic image interpretation of the experienced clinical radiologist. The goal of clinical imaging remains to reliably provide a positive impact on the treatment and outcome of our patients. I personally believe that this may be done best by integrating the new exciting biomarkers gradually as soon as they have been proved to be scientifically reproducible, following Theodore Roosevelt's advice, "Keep your eyes on the stars and keep your feet on the ground."

REFERENCES

1. Kuno H, Qureshi MM, Chapman MN, et al. **CT texture analysis potentially predicts local failure in head and neck squamous cell carcinoma treated with chemoradiotherapy.** *AJNR Am J Neuroradiol* 2017 Oct 12. [Epub ahead of print] CrossRef
2. Mancuso AA, Mukherji SK, Schmalfuss I, et al. **Preradiotherapy computed tomography as a predictor of local control in supraglottic carcinoma.** *J Clin Oncol* 1999;17:631–37 CrossRef Medline
3. Ljumanovic R, Langendijk JA, van Wattingen M, et al. **MR imaging predictors of local control of glottic squamous cell carcinoma treated with radiation alone.** *Radiology* 2007;244:205–12 CrossRef Medline
4. Becker M, Zbären P, Casselman JW, et al. **Neoplastic invasion of laryngeal cartilage: reassessment of criteria for diagnosis at MR imaging.** *Radiology* 2008;249:551–59 CrossRef Medline
5. Driessen JP, Caldas-Magalhaes J, Janssen LM, et al. **Diffusion-weighted MR imaging in laryngeal and hypopharyngeal carcinoma: association between apparent diffusion coefficient and histologic findings.** *Radiology* 2014;272:456–63 CrossRef Medline
6. Ohnishi K, Shioyama Y, Hatakenaka M, et al. **Prediction of local failures with a combination of pretreatment tumor volume and apparent diffusion coefficient in patients treated with definitive radiotherapy for hypopharyngeal or oropharyngeal squamous cell carcinoma.** *J Radiat Res* 2011;52:522–30 CrossRef Medline
7. Chawla S, Kim S, Dougherty L, et al. **Pretreatment diffusion-weighted and dynamic contrast-enhanced MRI for prediction of local treatment response in squamous cell carcinomas of the head and neck.** *AJR Am J Roentgenol* 2013;200:35–43 CrossRef Medline
8. Preda L, Conte G, Bonello L, et al. **Combining standardized uptake value of FDG-PET and apparent diffusion coefficient of DW-MRI improves risk stratification in head and neck squamous cell carcinoma.** *Eur Radiol* 2016;26:4432–41 CrossRef Medline
9. Alobaidli S, McQuaid S, South C, et al. **The role of texture analysis in**

imaging as an outcome predictor and potential tool in radiotherapy treatment planning. *Br J Radiol* 2014;87:20140369 CrossRef Medline

10. Buch K, Fujita A, Li B, et al. **Using texture analysis to determine human papillomavirus status of oropharyngeal squamous cell carcinomas on CT.** *AJNR Am J Neuroradiol* 2015;36:1343–48 CrossRef Medline
11. de Perrot T, Lenoir V, Domingo Ayllón M, et al. **Apparent diffusion coefficient histograms of human papillomavirus-positive and human papillomavirus-negative head and neck squamous cell carcinoma: assessment of tumor heterogeneity and comparison with histopathology.** *AJNR Am J Neuroradiol* 2017 Sep 14. [Epub ahead of print] CrossRef Medline
12. Zhang H, Graham CM, Elci O, et al. **Locally advanced squamous cell carcinoma of the head and neck: CT texture and histogram analysis allow independent prediction of overall survival in patients treated with induction chemotherapy.** *Radiology* 2013;269:801–09 CrossRef Medline

M. Becker
Division of Radiology
Department of Imaging and Medical Informatics
Geneva University Hospital
Geneva, Switzerland

http://dx.doi.org/10.3174/ajnr.A5451

Optimization of Quantitative Dynamic Postgadolinium MRI Technique Using Normalized Ratios for the Evaluation of Temporomandibular Joint Synovitis in Patients with Juvenile Idiopathic Arthritis

P. Caruso, K. Buch, S. Rincon, R. Hakimelahi, Z.S. Peacock, C.M. Resnick, C. Foster, L. Guidoboni, T. Donahue, R. Macdonald, H. Rothermel, H.D. Curtin, and L.B. Kaban

ABSTRACT

BACKGROUND AND PURPOSE: MR imaging has been shown to be useful in the diagnosis of juvenile idiopathic arthritis of the temporomandibular joint. Prior MR imaging approaches have relied mainly on the subjective interpretation of synovial enhancement as a marker for synovial inflammation. Although, more recently, several attempts have been made to quantify synovial enhancement, these methods have not taken into account the dynamic enhancement characteristics of the temporomandibular joint and the effect of sampling time. Our aim was to develop a clinically feasible, reproducible, dynamic, contrast-enhanced MR imaging technique for the quantitative assessment of temporomandibular joint synovitis in patients with juvenile idiopathic arthritis and to study the effect of sampling time on the evaluation of synovitis.

MATERIALS AND METHODS: This was a retrospective study of all patients who had dynamic, contrast-enhanced coronal T1 3T MR imaging through the temporomandibular joint at our institution between January 1, 2015, and July 8, 2016. Patients in this cohort included those with a history of juvenile idiopathic arthritis and control patients who underwent MR imaging for other routine, clinical purposes. Synovial enhancement was calculated for each temporomandibular joint using 3 different types of equations termed normalization ratios. The enhancement profiles generated by each equation were studied to determine which provided the best discrimination between affected and unaffected joints, was the least susceptible to sampling errors, and was the most clinically feasible.

RESULTS: A ratio of synovial enhancement (defined as the difference between the postgadolinium and the pregadolinium T1 signal of the synovium) to the postgadolinium signal of the longus capitis provided the best discrimination between affected and unaffected joints, the least susceptibility to sampling error, and was thought to be the most clinically feasible method of quantification of synovial inflammation. Additional synovial enhancement ratios studied did not provide the same level rates of discrimination between the affected and unaffected joints and were thought to be too temporally variable to provide reliable clinical use.

CONCLUSIONS: We provide a robust, reproducible, dynamic gadolinium-enhanced MR imaging technique for the quantitative assessment of temporomandibular joint synovitis in patients with juvenile idiopathic arthritis.

ABBREVIATIONS: JIA = juvenile idiopathic arthritis; LC = longus capitis; NR = normalization ratio; TMJ = temporomandibular joint

The International League of Associations for Rheumatology defines juvenile idiopathic arthritis (JIA) as an arthritis of unknown etiology that begins before the sixteenth birthday and lasts for a minimum of 6 weeks.[1] The incidence of JIA is estimated at 10.3/100,000.[2] The temporomandibular joint (TMJ) is frequently involved in JIA; TMJ involvement in patients with JIA occurs in 17%–87% of patients.[3]

MR imaging has been shown to be useful in the diagnosis of JIA of the TMJ.[4] While many prior MR imaging approaches have relied on subjective interpretation of synovial enhancement more recently, attempts have been made to assess the utility of quantitative analysis of TMJ synovial enhancements.[5-8] Peacock et al[6] defined a ratio of the TMJ synovial postgadolinium signal inten-

Received April 5, 2017; accepted after revision July 16.

From the Division of Neuroradiology, Department of Radiology, Massachusetts General Hospital (P.C., K.B., S.R., R.H., C.F., L.G., T.D., R.M.), Department of Pediatrics, Mass General Hospital for Children (H.R.), Department of Oral & Maxillofacial Surgery, Massachusetts General Hospital and Mass General Hospital for Children (Z.S.P., L.B.K.), Department of Plastic and Oral Surgery, Boston Children's Hospital (C.M.R.), Department of Radiology, Massachusetts Eye and Ear Infirmary (H.D.C.), Harvard Medical School and Harvard School of Dental Medicine, Boston, Massachusetts.

Paper previously presented in part at: Annual Meeting of the American Society of Head and Neck Radiology, September 7–11, 2016; Washington, DC.

Please address correspondence to Paul Caruso, MD, Division of Neuroradiology, Department of Radiology, Massachusetts General Hospital, 55 Fruit Street, Boston, MA 02114; e-mail: PCARUSO@mgh.harvard.edu

Indicates article with supplemental on-line tables.

http://dx.doi.org/10.3174/ajnr.A5424

Table 1: Dynamic gadolinium MRI technique for imaging of the TMJ

Parameters	Details
Sequence	Coronal T1 postgadolinium, 70-sec, 10-sec prescan
TR/TE (ms)	400/15
Frequency × phase	300 × 200
NEX	1
Section thickness	3 mm, 0-mm gap
FOV	14–16 cm
Timing of the serial runs	Runs: run 0, pregadolinium run, followed by 10 postgadolinium runs with the following timing intervals: run 1: 0 -1 min 10 sec, run 2: 1 min 20 sec to 2 min 30 sec; run 3: 2 min 40 sec to 3 min 50 sec; run 4: 4 min 00 sec to 5 min 10 sec; run 5: 5 min 20 sec to 6 min 30 sec; run 6: 6 min 40 sec to 7 min 50 sec; run 7: 8 min 00 sec to 9 min 10 sec; run 8: 9 min 20 sec to 10 min 30 sec; run 9: 10 min 40 sec to 11 min 50 sec; run 10: 12 min 00 sec to 13 min 10 sec
Injection technique	Standard supine position 22-ga angiocatheter in right antecubital fossa, attached to 20-cm length of standard tubing connected to a power injector
Contrast agent and dosing	Gadoterate meglumine (Dotarem)[a] maintained at room temperature was drawn up at a dose of 0.2 mL/kg (0.1 mmol/kg) of body weight Simultaneous with the start of the first coronal T1 dynamic sequence, run 1, gadoterate was administered by power injector as a single intravenous bolus injection at a flow rate of 2.5 mL/s followed by a 20-mL saline chaser at the same injection rate

[a] Guerbet, Aulnay-sous-Bois, France.

sity normalized to the longus capitis muscle in control patients and found a 95% specificity threshold of 1.55. Resnick et al[8] found that the 1.55 threshold had a 91% sensitivity and 96% specificity for detecting synovitis in symptomatic JIA TMJs. These results, however, rely on measurements of synovial enhancement at a single time point that may not reflect the dynamic contrast enhancement of the TMJ synovia and do not take into consideration the effect of sampling time. The purpose of our study was to establish a reproducible, practical technique for the study of dynamic enhancement curves of the TMJ in patients with JIA and in controls and to determine the effect of sampling time.

MATERIALS AND METHODS

Study Design

This is an institutional review board–approved, retrospective study in patients who had dynamic contrast-enhanced MR imaging through the TMJ at our institution between January 1, 2015, and July 8, 2016. The dynamic contrast-enhanced technique used in this study was performed on all TMJ MRIs for patients with JIA and for some patients with neuroendocrine MRIs who served as controls.

Patients 18 years of age or younger who underwent dynamic contrast-enhanced MR imaging through the TMJ and longus capitis muscles were included. For controls, only patients in whom dynamic coronal T1 sequences included both the TMJ and the longus capitis muscle (and the target sella turcica) were included.

Exclusion criteria included a history of mandibular/facial trauma, jaw/neck tumor, craniofacial malformation, prior radiation, chemotherapy, or vasculopathy. For controls, additional exclusion criteria included any history of jaw findings: pain, limited range of motion, clicking, mandibular asymmetry, or retrognathia. Any study with artifact that compromised interpretation of the images was excluded.

Clinical Data

For patients with JIA, electronic medical records were reviewed for sex; International League of Associations for Rheumatology classification; age at the time of JIA diagnosis, at first presentation with TMJ findings, and at time of MR imaging; TMJ findings including limitation of jaw opening, pain, mandibular asymmetry, retrognathia, bilateral/unilateral TMJ involvement, presence of TMJ symptoms at MR imaging; and medication history, as described in On-line Tables 1 and 2.

For control patients, electronic medical records were reviewed for sex, age at MR imaging, indications for MR imaging, and use of any immunosuppressants within 3 months of MR imaging, as listed in On-line Table 3.

Imaging Technique

MRIs were performed on 2 platforms, either a Tim Trio 3T (Siemens, Erlangen, Germany) using a 32-channel head coil or a Discovery MR750 3T (GE Healthcare, Milwaukee, Wisconsin) using an 8-channel head coil. Details of the MR dynamic imaging technique are shown in Table 1.

Normalized Ratios

Measurements of the TMJ synovial signal were performed as follows: Ten 0.5-mm^2 ROIs were measured over each TMJ on the precontrast sequence, 5 over the superior joint compartment and 5 over the lower joint compartment where the measurements were distributed in a standard fashion from lateral to medial across the joint (Fig 1). Ten 0.5-mm^2 ROIs were then measured similarly over each TMJ on each of the 10 postgadolinium runs for a total of 100 postgadolinium measurements per joint (Fig 1). This technique resulted in 110 measurements per joint (100 postgadolinium + 10 pregadolinium) and 220 measurements per patient (Fig 1).

We then defined 3 distinct quantitative measures of synovial inflammation that we normalized to an internal structure (the longus capitis muscles) to allow for comparison across different patients and time points, ER1, ER2, and R, that we termed collectively "normalized ratios". ER1 = (postgadolinium T1 signal of the TMJ synovium − the pregadolinium T1 signal of the TMJ synovium) divided by the (postgadolinium T1 signal of the longus capitis − the pregadolinium T1 signal of the longus capitis) where ER1 thus represents the ratio of the enhancement of the TMJ

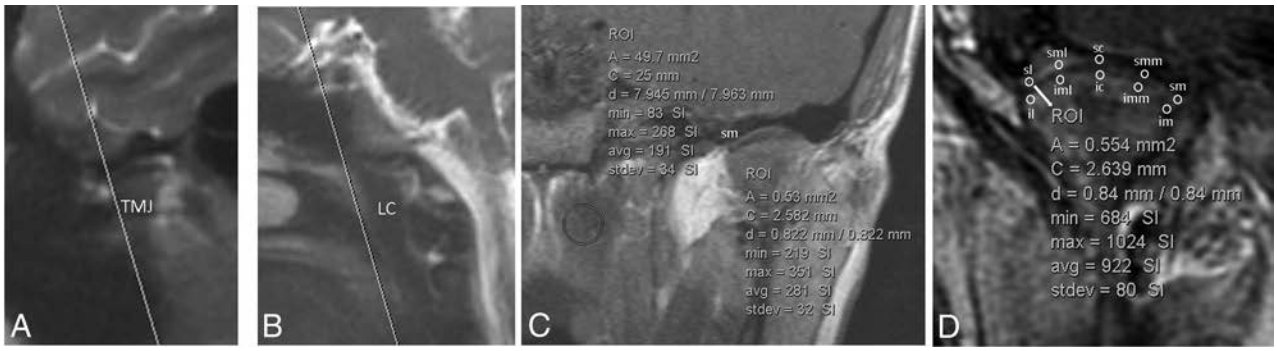

FIG 1. *A* and *B*, Coronal scanning plane and ROI-based measurements of the TMJ synovia. An oblique coronal plane was prescribed off the sagittal localizer to include the entire right and left TMJs and the longus capitis in the same coronal FOV. The coronal plane was angled superoanterior to posteroinferior to include both the TMJs from anterior to posterior and the longus capitis muscle; in controls, the oblique coronal plane included both TMJs, the longus capitis, and the sella turcica. *C*, An example of a single ROI at the superomedial synovial edge of the right TMJ (0.5 mm^2) on a precontrast MR imaging and a single ROI placed along the longus capitis muscle (50 mm^2), which was used for normalization. *D*, Example of the 10 ROIs placed on a postgadolinium MR imaging. These ROIs are placed along the superior and inferior synovial compartments of the left TMJ with the following designations: SL indicates superior compartment, lateral edge; SML, superior compartment, midlateral edge; SC, superior compartment, central; SMM, superior compartment, midmedial edge; SM, superior compartment, medial edge; IL, inferior compartment, lateral edge; IML, inferior compartment, midlateral edge, IC, inferior compartment, central; IMM, inferior compartment, midmedial edge; IM, inferior compartment, medial edge. Although attempts were made to measure the signal along the area closest to the disk edge in the expected location of the synovium, these measurements undoubtedly reflect a composite of signal produced by the synovium, cartilage, and perhaps the periosteum. Thus, the notion of "synovial signal" used in this report reflects this currently unavoidable composite measurement.

Table 2: Measurements of signal intensity over the synovium and longus capitis muscles and calculation of the normalized ratios ER1, ER2, and R

	Calculations
Synovial signal intensity	Pre = (SL+SML+SC+SMM+SM+IL+IML+IC+IMM+IM)/10, where, Pre = average precontrast synovial T1 signal intensity measured at 10 points along the synovia
	$Post_n$ = (SL+SML+SC+SMM+SM+IL+IML+IC+IMM+IM)$_n$ /10, where, $Post_n$ = average postgadolinium synovial signal, for run *n* (*n* = 1–10) measured at 10 points along the synovia
	Synovial enhancement$_n$ = $Post_n$–Pre, for each run *n* (*n* = 1–10)
Longus capitis intensity	LCPRE = precontrast T1 signal in the longus capitis
	$LCPOST_n$ = postcontrast T1 signal in the longus capitis, for run *n* (*n* = 1–10)
	Longus capitis enhancement$_n$ = $LCPOST_n$–LCPRE, for each run *n* (*n* = 1–10)
Normalized ratios	ER1 = (postgadolinium T1 signal of the TMJ synovium − the pregadolinium T1 signal of the TMJ synovium) divided by the (postgadolinium T1 signal of the longus capitis − the pregadolinium T1 signal of the longus capitis) where ER1 thus represents the ratio of the synovial enhancement$_n$ to the longus capitis enhancement$_n$ for each run n
	ER2 = (postgadolinium T1 signal of the TMJ synovium − the pregadolinium T1 signal of the TMJ synovium) divided by the postgadolinium T1 signal of the longus capitis where ER2 thus represents the ratio of the synovial enhancement$_n$ to the $LCPOST_n$ for each run n
	R = the postgadolinium T1 signal of the TMJ synovium divided by the postgadolinium T1 signal of the longus capitis and thus represents the ratio of $Post_n$ to $LCPOST_n$

Note:—n indicates each run; SL, superior compartment, lateral edge; SML, superior compartment, midlateral edge; SC, superior compartment, central; SMM, superior compartment, midmedial edge; SM, superior compartment, medial edge; IL, inferior compartment, lateral edge; IML, inferior compartment, midlateral edge; IC, inferior compartment, central; IMM, inferior compartment, midmedial edge, IM, inferior compartment medial edge; LCPRE, the measurement of the T1 signal in the longus capitis muscle on the coronal pregadolinium T1 sequence; $LCPOST_n$, the measurement of the T1 signal in the longus capitis on the postgadolinium coronal T1 sequence for runs 1–10.

synovium to the enhancement of the longus capitis. ER2 = (postgadolinium T1 signal of the TMJ synovium − the pregadolinium T1 signal of the TMJ synovium) divided by the postgadolinium T1 signal of the longus capitis where ER2 thus represents the ratio of the enhancement of the TMJ synovium to the postgadolinium T1 signal of the longus capitis. R = the postgadolinium T1 signal of the TMJ synovium divided by the postgadolinium T1 signal of the longus capitis and thus represents a ratio of postgadolininium signals. R is not a true "enhancement" ratio as measures of enhancement require a subtraction of pregadolinium signal from postgadolinium signal that is incorporated into ER1 and ER2 but not into R (Table 2). Then, the individual and average values for ER1, ER2, and R were plotted over the entire 13-minute 10-second sampling period for each patient, for each joint, and at each time point, to yield dynamic normalized ratio profiles.

The joints were then organized into 3 groups: 1) symptomatic joints in patients with JIA, 2) asymptomatic joints in patients with JIA, and 3) controls.

Peak, time to peak, and minimums for ER1, ER2, R, were plotted over the 13-minute 10-second sampling period for each joint.

The ER1s, ER2s, and Rs for each joint were grouped into 0 minutes 00 seconds to 3 minutes 50 seconds; 4 minutes 00 seconds to 7 minutes 50 seconds; and 8 minutes 00 seconds to 12 minutes 10 seconds minute intervals and averaged for each joint over these

sampling intervals. The average rate of change of ER1, ER2, and R for each sampling period was determined for symptomatic JIA, asymptomatic JIA, and control joints.

R, the ratio of the postgadolinium T1 signal of the synovium to the postgadolinium T1 signal of the longus capitis, (one of the 3 normalized ratios used in this study), corresponds to the ratio previously published by Resnick et al[8] and Peacock et al.[6] In these publications, a 1.55 threshold was proposed as a reliable discriminator between symptomatic JIA and control joints.[7,9] For each temporal sampling point, the relation of R, above or below, to the threshold 1.55 was recorded.

Similarly, for ER2, the relation of each sampling point, to a threshold value 0.95, above or below, was recorded.

Longus Capitis T1 Signal Measurements

The raw, non-normalized T1 signal from the longus capitis muscle was recorded on the pregadolinium T1 sequence and at each postgadolinium time point for the JIA and control patients.

Interrater Agreement

Measurements of synovial T1 signal intensity and the longus capitis were performed independently by 2 raters (K.B., a second-year neuroradiology fellow, and P.C., an attending neuroradiologist with 15 years of head and neck radiology experience).

In 10 joints, each at a different time points, both readers independently measured the lateral edge, center, and medial edge of either the superior or the inferior joint compartment. Thus, 30 ROIs were measured independently by both readers. Interrater agreement was calculated with a κ score.

Statistics

A Mann-Whitney *U* test was used to compare differences among symptomatic, asymptomatic, and control joints for the ER1 and ER2 equations among asymptomatic JIA and control joints, symptomatic JIA and asymptomatic JIA joints, and symptomatic JIA and control joints. These comparisons were made at each of the 10 postgadolinium sampling points.

Calculations were performed using MedCalc statistical software, Version 16.8.4 (MedCalc Software, Mariakerke, Belgium). A 2-tailed *t* test was used to evaluate differences in raw, non-normalized, average values of the longus capitis among the 3 clinical groups.

RESULTS

Study Design

Eight patients (1 male, 7 females) with JIA (16 joints) and 4 (1 male, 3 females) control patients (8 joints) were included in this study.

Clinical Data

The clinical data for the patients with JIA and control group are shown in On-line Tables 1–3.

The average age at MR imaging of the JIA group was 16.1 ± 7.9 years (range, 7.1–33.3 years). The average age at MR imaging of the control group was 15.5 ± 3.7 years (range, 10–18 years). Seven of 8 patients with JIA had been treated with some type of anti-inflammatory agent, and 5 had undergone intra-articular steroid injection before MR imaging.

Results of the Dynamic NR TMJ Profiles

ER1, the ratio of the whole joint (superior and inferior synovia) enhancement normalized to the enhancement of the longus capitis muscle, is shown in Fig 2*A–D*. ER2, the ratio of the whole joint (superior and inferior synovia) enhancement normalized to the postgadolinium T1 value of the longus capitis muscle is shown in Fig 2*E–H*. R, the ratio of the whole joint (superior and inferior synovia) postgadolinium T1 signal value normalized to the postgadolinium T1 value of the longus capitis muscle is shown in Fig 2*I–L*.

The individual patient and average group values for peak, time to peak, minimum, and average values grouped into 0–3:50, 4–7:50, and 8–12:10 minute intervals, and rates of change over these intervals for ER1, ER2, and R are reported in On-line Tables 4 and 5. For R, the number of times the NR profile for each joint fell below or above the 1.55 threshold is reported in On-line Table 4. For ER2, the number of times the NR profile for each joint fell below or above the maximum NR for the control joints of 0.94 is shown in On-line Table 5.

Longus Capitis T1 Signal

The longus capitis T1 signal profiles show a monomodal peak at 5 minutes 10 seconds for the JIA and control groups and a relative plateau from 5 minutes 10 seconds to 13 minutes 10 seconds (Fig 3).

Statistics

The results of the statistical analyses are shown in On-line Table 6.

The results of the interrater agreement between the 2 raters, K.B. and P.C., was 0.73, corresponding to a κ rating of good agreement. *P* values for the average longus capitis T1 signal showed no statistically significant difference between the JIA and control patients ($P = .99$).

Comparison of Synovial Enhancement Using the ER1 Equation

Asymptomatic JIA versus Control Joints. Significant differences in ER1 were noted between these 2 groups at the third postgadolinium time point ($P = .03$); however, ER1 values at the remaining postgadolinium time points did not demonstrate a statistically significant difference ($P = .10–.88$).

Symptomatic JIA versus Control Joints. Statistically significant differences in ER1 were noted between these 2 groups at all postgadolinium time points ($P \leq .001–.04$).

Asymptomatic JIA versus Symptomatic JIA Joints. A statistically significant difference in ER1 between these 2 groups for the eighth postgadolinium time point ($P = .009$) was noted. Otherwise, no statistically significant difference between synovial enhancement ratios at the remaining postgadolinium time points ($P = .08–.36$) was seen.

Comparison of Synovial Enhancement Using the ER2 Equation

Asymptomatic JIA versus Control Joints. No significant difference was observed for ER2 at all postgadolinium time points be-

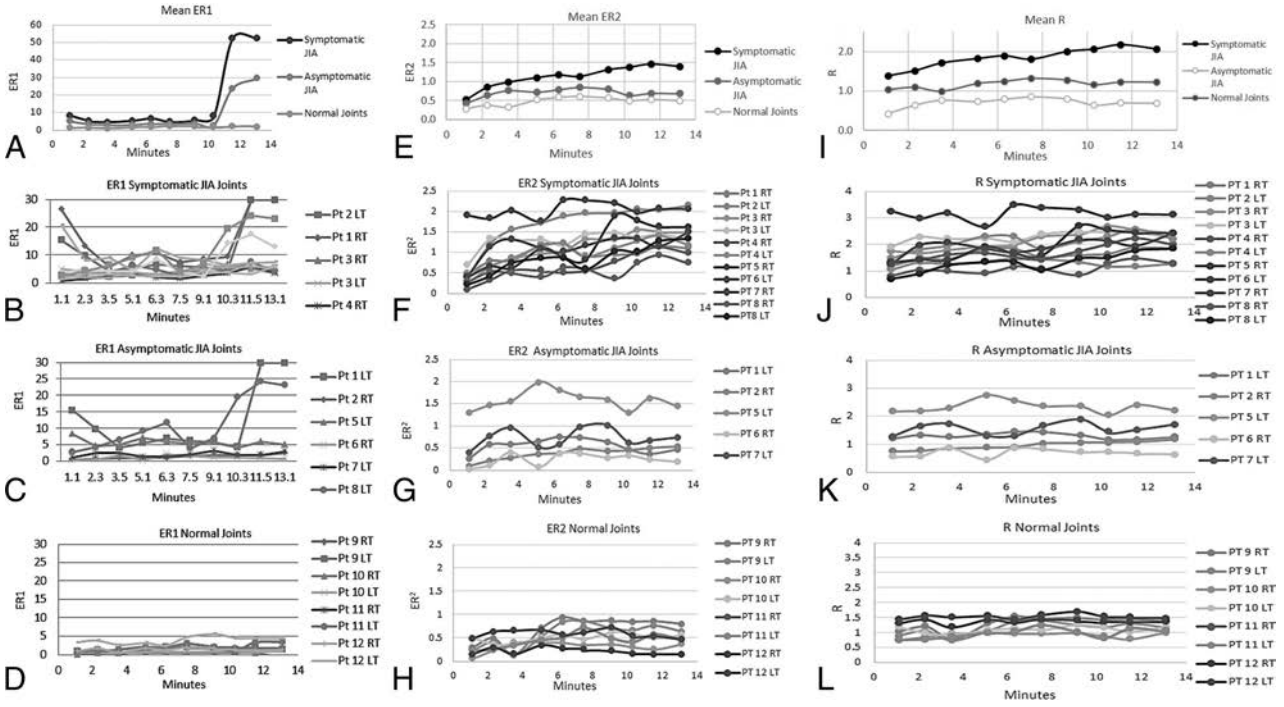

FIG 2. *A*, Mean ER1 for the symptomatic JIA, asymptomatic JIA, and control joints. ER1 shows a monopeak profile with an upward slope that starts at 10 minutes 30 seconds at the end of run 8 and clear separation of the curves between 10 minutes 30 seconds and 13 minutes 10 seconds during runs 9 and 10. *B*, Individual patient profiles for ER1 for the symptomatic JIA joints. *C*, Individual patient profiles for ER1 for the asymptomatic JIA joints. *D*, Individual patient profiles for ER1 for the control TMJ joints. These joints exhibit relatively constant enhancement ratios between 0.73 and 5 at all time points. *E*, Mean ER2 for the symptomatic JIA, asymptomatic JIA, and control joints. Note the clear separation among the 3 groups at all sampling time points with the mean profile for the symptomatic JIA group showing a monopeak profile. Also, the mean profile of the asymptomatic JIA group is higher at all time points than the mean profile for the control group. *F*, Individual patient profiles for ER2 for symptomatic JIA joints. All but one of the symptomatic joints, patient 8 RT TMJ, pass above the threshold value of normal (0.95) at multiple time points that thus results in correct classification of 10/11 symptomatic joints. *G*, Individual patient profiles for ER2 for asymptomatic JIA joints. Most profiles stay below the threshold normal value (0.94) while several pass above. *H*, Individual patient profiles for ER2 for control TMJ joints. The initial ER2 at 1 minute 10 seconds ranges from 0.15 to 0.5, and the end ER2 for this group at 13 minutes 10 seconds ranges from 0.14 to 0.63. The maximum ratio (peak) reached by any single patient at any time point is 0.94 that serves as a threshold value for normal for ER2. *I*, Mean R for the symptomatic JIA, asymptomatic JIA, and control joints. Note the clear separation among the 3 groups at all sampling time points. The mean profile for the symptomatic JIA group shows a monopeak profile. *J*, Individual patient profiles for R for the symptomatic JIA joints. Two joints, patient 2 L TMJ and patient 8 R TMJ, never pass above the 1.55 threshold and thus would be misclassified by R as asymptomatic joints. A third joint, patient 8 L TMJ, passes above the threshold only twice that may result in an indeterminate or borderline classification. *K*, Individual patient profiles for R for the asymptomatic JIA joints. Two of these joints, patient 5 L TMJ and patient 7 L TMJ pass above the normal threshold. *L*, Individual patient profiles for R for the control TMJ joints. While most of these joints stay below the 1.55 threshold, one joint, patient 12 L TMJ passes above the threshold at 4 time points, that may lead to misclassification of this joint.

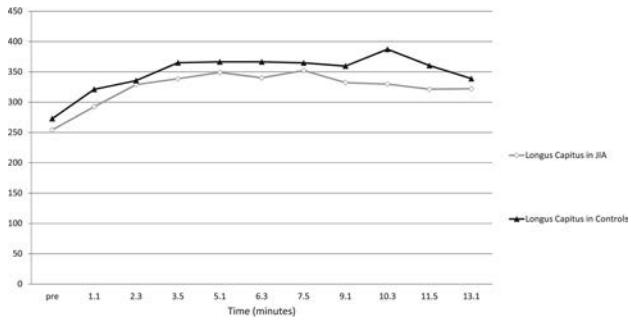

FIG 3. Raw T1 hyperintensity curves of the longus capitis muscle as measured on the precontrast image and each of the 10 postgadolinium dynamic images. The raw signal of the longus capitis is similar at all sampling time points in both the JIA and control groups: no statistically significant difference ($P = .99$) was seen at any time point, suggesting that the longus capitis may serve as a normalization standard for both normal and symptomatic groups.

tween these 2 groups ($P = .06–1.0$). Of note, the third postgadolinium time point trended toward significance with $P = .06$.

Symptomatic JIA versus Control Joints. Significant differences were seen at all postgadolinium time points except for the first postgadolinium time point ($P = .001–.006$).

Asymptomatic JIA versus Symptomatic JIA Joints. Significant differences were seen at later postgadolinium time points, between 9 minutes 20 seconds and 13 minutes 10 seconds ($P = .01$, .03, .01, respectively). There was no statistically significant difference at earlier time points ($P = .08–.33$).

DISCUSSION

We propose the current study as an illustration of a rigorous technique for quantification of TMJ synovial inflammation in patients with JIA. The technique was controlled for hardware, sequences, injection technique, scan plane, mouth position, and timing of the postgadolinium images. We used 3T platforms with either 32-

or 8-channel head coils, readily commercially available standard T1 postgadolinium spin-echo sequences in the coronal plane, and 10 sampling points during a 13-minute postinjection period. Prior studies using dynamic, contrast-enhancement techniques of the TMJ in patients with JIA were retrospective and thus have not been controlled rigorously for hardware, injection technique, or sampling timing.

Our results show that synovial enhancement curves for patients with JIA are, on average, notably temporally dependent so that technical variations in the acquisition of postgadolinium sequences can place the interpretation at risk of misclassification of a joint, underestimate degree of synovial inflammation, and, over serial scans, compromise evaluation of the response to treatment.

We used 5 separate ROIs spaced evenly across the TMJ in the coronal plane to sample synovial enhancement. The ROI-based assessment performed in this study using a small, 0.5-mm^2 sampling area minimizes contamination of T1 signal intensity from the intra-articular disk. We found that 5 separate ROI measurements were associated with a good interrater agreement. We think that the coronal plane is superior to the axial plane in that it allows a more precise placement of ROIs along the synovia and allows inclusion of both TMJ in the same dynamic run.[10]

Our results show the longus capitis muscle to be an excellent candidate for normalization. No significant difference was seen between enhancement of the longus capitis muscle in JIA and control patients, and the longus capitis demonstrates a long postinjection temporal signal plateau. Synovial TMJ postcontrast T1 signal depends on multiple technical parameters, including magnet strength, scanner platform, TR/TE parameters and injection technique, patient hemodynamics, and intrinsic T1 signal intensity of the TMJ synovium. Because of these variations in both technical and physiologic parameters, it is important to adopt a method for normalizing the quantitative measurements of the synovium to allow comparisons between scans performed on different patients and at different time points. Prior publications have chosen different normalization ratios, normalizing to the same joint or normalizing by the signal-to-noise ratio.[8,10] The longus capitis muscle was chosen as a candidate for normalization because it is not known to be affected in JIA; it lies in the center of the FOV and thus is less susceptible to peripheral scan artifacts or motion artifacts; and it can be feasibly included in coronal T1 sequences.

ER2 is preferable to ER1 and R in that ER2 provides the most favorable ratio of average peak values for symptomatic to asymptomatic joints at 1.73 (1.52/0.88), compared with ER1 1.65 (50.34/30.30) and R 1.4 (2.27/1.6), shows a more favorable ratio of average peak values between symptomatic joints and controls 2.27 (1.52/0.67) compared to R 1.67 (2.27/1.36), and exhibits a slightly more favorable ratio of average peak values between asymptomatic joints and controls 1.3 (0.88/0.67) compared to R, 1.2 (1.6/1.36).

ER2 is preferable to ER1 in that ER2 similar to ER1 discriminates with statistical significance between symptomatic JIA joints and controls at nearly all postgadolinium time points and ER2, unlike ER1, also discriminates with statistical significance between symptomatic and asymptomatic JIA joints beyond 10 minutes, a feasible sampling point for clinical use.

ER2 is preferable to ER1 also in that ER2 provides a longer temporal plateau from 9–13 minutes post injection, compared to ER1 that undergoes a steep upswing during this period (compare Fig 2*A* to Fig 2*E*). The long temporal plateau of ER2 is preferable in that it is less susceptible to technical variations in sampling time.

ER2 is preferable to R in that it classifies the TMJ joints better than R. We used the peak ER2 value among control patients over the entire dynamic profile (0.95, patient 9 [right TMJ] at 6 minutes 30 seconds) as a threshold for ER2 and the published 1.55 R threshold.[6,8] Using these thresholds, we found that ER2 classified 10/11 symptomatic JIA joints correctly compared with 9/11 joints for R.

ER2 is also conceptually preferable to R in that ER2 is a measure of true synovial enhancement (postgadolinium T1 signal–pregadolinium T1 signal) whereas R reflects the ratio of postgadolinium signal in the synovium to postgadolinium signal in the longus capitis muscle but does not reflect synovial enhancement in the strict sense.

We determined the optimal sampling time to be between 7 minutes 50 seconds and 13 minutes 10 seconds. We studied the average NRs for ER1, ER2, and R over 3 sampling periods, 0–3 minutes 50 seconds; 3 minutes 50 seconds to 7 minutes 50 seconds; and 7 minutes 50 seconds to 13 minutes 10 seconds, reasoning that the most favorable sampling period would be when differences among the NRs for each group were greatest and the profiles exhibited a steady-state or temporal plateau. Our results showed the 7 minute 50 second to 13 minute 10 second periods to be preferable for such.

Our results raise some interesting considerations regarding the effect of medication. For ER2, for example, 3/5 asymptomatic JIA joints (patient 1, left TMJ; patient 2, right TMJ; and patient 6, right TMJ) fell below the control maximum at all sampling time points, thus showing an ER2 consistent with control joints. All 3 of these patients were on antitumor necrosis factor medications at the time of imaging. Two of 5 asymptomatic JIA joints fell above the control threshold, and one of these joints was above the control threshold at all time points, producing a profile curve like that of symptomatic JIA joints. This patient was not on systemic therapy and had no prior exposure to antitumor necrosis factor medications. These preliminary results allow the consideration that asymptomatic joints in patients with JIA behave differently than control joints and are suggestive of a possible normalizing effect of the antitumor necrosis factor medications on NRs that may reflect a therapeutic effect on clinically silent joints in patients with JIA.

Our study provides a robust technique for the quantitative evaluation of synovial enhancement as a biomarker for TMJ synovitis in JIA. Although our patient numbers are low, our data illustrate this method, for which larger numbers of patients would be required for more definitive characterization of enhancement profiles. The study is limited by image resolution. It is not currently feasible to sample the synovia separate from adjacent cartilage and periosteum. The study is limited by heterogeneity of patient treatment regimens. This limitation is nearly unavoidable because only rarely do patients with JIA present initially with TMJ symptoms. A future direction would be to develop a standardized imaging-treatment algorithm to monitor synovial enhancement

in response to a controlled treatment regimen to understand the pathophysiology of JIA.

Our study is labor intensive in that each joint requires 110 measurements; however, we consider this limitation as a temporary step needed to characterize the temporal enhancement profile of the TMJ so that, in practice, once these profiles are fully characterized, the radiologist may target a particular number of samples and a particular temporal sampling point, for example, from 8–10 minutes post injection.

CONCLUSIONS

We provide a robust, clinically feasible, reproducible, dynamic gadolinium-enhanced technique for the quantitative assessment of TMJ synovitis in JIA. We explored 3 NRs, each of which normalizes the postgadolinium synovial signal to an easily measurable, internal reference and found that ER2 is the preferred equation for the quantitative assessment of synovial inflammation. Our data show the dependency of synovial enhancement on sampling time and the misclassification of joints that may result from sampling time inconsistencies and suggest that the preferred sampling time for synovial enhancement lies between 7 minutes 50 seconds and 13 minutes 10 seconds. We therefore provide what we hope will serve as a platform for the quantitative assessment of TMJ synovitis in JIA and areas for future research.

Disclosures: Zachary S. Peacock—*UNRELATED*: *Grants/Grants Pending*: Oral and Maxillofacial Surgery Foundation, AO Foundation, *Comments*: for research on distraction osteogenesis*; *Payment for Lectures Including Service on Speakers Bureaus*: Ethicon/Depuy Synthes, *Comments*: provided lecture to Ethicon employees on the use of their products for distraction osteogenesis in June 2016 and received honorarium. Hugh D. Curtin—*UNRELATED*: *Royalties*: Elsevier, *Comments*: royalties for a book. *Money paid to the institution.

REFERENCES

1. Petty RE, Southwood TR, Manners P, et al; International League of Associations for Rheumatology. **International League of Associations for Rheumatology classification of juvenile idiopathic arthritis: second revision, Edmonton, 2001.** *J Rheumatol* 2004;31:390–92 Medline
2. Krause ML, Crowson CS, Michet CJ, et al. **Juvenile idiopathic arthritis in Olmsted County, Minnesota, 1960–2013.** *Arthritis Rheumatol* 2016;68:247–54 CrossRef Medline
3. Keller H, Müller LM, Markic G, et al. **Is early TMJ involvement in children with juvenile idiopathic arthritis clinically detectable? Clinical examination of the TMJ in comparison with contrast enhanced MRI in patients with juvenile idiopathic arthritis.** *Pediatr Rheumatol Online J* 2015;13:56 CrossRef Medline
4. Küseler A, Pedersen TK, Herlin T, et al. **Contrast-enhanced magnetic resonance imaging as a method to diagnose early inflammatory changes in the temporomandibular joint in children with juvenile chronic arthritis.** *J Rheumatol* 1998;25:1406–12 Medline
5. Ma GM, Amirabadi A, Inarejos E, et al. **MRI thresholds for discrimination between normal and mild temporomandibular joint involvement in juvenile idiopathic arthritis.** *Pediatr Rheumatol Online J* 2015;13:53 CrossRef Medline
6. Peacock ZS, Vakilian P, Caruso P, et al. **Quantifying synovial enhancement of the pediatric temporomandibular joint.** *J Oral Maxillofac Surg* 2016;74:1937–45 CrossRef Medline
7. von Kalle T, Stuber T, Winkler P, et al. **Early detection of temporomandibular joint arthritis in children with juvenile idiopathic arthritis: the role of contrast-enhanced MRI.** *Pediatr Radiol* 2015;45:402–10 CrossRef Medline
8. Resnick CM, Vakilian PM, Kaban LB, et al. **Quantifying the effect of temporomandibular joint intra-articular steroid injection on synovial enhancement in juvenile idiopathic arthritis.** *J Oral Maxillofac Surg* 2016;74:2363–69 CrossRef Medline
9. Weiss PF, Arabshahi B, Johnson A, et al. **High prevalence of temporomandibular joint arthritis at disease onset in children with juvenile idiopathic arthritis, as detected by magnetic resonance imaging but not by ultrasound.** *Arthritis Rhem* 2008;58:1189–96 CrossRef Medline

Efficacy and Safety of Ethanol Ablation for Branchial Cleft Cysts

E.J. Ha, S.M. Baek, J.H. Baek, S.Y. Shin, M. Han, and C.-H. Kim

ABSTRACT

BACKGROUND AND PURPOSE: Branchial cleft cyst is a common congenital lesion of the neck. This study evaluated the efficacy and safety of ethanol ablation as an alternative treatment to surgery for branchial cleft cyst.

MATERIALS AND METHODS: Between September 2006 and October 2016, ethanol ablation was performed in 22 patients who refused an operation for a second branchial cleft cyst. After the exclusion of 2 patients who were lost to follow-up, the data of 20 patients were retrospectively evaluated. All index masses were confirmed as benign before treatment. Sonography-guided aspiration of the cystic fluid was followed by injection of absolute ethanol (99%) into the lesion. The injected volume of ethanol was 50%–80% of the volume of fluid aspirated. Therapeutic outcome, including the volume reduction ratio, therapeutic success rate (volume reduction ratio of >50% and/or no palpable mass), and complications, was evaluated.

RESULTS: The mean index volume of the cysts was 26.4 ± 15.7 mL (range, 3.8–49.9 mL). After ablation, the mean volume of the cysts decreased to 1.2 ± 1.1 mL (range, 0.0–3.5 mL). The mean volume reduction ratio at last follow-up was 93.9% ± 7.9% (range, 75.5%–100.0%; $P < .001$). Therapeutic success was achieved in all nodules (20/20, 100%), and the symptomatic ($P < .001$) and cosmetic ($P < .001$) scores had improved significantly by the last follow-up. In 1 patient, intracystic hemorrhage developed during the aspiration; however, no major complications occurred in any patient.

CONCLUSIONS: Ethanol ablation is an effective and safe treatment for patients with branchial cleft cysts who refuse, or are ineligible for, an operation.

ABBREVIATIONS: BCC = branchial cleft cyst; EA = ethanol ablation; US = ultrasonography

Branchial cleft cyst (BCC) is a congenital epithelial cyst, which may arise in the lateral neck. The lesions are thought to represent failed obliteration of one of the brachial clefts during embryonic development.[1] Although BCC is benign, some patients have pain, swelling, neck discomfort, and cosmetic problems. Surgery is curative in patients with BCC, but in addition to the need for general anesthesia, its drawbacks include scarring and postoperative morbidity. Therefore, minimally invasive treatment such as ultrasonography (US)-guided chemical ablation has been suggested as an alternative treatment for BCC.[2-7]

Both chemical ablation with picibanil (OK-432) and ethanol ablation (EA) are widely used to treat cystic lesions of the neck and oral cavity, such as thyroid cyst, ranula, and lymphatic malformation,[8-13] but only a few studies have focused on the use of either treatment in BCCs. Since Fukumoto et al[2] initially used EA on 3 BCCs in 1994, several studies have reported success rates of roughly 60% in patients with BCC treated with OK-432.[3-7] However, OK-432 is not widely accepted as an alternative to an operation because of its limited efficacy and adverse effects such as fever and local pain after the procedure.[3-7] In patients with thyroid cysts, EA has been recommended as a first-line treatment technique, rather than OK-432, due to its higher efficacy and safety.[14-17] However, except for a case report by Fukumoto et al, there have been no studies on the efficacy and safety of EA in BCC, to our knowledge. Therefore, in this retrospective study, we evaluated the efficacy and safety of EA for the treatment of BCC in patients from 2 hospitals (Ajou Univeristy Medical Center, Sharing and Happiness Hospital).

Received January 28, 2017; accepted after revision July 10.

From the Departments of Radiology (E.J.H., M.H.) and Otolaryngology (C.-H.K.), Ajou University School of Medicine, Suwon, Korea; Department of Radiology (S.M.B., S.Y.S.), Sharing and Happiness Hospital, Busan, Korea; and Department of Radiology and Research (J.H.B.), Institute of Radiology, University of Ulsan College of Medicine, Asan Medical Center, Seoul, Korea.

Please address correspondence to Seon Mi Baek, MD, Department of Radiology, Sharing and Happiness Hospital, Haeundae-gu, Busan 613-101, Korea; e-mail: radbsm@nate.com

http://dx.doi.org/10.3174/ajnr.A5373

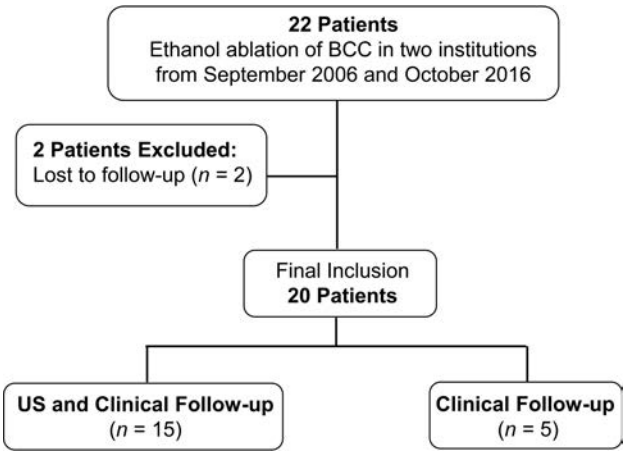

FIG 1. Flowchart of the patient enrollment process.

MATERIALS AND METHODS

This retrospective study was approved by the institutional review boards of the 2 participating hospitals. Written informed consent was obtained from all patients before the EA procedure.

Patients

Between September 2006 and October 2016, EA was performed in 22 patients who presented with a second BCC. After the exclusion of 2 patients who were lost to follow-up (Fig 1), 20 patients were included in this study (male/female ratio = 8:12; mean age, 30.9 years; range, 2–72 years). All of the included patients fulfilled the following criteria: cosmetic problems and/or symptoms, such as pain, swelling, or neck discomfort; a single clinically palpable neck mass in the anterolateral aspect of the neck (ie, posterolateral to the submandibular gland, lateral to the carotid space, anteromedial to the sternocleidomastoid muscle) previously diagnosed as a benign lesion by fine-needle aspiration; a completely cystic lesion; recurrence after at least 1 simple aspiration procedure; and refusal of or ineligibility for an operation.

Preprocedural Assessment

Ultrasonography and US-guided fine-needle aspiration were performed in all patients before EA. Two radiologists (S.M.B. and E.J.H.), with 12 and 17 years of clinical experience, respectively, in performing and evaluating neck US images, conducted all US examinations and US-guided fine-needle aspirations. The former imaging was performed with 1 of 3 US systems: an iU22 ultrasound machine (Philips Healthcare, Best, the Netherlands), Acuson S2000 (Siemens, Erlangen, Germany), or an EUB-7500 HV (Hitachi Medical Systems, Tokyo, Japan). All 3 were equipped with a high-frequency linear probe (5–14 MHz). The index cyst volume was calculated as $V = \pi abc/6$, where V is the volume, a is the largest diameter, and b and c are the other 2 perpendicular diameters. Before fine-needle aspiration of the cyst wall, as much of the internal fluid as possible was aspirated with a 23-ga needle. A smear for aspirates and a cell block for internal fluid assessment were prepared for use in cytologic evaluations by an experienced cytologist.

Before the procedure, patients were asked to rate their symptoms on a visual analog scale (0–10). The physicians assigned a cosmetic grading score (grade 1, no palpable mass; grade 2, invisible but palpable mass; grade 3, mass visible only to experienced clinician; grade 4, easily visible mass) to the lesions before the procedure.[18]

Procedure

EA was performed by the same radiologists (S.M.B. and E.J.H.). The patient was placed in the supine position with mild neck extension. After sterilization of the neck skin, local anesthesia consisting of 2% lidocaine was applied to the puncture site. A 16- or 18-ga needle was then inserted into the cyst under US guidance, and a 10- or 25-mL syringe, depending on the cyst size, was connected to the needle. After aspiration of as much of the cyst content as possible, the cyst wall was irrigated with normal saline to remove the debris coating its inner aspect. Because BCC lumina contain watery or cheesy secretions with exfoliated cells, multiple flushes were usually performed to clear the cystic cavity and enable direct contact of the sclerosing agent with the inner epithelial surface. The same needle was used to inject a volume of 99% sterile ethanol corresponding to 50%–80% of the aspirated fluid volume. If ethanol leakage through the puncture site was seen on real-time US, the ethanol injection was stopped immediately. After 5–10 minutes with the needle in place, the injected ethanol was removed completely and the needle was withdrawn. The patient was observed for 1 hour postoperatively. Complications arising during or immediately after the procedure were evaluated on the basis of the clinical signs and symptoms. Cosmetic and/or symptomatic problems that were incompletely resolved during the follow-up period were treated by repeat EA.

Follow-Up

Clinical symptoms, US examination, and complications during the follow-up after EA were evaluated. The volume reduction ratio, calculated as Volume Reduction Ratio (%) = {[Initial Volume (mL) − Final Volume (mL)] × 100}/Initial Volume, was assessed by US and used to determine the efficacy of EA in treating the nodule. The technical success of EA was defined as a volume reduction ratio of >50% and/or no palpable mass at the last follow-up. The occurrence of adverse events during the follow-up period was also investigated to assess EA-related complications.

Statistical Analysis

Statistical analysis was performed with the SPSS for Windows statistical software package (Version 23.0; IBM, Armonk, New York). The Wilcoxon signed rank test was used to compare nodule volumes, as well as symptomatic and cosmetic scores, before and after EA. The Mann-Whitney U test was used to compare variables between patients treated in single-versus-multiple sessions of EA. A P value < .05 was considered to indicate statistical significance.

RESULTS

Initial characteristics of the patients and lesions, treatment characteristics, and changes in the volume of the BCCs after-versus-before EA are summarized in Table 1. All BCCs contained white-to-yellowish fluid and keratinaceous cellular debris. Of the 20 nodules, 9 (45.0%) were treated in a single session, and 11 (55.0%), in multiple sessions (twice, $n = 8$; three times, $n = 2$; six

Table 1: Initial patient, brachial cleft cyst, and treatment characteristics and changes in the cysts (before versus after ethanol ablation)

Patient	Sex	Age (yr)	Index Volume (mL)	Aspiration Volume (mL)	Ethanol Volume (mL)	Treatment Sessions (No.)	Fluid Volume (mL) at Follow-Up				VRR (%)	Therapeutic Success
							1–2 mo (*n* = 17)	3–6 mo (*n* = 9)	7–12 mo (*n* = 7)	Final Evaluation (*n* = 15)		
1	M	17	29.4	30.0	10	2			57.9[a]	0.4 (14)	98.6	Yes
2	F	13	3.8	3.0	2	2	1.1	4.4[a]	0.3	0.3 (8)	92.1	Yes
3	M	33	41.4	40.0	20	2	35.6[a]	2.4	NA	2.4 (4)	94.2	Yes
4	M	15	36.6	36.0	10	2	33.7[a]	9.7	1.2	0.1 (25)	99.7	Yes
5	M	30	49.9	50.0	20	1	NA	NA	NA	NA (12)	NA	Yes
6	F	60	6.1	5.8	4	1	0.2	0.2		0.0 (18)	100.0	Yes
7	F	38	38.2	20.0	10	2	6.6[a]	NA	NA	NA (12)	NA	Yes
8	F	25	38.0	21.0	10	6	5.7[a]/25.12[a]	30.4[a]/9.3[a]	2.2	0.5 (16)	98.7	Yes
9	M	6	12.4	12.0	4	1	NA	NA	NA	NA (22)	NA	Yes
10	M	37	42.2	31.0	10	2	15.1[a]	1.2	0.3	0.3 (12)	99.3	Yes
11	M	41	7.5	7.0	7	2	7.4[a]	NA	NA	NA (12)	NA	Yes
12	F	26	11.8	12.0	5	1	1.4	0.4	NA	0.4 (6)	96.6	Yes
13	F	49	32.8	30.0	10	1	0.8	NA	NA	0.8 (2)	97.6	Yes
14	F	34	37.7	15.0	10	2	30.3[a]	NA	NA	NA (12)	NA	Yes
15	F	22	48.1	33.0	25	3	116.1[a]	86.4[a]	2.5	2.5 (9)	94.8	Yes
16	F	25	13.9	10.0	6	2	13.0[a]	4.3[a]	2.2	2.2 (7)	84.2	Yes
17	F	32	5.5	5.0	4	1	1.1	NA	NA	1.1 (1)	80.0	Yes
18	F	72	25.1	17.0	20	1	3.5	NA	NA	3.5 (1)	86.1	Yes
19	M	2	37.6	36.0	10	1	0.7	NA	NA	0.7 (2)	98.1	Yes
20	F	38	10.6	10.0	6	1	2.6	NA	NA	2.6 (2)	75.5	Yes
Mean		30.8 ± 17.0	26.4 ± 15.7	21.2 ± 13.6	10.2 ± 6.3	1.8 ± 1.2	17.3 ± 28.3	15.5 ± 28.2	9.5 ± 21.4	1.2 ± 1.1	93.0 ± 7.9	

Note:—VRR indicates volume reduction rate; NA, not available.
[a] Additional EA treatment during the follow-up period. The clinical follow-up duration for each patient is shown in parentheses.

times, $n = 1$). The mean number of ablation sessions was 1.9 ± 1.2 (range, 1–6). Data from the follow-up US examination were available for 15 patients. The other 5 patients refused US examination because they felt well and had no palpable lesion in the treated area of the neck. These 5 patients were followed-up clinically.

The mean index volume of the BCCs was 26.4 ± 15.7 mL (range, 3.8–49.9 mL). The mean volume of the aspirated internal content was 21.1 ± 13.6 mL (range, 3.0–55.0 mL), and the mean amount of ethanol injected was 10.2 ± 6.3 mL (range, 2.0–25 mL), corresponding to 50.3% ± 24.4% of the aspirated volume. The mean follow-up in the 20 patients was 9.9 ± 7.0 months (range, 1–25 months). By the last follow-up examination, the volume of the treated BCC had decreased significantly to 1.2 ± 1.1 mL ($P = .001$), which corresponded to a mean volume reduction at the last follow-up examination of 93.0% ± 7.9%. Technical success was achieved in all patients (20/20, 100%). The mean symptomatic and cosmetic grading scores improved significantly, from 9.2 ± 1.7 to 0.6 ± 0.8 ($P < .001$) and from 4.0 ± 0.0 to 1.3 ± 0.4, respectively ($P < .001$).

Additional EA was performed in 11 patients (11/20, 55.0%) due to incompletely resolved clinical symptoms and cosmetic problems (Table 2). Improvement was achieved in 8 of these patients after the second treatment; the remaining 3 patients still had incompletely resolved clinical symptoms. However, their clinical symptoms and cosmetic problems improved after a third session of EA in 2 patients and a sixth session of EA in 1 patient, respectively (Fig 2). In patients undergoing multiple treatment sessions, the mean index volume of the cyst was larger, and the initial symptom score, therefore, higher, than in patients treated in a single session. After the procedure, the volume of BCCs in patients in both groups improved significantly, as did the symptomatic and cosmetic scores. Intracystic hemorrhage developed during the aspiration in 1 patient, which delayed the procedure (Fig 3); however, there were no significant complications such as infection, skin necrosis, fever, or nerve palsy. Only mild local pain related to the procedure occurred.

Table 2: Efficacy of ethanol ablation according to the number of treatment sessions[a]

No. of Sessions	Single Session (*n* = 9)	Multiple Sessions (*n* = 11)	*P* Value
Initial volume	21.3 ± 15.8	30.6 ± 15.3	.160
Symptom score	8.1 ± 2.2	10.0 ± 0.0	.011
Cosmetic score	3.9 (3–4)	4.0 (4)	.710
Final volume (VRR)	1.3 ± 1.3	1.1 ± 1.1	.487
P value	.028	.018	
Symptomatic score	0.4 (0–1)	0.5 (0–2)	.809
P value	.017	.004	
Cosmetic score	1.2 (1–2)	1.2 (1–2)	.827
P value	.009	.003	

Note:—VRR indicates volume reduction rate.
[a] Data are means unless otherwise indicated. Range is shown in parentheses.

DISCUSSION

This study evaluated the efficacy and safety of EA for the treatment of BCCs based on the largest number of cases (drawn from 2 hospitals) reported thus far. The results demonstrated a mean volume reduction in the EA-treated BCCs of 93.0%, as well as improvement in clinical symptoms and cosmetic problems. There were no major complications or procedure-related deaths. After a single session, 55.0% of the patients had incompletely resolved clinical problems, but they responded well to additional EA, which was effective and safe and had a therapeutic success rate of 100.0%. These results support the use of EA as a first-line treatment for BCC.

BCC is a congenital neck mass that usually manifests as a painless lateral neck mass in children and young adults.[1] However, it may also be symptomatic, with fever, tenderness, and erythema developing in infected cysts, and may cause a cosmetic problem if it enlarges. Complete surgical resection has been the treatment of choice for BCC, but surgery carries the risk of complications re-

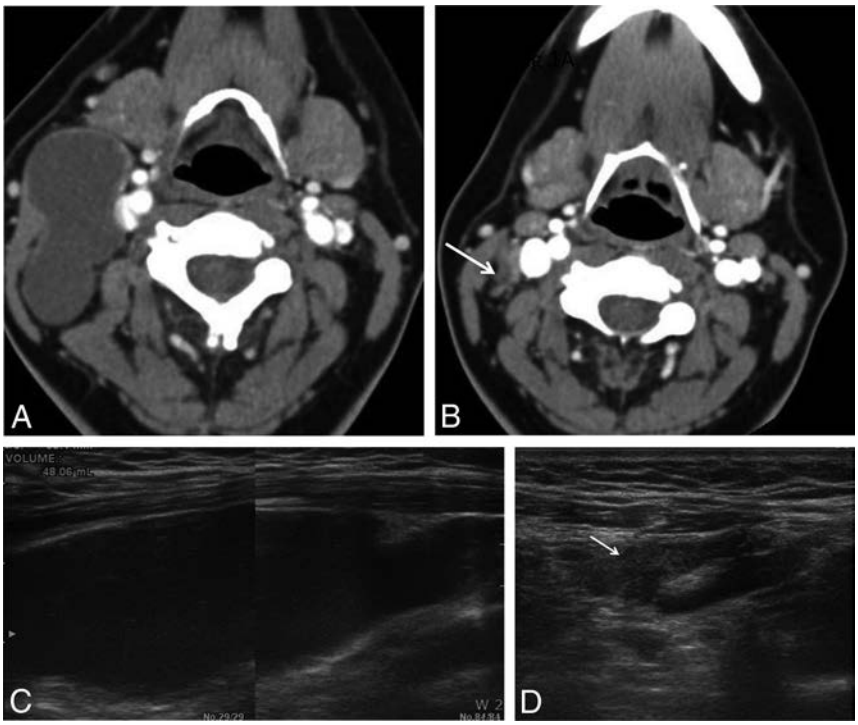

FIG 2. A 22-year-old woman with a right-neck mass. *A*, A CT scan reveals a 6.5-cm second branchial cleft cyst anteromedial to the sternocleidomastoid muscle and lateral to the carotid sheath. *B*, After 3 sessions of ethanol ablation, it is nearly obliterated on follow-up CT (*arrow*). *C* and *D*, Transverse sonogram also shows a large cystic mass in the right neck (volume, 48.1 mL) nearly disappeared after the treatment (*arrow*).

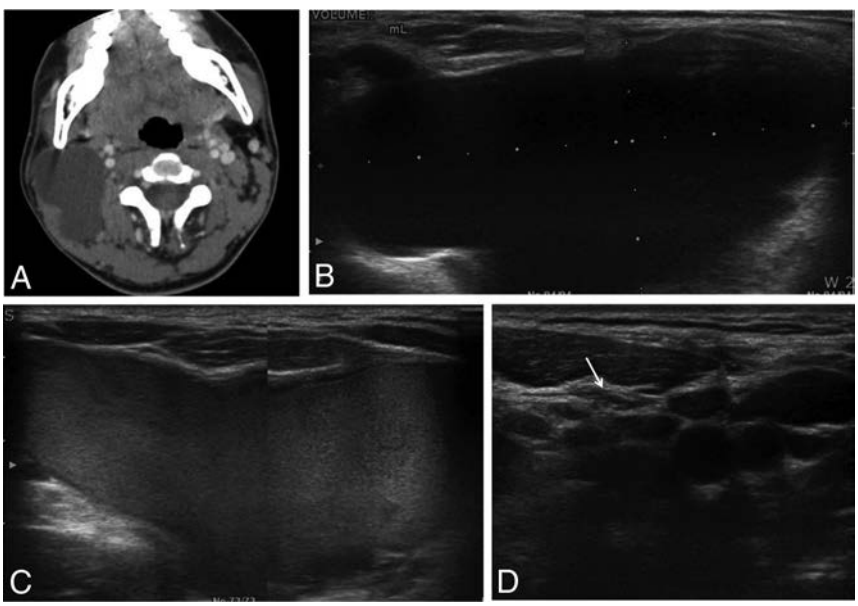

FIG 3. A 15-year-old adolescent boy with a right-neck mass. *A* and *B*, Transverse US and CT scans show a 7-cm cystic mass in the right neck (volume, 36.6 mL). *C*, During the ethanol ablation, intracystic hemorrhage developed after aspiration of internal contents. *D*, However, after a second session of ethanol ablation, the cystic mass had disappeared on follow-up US (*arrow*).

lated to general anesthesia, postoperative morbidity, and scarring of the surgical wound. In addition, surgeons may be reluctant to undertake open surgical treatment, which might seem inappropriate, particularly in view of the often relatively mild symptomatology.[19] Alternative treatment of BCCs, specifically US-guided chemical ablation with OK-432 or EA, has been suggested to overcome the limitations of surgery. The main advantages of US-guided chemical ablation are the absence of external scarring and the low morbidity and complication rates.[3-7]

OK-432 is a lyophilized mixture of group A *Streptococcus pyogenes,* which has antineoplastic activity. Despite success rates of 50.0%–60.8% in BCCs treated with OK-432 (Table 3), 25.0%–41.7% of patients required an operation due to either partial or no response.[3-7,13] OK-432 induces a strong inflammatory reaction, including the activation of macrophages and production of cytokines so that fever and local pain develop as adverse effects, though no major complications have been reported. The potential for adverse effects related to the streptococcal preparation, such as post-rheumatic fever sequelae and glomerulonephritis, as well as penicillin-induced anaphylaxis, has also been suggested.[7] Accordingly, in patients with cystic thyroid nodules, EA may be a better first-line treatment than OK-432.[14,15,17,20] Our study demonstrated a therapeutic success rate with EA higher than that previously reported for OK-432 on the basis of a mean volume reduction ratio in our patients with BCC of 93.0%. Although some patients had mild pain and discomfort related to needle puncture, none had fever or severe pain either during or after treatment, and there were no significant complications.

In terms of the number of treatment sessions, 55% (11/20) of the patients in this study required >2 sessions of EA due to incompletely resolved clinical problems after the initial EA. This rate is higher than the reported rate of recurrence after an operation.[21-23] However, these extra sessions were effective in all cases. The number of patients who required additional EA was higher than the 4.7% reported in previous studies of patients with thyroid cysts.[15] This finding may be because the BCC lumen contains watery or cheesy secretions with exfoliated cells, and direct contact of the sclerosing agent with the inner epithelial surface may be difficult. Aspiration of as much of the cystic content as possible and irrigation of the cyst wall with normal saline may increase the efficacy of EA by removing the debris or viscous material coating the inner wall of the cyst.[24] Another possible explanation is that the BCC wall may be thicker than the wall of thyroid cysts; this feature makes complete penetration by the ethanol difficult. Although BCCs are usually

Table 3: Summary of published data for chemical ablation in patients with brachial cleft cysts[a]

Study	Year	No. of Patients	Sclerosing Agent	Mean Treatment Sessions (No.)	Complete Response	Partial (≥50%) Response	Partial (<50%) Response	No Response	Complications
Fukumoto et al[2]	1994	3	Ethanol	1.0	100.0% (3/3)	–		–	None
Roh et al[5]	2006	12	OK-432	2.3	58.3% (7/12)	25.0% (3/12)		16.7% (2/12)	Fever
Kim et al[4]	2009	23	OK-432	1.7	60.8% (14/23)	13.0% (3/23)	8.7% (2/23)	17.4% (4/23)	Fever, local pain
Ohta et al[6]	2010	12	OK-432	2.9	50.0% (6/12)	16.7% (2/12)	8.3% (1/12)	25.0% (3/12)	Fever

[a] Numbers in parentheses are the numbers of patients among all those included in the study.

lined with a stratified squamous epithelium, in some cases, the lining consists of a thick columnar ciliated epithelium surrounded by dense lymphoid tissue. There may also be marked inflammatory changes and the epithelium may be attenuated.[25] Thus, a longer ethanol retention time may be needed for BCCs than for thyroid cysts because slower diffusion of the ethanol would induce continuous ablation. A previous study of cystic thyroid nodules (cystic component of ≥50%) demonstrated a higher therapeutic success rate in a group of patients treated with a longer ethanol retention time, suggesting that this would also be the case in EA-treated BCCs.[26]

Despite the need for additional EA, technical success was achieved in all patients. This is in contrast to the repeat treatment of cystic thyroid nodules, as in 5%–25% of patients refractory to the first round of EA and there was a marked decline in the therapeutic efficacy of subsequent rounds.[27] Bennedbaek and Hegedüs[28] also reported a decrease in the efficacy of additional EA in patients with thyroid cysts: 63.6% after the first, 33.3% after the second, and 25% after the third round of EA. However, in our patients with BCCs, additional EA was effective; 45% (9/20) of the patients were treated successfully with 1 round; 81.8% (9/11), with 2 rounds; and 50% (1/2), with 3 rounds. In BCC, the additional EA probably destroys the remaining viable epithelial cell layer that was not in contact with ethanol in the previous ablation, whereas in thyroid nodules, the solid component is more resistant to ethanol diffusion and is likely to bleed, as reported in previous retrospective and prospective studies.[27,29]

In our study, all BCCs were cytologically confirmed as benign at fine-needle aspiration. Nonetheless, CT was performed to exclude the possibility of solitary cystic lymph node metastasis from head and neck cancers.[13,30,31] A cystic lymph node metastasis from an occult tumor can mimic a benign BCC, and their cytologic features may not be distinguishable by fine-needle aspiration. Thus, especially in older patients, careful evaluation of the imaging features is a prerequisite of EA application. The possibility of a carcinoma arising from a BCC is extremely low and may even be zero.[32]

There were several limitations to this study. First, because the mean follow-up was relatively short, it did not allow an accurate evaluation of recurrence. Second, the number of patients included was small. However, BCC is relatively uncommon, and EA is currently not a primary treatment method for these cysts. Only patients who refused or were ineligible for an operation were included in this study. Therefore, the generalizability of these results may be limited. However, this study of the efficacy of EA for the treatment of BCC is the largest conducted thus far and serves as a basis for further, larger scale studies. Third, only patients with unilocular cystic lesions were included. The effects of EA on other types of brachial sinuses or fistulas may be different.

CONCLUSIONS

Our results demonstrated that EA offers an effective and safe alternative treatment for patients with BCC who refuse or are ineligible for an operation. It should, therefore, also be considered as a first-line treatment in patients with BCC.

REFERENCES

1. Benson MT, Dalen K, Mancuso AA, et al. **Congenital anomalies of the branchial apparatus: embryology and pathologic anatomy.** *Radiographics* 1992;12:943–60 CrossRef Medline
2. Fukumoto K, Kojima T, Tomonari H, et al. **Ethanol injection sclerotherapy for Baker's cyst, thyroglossal duct cyst, and branchial cleft cyst.** *Ann Plast Surg* 1994;33:615–19 CrossRef Medline
3. Kim MG, Kim SG, Lee JH, et al. **The therapeutic effect of OK-432 (picibanil) sclerotherapy for benign neck cysts.** *Laryngoscope* 2008; 118:2177–81 CrossRef Medline
4. Kim MG, Lee NH, Ban JH, et al. **Sclerotherapy of branchial cleft cysts using OK-432.** *Otolaryngol Head Neck Surg* 2009;141:329–34 CrossRef Medline
5. Roh JL, Sung MW, Kim KH, et al. **Treatment of branchial cleft cyst with intracystic injection of OK-432.** *Acta Otolaryngol* 2006;126: 510–14 CrossRef Medline
6. Ohta N, Fukase S, Suzuki Y, et al. **Treatments of various otolaryngological cystic diseases by OK-4321: its indications and limitations.** *Laryngoscope* 2010;120:2193–96 CrossRef Medline
7. Ohta N, Fukase S, Watanabe T, et al. **Effects and mechanism of OK-432 therapy in various neck cystic lesions.** *Acta Otolaryngol* 2010; 130:1287–92 CrossRef Medline
8. Lee DK, Seo JW, Park HS, et al. **Efficacy of ethanol ablation for thyroglossal duct cyst.** *Ann Otol Rhinol Laryngol* 2015;124:62–67 CrossRef Medline
9. Sung JY, Baek JH, Kim KS, et al. **Symptomatic nonfunctioning parathyroid cysts: role of simple aspiration and ethanol ablation.** *Eur J Radiol* 2013;82:316–20 CrossRef Medline
10. Sung MW, Lee DW, Kim DY, et al. **Sclerotherapy with picibanil (OK-432) for congenital lymphatic malformation in the head and neck.** *Laryngoscope* 2001;111:1430–33 CrossRef Medline
11. Tu JH, Do HM, Patel V, et al. **Sclerotherapy for lymphatic malformations of the head and neck in the pediatric population.** *J Neurointerv Surg* 2016 Oct 5. [Epub ahead of print] CrossRef Medline
12. Kim KH, Sung MW, Roh JL, et al. **Sclerotherapy for congenital lesions in the head and neck.** *Otolaryngol Head Neck Surg* 2004;131: 307–16 CrossRef Medline
13. Kim JH. **Ultrasound-guided sclerotherapy for benign non-thyroid cystic mass in the neck.** *Ultrasonography* 2014;33:83–90 CrossRef Medline
14. Gharib H, Hegedüs L, Pacella CM, et al. **Clinical review: nonsurgical, image-guided, minimally invasive therapy for thyroid nodules.** *J Clin Endocrinol Metab* 2013;98:3949–57 CrossRef Medline
15. Sung JY, Baek JH, Kim KS, et al. **Single-session treatment of benign cystic thyroid nodules with ethanol versus radiofrequency ablation: a prospective randomized study.** *Radiology* 2013;269:293–300 CrossRef Medline
16. Sung JY, Baek JH, Kim YS, et al. **One-step ethanol ablation of viscous cystic thyroid nodules.** *AJR Am J Roentgenol* 2008;191:1730–33 CrossRef Medline

17. Sung JY, Kim YS, Choi H, et al. **Optimum first-line treatment technique for benign cystic thyroid nodules: ethanol ablation or radiofrequency ablation?** *AJR Am J Roentgenol* 2011;196:W210–14 CrossRef Medline
18. Baek JH, Ha EJ, Choi YJ, et al. **Radiofrequency versus ethanol ablation for treating predominantly cystic thyroid nodules: a randomized clinical trial.** *Korean J Radiol* 2015;16:1332–40 CrossRef Medline
19. Nixon PP, Healey AE. **Treatment of a branchial sinus tract by sclerotherapy.** *Dentomaxillofac Radiol* 2011;40:130–32 CrossRef Medline
20. Na DG, Lee JH, Jung SL, et al; Korean Society of Thyroid Radiology (KSThR), Korean Society of Radiology. **Radiofrequency ablation of benign thyroid nodules and recurrent thyroid cancers: consensus statement and recommendations.** *Korean J Radiol* 2012;13:117–25 CrossRef Medline
21. Spinelli C, Rossi L, Strambi S, et al. **Branchial cleft and pouch anomalies in childhood: a report of 50 surgical cases.** *J Endocrinol Invest* 2016;39:529–35 CrossRef Medline
22. Prasad SC, Azeez A, Thada ND, et al. **Branchial anomalies: diagnosis and management.** *Int J Otolaryngol* 2014;2014:237015 CrossRef Medline
23. Ford GR, Balakrishnan A, Evans JN, et al. **Branchial cleft and pouch anomalies.** *J Laryngol Otol* 1992;106:137–43 CrossRef Medline
24. Kim SM, Baek JH, Kim YS, et al. **Efficacy and safety of ethanol ablation for thyroglossal duct cysts.** *AJNR Am J Neuroradiol* 2011;32:306–09 CrossRef Medline
25. Thomaidis V, Seretis K, Tamiolakis D, et al. **Branchial cysts: a report of 4 cases.** *Acta Dermatovenerol Alp Pannonica Adria* 2006;15:85–89 Medline
26. Kim DW, Rho MH, Kim HJ, et al. **Percutaneous ethanol injection for benign cystic thyroid nodules: is aspiration of ethanol-mixed fluid advantageous?** *AJNR Am J Neuroradiol* 2005;26:2122–27 Medline
27. Lee JH, Kim YS, Lee D, et al. **Radiofrequency ablation (RFA) of benign thyroid nodules in patients with incompletely resolved clinical problems after ethanol ablation (EA).** *World J Surg* 2010;34:1488–93 CrossRef Medline
28. Bennedbaek FN, Hegedüs L. **Treatment of recurrent thyroid cysts with ethanol: a randomized double-blind controlled trial.** *J Clin Endocrinol Metab* 2003;88:5773–77 CrossRef Medline
29. Jang SW, Baek JH, Kim JK, et al. **How to manage the patients with unsatisfactory results after ethanol ablation for thyroid nodules: role of radiofrequency ablation.** *Eur J Radiol* 2012;81:905–10 CrossRef Medline
30. Foss RD, Warnock GR, Clark WB, et al. **Malignant cyst of the lateral aspect of the neck: branchial cleft carcinoma or metastasis?** *Oral Surg Oral Med Oral Pathol* 1991;71:214–17 CrossRef Medline
31. Briggs RD, Pou AM, Schnadig VJ. **Cystic metastasis versus branchial cleft carcinoma: a diagnostic challenge.** *Laryngoscope* 2002;112:1010–14 CrossRef Medline
32. Girvigian MR, Rechdouni AK, Zeger GD, et al. **Squamous cell carcinoma arising in a second branchial cleft cyst.** *Am J Clin Oncol* 2004;27:96–100 CrossRef Medline

Head and Neck MRI Findings in CHARGE Syndrome

M.J. Hoch, S.H. Patel, D. Jethanamest, W. Win, G.M. Fatterpekar, J.T. Roland Jr, and M. Hagiwara

ABSTRACT

SUMMARY: Coloboma of the eye, Heart defects, Atresia of the choanae, Retardation of growth and/or development, Genital and/or urinary abnormalities, and Ear abnormalities and deafness (CHARGE) syndrome is a disorder with multiple congenital anomalies seen on imaging. A retrospective review of 10 patients with CHARGE syndrome who underwent MR imaging of the brain as part of a preoperative evaluation for cochlear implantation was conducted. Structural abnormalities of the entire MR imaging of the head were evaluated, including the auditory system, olfactory system, face, skull base, and central nervous system. The most frequent MR imaging findings included dysplasias of the semicircular canals and hypoplasia of the frontal lobe olfactory sulci. Less frequent findings included cleft lip/palate and coloboma. Our study uncovered new findings of a J-shaped sella, dorsal angulation of the clivus, and absent/atrophic parotid glands, not previously described in patients with CHARGE. Our results emphasize the utility of MR imaging in the diagnosis and management of patients with CHARGE syndrome.

ABBREVIATIONS: CHARGE = Coloboma of the eye, Heart defects, Atresia of the choanae, Retardation of growth and/or development, Genital and/or urinary abnormalities, and Ear abnormalities and deafness; IAC = internal auditory canal; SCC = semicircular canal; SPACE = sampling perfection with application-optimized contrasts using different flip angle evolutions

Coloboma of the eye, Heart defects, Atresia of the choanae, Retardation of growth and/or development, Genital and/or urinary abnormalities, and Ear abnormalities and deafness (CHARGE) syndrome was first described in 1979 by Hall[1] in 17 children with multiple congenital anomalies, including choanal atresia, and separately by Hittner et al[2] in 10 patients with coloboma. It is an autosomal dominant disorder with a North American prevalence of 1/10,000 live births.[3,4] Most cases are sporadic with the *CHD7* gene mutation identified as a cause in 2 of 3 patients.[5,6] The 6 classic diagnostic criteria of the acronym described by Pagon et al[7] in 1981 are ocular Coloboma, Heart defects, choanal Atresia, Retardation, Genital anomalies, and Ear anomalies. Additional anomalies have been reported, and revised criteria for the diagnosis have been proposed. Blake et al[3] expanded the original criteria to include brain stem anomalies and visceral malformations. Verloes[8] focused on the "3C triad" of coloboma, choanal atresia, and abnormal semicircular canals and formally defined partial and atypical CHARGE syndromes.

Multiple anomalies are seen on imaging involving the ear, orbit, nasal cavity, and brain. Most neuroimaging reviews of patients with CHARGE syndrome focus on the CT findings within the temporal bone.[9-12] While many temporal bone findings are clinically important for diagnosis and treatment, other findings such as cochlear nerve abnormalities are better characterized with MR imaging. However, MR imaging reviews of CHARGE syndrome are limited, focusing on only 1 or a few anomalies.[13-15] To date, no single study comprehensively reports all key head and neck MR imaging findings in CHARGE syndrome, to our knowledge. The purpose of our article was to determine, by retrospective review, the head and neck structural anomalies in patients with CHARGE detected on MR imaging. Our findings will be compared with other works in the literature for concordance when available. Instructive images of the structural anomalies will be included for educational purposes.

CASE SERIES

Retrospective review of the radiology data base from 2006 to 2015 yielded 10 patients with CHARGE syndrome who underwent MR imaging of the brain as part of a preoperative evaluation for cochlear implantation. Inclusion criteria used for the clinical diagnosis of CHARGE syndrome were based on those set by Verloes.[8] Typical CHARGE syndrome requires all 3 of the major criteria or 2 of the major and at least 2 minor criteria. Classification as atypical CHARGE is used for patients with 2 major and no minor or 1

Received October 6, 2016; accepted after revision May 13, 2017.

From the Department of Radiology (M.J.H., S.H.P., W.W., G.M.F., M.H.), Section of Neuroradiology, and Department of Otolaryngology (D.J., J.T.R.), New York University Langone Medical Center, New York, New York.

Abstract previously presented at: Annual Meeting and Symposium of the American Society of Neuroradiology, April 25–30, 2015; Chicago, Illinois.

Please address correspondence to Michael J. Hoch, MD, Department of Radiology, 1364 Clifton Rd NE, Atlanta, GA 30322; e-mail: michael.hoch@emory.edu

http://dx.doi.org/10.3174/ajnr.A5297

Summary of clinical documentation of CHARGE diagnosis for the 10 subjects according to the criteria set by Verloes[8]

	Subject									
	1	2	3	4	5	6	7	8	9	10
Sex	M	M	F	F	M	M	M	M	F	F
Age at MRI (yr)	1	2	18	1	1	7	4	8 mo	1	19
Major criteria										
Coloboma		+	+			+			+	+
Choanal atresia						+			+	
SCC hypoplasia	+	+	+	+	+	+	+	+	+	+
Minor criteria										
Rhombencephalic dysfunction	$+^{1,2}$	$+^{1,2}$	$+^{1}$	$+^{1,2}$	$+^{1,2}$	$+^{1}$	$+^{1}$	$+^{2}$	$+^{1,2}$	
Hypothalamohypophyseal dysfunction	$+^{3}$	$+^{4}$		$+^{4}$	$+^{3}$	$+^{4}$		$+^{4}$	$+^{4}$	
Malformation of ear	$+^{5,6}$	$+^{6}$	$+^{6}$	$+^{5,6}$	$+^{6}$	$+^{6}$	$+^{6}$	$+^{6}$	$+^{6}$	$+^{6}$
Malformation of mediastinum	$+^{7}$	$+^{7}$		$+^{7}$	$+^{7}$	$+^{7}$		$+^{7}$	$+^{7,8}$	$+^{7}$
Mental retardation	+	+		+	+			+		
Typical CHARGE		+	+			+			+	+
Atypical CHARGE	+			+	+		+	+		

Note:— + indicates present criteria; $+^{1}$, cochlear nerve hypoplastic or absent; $+^{2}$, brain stem hypoplasia; $+^{3}$, undescended testes; $+^{4}$, growth delay; $+^{5}$, external ear malformation; $+^{6}$, inner ear malformation; $+^{7}$, cardiac malformation; $+^{8}$, tracheoesophageal fistula.

major and at least 3 minor criteria. The clinical diagnostic information is summarized in the Table. Five of the 10 patients were classified as having typical CHARGE syndrome. The other 5 were classified as having atypical CHARGE syndrome. None of the patients met the criteria for partial CHARGE syndrome. Three of the 5 patients with typical CHARGE had *CHD7* genetic testing, and all 3 had findings positive for the mutation. Patient ages ranged from 8 months to 19 years of age (average age, 6.4 years). Seven patients were 2 years of age or younger at the time of imaging. Six patients were male. All patients were imaged on 1.5T MR imaging scanners (Aera and Avanto; Siemens, Erlangen, Germany). Nine of the 10 patients had high-resolution heavily T2-weighted 3D imaging of the temporal bones, such as CISS ($n = 8$) or T2 sampling perfection with application-optimized contrasts using different flip angle evolutions (SPACE sequence; Siemens) ($n = 1$). Five of the 10 patients had intravenous contrast administered during their MR imaging examinations.

Each bilateral structure, including the ears and orbits, was evaluated separately. The 10 cases were reviewed in consensus by 2 Certificate of Added Qualification–certified neuroradiologists with 8 and 3 years of experience, specializing in head and neck imaging. Because of the variability in MR imaging sequences, not all structures were visualized equally. This discrepancy was reflected in the final analysis. Structural abnormalities of the entire MR imaging of the head were evaluated, including the auditory system, olfactory system, face, skull base, and central nervous system.

Imaging criteria of most temporal bone findings were based on previously reported findings.[16,17] Readers assessed findings of vestibular dysplasia, semicircular canal (SCC) dysplasia, cochlear dysplasia, absence of the cochlear aperture, cochlear nerve deficiency, internal auditory canal (IAC) dysplasia, and an enlarged vestibular aqueduct.[9,14,16,17]

The olfactory apparatus and facial structures were evaluated for abnormalities, some of which were based on other published works involving CHARGE syndrome,[7,9,13-15] including olfactory bulb and sulcal hypoplasia/aplasia, choanal atresia, nasal septal integrity, cleft lip and palate, and chorioretinal coloboma. The parotid glands were included in the FOV of all examinations and were also evaluated for any abnormality.

The skull base was evaluated for abnormalities, with basiocciptal hypoplasia and basilar invagination previously reported in patients with CHARGE syndrome.[13] Basilar invagination was recorded if the tip of the odontoid process extended >5 mm above the Chamberlain line. Other observed abnormalities of the skull base were also recorded.

Readers evaluated variations in venous drainage as previously described in patients with CHARGE. These included enlarged transmastoid emissary veins, hypoplastic sigmoid sinus or jugular foramen, aberrant petrosal sinus, venous lakes, condylar canal veins, and high-riding jugular bulbs.[18]

The brain was evaluated for known reported associated findings of CHARGE syndrome such as Chiari I malformation, Dandy-Walker spectrum, holoprosencephaly spectrum, brain stem hypoplasia, other cranial nerve dysplasia, cerebellar hypoplasia, and ventriculomegaly,[19,20] and for other potential abnormalities.

MR imaging data for the 10 patients included mild variability in sequence acquisitions among patients. Therefore, the findings provided for each of the sections reflect the variability of the data. When MR imaging did not cover a pertinent area of interest, relevant data were not recorded. Fig 1 shows the percentage of structures evaluated when the finding was present.

Temporal Bone

Of the inner ears evaluated, 20 of 20 had both vestibular and SCC dysplasia (Fig 2). Because 1 patient did not have high-resolution 3D T2-weighted or CISS imaging, the following were scored of 18 total ears: Fifteen had cochlear nerve deficiency (bilateral in 7 subjects) (Fig 3), 8 had an absent cochlear aperture (bilateral in 3), and 1 had a unilateral enlarged vestibular aqueduct. One patient with bilateral cochlear nerve deficiency also had unilateral vestibular nerve deficiency. Eighteen of 18 patients also had IAC dysplasia (bilateral in 9), of which 4 were enlarged and 14 were stenotic. Sixteen of 18 patients had cochlear dysplasia (bilateral in 7) with most patients ($n = 7$) having 1.5 turns.

Olfactory Apparatus and Face

Only 2 patients of 10 had choanal atresia (Fig 4), and 1 of those 2 had a deficient posterior nasal septum. Due to FOV coverage variability, 16 olfactory structures (8 patients) could be evaluated;

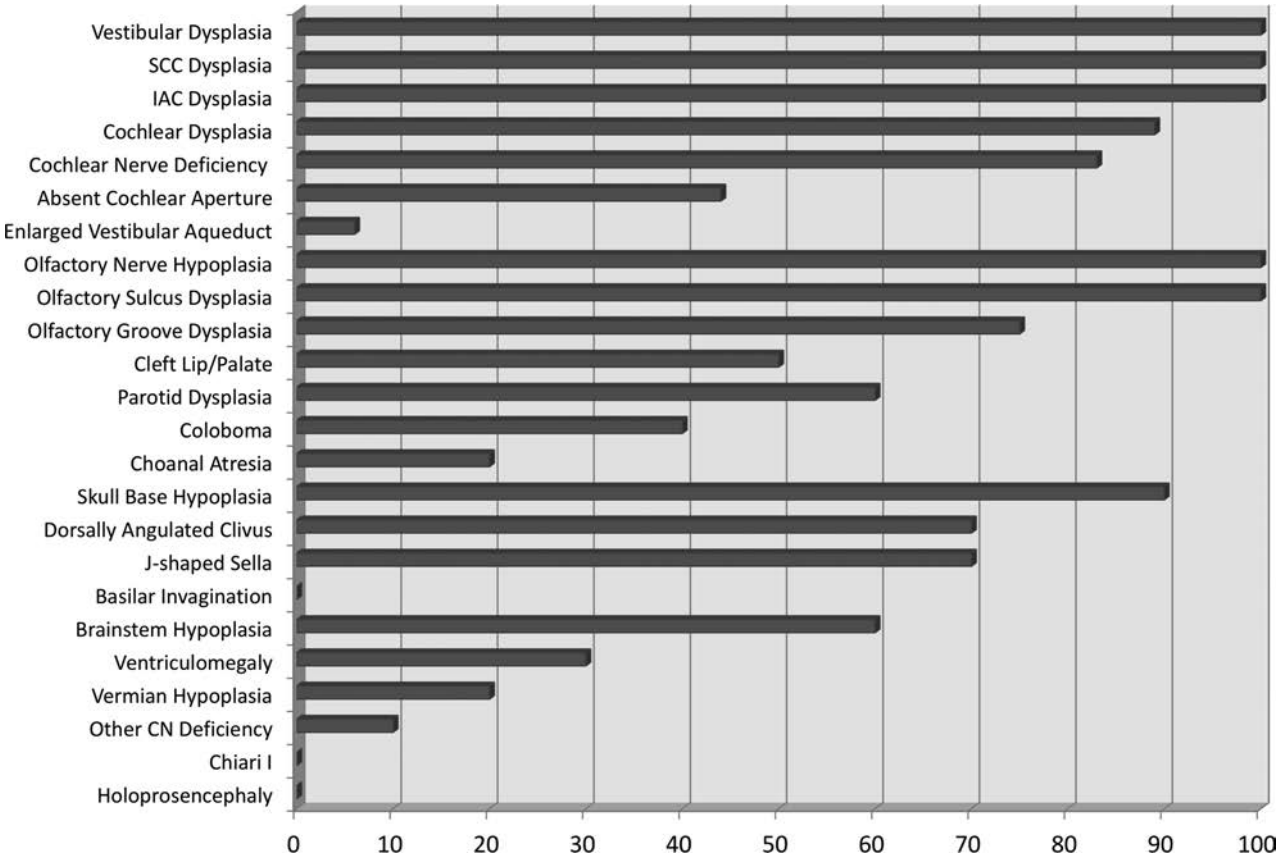

FIG 1. Bar graph of the percentage of findings present in all 10 patients with CHARGE. A percentage was chosen as the representation because some findings were bilateral and others were singular, and some of the structures could not be evaluated in all patients due to differences in imaging technique. Inner ear dysplasia, olfactory structure hypoplasia, and skull base hypoplasia were the most frequent findings.

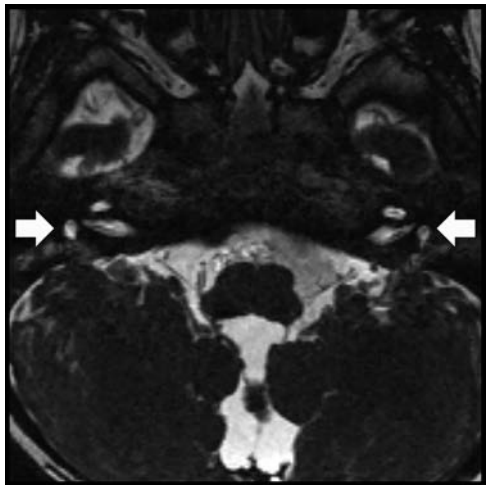

FIG 2. Axial CISS image at the level in the inner ears shows bilateral vestibular dysplasia (*arrows*) and absence of the semicircular canals. Inner ear malformations are among the most frequent head and neck findings in CHARGE syndrome.

however, all 16 demonstrated olfactory nerve hypoplasia with associated absent or hypoplastic olfactory sulci (Fig 5). Twelve of those 16 showed small bony olfactory grooves. Five of 10 patients had a cleft lip and cleft palate (Fig 6). Coloboma was seen in 8 of 20 imaged globes (Fig 7).

All temporal bone MRIs covered the entire parotid and parapharyngeal spaces. Two of 10 patients demonstrated aplastic bilateral parotid glands (Fig 8). Four additional patients had hypoplastic parotid glands bilaterally (2 of which had accessory salivary tissue along the masseter). The MR imaging scans covered the submandibular glands in 9 of 10 patients. Those 9 patients had normal-appearing submandibular glands. No ectopic salivary glands were identified in any patients.

Skull Base

Only 1 patient had a normally formed skull base. The other 9 patients had basioccipital hypoplasia, none of which had classic basilar invagination. All 10 patients had a normal relationship of the superior ossification center of the dens with respect to the anterior arch of C1. However, 7 of 10 demonstrated a dorsally angled clivus, with posterior displacement of an ossific density, which we interpreted to reflect an underdeveloped basioccipital ossification center and widening of the spheno-occipital synchondrosis (Fig 9). Eight of 10 had hypoplasia of the sella with 7 of those patients having a "J-shaped" appearance, with flattening and elongation of the tuberculum sella (Fig 9*B*).[21]

Venous Anomalies

In 2 of the 10 patients, the readers reported insufficient imaging data to accurately assess the venous structures. Of the remaining 8 patients, 6 demonstrated large anomalous transmastoid emissary veins (Fig 10), with 3 of these patients demonstrating this finding bilaterally. In 5 of the 6 patients with anomalous transmastoid emissary veins, the ipsilateral sigmoid sinus was hypoplastic. One

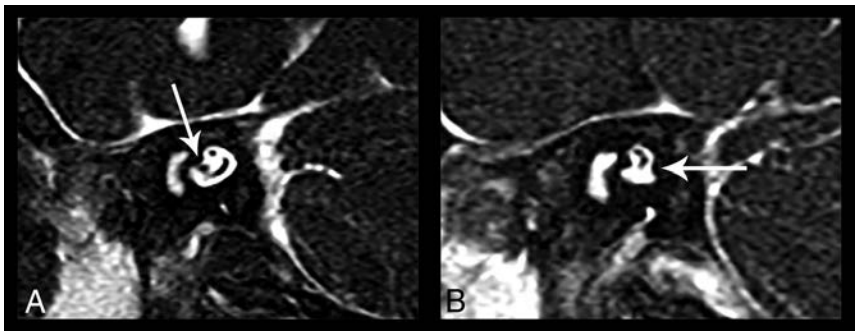

FIG 3. Oblique sagittal CISS images of the bilateral internal auditory canals show unilateral cochlear nerve deficiency. *A*, The normal right IAC has all 4 nerves. The cochlear nerve is seen in the anterior inferior quadrant of the IAC (*arrow*). *B*, The cochlear nerve is not visualized in the left IAC. There is also the suggestion of left inferior vestibular nerve hypoplasia (*arrow*).

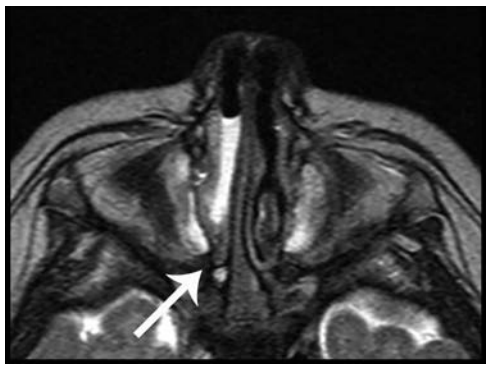

FIG 4. Axial CISS image at the level of the nasal cavity shows right choanal atresia (*arrow*) with retained secretions in the nasal cavity.

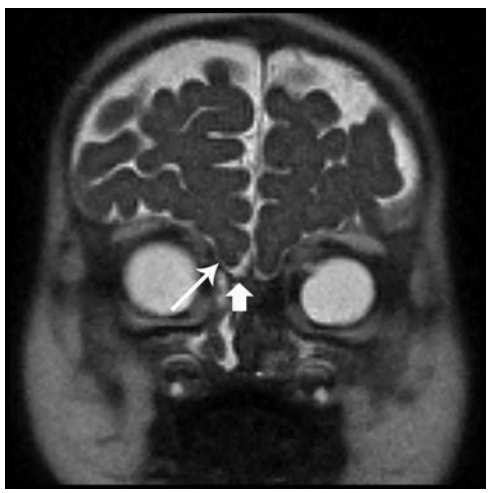

FIG 5. Coronal HASTE image shows bilateral shallow olfactory grooves with absent olfactory nerves (*short arrow*) and absent olfactory sulci (*long arrow*). The findings are labeled unilaterally.

of the patients with bilateral transmastoid emissary veins also demonstrated bilateral enlarged transoccipital emissary veins.

Central Nervous System

None of the 10 patients had findings of Chiari I malformation or holoprosencephaly. However, 5 patients showed brain stem hypoplasia, 1 had vermian hypoplasia, and 1 had both vermian and brain stem hypoplasia. Three of 10 patients had ventriculomegaly.

DISCUSSION

This is the largest comprehensive review of the structural head and neck MR imaging findings in CHARGE syndrome. As in other reviews of CHARGE syndrome, findings reflecting the acronym were variable in frequency. Inner ear abnormalities were the most frequent finding, whereas coloboma and choanal atresia were infrequent findings. Most interesting, skull base dysplasia and olfactory complex hypoplasia, which are not part of the acronym, were 2 of the most frequent findings.

While complementary, MR imaging has advantages over CT in the preoperative evaluation of pediatric deafness.[22] MR imaging can identify cochlear nerve aplasia and can better delineate brain abnormalities that can potentially alter management in patients with CHARGE, who often require brain stem or cochlear implantation. While sedation is often needed for pediatric patients, MR imaging does not use radiation, which is of particular concern in the pediatric population.

There are 2 recently described and potentially major new diagnostic criteria for CHARGE syndrome. The first is olfactory complex anomalies, which include either absence or hypoplasia of the olfactory nerve, sulcus, and bony groove. This was described by Pinto et al in 2005[23] and later by Blustajn et al in 2008.[15] Our findings of 8 of 8 visible cases with olfactory complex anomalies are in agreement with the prior works. Pinto et al[23] proposed that the olfactory abnormality and hypogonadotropic hypogonadism in patients with CHARGE syndrome overlap the main features of Kallmann syndrome. Deficiency of fibroblast growth factor signaling is thought to be responsible for olfactory bulb dysgenesis in Kallmann syndrome,[24] and Pinto et al theorized that there may be potentially a functional connection between *CHD7* and fibroblast growth factor signaling in olfactory bulb differentiation.[15,23]

The second newly proposed potential major criterion for CHARGE syndrome is abnormal basiocciput development.[13] Basiocciput hypoplasia results in shortening of the clivus and was previously reported to be closely associated with basilar invagination.[25] The work of Fujita et al[13] showed that 7 of 8 patients with CHARGE syndrome had basioccipital hypoplasia, and of those, 5 had basilar invagination. Our series demonstrated 9 of 10 patients with basioccipital hypoplasia, similar to the work of Fujita et al. However, none of our patients were judged to demonstrate basilar invagination. Instead, 7 of 10 patients demonstrated a dorsally angulated clivus with posterior displacement of an ossific density forming the inferior clivus; we interpreted this ossific density to reflect an underdeveloped basioccipital ossification center, with associated widening of the spheno-occipital synchondrosis. This finding has not been previously reported. The spheno-occipital synchondrosis is often not fused in the teenage years. We suspect that the posteriorly displaced basioccipital ossification center can mimic basilar invagination. All our patients demonstrated a normal relationship of the superior ossification center of the dens with the anterior arch of C1.

Our study is the first to describe a J-shaped sella associated

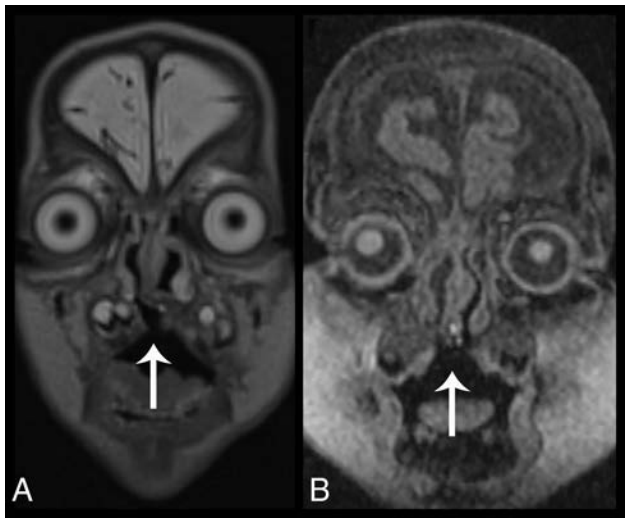

FIG 6. Cleft palate in 2 different patients. Coronal T2 SPACE reconstruction (*A*) and 3D T1-weighted coronal image (*B*) demonstrate a bony defect in the hard palate (*arrows*), allowing communication between the oral and nasal cavities.

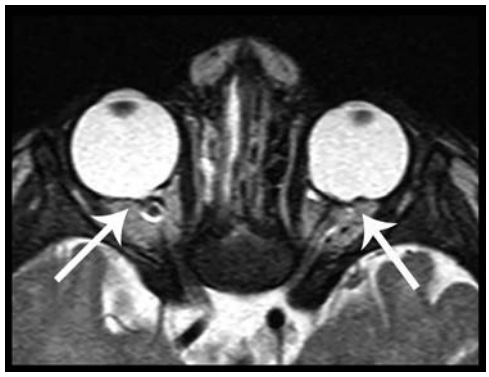

FIG 7. Axial CISS image at the level of the orbits demonstrates focal outpouching of the posterior globes at the optic disc, consistent with bilateral colobomas (*arrows*).

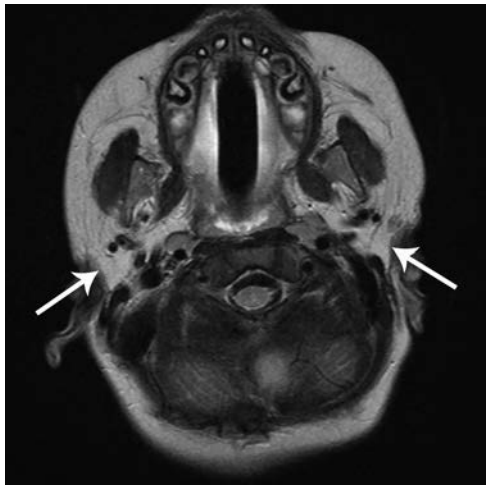

FIG 8. Axial T2-weighted image shows absent bilateral parotid glands. There is fatty tissue in both parotid spaces (*arrows*), with no identifiable salivary gland tissue. This finding has not been previously reported in CHARGE syndrome, to our knowledge. The normal-appearing masticator muscles argue against denervation atrophy and early fatty replacement as a cause of the parotid abnormality.

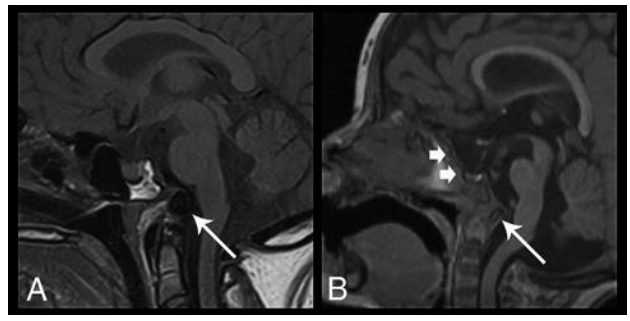

FIG 9. Sagittal images of skull base dysplasia in 2 different patients. *A*, Sagittal T1-weighted image demonstrates skull base hypoplasia with dorsal angulation and posterior displacement of a hypoplastic basioccipital ossification center (*arrow*) and widening of the spheno-occipital synchondrosis. *B*, Sagittal 3D T1-weighted image shows a J-shaped sella (*short arrows*) with flattening and elongation of the tuberculum sella. There is also evidence of a dorsally angulated clivus (*long arrow*), with findings similar to those in *A*. None of the patients had basilar invagination.

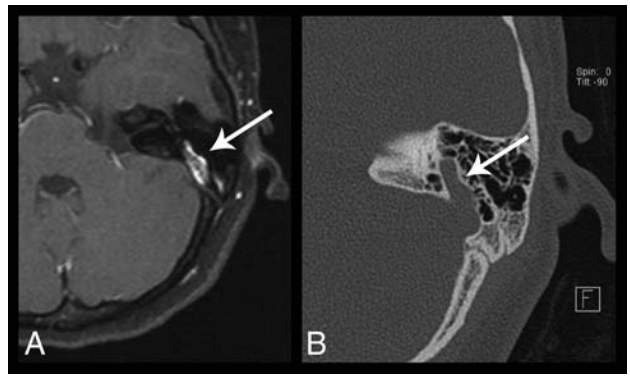

FIG 10. Axial postcontrast fat-saturated T1-weighted image (*A*) and axial temporal bone CT image (*B*) of the left temporal bone demonstrate a prominent left transmastoid emissary vein (*arrows*).

with CHARGE syndrome. This appearance was described in 1923 as a skull plain film finding suggestive of intracranial extension of optic nerve glioma.[26] This has been reported in patients with achondroplasia and mucopolysaccharidoses related to skull base hypoplasia, as well as in patients with intracranial aneurysms due to bony remodeling.[21,27] In our patients with CHARGE syndrome, the J-shaped sella is also potentially related to the basioccipital hypoplasia.

Most surprising, 6 of 10 patients had aplastic or hypoplastic bilateral parotid glands. To our knowledge, this finding has not been previously described in association with CHARGE syndrome. Congenital absence of the salivary glands is infrequent and often involves multiple major salivary glands.[28,29] In the 9 patients in whom the submandibular glands were included in the FOV, all 9 had normal-appearing submandibular glands. Furthermore, all subjects had normal-appearing masticator muscles and bilateral cranial nerve V, which would argue against denervation atrophy and early fatty replacement as a cause of the parotid abnormalities.

The etiology of parotid gland dysplasia in patients with CHARGE is unclear. Salivary gland dysplasia can be associated with Treacher Collins syndrome and other facial anomalies,[30] as well as with deafness and ear malformations.[31] Parotid glands

develop in the sixth-to-eighth week of gestation from oral ectoderm. Abnormalities of the inner ear associated with CHARGE such as vestibular and SCC dysplasias tend to occur with an insult in the sixth-to-eighth week of gestation.[32] The similar timeframes of growth arrest could be explained by an insult to both developing parotid buds and primitive inner ears. Disruption of the fibroblast growth factor pathway has been reported in autosomal dominant salivary gland aplasia; as theorized with olfactory bulb dysplasia, the *CHD7* mutation in a patient with CHARGE could potentially affect fibroblast growth factor signaling for parotid gland development.[33]

Our MR imaging findings of inner ear malformations were similar to those in prior CT reviews. When the area of interest was imaged appropriately, 100% of our patients had bilateral vestibular, SCC, and IAC dysplasia. This finding is similar to that in the studies of Lemmerling et al,[11] in which all 7 patients also had these 3 abnormalities bilaterally, and Morimoto et al, [9] in which all 13 patients had bilateral SCC dysplasia.[9,11] In the work of Morimoto et al, only 15 of 26 ears studied had vestibular dysplasia. In the work of Admiraal et al,[10] all cases had bilateral SCC absence on CT, but 2 cases had normally formed vestibules. On MR imaging, SCC abnormalities remain the most frequent temporal bone finding in patients with CHARGE.

In our study, 15 of 18 ears had cochlear nerve deficiency. This finding is similar to that in the work of Holcomb et al,[12] who also showed, on MR imaging, that 13 of 14 ears in patients with CHARGE with sensorineural hearing loss also had deficient or absent cochlear nerves. There were 14 ears with stenotic IAC dysplasia, of which 3 demonstrated the presence of a normal-caliber cochlear nerve. We conclude that abnormal IAC morphology is not a reliable indicator of cochlear nerve integrity. This was similarly demonstrated by Adunka et al,[14] who studied the relationship of the IAC morphology to cochlear nerve abnormalities in 14 children.

Brain stem and cerebellar hypoplasia and ventriculomegaly have been previously reported in patients with CHARGE syndrome[3,19] and were demonstrated in our patients. Six of our patients had brain stem hypoplasia, 2 patients had vermian hypoplasia without other findings of Dandy-Walker malformation, and 3 patients had ventriculomegaly. While there is a reported increased prevalence of Chiari I malformation, Dandy-Walker malformation, and holoprosencephaly in patients with CHARGE syndrome,[34] none of the patients in our study demonstrated these findings.

Temporal bone venous anomalies have also been reported in patients with CHARGE syndrome,[18] with large emissary veins being the most common finding. Six of our patients demonstrated large transmastoid emissary veins, with half of those present bilaterally; most of these patients showed an ipsilateral hypoplastic sigmoid sinus. Other reported anomalies, including a high-riding jugular bulb and venous lakes, were not found in our study.

This retrospective study enumerates the head and neck MR imaging findings in 10 patients with CHARGE syndrome. Because MR imaging and CT play a complementary role in surgical treatment of these patients, knowledge of the common and less frequently associated MR imaging abnormalities is necessary. Frequent findings such as basioccipital dysplasia and olfactory hypoplasia are not found in the CHARGE acronym; thus, further discussion into revising the diagnostic criteria of this syndrome is warranted. Novel findings reported in our study include dorsal angulation of the clivus, a J-shaped sella, and absent parotid glands.

Disclosures: J. Thomas Roland Jr—*UNRELATED: Board Membership:* Cochlear Americas, Advance Bionics; *Comments*: on advisory boards; no money paid to individual.

REFERENCES

1. Hall BD. **Choanal atresia and associated multiple anomalies.** *J Pediatr* 1979;95:395–98 CrossRef Medline
2. Hittner HM, Hirsch NJ, Kreh GM, et al. **Colobomatous microphthalmia, heart disease, hearing loss, and mental retardation: a syndrome.** *J Pediatr Ophthalmol Strabismus* 1979;16:122–28 Medline
3. Blake KD, Davenport SL, Hall BD, et al. **CHARGE association: an update and review for the primary pediatrician.** *Clin Pediat (Phila)* 1998;37:159–73 CrossRef Medline
4. Issekutz KA, Graham JM Jr, Prasad C, et al. **An epidemiological analysis of CHARGE syndrome: preliminary results from a Canadian study.** *Am J Med Genet A* 2005;133A:309–17 Medline
5. Jongmans M, Admiraal R, van der Donk KP, et al. **CHARGE syndrome: the phenotypic spectrum of mutations in the CHD7 gene.** *J Med Genet* 2006;43:306–14 Medline
6. Lalani SR, Safiullah AM, Fernbach SD, et al. **Spectrum of CHD7 mutations in 110 individuals with CHARGE syndrome and genotype-phenotype correlation.** *Am J Hum Genet* 2006;78:303–14 CrossRef Medline
7. Pagon RA, Graham JM Jr, Zonana J, et al. **Coloboma, congenital heart disease, and choanal atresia with multiple anomalies: CHARGE association.** *J Pediatr* 1981;99:223–27 CrossRef Medline
8. Verloes A. **Updated diagnostic criteria for CHARGE syndrome: a proposal.** *Am J Med Genet A* 2005;133A:306–08 CrossRef Medline
9. Morimoto AK, Wiggins RH 3rd, Hudgins PA, et al. **Absent semicircular canals in CHARGE syndrome: radiologic spectrum of findings.** *AJNR Am J Neuroradiol* 2006;27:1663–71 Medline
10. Admiraal RJ, Joosten FB, Huygen PL. **Temporal bone CT findings in the CHARGE association.** *Int J Pediatr Otorhinolaryngol* 1998;45:151–62 CrossRef Medline
11. Lemmerling M, Dhooge I, Mollet P, et al. **CT of the temporal bone in the CHARGE association.** *Neuroradiology* 1998;40:462–65 CrossRef Medline
12. Holcomb MA, Rumboldt Z, White DR. **Cochlear nerve deficiency in children with CHARGE syndrome.** *Laryngoscope* 2013;123:793–96 CrossRef Medline
13. Fujita K, Aida N, Asakura Y, et al. **Abnormal basiocciput development in CHARGE syndrome.** *AJNR Am J Neuroradiol* 2009;30:629–34 CrossRef Medline
14. Adunka OF, Roush PA, Teagle HF, et al. **Internal auditory canal morphology in children with cochlear nerve deficiency.** *Otol Neurotol* 2006;27:793–801 CrossRef Medline
15. Blustajn J, Kirsch CF, Panigrahy A, et al. **Olfactory anomalies in CHARGE syndrome: imaging findings of a potential major diagnostic criterion.** *AJNR Am J Neuroradiol* 2008;29:1266–69 CrossRef Medline
16. Romo LV, Casselman JW, Robson CD. **Temporal bone: congenital anomalies.** In: Som PM, Curtin HD, eds. *Head and Neck Imaging.* Vol 2. 4th ed. St Louis: Mosby; 2003:1119–40
17. Swartz JD, Loevner LA. **The inner ear and otodystrophies.** In: Swartz JD, Loevner LA, eds. *Imaging of the Temporal Bone*. 4th ed. New York: Thieme; 2009:298–411
18. Friedmann DR, Amoils M, Germiller JA, et al. **Venous malformations of the temporal bone are a common feature in CHARGE syndrome.** *Laryngoscope* 2012;122:895–900 CrossRef Medline
19. Lin AE, Siebert JR, Graham JM. **Central nervous system malforma-**

tions in the CHARGE association. *Am J Med Genet* 1990;37:304–10 CrossRef Medline
20. Byerly K, Pauli RM. **Cranial nerve abnormalities in CHARGE association.** *Am J Med Gen* 1993;45:751–57 CrossRef Medline
21. Wren MW. **Significance of the so-called J-shaped sella in the diagnosis of intracranial aneurysm.** *Br J Ophthal* 1969;53:307–09 CrossRef Medline
22. Parry DA, Booth T, Roland PS. **Advantages of magnetic resonance imaging over computed tomography in preoperative evaluation of pediatric cochlear implant candidates.** *Otol Neurotol* 2005;26: 976–82 CrossRef Medline
23. Pinto G, Abadie R, Mesnage R, et al. **CHARGE syndrome includes hypogonadotropic hypogonadism and abnormal olfactory bulb development.** *J Clin Endocrinol Metab* 2005;90:5621–26 CrossRef Medline
24. Dodé C, Hardelin JP. **Kallmann syndrome: fibroblast growth factor signaling insufficiency?** *J Mol Med (Berl)* 2004;82:725–34 CrossRef Medline
25. Smoker WR. **Craniovertebral junction: normal anatomy, craniometry, and congenital anomalies.** *Radiographics* 1994;14:255–77 CrossRef Medline
26. Martin P, Cushing H. **Primary gliomas of the chiasm and optic nerves in their intracranial portion.** *Arch Ophthal (NY)* 1923; 52:209–41
27. Zafeiriou DI, Batzios SP. **Brain and spinal MR imaging findings in mucopolysaccharidoses: a review.** *AJNR Am J Neuroradiol* 2013;34: 5–13 CrossRef Medline
28. McDonald FG, Mantas J, McEwen CG, et al. **Salivary gland aplasia: an ectodermal disorder?** *J Oral Pathol* 1986;15:115–17 CrossRef Medline
29. Higashino H, Horii T, Ohkusa Y, et al. **Congenital absence of lacrimal puncta and of all major salivary glands: case report and literature review.** *Clin Pediatr (Phila)* 1987;26:366–68 CrossRef Medline
30. Cohen M. **Mandibulofacial dysostosis.** In: Bergsma D, ed. *Birth Defect*. Baltimore: Williams and Wilkins; 1974:465–74
31. Hollister DW, Klein SH, De Jager HJ, et al. **The lacrimo-auriculo-dento-digital syndrome.** *J Pediatr* 1973;83:438–44 CrossRef Medline
32. Joshi VM, Navlekar SK, Kishore GR, et al. **CT and MR imaging of the inner ear and brain in children with congenital sensorineural hearing loss.** *Radiographics* 2012;32:683–98 CrossRef Medline
33. Nie X, Luukko K, Kettunen P. **FGF signalling in craniofacial development and developmental disorders.** *Oral Dis* 2006;12:102–11 CrossRef Medline
34. VanGilder JC, Menezes AH, Dolan KD. *The Craniovertebral Junction and Its Abnormalities.* Mount Kisco: Furuta; 1987:113–18

Quantitative Synthetic MRI in Children: Normative Intracranial Tissue Segmentation Values during Development

A. McAllister, J. Leach, H. West, B. Jones, B. Zhang, and S. Serai

ABSTRACT

BACKGROUND AND PURPOSE: Synthetic MR imaging is a new technique to create absolute R1 relaxivity (1/T1), R2 relaxivity (1/T2), and proton-density maps using a single multiple-spin-echo saturation recovery sequence. These relaxivity maps allow rapid automated intracranial segmentation of tissue types. To assess its utility in children, we created a normative data base of intracranial volume and brain parenchymal, GM, WM, CSF, and myelin volumes in a pediatric population with normal brain MRI findings using synthetic MR imaging.

MATERIALS AND METHODS: All multiple-spin-echo saturation recovery sequences containing brain MR imaging examinations performed during 34 months were retrospectively reviewed. Abnormal examination findings were excluded following a detailed radiographic and clinical chart review. The remaining normal examination findings were then quantitatively analyzed with synthetic MR imaging. Intracranial, brain parenchymal, GM, WM, CSF, and myelin volumes were plotted versus age. Qualitative assessment of segmentation accuracy was performed. Selected abnormal examination findings were compared with these normative curves.

RESULTS: One hundred twenty-two MRI examinations with normal findings were included of individuals ranging from 0.1 to 21.5 years of age (median, 11.8 years). Resulting normative data plots compared favorably with previously published data obtained using more onerous techniques. Differentiation from pathologic states was possible using quantitative values in select cases.

CONCLUSIONS: A pediatric data base of normal intracranial tissue volumes using a single sequence and rapid software analysis has been compiled and correlates with previously published data. This provides a framework for clinical interpretation of quantitative synthetic MR images during development. Improved age-based segmentation algorithms in young children are needed.

ABBREVIATIONS: BPF = brain parenchymal fraction; BPV = brain parenchymal volume; ICV = intracranial volume; MY = myelin; MYF = myelin fraction; PD = proton density; QMAP = quantitative map; R1 = 1/T1; R2 = 1/T2

Many complex subjective assessments are made when radiologists interpret imaging of the pediatric brain, including evaluation of brain parenchymal volume (BPV), morphology, CSF volume, and myelination extent, all in the context of the patient's age.[1] There is clinical interest in automated quantitative methods of segmenting intracranial tissues that allow longitudinal tracking and comparison against normative standards. Many segmentation methods have been described,[2] and multiple software packages are available, including FSL (http://www.fmrib.ox.ac.uk/fsl),[3] FreeSurfer (http://surfer.nmr.mgh.harvard.edu),[4] NeuroQuant (CorTech Labs, San Diego, California),[5] and NeuroReader (https://brainreader.net/),[6] but to date, there has been relatively limited impact on the clinical interpretation of pediatric neuroimaging studies.

Synthetic MRI is a quantitative MR imaging method in which a multiple-spin-echo saturation recovery sequence (QMAP sequence) is used with 4 saturation delays and 5 echoes to measure absolute R1 relaxivity (1/T1), R2 relaxivity (1/T2), and proton-density (PD) values.[7] Fully automated synthetic MR imaging visualization software loads the raw DICOM data, performs relaxivity curve fitting to the Bloch equations, and calculates whole-brain R1, R2, and PD maps used to synthesize MR images with standard contrast.[7-9] Additionally, the R1, R2, and PD maps are used as input to calculate an intracranial mask that determines the intracranial volume (ICV). A look-up table is used to convert R1, R2, and PD values of each voxel into tissue volume fractions with no atlas, manual tracing, or a priori assumptions of tissue distribution or anatomy.[10] Whole intracranial volumes of CSF, GM, WM, nonassignable tissues, and myelin (MY) are calculated by summing the partial volume fraction of each voxel within the

Received May 2, 2017; accepted after revision August 3.

From the Department of Radiology, Cincinnati Children's Hospital Medical Center, University of Cincinnati College of Medicine, Cincinnati, Ohio.

Please address correspondence to Aaron S. McAllister, MD, Department of Radiology, Nationwide Children's Hospital, 700 Children's Dr, Columbus, OH 43205; e-mail: Aaron.mcallister@nationwidechildrens.org


Indicates article with supplemental on-line photos.

http://dx.doi.org/10.3174/ajnr.A5398

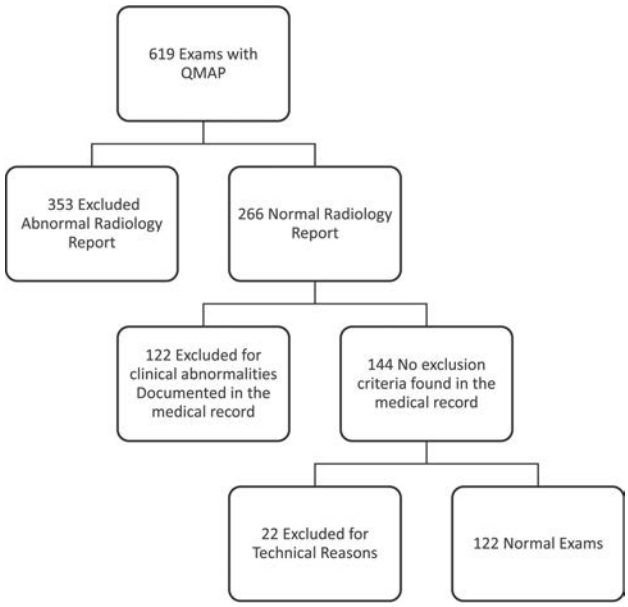

FIG 1. Examination evaluation path/exclusion diagram.

ICV.[10,11] The partial volume method accounts for voxels containing multiple tissue types and decreases dependence on the acquired resolution of the dataset.[12] A key advantage of this segmentation method is that unlike voxel intensity in standard MR images, R1, R2, and PD values are inherent physical properties of a given tissue/voxel at a given field strength and are otherwise independent of the acquisition strategy or hardware.[10]

To date, synthetic MR imaging–based segmentation has been primarily performed in adults.[10] There are a few published case reports demonstrating the value of synthetic MR imaging in pediatric brain imaging,[8,9,13,14] but widespread clinical utility of volumetrics requires the documentation of normative segmentation volumes during development. To address this need, we have created a normative data base of ICV, BPV, brain parenchymal fraction (BPF), GM, WM, CSF, MY, and myelin fraction (MYF) in a pediatric population with normal brain MRI findings using this methodology.

MATERIALS AND METHODS

An institutional review board–approved retrospective review was performed of all brain MR imaging examinations during a 34-month period in which the QMAP sequence was performed (619 examinations). The axial QMAP sequence (4-mm section thickness, 1-mm gap, matrix size of 320 × 256, acquisition time of 6 minutes) was included as an optional sequence (when time allowed) and has been described previously.[7-9] The algorithm for subject inclusion is shown in Fig 1. Studies with abnormal findings on clinical radiology reports were excluded. A systematic medical chart review was performed on the remaining 266 examinations to exclude those with clinical diagnoses or medications potentially affecting intracranial tissue volumes (Table 1). The remaining MR imaging examinations were reviewed by 1 of 3 board-certified pediatric neuroradiologists to identify any abnormalities not described on the clinical report.

The QMAP sequences on the remaining 144 studies were analyzed with SyMRI, Version 8 (Synthetic MR AB, Linköping, Sweden) with output of ICV, GM, WM, CSF, and MY. Descriptions of the segmentation method have been published previously.[10,11] BPV is calculated as the sum of GM, WM, and nonassignable tissues. BPF is BPV/ICV and MYF is MY/BPV.[10,11]

Table 1: Clinical and radiographic exclusion criteria

Exclusion Criteria
Identified pathology in the brain
Prior intracranial operation
Motion or susceptibility artifacts causing image distortion of SyMRI
Known developmental delay in language or motor domains requiring therapy
Autism spectrum disorder
Fixed neurologic deficit related to intracranial disease
Spasticity with cerebral cause requiring therapy
Chronic epilepsy
Significant prematurity (younger than 34 weeks' GA at delivery)
Significant macrocephaly (head circumference >97th percentile)
Significant microcephaly (head circumference <3rd percentile)
Hydrocephalus
Head trauma with extra-axial hemorrhage
Genetic disorder known to involve brain development
Systemic steroid therapy within 1 mo of examination

Note:—GA indicates gestational age.

Resultant segmentation maps were assessed for image quality, artifacts, errors in intracranial volume segmentation, and appropriate anatomic coverage. Twenty-two examinations were excluded from analysis because of image degradation caused by motion artifacts or insufficient coverage of the intracranial compartment. In a small number of cases (16), minor manual adjustments were made to the segmented intracranial contour. In 14 cases, extracranial tissues were included in the ICV (primarily the diploic space). Following adjustment, the average ICV decreased by only 6 mL (0.4%). The effect was largest on myelin volume, which decreased by 0.6%, and CSF, which decreased by 0.9%. In 2 cases, small portions of the occipital lobes were incorrectly excluded from the ICV. Following adjustment, the ICV increased by 15 mL (1%), with corresponding increases in GM and WM of 1%.

The adequacy of segmentation was assessed in all subjects (n = 26) younger than 4 years of age (relative to that expected by visual assessment of the anatomic images) with the following scoring system for GM/WM segmentation: 1, all WM was labeled as GM; 2, marked mislabeling of WM as GM though correct in the central WM tracts; 3, clear extension of GM labeling into the WM; 4, overall correctly labeled, with mislabeling of subcortical WM in the frontal and/or temporal lobes; and 5, correctly labeled. The fractional assignment of brain to the CSF compartment was assessed as follows: 1, large confluent areas of parenchyma incorrectly classified as CSF; 2, small noncontiguous areas of parenchyma incorrectly classified as CSF; and 3, no parenchyma incorrectly classified as CSF.

Of the 122 final examinations, 60 were performed at 3T and 62 were performed at 1.5T. All 3T examinations were performed on a Discovery MR750w scanner (GE Healthcare, Milwaukee, Wisconsin). Of those performed at 1.5T, 51 were performed on an Optima MR450w (GE Healthcare) and 11 were performed on an Ingenia scanner (Philips Healthcare, Best, the Netherlands). All examinations on children younger than 6 years of age were performed at 3T. Data plotting, curve fitting, and confidence interval

calculation was performed with SAS, Version 9.4 (SAS Institute, Cary, North Caroline) and Matlab 2016b (MathWorks, Natick, Massachusetts) using the cftool function in Matlab. For each tissue type, data were plotted versus patient age. Curve fits and 95% confidence intervals were calculated and superimposed on the respective scatterplots. For BPV, BPF, ICV, WM, CSF, MY, and MYF, the data were fit to a double exponential curve $y = a \times \exp(b \times x) + c \times \exp(d \times x)$. GM data were fit to a double exponential equation modified with a linear term $y = a \times \exp(b \times x) + c \times \exp(d \times x) + f \times x + g$. Additional plots for MY and MYF were made with a subset of data limited to subjects 0–18 months of age, the period of most rapid myelination. Curve fits were performed to the equation $y = m \times x + b$.

RESULTS

The included 122 subjects ranged in age from 0.1 to 21.5 years (median, 11.8 years), with 49 males and 73 females. Clinical indications for the examinations are given in Table 2.

Table 2: Clinical indications for included MRI examinations

Indication for Brain MRI	No.
Headaches	69
Seizure (suspected or first-time seizure)	10
Suspected brain lesion	8
Dizziness, vertigo, or vomiting	7
Neurologic findings	7
Concussion	4
Other	17

Representative automated segmentation images for patients 0.1, 0.4, 0.8, 1.2, 2.5, 7, and 15 years of age are shown in Fig 2. Resultant normative curves for ICV, BPV, GM, WM, CSF, MY, and MYF are given in Fig 3. MY and MYF for subjects 0–18 months of age are given in Fig 4.

ICV increased rapidly from 0 to 18 months, with progressive slowing, reaching a plateau in early adolescence with an ICV of approximately 1400 mL. A similar rapid growth and plateau are seen with BPV, reaching a plateau of 1300 mL in early adolescence. BPF rises rapidly in infancy and early childhood to a peak of 0.96 at 45 months, followed by a gradual linear decline in late childhood and adolescence, reaching a value of 0.92 at 18 years of age.

Values of intracranial CSF volume demonstrated a gradual increase throughout childhood and adolescence from a value of approximately 50 mL in neonates and infants to a mean value of approximately 100 mL, with a range of 50–150 mL in the late teenage and young adult period.

GM volume increases rapidly during the first 18 months of life, with subsequent slowing of the growth rate. A maximum GM volume of 920 mL was reached at 6–7 years of age, followed by a gradual decline throughout the teenage years to a value of 790 at 18 years of age.

WM demonstrates rapid linear growth during the first 18 months with subsequent slowing of the growth rate through childhood and adolescence, with continued increases throughout the age range of the study population. No maximum was reached.

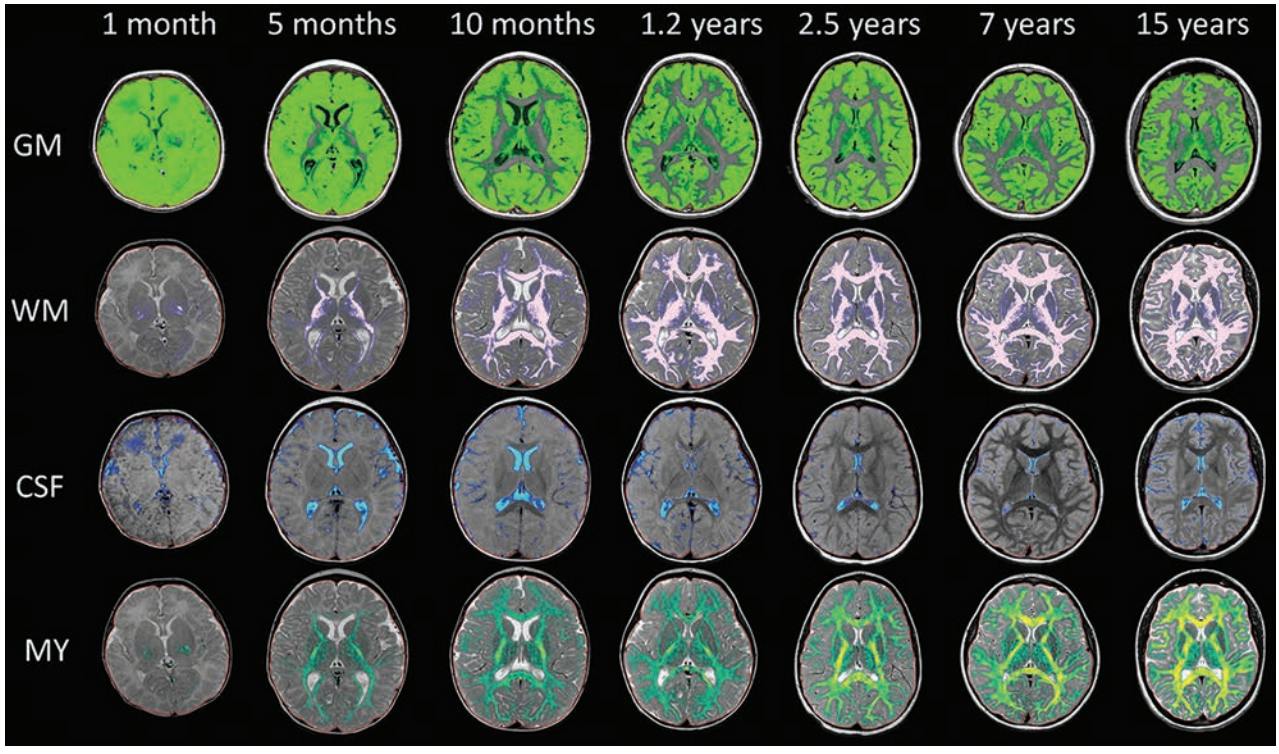

FIG 2. Representative segmentation images. Age is organized in columns increasing from *left* to *right*: 1 month, 5 months, 10 months, 1.2 years, 2.5 years, 7 years, and 15 years of age. Tissue types are arranged in *upper-to-lower rows*: GM, WM, CSF, and MY. The *faint red line* denotes the boundary of the intracranial mask. Note the suboptimal GM/WM segmentation in young children (*upper 2 rows*). At 0.1 year, there is complete assignment of WM as GM (*upper left image*); at 0.4 year, there is mislabeling with correct assignment of the internal capsule and centrum semiovale (not shown). At 0.8 year, some peripheral WM is assigned as GM. At 1.2 years, there is overall good segmentation with areas of mislabeling in the frontal and temporal lobes. By 2.5 years and beyond, GM and WM are correctly segmented. Note the assignment of parenchymal voxels as CSF in the youngest children (*first column, third row*).

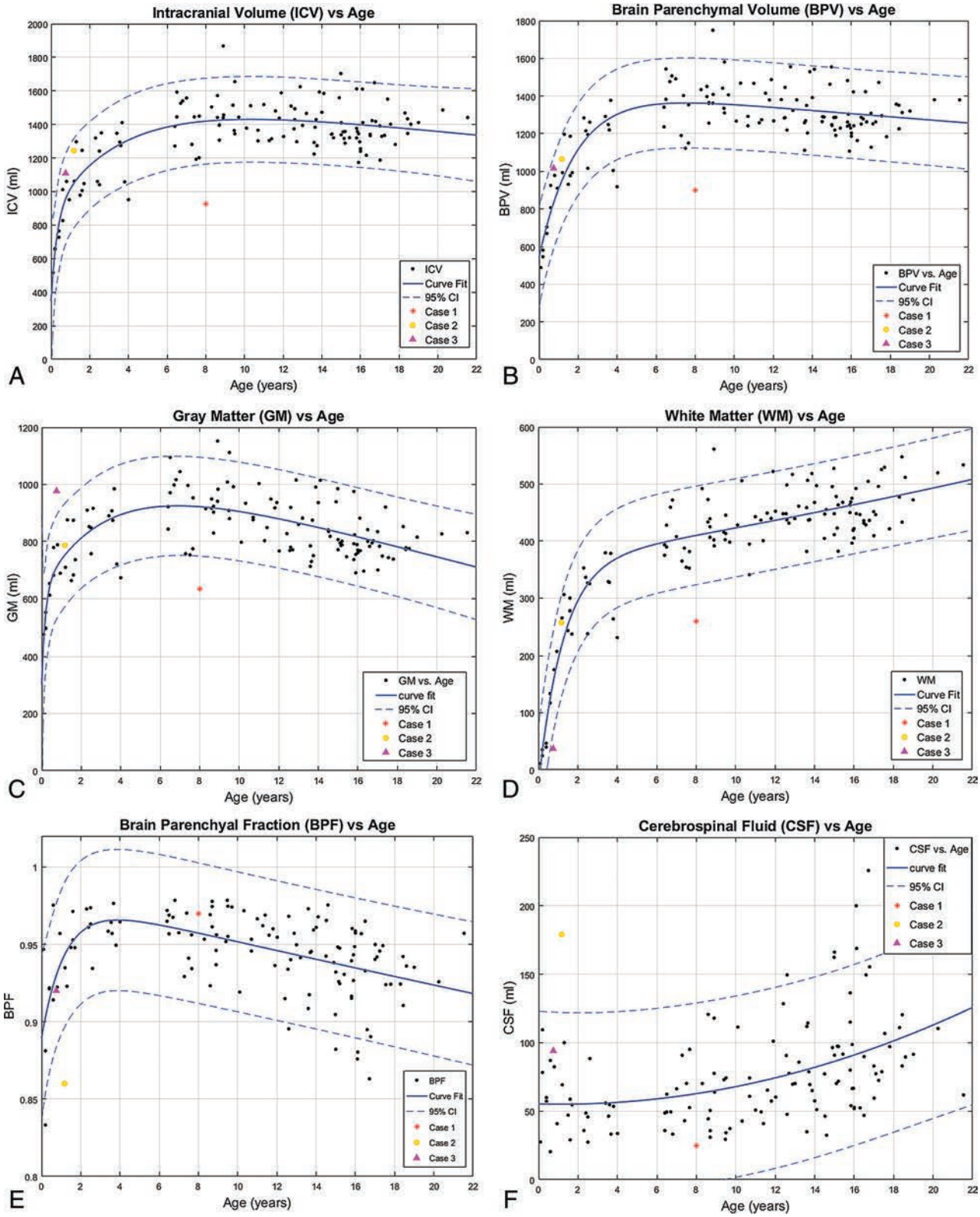

FIG 3. Segmentation volume plots versus patient age. *A*, ICV. *B*, BPV. *C*, GM. *D*, WM. *E*, BPF. *F*, CSF. *G*, MY. *H*, MYF. *Solid lines* denote curve fit functions. *Dashed lines* denote 95% confidence intervals. Data points for the 122 healthy patients are denoted by *black dots*. Three illustrative cases with abnormal exams are superimposed on the normal plots. Case 1 is a *purple triangle,* Case 2 is an orange *circle*, and unhealthy Case 3 is a *red asterisk*. (Normal plots without the superimposed cases can be found in the On-line Figs 1 and 2).

MY and MYF demonstrate rapid linear growth during the first 18 months of age, with a gradually decreasing rate of growth throughout childhood and further decreased-but-persistent growth through adolescence. To better assess the rapid early growth phase, we plotted a subset of the data limited to subjects 0–18 months of age demonstrating rapid linear growth (Fig 4). As

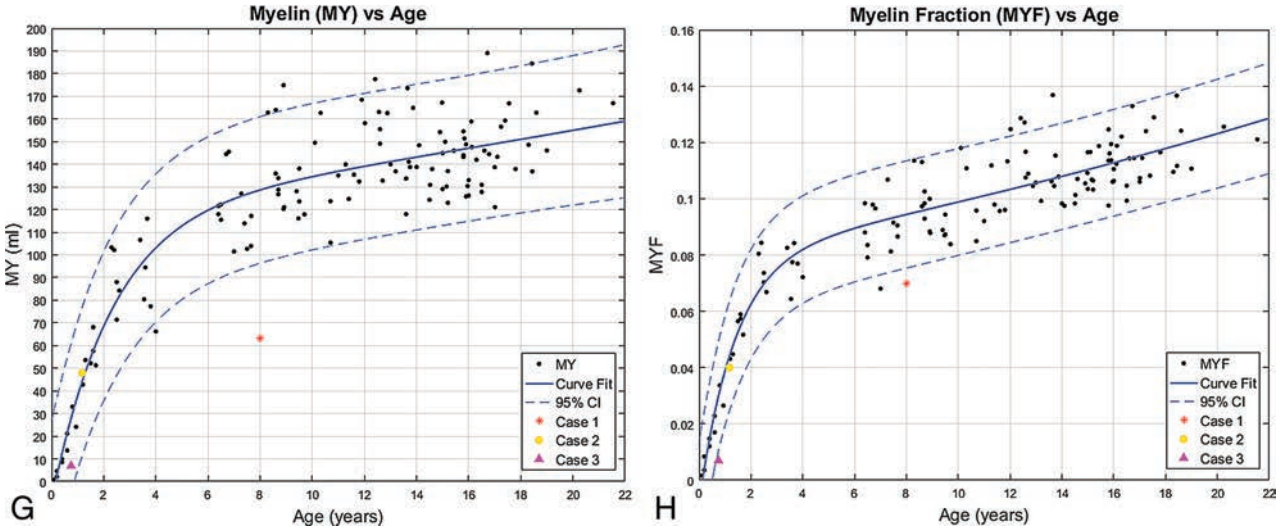

FIG 3. Continued.

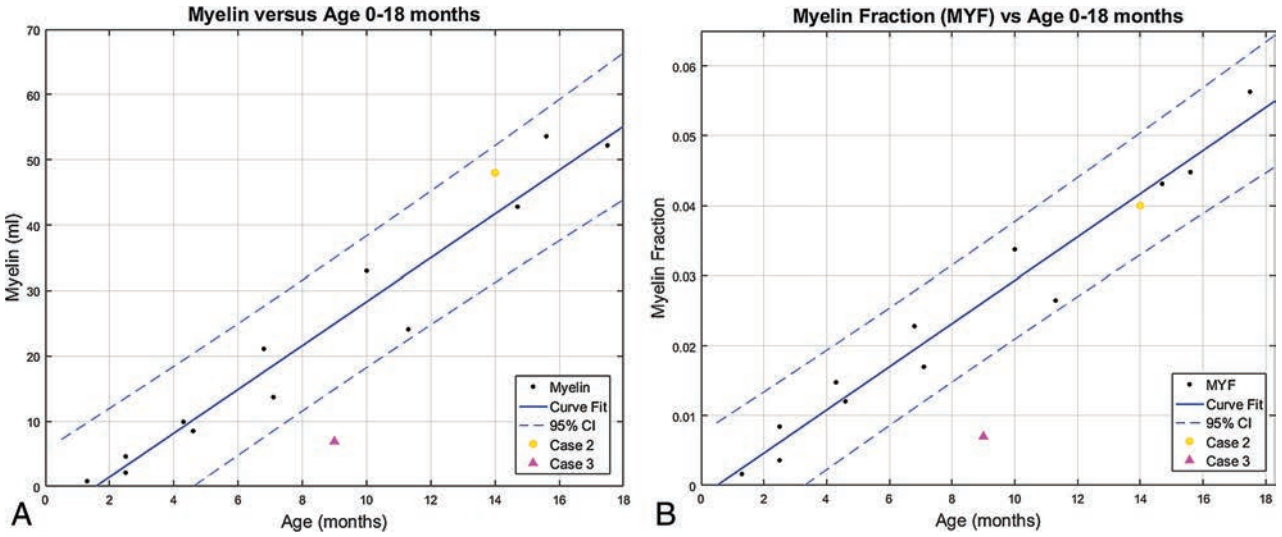

FIG 4. Segmentation volume plots versus patient age from 0 to 18 months. *A*, Myelin volume versus age. *B*, Myelin fraction versus age. Data points for the 12 healthy patients 0–18 months of age are denoted by *black dots*. Two illustrative cases with abnormal exams are superimposed on the normal plots. Case 1 is a *purple triangle*, and Case 2 is an *orange circle*. (Normal plots without the superimposed cases can be found in the On-line Figs 1 and 2). *Solid lines* denote curve fit functions. *Dashed lines* denote 95% confidence intervals.

expected, the limited dataset has narrower confidence intervals for the 0- to 18-month age range than the full dataset.

Qualitative assessment of the accuracy of segmentation demonstrated improved segmentation of CSF, GM, and WM with increasing subject age up to 18 months of age (Fig 5).

To provide an initial assessment of the potential clinical applications of the automated segmentation process and normative curves, we evaluated selected studies with abnormal findings and compared segmentation volumes with the normative values (Figs 6–8).

DISCUSSION

To the best of our knowledge, this is the first study to evaluate normative quantitative segmentation of intracranial tissue types in children using the SyMRI technique. Understanding the normal developmental trajectories and limitations of these analyses is critical for eventual clinical use. Assessment of intracranial tissue volumes is a key component of interpretation of brain imaging studies, but currently, this is almost exclusively subjective and qualitative in clinical practice. Readily obtained linear measurements of complex volumes like the ventricular system have been shown to be representative of absolute volumes,[15] but the degree of correlation is limited. Moreover, such subjective analyses do not lend themselves to accurate assessment of changes with time or to meaningful population comparisons. The ability to quantify the volumes of intracranial CSF and parenchyma in a patient during multiple time points or in comparison with a healthy population will increase the accuracy and value of the imaging analysis and will likely lead to greater insight into the evolution of multiple pathologic processes.

Obtaining quantitative data in our subjects with synthetic MR imaging was rapid and easily translatable to clinical practice. The QMAP sequence requires <6 minutes to acquire, and the segmentation with synthetic MR imaging is automated and provides

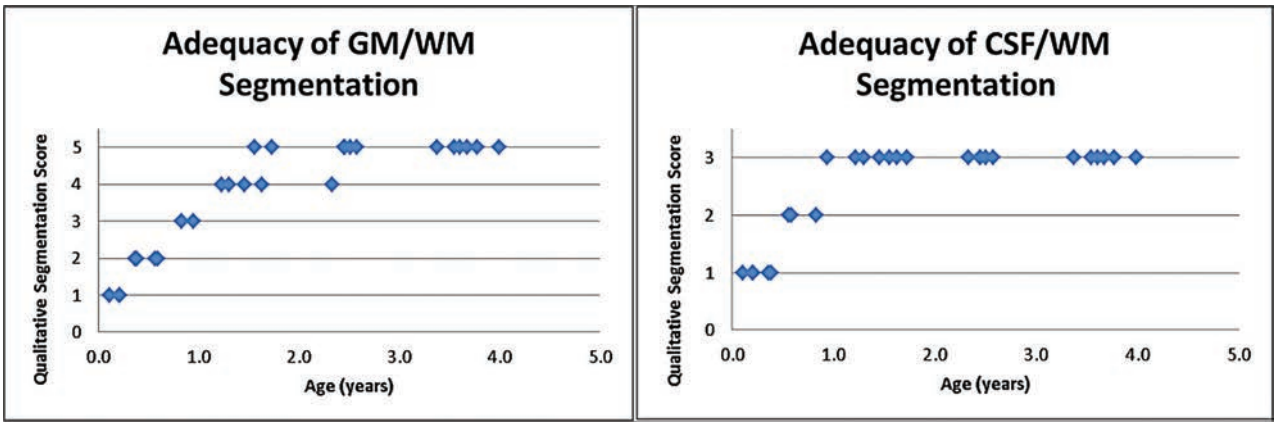

FIG 5. Adequacy of segmentation. Qualitative segmentation scores versus patient age. GM/WM segmentation (*left*) and CSF/WM segmentation (*right*). In subjects younger than 3 months of age, most anatomic WM was labeled as GM with a qualitative score of 1. In subjects between 3 and 7 months of age, there was moderate mislabeling of WM as GM, but WM tracts in the centrum semiovale and internal capsule were correctly labeled with a qualitative score of 2. From 8 to 11 months, there was less prominent-but-definite extension of GM labeling into WM with a score of 3. From 12 to 18 months of age, there was minor mislabeling of subcortical WM in the frontal and/or temporal lobes with otherwise excellent segmentation, with a qualitative score of 4. The WM was correctly labeled in children older than 18 months of age with a qualitative score of 5. Subjects younger than 5 months of age had large confluent areas of parenchyma and unmyelinated WM, which were labeled fractionally as CSF (score of 1). Subjects between 5 and 10 months of age had small noncontiguous areas, primarily in the subcortical white matter, which were fractionally labeled as CSF (score of 2). No parenchyma was designated as CSF in subjects older than 10 months of age (score of 3).

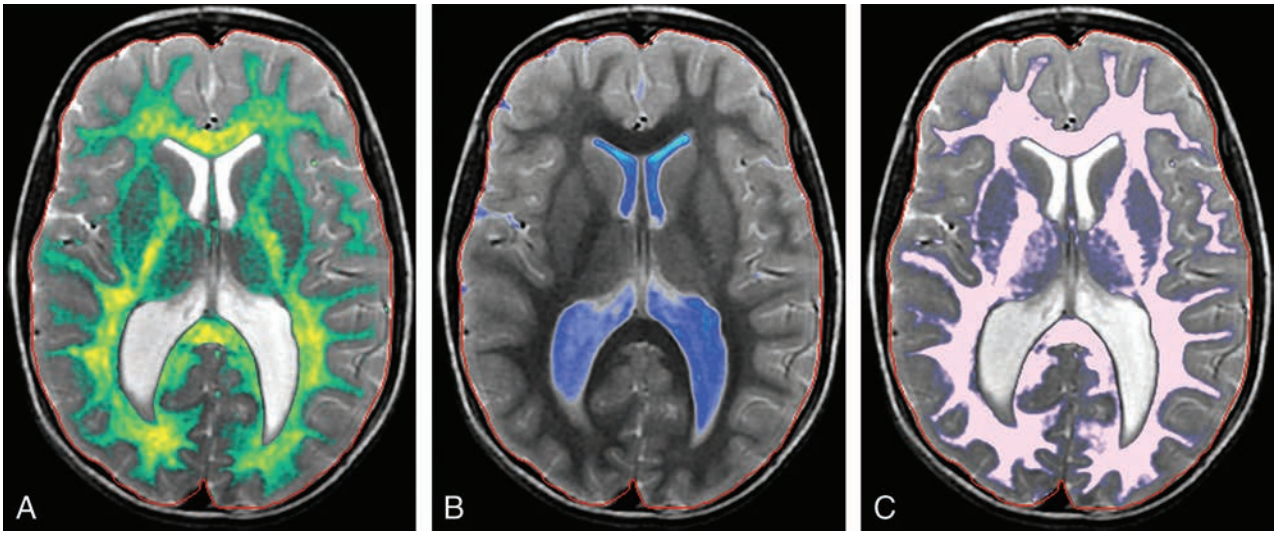

FIG 6. Case 1. *A*, Myelin. *B*, CSF. *C*, WM. An 8-year-old girl with a history of trisomy 21 and microcephaly. Volumetric data are superimposed on the normal plots such as the red asterisk on Fig 3. The ICV (925 mL), BPV (900 mL), GM (634 mL), WM (259 mL), myelin (63 mL), and MYF (0.07) are abnormal and plot below the 95% CI. The CSF (25 mL) and BPF (0.97) are normal. Consistent with microcephaly, the ICV and BPV are small. The BPF is normal; this finding indicates that the brain is proportional to the intracranial compartment. A low myelin volume would be expected with a small BPV; however, the MYF is also low. This finding indicates abnormal myelination, which has been described in patients with Down syndrome.[32-34]

quantitative maps, volumetric segmentation, and anatomic datasets with standard MR imaging contrasts (T1, T2, FLAIR, and so forth) in <1 minute on a standard workstation and a timeframe and format optimized for clinical use, allowing concurrent analysis of quantitative and anatomic data.[7-9]

Useful as they are, the descriptive terms "gray matter" and "white matter" can be misleading when used to describe the brain parenchyma. These descriptions of the various compartments of the brain, based on gross anatomic observation, imply that there is little or no contamination of either tissue type by the other, but we know that axons and myelin exist within gray matter structures, and neurons are present in white matter. Additionally, in the immature brain, the absence of myelin on many of the axons requires recognition of unmyelinated axons and those acquiring myelin.

The R1, R2, and PD characteristics of WM change considerably as myelination progresses. In young children, the WM has low R1 and R2 values secondary to the large water content, but as the tissue myelinates, the water is expressed and myelin is deposited, lengthening R1 and R2. The SyMRI technique segments WM and myelin and calculates myelin fraction.[11] WM reflects the total volume of myelinated axons, myelin represents the total volume of myelin (excluding axons, extracellular water, and other material that is not myelin), and myelin fraction represents the fraction

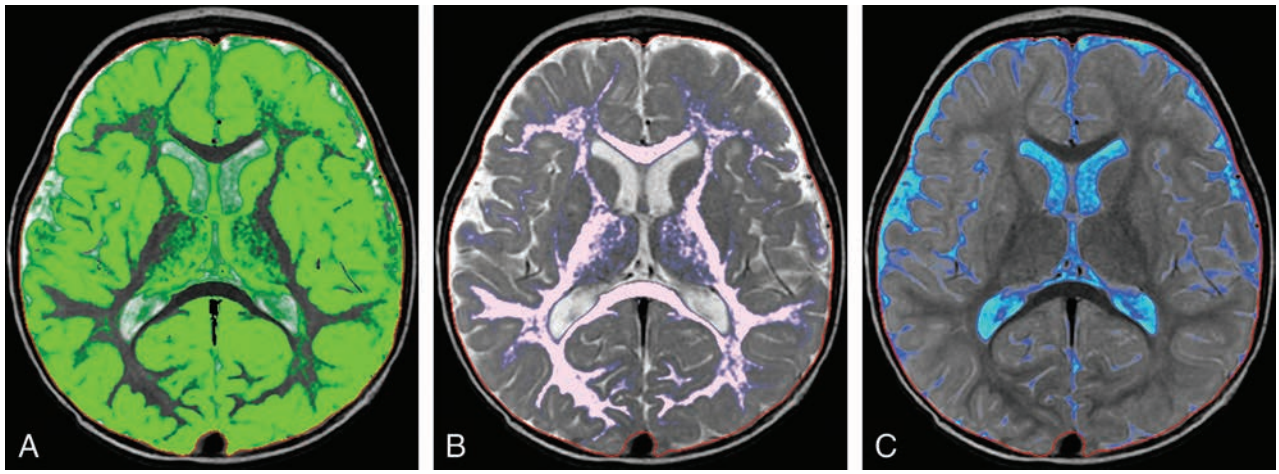

FIG 7. Case 2. A 14-month-old boy with a history of increased head circumference and developmental delay. *A*, GM. *B*, WM. *C*, CSF. Volumetric data are superimposed on the normal plots such as the orange circle Fig 3 and on the 0- to 18-month curves in Fig 4. The ICV (1244 mL), BPV (1065 mL), GM (787 mL), WM (257 mL), MY (48 mL), and MYF (0.04) are normal for age; however, the CSF (179 mL) is above the 95% CI for age. The BPF (0.86) is below the 95% CI for age. Despite the enlarged head circumference, the ICV is at the upper range of normal. The normal BPV, GM, WM, and MY are reassuring. The CSF volume is higher than that of age-matched peers, seen with benign macrocrania, but the developmental delay is concerning and this patient will be followed.

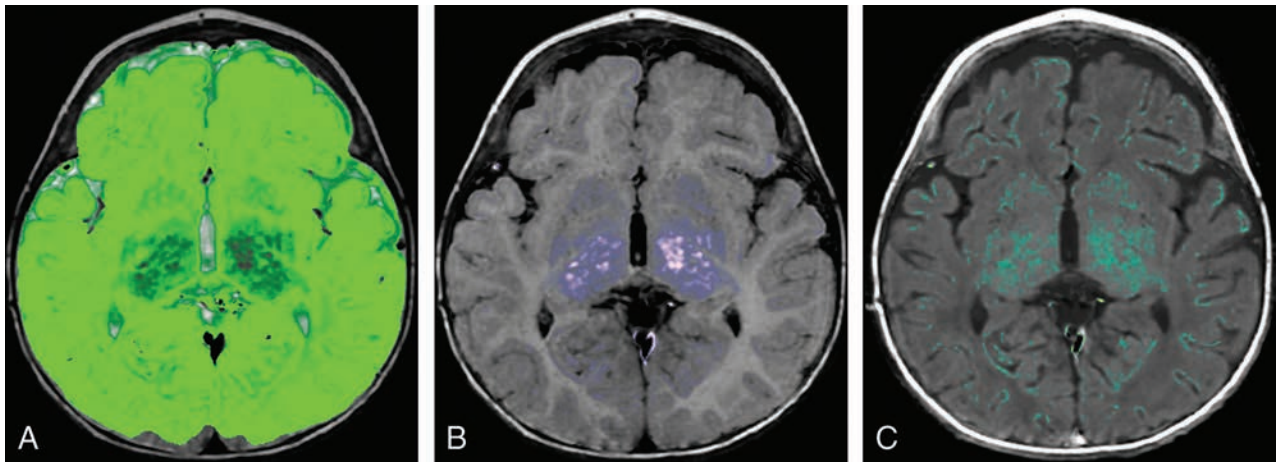

FIG 8. Case 3. A 9-month-old boy with a known history of Pelizaeus-Merzbacher disease. *A*, GM. *B*, WM. *C*, Myelin. Volumetric data are superimposed on the normal plots like the purple triangle Fig 3 and on the 0- to 18-month-old curves in Fig 4. The ICV (1109 mL), BPV (1016 mL), BPF (0.92), and CSF (94 mL) are normal. The brain parenchyma was almost exclusively segmented as GM (971 mL), higher than the 95% CI, with only a small component of WM (37 mL) lower than the 95% CI. The myelin volume (7 mL) and MYF (0.007) are both below the 95% CI for age as expected for a patient with Pelizaeus-Merzbacher disease, a primary hypomyelination disease.[35]

of the brain that is myelin.[11] The MY and MYF curves are similar to those produced by Dean et al[16] using different techniques, supporting the validity of the SyMRI myelin segmentation in children. A relative reduction in myelin or myelin fraction may provide the earliest indication of disruption of the myelination process. In cases of parenchymal volume loss, though the volumes of both WM and myelin will be lower than normal, myelin fraction can inform whether the parenchyma that is present is normally myelinated.

The present methodology is sensitive to the presence of myelinated axons and those in the early stages of acquiring myelination, but it has difficulty in accurately segregating unmyelinated axons from GM (Fig 5). In R1–R2 space, the unmyelinated and myelinated WM flank GM on opposite sides. As unmyelinated WM myelinates, it passes immediately adjacent to GM with overlap, making separation difficult. Similar WM/GM segmentation difficulties in children using other techniques have been reported previously.[2,17,18] Therefore, visual review of the segmentation in subjects younger than 18 months of age shows that the GM compartment contains large areas of what we know to be unmyelinated axons (Fig 2). GM is therefore overestimated in subjects younger than 18 months of age, while WM is underestimated. This error in estimation results in an artificially shallow growth rate of GM through the first 18 months of life and an artificially steep growth rate of WM. An article limited to neonates up to 2 months of age demonstrated substantially lower GM volumes than in our youngest patients.[19] However, despite this overestimation, the curves of GM volume across time parallel those generated by previously published pediatric studies, even in the 0- to 5-year age range.[17,20-24] This similarity suggests that either these other techniques have a similar error, young subjects were underrepresented in the samples, or the inclusion of

unmyelinated axons during the first 18 months of development does not substantially skew the pattern of GM growth. Our data demonstrated the maximum GM volume occurring at 6 years of age, which is later than the 4 years reported in prior articles.[22,23] The GM/WM segmentation error does not render the data clinically useless. If the algorithm is consistent and the clinical case is compared with healthy cases segmented with the same algorithm, the patient's location on the nomogram and growth trajectory can provide useful clinical information.

The readily available quantification of the CSF compartment and the ability to generate ratios of CSF to BPV may allow a more accurate and translatable assessment of hydrocephalus and other pathologies of CSF homeostasis. Tracking these volumes across time in individual patients may allow a more sensitive and meaningful understanding of the effectiveness of CSF diversion strategies, as will comparison of values with a healthy population data base, such as that presently done with head circumference measurements. It is reasonable to think that such ready quantification may increase the sensitivity and accuracy of the diagnosis of more pervasive disorders of CSF volume and intracranial pressure. One could assume that future software iterations will segment intraventricular CSF as a separate compartment, an additional valuable data source in these patients.

In our youngest subjects, we identified regions of the parenchyma partially assigned to the CSF compartment (Fig 2). This misclassification is most evident in subjects younger than 5 months of age and is secondary to the fractional volume assignment of each pixel and the relative high water content of the infant brain. The degree to which this misclassification alters the assessment in an individual case is unclear, given the wide range of normal CSF volumes, but it does suggest that intracranial CSF is mildly overestimated in very young children.

Many diseases result in focal parenchymal abnormalities and would not be detected by whole-brain volumetric analysis. This technique will be most advantageous in the assessment of diffuse disease processes. Current tools for clinically assessing brain size are crude, consisting of head circumference and cranial facial ratios. These do not distinguish a large/thick calvaria and scalp from a large ICV and a large CSF volume from a large BPV. Comparison of tissue volumes using synthetic MR imaging can easily and rapidly make these distinctions. Furthermore, quantitative longitudinal tracking is also readily accomplished.

During our secondary review, in 16 subjects, the radiologist thought that the intracranial contour should be adjusted to accurately reflect the ICV. The normative curves were created by using manually corrected data for these subjects. Correcting the intracranial contour is easy to accomplish, but it is a nuisance when interpreting examinations clinically. The resulting changes in the observed volumes were $<1\%$, which we think is clinically insignificant and within the range of variability reported by other segmentation algorithms[25] and small in comparison with the width of the current confidence bands. Therefore, adjustment during clinical practice will rarely be necessary and only in borderline cases.

Synthetic MR imaging is a relatively new method of image acquisition and analysis and will continue to undergo modification as the technique matures. Segmentation algorithms and tissue look-up tables may be improved with future releases, with slightly different volumetric results for a given dataset. Therefore, the subject being clinically assessed should be analyzed with the same software version used to create the nomograms.

There are some limitations to the present study. As opposed to categoric voxel assignment, synthetic MR imaging segmentation uses a partial volume tissue model, which reduces the partial volume errors introduced by low-resolution images and accounts for the complex anatomy and heterogeneity of intracranial tissues.[10,26,27] As a result, although our resolution is lower than that in other segmentation techniques, the resultant volumetric nomogram curves are very like those that have been published previously.[22]

This data base was compiled from a retrospective review of clinical examinations. The patients in this data base had symptoms warranting neuroimaging, and in that context, they were not completely healthy; however, the exclusion process was extensive. We understand the advantages of developing nomograms using clinically healthy subjects; however, there are challenges. Most notably, the required sedation of healthy pediatric subjects is ethically dubious; subsequently, few articles have data in the 1- to 4-year age group.[28] Several articles included patients in the perinatal period,[19,29] a time when subjects do not require sedation, while others have used a mixed subject pool with 3-month to 2-year-old patients and healthy volunteers for the older age groups.[22]

Although respectable, our sample size of 122 subjects is small in comparison with the sample sizes that number in the thousands used for the development of the CDC growth charts.[30] Larger sample sizes are desirable to define percentiles with appropriate precision for each age group, most important for the outlying percentiles.[31] Larger sample sizes will also allow detailed sex-specific nomograms.

The use of SyMRI segmentation is promising for routine clinical use; however, there is need for further study. Improved segmentation algorithms are needed for patients younger than 18 months of age. The sensitivity and specificity to identify abnormalities using this method need to be determined, and a larger dataset of healthy patients would be of benefit.

CONCLUSIONS

We present the implementation of rapid segmentation of intracranial content using synthetic MR imaging in children. The compiled pediatric data base of normal intracranial tissue volumes using this technique correlates with previously published data and may provide a framework for more quantitative clinical interpretation of MR images during development. Improved age-based segmentation algorithms in young children are needed.

Disclosures: Blaise Jones—*RELATED*: *Support for Travel to Meetings for the Study or Other Purposes*: SyMRI, *Comments*: They reimbursed me for travel expenses to Maryland to describe my experience with the software to the FDA.

REFERENCES

1. Barkovich AJ, Kjos BO, Jackson DE Jr, et al. **Normal maturation of the neonatal and infant brain: MR imaging at 1.5 T.** *Radiology* 1988; 166:173–80 CrossRef Medline
2. Despotović I, Goossens B, Philips W. **MRI segmentation of the hu-**

man brain: challenges, methods, and applications. *Comput Math Methods Med* 2015;2015:450341 CrossRef Medline
3. Jenkinson M, Beckmann CF, Behrens TE, et al. **FSL.** *Neuroimage* 2012;62:782–90 CrossRef Medline
4. Fischl B. **FreeSurfer**. *Neuroimage* 2012;62:774–81 CrossRef Medline
5. Brewer JB. **Fully-automated volumetric MRI with normative ranges: translation to clinical practice.** *Behav Neurol* 2009;21:21–28 CrossRef Medline
6. Ahdidan J, Raji CA, DeYoe EA, et al. **Quantitative neuroimaging software for clinical assessment of hippocampal volumes on MR imaging.** *J Alzheimers Dis* 2016;49:723–32 CrossRef Medline
7. Warntjes JB, Leinhard OD, West J, et al. **Rapid magnetic resonance quantification on the brain: optimization for clinical usage.** *Magn Reson Med* 2008;60:320–29 CrossRef Medline
8. Betts AM, Leach JL, Jones BV, et al. **Brain imaging with synthetic MR in children: clinical quality assessment.** *Neuroradiology* 2016;58: 1017–26 CrossRef Medline
9. West H, Leach JL, Jones BV, et al. **Clinical validation of synthetic brain MRI in children: initial experience.** *Neuroradiology* 2017;59: 43–50 CrossRef Medline
10. West J, Warntjes JB, Lundberg P. **Novel whole brain segmentation and volume estimation using quantitative MRI.** *Eur Radiol* 2012;22: 998–1007 CrossRef Medline
11. Warntjes M, Engström M, Tisell A, et al. **Modeling the presence of myelin and edema in the brain based on multi-parametric quantitative MRI.** *Front Neurol* 2016;7:16 CrossRef Medline
12. Van Leemput K, Maes F, Vandermeulen D, et al. **A unifying framework for partial volume segmentation of brain MR images.** *IEEE Trans Med Imaging* 2003;22:105–19 CrossRef Medline
13. Andica C, Hagiwara A, Nakazawa M, et al. **The advantage of synthetic MRI for the visualization of early white matter change in an infant with Sturge-Weber syndrome.** *Magn Reson Med Sci* 2016;15: 347–48 CrossRef Medline
14. Andica C, Hagiwara A, Nakazawa M, et al. **Synthetic MR imaging in the diagnosis of bacterial meningitis.** *Magn Reson Med Sci* 2017;16: 91–92 CrossRef Medline
15. Ragan DK, Cerqua J, Nash T, et al. **The accuracy of linear indices of ventricular volume in pediatric hydrocephalus: technical note.** *J Neurosurg Pediatr* 2015;15:547–51 CrossRef Medline
16. Dean DC 3rd, O'Muircheartaigh J, Dirks H, et al. **Characterizing longitudinal white matter development during early childhood.** *Brain Struct Funct* 2015;220:1921–33 CrossRef Medline
17. Wilke M, Krägeloh-Mann I, Holland SK. **Global and local development of gray and white matter volume in normal children and adolescents.** *Exp Brain Res* 2007;178:296–307 CrossRef Medline
18. Wilke M, Schmithorst VJ, Holland SK. **Normative pediatric brain data for spatial normalization and segmentation differs from standard adult data.** *Magn Reson Med* 2003;50:749–57 CrossRef Medline
19. Gilmore JH, Lin W, Prastawa MW, et al. **Regional gray matter growth, sexual dimorphism, and cerebral asymmetry in the neonatal brain.** *J Neurosci* 2007;27:1255–60 CrossRef Medline
20. Jernigan TL, Tallal P. **Late childhood changes in brain morphology observable with MRI.** *Dev Med Child Neurol* 1990;32:379–85 Medline
21. Jernigan TL, Trauner DA, Hesselink JR, et al. **Maturation of human cerebrum observed in vivo during adolescence.** *Brain* 1991;114(pt 5): 2037–49 CrossRef Medline
22. Groeschel S, Vollmer B, King MD, et al. **Developmental changes in cerebral grey and white matter volume from infancy to adulthood.** *Int J Dev Neurosci* 2010;28:481–89 CrossRef Medline
23. Pfefferbaum A, Mathalon DH, Sullivan EV, et al. **A quantitative magnetic resonance imaging study of changes in brain morphology from infancy to late adulthood.** *Arch Neurol* 1994;51:874–87 CrossRef Medline
24. Reiss AL, Abrams MT, Singer HS, et al. **Brain development, gender and IQ in children: a volumetric imaging study.** *Brain* 1996;119(pt 5): 1763–74 CrossRef Medline
25. Courchesne E, Chisum HJ, Townsend J, et al. **Normal brain development and aging: quantitative analysis at in vivo MR imaging in healthy volunteers.** *Radiology* 2000;216:672–82 CrossRef Medline
26. Shattuck DW, Sandor-Leahy SR, Schaper KA, et al. **Magnetic resonance image tissue classification using a partial volume model.** *Neuroimage* 2001;13:856–76 Medline
27. Bonar DC, Schaper KA, Anderson JR, et al. **Graphical analysis of MR feature space for measurement of CSF, gray-matter, and white-matter volumes.** *J Comput Assist Tomogr* 1993;17:461–70 CrossRef Medline
28. Zhang L, Thomas KM, Davidson MC, et al. **MR quantitation of volume and diffusion changes in the developing brain.** *AJNR Am J Neuroradiol* 2005;26:45–49 Medline
29. Hüppi PS, Warfield S, Kikinis R, et al. **Quantitative magnetic resonance imaging of brain development in premature and mature newborns.** *Ann Neurol* 1998;43:224–35 CrossRef Medline
30. Kuczmarski RJ, Ogden CL, Guo SS, et al. **CDC Growth Charts for the United States: methods and development.** *Vital Health Stat 1* 2002: 1–190 Medline
31. Guo SS, Roche AF, Chumlea WC, et al. **Statistical effects of varying sample sizes on the precision of percentile estimates.** *Am J Hum Biol* 2000;12:64–74 Medline
32. Olmos-Serrano JL, Kang HJ, Tyler WA, et al. **Down syndrome developmental brain transcriptome reveals defective oligodendrocyte differentiation and myelination.** *Neuron* 2016;89:1208–22 CrossRef Medline
33. Becker L, Mito T, Takashima S, et al. **Growth and development of the brain in Down syndrome.** *Prog Clin Biol Res* 1991;373:133–52 Medline
34. Wisniewski KE, Schmidt-Sidor B. **Postnatal delay of myelin formation in brains from Down syndrome infants and children.** *Clin Neuropathol* 1989;8:55–62 Medline
35. Boespflug-Tanguy O. **Inborn errors of brain myelin formation.** *Handb Clin Neurol* 2013;113:1581–92 CrossRef Medline

Gestational Age at Birth and Brain White Matter Development in Term-Born Infants and Children

X. Ou, C.M. Glasier, R.H. Ramakrishnaiah, A. Kanfi, A.C. Rowell, R.T. Pivik, A. Andres, M.A. Cleves, and T.M. Badger

ABSTRACT

BACKGROUND AND PURPOSE: Studies on infants and children born preterm have shown that adequate gestational length is critical for brain white matter development. Less is known regarding how variations in gestational age at birth in term infants and children affect white matter development, which was evaluated in this study.

MATERIALS AND METHODS: Using DTI tract-based spatial statistics methods, we evaluated white matter microstructures in 2 groups of term-born (≥37 weeks of gestation) healthy subjects: 2-week-old infants ($n = 44$) and 8-year-old children ($n = 63$). DTI parameters including fractional anisotropy, mean diffusivity, axial diffusivity, and radial diffusivity were calculated by voxelwise and ROI methods and were correlated with gestational age at birth, with potential confounding factors such as postnatal age and sex controlled.

RESULTS: Fractional anisotropy values, which are markers for white matter microstructural integrity, positively correlated ($P < .05$, corrected) with gestational age at birth in most major white matter tracts/regions for the term infants. Mean diffusivity values, which are measures of water diffusivities in the brain, and axial and radial diffusivity values, which are markers for axonal growth and myelination, respectively, negatively correlated ($P < .05$, corrected) with gestational age at birth in all major white matter tracts/regions excluding the body and splenium of the corpus callosum for the term infants. No significant correlations with gestational age were observed for any tracts/regions for the term-born 8-year-old children.

CONCLUSIONS: Our results indicate that longer gestation during the normal term period is associated with significantly greater infant white matter development (as reflected by higher fractional anisotropy and lower mean diffusivity, axial diffusivity, and radial diffusivity values); however, similar associations were not observable in later childhood.

ABBREVIATIONS: AD = axial diffusivty; FA = fractional anisotropy; MD = mean diffusivity; RD = radial diffusivity

It is well known that infants born with low gestational age (preterm, <37 completed weeks of gestation) are relatively more vulnerable to brain white matter injury or abnormal white matter development. White matter damage in extremely or very preterm infants (<32 completed weeks of gestation) is common, and increased risk is associated with lower gestational age[1]; white matter microstructural differences in moderate or late preterm infants (32–36 completed weeks of gestation) compared with term infants have also been reported.[2] The abnormality of white matter development associated with low gestational age in preterm infants may extend well beyond infancy, as indicated by observed differences in adolescents born prematurely compared with term-born controls.[3-5] Furthermore, abnormal white matter development associated with preterm birth is also linked to adverse long-term neurodevelopmental outcomes in children at different ages.[6-8]

The effects of gestational age on neurologic or neurodevelopment for term-born children (≥37 completed weeks of gestation) have not been investigated until recently. Several new studies (most of them population-based) reported positive associations between longer gestational age (excluding postterm, which is ≥42 weeks of gestation) and better cognitive and/or neurodevelopment in term-born children, such as higher scores on Bayley scales of mental and motor development during the first year of life[9,10];

Received March 23, 2017; accepted after revision July 22.

From the Departments of Radiology (X.O., C.M.G., R.H.R., A.K., A.C.R.) and Pediatrics (X.O., C.M.G., R.T.P., A.A., M.A.C., T.M.B.), University of Arkansas for Medical Sciences, Little Rock, Arkansas; Arkansas Children's Nutrition Center (X.O., R.T.P., A.A., T.M.B.), Little Rock, Arkansas; and Department of Radiology (X.O., C.M.G., R.H.R., A.K., A.C.R.), Arkansas Children's Hospital, Little Rock, Arkansas.

These studies were supported in part by United States Department of Agriculture Agricultural Research Service Project 6026-51000-010-05S and the Marion B. Lyon Award from the Arkansas Children's Research Institute.

Please address correspondence to Xiawei Ou, PhD, Arkansas Children's Hospital, 1 Children's Way, Slot 105, Little Rock, AR 72202; e-mail: ouxiawei@uams.edu

Indicates open access to non-subscribers at www.ajnr.org

Indicates article with supplemental on-line photo.

http://dx.doi.org/10.3174/ajnr.A5408

more school readiness and cognitive and educational ability at age 3 years[11]; higher intelligence quotient scores[12] and less vulnerability to low early developmental index at age 6–7 years[13]; greater reading, math, and achievement scores in the third grade[14]; and better test scores in elementary and middle school and higher probability of being gifted.[15]

Brain structural and functional development is directly related with neurodevelopment and cognitive performance in children. However, very few studies have addressed whether length of gestation at term birth is associated with differences in later brain development in children as measured by neuroimaging, particularly for white matter development (a recent study reported associations between longer gestation and higher brain gray matter density measured by MR imaging in term-born healthy 6–10-year-old children[16]). In addition, although white matter maturation before and after term has been investigated via imaging studies,[17] there is insufficient quantitative characterization of white matter maturation during the normal term period beyond the common perception that white matter is developing rapidly during this time. In each week of gestation and/or week of life during the term period, white matter continues to mature in patterns of posterior to anterior and central to peripheral.[18] A few studies have evaluated white matter microstructures in relation to term gestational ages[19,20]; nevertheless, studies including white matter imaging data for term-born infants have mostly focused on the comparison to preterm,[20,21] but not on the trajectory of white matter development in term-born infants during the normal term period. Nor is it clear whether gestational lengths at birth of term-born infants impact this trajectory and longer-term development into childhood. In this study, DTI measures were used to examine potential associations between gestational age at birth and brain white matter microstructural development in 2 well-characterized cohorts of healthy term-born subjects (2-week old infants and 8-year-old children).

MATERIALS AND METHODS

Study Population

All study subjects were from the existing prospective Brain Power (ClinicalTrials.gov identifier: NCT00735423) or Glowing (ClinicalTrials.gov identifier: NCT01131117) research cohorts at the Arkansas Children's Nutrition Center, and all experimental procedures were approved by the institutional review board at the University of Arkansas for Medical Sciences with parental consent. Inclusion and exclusion criteria for these 2 research cohorts apply to this retrospective secondary analysis study. Briefly, all infants ($n = 44$) were born to healthy women with uncomplicated singleton pregnancy; had term gestation at birth (≥37 completed weeks); were born with size appropriate for gestational age; and had no birth defects or congenital abnormalities and no medical issues at or after birth. All 8-year-old children ($n = 63$) were term-born (≥37 completed weeks) with birth weight and current body mass index between the 5th and 95th percentile for age; were healthy with normal neurodevelopment; and had no history of neurologic impairment or injury, psychologic or psychiatric diagnoses, or any other serious illnesses or diseases. Reynolds Intellectual Assessment Scales of intelligence quotient were measured, and all subjects had composite intelligence quotient >80. All infants included in this study had an MR imaging examination of the brain during natural sleep at Arkansas Children's Hospital around age 2 weeks, which included conventional sequences to screen for apparent abnormalities and DTI for evaluation of white matter development, as part of the Glowing study. All 8-year-old children included in this study were scanned with similar DTI pulse sequences as part of the Brain Power study.

MR Imaging Data Acquisition

The MR imaging data were acquired by using a 1.5T Achieva scanner (Philips Healthcare, Best, the Netherlands) with an 8-channel SENSE head coil (Philips Healthcare). Infants were fed approximately 30 minutes before the scan and wrapped by a MedVac infant immobilizer (CFI Medical Solutions, Fenton, MI). Mini muffs were used to block the noise from the scanner, a pulse oximeter probe was used to monitor oxygen saturation and heart rate, and an MR imaging–compatible camera was used to monitor the infants during the scan. Pulse sequences included diffusion, susceptibility, 3D T1- and/or T2-weighted imaging to exclude apparent brain abnormalities, and a single-shot spin-echo EPI sequence with diffusion-weighting gradients in 15 uniformly distributed directions and a maximum b-value of 700 seconds/mm^2 to acquire DTI data with $2 \times 2 \times 3$ mm^3 voxel size. For 8-year-old children, a headset was used to block scanner noise and to play audio associated with a movie played during the scan by using an MR imaging–compatible entertainment system. The children were instructed to remain still inside the scanner, but were given a panic button for emergency use. DTI data were acquired by using a similar EPI sequence with 15 diffusion-weighting directions and a maximum b-value of 800 seconds/mm^2.

DTI Data Analysis

All DTI raw data were exported to a workstation with the FMRIB Software Library (FSL, created by the Oxford Center for Functional MR Imaging of the Brain, United Kingdom [http://www.fmrib.ox.ac.uk/fsl]) installed on a VMware Linux virtual machine (VMware, Palo Alto, California) and with Matlab software (MathWorks, Natick, Massachusetts). First, FSL tools were used for eddy current and head movement correction in the raw data and for creating a brain mask for each subject. The preprocessed DTI data were then fed to the DTIfit tool (http://fsl.fmrib.ox.ac.uk/fsl/fsl-4.1.9/fdt/fdt_dtifit.html) to calculate DTI parameter maps for each subject, including fractional anisotropy (FA), mean diffusivity (MD), axial diffusivity (AD), and radial diffusivity (RD). The FA maps were then processed by the tract-based spatial statistics tool (http://fsl.fmrib.ox.ac.uk/fsl/fslwiki/TBSS) for further analysis.[22] Specifically, FA maps were preprocessed to remove outliers from the DTI fitting and then aligned to each other to identify a most representative subject with the least total imaging warping. The FA maps for all subjects were then registered to the FA maps for this representative subject by using nonlinear transformation and were skeletonized by using the tract-based spatial statistics tool. A threshold of FA >0.1 was chosen for the infants' data and a threshold of FA >0.15 was chosen for the 8-year-old children's data to delineate the major white matter tracts (white matter skeletons) on the FA maps for each subject,

which were used for voxelwise statistical analysis. In addition, the MD, AD, and RD maps were transformed and skeletonized according to the existing template and logistics for FA maps and were processed for voxelwise statistical analysis as well. Furthermore, major white matter tracts/regions with known anatomy were sketched on the FA maps, and mean DTI parameter values for each ROI for each subject were exported to Matlab for additional ROI analysis.

Statistics

Randomization with 5000 permutations was used for the voxelwise correlation analysis in tract-based spatial statistics. The threshold-free cluster enhancement option[23] was used to identify voxels with significant correlation ($P < .05$, corrected for multiple comparisons) between gestational age and DTI parameters. The analysis was also adjusted for potential confounding factors including postnatal age at MR imaging and the subject's sex, because the brain continues to develop rapidly after birth and sex differences in DTI measures in children have been reported.[24] For the ROI analysis, Spearman partial correlation tests were used to calculate the coefficients and *P* values for the correlation between gestational ages and mean DTI parameters in each ROI, controlling for postnatal age at MR imaging and sex.

RESULTS

The demographic information for the healthy term infants and 8-year-old healthy children are listed in Table 1. The standard deviation of age at the time of MR imaging examination was relatively small compared with the mean age at MR imaging for both groups, indicating well-defined age groups with potentially low confounding by postnatal age.

For the term infants, DTI tract-based spatial statistics analysis revealed that FA values, a marker for white matter microstructural integrity, positively correlated ($P < .05$, corrected) with gestational age at birth in most white matter voxels in the brain (Fig 1 and Table 2). These voxels involved the frontal, parietal, temporal, and occipital lobes and the pons as well as the cerebellum. However, the corpus callosum (especially the splenium and the body), which develops the fastest at the first trimester of pregnancy,[25] did not show significant correlations. On the other hand, MD, AD, and RD parameters negatively correlated ($P < .05$, corrected) with gestational age at birth in most white matter voxels in the brain (Fig 1 and Table 2), again with the exception of the splenium and body of the corpus callosum. For the 8-year-old children, no voxels in the white matter tracts showed significant correlation (positive or

Table 1: Demographic information for the healthy term infants and 8-year-old term-born children

Demographics	Infants	Children
No. of patients	44	63
Gestational age at birth, wks (mean ± SD [min, max])	39.3 ± 1.0 [37.3, 40.7]	39.4 ± 1.2 [37.0, 42.1]
Age at MRI (mean ± SD [min, max])[a]	14.3 ± 1.6 [11, 19]	7.90 ± 0.25 [7.52, 8.51]
Gender (M, F)	23, 21	28, 35
RIAS IQ (mean ± SD [min, max])	N/A	110.8 ± 12.5 [82, 147]

Note:—IQ indicates intelligence quotient; max, maximum; min, minimum; RIAS, Reynolds Intellectual Assessment Scales.

[a] Unit for infant ages is weeks; for children, years.

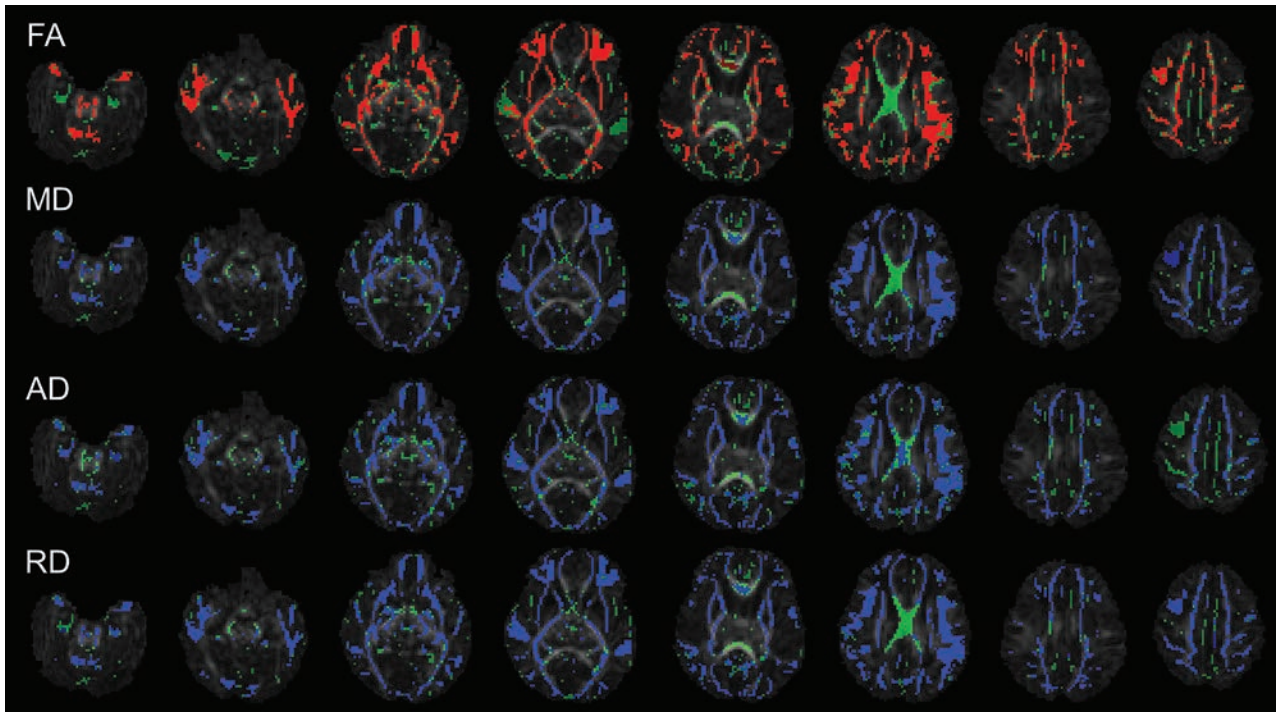

FIG 1. Tract-based spatial statistics analysis of the correlation between gestational age at birth and DTI parameters (FA, MD, AD, and RD) in term infants. Background images are FA maps; major white matter tracts are *green*; voxels in the tract with significant positive correlations ($P < .05$, corrected) are *red*; voxels with significant negative correlations ($P < .05$, corrected) are *blue*. Widespread positive correlations between FA and gestational age at birth and negative correlations between MD, AD, and RD and gestational age at birth were observed.

negative) between gestational age at birth and any of the DTI parameters (Table 2). Sex effects on DTI parameter values were observed in several white matter tracts for the 8-year-old children (data presented in the On-line Figure), but were not observed for the term infants.

ROI analysis of brain white matter regions/tracts showed results similar to those observed for the tract-based spatial statistics analyses (Fig 2). Correlation coefficients and *P* values for all ROIs for the 2 study groups are listed in Table 3. For the term infants, of the 14 regions/tracts included, mean FA values positively correlated ($P < .05$) with gestational age at birth in 6 regions, and mean MD, AD, and RD values negatively correlated ($P < .05$) with gestational age at birth in 11 regions. The genu, splenium, and body of the corpus callosum did not show any significant correlations. For the 8-year-old children, no ROI showed a significant correlation ($P < .05$) between gestational age at birth and any DTI parameter (Fig 2 and Table 3).

Table 2: Percentage of imaging voxels in major white matter tracts that showed significant correlation ($P < .05$, corrected) between DTI parameters (FA, MD, AD, and RD) and gestational age at birth

	Infants[a]	Children[a]
FA	80, all positive	0
MD	91, all negative	0
AD	87, all negative	0
RD	91, all negative	0

[a] Information presented as percentage of voxels, correlation type.

DISCUSSION

Our DTI study shows that gestational age at birth is associated with significant differences in white matter microstructural development in term infants, but not in term-born children at age 8

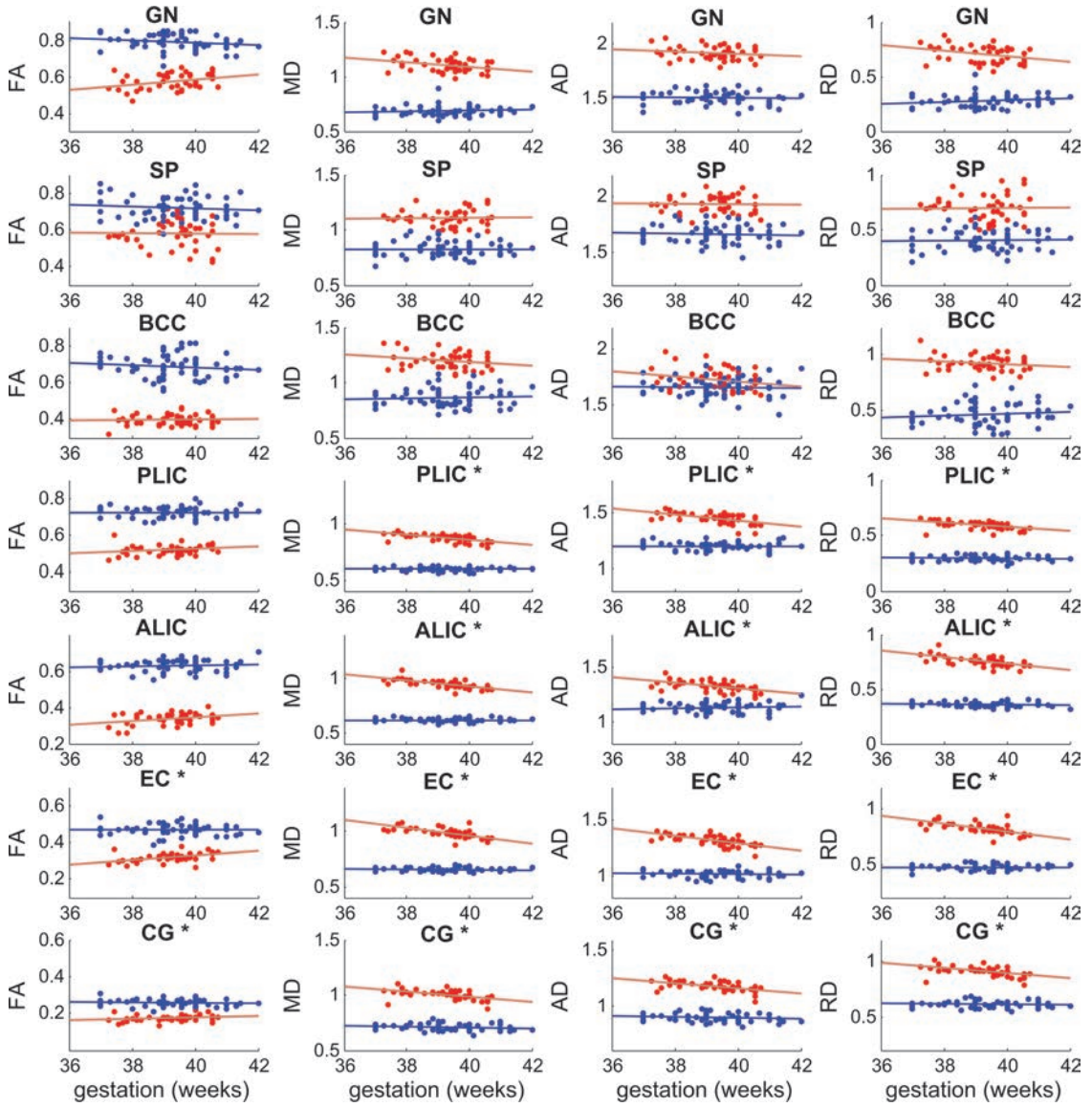

FIG 2. Scatterplots for correlation analyses between gestational age at birth and DTI parameters in white matter ROIs of term infants and children. Data for term infants are in *red*, and data for 8-year-old children are in *blue*. Least-square fit lines are also shown. Units for DTI parameters are: FA (no unit); MD, AD, and RD (μm^2/ms). Positive correlations ($P < .05$) between gestational age and FA were observed in many ROIs (marked with an *asterisk*) for the term infants, but not in any ROI for the 8-year-old children. Likewise, negative correlations ($P < .05$) between gestational age and MD, AD, and RD were observed for most ROIs (marked with an *asterisk*) for the term infants, but none were observed for any ROI for the 8-year-old children. (Details of correlation statistics are provided in Table 3.)

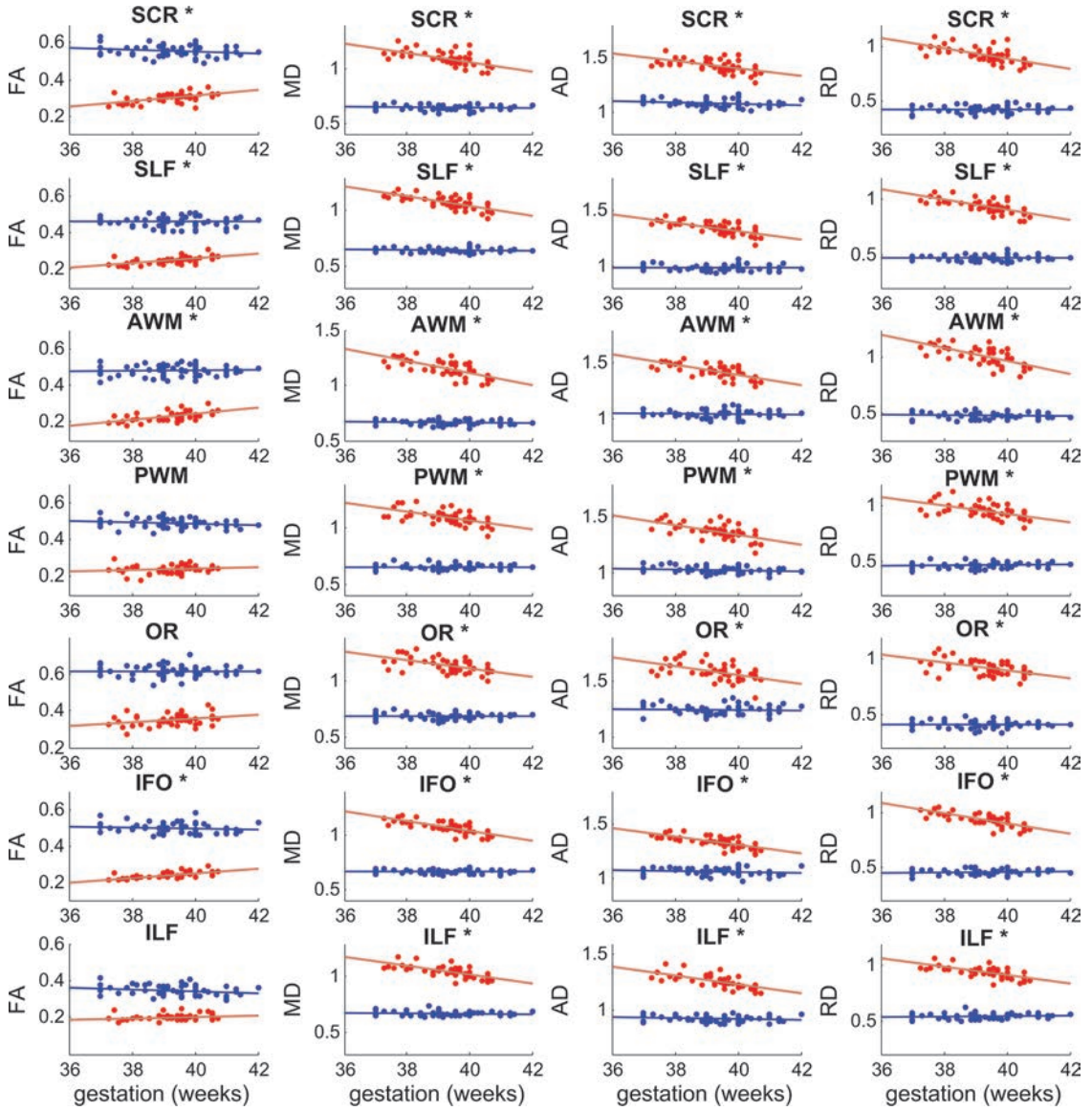

FIG 2. Continued.

years. Specifically, for term infants, significant positive correlations between gestational age at birth and FA values and negative correlations between gestational age at birth and MD, AD, and RD values were observed in most white matter tracts, indicating that increased myelination (reflected by lower RD) and axonal growth (reflected by lower AD) as well as overall higher white matter integrity (reflected by higher FA and lower MD) are associated with longer gestational age during the normal term period before birth. One major white matter region not displaying these significant gestation-related associations was the corpus callosum, which typically starts development at the first trimester of pregnancy with a faster growth rate than at other trimesters.[25] It is possible that the development of the corpus callosum is less vulnerable to gestational influences at the end of the normal term period, in which case relatively small differences in gestational age within the normal term period may not result in measurable changes in its myelination and growth. For the DTI parameters, it appears that diffusivity measures (MD, AD, and RD) were more sensitive than anisotropy (FA) to white matter microstructural changes during the normal term period. For example, tract-based spatial statistics analyses revealed a higher percentage of white matter voxels with significant correlations related to gestational age at birth (Table 2) for MD, AD, and RD than for FA, and ROI analyses showed significant correlations with gestational age at birth for more regions for MD, AD, and RD than for FA (Table 3). To our knowledge, there is only 1 other published study focused on white matter microstructural development in term infants at young postnatal ages similar to those in our study.[20] In that study, a positive correlation with gestational age was found in several white matter regions for FA values. Analyses on diffusivities were not available. Another study investigated white matter microstructural development in term infants at a larger postnatal age range by using DTI tractography methods, but the evaluation was limited to only a few white matter regions.[19] Their results showed increased FA and decreased MD with gestational age at MR imaging (gestational age at birth plus postnatal age at MR imaging) in corticospinal tracts, but not in the splenium of the corpus callosum, consistent with our findings. Overall, our DTI results for

Table 3: Correlation coefficients (*r* values) and correlation statistics (*P* values) between gestational age at birth and DTI parameters in white matter ROIs for the term infants and children

	FA Correlation		MD Correlation		AD Correlation		RD Correlation	
	r Value	*P* Value	*r* Value	*P* Value	*r* Value	*P* Value	*r* Value	*P* Value
Infants								
GN	0.28	.07	−0.24	.13	−0.06	.72	−0.29	.06
SP	−0.02	.90	0.06	.73	−0.05	.78	0.06	.69
BCC	−0.06	.70	−0.15	.34	−0.25	.10	−0.08	.60
PLIC	0.29	.06	−0.67	<.001[a]	−0.54	<.001[a]	−0.59	<.001[a]
ALIC	0.18	.25	−0.72	<.001[a]	−0.59	<.001[a]	−0.61	<.001[a]
EC	0.45	.003[a]	−0.71	<.001[a]	−0.65	<.001[a]	−0.69	<.001[a]
CG	0.32	.04[a]	−0.63	<.001[a]	−0.51	<.001[a]	−0.62	<.001[a]
SCR	0.48	.001[a]	−0.63	<.001[a]	−0.54	<.001[a]	−0.63	<.001[a]
SLF	0.59	<.001[a]	−0.65	<.001[a]	−0.63	<.001[a]	−0.66	<.001[a]
AWM	0.60	<.001[a]	−0.69	<.001[a]	−0.66	<.001[a]	−0.67	<.001[a]
PWM	0.23	.13	−0.59	<.001[a]	−0.61	<.001[a]	−0.52	<.001[a]
OR	0.28	.07	−0.52	<.011[a]	−0.49	.001[a]	−0.47	.001[a]
IFO	0.66	<.001[a]	−0.72	<.001[a]	−0.70	<.001[a]	−0.70	<.001[a]
ILF	0.24	.13	−0.71	<.001[a]	−0.69	<.001[a]	−0.68	<.001[a]
Children								
GN	−0.25	.05	0.16	.21	−0.15	.25	0.22	.08
SP	−0.05	.68	0.04	.78	−0.03	.79	0.04	.78
BCC	−0.13	.33	0.03	.81	0.00	.99	0.06	.63
PLIC	−0.03	.81	−0.02	.88	−0.04	.73	0.01	.93
ALIC	0.08	.54	−0.05	.68	0.09	.51	−0.10	.46
EC	−0.05	.69	−0.00	.95	−0.07	.61	0.01	.93
CG	−0.08	.53	−0.19	.14	−0.02	.10	−0.16	.21
SCR	−0.17	.18	−0.02	.91	−0.24	.06	0.04	.77
SLF	0.01	.95	−0.01	.94	−0.02	.84	−0.02	.89
AWM	−0.01	.91	−0.10	.44	−0.06	.64	−0.09	.49
PWM	−0.19	.14	−0.00	.97	−0.18	.17	0.08	.52
OR	−0.04	.76	−0.05	.72	−0.00	.99	−0.04	.77
IFO	−0.21	.10	−0.04	.77	−0.22	.09	0.05	.71
ILF	−0.21	.10	0.00	.98	−0.24	.06	0.10	.43

Note:—ALIC indicates anterior limb of internal capsule; AWM, anterior white matter; BCC, body of corpus callosum; CG, cingulum; EC, external capsule; GN, genu of corpus callosum; IFO, inferior frontal occipital fasciculus; ILF, inferior longitudinal fasciculus; OR, optic radiation; PLIC, posterior limb of internal capsule; PWM, posterior white matter; SCR, superior corona radiata; SLF, superior longitudinal fasciculus; SP, splenium of corpus callosum.

[a] Indicates *P* values for significant correlations.

term infants agree with the general consensus that the normal term period (37–41 weeks of gestation) is a critical timeframe for the developing brain. Furthermore, the results in the current study can provide additional normative data for DTI parameter changes in white matter during this period.

For 8-year-old term-born children, significant correlations between gestational age at birth and DTI parameters at age 8 years were not observed. This may be a reflection of a "catch-up" effect (ie, the deficits presumably related to less in utero development because of shorter gestational length within the normal term period were compensated for during 8 years of postnatal development, with the white matter microstructures in term-born children with all gestational ages eventually reaching the same level). However, extensive exposure to potential confounding factors (such as diet, lifestyle, and family environment) during the 8 years of postnatal brain development could also be a mediating factor and cannot be ruled out as a contributing factor underlying the observed absence of gestational age-associated white matter differences. Although there was no significant correlation between gestational age and intelligence quotient for the 8-year-old children ($r = -0.09$, $P = .49$) in our study, population-based studies have shown that white matter development is associated with cognitive functioning in 6–10-year-old healthy children,[18] and recent large-scale studies have revealed associations between cognitive development and length of gestation in school-age children born at term.[12-15] Our results indicate that white matter changes are not likely the driving force for reported relationships between gestational age and cognitive performance in term-born children. It is noteworthy that reported white matter changes in older children/adolescents associated with preterm birth were mostly for those born very preterm or with very low birth weight,[3-5,8,26] and a study of 9-year-old children with low risk preterm birth (30–34 weeks of gestation) showed more changes in gray matter than white matter compared with term controls.[27] In addition, 1 study showed increased regional gray matter attenuation associated with gestational age at birth in 6–10-year-old children for both the preterm and term subgroups.[16] Therefore, the development of gray matter, the other major structural component of the brain, may need to be the future focus for exploring potential relationships between gestational age and brain development in term-born children. This may be achieved by either global/regional volume or cortical thickness measurements of gray matter or fMRI measurements of stimulated brain activation or connectivity at resting state in gray matter.

One limitation for this study is that the gestational age for the 8-year-old children was parent reported. Medical records containing relevant information were not available for some subjects. Parents were asked to provide the due date (and/or the exact gestational length at birth of their children) as part of the Brain

Power study (those unable to provide this information were excluded from this study), and gestational age at birth was then calculated by comparing the due date (assume 40 weeks of gestation) and the actual date of birth. Although potential inaccuracy (likely on the order of days, if any) is possible, the distribution and mean/standard deviation (Table 1) of gestational age at birth were comparable with that for the infant cohort, and therefore did not suggest apparent issues. Furthermore, additional analyses were performed to test the effects of gestational age at term birth on DTI parameters in these 8-year-old children, such as group comparisons of those with reported gestational age 37–38 completed weeks versus 39–41 or 40–41 completed weeks; 37 or 38 completed weeks versus 39, 40, or 41 completed weeks; and so forth. None of those comparisons showed any effect of gestational age at birth on DTI parameters for the 8-year-old children.

CONCLUSIONS

Our DTI findings indicate that longer gestational length is associated with greater white matter microstructural development in term healthy infants, but not in term-born 8-year-old healthy children.

ACKNOWLEDGMENTS

We thank the staff of the Arkansas Children's Nutrition Center Clinical Research Core and the Arkansas Children's Hospital Radiology MR imaging team for their assistance with these studies. We also thank Dr. Sean Adams and Dr. Sherry Courtney for helpful discussion as well as reviewing this manuscript.

Disclosures: Xiawei Ou—*RELATED*: *Grants/Grants Pending*: United States Department of Agriculture (USDA) grant, *Comments*: this study was partly supported by a USDA Agricultural Research Service (USDA-ARS) grant, which is acknowledged in the manuscript*. Charles M. Glasier—*UNRELATED*: *Board Membership*: *Pediatric Radiology*, *Comments*, editorial board; Arkansas Foodbank. R.T. Pivik—*RELATED*: *Grants/Grants Pending*: USDA-ARS*; *Support for Travel to Meetings for the Study or Other Purposes*: USDA-ARS*; *Provision of Writing Assistance, Medicines, Equipment, or Administrative Support*: USDA-ARS*; *UNRELATED*: *Grants/Grants Pending*: USDA-ARS*. Aline Andres—*RELATED*: *Grants/Grants Pending*: USDA-ARS*; *Support for Travel to Meetings for the Study or Other Purposes*: USDA-ARS, *Comments*: grant-supported travel to scientific conferences*. *Money paid to the institution.

REFERENCES

1. Larroque B, Marret S, Ancel PY, et al. **White matter damage and intraventricular hemorrhage in very preterm infants: the EPIPAGE study.** *J Pediatr* 2003;143:477–83 CrossRef Medline
2. Kelly CE, Cheong JL, Fam LG, et al. **Moderate and late preterm infants exhibit widespread brain white matter microstructure alterations at term-equivalent age relative to term-born controls.** *Brain Imaging Behav* 2016;10:41–49 CrossRef Medline
3. Giménez M, Junqué C, Narberhaus A, et al. **White matter volume and concentration reductions in adolescents with history of very preterm birth: a voxel-based morphometry study.** *Neuroimage* 2006;32:1485–98 CrossRef Medline
4. Nagy Z, Westerberg H, Skare S, et al. **Preterm children have disturbances of white matter at 11 years of age as shown by diffusion tensor imaging.** *Pediatr Res* 2003;54:672–79 CrossRef Medline
5. Vangberg TR, Skranes J, Dale AM, et al. **Changes in white matter diffusion anisotropy in adolescents born prematurely.** *Neuroimage* 2006;32:1538–48 CrossRef Medline
6. Counsell SJ, Edwards AD, Chew AT, et al. **Specific relations between neurodevelopmental abilities and white matter microstructure in children born preterm.** *Brain* 2008;131:3201–08 CrossRef Medline
7. Feldman HM, Lee ES, Yeatman JD, et al. **Language and reading skills in school-aged children and adolescents born preterm are associated with white matter properties on diffusion tensor imaging.** *Neuropsychologia* 2012;50:3348–62 CrossRef Medline
8. Murray AL, Thompson DK, Pascoe L, et al. **White matter abnormalities and impaired attention abilities in children born very preterm.** *Neuroimage* 2016;124:75–84 CrossRef Medline
9. Espel EV, Glynn LM, Sandman CA, et al. **Longer gestation among children born full term influences cognitive and motor development.** *PLoS One* 2014;9:e113758 CrossRef Medline
10. Rose O, Blanco E, Martinez SM, et al. **Developmental scores at 1 year with increasing gestational age, 37–41 weeks.** *Pediatrics* 2013;131:E1475–81 CrossRef Medline
11. Poulsen G, Wolke D, Kurinczuk JJ, et al. **Gestational age and cognitive ability in early childhood: a population-based cohort study.** *Paediatr Perinat Epidemiol* 2013;27:371–79 CrossRef Medline
12. Yang S, Platt RW, Kramer MS. **Variation in child cognitive ability by week of gestation among healthy term births.** *Am J Epidemiol* 2010;171:399–406 CrossRef Medline
13. Smithers LG, Searle AK, Chittleborough CR, et al. **A whole-of-population study of term and post-term gestational age at birth and children's development.** *BJOG* 2015;122:1303–11 CrossRef Medline
14. Noble KG, Fifer WP, Rauh VA, et al. **Academic achievement varies with gestational age among children born at term.** *Pediatrics* 2012;130:e257–64 CrossRef Medline
15. Figlio DN, Guryan J, Karbownik K, et al. **Long-term cognitive and health outcomes of school-aged children who were born late-term vs full-term.** *JAMA Pediatr* 2016;170:758–64 CrossRef Medline
16. Baym CL, Khan NA, Monti JM, et al. **Dietary lipids are differentially associated with hippocampal-dependent relational memory in prepubescent children.** *Am J Clin Nutr* 2014;99:1026–32 CrossRef Medline
17. Dubois J, Dehaene-Lambertz G, Kulikova S, et al. **The early development of brain white matter: a review of imaging studies in fetuses, newborns and infants.** *Neuroscience* 2014;276:48–71 CrossRef Medline
18. Muetzel RL, Mous SE, van der Ende J, et al. **White matter integrity and cognitive performance in school-age children: a population-based neuroimaging study.** *Neuroimage* 2015;119:119–28 CrossRef Medline
19. Alcauter S, Lin W, Keith Smith J, et al. **Consistent anterior-posterior segregation of the insula during the first 2 years of life.** *Cereb Cortex* 2015;25:1176–87 CrossRef Medline
20. Broekman BF, Wang C, Li Y, et al. **Gestational age and neonatal brain microstructure in term born infants: a birth cohort study.** *PLoS One* 2014;9:e115229 CrossRef Medline
21. Davids S, Lauffer H, Thoms K, et al. **Increased dorsolateral prefrontal cortex activation in obese children during observation of food stimuli.** *Int J Obesity (Lond)* 2010;34:94–104 CrossRef Medline
22. Smith SM, Jenkinson M, Johansen-Berg H, et al. **Tract-based spatial statistics: voxelwise analysis of multi-subject diffusion data.** *Neuroimage* 2006;31:1487–505 CrossRef Medline
23. Smith SM, Nichols TE. **Threshold-free cluster enhancement: addressing problems of smoothing, threshold dependence and localisation in cluster inference.** *Neuroimage* 2009;44:83–98 CrossRef Medline
24. Schmithorst VJ, Holland SK, Dardzinski BJ. **Developmental differences in white matter architecture between boys and girls.** *Hum Brain Mapp* 2008;29:696–710 CrossRef Medline
25. Achiron R, Achiron A. **Development of the human fetal corpus callosum: a high-resolution, cross-sectional sonographic study.** *Ultrasound Obstet Gynecol* 2001;18:343–47 CrossRef Medline
26. Nosarti C, Giouroukou E, Healy E, et al. **Grey and white matter distribution in very preterm adolescents mediates neurodevelopmental outcome.** *Brain* 2008;131:205–17 CrossRef Medline
27. Soria-Pastor S, Padilla N, Zubiaurre-Elorza L, et al. **Decreased regional brain volume and cognitive impairment in preterm children at low risk.** *Pediatrics* 2009;124:e1161–70 CrossRef Medline

Basion–Cartilaginous Dens Interval: An Imaging Parameter for Craniovertebral Junction Assessment in Children

A.K. Singh, Z. Fulton, R. Tiwari, X. Zhang, L. Lu, W.B. Altmeyer, and B. Tantiwongkosi

ABSTRACT

BACKGROUND AND PURPOSE: Widening of the basion-dens interval is an important sign of cranioverterbral junction injury. The current literature on basion-dens interval in children is sparse and based on bony measurements with variable values. Our goal was to establish the normal values of a recently described new imaging parameter, the basion–cartilaginous dens interval in children.

MATERIALS AND METHODS: Three hundred healthy pediatric patients (0–10 years of age) were selected retrospectively. These patients were divided into 3 different groups: A (0–3 years), B (3–6 years), and C (6–10 years). The basion–cartilaginous dens interval was calculated on the sagittal MPR image of cervical spine CT in a soft-tissue window. The mean, SD, and the upper limit of normal (mean +2 SDs) of the 3 groups were calculated, and statistical tests were used to check for significant differences of the basion–cartilaginous dens interval among these 3 groups.

RESULTS: The upper limits of the basion–cartilaginous dens interval for the 3 groups were 5.34 mm in group A, 5.64 mm in group B, and 7.24 mm in group C. There were statistically significant differences in the basion–cartilaginous dens interval values among the 3 groups. There was no statistically significant difference in basion–cartilaginous dens interval values between groups A and B; however, values in group C were significantly different from those in both A and B. There was no statistically significant difference in the basion–cartilaginous dens interval values between males and females.

CONCLUSIONS: The basion–cartilaginous dens interval is a novel imaging parameter to assess cranioverterbral junction integrity in children, which includes the nonossified cartilage in the measurement.

ABBREVIATIONS: BDI = basion-dens interval; BCDI = basion–cartilaginous dens interval; CVJ = craniovertebral junction

The incidence of pediatric cervical spine injuries is between 1% and 2% of all patients with trauma.[1,2] Upper cervical spine injuries are approximately twice as common as lower cervical spine injuries in children.[3] Pure ligamentous injuries without fractures are more common in children younger than 9 years of age.[4,5] Younger children are more susceptible to craniovertebral junction (CVJ) injuries due to a disproportionately large head size, laxity of the ligaments, and increased mobility at the craniovertebral junction.[6,7] The basion-dens interval (BDI) is an important imaging marker for CVJ injuries; however, the literature on pediatric BDI is limited. Moreover, BDI does not include the cartilaginous portion of the dens and is susceptible to variability in measurements. To address these limitations, a novel pediatric imaging parameter, the basion–cartilaginous dens interval (BCDI) has recently been introduced and described by Birchansky et al.[8] As a substitute for BDI, we apply this new BCDI measurement in order to assess the normal values in children.

MATERIALS AND METHODS

This study was approved by our institutional review board for research. We retrospectively examined cervical spine CT scans in 300 pediatric patients (0–10 years of age) from 2013 to 2016. These patients were divided into 3 groups: 0–3 years of age, 3–6 years of age, and 6–10 years of age. Seven radiologists (3 attending neuroradiologists and 4 second-year radiology residents) reviewed the CT scans in these patients. Each of the 3 attending neuroradiologists and 2 residents reviewed images in 50 different patients ($n = 250$), and each of the 2 other residents reviewed images in 25 different patients ($n = 50$). The patients were divided

Received May 25, 2017; accepted after revision August 3.

From the Department of Radiology, University of Texas Health Science Center San Antonio, San Antonio, Texas.

Paper previously presented at: Annual Meeting of American Society of Neuroradiology, April 22–27, 2017; Long Beach, California.

Please address correspondence to Achint K. Singh, MD, Department of Radiology, University of Texas Health Science Center San Antonio, 7703 Floyd Curl Dr, MC 7800, San Antonio, TX 78229; e-mail: singhak@uthscsa.edu

Indicates open access to non-subscribers at www.ajnr.org

http://dx.doi.org/10.3174/ajnr.A5400

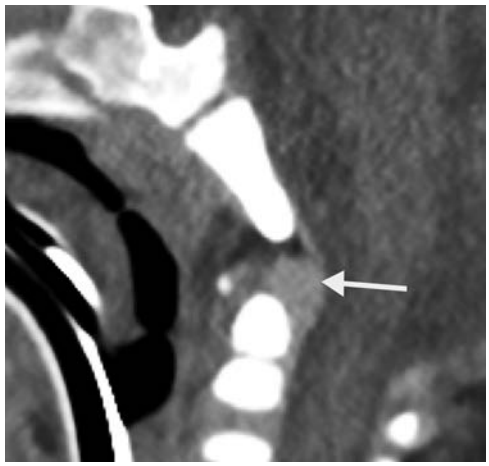

FIG 1. Sagittal CT cervical spine image (soft-tissue window) in a 6-month-old boy shows the soft-tissue cartilage around the dens (*arrow*).

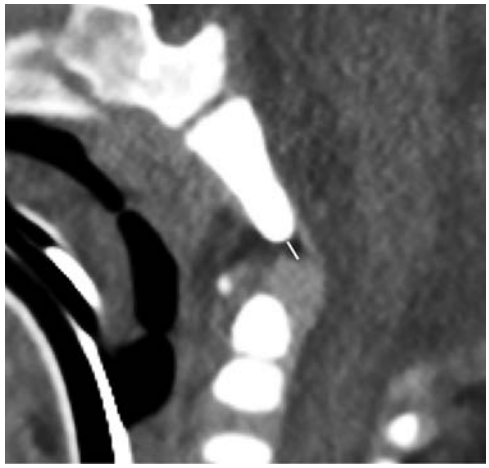

FIG 2. Sagittal CT cervical spine image (soft-tissue window) in a 6-month-old boy shows the technique for measuring BCDI as indicated by the *line*.

again among radiologists for a second review so that a different radiologist reviewed images in each patient. All radiologists received training on how to measure the BCDI. These measurements were obtained in sagittal reformatted images of the cervical spine in a soft-tissue window where cartilage can be easily seen around the dens (Fig 1). The minimum distance between the basion and tip of the dens was measured. If cartilage was seen, then the tip of the cartilage was used for measurement (Fig 2). If the dens was completely formed and the cartilage was not seen, then the tip of the bony dens was used for measurement. The BCDI measurement on each patient was obtained by 2 different readers, and an average of these 2 values was obtained for the data analysis.

Inclusion criteria for this study were normal cervical spine CT findings without any signs of craniovertebral junction injury based on imaging and clinical grounds. Exclusion criteria were any sign of craniovertebral junction injury, congenital anomalies of the CVJ, motion artifacts, and inadequate sagittal reformatted images in the soft-tissue window.

These patients were scanned on 2 similar machines (128-section Ingenuity; Philips Healthcare, Best, the Netherlands) with the same technical parameters: 128 × 0.625-mm collimation, 0.9-mm section thickness, 0.5-mm interval, with a pitch of 0.914, 100 kV(peak), and 70–100 mAs. Axial images were reconstructed at 1 and 3 mm. Sagittal and coronal MPR images were reconstructed from axial 1-mm sections. Images were reviewed in the bone window (window level, 400 HU; window width, 2000 HU) and soft-tissue window (window level, 50 HU; window width, 450 HU).

BCDI values in 3 different groups

Group	Mean	SD	Upper Limit of Normal (Mean +2 SDs)
A (0–3 yr)	3.87	0.73	5.34
B (3–6 yr)	3.80	0.92	5.64
C (6–10 yr)	5.31	0.96	7.24

Statistical Analysis

All statistical analyses were performed on SAS statistical software, Version 9.4 (SAS Institute, Cary, North Carolina). All the patients were divided into 3 groups: group A (0–3 years), group B (3–6 years), and group C (6–10 years). There were 172 males and 128 females. Descriptive statistical analysis was performed for the BCDI values in the 3 groups, and the mean, SD, and upper limit of normal values were obtained (Table). The upper limit of normal was defined as mean +2 SDs. The 1-way ANOVA test was performed to check the statistically significant difference in BCDI values among the 3 groups followed by a post hoc statistical test (Tukey) to check which group differed from the other groups. The Student *t* test was performed to check the statistically significant difference in BCDI values between males and females. Interobserver agreement for the BCDI values was checked by using an intraclass correlation test. Descriptive analysis was also performed regarding the appearance and fusion of the os terminale, and the mean and SD were calculated. A *P*-value of .05 was considered significant.

RESULTS

The results for the BCDI values are summarized in the Table. There were statistically significant differences in the BCDI values among the 3 groups as calculated by 1-way ANOVA (*P* value < .001). The post hoc statistical tests were performed to compare which group differed from another. There was no statistically significant difference in BCDI values between groups A and B; however, values in group C were significantly different from those in both A and B. There were 172 males and 128 females. There was no statistically significant difference in the BCDI values between males and females (*t* test, *P* value > .05). The interobserver reliability was measured with the intraclass correlation coefficient, which was very good, with a coefficient of 0.89 with a 95% confidence interval of 0.84–0.90. The data were also analyzed regarding the appearance and fusion of the os terminale ossification center. The mean age at which the ossification center of the os terminale appeared was 47 months, with an SD of 12 months (Fig 3). The mean age at which the os terminale ossification center showed fusion was 8.6 years, with an SD of 1.1 years (Fig 4).

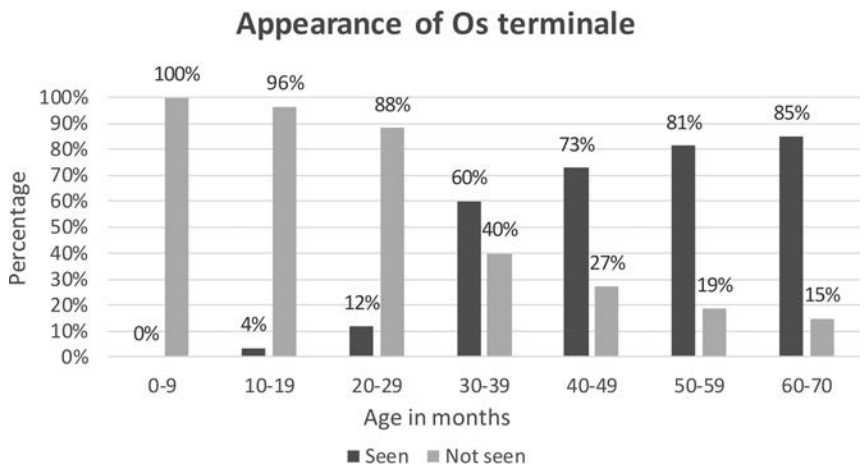

FIG 3. Bar chart for the appearance of the os terminale ossification center in children.

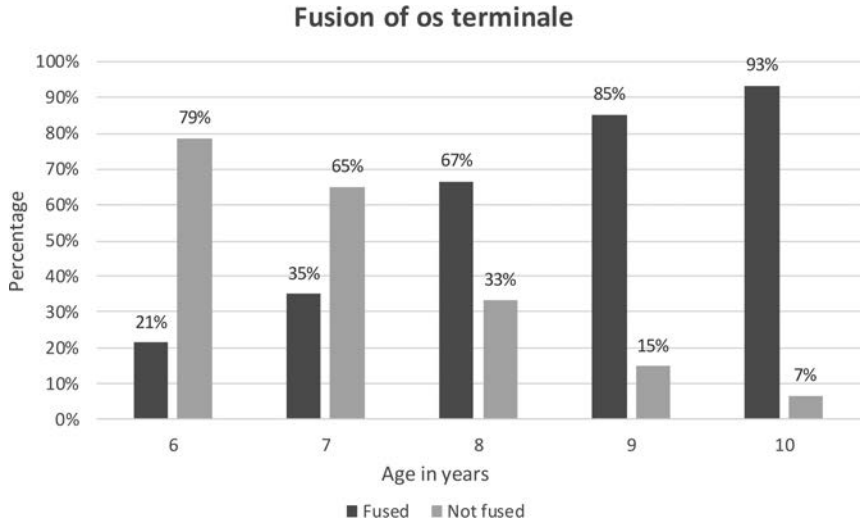

FIG 4. Bar chart for the fusion of the os terminale ossification center in children.

DISCUSSION

The craniovertebral junction comprises the occiput, atlas, and axis with associated ligaments. These ligaments play an important role in the stability of the CVJ. The anterior atlanto-occipital membrane is the cranial extension of the anterior longitudinal ligament and extends superiorly to the clivus. The apical ligament extends from the dens to the clivus. The transverse band of the cruciform ligament is the main stabilizing ligament of atlantoaxial joint and passes behind the dens to attach to the lateral masses of the atlas. The ascending and descending bands of the cruciform ligament attach to the clivus and body of C2, respectively. The tectorial membrane is the cranial extension of the posterior longitudinal ligament and passes behind the cruciform ligament to attach to the clivus. The paired alar ligaments extend from the superolateral margins of the dens to the medial aspect of the occipital condyles. The posterior atlanto-occipital membrane is the cranial extension of the ligamentum flavum and extends from the anterior aspect of the posterior arch of the atlas to the posterior aspect of the foramen magnum.[9,10]

It is important to be aware of the embryology of the CVJ to understand the anatomy. The craniovertebral junction is formed from the 4 occipital and 2 upper spinal sclerotomes. First, 2 occipital sclerotomes form the clivus below the spheno-occipital synchondrosis (basiocciput). The third occipital sclerotome forms the exoccipital bone, which forms the jugular tubercle. The fourth occipital sclerotome (proatlas) divides into cranial and caudal halves, with the cranial half forming the tip of the clivus, occipital condyles, and the margin of foramen magnum. The lateral mass and superior portion of the posterior arch are formed by the caudal division of the proatlas (fourth occipital sclerotome), and the posterior and inferior portions of the arch are formed by the first spinal sclerotome. The anterior arch is formed by the hypocentrum of the first spinal sclerotome. The centrum of the second spinal sclerotome forms the body of the axis, and the neural arch forms the facets and posterior arch of the axis. The centrum of the first spinal sclerotome forms the odontoid process.

In a 17-mm embryo (Carnegie stages 18 and 19, 44–46 days after fertilization), the odontoid process is a dense mass of mesenchymal tissue located close to the future anterior foramen magnum. The chondrification of the odontoid starts from the base in stage 21 (51 days after fertilization).[11,12] The odontoid ossification begins at the base from 2 ossification centers that fuse in the midline by the seventh gestational month. The terminal portion of odontoid arises from the proatlas (the fourth occipital sclerotome). The most inferior portion of the axis body is formed by the second spinal sclerotome.[13-15] The body of C2 fuses with the odontoid by 3–6 years of age. A secondary ossification center (os terminale) at the apex of the odontoid process appears between 3 and 6 years of age and usually fuses by 12 years.[16,17] The cruciate and alar ligaments share the common mesenchymal origin in the tip of the primitive odontoid process.[12,18] The apical ligament is a functional vestige of the notochord and arises from either the notochord or its sheath.[12,19,20]

Craniovertebral junction injuries are unstable, potentially fatal injuries and should be diagnosed promptly on the initial imaging studies. The basion-dens interval is an important imaging parameter for CVJ injuries, described by Wholey et al in 1958.[21] Normal values of the basion-dens interval in the adult population have been well-described in the literature. In a study by Harris et al,[22] the basion-dens interval was <12 mm in 95% of adult patients on lateral cervical spine radiographs.

However, BDI values on CT are different from those of radiographs due to better delineation of the anatomy. Gonzalez et al[23] reported that a BDI of >9 mm on CT is suggestive of injury to the craniovertebral junction. In a study by Rojas et al,[24] BDI values of

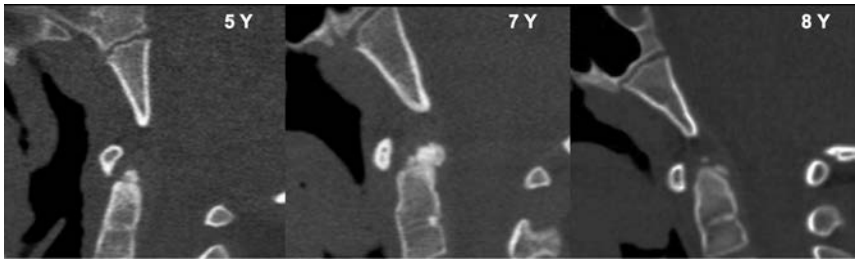

FIG 5. Sagittal CT cervical spine images in 3 children of different ages show the variable appearance of the os terminale.

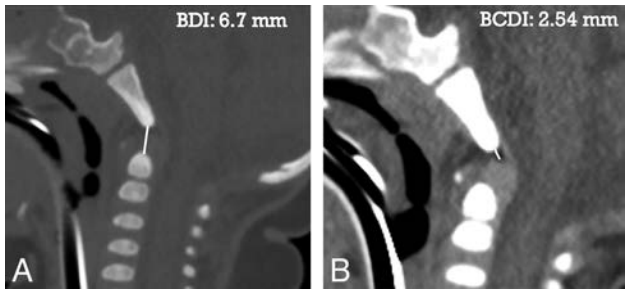

FIG 6. Comparison of BDI versus BCDI in a 6-month-old child. *A*, Sagittal CT cervical spine image in a bone window shows the BDI as 6.7 mm. *B*, Sagittal CT cervical spine image in a soft-tissue window shows the BCDI as 2.54 mm.

<8.5 mm were seen in 95% of patients (of 200) on CT. Omercikoglu et al[25] also reported a BDI of 8.5 mm as the optimal upper limit of normal on CT in their study of 499 patients.

The literature on the BDI in the pediatric population is very limited. Bulas et al[26] mentioned 12.5 mm as an upper limit of normal on cervical spine radiographs in a study on 110 patients. Bertozzi et al[27] studied the basion-dens interval in 117 healthy children and found that the normal maximum value of the BDI is 9.5 mm if the os terminale is ossified and 11.6 mm if it is not ossified. Vachhrajani et al[28] reported 7.49 mm as the upper tolerance limit for the BDI in 42 pediatric patients. The basion-dens interval is highly variable in children due to the developing dens and the variable ossification of the os terminale (Fig 5).

Recognizing that an inherent problem with the BDI in the pediatric population is that it does not include cartilage in the measurement, Birchansky et al[8] were the first group to devise a new imaging parameter utilizing sagittal CT soft tissue window reformats to measure the distance from the basion to the readily observed cartilaginous dens tip. In their study, this novel distance was coined as the "basion-cartilaginous dens interval" (BCDI). They measured the BCDI in 86 children between 0–24 months of age and calculated the upper limit of normal to be 4.4 mm.[8]

Our results show that the BCDI varies with age, with the upper tolerance limit of 5.6 mm in children up to 6 years of age and 7.2 mm in children 6–10 years of age. Our results for the BCDI are smaller than those in prior studies that measured the BDI because the 2 measurements used different landmarks. The BCDI should serve as a substitute for the BDI in the pediatric population, especially in younger children in whom the dens is not completely formed because BCDI is measured from the clivus to the cartilaginous dens where ligaments attach. An example is shown in Fig 6 for comparing the BCDI versus BDI.

Some limitations of our study are due to its retrospective nature, such as selection bias; however, we tried to minimize this bias by prospectively selecting patients in the PACS from 2013 to 2016 after the careful application of exclusion criteria. The other limitation of this study is that we only looked at the BCDI values in the healthy pediatric population. We need to compare these data with data from patients with actual CVJ injury to validate these measurements.

CONCLUSIONS

The BDI is an important imaging parameter of a craniovertebral junction injury in adults on cervical spine CT. However, its use in pediatric patients is limited due to the variable appearance of the developing os terminale. The BCDI is a recently described novel imaging parameter to assess the CVJ integrity in children that includes nonossified cartilage in the measurement. We believe that the BCDI may be a helpful imaging marker of CVJ injury in children; however, more studies are needed to validate this claim.

REFERENCES

1. Dietrich AM, Ginn-Pease ME, Bartkowski HM, et al. **Pediatric cervical spine fractures: predominantly subtle presentation.** *J Pediatr Surg* 1991;26:995–99; discussion 99–100 CrossRef Medline
2. Kokoska ER, Keller MS, Rallo MC, et al. **Characteristics of pediatric cervical spine injuries.** *J Pediatr Surg* 2001;36:100–05 CrossRef Medline
3. Patel JC, Tepas JJ 3rd, Mollitt DL, et al. **Pediatric cervical spine injuries: defining the disease.** *J Pediatr Surg* 2001;36:373–76 CrossRef Medline
4. Hamilton MG, Myles ST. **Pediatric spinal injury: review of 174 hospital admissions.** *J Neurosurg* 1992;77:700–04 CrossRef Medline
5. Hadley MN, Zabramski JM, Browner CM, et al. **Pediatric spinal trauma: review of 122 cases of spinal cord and vertebral column injuries.** *J Neurosurg* 1988;68:18–24 CrossRef Medline
6. Junewick JJ. **Pediatric craniocervical junction injuries.** *AJR Am J Roentgenol* 2011;196:1003–10 CrossRef Medline
7. Goldstein HE, Anderson RC. **Classification and management of pediatric craniocervical injuries.** *Neurosurg Clin N Am* 2017;28:73–90 CrossRef Medline
8. Birchansky S, Syed H, Jea A, et al. **Pediatric craniocervical metrics revisited: establishing landmark CT measurements of basion-cartilaginous dens interval (BCDI) in infants using soft tissue window.** In: *Proceeding of the American Society of Head and Neck Radiology 50th Annual Meeting*, Washington, DC. September 7–11, 2016
9. Junewick JJ, Meesa IR, Luttenton CR, et al. **Occult injury of the pediatric craniocervical junction.** *Emerg Radiol* 2009;16:483–88 CrossRef Medline
10. Grabb BC, Frye TA, Hedlund GL, et al. **MRI diagnosis of suspected atlanto-occipital dissociation in childhood.** *Pediatr Radiol* 1999;29:275–81 CrossRef Medline
11. O'Rahilly R, Müller F. **Developmental stages in human embryos: revised and new measurements.** *Cells Tissues Organs* 2010;192:73–84 CrossRef Medline
12. Hita-Contreras F, Roda O, Martinez-Amat A, et al. **Embryonic and early fetal period development and morphogenesis of human craniovertebral junction.** *Clin Anat* 2014;27:337–45 CrossRef Medline
13. Menezes AH. **Craniocervical developmental anatomy and its implications.** *Childs Nerv Syst* 2008;24:1109–22 CrossRef Medline

14. Raybaud C. **Anatomy and development of the craniovertebral junction.** *Neurol Sci* 2011;32(suppl 3):S267–70 CrossRef Medline
15. Pang D, Thompson DN. **Embryology and bony malformations of the craniovertebral junction.** *Childs Nerv Syst* 2011;27:523–64 CrossRef Medline
16. Akobo S, Rizk E, Loukas M, et al. **The odontoid process: a comprehensive review of its anatomy, embryology, and variations.** *Childs Nerv Syst* 2015;31:2025–34 CrossRef Medline
17. Lustrin ES, Karakas SP, Ortiz AO, et al. **Pediatric cervical spine: normal anatomy, variants, and trauma.** *Radiographics* 2003;23:539–60 CrossRef Medline
18. Ludwig KS. **Early development of atlas and occipital vertebra in man** [in German]. *Acta Anat (Basel)* 1957;30:444–61 CrossRef Medline
19. O'Rahilly R, Müller F, Meyer DB. **The human vertebral column at the end of the embryonic period proper, 2: the occipitocervical region.** *J Anat* 1983;136(pt 1):181–95 Medline
20. Abe H, Ishizawa A, Cho KH, et al. **Fetal development of the transverse atlantis and alar ligaments at the craniovertebral junction.** *Clin Anat* 2012;25:714–21 CrossRef Medline
21. Wholey MH, Bruwer AJ, Baker HL Jr. **The lateral roentgenogram of the neck; with comments on the atlanto-odontoid-basion relationship.** *Radiology* 1958;7:350–56 CrossRef Medline
22. Harris JH Jr, Carson GC, Wagner LK. **Radiologic diagnosis of traumatic occipitovertebral dissociation, 1: normal occipitovertebral relationships on lateral radiographs of supine subjects.** *AJR Am J Roentgenol* 1994;162:881–86 CrossRef Medline
23. Gonzalez LF, Fiorella D, Crawford NR, et al. **Vertical atlantoaxial distraction injuries: radiological criteria and clinical implications.** *J Neurosurg Spine* 2004;1:273–80 CrossRef Medline
24. Rojas CA, Bertozzi JC, Martinez CR, et al. **Reassessment of the craniocervical junction: normal values on CT.** *AJNR Am J Neuroradiol* 2007;28:1819–23 CrossRef Medline
25. Omercikoglu S, Altunbas E, Akoglu H, et al. **Normal values of cervical vertebral measurements according to age and sex in CT.** *Am J Emerg Med* 2017;35:383–90 CrossRef Medline
26. Bulas DI, Fitz CR, Johnson DL. **Traumatic atlanto-occipital dislocation in children.** *Radiology* 1993;188:1555–58 CrossRef Medline
27. Bertozzi JC, Rojas CA, Martinez CR. **Evaluation of the pediatric craniocervical junction on MDCT.** *AJR Am J Roentgenol* 2009;192:26–31 CrossRef Medline
28. Vachhrajani S, Sen AN, Satyan K, et al. **Estimation of normal computed tomography measurements for the upper cervical spine in the pediatric age group.** *J Neurosurg Pediatr* 2014;14:425–33 CrossRef Medline

Anterior Mesencephalic Cap Dysplasia: Novel Brain Stem Malformative Features Associated with Joubert Syndrome

F. Arrigoni, R. Romaniello, D. Peruzzo, A. De Luca, C. Parazzini, E.M. Valente, R. Borgatti, and F. Triulzi

ABSTRACT

SUMMARY: In Joubert syndrome, the "molar tooth" sign can be associated with several additional supra- and infratentorial malformations. Here we report on 3 subjects (2 siblings, 8–14 years of age) with Joubert syndrome, showing an abnormal thick bulging of the anterior profile of the mesencephalon causing a complete obliteration of the interpeduncular fossa. DTI revealed that the abnormal tissue consisted of an ectopic white matter tract with a laterolateral transverse orientation. Tractographic reconstructions support the hypothesis of impaired axonal guidance mechanisms responsible for the malformation. The 2 siblings were compound heterozygous for 2 missense variants in the *TMEM67* gene, while no mutations in a panel of 120 ciliary genes were detected in the third patient. The name "anterior mesencephalic cap dysplasia," referring to the peculiar aspect of the mesencephalon on sagittal MR imaging, is proposed for this new malformative feature.

ABBREVIATIONS: AMCD = anterior mesencephalic cap dysplasia; CST = corticospinal tract; IQ = Intelligence Quotient; JS = Joubert syndrome; SCP = superior cerebellar peduncle

The "molar tooth" sign is the distinctive imaging feature and a mandatory criterion for the diagnosis of Joubert syndrome (JS), a rare group of conditions characterized by a complex malformation of the midbrain-hindbrain. The molar tooth sign owes its name to the appearance of the pons and superior cerebellar peduncles (SCPs) on axial MR images, resembling a molar tooth. It is related to a moderate-to-severe vermian hypodysplasia, associated with a narrow pontine-mesencephalic junction and a thickened, elongated, horizontal SCP.[1]

The typical clinical signs of JS (episodic hyperpnea, abnormal eye movements, developmental delay, and ataxia[2]) may be associated with heterogeneous neurologic and non-neurologic symptoms and defects in other organs, including the kidneys, retina, liver, and skeleton,[1,3,4] giving rise to an extremely large spectrum of phenotypes, from relatively mild to severe conditions.[5]

JS is part of an expanding group of disorders called ciliopathies, caused by dysfunction of the primary cilium, a ubiquitous subcellular organelle that plays a key role in brain development and in many cellular functions.[6] To date, >35 genes encoding for proteins of the primary cilium or its apparatus have been identified as causing JS[5,7]; however, many patients remain undiagnosed; thus, further genetic heterogeneity is suggested.

The variable degree of vermian hypodysplasia and the presence of associated supratentorial findings (hippocampal malrotation, callosal dysgenesis, migration disorders, hypothalamic hamartomas, cephaloceles, and ventriculomegaly) may further complicate the spectrum.[8,9]

We report on 3 patients from 2 different families (2 brothers with genetically defined JS and 1 unrelated girl), presenting an additional complex malformation of the brain stem characterized by an abnormal thick bulging of the anterior profile of the mesencephalon. DTI revealed that the abnormal tissue consisted of an ectopic bundle of white matter with a laterolateral transverse orientation, likely resulting from impaired axonal guidance mechanisms during the early stages of brain development.

Received March 9, 2017; accepted after revision June 30.

From the Neuroimaging Lab (F.A., D.P., A.D.L.) and Neuropsychiatry and Neurorehabilitation Unit (R.R., R.B.), Scientific Institute Istituto Di Ricovero e Cura a Carattere Scientific Eugenio Medea, Bosisio Parini, Italy; Department of Information Engineering (A.D.L.), University of Padova, Padova, Italy; Department of Pediatric Radiology and Neuroradiology (C.P.), "V. Buzzi" Children's Hospital, Milan, Italy; Department of Molecular Medicine (E.M.V.), University of Pavia, Pavia, Italy; Neurogenetics Unit (E.M.V.), Istituto Di Ricovero e Cura a Carattere Scientific Santa Lucia Foundation, Rome, Italy; and Department of Neuroradiology (F.T.), Scientific Institute Istituto Di Ricovero e Cura a Carattere Scientific Cà Granda Foundation—Ospedale Maggiore Policlinico, Milan, Italy.

This work was supported by the Italian Ministry of Health (Ricerca Corrente 2016–17) and by the European Research Council Starting Grant 260888.

Paper previously presented at: Annual Meeting of the European Society of Neuroradiology, September 13–17, 2017; Malmö, Sweden.

Please address correspondence to Filippo Arrigoni, MD, Neuroimaging Lab, Scientific Institute IRCCS Eugenio Medea, Via Don Luigi Monza 20, 23842 Bosisio Parini, Italy; e-mail: filippo.arrigoni@bp.lnf.it

Indicates open access to non-subscribers at www.ajnr.org

Indicates article with supplemental on-line table.

http://dx.doi.org/10.3174/ajnr.A5360

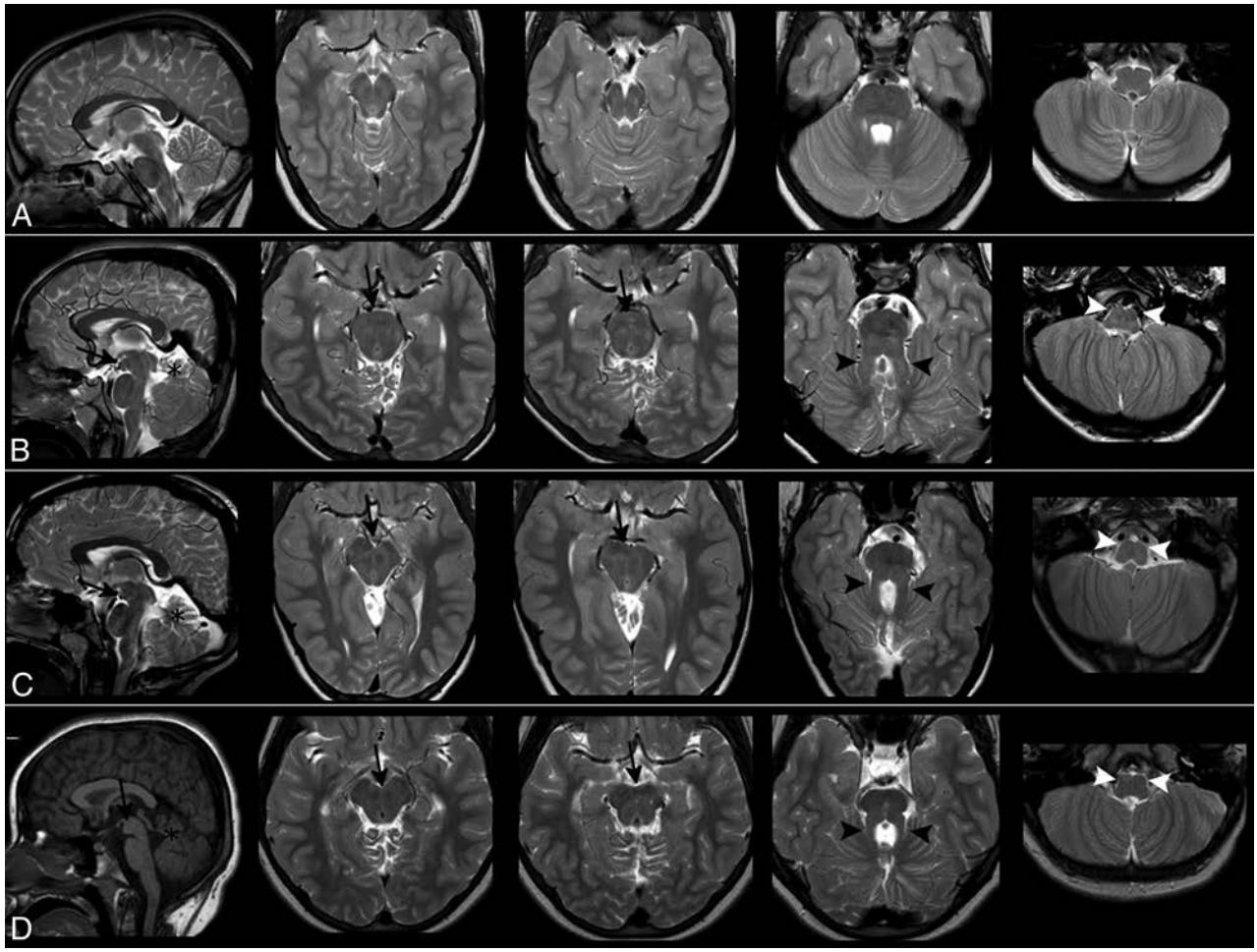

FIG 1. Morphologic findings. Images show T1- and T2-weighted sagittal and axial sections of a healthy subject (row *A*), patient 1 (row *B*), patient 2 (row *C*), and patient 3 (row *D*). In the 3 patients, the mesencephalon shows an anterior bulging (*black arrows*) that fills the interpeduncular cistern, visible both on sagittal and axial sections. The signal intensity of the abnormal mass is like that of white matter. Patients also share the classic features of mesial temporal sclerosis: cerebellar hypodysplasia (*black asterisks*), a thickened and horizontal SCP (*black arrowheads*), and hypoplasia of the medullary pyramids and inferior olivary nuclei (*white arrowheads*).

MATERIALS AND METHODS

Neuroimaging Data

Patients underwent MR imaging studies on either 3T (patients 1 and 2) or 1.5T (patient 3) scanners at 2 different institutions (Eugenio Medea Research Institute and "V. Buzzi" Children's Hospital). Axial and coronal T2-weighted (thickness, 3 mm), axial and coronal FLAIR (thickness, 3 mm), and 3D T1-weighted echo-spoiled gradient-echo images (voxel size, 1 mm^3) were acquired. Balanced steady-state free precession sequences were acquired at 3T to evaluate the cranial nerves. High-resolution DTI data (voxel size, 2 mm^3; b-values, 0, 300, 1100 s/mm^2; number of directions, 32) were available for the 2 patients examined at 3T, while the third patient had low-resolution DTI (voxel size, 3 mm^3; b-values, 0, 1100 s/mm^2; number of directions, 15).

DTI data were preprocessed with the DIFF_PREP module of TORTOISE (https://science.nichd.nih.gov/confluence/display/nihpd/TORTOISE) to remove motion and eddy current artifacts; then, correction of geometric EPI distortions was performed with DR-BUDDI using the dual-phase encoding acquisition.[10] Fiber tractography was performed with TrackVis (http://www.trackvis.org/dtk/)[11] in patients 1 and 2. We did not perform tractography in patient 3 because of the lower quality (ie, signal-to-noise ratio, resolution) of the data.

Clinical and Genetic Data

Neurologic, neuropsychological, and instrumental evaluations as well as genetic analysis were performed in all patients.

The local ethics committee approved the study. Written informed consent was obtained from all participating families.

RESULTS

Neuroimaging

The 3 patients showed a complex brain stem and cerebellar malformation, with normal findings in the supratentorial brain.

The main features of the common midbrain-hindbrain malformation were the following:

- A severe vermian hypodysplasia with a thickened, horizontal SCP determining a molar tooth shape of the superior brain stem on axial images (Fig 1)
- A flattening of the inferior olives and medullary pyramids (Fig 1)

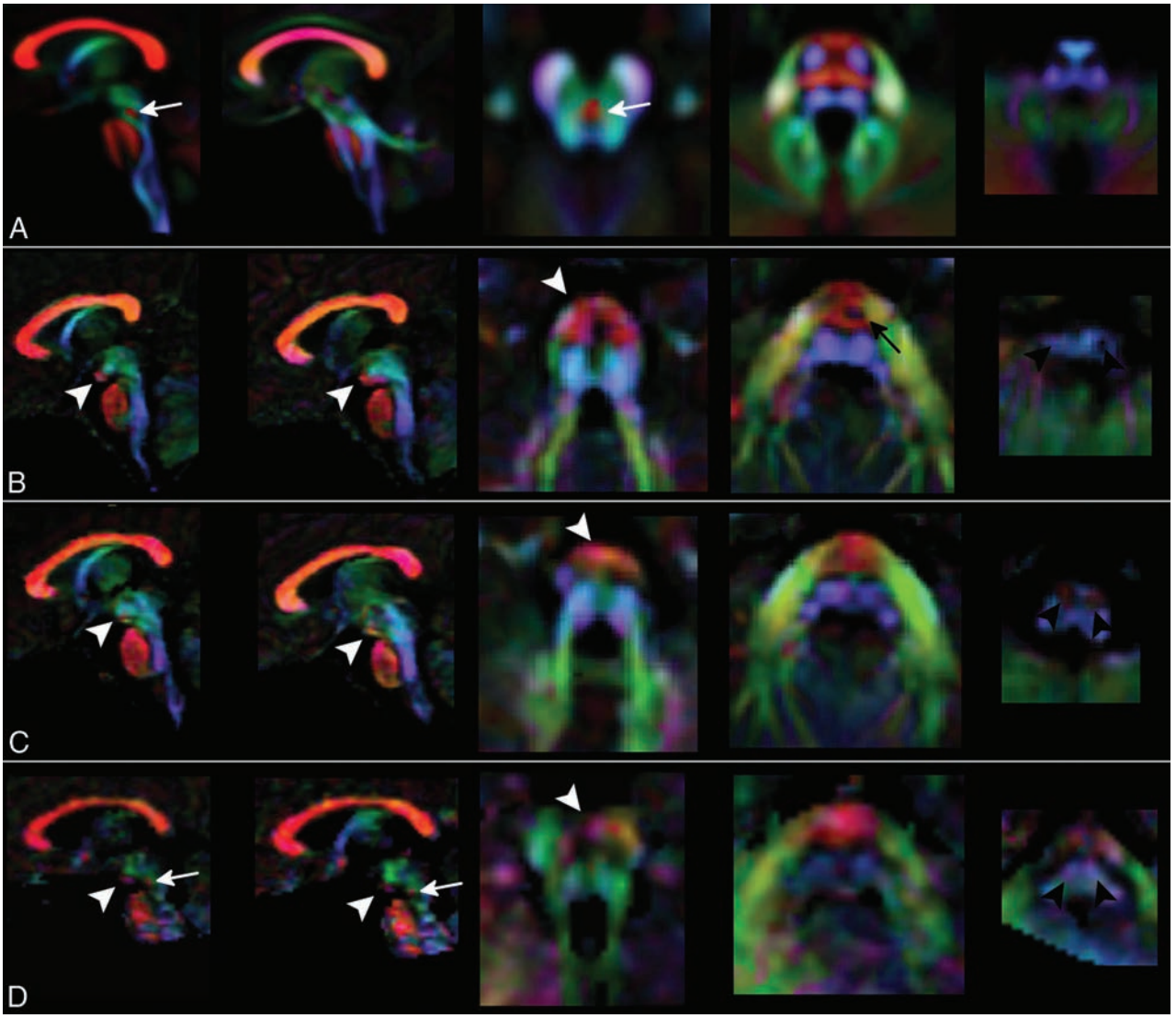

FIG 2. Color-coded DTI maps. Patients 1 (row *B*), 2 (row *C*), and 3 (row *D*) show an altered organization of white matter tracts if compared with a template of healthy subjects (row *A*). The anterior bulging of the mesencephalon corresponds to an area of transversely oriented diffusivity located anteriorly in the interpeduncular fossa (*white arrowheads*). CSTs in the pons are thinned (*black arrow*) or not clearly recognizable, and transverse pontine fibers appear as a unique bundle displaced in the anterior part of the pons. In the medulla, CST and lemnisci are hypoplastic/atrophic and the olives are reduced in volume. The decussation of SCP (*white arrow* in the normal template) is absent in patients 1 and 2 and markedly thinned in patient 3 (*white arrows* in *D*). Red, green, and blue represent areas of transverse, anteroposterior, and caudocranial orientation of diffusivity and white matter, respectively.

- A narrow isthmus, with a thin pontine-mesencephalic junction
- A thickened tectum on the sagittal plane in patient 1
- An abnormal bulging of the anterior profile of the mesencephalon on sagittal planes. On axial images, such bulging resulted in a complete obliteration of the interpeduncular fossa, giving to the mesencephalon a more rounded anterior profile. Most interesting, the ectopic mass had the same signal intensity as white matter in all MR imaging weightings, and it did not look like a single, nodular interpeduncular structure (Fig 1).
- The third, fifth, sixth, seventh, and eighth cranial nerves could be recognized. The trochlear nerves were not identified, probably because of technical limits; extraocular muscles, including the oblique superior muscles, appeared regular in terms of signal intensity and volume. The optic nerves were thinned in patient 3.
- Cranial nerves IX and X could be detected on balanced steady-state free precession sequences in patients 1 and 2. Patient 1 showed an agenesis of the left cranial nerve XII. The lower cranial nerves could not be assessed in patient 3.
- Color-encoded DTI maps and tractography reconstructions revealed that the anterior mesencephalic bulging corresponded to a transversely orientated white matter tract in the interpeduncular cistern (Fig 2). On tractography, an apparent merging of corticospinal tracts (CSTs) with the abnormal mesencephalic bundle could be suspected.
- On color-encoded DTI maps, CSTs could be regularly recognized only until the upper part of the pons (Fig 2). On tractography, pontine transverse fibers and middle cerebellar peduncles appeared as a thick unique bundle anteriorly displaced in the pons (Fig 3). The SCPs were thickened, while the inferior cerebellar peduncles were atrophic in patient 1. SCP decussation was absent in patients 1 and 2, and it was thinned in patient 3.

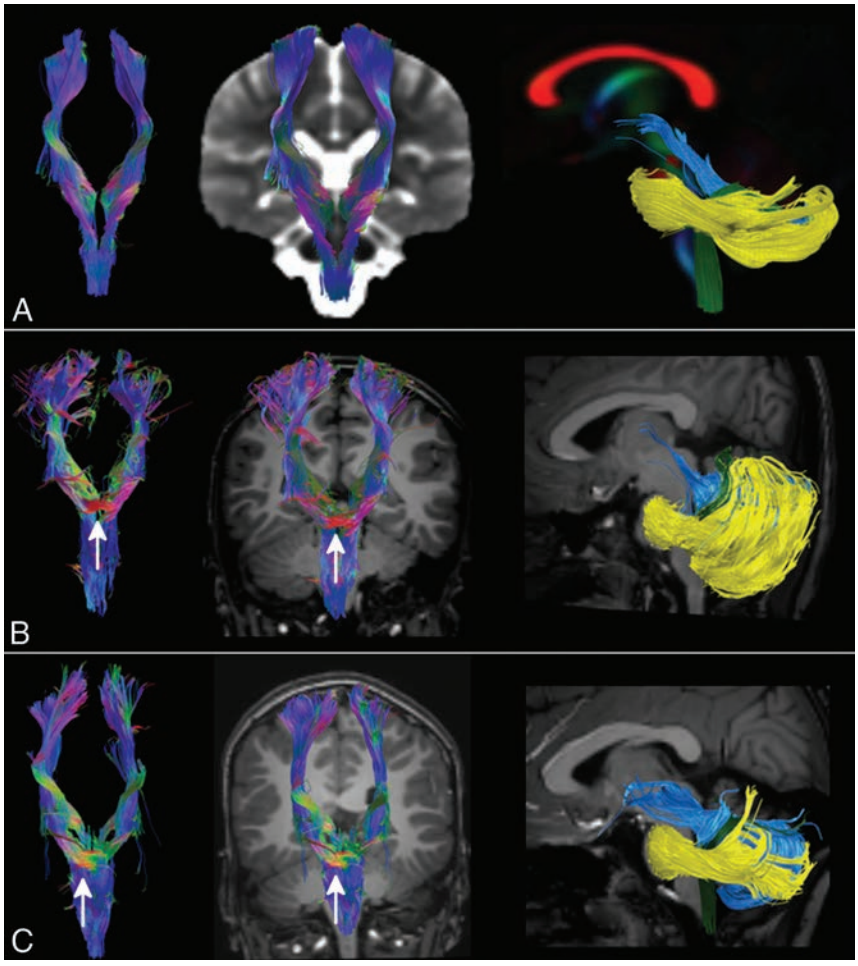

FIG 3. Tractography. CST (first 2 columns) and cerebellar peduncles (last column) were reconstructed with DTI data and the FACT algorithm from a template of healthy subjects (row *A*) and in patients 1 and 2 (rows *B* and *C*). The ectopic mass seen on morphologic sections corresponds to a transvers bundle that seems to be located along the CST (*white arrow*). No transverse fibers are seen in the normal CST at the same level (row *A*). SCPs (*light blue tract* in the last column) of both patients are thickened and more horizontal than normal and do not pass through the anterior mesencephalon. The inferior cerebellar peduncles (*green tract*) in patient 1 are thinned, while in both patients, the middle cerebellar peduncles (*yellow tract*) are displaced anteriorly in the pons.

Genetic Findings

Clinical and genetic findings of the 2 siblings were reported in 2009 as part of a molecular genetic screening of the *TMEM67* gene in patients with JS. They both were compound heterozygous for *TMEM67* missense variants c. 1115C>A/p.(T372K) and c.2345A>G/p.(H782R), which were inherited from the healthy father and mother, respectively (Family COR32 in Brancati et al[12]). The third patient underwent next-generation sequencing-based analysis of a panel of 120 ciliopathy-related genes,[13] which failed to identify any pathogenic variant.

Clinical Findings

Patient 1 is now a 14-year-old boy. He had impaired psychomotor development, with delayed motor acquisitions (able to walk independently at 6 years of age) and absence of expressive language. Currently, he can use sign language and is able to read and write words in uppercase letters. Good social skills are present. Neurologic examination showed diffuse hypotonia, nystagmus, oculomotor apraxia, dysmetria, severe oromotor dyspraxia, and gait ataxia. Cognitive testing showed moderate intellectual disability (Wechsler Intelligence Scale for Children-Revised, Third Edition; Intelligence Quotient [IQ] = 46 at performance subitems). Visual assessment detected a reduced visual acuity and bilateral optical nerve coloboma. The right kidney was polycystic and atrophic, while the left one showed compensatory hypertrophy at sonography. Liver biopsy at 8 years of age documented congenital hepatic fibrosis associated with mild portal hypertension, normal liver functioning, and the absence of esophageal varices.

Patient 2 is an 8-year-old boy. As with his older brother, he had delayed psychomotor development, walking unaided at 3 years of age and lacking any expressive language. Currently, he uses sign language with good social interactions and skills. Diffuse hypotonia, dysmetria, oromotor dyspraxia, and gait ataxia with moderate intellectual disability (Performance IQ = 41) were evident at neurologic examination. A liver biopsy performed at 4 years of age demonstrated congenital hepatic fibrosis, hepatosplenomegaly, portal hypertension, and small esophageal varices. He also had an increase of transaminase and γ glutamyltranspeptidase levels and thrombocytopenia secondary to hypersplenism.

Patient 3 is an 11-year-old girl, the only child of consanguineous healthy parents (second-grade cousins). She presented early in life with mild motor delay, severe intellectual impairment, marked visual deficits, and nystagmus. On the latest neurologic examination, she presented with severe intellectual disability with poor expressive language and social skills, diffuse hypotonia, and clumsiness. She had severe visual impairment (1/50 bilaterally), nystagmus, and roving ocular movements. Fundus oculi showed nerve optic hypoplasia and small vessels, and electroretinography could not elicit any response. Abdominal sonography and audiometric evaluation findings were normal.

Clinical findings and instrumental evaluation are summarized in the On-line Table.

DISCUSSION

The presence of an anterior mesencephalic bulging due to an ectopic transverse white matter bundle represents a new malformative pattern of the midbrain for which we propose the name "anterior mesencephalic cap dysplasia" (AMCD). This definition is adopted and adapted from a previously described malformation of the brain stem, pontine tegmental cap dysplasia,[14] which shares some common features with AMCD. In both cases, the

sagittal profile of the brain stem shows an abnormal "cap," which, in AMCD, is located anteriorly, at the mesencephalic level, while in pontine tegmental cap dysplasia, the cap is located posteriorly at the pontine level. Moreover, in both cases, on axial sections and DTI, the cap looks like a white matter ectopic bundle with a transverse laterolateral orientation.

Other diagnoses, like tumors, metastasis, or other proliferative disorders, could be easily excluded, considering their signal intensity and expansive/infiltrative features.

The presence of an interpeduncular mass in patients with JS was previously reported by Harting et al,[15] who described 3 patients with a nodular structure within the interpeduncular fossa. Similar tissue can also be depicted, but not discussed, in several articles by Huppke et al[16] and Alorainy et al.[17] Interpeduncular masses in JS probably represent a continuum, but we believe that according to their appearance on both morphologic sequences and DTI, a distinction between pedunculated and nonpedunculated structures can be maintained. Interpeduncolar heterotopia is a nodular rounded structure, isointense to gray matter, with a peduncle that connects the mass to the brain stem, while AMCD is isointense to white matter, has no peduncle, and completely fills the interpeduncular fossa. Moreover, in AMCD, DTI confirmed the presence of an ectopic transverse white matter bundle anterior to the mesencephalon. Most interesting, according to tractographic reconstructions, the bundle appears to be in continuity with corticospinal tracts and may represent an ectopic decussation of the motor tracts. Careful interpretation of these findings is needed because the algorithm we used for tractography has limitations in resolving crossing or sharply angulated fibers,[18] which are better handled by more sophisticated approaches, such as high angular resolution diffusion imaging (HARDI). Unfortunately, because of the characteristics of our protocol (low b-values, few diffusion directions), spheric deconvolution–based tractography did not improve the resolution of the tracts.

Anomalies in tract decussations (both CST and SCP) have been frequently described in neuropathologic reports of patients with JS.[19-23] Moreover, the absence of CST decussation has been described in other conditions such as occipital encephalocele, Dandy-Walker malformation, Möbius syndrome, horizontal gaze palsy and progressive scoliosis, L1 syndrome, Kallmann syndrome, and trisomy 18,[24,25] while there is no report of aberrant ectopic mesencephalic decussation.

More recently, Poretti et al[9] described a convex protuberance of the ventral contour of the midbrain due to a nodular structure in 13 of 110 patients with JS, expanding the findings from Harting et al.[15] No DTI data are shown, and the lesions are interpreted as gray matter heterotopias; however, the possibility of ectopic white matter projections is left open.

Only a single case has been previously reported of a fetus with JS at 22 weeks' gestation, showing AMCD both at MR imaging and postmortem histology.[26] As in our patients, in utero- and histology-based tractography confirmed the abnormal projection of the CSTs into the interpeduncular cistern. Both in the fetus and in our patients, the motor tracts were atrophic/barely recognizable in the pons and medulla.

The alternative hypothesis that the abnormal mesencephalic bundle represents an ectopic, aberrant white matter tract connecting either the cerebral or cerebellar hemispheres cannot be completely discarded, even if it is not supported by tractography. We also hypothesized that the tract could represent the decussation of the SCP displaced anteriorly, but in patient 3, SCP decussation was present (even if uncommon in JS, the persistence of SCP decussation is not exceptional because it was already reported in neuropathologic studies[21]); in the 2 siblings, we could not identify a direct connection between SCP and the bundle. Pathologic confirmation is needed to fully understand the course of the abnormal tract and its origin.

Mirror movements, often associated with abnormal pyramidal decussation, resulting in bilateral CST projections to the spinal cord were not detected in our patients.[27] Functional MR imaging during motor tasks would be of help to verify the decussation of the CST, but it could not be performed due to the insufficient cooperation of patients.

The 2 siblings had mutations in the *TMEM67* gene, a ciliary gene that is expressed in the brain midline, hindbrain, retina, kidney, liver, and developing sphenoid bone and plays a fundamental role in centriole migration to the apical membrane and formation of the primary cilium.[28] Most interesting, *TMEM67* represents the gene for which the strongest gene-phenotype correlates have been drawn.[29-31] In fact, nearly all patient with JS and the *TMEM67* mutation have congenital liver fibrosis, variably associated with optic nerve or chorioretinal coloboma, retinal dystrophy, and renal involvement (COACH syndrome).[32-34]

Mounting evidence suggests a central role for the primary cilia in modulating neurogenesis, cell polarity, axonal guidance, and possibly adult neuronal functions.[5,6] The lack of decussation of the CST and SCP reported in neuropathologic and DTI tractography studies of patients with JS suggested that defective primary cilia could also impair the process of axonal guidance, and the presence of an aberrant/ectopic white matter tract in patients with a proved ciliopathy can further support this theory.

Aberrant or ectopic white matter tracts have been detected in a wide spectrum of malformations involving the brain stem and corpus callosum,[26,35-40] as a result of defects in axonal guidance or other mechanisms. The advent of high-resolution MR imaging and DTI along with the advances in genetic technologies helped to define and expand human disorders of axon guidance and will probably contribute to the discovery of many additional similar conditions in the future.

CONCLUSIONS

Through high-resolution MR imaging, DTI, and tractography, we demonstrated that nonpedunculated interpeduncular tissue in JS may represent an ectopic transverse white matter tract located in the mesencephalon, for which the name "AMCD" is proposed.

ACKNOWLEDGMENTS

We are grateful to patients and their family for cooperation in this study.

Disclosures: Filippo Arrigoni—*RELATED*: *Grant*: Italian Ministry of Health, *Comments*: Ricerca Corrente 2016.* Enza Maria Valente—*RELATED*: *Grant*: European Research Council, *Comments*: European Research Council Starting Grant 260888 to E.M.V.*; *UNRELATED*: *Board Membership*: Pediatric Research, *Comments*: Genetic Section Editor, Pediatric Research; *Grants/Grants Pending*: Telethon Italy, Italian

Ministry of Health, Italian Ministry of University and Research.* *Money paid to the institution.

REFERENCES

1. Romani M, Micalizzi A, Valente EM. **Joubert syndrome: congenital cerebellar ataxia with the molar tooth.** *Lancet Neurol* 2013;12:894–905 CrossRef Medline
2. Joubert M, Eisenring JJ, Robb JP, et al. **Familial agenesis of the cerebellar vermis: a syndrome of episodic hyperpnea, abnormal eye movements, ataxia, and retardation.** *Neurology* 1969;19:813–25 CrossRef Medline
3. Zaki MS, Abdel-Aleem A, Abdel-Salam G, et al. **The molar tooth sign: a new Joubert syndrome and related cerebellar disorders classification system tested in Egyptian families.** *Neurology* 2008;70:556–65 CrossRef Medline
4. Valente EM, Brancati F, Dallapiccola B. **Genotypes and phenotypes of Joubert syndrome and related disorders.** *Eur J Med Genet* 2008;51:1–23 CrossRef Medline
5. Mitchison HM, Valente EM. **Motile and non-motile cilia in human pathology: from function to phenotypes.** *J Pathol* 2017;241:294–309 CrossRef Medline
6. Engle EC. **Human genetic disorders of axon guidance.** *Cold Spring Harb Perspect Biol* 2010;2:a001784 CrossRef Medline
7. Vilboux T, Doherty DA, Glass IA, et al. **Molecular genetic findings and clinical correlations in 100 patients with Joubert syndrome and related disorders prospectively evaluated at a single center.** *Genet Med* 2017 Jan 26. [Epub ahead of print] CrossRef Medline
8. Poretti A, Huisman TA, Scheer I, et al. **Joubert syndrome and related disorders: spectrum of neuroimaging findings in 75 patients.** *AJNR Am J Neuroradiol* 2011;32:1459–63 CrossRef Medline
9. Poretti A, Snow J, Summers AC, et al. **Joubert syndrome: neuroimaging findings in 110 patients in correlation with cognitive function and genetic cause.** *J Med Genet* 2017 Jan 13. [Epub ahead of print] CrossRef Medline
10. Pierpaoli C, Walker L, Irfanoglu MO, et al. **Tortoise: an integrated software package for processing of diffusion MRI data.** In: *Proceedings of the International Society of Magnetic Resonance in Medicine,* Stockholm, Sweden. May 1–7, 2010:1597
11. Wang R, Benner T, Sorensen AG, et al. **Diffusion toolkit: a software package for diffusion imaging data processing and tractography.** In: *Proceedings of the International Society of Magnetic Resonance in Medicine,* Berlin, Germany. May 19–25, 2007:3720
12. Brancati F, Iannicelli M, Travaglini L, et al; International JSRD Study Group. **MKS3/TMEM67 mutations are a major cause of COACH Syndrome, a Joubert syndrome related disorder with liver involvement.** *Hum Mutat* 2009;30:E432–42 CrossRef Medline
13. Roosing S, Romani M, Isrie M, et al. **Mutations in CEP120 cause Joubert syndrome as well as complex ciliopathy phenotypes.** *J Med Genet* 2016;53:608–15 CrossRef Medline
14. Barth PG, Majoie CB, Caan MWA, et al. **Pontine tegmental cap dysplasia: a novel brain malformation with a defect in axonal guidance.** *Brain* 2007;130:2258–66 CrossRef Medline
15. Harting I, Kotzaeridou U, Poretti A, et al. **Interpeduncular heterotopia in Joubert syndrome: a previously undescribed MR finding.** *AJNR Am J Neuroradiol* 2011;32:1286–89 CrossRef Medline
16. Huppke P, Wegener E, Böhrer-Rabel H, et al. **Tectonic gene mutations in patients with Joubert syndrome.** *Eur J Hum Genet* 2015;23:616–20 CrossRef Medline
17. Alorainy IA, Sabir S, Seidahmed MZ, et al. **Brain stem and cerebellar findings in Joubert syndrome.** *J Comput Assist Tomogr* 2006;30:116–21 CrossRef Medline
18. Jeurissen B, Leemans A, Tournier J-D, et al. **Investigating the prevalence of complex fiber configurations in white matter tissue with diffusion magnetic resonance imaging.** *Hum Brain Mapp* 2013;34:2747–66 CrossRef Medline
19. Friede RL, Boltshauser E. **Uncommon syndromes of cerebellar vermis aplasia, I: Joubert syndrome.** *Dev Med Child Neurol* 1978;20:758–63 Medline
20. Yachnis AT, Rorke LB. **Neuropathology of Joubert syndrome.** *J Child Neurol* 1999;14:655–59; discussion 669–72 CrossRef Medline
21. Ferland RJ, Eyaid W, Collura RV, et al. **Abnormal cerebellar development and axonal decussation due to mutations in AHI1 in Joubert syndrome.** *Nat Genet* 2004;36:1008–13 CrossRef Medline
22. Juric-Sekhar G, Adkins J, Doherty D, et al. **Joubert syndrome: brain and spinal cord malformations in genotyped cases and implications for neurodevelopmental functions of primary cilia.** *Acta Neuropathol* 2012;123:695–709 CrossRef Medline
23. Poretti A, Boltshauser E, Loenneker T, et al. **Diffusion tensor imaging in Joubert syndrome.** *AJNR Am J Neuroradiol* 2007;28:1929–33 CrossRef Medline
24. Miyata H, Miyata M, Ohama E. **Pyramidal tract abnormalities in the human fetus and infant with trisomy 18 syndrome.** *Neuropathology* 2014;34:219–26 CrossRef Medline
25. ten Donkelaar HJ, Lammens M, Wesseling P, et al. **Development and malformations of the human pyramidal tract.** *J Neurol* 2004;251:1429–42 CrossRef Medline
26. Mitter C, Jakab A, Brugger PC, et al. **Validation of in utero tractography of human fetal commissural and internal capsule fibers with histological structure tensor analysis.** *Front Neuroanat* 2015;9:164 CrossRef Medline
27. Welniarz Q, Dusart I, Roze E. **The corticospinal tract: evolution, development, and human disorders.** *Dev Neurobiol* 2017;77:810–29 CrossRef Medline
28. Dawe HR, Smith UM, Cullinane AR, et al. **The Meckel-Gruber syndrome proteins MKS1 and meckelin interact and are required for primary cilium formation.** *Hum Mol Genet* 2007;16:173–86 Medline
29. Smith UM, Consugar M, Tee LJ, et al. **The transmembrane protein meckelin (MKS3) is mutated in Meckel-Gruber syndrome and the wpk rat.** *Nat Genet* 2006;38:191–16 CrossRef Medline
30. Baala L, Khaddour R, Saunier S, et al. **The Meckel-Gruber syndrome gene, MKS3, is mutated in Joubert syndrome.** *Am J Hum Genet* 2007;80:186–94 CrossRef Medline
31. Suzuki T, Miyake N, Tsurusaki Y, et al. **Molecular genetic analysis of 30 families with Joubert syndrome.** *Clin Genet* 2016;90:526–35 CrossRef Medline
32. Otto EA, Tory K, Attanasio M, et al. **Hypomorphic mutations in meckelin (MKS3/TMEM67) cause nephronophthisis with liver fibrosis (NPHP11).** *J Med Genet* 2009;46:663–70 CrossRef Medline
33. Iannicelli M, Brancati F, Mougou-Zerelli S, et al; International JSRD Study Group. **Novel TMEM67 mutations and genotype-phenotype correlates in meckelin-related ciliopathies.** *Hum Mutat* 2010;31:E1319–31 CrossRef Medline
34. Bachmann-Gagescu R, Phelps IG, Dempsey JC, et al. **KIAA0586 is mutated in Joubert syndrome.** *Hum Mutat* 2015;36:831–35 CrossRef Medline
35. Poretti A, Meoded A, Rossi A, et al. **Diffusion tensor imaging and fiber tractography in brain malformations.** *Pediatr Radiol* 2013;43:28–54 CrossRef Medline
36. Briguglio M, Pinelli L, Giordano L, et al. **Pontine tegmental cap dysplasia: developmental and cognitive outcome in three adolescent patients.** *Orphanet J Rare Dis* 2011;6:36 CrossRef Medline
37. Haller S, Wetzel SG, Lütschg J. **Functional MRI, DTI and neurophysiology in horizontal gaze palsy with progressive scoliosis.** *Neuroradiology* 2008;50:453–59 CrossRef Medline
38. Caan MW, Barth PG, Niermeijer JM, et al. **Ectopic peripontine arcuate fibres, a novel finding in pontine tegmental cap dysplasia.** *Eur J Paediatr Neurol* 2014;18:434–38 CrossRef Medline
39. Sicotte NL, Salamon G, Shattuck DW, et al. **Diffusion tensor MRI shows abnormal brainstem crossing fibers associated with ROBO3 mutations.** *Neurology* 2006;67:519–21 CrossRef Medline
40. Arrigoni F, Romaniello R, Peruzzo D, et al. **Aberrant supracallosal longitudinal bundle: MR features, pathogenesis and associated clinical phenotype.** *Eur Radiol* 2016;26:2587–96 CrossRef Medline

Predictive Models in Differentiating Vertebral Lesions Using Multiparametric MRI

R. Rathore, A. Parihar, D.K. Dwivedi, A.K. Dwivedi, N. Kohli, R.K. Garg, and A. Chandra

ABSTRACT

BACKGROUND AND PURPOSE: Conventional MR imaging has high sensitivity but limited specificity in differentiating various vertebral lesions. We aimed to assess the ability of multiparametric MR imaging in differentiating spinal vertebral lesions and to develop statistical models for predicting the probability of malignant vertebral lesions.

MATERIALS AND METHODS: One hundred twenty-six consecutive patients underwent multiparametric MRI (conventional MR imaging, diffusion-weighted MR imaging, and in-phase/opposed-phase imaging) for vertebral lesions. Vertebral lesions were divided into 3 subgroups: infectious, noninfectious benign, and malignant. The cutoffs for apparent diffusion coefficient (expressed as 10^{-3} mm^2/s) and signal intensity ratio values were calculated, and 3 predictive models were established for differentiating these subgroups.

RESULTS: Of the lesions of the 126 patients, 62 were infectious, 22 were noninfectious benign, and 42 were malignant. The mean ADC was 1.23 ± 0.16 for infectious, 1.41 ± 0.31 for noninfectious benign, and 1.01 ± 0.22 mm^2/s for malignant lesions. The mean signal intensity ratio was 0.80 ± 0.13 for infectious, 0.75 ± 0.19 for noninfectious benign, and 0.98 ± 0.11 for the malignant group. The combination of ADC and signal intensity ratio showed strong discriminatory ability to differentiate lesion type. We found an area under the curve of 0.92 for the predictive model in differentiating infectious from malignant lesions and an area under the curve of 0.91 for the predictive model in differentiating noninfectious benign from malignant lesions. On the basis of the mean ADC and signal intensity ratio, we established automated statistical models that would be helpful in differentiating vertebral lesions.

CONCLUSIONS: Our study shows that multiparametric MRI differentiates various vertebral lesions, and we established prediction models for the same.

ABBREVIATIONS: AUC = area under the curve; FNA = fine-needle aspiration; GPI = infectious; GPN = noninfectious benign; GPM = malignant; mpMRI = multiparametric MRI; SE = sensitivity; SIR = signal intensity ratio; Sp = specificity

MR imaging is the preferred technique in the diagnostic work-up of benign and malignant vertebral lesions. Morphologic criteria alone could not differentiate benign and malignant spinal lesions in 6%–21% of cases.[1-3] Due to the limited specificity of conventional MR imaging,[4] radiologists often have trouble differentiating common spinal pathologies such as osteoporotic vertebral collapse, infectious spondylodiscitis, and metastasis. Recently, multiparametric MR imaging (mpMRI) has shown the ability to localize, detect, and stage various diseases.[5-8] The mpMRI approach combines anatomic sequences (T1- and T2-weighted MR imaging) with functional imaging sequences. Functional and quantitative MR imaging methods, such as DWI, dynamic contrast-enhanced MR imaging, and in-phase/opposed-phase imaging, measure the Brownian motion of water molecules, regional vascular properties of the tumor, and fat quantification, respectively.[6-9]

DWI has been used in the differentiation of benign and malignant spinal lesions.[10-12] Signal characteristics of vertebral lesions were evaluated on DWI for qualitative assessment, and the ADC was calculated for quantitative analysis. In general, malignant lesions yield lower ADC compared with noninfectious benign and infectious lesions due to increased cellularity and decreased extracellular space in malignant lesions.[10-12] In-phase/opposed-phase MR imaging quantifies fat in tissues and has been used in lesions of the adrenal gland and liver.[13-17] It has also been used in diagnostic work-up of spinal lesions, and the results demonstrated a

Received April 6, 2017; accepted after revision July 22.

From the Departments of Radiodiagnosis (R.R., A.P., D.K.D., N.K.), Neurology (R.K.G.), and Neurosurgery (A.C.), King George's Medical University, Lucknow, Uttar Pradesh, India; and Division of Biostatistics & Epidemiology (A.K.D.), Department of Biomedical Sciences, Texas Tech University Health Sciences Center, El Paso, Texas.

Please address correspondence to Anit Parihar, MD, Department of Radiodiagnosis, King George's Medical University, Lucknow, UP, India—226003; e-mail: anitparihar@gmail.com

Indicates article with supplemental on-line tables.

Indicates article with supplemental on-line photos.

http://dx.doi.org/10.3174/ajnr.A5411

significant difference in the signal intensity ratio (SIR) between benign and malignant vertebral lesions.[9,18-21]

The hypothesis for this study was that the mpMRI approach would increase the discriminatory ability of different vertebral lesions. The aim of the present study was to evaluate the ability of mpMRI in differentiating vertebral lesions and to establish statistical models for predicting the probability of malignant (GPM) lesions compared with noninfectious benign (GPN) and infectious (GPI) ones. The cutoffs of the ADC and SIR values were obtained to differentiate GPM lesions from GPI and GPN lesions. Furthermore, we considered GPI and GPN as all benign compared with the malignant lesions. The cutoff values of the ADC and SIR for differentiating malignant from all benign lesions were also obtained.

Although attempts have been made to assess the role of quantitative DWI or in-phase/opposed-phase imaging in differentiating vertebral lesions, to the best of our knowledge, no previous study has evaluated the ability of mpMRI to differentiate malignant or infectious lesions from noninfectious benign lesions.

MATERIALS AND METHODS

Patients and Inclusion Criteria

The institutional ethics committee of King George's Medical University approved this prospective cross-sectional study. All patients gave written informed consent before MR imaging. We included all consecutive patients presenting with vertebral lesions on spine MR imaging between July 2011 and August 2015 who also had CT-guided fine-needle aspiration cytology/biopsy in the absence of trauma. We performed CT-guided fine-needle aspiration (FNA)/biopsy on the basis of clinical indications communicated by the referring department and/or mpMRI findings. We used CT-guided FNA/biopsy (cytohistology/biopsy culture) as a reference standard test. We excluded 9 patients: 5 with motion artifacts and 4 due to indeterminate results of the biopsy. As a result, a cohort of 126 patients was included in the analysis of this study.

The exclusion criteria in the study were patients showing classic features of degenerative changes in the spine, vertebral hemangioma, or innumerable bony metastases. Although the classic cases of Modic degenerative endplate changes were excluded, patients showing signal changes in vertebrae other than the endplates, such as in the region of the vertebral body or posterior elements without any obvious bone destruction, were not excluded. For example, early cases of infectious vertebral lesion or marrow infiltration present as isolated signal changes (marrow edema) without any bone destruction, preparavertebral soft-tissue component, disc involvement, or frank abscess formation were not excluded. The other exclusion criteria were patients with metallic implants, cardiac pacemakers, and claustrophobia; follow-up of vertebral lesions; and postoperative patients. Moreover, patients with abnormal coagulation profiles and those not willing to undergo CT-guided FNA/biopsy were also excluded from the study.

In the study population, 5 patients had a history of other cancers (2 had carcinoma breast, 1 had carcinoma larynx, 1 had carcinoma cervix, and 1 had carcinoma penis). The patient's blood or previous radiologic investigations available at the time of presentation were not collected or analyzed in this study.

MR Image Acquisitions

MR imaging was performed on a 1.5T scanner (Signa Excite; GE Healthcare, Milwaukee, Wisconsin). All patients underwent MR imaging of the spine (T1WI, T2WI, STIR, contrast-enhanced MR imaging, DWI, and in-phase/opposed-phase MR imaging). T1WI in axial (TR/TE = 500/11.7 ms, section thickness = 4 mm) and sagittal planes (TR/TE = 600/10.7 ms, section thickness = 4 mm) was performed. Fast recovery fast spin-echo T2WI (TR/TE = 3400/102 ms, section thickness = 4 mm) in the axial and sagittal planes was performed. The STIR sequence (TR/TE = 3200/110 ms, section thickness = 5 mm, TI = 150 ms) in the sagittal plane was acquired. Phase sequences were obtained in the sagittal plane with the following parameters: in-phase (TR/TE = 118/5 ms; flip angle = 80°), opposed-phase (TR/TE = 118/2.5 ms; flip angle = 80°), section thickness = 5 mm with an intersection gap of 0.5 mm, matrix size = 256 × 160, NEX = 1, FOV = 32 cm, and number of sections = 15.

A single-shot DWI echo-planar sequence was used to acquire data in the sagittal plane: TR/TE = 6200/104.6 ms, b-values of 0 and 600 s/mm^2, FOV = 32 cm, section thickness = 5 mm, intersection gap = 1 mm, and NEX = 3. The ADC maps were generated with minimum and maximum b-values.

Contrast-enhanced imaging including non-fat-saturated T1WI (TR/TE = 400/10.8 ms, section thickness = 4 mm) in the axial and sagittal planes was performed. The dosage of gadodiamide (Omniscan; GE Healthcare, Piscataway, New Jersey) contrast given was 0.1 mmol/kg of body weight.

Image Interpretation and Data Analysis

After MR imaging acquisition, images were interpreted prospectively by 2 independent radiologists. All the imaging features, ADC, and SIR values of vertebral lesions were calculated and recorded before the CT-guided FNA/biopsy for each patient. One radiologist had 3 years' experience in neuroradiology and the other had 10 years'. The radiologists were blinded to the patients' clinical information, findings from other imaging modalities, and blood investigations, if any. However, the history of other cancers was available to the radiologists. Due to increased incidence of infectious vertebral lesions in our setup,[22] various lesions were classified into 3 subgroups as GPI, GPN, and GPM.

On conventional MR imaging, lesions were primarily vertebral in nature, involving the vertebral body, the posterior elements, or both. We observed associated preparavertebral and/or intraspinal (epidural) soft-tissue components in many of them, but none of the patients had intradural extramedullary or intramedullary involvement.

Mean ADC and SIR were calculated with the ADC map and in-phase/opposed-phase images, respectively. Circular ROIs were drawn on the ADC and in-phase/opposed-phase images manually 3 times within the lesion, and the averages of these values were calculated and used. Although ROIs were not drawn on conventional MR images, T1WI, T2WI, and postcontrast T1WI were used in defining the anatomic landmarks. Also, DWI was used for placement of ROIs at the region with lowest signal on the ADC image. We attempted to keep the ROI locations the same for the ADC and SIR calculations, guided by conventional MR images. The average size of manually drawn ROIs was 20–30 mm^2. The

ROIs were drawn on the solid, preferably enhancing, bony components of the lesion, avoiding paravertebral soft tissue/collection, if present. The areas of hemorrhage, necrosis, and calcification were avoided. Hypointense signals on T2-weighted and hyperintense signals on T1-weighted images were assumed to indicate hemorrhage/calcification. Furthermore, nonenhancing hypointense areas on T2- and T1-weighted images were considered calcifications. Nonenhancing hyperintense areas similar to fluid on T2-weighted and hypointense areas on T1-weighted images were used for necrosis. Care was taken to exclude endplates, cortical margins, disc spaces, or adjacent normal marrow while drawing the ROIs.

The ADC values were expressed in 10^{-3} mm^2/s. For the calculation of SIR, the signal intensity was measured on in-phase and opposed-phase images in the affected vertebrae. The mean SIR was calculated by dividing the marrow signal intensity recorded on opposed-phase by the in-phase images.

Reference Standard Test

In this study, lesions were identified on mpMRI examinations followed by CT-guided FNA/biopsy from the representative lesions. However, the decision for biopsy was not based merely on the results of mpMRI analysis but also included other clinical parameters for appropriate patient management. The radiologist who interpreted MR images subsequently performed the CT-guided FNA/biopsy on the preselected target vertebra.

The vertebral FNA/biopsy specimen was obtained from 1 vertebra/contiguous soft tissue. A patient may have had >1 type of lesion. However, we recorded 1 type of lesion for each patient when cytohistology was performed. The mean time interval between MR imaging and CT-guided FNA/biopsy was 5 days (range, 3–7 days). If the results of the CT-guided FNA were indeterminate, a repeat CT-guided biopsy was performed in another 6 days (range, 5–8 days). None of the patients underwent open biopsy.

Statistical Analysis

We used previously published data to estimate the sample size for this study. In previous studies, the mean ADC values were reported for the benign group as 1.75–1.98 SD 0.30–0.44; for the infectious group, as 0.91–1.54 SD 0.14–0.38; and for the malignant group, as 0.5–0.77 SD 0.23–0.30.[23,24] On the basis of these data, we estimated a sample size of 19 per group to detect significant differences in mean ADC values between GPN and GPI and 34 per group to detect significant differences in mean ADC values between GPI and GPM with >80% power at the 5% level of significance using a 2-sided unpaired *t* test. Thus, we proposed to include at least 20 cases of GPN, 40 cases of GPI, and 40 cases of GPM. The proposed sample size is more than sufficient to detect differences in mean SIR values between benign and malignant cases on the basis of the data previously reported in studies.[9,20] The sample size is also sufficient to develop predictive logistic regression models to differentiate these groups.

Quantitative data were described with mean ± SD and range, while categoric data were presented using frequency and proportion. A weighted κ agreement along with the 95% confidence interval was estimated between 2 independent radiologists. The average ADC and SIR values were compared among 3 groups by using 1-way analysis of variance followed by the Bonferroni correction for multiple comparisons in post hoc analysis. The thresholds of the ADC and SIR in classifying different disease groups were calculated with receiver operating characteristic analysis. The cutoff was selected where the maximum Youden index (sensitivity + specifity − 1) and the minimum distance on the receiver operating characteristic curve from points 0 and 1 were observed. The performance of the cutoff was summarized using sensitivity (SE), and specificity (Sp). The area under the curve (AUC) was summarized to evaluate the overall discriminatory ability of different tests. The likelihood ratios (positive likelihood ratio and negative likelihood ratio) and correct classification measures were also reported for the obtained cutoffs. The receiver operating characteristic curves were constructed for important findings. The individual and combined predictive models of ADC and SIR in differentiating disease groups were developed using logistic regression analysis. Furthermore, the discriminatory performance of the model was summarized with the area under the receiver operating characteristic curve along with the 95% CI. The 95% CI for the AUC was obtained with an asymptotic normal distribution approach. We also conducted internal validation of the developed models by using leave-one-out methods. The indices for model performance were reported for both original and validation analysis. A value of $P < .05$ was significant. All the statistical analyses were performed with STATA 12.1 (StataCorp, College Station, Texas).

RESULTS

A total of 126 subjects (73 men [57.9%], 53 women [42.1%]; mean age, 45.3 ± 15.2 years, range, 4–76 years) were analyzed. Of the total, 49% (62/126) had GPI lesions, 18% (22/126) had GPN lesions, and 33% (42/126) had GPM lesions using the reference standard. In malignancy, 85.7% (36/42) of cases were metastatic (solitary, 25; multiple, 11) and the remaining 14.2% (6/42) were primary bone tumor. Excellent agreement was obtained on the data generated by the 2 independent radiologists (κ agreement = 0.96; 95% CI, 0.94–0.97).

Most of the patients in the GPI subgroup had tuberculosis, 82% (51/62); the rest of the cases were pyogenic in nature, 18% (11/62), while in the GPN subgroup, most had osteoporotic vertebral collapse, 63% (14/22). The different types of lesions are summarized in On-line Table 1. The morphologic and quantitative imaging of GPI, GPN, and GPM lesions is shown in Figs 1–3, respectively. On-line Fig 1 is a GPN lesion with a histopathologic diagnosis of inflammatory pseudotumor.

The mean ADC value was 1.23 ± 0.16 for GPI, 1.41 ± 0.31 for GPN, and 1.01 ± 0.22 for GPM lesions (On-line Table 2). The SIR was 0.80 ± 0.13 for GPI, 0.75 ± 0.19 for GPN, and 0.98 ± 0.11 for GPM lesions (On-line Table 2). Overall, the mean ADC and SIR values for 3 different categories of vertebral lesions were significantly different ($P < .000$ and $P < .000$). For the ADC values, a statistically significant difference was observed between GPI and GPN lesions ($P < .002$), GPI and GPM lesions ($P < .000$), and GPN and GPM lesions ($P < .000$). In the post hoc analysis of the SIR comparison, a statistically significant difference was observed between GPI and GPM lesions ($P < .000$) and between GPN and GPM lesions ($P < .000$). However, for GPI and GPN lesions, the difference was not statistically significant ($P = .46$) (On-line Table 2).

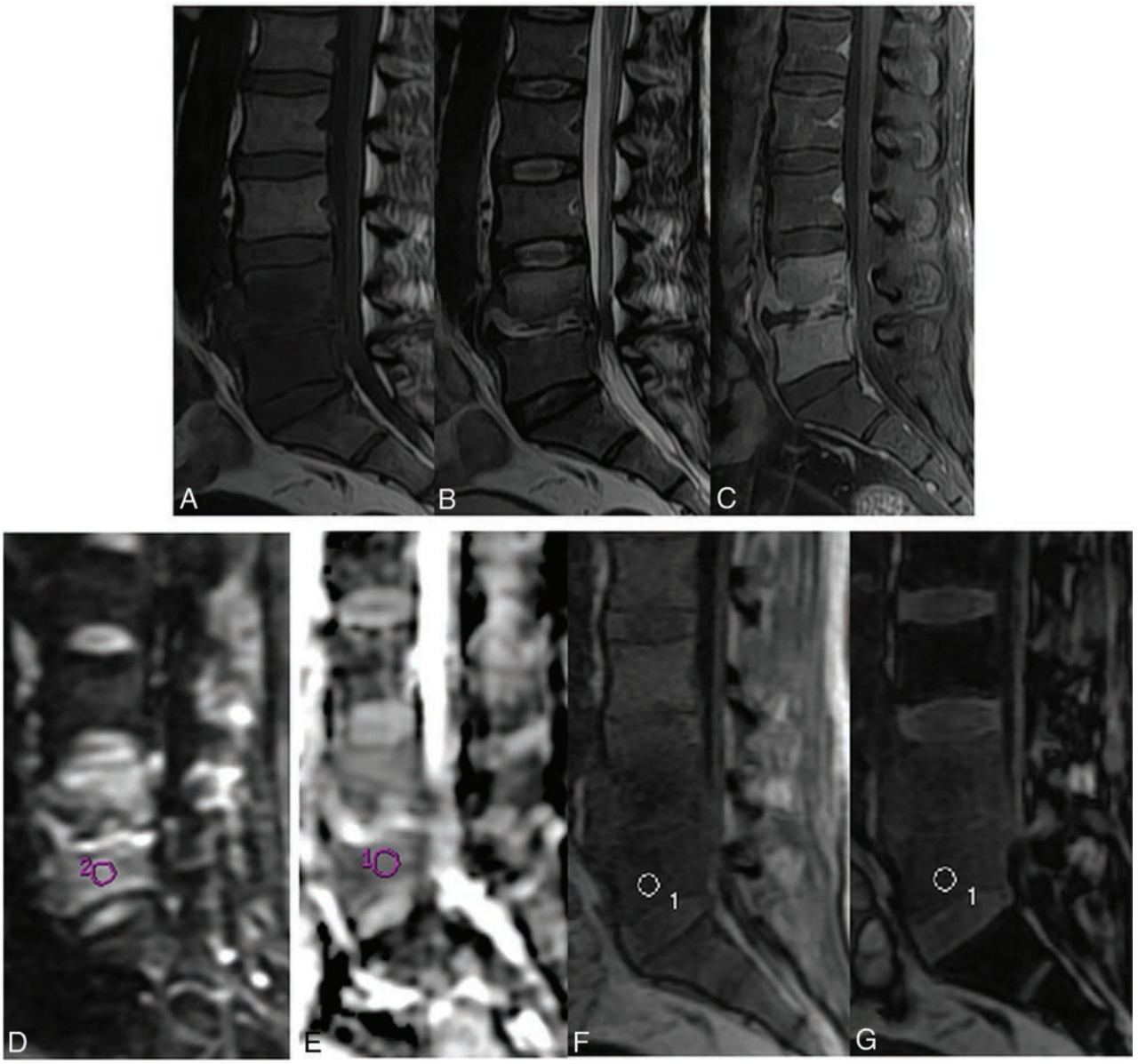

FIG 1. A 35-year-old man with biopsy-proved vertebral tuberculosis shows diffusely hypointense signal in the L4 and L5 vertebrae on sagittal T1WI (*A*) and hyperintense signal on sagittal T2WI (*B*). The intervening disc space has a small amount of prevertebral and epidural soft tissue. Heterogeneous enhancement of both the involved vertebrae, intervertebral disc space, and prevertebral and epidural soft tissue is noted on the contrast study (*C*). The lesion is mildly hyperintense on DWI (*D*). ADC measured from the L5 vertebral body is 1.2×10^{-3} mm^2/s (*E*). Sagittal in-phase (*F*) and opposed-phase (*G*) images with the ROI cursor drawn in the lesion are shown. The measured SIR is 0.88.

The diagnostic accuracy of MR imaging quantitative traits for characterizing different vertebral lesions and the results of receiver operating characteristic analysis are summarized in On-line Table 3. The cutoff for ADC to differentiate GPN and GPM lesions was found to be 1.2 with a sensitivity of 86.4% and a specificity of 78.6%. The cutoff for ADC was 1.0 (with an SE of 96.8% and an Sp of 69.1%) in differentiating GPI and GPM lesions, whereas the cutoff for ADC in differentiating GPI and GPN lesions was found to be 1.3 with an SE of 72.7% and an Sp of 59.7% (On-line Table 3). The AUC for the ADC model in differentiating GPN and GPM lesions was 0.89 (95% CI, 0.81–0.96) followed by 0.82 (95% CI, 0.73–0.92) for differentiating GPI and GPM lesions. The cutoffs for SIR in differentiating various categories are depicted in On-line Table 3. The cutoff for SIR was 0.91 with an SE of 85.7% and an Sp of 85.5% in differentiating GPI and GPM lesions, and the SIR model provided an AUC of 0.90 (95% CI, 0.84–0.96). Differentiating GPN and GPM lesions with the SIR cutoff value as 0.90 correctly classified 84.3% cases, and the calculated AUC was 0.86 (95% CI, 0.76–0.97). The ADC cutoff for differentiating all benign from malignant lesions was estimated to be 1.0, whereas the SIR cutoff was estimated to be 0.91 for differentiating malignant lesions from all benign lesions. On-line Fig 1 represents a case with an expansile lesion with endplate erosion and mild homogeneous contrast enhancement. These findings favored a malignant etiology, while its ADC was 1.3×10^{-3} mm^2/s and the SIR was 0.64. These features pointed to a benign lesion, which proved to be an inflammatory pseudotumor on histopathology.

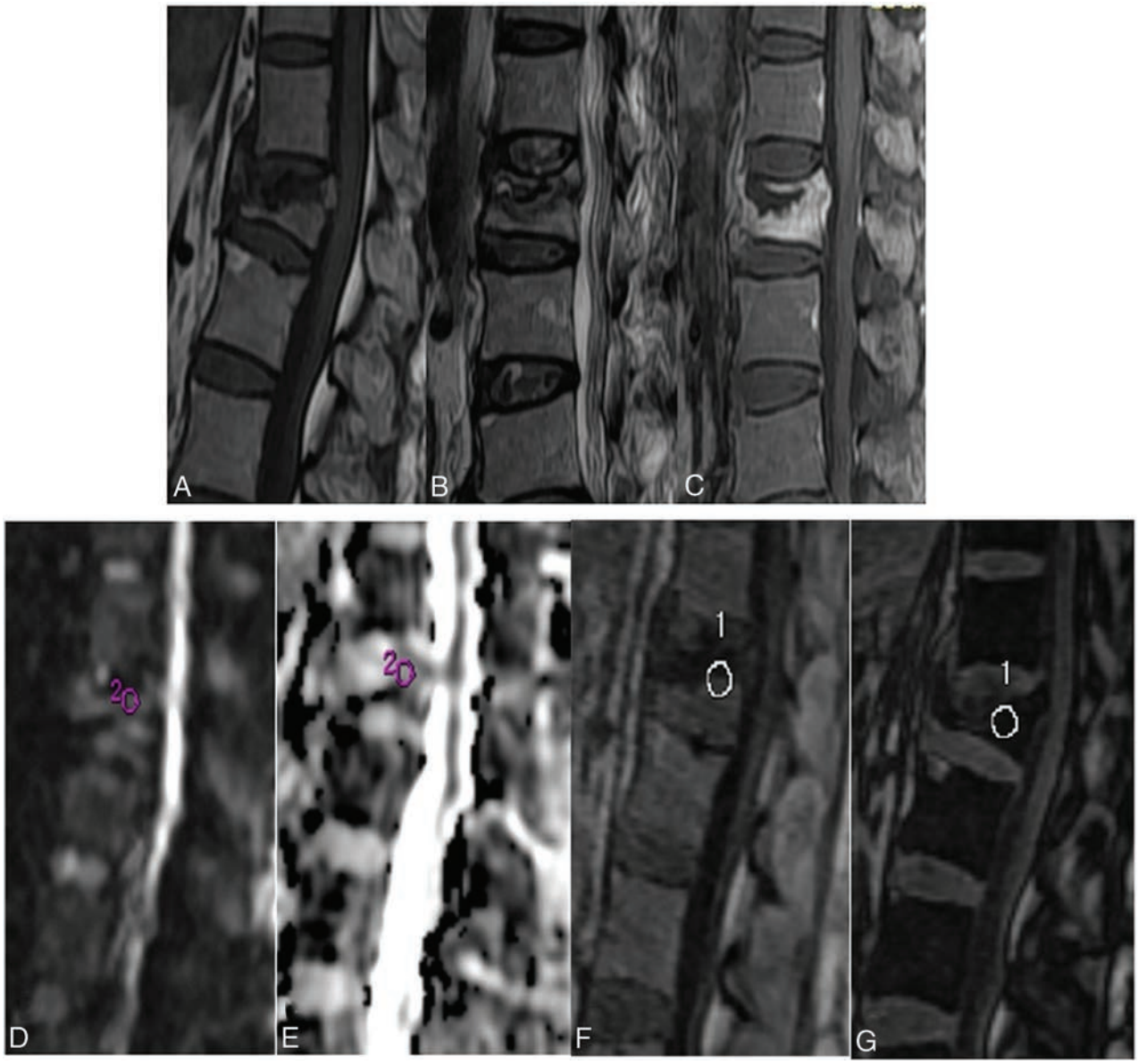

FIG 2. A 63-year-old woman with biopsy-proved osteoporotic vertebral collapse of the L1 vertebra shows partial collapse of the vertebra with retropulsion of the posterosuperior part of the vertebral body, the presence of the fluid sign, and the absence of prevertebral and epidural soft tissue on T1WI (*A*) and T2WI (*B*). The collapsed vertebra shows diffuse heterogeneous enhancement on the contrast study (*C*). Sagittal DWI obtained at the same level shows isointense signals (*D*). ADC measured from the L1 vertebral body is 1.3×10^{-3} mm^2/s (*E*). Sagittal in-phase (*F*) and opposed-phase (*G*) images with the ROI cursor drawn in the lesion are shown. The measured SIR is 0.56.

With estimated cutoffs for the ADC and SIR, 28 lesions (22.2%) had contradictory ADC and SIR in differentiating malignant from all benign lesions. In these cases, the sensitivity and specificity of ADC values were found to be 26.7% and 92.3%, respectively. Whereas, the sensitivity and specificity of SIR were found to be 73.3% and 7.7%, respectively. Therefore, the joint evaluation of the ADC and SIR values could improve classifications. In differentiating all groups, 45 (35.7%) lesions had different results between ADC and SIR. Overall, misclassification was found to be similar with the ADC and SIR values.

Multivariable logistic regression analysis showed that the ADC and SIR values were significantly associated with GPM compared with GPN or GPI lesions and all benign lesions (On-line Table 4). The AUC for the statistical model (model 1) with ADC and SIR to differentiate GPM from GPI lesions was found to be 0.92 (95% CI, 0.87–0.97), while the AUC for the statistical model (model 2) with ADC and SIR to differentiate GPM from GPN lesions was observed to be 0.91 (On-line Fig 2). The AUC for differentiating malignant lesions from all benign lesions (model 3) was 0.92 (95% CI, 0.87–0.97). The probability of malignant lesions in model 1 can be obtained as $\exp(-10.50 - 5.67 \times \text{ADC} + 18.35 \times \text{SIR}) / [1 + \exp(-10.5 - 5.67 \times \text{ADC} + 18.35 \times \text{SIR})]$. Moreover, the probability of malignant lesions in model 2 can be obtained by using the equation, $\exp(-5.93 - 4.59 \times \text{ADC} + 13.33 \times \text{SIR}) / [1 + \exp(-5.93 - 4.59 \times \text{ADC} + 13.33 \times \text{SIR})]$. The probability of malignant lesions compared with all benign lesions in model 3 can be estimated by using the following equation: $\exp(-8.25 - 5.42 \times \text{ADC} + 15.27 \times \text{SIR}) / [1 + \exp(-8.25 - 5.42 \times \text{ADC} + 15.27 \times$

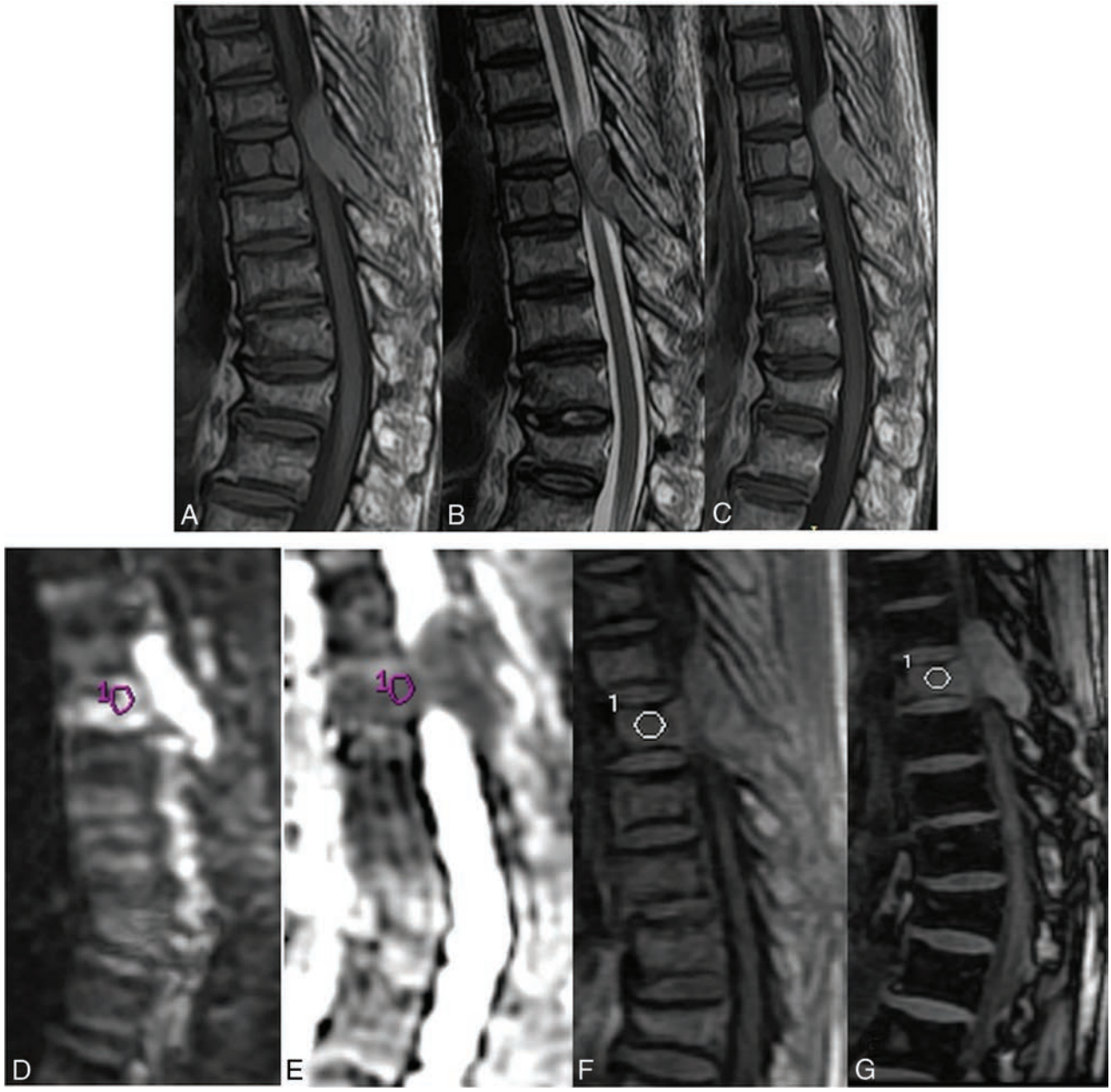

FIG 3. A 55-year-old man with biopsy-proved vertebral metastasis from transitional cell carcinoma of the D6 vertebra shows an isointense lesion at the D6 vertebra on sagittal T1WI (*A*) and sagittal T2WI (*B*). The lesion shows diffuse enhancement on the contrast study (*C*). The lesion is hyperintense on DWI (*D*). ADC measured from the lesion is 0.92×10^{-3} mm^2/s (*E*). Sagittal in-phase (*F*) and opposed-phase (*G*) images with the ROI cursor drawn in the lesion are shown. The measured SIR is 0.96.

SIR)]. The model validation on the test data (using the leave-one-out method) showed an AUC of 0.91 for model 1, an AUC of 0.88 for model 2, and an AUC of 0.90 for model 3 (On-line Table 4).

Model 1 can differentiate GPI and GPM lesions. A cutoff of 0.39 for model 1 provided the positive likelihood ratio of 4.18. The proposed model 1 achieved a sensitivity of 81% and a specificity of 80.7% at the determined cutoff. This model correctly characterized 81% of cases. Model 2 differentiates GPN and GPM lesions. A cutoff value of 0.68 was determined for the second model; it differentiated GPN and GPM lesions with a high sensitivity and specificity (83.3% and 81.8%, respectively), and it correctly characterized 83% of cases. The positive likelihood ratio for model 2 was 4.58. Model 3 differentiated malignant compared with all benign lesions. A cutoff value of 0.32 for this model provided the positive likelihood ratio of 4.67 with a sensitivity of 83.3% and specificity of 82.1%, and it correctly characterized 82% lesions. (On-line Table 5).

DISCUSSION

A vertebral lesion may be diagnosed with x-ray, CT, and other imaging modalities such as hybrid single-photon emission CT. Among all imaging techniques available, MR imaging is the method of choice in spinal pathology because of its excellent tissue contrast.[10,23] Overdiagnosis due to the limited specificity of conventional MR imaging puts patients at risk of unnecessary investigations and delays proper treatment.[24,25] Furthermore,

spinal tuberculosis, which mimics a malignant condition, is a frequent diagnosis in our experience.[22] It is challenging to distinguish atypical variants of spinal tuberculosis from malignancy, especially in the early stage when the isolated vertebral body does not involve any soft-tissue component, adjacent disc involvement, or abscess formation.

Quantitative parameters derived from the mpMRI approach using a combination of DWI and in-phase/opposed-phase imaging could improve patient management. In this study, we have presented 3 statistical models for predicting the probability of malignant vertebral lesions for proper patient management using the mpMRI methods.

DWI has been used previously in various diseases.[26-29] Initial studies showed that qualitative DWI offers no advantage over conventional unenhanced MR imaging in the detection of vertebral lesions.[10-12,30] Quantitative DWI studies using ADC maps also showed overlapping results in differentiating various vertebral lesions.[31,32] Balliu et al[32] reported no significant difference in ADC values for differentiating infectious and malignant lesions. In contrast, our study showed a significant difference in ADC values of malignant and infectious vertebral lesions, which could help differentiate malignant and benign vertebral lesions. We observed the lowest ADC values for malignant lesions, the highest ADC values for noninfectious benign lesions, and values in the intermediate range for infectious lesions. A similar trend of ADC values for malignant, acute benign, and infectious vertebral lesions was observed by Dewan et al.[33] However, in contrast to our study, they observed overlapping mean ADC values between tuberculous spondylodiscitis and malignant compression fracture. Palle et al[31] reported considerable overlap of ADC values in metastatic and tubercular vertebrae. The cutoff value of the ADC determined in our study could be helpful in differentiating various vertebral lesions. An important aspect of the present study is the method of ROI placement and the relatively larger patient population. In contrast to the ADC calculation method used in previous studies, the circular ROIs were placed at the site of maximum restriction observed on the ADC images in this study.[33] Furthermore, using the established cutoff in our study, we could achieve higher sensitivity, specificity, and AUC for various predictive models in differentiating vertebral lesions. We could correctly classify >80% of various vertebral lesions using the different statistical models.

In-phase/opposed-phase imaging quantifies fat in tissues because water and fat protons have different precession frequencies and are in-phase at a TE of 4.8 ms and are 180° opposed at a TE of 2.4 ms at 1.5T. The presence of both fat and water in normal marrow results in suppression of signal intensity on the opposed-phase images. In benign compression fractures, no marrow-replacing process occurs, so there is signal loss in opposed-phase images. In case of malignant lesions, the bone marrow fat is replaced by tumor cells, so there is a lack of signal loss on opposed-phase images. Therefore, a substantial decrease in signal intensity occurs in normal vertebrae and for benign lesions, but malignant lesions exhibit either a minimal decrease or an increase in signal intensity.[34]

A similar trend in our study was also observed. The mean SIR in this study was found to be highest in malignant lesions and lowest in the noninfectious benign lesions. We found that the SIR of affected vertebrae was 0.80 in infectious vertebral lesions, 0.75 in noninfectious benign lesions, and 0.98 in malignant lesions. An optimal cutoff value of SIR was also calculated to differentiate infectious, noninfectious benign, and malignant vertebral lesions. We could differentiate noninfectious benign and malignant vertebral lesions as well as infectious and malignant vertebral lesions with a high sensitivity and specificity using cutoffs for the SIR value of 0.90 and 0.91, respectively. This result coincides with the results of previous studies performed with in-phase/opposed-phase imaging in vertebral lesions.[9,20] Disler et al[20] reported a relative SIR of 1.03 ± 0.13 for the neoplastic group and 0.62 ± 0.13 for the non-neoplastic group, and a ratio cutoff value of 0.81 resulted in a 95% sensitivity and a 95% specificity for detection of neoplasms. Erly et al[9] reported that the mean SIR for benign lesions was 0.58 compared with a malignant lesion cutoff of 0.98, and if 0.80 was chosen as a cutoff, it correctly identifies malignant and benign lesions with a sensitivity of 0.95 and a specificity of 0.89.[9] Our findings are consistent with those in that previous study.[9]

A major strength of this study was developing statistical models for malignant vertebral lesions using mpMRI and determining thresholds for different parameters of mpMRI. Multivariate logistic regression analysis showed ADC and SIR as independent predictors of malignancy in vertebral lesions. On the basis of the mean ADC and SIR, we established automated statistical models that would be helpful in differentiating vertebral lesions. Various predictive models demonstrated excellent validation with leave-one-out analysis.

Our study has several limitations. We recruited patients irrespective of their duration of symptoms (ie, both acute and chronic cases of vertebral lesions) because most of the patients in our institution had poor socioeconomic status and there is a tendency to avoid the costly investigations until later in the disease progression. Another limitation was the modest number of noninfectious benign cases compared with infectious and malignant vertebral lesions. Spinal tuberculosis is more common and a major public health hazard in developing nations such as India, and a similar proportion of the infectious group was reflected in our study. Osteoporotic compression forms a large proportion of noninfectious benign group and is more likely to be managed conservatively. Such patients are less likely to undergo biopsy and hence are under-represented in our study population. The ADC and SIR values were recorded before the CT-guided FNA/biopsy. Because the same radiologists were involved in biopsy procedures as well, performance bias cannot be ignored completely. Although all the models established in this study provided high accuracy in differentiating various vertebral lesions, the output of models needs to be externally validated in a larger study; therefore, future prospective studies are warranted.

CONCLUSIONS

Our study shows that mpMRI can differentiate various vertebral lesions. The prediction model established in this study using mpMRI can be used to assess the probability of malignancy in vertebral lesions and may help in accurate diagnosis and proper patient management. The potential utility of statistical models using mpMRI requires further prospective validation.

ACKNOWLEDGMENTS

The authors thank Dr Josh Greer, Radiology, University of Texas Southwestern Medical Center, Dallas, Texas, for help in language correction and many useful comments.

Disclosures: Alok K. Dwivedi—*UNRELATED*: *Consultancy*: Texas Tech University Health Sciences Center El Paso*; *Grants/Grants Pending*: National Institutes of Health, Cancer Prevention and Research Institute of Texas*; *Travel/Accommodations/Meeting Expenses Unrelated to Activities Listed*: Joint Statistical Meeting, Conference on Statistical Practices. Ravindra Kumar Garg—*RELATED*: *Payment for Writing or Reviewing the Manuscript*: MedLink Neurology, *Comments*: 22 chapters for this e-book. *Money paid to the institution.

REFERENCES

1. Cuénod CA, Laredo JD, Chevret S, et al. **Acute vertebral collapse due to osteoporosis or malignancy: appearance on unenhanced and gadolinium-enhanced MR images.** *Radiology* 1996;199:541–49 CrossRef Medline
2. An HS, Andreshak TG, Nguyen C, et al. **Can we distinguish between benign versus malignant compression fractures of the spine by magnetic resonance imaging?** *Spine (Phila Pa 1976)* 1995;20:1776–82 CrossRef Medline
3. Yuh WT, Zachar CK, Barloon TJ, et al. **Vertebral compression fractures: distinction between benign and malignant causes with MR imaging.** *Radiology* 1989;172:215–18 CrossRef Medline
4. Baur A, Stäbler A, Arbogast S, et al. **Acute osteoporotic and neoplastic vertebral compression fractures: fluid sign at MR imaging.** *Radiology* 2002;225:730–35 CrossRef Medline
5. Dwivedi DK, Kumar R, Bora GS, et al. **Stratification of the aggressiveness of prostate cancer using pre-biopsy multiparametric MRI (mpMRI).** *NMR Biomed* 2016;29:232–38 CrossRef Medline
6. Kimura M, da Cruz LC Jr. **Multiparametric MR imaging in the assessment of brain tumors.** *Magn Reson Imaging Clin N Am* 2016;24:87–122 CrossRef Medline
7. Rahbar H, Partridge SC. **Multiparametric MR imaging of breast cancer.** *Magn Reson Imaging Clin N Am* 2016;24:223–38 CrossRef Medline
8. Ro SR, Asbach P, Siebert E, et al. **Characterization of orbital masses by multiparametric MRI.** *Eur J Radiol* 2016;85:324–36 CrossRef Medline
9. Erly WK, Oh ES, Outwater EK. **The utility of in-phase/opposed-phase imaging in differentiating malignancy from acute benign compression fractures of the spine.** *AJNR Am J Neuroradiol* 2006;27:1183–88 Medline
10. Castillo M, Arbelaez A, Smith JK, et al. **Diffusion-weighted MR imaging offers no advantage over routine noncontrast MR imaging in the detection of vertebral metastases.** *AJNR Am J Neuroradiol* 2000;21:948–53 Medline
11. Maeda M, Sakuma H, Maier SE, et al. **Quantitative assessment of diffusion abnormalities in benign and malignant vertebral compression fractures by line scan diffusion-weighted imaging.** *AJR Am J Roentgenol* 2003;181:1203–09 CrossRef Medline
12. Zhou XJ, Leeds NE, McKinnon GC, et al. **Characterization of benign and metastatic vertebral compression fractures with quantitative diffusion MR imaging.** *AJNR Am J Neuroradiol* 2002;23:165–70 Medline
13. Israel GM, Korobkin M, Wang C, et al. **Comparison of unenhanced CT and chemical shift MRI in evaluating lipid-rich adrenal adenomas.** *AJR Am J Roentgenol* 2004;183:215–19 CrossRef Medline
14. Namimoto T, Yamashita Y, Mitsuzaki K, et al. **Adrenal masses: quantification of fat content with double-echo chemical shift in-phase and opposed-phase FLASH MR images for differentiation of adrenal adenomas.** *Radiology* 2001;218:642–46 CrossRef Medline
15. Haider MA, Ghai S, Jhaveri K, et al. **Chemical shift MR imaging of hyperattenuating (>10 HU) adrenal masses: does it still have a role?** *Radiology* 2004;231:711–16 CrossRef Medline
16. Earls JP, Krinsky GA. **Abdominal and pelvic applications of opposed-phase MR imaging.** *AJR Am J Roentgenol* 1997;169:1071–77 CrossRef Medline
17. Rofsky NM, Weinreb JC, Ambrosino MM, et al. **Comparison between in-phase and opposed-phase T1-weighted breath-hold FLASH sequences for hepatic imaging.** *J Comput Assist Tomogr* 1996;20:230–35 CrossRef Medline
18. Baker LL, Goodman SB, Perkash I, et al. **Benign versus pathologic compression fractures of vertebral bodies: assessment with conventional spin-echo, chemical-shift, and STIR MR imaging.** *Radiology* 1990;174:495–502 CrossRef Medline
19. Rosen BR, Fleming DM, Kushner DC, et al. **Hematologic bone marrow disorders: quantitative chemical shift MR imaging.** *Radiology* 1988;169:799–804 CrossRef Medline
20. Disler DG, McCauley TR, Ratner LM, et al. **In-phase and out-of-phase MR imaging of bone marrow: prediction of neoplasia based on the detection of coexistent fat and water.** *AJR Am J Roentgenol* 1997;169:1439–47 CrossRef Medline
21. Eito K, Waka S, Naoko N, et al. **Vertebral neoplastic compression fractures: assessment by dual-phase chemical shift imaging.** *J Magn Reson Imaging* 2004;20:1020–24 CrossRef Medline
22. Garg RK, Somvanshi DS. **Spinal tuberculosis: a review.** *J Spinal Cord Med* 2011;34:440–54 CrossRef Medline
23. Daffner RH, Lupetin AR, Dash N, et al. **MRI in the detection of malignant infiltration of bone marrow.** *AJR Am J Roentgenol* 1986;146:353–58 CrossRef Medline
24. Baur A, Stäbler A, Bruning R, et al. **Diffusion-weighted MR imaging of bone marrow: differentiation of benign versus pathologic compression fractures.** *Radiology* 1998;207:349–56 CrossRef Medline
25. Spuentrup E, Buecker A, Adam G, et al. **Diffusion-weighted MR imaging for differentiation of benign fracture edema and tumor infiltration of the vertebral body.** *AJR Am J Roentgenol* 2001;176:351–58 CrossRef Medline
26. Durando M, Gennaro L, Cho GY, et al. **Quantitative apparent diffusion coefficient measurement obtained by 3.0Tesla MRI as a potential noninvasive marker of tumor aggressiveness in breast cancer.** *Eur J Radiol* 2016;85:1651–58 CrossRef Medline
27. Dwivedi DK, Kumar R, Bora GS, et al. **Multiparametric MR can identify high grade prostatic intraepithelial neoplasia (HGPIN) lesions and predict future detection of prostate cancer in men with a negative initial prostate biopsy.** *Magn Reson Imaging* 2016;34:1081–86 CrossRef Medline
28. Traboulsee A, Simon JH, Stone L, et al. **Revised recommendations of the Consortium of MS Centers Task Force for a standardized MRI protocol and clinical guidelines for the diagnosis and follow-up of multiple sclerosis.** *AJNR Am J Neuroradiol* 2016;37:394–401 CrossRef Medline
29. Yanagihara TK, Grinband J, Rowley J, et al. **A simple automated method for detecting recurrence in high-grade glioma.** *AJNR Am J Neuroradiol* 2016;37:2019–25 CrossRef Medline
30. Padhani AR, Liu G, Koh DM, et al. **Diffusion-weighted magnetic resonance imaging as a cancer biomarker: consensus and recommendations.** *Neoplasia* 2009;11:102–25 CrossRef Medline
31. Palle L, Reddy MB, Reddy KJ. **Role of magnetic resonance diffusion imaging and apparent diffusion coefficient values in the evaluation of spinal tuberculosis in Indian patients.** *Indian J Radiol Imaging* 2010;20:279–83 CrossRef Medline
32. Balliu E, Vilanova JC, Peláez I, et al. **Diagnostic value of apparent diffusion coefficients to differentiate benign from malignant vertebral bone marrow lesions.** *Eur J Radiol* 2009;69:560–66 CrossRef Medline
33. Dewan KA, Salama AA, El habashy HM, et al. **Evaluation of benign and malignant vertebral lesions with diffusion weighted magnetic resonance imaging and apparent diffusion coefficient measurements.** *The Egyptian Journal of Radiology and Nuclear Medicine* 2015;46:423–33 CrossRef
34. Ishijima H, Ishizaka H, Horikoshi H, et al. **Water fraction of lumbar vertebral bone marrow estimated from chemical shift misregistration on MR imaging: normal variations with age and sex.** *AJR Am J Roentgenol* 1996;167:355–58 CrossRef Medline

Advantages of 70-kV CT Angiography for the Visualization of the Adamkiewicz Artery: Comparison with 120-kV Imaging

S. Shimoyama, T. Nishii, Y. Watanabe, A.K. Kono, K. Kagawa, S. Takahashi, and K. Sugimura

ABSTRACT

BACKGROUND AND PURPOSE: Preprocedural identification of the Adamkiewicz artery is crucial in patients with aortic diseases. This study aimed to compare 70-kV CTA with conventional 120-kV CTA for the identification of the Adamkiewicz artery, examining differences in radiation dose and image quality.

MATERIALS AND METHODS: We retrospectively analyzed 2 equal groups of 60 patients who had undergone 70-kV or 120-kV CTA to detect the Adamkiewicz artery before aortic repair. Size-specific dose estimate, the CT number of the aorta, and the contrast-to-noise ratio of the anterior spinal artery to the spinal cord were recorded. Furthermore, detectability of the Adamkiewicz artery was evaluated by using a 4-point continuity score (3, definite to 0, undetectable).

RESULTS: There was significantly lower radiation exposure with 70-kV CTA than 120-kV CTA (median size-specific dose estimate, 23.1 versus 61.3 mGy, respectively; $P < .001$). CT number and contrast-to-noise ratio were both significantly higher in the 70-kV CTA group than the 120-kV group (999.1 HU compared with 508.7 HU, and 5.6 compared with 3.4, respectively; $P < .001$ for both). Detectability of the Adamkiewicz artery was not impaired in the 70-kV CTA group (90.0% versus 83.3% in the 120-kV group, $P = .28$). Moreover, the Adamkiewicz artery was detected with greater confidence with 70-kV CTA, reflected by a significantly superior continuity score (median, 3) compared with 120-kV CTA (median, 2; $P = .001$).

CONCLUSIONS: Seventy-kilovolt CTA has substantial advantages for the identification of the Adamkiewicz artery before aortic repair, with a significantly lower radiation exposure and superior image quality than 120-kV CTA.

ABBREVIATIONS: AKA = Adamkiewicz artery; ASA = anterior spinal artery; CSA = critical segmental artery; CNR = contrast-to-noise ratio; $CTDI_{vol}$ = volume CT dose index; IQR = interquartile range; SSDE = size-specific dose estimate

Spinal cord ischemia is a serious complication of surgical and endovascular stent-graft repair of thoracic or thoracoabdominal aortic aneurysms and aortic dissection.[1] Preservation of spinal cord blood supply, especially from the Adamkiewicz artery (AKA) and its tributary the critical segmental artery (CSA) during the procedure is mandatory to prevent neurologic complications.[2,3] Thus, accurate preprocedural knowledge of the anatomy of the AKA and CSA is crucial, particularly in surgical repair.[4]

Recently, CTA has been used for noninvasive identification of the AKA[5,6] in place of invasive selective spinal angiography. However, the anatomic features of the AKA—a small vessel surrounded by osseous structures—may frequently be obscured in the contrast-to-noise ratio (CNR) of the spinal vasculature.[7] A higher contrast-to-noise ratio in spinal CTA has previously been achieved with a high tube current–time product with a slow rotation speed and a small helical pitch to reduce image noise,[8] and CTA with intra-arterial injection has been used to increase the contrast of the vessel.[7,9,10] Consequently, the detection rate of the AKA has been improved to 85%–100%[7,8,10-12]; however, these techniques require either high radiation exposure or the insertion of a pigtail catheter into the pathologic aorta.[8]

Seventy-kilovolt CT can substantially increase vascular iodine enhancement compared with conventional 120-kV imaging because the effective photon energy achieved with a 70-kV scan lies in the range of maximum absorption close to the K-edge of iodine (33.2 keV).[13,14] The mean CT number in the aorta with 70-kV CTA is reported to be approximately 700 HU, even with intravenous injection,[14] which approaches the attenuation in the aorta with intra-arterial injection in 120-kV imaging.[7] Moreover, radi-

Received May 21, 2017; accepted after revision July 7.

From the Department of Radiology (S.S., T.N., Y.W., A.K.K., S.T., K.S.), Kobe University Graduate School of Medicine, Kobe, Hyogo, Japan; Department of Radiology (Y.W., A.K.K.), National Cerebral and Cardiovascular Center, Suita, Osaka, Japan; and Division of Radiology (K.K.), Center for Radiology and Radiation Oncology, Kobe University Hospital, Kobe, Hyogo, Japan.

Please address correspondence to Shinsuke Shimoyama, MD, Department of Radiology, Kobe University Graduate School of Medicine, 7-5-1 Kusunoki-cho, Chuo-ku, Kobe, Hyogo 650-0017 Japan; e-mail: road6185@yahoo.co.jp

http://dx.doi.org/10.3174/ajnr.A5372

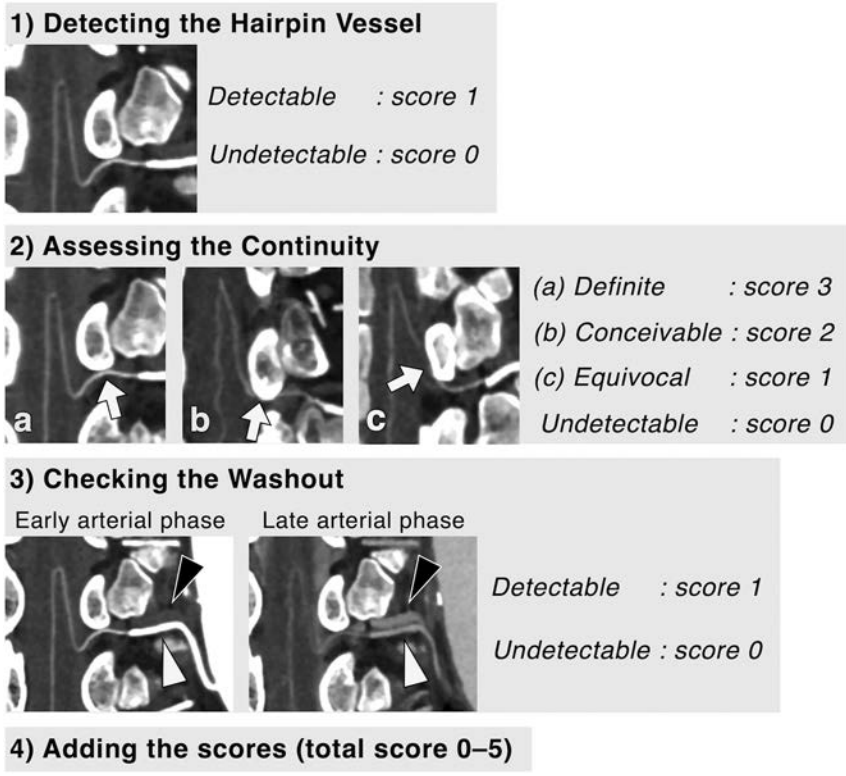

FIG 1. The AKA was identified according to the following stepwise approach: 1) detect the hairpin vessel; 2) assess the continuity of the vessel to the aorta mainly around the pedicle of the vertebral arch (*white arrows*) as definite (*a*), conceivable (*b*), equivocal (*c*), or undetectable; 3) check the washout from the early-to-late arterial phase (*white arrowhead*), because vessels that are more prominent in the late arterial phase are likely to be veins (*black arrowhead*); and 4) sum the scores. We defined positive identification of the AKA as a total score of ≥3.

ation exposure is significantly reduced with lower voltage scanning.[14-16] We hypothesized that 70-kV CTA would be associated with superior AKA visualization, with high vessel attenuation and lower radiation exposure. The aim of this study was to compare 70-kV CTA with conventional 120-kV imaging for the identification of the AKA and the CSA regarding the radiation dose and qualitative and quantitative image quality.

MATERIALS AND METHODS

Ethics

Our institutional review board of Kobe University Hospital approved this retrospective study; the requirement for written, informed consent was waived because of its design. All patient records and information were anonymized before analysis.

Study Population

A total of 185 consecutive subjects who underwent CTA to detect the AKA between January 2014 and September 2016 were enrolled in this study. Subjects who had a history of aortic repair, spinal arteriovenous fistula, or vertebral or spinal tumor were excluded. Ultimately, we included 120 patients (median age, 69 years; range, 28–85 years; 25.8% women) who underwent CTA to detect the AKA before aortic repair. Because we changed scan mode in January 2015 when a new CT scanner was installed, CTA was performed with a 120-kV scanner in the first 60 subjects and a 70-kV scanner in next 60 subjects.

Data Acquisition

Seventy-kilovolt CTA was performed on a 192-section dual-source CT scanner (Somatom Force; Siemens, Erlangen, Germany). Dual-power scan mode was applied with the following parameters: 128 × 0.6 mm detector configuration, 0.5 seconds per rotation, 0.45 pitch, 1170-mA tube current, and 1300-mAs effective tube current–time product. In dual-power scan mode, the total radiation is divided equally between each x-ray tube, and the data from each detector are summed.[17] Thus, the maximum photon flux is expected to double, and because of the reduction in load on the x-ray tube, we achieved high tube current with a long scan range. One hundred twenty-kilovolt CTA was performed on a 64- or a 320-section multidetector CT scanner (Aquilion 64 or Aquilion ONE; Toshiba Medical Systems, Tokyo, Japan). The scanning parameters used were like those in previous reports[8,12,18] and were as follows: 64-section helical scan mode, 64 × 0.5 mm detector configuration, 0.5 seconds per rotation, 0.64 pitch, 400-mA tube current, and 312.5-mAs effective tube current–time product. The scan range extended from the thoracic inlet to the lesser trochanter of the hip.

Injection Protocol and Scan Timing

Iopamidol 370 mg I/mL (Iopamiron 370; Bayer Yakuhin, Osaka, Japan) was administered through a 20-ga intravenous catheter placed in the right antecubital vein at 5 mL/s, followed by a 30-mL physiologic saline flush at the same rate using a dual-head power injector (Dual Shot GX 7; Nemoto Kyorindo, Tokyo, Japan). Scan timing was set as the peak timing in the true lumen of the descending aorta, which was determined by the timing-bolus method in 70-kV CTA, and by the bolus-tracking method in 120-kV CTA. This technical limitation meant that the ROI could not be moved simultaneously during acquisition of the time-intensity curve in the ROI in the 192-section dual-source CT scanner. For the timing-bolus method, 10 mL of contrast material followed by a 20-mL physiologic saline flush was injected at 5 mL/s, respectively. Timing-bolus scanning was started 10 seconds after the start of injection. The peak time of the CT number in the ROI placed in the true lumen of the descending aorta at the level of the tenth thoracic vertebra was obtained with console software (DynEva, syngo VA50A; Siemens). The 70-kV scan was then started 10 seconds after the peak time. In the bolus-tracking method, the ROI was placed in the descending aorta at the level of the sixth thoracic vertebra, and the trigger threshold was set at 200 HU. The 120-kV scan was automatically started 5 seconds after the trigger. The volume of contrast material used for CTA in the 70- and 120-kV scans was 90 and 100 mL, respectively. The scans

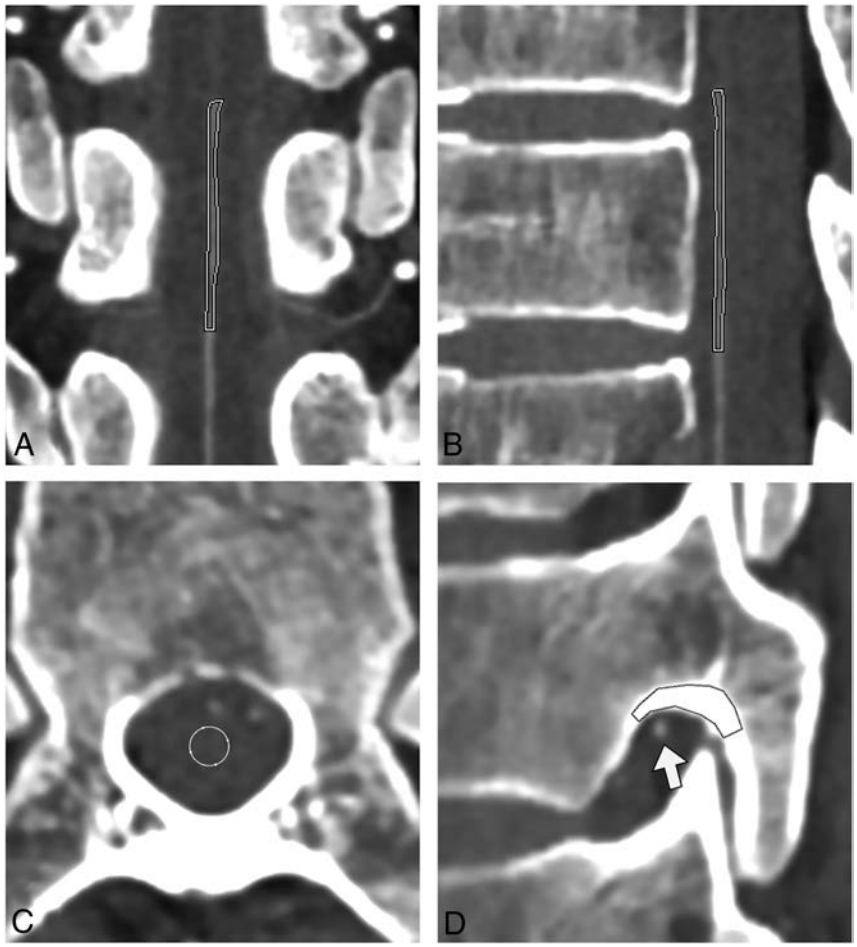

FIG 2. The ROIs placed for measuring CT numbers are shown in a coronal image of the ASA (*A*), a sagittal image of the ASA (*B*), an axial image of the spinal cord (*C*), and a sagittal image of the vertebral bone cortex around the vertebral foramen at the AKA (*white arrow*) running level (*D*).

were repeated to obtain images in the early and late arterial phases. The scan of the late arterial phase was obtained approximately 10 seconds after the end of the first phase, to evaluate the washout of contrast material in the vessels to distinguish the AKA from the similar hairpin-shaped radiculomedullary vein,[7] because vessels that are more prominent in the late phase are likely to be veins.

Image Reconstruction

Seventy-kilovolt CTA image data were reconstructed in the axial plane with 0.6-mm thickness, 0.6-mm interval, 200-mm FOV, and a vascular convolution kernel (Bv44) with Advanced Modeled Iterative Reconstruction (Siemens) with strength level 3. One hundred twenty-kilovolt CTA image data were reconstructed in the axial plane with 0.5-mm thickness, 0.5-mm reconstruction interval, and 200-mm FOV using a soft-tissue convolution kernel (FC13) with the filter back-projection method. The assignable values of both protocols were set as the parameters of reconstruction. Image data were then transferred to a workstation (Ziostation 2, Version 2.4.2.3; Ziosoft, Tokyo, Japan) for further processing and analysis. Curved coronal multiplanar reformatted images (1.0-mm thickness at 1.0-mm intervals) fitted to the curvature of the spinal cord in the early and late arterial phases were obtained.[19]

Radiation Dose Metrics

The volume CT dose index ($CTDI_{vol}$) and the dose-length product reported by the scanner after imaging of a 32-cm phantom were recorded. The size-specific dose estimate (SSDE) was calculated by multiplying the $CTDI_{vol}$ by a conversion factor based on the effective diameter,[20] which was measured using the lateral diameter of the upper abdomen on the standard posterior-anterior CT radiograph.

Qualitative Image Analysis

To assess performance for identifying the AKA, we initially evaluated the image datasets with the 2 scan modes in a consensus reading by 2 board-certified diagnostic radiologists (T.N. with 10 years of experience and A.K.K. with 15 years of experience), who were unaware of the identity of subjects and CTA protocols. The AKA was identified with a stepwise approach and a 6-point scoring system (Fig 1), modified from a previously published report.[8] First, we sought the "hairpin vessel" and assessed it as detectable or undetectable (score 1 or 0, respectively). Second, we assessed continuity to the aorta as definite, conceivable, equivocal, or undetectable (score 3, 2, 1, or 0, respectively). We carefully evaluated the presence of the collateral pathway from the aorta. Third, we evaluated the washout of the attenuation of the vessel from the early-to-late arterial phase (score 1 or 0). Finally, we summed the scores and defined positive identification of the vessel as the AKA when the total score was ≥3. Furthermore, the artery connecting the aorta to the AKA was defined as the CSA. The origin level and the side of the AKA and the CSA were recorded.

The results of the consensus image interpretation by 2 board-certified diagnostic radiologists were determined to be the reference standard for following analyses. To assess the reproducibility of CSA identification in both imaging protocols, 2 radiologists who were unaware of the identity of subjects and CTA protocols evaluated images independently (observer A, T.N., ≥2 months after the first consensus reading, which was judged to be acceptable to minimize the influence of the first review; observer B, S.S., with 6 years of experience).

Quantitative Image Analysis

For the quantitative image analyses, a cardiovascular radiologist (S.S., observer B) unaware of the scan protocols evaluated the following measurements: Mean CT number and SD of the aorta were calculated from the measurement with the circular ROIs placed at the fifth, eighth, and twelfth thoracic vertebrae and the third lumbar vertebra.[18] The ROIs were drawn to include as much vessel lumina as possible, while avoiding areas of artifacts and

calcification. Furthermore, for subjects in whom the AKA had been identified with the previous consensus reading, we performed the following measurement: Because it was difficult to measure the CT number of the AKA accurately due to its small diameter and tortuous route, the CT number of the anterior spinal artery (ASA) was used as an indicator.[21] The mean CT number of the ASA was obtained from the mean of the measured CT number on a sagittal and a coronal multiplanar reformation adjusted to the ASA course along the length of 1 vertebral body (Fig 2). Furthermore, the mean CT number and SD of the spinal cord were calculated from measurements at 3 positions in the spinal cord in the axial plane (top, middle, and bottom level of the previously set ROI for the ASA, Fig 2). The mean CT number of the bone cortex of the vertebral body was calculated from the measurement of the cortex around the right and left intervertebral foramina at the AKA running level (Fig 2). The SNR and CNRs were calculated with the following equations:

$$SNR_{Aorta} = \frac{\text{Mean CT Number of the Aorta}}{\text{SD of the Aorta}},$$

$$CNR_{ASA\text{-}Cord} = \frac{\text{Mean CT Number of the ASA} - \text{Mean CT Number of the Spinal Cord}}{\text{SD of the Spinal Cord}},$$

$$CNR_{ASA\text{-}Bone} = \frac{\text{Mean CT Number of the Bone Cortex} - \text{Mean CT Number of the ASA}}{\text{SD of the Spinal Cord}}.$$

Statistical Analysis

Continuous variables are expressed as the mean ± SD or median and interquartile range (IQR). Categoric variables are expressed as proportions. To evaluate differences between 70- and 120-kV CTA, we used the Welch *t* test for body mass index, mean CT number of the aorta, SNR_{Aorta}, mean CT number of the ASA, SD of the spinal cord, $CNR_{ASA\text{-}Cord}$, and $CNR_{ASA\text{-}Bone}$. The Wilcoxon test was used to compare age, $CTDI_{vol}$, SSDE, and dose-length product. The χ^2 test was used to evaluate differences in AKA detection rates, CSA location, presence of the collateral pathway, aortic disease (aneurysm versus dissection), and sex. The Cochran-Armitage test was used to evaluate differences between the scores.

Diagnostic accuracy and the Cohen κ for agreement were evaluated by comparing the side and level of the CSA interpreted by 2 independent observers against the reference standard. We also assessed the effect of the presence of the collateral pathway to the AKA on diagnostic accuracy.

For statistical analysis, commercially available (JMP 13.0; SAS Institute, Cary, North Carolina) and open-source (R statistical and computing software; http://www.r-project.org/) programs were used. For all analyses, $P < .05$ indicated statistical significance.

RESULTS

Subject Characteristics and Radiation Metrics

There was no significant difference in the demographic or clinical characteristics of subjects undergoing each of the imaging protocols (Table 1). No adverse events during CT were noted in the medical records. Radiation metrics for 1 phase were significantly reduced in 70-kV compared with 120-kV CTA ($CTDI_{vol}$ median, 16.2 mGy [IQR, 16.2–16.2 mGy] versus 47.1 mGy [IQR, 42.3–47.1 mGy]; SSDE median, 23.1 mGy [IQR, 21.1–25.1 mGy] compared with 61.3 mGy [IQR, 57.5–68.3 mGy]; dose-length product, 1147 mGy × cm [IQR, 1107–1211 mGy × cm] compared with 3293 mGy × cm [IQR, 3093–3487 mGy × cm], respectively; $P < .001$ for all analyses) (Fig 3).

Table 1: Subject demographic and clinical characteristics

Variables	120-kV (*n* = 60)	70-kV (*n* = 60)	*P* Value
Age (yr)			.81
Mean	69	69	
Range	57.0–76.3	54.8–76.0	
Sex			.83
Male (No.)	44	45	
Female (No.)	16	15	
Mean body mass index (kg/m^2)	23.7 ± 3.3	23.2 ± 3.6	.48
Aortic disorder			.46
Aneurysm (No.)	35	31	
Dissection (No.)	25	29	

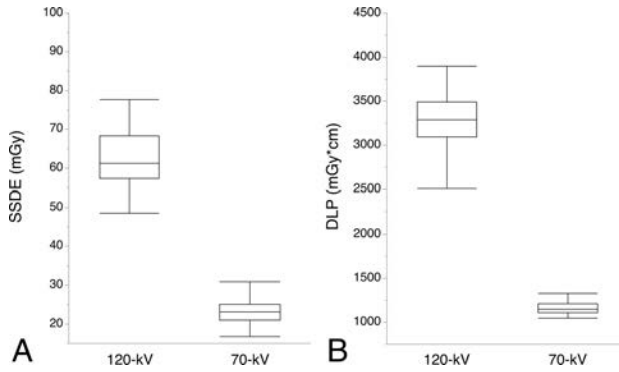

FIG 3. Box range shows the first and third quartiles; whisker range, from the 5th to 95th percentiles. Seventy-kilovolt CTA yields significantly lower SSDE (*A*) and dose-length product (*B*) than 120-kV CTA ($P < .001$ for both).

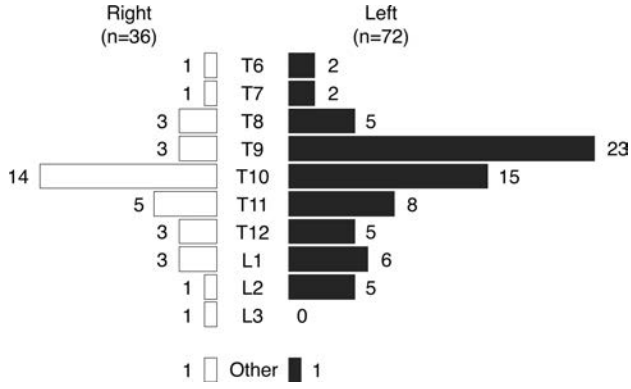

FIG 4. Distribution of the side and level of the CSA to the AKA is shown. Two cases in which the CSA and the AKA were supplied by the axillary artery were described as "other."

Identification of the AKA/CSA

The AKA was identified in 104 of 120 subjects (86.7%). We identified 108 AKAs because there were 2 or 3 AKAs in 3 patients. The CSA originated from a left segmental artery in 66.7% (72/108) and at the level of the eighth intercostal artery to the first lumbar artery in 86.1% (93/108) (Fig 4). A collateral pathway was found in 26 of 120 subjects (21.7%), 13 in each group (Table 2).

Continuity and total scores for 70-kV CTA were significantly superior to those in 120-kV CTA ($P = .001$ and 0.009, respectively; Fig 5); however, the detection rate was not significantly higher (90.0% versus 83.3%, respectively; $P = .28$) (Table 2). The difference in detectability between 70- and 120-kV CTA was +6.6% (90% CI, −3.9% to +16.8%). For accuracy of detection of the correct CSA, 70-kV CTA was significantly more accurate than 120-kV CTA for observer A ($P = .035$), but it was not significantly different for observer B ($P = .084$, Table 3). For detection of the presence of a collateral pathway, 70-kV CTA showed significantly higher accuracy for both observers ($P = .004$ for observer A and .047 for observer B). The Cohen κ for agreement between observers A and B and the reference standard was as follows: 0.81 (95% CI, 0.71–0.92) and 0.81 (95% CI, 0.70–0.92) for 120-kV CTA and 0.94 (95% CI, 0.88–1.00) and 0.92 (95% CI, 0.85–1.00) for 70-kV CTA, respectively. Representative CTA images with the highest continuity score in both protocols are presented in Fig 6.

Table 2. Results of consensus interpretation of the critical segmental artery

Variables	120-kV	70-kV	*P* Value
Detection of collateral pathway (No.) (%)	13 (21.7)	13 (21.7)	1.00
Detection of critical segmental artery (No.) (%)	50 (83.3)	54 (90.0)	.28

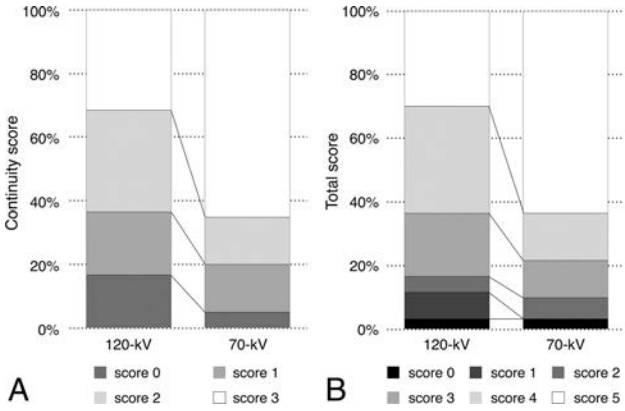

FIG 5. Seventy-kilovolt CTA yielded significantly higher scores than 120-kV CTA. *A*, Continuity score, median 3 (interquartile range, 2–3) compared with 2 (interquartile range, 1–3), respectively. *B*, Total score, median 5 (interquartile range, 4–5), compared with 4 (interquartile range, 3–5), respectively ($P < .05$ for both).

Table 3: Accuracy of interpretation of the critical segmental artery

Variables	120-kV	70-kV	*P* Value
Accuracy in all subjects			
Observer A	83.3	95.0	.035[a]
Observer B	83.3	93.3	.084
Accuracy in subjects with a collateral pathway			
Observer A	61.5	100	.004[a]
Observer B	30.8	69.2	.047[a]

[a] Statistically significant.

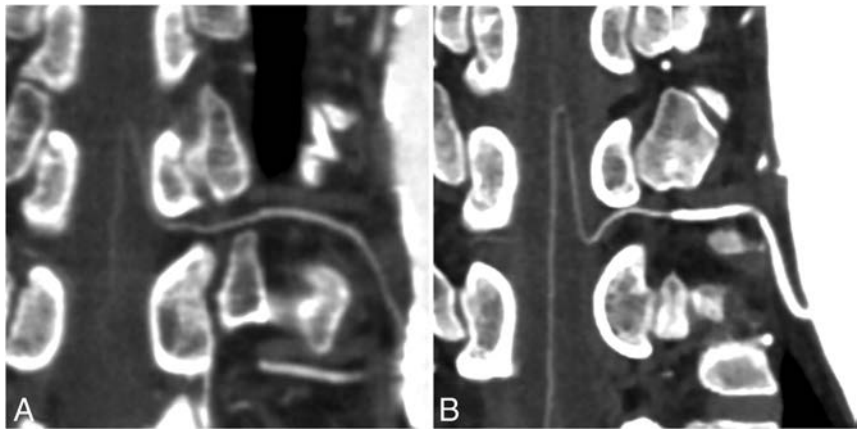

FIG 6. *A*, Curved multiplanar reformatted image of a 77-year-old woman scanned with a 120-kV protocol shows definite continuity between the AKA and the segmental artery. *B*, Curved multiplanar reformatted image of a 68-year-old man scanned with a 70-kV protocol shows clearer visualization of the AKA and the segmental artery from the aorta. Window center and width were set at 200 and 800.

Quantitative Image-Quality Analysis

Seventy-kilovolt CTA achieved a significantly higher mean CT number in the aorta and SNR_{Aorta} than 120-kV CTA (mean CT number, 999.1 ± 187.3 HU compared with 508.7 ± 96.5 HU; SNR_{Aorta}, 51.0 ± 11.0 HU compared with 28.8 ± 9.2 HU, respectively; $P < .001$ for both) (Fig 7). In 70-kV CTA, the CT numbers of the ASA, spinal cord, and bone cortex were significantly higher; however, there was no significant difference in the SD of the spinal cord (Table 4). Consequently, $CNR_{ASA\text{-}Cord}$ and $CNR_{ASA\text{-}Bone}$ were both significantly superior with 70-kV CTA than with 120-kV CTA ($P < .001$ for both, Table 4).

DISCUSSION

We found that 70-kV CTA has substantial advantages over 120-kV CTA for the detection of the AKA. With 70-kV CTA, a 66% reduction of the radiation dose (mean $CTDI_{vol}$, 16.2 mGy), while fulfilling the diagnostic reference level for chest or abdominal CT (21–25 mGy)[22] was possible without impairing the detection rate of the AKA and the CSA. Moreover, 70-kV CTA yielded significantly higher continuity and total scores and quantitative image-quality metrics, such as CT number of vessels, SNRs, and CNRs.

The use of the 70-kV scanning technique for cervical vascular CT has been reported before[23]; however, its utility is thought to be limited by image noise and artifacts. Image noise depends on photon flux, which, in turn, is dependent on tube current and voltage.[24] Because decreasing the tube voltage reduces photon flux, image noise would be expected to be higher in a 70-kV scan, but this can be addressed with the high tube current provided by the dual-power scan mode and an iterative reconstruction algorithm.[25] Using 2 state-of-the-art CT techniques, we were able to control image noise while significantly reducing the radiation dose compared with 120-kV CTA, thereby also improving contrast material enhancement to increase the SNR_{Aorta} and $CNR_{ASA\text{-}Cord}$ in 70-kV CTA. Although the quality of images obtained with 70-kV CT could theoretically

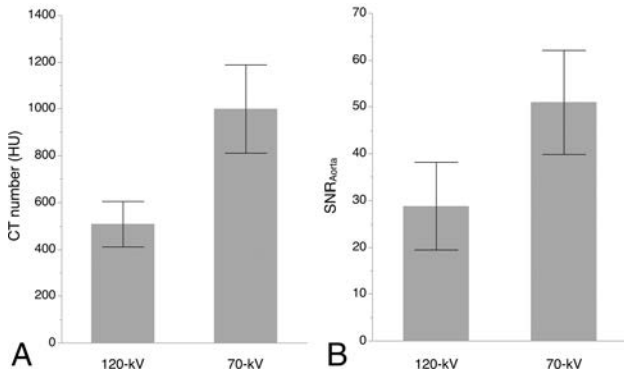

FIG 7. Seventy-kilovolt CTA yielded a significantly higher CT number (*A*) and SNR_{Aorta} (*B*) than 120-kV CTA ($P < .001$ for both analyses).

Table 4: Results of quantitative image-quality analysis[a]

Variables	120-kV	70-kV	*P* Value
Spinal cord			
CT number (HU)	39.4 ± 7.1	54.3 ± 11.6	<.001[b]
SD (HU)	12.5 ± 3.4	13.7 ± 3.9	.059
Bone cortex around the vertebral foramen			
CT number (HU)	657.4 ± 134.0	1,106.1 ± 246.2	<.001[b]
Anterior spinal artery			
CT number (HU)	78.7 ± 13.3	127.7 ± 30.0	<.001[b]
$CNR_{ASA\text{-}Cord}$	3.4 ± 1.6	5.6 ± 2.5	<.001[b]
$CNR_{ASA\text{-}Bone}$	50.3 ± 17.0	75.9 ± 30.5	<.001[b]

Note:—$CNR_{ASA\text{-}Cord}$ indicates contrast-to-noise ratio of the anterior spinal artery to the spinal cord; $CNR_{ASA\text{-}Bone}$, contrast-to-noise ratio of the anterior spinal artery to bone cortex around the vertebral foramen.

[a] Data are presented as the mean ± SD.

[b] Statistically significant.

be impaired by the presence of metal foreign bodies or stents or streak artifacts from extensive contrast attenuation, we did not observe any substantial diminution in image quality.

To identify the AKA, it is important to establish its continuity with the aorta, because the anterior radiculomedullary vein is similar in shape and size to the AKA and may run close to it.[12,18] When aortic disease has occluded the segmental arteries, it is necessary to identify the collateral supply via the CSA at a different vertebral level from the AKA.[3,26] The proximity between the AKA (or the collateral supply from the CSA) and the vertebral bone cortex makes the evaluation of continuity of the AKA or correct identification of the CSA challenging and time-consuming in spinal CTA.[27] However, due to the improvement of $CNR_{ASA\text{-}Bone}$ in 70-kV CTA, the continuity score was significantly higher than with 120-kV CTA. The accuracy of detection of the CSA was also improved in 70-kV CTA, especially when there was a collateral pathway to the AKA. Use of the continuity and total scores to detect the CSA allows surgical strategies for spinal protection to be identified with confidence, potentially informing the choice to undertake segmental artery reconstruction.[8]

Despite improvement in the continuity score, the AKA detection rate with 70-kV CTA was not significantly different from that of 120-kV CTA. However, 85%–90% is considered the upper limit of detectability of the AKA with CTA. Even in postmortem studies, the AKA detection rate (of anterior radiculomedullary arteries of ≥0.5-mm diameter) is reported to be 88%.[28] Furthermore, the detection rate of selective spinal angiography in a cohort of 487 patients with aortic disease has been reported as 86%,[29] and the combination of CTA and MR arteriography can achieve a detection rate of 89%.[12] The remaining 10%–15% of individuals in whom the AKA is undetectable are thought to have a greater number of smaller-caliber anterior radiculomedullary arteries (<0.5-mm diameter), according to an inverse association between the number and caliber of the anterior radiculomedullary arteries contributing to entire spinal blood supply.[30] Further advances in spatial resolution with CT might address limitations in visualization of the AKA; however, future studies should focus on fine-tuning CTA protocols to reduce radiation exposure and contrast material volume.

Our study had several limitations because of its single-center retrospective design. First, differences among CT scanners, especially reconstruction methods and the detectors, may have affected image quality. Nonetheless, image noise was not significantly different between the 2 CTA techniques, and consequently, we concluded that the higher vessel CT number of 70-kV CTA made it superior for AKA visualization. Because the scan mode was changed on installation of the new CT scanner at our institution, selection bias should also have been minimized. Second, we used a reference standard for CSA detection of the consensus interpretation of 2 specialists rather than conventional selective spinal angiography. Because selective spinal angiography is associated with complications in patients with aortic disease, we judge that using it to identify the AKA for validation purposes would not have been clinically or ethically acceptable.[12]

Finally, because all our subjects were Asian, the contrast material volume and usability of the low-kilovolt images may not be representative of those needed by subjects of other ethnicities or body sizes. However, even in obese patients, the low-kilovolt scanning technique can reportedly be successfully adapted by automated tube-voltage selection.[31] Further study is required to establish the optimum tube-voltage setting, radiation dose, and contrast material dose and injection rate to visualize the AKA according to body size.

CONCLUSIONS

Seventy-kilovolt CTA has substantial advantages over 120-kV CTA for the identification of the blood supply to the spinal cord, requiring a lower radiation dose but improving image quality sufficiently to allow confident and correct interpretation of the AKA and the CSA.

ACKNOWLEDGMENTS

The authors thank the following CT technologists for their support in image acquisition and processing: Tomoki Maebayashi, Ryuji Shimada, Erina Suehiro, Wakiko Tani, Toshinori Sekitani. and Noriyuki Negi.

Disclosures: Satoru Takahashi—*UNRELATED*: *Grant*: Siemens Healthcare*; *Consulting Fee or Honorarium*: Siemens Healthcare, *Comments*: honorarium for lectures; *Support for Travel to Meetings for the Study or Other Purposes*: Siemens Healthcare, *Comments*: travel fee for the presentation at Siemens SOMATOM World Summit meeting; *Payment for Writing or Reviewing the Manuscript*: Siemens Healthcare; *Payment for Lectures Including Service on Speakers Bureaus*: Siemens Healthcare, Philips Healthcare, Toshiba Medical Systems, GE Healthcare, Bayer Yakuhin, Esai, Fujifilm RI Pharma, Nihon Medi-physics, Daiichi Sankyo, Fuji Yakuhin, Astellas Pharma, AstraZeneca, Novartis International AG. *Money paid to the institution.

REFERENCES

1. Messé SR, Bavaria JE, Mullen M, et al. **Neurologic outcomes from high risk descending thoracic and thoracoabdominal aortic operations in the era of endovascular repair.** *Neurocrit Care* 2008;9: 344–51 CrossRef Medline
2. Jacobs MJ, de Mol BA, Elenbaas T, et al. **Spinal cord blood supply in patients with thoracoabdominal aortic aneurysms.** *J Vasc Surg* 2002;35:30–37 Medline
3. Kamada T, Yoshioka K, Tanaka R, et al. **Strategy for thoracic endovascular aortic repair based on collateral circulation to the artery of Adamkiewicz.** *Surg Today* 2016;46:1024–30 CrossRef Medline
4. Tanaka H, Ogino H, Minatoya K, et al; Japanese Study of Spinal Cord Protection in Descending and Thoracoabdominal Aortic Repair investigators. **The impact of preoperative identification of the Adamkiewicz artery on descending and thoracoabdominal aortic repair.** *J Thorac Cardiovasc Surg* 2016;151:122–28 CrossRef Medline
5. Kudo K, Terae S, Asano T, et al. **Anterior spinal artery and artery of Adamkiewicz detected by using multi-detector row CT.** *AJNR Am J Neuroradiol* 2003;24:13–17 Medline
6. Takase K, Sawamura Y, Igarashi K, et al. **Demonstration of the artery of Adamkiewicz at multi-detector row helical CT.** *Radiology* 2002; 223:39–45 CrossRef Medline
7. Uotani K, Yamada N, Kono AK, et al. **Preoperative visualization of the artery of Adamkiewicz by intra-arterial CT angiography.** *AJNR Am J Neuroradiol* 2008;29:314–18 CrossRef Medline
8. Nishii T, Kono AK, Negi N, et al. **The feasibility of a 64-slice MDCT for detection of the Adamkiewicz artery: comparison of the detection rate of intravenous injection CT angiography using a 64-slice MDCT versus intra-arterial and intravenous injection CT angiography using a 16-slice MDCT.** *Int J Cardiovasc Imaging* 2013; 29(suppl 2):127–33 CrossRef Medline
9. Nojiri J, Matsumoto K, Kato A, et al. **The Adamkiewicz artery: demonstration by intra-arterial computed tomographic angiography.** *Eur J Cardiothorac Surg* 2007;31:249–55 CrossRef Medline
10. Clarencon F, Di Maria F, Cormier E, et al. **Comparison of intra-aortic computed tomography angiography to conventional angiography in the presurgical visualization of the Adamkiewicz artery: first results in patients with thoracoabdominal aortic aneurysms.** *Neuroradiology* 2013;55:1379–87 CrossRef Medline
11. Melissano G, Chiesa R. **Advances in imaging of the spinal cord vascular supply and its relationship with paraplegia after aortic interventions: a review.** *Eur J Vasc Endovasc Surg* 2009;38:567–77 CrossRef Medline
12. Takagi H, Ota H, Natsuaki Y, et al. **Identifying the Adamkiewicz artery using 3-T time-resolved magnetic resonance angiography: its role in addition to multidetector computed tomography angiography.** *Jpn J Radiol* 2015;33:749–56 CrossRef Medline
13. Lell MM, Jost G, Korporaal JG, et al. **Optimizing contrast media injection protocols in state-of-the art computed tomographic angiography.** *Invest Radiol* 2015;50:161–67 CrossRef Medline
14. Meyer M, Haubenreisser H, Schoepf UJ, et al. **Closing in on the K edge: coronary CT angiography at 100, 80, and 70 kV-initial comparison of a second- versus a third-generation dual-source CT system.** *Radiology* 2014;273:373–82 CrossRef Medline
15. Nakaura T, Awai K, Oda S, et al. **Low-kilovoltage, high-tube-current MDCT of liver in thin adults: pilot study evaluating radiation dose, image quality, and display settings.** *AJR Am J Roentgenol* 2011;196: 1332–38 CrossRef Medline
16. Nishii T, Watanabe Y, Shimoyama S, et al. **Tailored duration of contrast material injection in high-pitch computed tomographic aortography with a double-level test bolus method.** *Invest Radiol* 2017; 52:274–80 CrossRef Medline
17. Petersilka M, Bruder H, Krauss B, et al. **Technical principles of dual source CT.** *Eur J Radiol* 2008;68:362–68 CrossRef Medline
18. Utsunomiya D, Yamashita Y, Okumura S, et al. **Demonstration of the Adamkiewicz artery in patients with descending or thoracoabdominal aortic aneurysm: optimization of contrast-medium application for 64-detector-row CT angiography.** *Eur Radiol* 2008;18:2684–90 CrossRef Medline
19. Yoshioka K, Niinuma H, Ehara S, et al. **MR angiography and CT angiography of the artery of Adamkiewicz: state of the art.** *Radiographics* 2006;26(suppl 1):S63–73 CrossRef Medline
20. Size-specific dose estimates (SSDE) in pediatric and adult body CT examinations. http://www.aapm.org/pubs/reports/rpt_204.pdf. Accessed March 8, 2017
21. Nishida J, Kitagawa K, Nagata M, et al. **Model-based iterative reconstruction for multi-detector row CT assessment of the Adamkiewicz artery.** *Radiology* 2014;270:282–91 CrossRef Medline
22. ACR-AAPM practice parameter for diagnostic reference levels and achievable doses in medical x-ray imaging. https://www.acr.org/~/media/ACR/Documents/PGTS/guidelines/Reference_Levels_Diagnostic_Xray.pdf. Accessed March 8, 2017
23. Gnannt R, Winklehner A, Goetti R, et al. **Low kilovoltage CT of the neck with 70 kVp: comparison with a standard protocol.** *AJNR Am J Neuroradiol* 2012;33:1014–19 CrossRef Medline
24. Huda W, Scalzetti EM, Levin G. **Technique factors and image quality as functions of patient weight at abdominal CT.** *Radiology* 2000;217: 430–35 CrossRef Medline
25. Scholtz JE, Kaup M, Hüsers K, et al. **Advanced modeled iterative reconstruction in low-tube-voltage contrast-enhanced neck CT: evaluation of objective and subjective image quality.** *AJNR Am J Neuroradiol* 2016;37:143–50 CrossRef Medline
26. Backes WH, Nijenhuis RJ, Mess WH, et al. **Magnetic resonance angiography of collateral blood supply to spinal cord in thoracic and thoracoabdominal aortic aneurysm patients.** *J Vasc Surg* 2008;48: 261–71 CrossRef Medline
27. Nishii T, Kono AK, Nishio M, et al. **Bone-subtracted spinal CT angiography using nonrigid registration for better visualization of arterial feeders in spinal arteriovenous fistulas.** *AJNR Am J Neuroradiol* 2015;36:2400–06 CrossRef Medline
28. Koshino T, Murakami G, Morishita K, et al. **Does the Adamkiewicz artery originate from the larger segmental arteries?** *J Thorac Cardiovasc Surg* 1999;117:898–905 CrossRef Medline
29. Kieffer E, Fukui S, Chiras J, et al. **Spinal cord arteriography: a safe adjunct before descending thoracic or thoracoabdominal aortic aneurysmectomy.** *J Vasc Surg* 2002;35:262–68 CrossRef Medline
30. Thron AK. *Vascular Anatomy of the Spinal Cord: Radioanatomy as the Key to Diagnosis and Treatment.* Switzerland: Springer; 2016:9–83
31. Mangold S, Wichmann JL, Schoepf UJ, et al. **Diagnostic accuracy of coronary CT angiography using 3(rd)-generation dual-source CT and automated tube voltage selection: clinical application in a non-obese and obese patient population.** *Eur Radiol* 2017;27:2298–308 CrossRef Medline

Zika Virus Iceberg: Very Large

Aragao et al[1] reported an interesting finding in "Nonmicrocephalic Infants with Congenital Zika Syndrome Suspected Only after Neuroimaging Evaluation Compared with Those with Microcephaly at Birth and Postnatally" and raised an interesting question, "How Large Is the Zika Virus 'Iceberg'?" In the report by Aragao et al, the important observations are "Among 77 infants, 24.6% had congenital Zika syndrome (11.7% microcephaly at birth, 9.1% postnatal microcephaly, 3.9% without microcephaly)."[1] It is interesting that there are many children with congenital Zika virus syndrome with no microcephaly but abnormal neurologic findings from neuroimaging evaluation. This finding might imply that there may be many cases of Zika infection that present no external phenotypic abnormality but have hidden neurologic abnormalities. The cases with Zika virus infections are usually asymptomatic,[2] and the tip of iceberg phenomenon is usually mentioned.[3]

Regarding the magnitude of underdiagnosed "iceberg" Zika virus infection, one might assume that 0.96% of infected cases (3.9% from 24.6%) can be underdiagnosed if there is no neuroimaging evaluation. Based on a recent publication of an immunologic study in an endemic area in Southeast Asia, the silent immunologic asymptomatic cases are 63%.[4] This finding can imply that the Zika virus iceberg is very large, and it might be necessary to consider the role and cost-effectiveness of using laboratory tools, including neuroimaging, for assessment of any suspicious cases.

http://dx.doi.org/10.3174/ajnr.A5351

REFERENCES

1. Aragao MFVV, Holanda AC, Brainer-Lima AM, et al. **Nonmicrocephalic infants with congenital Zika syndrome suspected only after neuroimaging evaluation compared with those with microcephaly at birth and postnatally: how large is the Zika virus "iceberg"?** *AJNR Am J Neuroradiol* 2017;38:1427–34 CrossRef Medline
2. Wiwanitkit S, Wiwanitkit V. **Afebrile, asymptomatic and non-thrombocytopenic Zika virus infection: don't miss it!** *Asian Pac J Trop Med* 2016;9:513 CrossRef Medline
3. Duarte G, Moron AF, Timerman A, et al. **Zika virus infection in pregnant women and microcephaly.** *Rev Bras Ginecol Obstet* 2017;39:235–48 CrossRef Medline
4. San K, Rajadhan V. **Seroprevalence of Zika virus in Cambodia: a preliminary report.** *Adv Lab Med Int* 2016;6:37–40

W. Sriwijitalai
RVT Medical Center
Bangkok, Thailand
V. Wiwanitkit
Joseph Ayobabalola University
Lagos, Nigeria

Regarding "Perfusion MR Imaging Using a 3D Pulsed Continuous Arterial Spin-Labeling Method for Acute Cerebral Infarction Classified as Branch Atheromatous Disease Involving the Lenticulostriate Artery Territory"

We read the article on the use of 3D pulsed continuous arterial spin-labeling (ASL) MR imaging for acute infarction associated with presumed branch atheromatous disease (BAD) by Shinohara et al[1] with great interest. The authors suggested that the baseline NIHSS score was significantly correlated with the asymmetry index of CBF in the contralateral cerebellar hemisphere (crossed cerebellar diaschisis, AI_{CCD}) ($r = 0.515$) and DWI lesion volume ($r = 0.664$), whereas it was not with the asymmetry index of CBF in the affected area (DWI lesion). The point of this study would be that even acute cerebral infarction by presumed BAD can show crossed cerebellar diaschisis on ASL MR imaging, which is correlated with the degree of neurologic severity. Their observations will draw the interest of the *American Journal of Neuroradiology* readers. As the authors pointed out, however, the clinical implication of the so-called BAD-type DWI lesions, which is usually determined by their location and size, is that they are strongly associated with early neurologic deterioration (END). A recent study with 587 patients showed that BAD-type DWI lesions and relevant artery stenosis can predict END, whereas the baseline NIHSS score cannot.[2] Thus, we already know that larger or longer DWI lesions may be a red flag for END, particularly when they are associated with relevant artery stenosis. In this circumstance, it would be better to provide firm evidence for obtaining ASL MR imaging by assessing its utility for the prediction of END. We also would like to comment on the methods in this study. First, the correlation between the AI_{CCD} and the baseline DWI lesion volume should be tested because it is expected that baseline DWI lesion volumes correlate well with baseline NIHSS scores, and larger DWI lesions have CCD more frequently. Thus, AI_{CCD} and baseline DWI lesion volume may have collinearity. If that is the case, the authors should conduct multivariable regression analysis to determine which one is independently associated with baseline NIHSS score. Second, it seems that the baseline NIHSS scores of 23 patients are not normally distributed (based on the Shapiro-Wilk test). Thus, nonparametric linear regression and Spearman rank correlation are rather appropriate. Third, the prevalence of END and clinical outcomes (such as discharge NIHSS scores or mRS at 3 months) should be compared between the patients with higher AI_{CCD} and those with lower value to confirm the clinical implication of obtaining ASL MR imaging in these patients. The authors only showed that the AI_{CCD} detected by ASL MR imaging is correlated with the baseline NIHSS score in this study. Finally, if they obtained ASL MR imaging in patients with non-BAD acute infarction, it would be better to include them for further analysis to determine whether they are different from those with BAD-type acute infarction in terms of prediction of END or baseline neurologic severity.

REFERENCES

1. Shinohara Y, Kato A, Kuya K, et al. **Perfusion MR imaging using a 3D pulsed continuous arterial spin-labeling method for acute cerebral infarction classified as branch atheromatous disease involving the lenticulostriate artery territory.** *AJNR Am J Neuroradiol* 2017 Jun 8. [Epub ahead of print] CrossRef Medline
2. Jeong HG, Kim BJ, Yang MH, et al. **Neuroimaging markers for early neurologic deterioration in single small subcortical infarction.** *Stroke* 2015;46:687–91 CrossRef Medline

D.H. Shin
Department of Neurology
E.Y. Kim
Department of Radiology
Gachon University Gil Medical Center
Incheon, South Korea

http://dx.doi.org/10.3174/ajnr.A5356

REPLY:

We appreciate the comments from Drs Shin and Kim regarding our publication, "Perfusion MR Imaging Using a 3D Pulsed Continuous Arterial Spin-Labeling Method for Acute Cerebral Infarction Classified as Branch Atheromatous Disease Involving the Lenticulostriate Artery Territory."[1]

It is well-established that branch atheromatous disease (BAD) is a risk factor for early neurologic deterioration (END).[2-5] Jeong et al[2] reported that the baseline NIHSS score in patients with a single small subcortical infarction, including BAD, cannot predict END, whereas another article showed that the baseline NIHSS score in patients with BAD can predict END.[3] Therefore, we focused on the initial MR imaging findings of lenticulostriate artery (LSA)-type BAD in comparison with the baseline NIHSS score. To our knowledge, only a few reports thus far have referred to the association between DWI infarct volume and clinical outcome in patients having radiologically defined LSA-type BAD.[4,5] Because the clinical entity, including the radiologic definition of BAD, remains uncertain, further investigations are needed to prove the relationship between the imaging characteristics of BAD and END.[5]

Regarding the collinearity between asymmetry index of the contralateral cerebellar hemisphere (crossed cerebellar diaschisis, AI_{CCD}) on 3D-arterial spin-labeling (ASL) and DWI infarct volume, we also considered that it would be better to perform multivariable regression analysis to clarify the relationship. However, our sample size was not large enough to obtain reliable statistical data. The Pearson correlation coefficient was used to compare the admission NIHSS score with each AI_{CCD} and infarct volume for the same reason. These decisions about the methods were based on statistical consultation with a specialist.

In addition, we previously reported the correlation between AI_{CCD} on 3D-ASL and the initial NIHSS score in patients with cardioembolic infarction (CE, $n = 44$) and large-artery atherosclerosis (LAA, $n = 38$) as well as LSA-type BAD at the 46th Annual Meeting of the Japanese Society of Neuroradiology, February 17–19, 2017, Tokyo, Japan. Our findings revealed that there was no significant correlation between AI_{CCD} and the initial NIHSS score in CE or LAA ($r = 0.147$, $P = .340$; $r = 0.086$, $P = .606$, respectively). Although LSA-type BAD usually affects the pyramidal tract at the corona radiata or internal capsule, easily resulting in a remote effect along the corticopontocerebellar pathway, the ischemic lesions of CE and LAA might be more variable depending on the collateral status or vascular territories compared with the LSA-type BAD.

Finally, as noted by Drs Shin and Kim, the main message of our study was that acute LSA-type BAD can show crossed cerebellar diaschisis on 3D-ASL and there is a significant correlation between the degree of perfusion asymmetry of crossed cerebellar diaschisis and initial neurologic severity. Further studies are warranted to validate the relationship between AI_{CCD} and neurologic outcome, including follow-up NIHSS score, and to clarify the collinearity between AI_{CCD} and baseline lesion volume with a larger sample size.

REFERENCES

1. Shinohara Y, Kato A, Kuya K, et al. **Perfusion MR imaging using a 3D pulsed continuous arterial spin-labeling method for acute cerebral infarction classified as branch atheromatous disease involving the lenticulostriate artery territory.** *AJNR Am J Neuroradiol* 2017 Jun 8. [Epub ahead of print] CrossRef Medline
2. Jeong HG, Kim BJ, Yang MH, et al. **Neuroimaging markers for early neurologic deterioration in single small subcortical infarction.** *Stroke* 2015;46:687–91 CrossRef Medline
3. Yamamoto Y, Ohara T, Hamanaka M, et al. **Predictive factors for progressive motor deficits in penetrating artery infarctions in two different arterial territories.** *J Neurol Sci* 2010;288:170–74 CrossRef Medline
4. Moriya S, Adachi T, Goto J, et al. **Relationship between MRI findings and outcome in supratentorial branch atheromatous disease (BAD).** *Nosotchu* 2006;28:504–09 CrossRef
5. Petrone L, Nannoni S, Del Bene A, et al. **Branch atheromatous disease: a clinically meaningful, yet unproven concept.** *Cerebrovasc Dis* 2016; 41:87–95 CrossRef Medline

Y. Shinohara
T. Ogawa
Division of Radiology
Department of Pathophysiological and Therapeutic Science
Faculty of Medicine
Tottori University
Yonago, Japan

http://dx.doi.org/10.3174/ajnr.A5364

Regarding "Determining the Orientation of Directional Deep Brain Stimulation Electrodes Using 3D Rotational Fluoroscopy"

We read with great interest the recently published article of Reinacher et al[1] on the determination of the precise 3D orientation of directional leads for deep brain stimulation (DBS) with rotational fluoroscopy. We agree with the authors that for targeted directional steering of DBS the "detailed knowledge of the exact orientation of the electrode array with respect to its functional environment" is essential. We also like the idea of using not only the directional marker but also the signal of the segmented electrode contacts to improve the accuracy of the measured orientation angle. However, we would like to raise concerns about the solution presented and the conclusions drawn.

To describe the position of a directional lead in its functional environment requires at least 6 parameters, for example, the X, Y, Z coordinates of the lead tip and the 3 angles of lead orientation defined in 3D stereotactic space. Coordinates and angles of leads as they appear in a volumetric image may be transformed into another coordinate system by applying a transformation matrix comprising 3 translations along the coordinate axes and 3 rotations with respect to the coordinate axes. Furthermore, the location and shape of implants, as they appear in a sectional image, may be calculated from the intersection of the 3D object describing the implant itself and a plane representing the image geometry. For leads that do not intersect the plane at right angles, both shape and angles commonly incline; thus, the angles between the lines connecting the gaps among the 3 electrode segments are no longer 60° but vary in the range of 40°–80°.[2]

The method described by the authors determines the directional angle of the lead as it projects into a plane defined by the path of the x-ray focus of the 3D-flouroscopy device used. In order to account for patient orientation during 3D fluoroscopy, measured angles were referenced to the patient's sagittal direction as it appeared in the plane of the x-ray focus path. The so-determined angle was then taken as the searched lead orientation angle, disregarding any inclinations due to oblique orientations of the lead inside the brain and the further tilt angles of the patient's head with respect to the imaging system.

Problems associated with the oblique and tilted courses of the leads were not addressed by the authors and not investigated in their experiments. Therefore, and also because the authors did not compare their results against a ground truth, we believe that the proposed method is insufficient for detecting "the exact orientation of the electrode array with respect to its functional environment."

Disclosures: Veerle Visser-Vandewalle—*UNRELATED*: *Consultancy*: Medtronic, Abbott, Boston Scientific; *Payment for Lectures Including Service on speakers Bureaus*: Medtronic, Abbott, Boston Scientific.

REFERENCES

1. Reinacher PC, Krüger MT, Coenen VA, et al. **Determining the orientation of directional deep brain stimulation electrodes using 3D rotational fluoroscopy.** *AJNR Am J Neuroradiol* 2017;38:1111–16 CrossRef Medline
2. Sitz A, Hoevels M, Hellerbach A, et al. **Determining the orientation angle of directional leads for deep brain stimulation using computed tomography and digital x-ray imaging: a phantom study.** *Med Phys* 2017 Jun 22. [Epub ahead of print] CrossRef Medline

H. Treuer
A. Hellerbach
Department of Stereotactic and Functional Neurosurgery
University Hospital of Cologne
Cologne, Germany
J. Borggrefe
Division of Neuroradiology, Institute of Diagnostic and Interventional Radiology
University Hospital of Cologne
Cologne, Germany
V. Visser-Vandewalle
Department of Stereotactic and Functional Neurosurgery
University Hospital of Cologne
Cologne, Germany

http://dx.doi.org/10.3174/ajnr.A5377

REPLY:

We thank Treuer et al for their interest in our article "Determining the Orientation of Directional Deep Brain Stimulation Electrodes Using 3D Rotational Fluoroscopy."[1] The coordinates (x, y, z) and 2 angles (pitch and yaw angles) are required to describe the position of a nondirectional deep brain stimulation (DBS) lead, and determining these is routine clinically. In directional leads, a third angle (roll) needs to be considered. We investigated the "iron sights method" to additionally determine this angle because there was no known imaging technique allowing us to do so precisely. We could demonstrate that this method allows determining a lead orientation angle with high interrater reliability.[1] We are aware that this angle is determined in a plane defined by 3D rotational fluoroscopy. As used in CT scans, the rotational fluoroscopy should be aligned to the tuberculum sellae–occipital protuberance line, and head tilt must be excluded by aligning both external acoustic meatus. This line closely correlates to the anterior/posterior commissure line,[2] which defines the relevant plane in clinical DBS practice. In publications, typically the orientation of directional leads is described and depicted in this plane.[3]

3D rotational fluoroscopy allows reconstructing a volumetric dataset that can be fused with the preoperative, stereotactic CT or MR imaging scan as shown in Fig 1. Thus, after fusion with these images, the stereotactic coordinates together with the pitch and yaw angles can be determined in a stereotactic planning system, allowing the roll angle to be calculated for any desired plane. In addition, the surrounding anatomic structures can be visualized (eg, in the preoperative MR imaging).

To address the authors' comment (additionally using ground truth and to further investigate the influence of different implantation angles on the iron sights method), we embedded a directional lead in an acrylic glass cylinder. This model was fixed in a stereotactic frame (Leksell G frame; Elekta Instruments, Stockholm, Sweden) and oriented visually with the marker exactly facing anteriorly. This orientation was confirmed by a strictly lateral x-ray in respect to the stereotactic frame. To investigate in which angles the overlap of the gaps between the electrode segments was still visible, we performed digital x-ray and 3D fluoroscopy in different settings of the stereotactic system. We systematically (in steps of 10°) changed the arc and ring angles, resulting in polar lead angles of 0°–90° (ring, rotation in the sagittal plane) and 0°–60° (arc, rotation in the coronal plane) (Fig 2).

Fluoroscopically with unchanged rotation of the lead, the overlap of the gaps between the directional contacts remained visible up to a polar angle of 50° when tilting the lead toward the observer (arc angle). It was overlaid by the other contacts at 60°. The overlap of the gaps remained visible from 0° to 90° on rotation of the electrode in a sagittal plane (ie, the ring angle of the stereotactic system). Within these ranges, the iron sights visualization was possible for combinations of lead rotations in both planes.

As long as the overlap of the gaps was visible, 3D rotational angiography allowed determining the lead rotation using the iron sights method as in our previous phantom study.[1] High polar angles (in our method, >50° in the coronal plane) require an oblique 3D fluoroscopy plane.

Sitz et al[4] have shown in their phantom study, evaluating the CT artifacts of the directional marker to determine the lead orientation, that "for polar angles >40°, the results became erratic and the uncertainty increased to ± 8.9° (range −23° to 34°)." They explained this with the marker anatomy, "Distal parts of the marker with the ring-shaped structures also appear within the CT-sections, giving rise to an additional nonisotropic artifact."[4]

We analyzed the polar angles of all DBS implantations performed in our center in 2016. Regarding 107 DBS electrodes in 54 patients, the mean sagittal polar angle was 15.5° ± 29.8° and the mean coronal polar angle was 23.1° ± 9.9°. In 9/214 measured polar angles (4.2%), the value was >50°. In these cases, a modification of our standard 3D fluoroscopy scanning protocol (ie, alignment to the tuberculum sellae–occipital protuberance line) with an oblique scan is necessary. However, this can be precisely predicted from the stereotactic planning of the DBS procedure.

REFERENCES

1. Reinacher PC, Krüger MT, Coenen VA, et al. **Determining the orientation of directional deep brain stimulation electrodes using 3D rotational fluoroscopy.** *AJNR Am J Neuroradiol* 2017;38:1111–16 CrossRef Medline
2. Kim YI, Ahn KJ, Chung YA, et al. **A new reference line for the brain CT: the tuberculum sellae-occipital protuberance line is parallel to the anterior/posterior commissure line.** *AJNR Am J Neuroradiol* 2009;30:1704–08 CrossRef Medline
3. Kühn AA, Volkmann J. **Innovations in deep brain stimulation methodology.** *Mov Disord* 2017;32:11–19 CrossRef Medline
4. Sitz A, Hoevels M, Hellerbach A, et al. **Determining the orientation angle of directional leads for deep brain stimulation using computed tomography and digital x-ray imaging: a phantom study.** *Med Phys* 2017 Jun 22. [Epub ahead of print] CrossRef Medline

P.C. Reinacher
Department of Stereotactic and Functional Neurosurgery
M.T. Krüger
Department of Neurosurgery
V.A. Coenen
Department of Stereotactic and Functional Neurosurgery
M. Shah
R. Roelz
Department of Neurosurgery
C. Jenkner
Clinical Trial Unit
K. Egger
Department of Neuroradiology
Medical Center, Faculty of Medicine
University of Freiburg, Freiburg, Germany

http://dx.doi.org/10.3174/ajnr.A5386

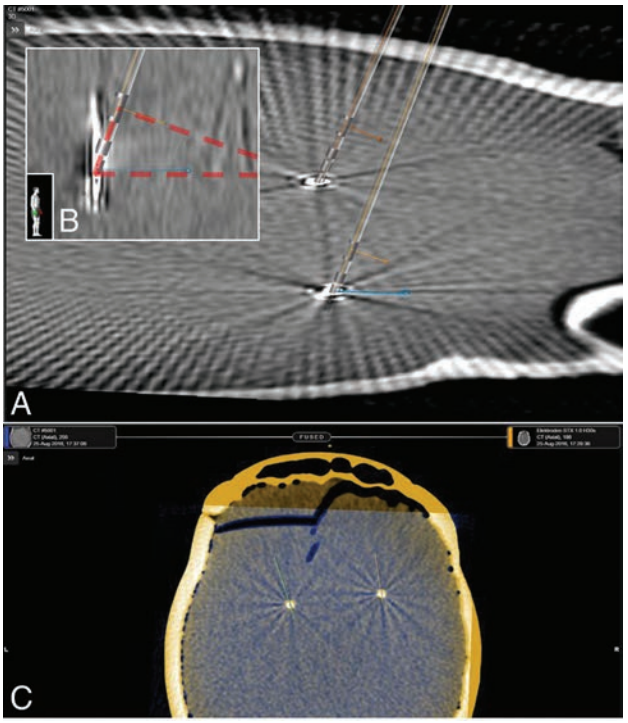

FIG 1. *A*, Visualization of 3D directional electrode models in a 3D reconstruction of rotational fluoroscopy imaging. The *blue line* (in-plane) indicates the detected orientation in the axial plane based on the iron sights method. The *orange line* originating out of the marker indicates the lead orientation. *B*, The same scene from a lateral view. The in-plane orientation and marker orientation form a *rectangular triangle* (red transparent) with the right angle at the marker. *C*, Fusion of rotational fluoroscopy 3D reconstruction and the CT scan in Brainlab Elements (Brainlab, Munich, Germany).

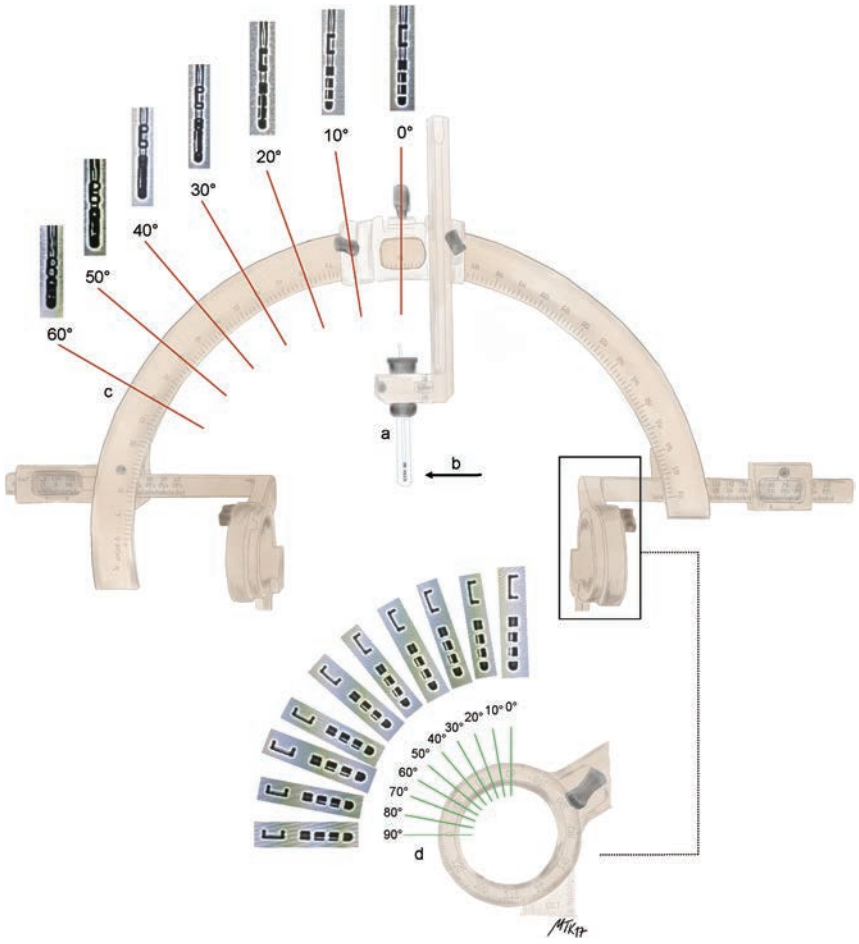

FIG 2. *A*, A directional lead embedded in an acrylic glass cylinder (ground truth). This model was fixed in a stereotactic Leksell G frame (Elekta Instruments) and oriented visually and with stereotactic fluoroscopy with the marker exactly facing anteriorly. *B*, Fluoroscopy was aligned with the stereotactic frame. *C*, The arc angle (lead rotation in the coronal plane) was changed, resulting in polar angles of 0°–60° in steps of 10°. *D*, The ring angle (lead rotation in the sagittal plane) was changed, resulting in polar angles of 0°–90° in steps of 10°. Digital x-ray and 3D fluoroscopy were performed for each setting to investigate in which angles the overlap of the gaps between the electrode segments (iron sights) is visible.

Safety and Efficacy of Aneurysm Treatment with the WEB

We read with interest the article by Pierot et al[1] regarding the results of the WEBCAST 2 study. We do, however, take issue with the statement that it confirms the "high" efficacy of the device. They reported a complete occlusion rate of 54% and "adequate" occlusion, including neck remnants, in 80% of 50 aneurysms (93% unruptured). The complete occlusion rate from neurosurgical clipping in the largest randomized controlled trials of coiling versus clipping of ruptured aneurysms was 96%.[2,3] A meta-analysis of clipping of unruptured aneurysms showed a complete occlusion rate of 92%.[4] Although the decision to proceed with endovascular therapy in WEBCAST was made by a multidisciplinary team, it may be wise to temper one's enthusiasm for novel endovascular devices when open neurosurgical treatment may offer a truly "high" level of efficacy.

http://dx.doi.org/10.3174/ajnr.A5387

REFERENCES

1. Pierot L, Gubucz I, Buhk JH, et al. **Safety and efficacy of aneurysm treatment with the WEB: results of the WEBCAST 2 study.** *AJNR Am J Neuroradiol* 2017;38:1151–55 CrossRef Medline
2. Spetzler RF, McDougall CG, Zabramski JM, et al. **The Barrow Ruptured Aneurysm Trial: 6-year results.** *J Neurosurg* 2015;123:609–17 CrossRef Medline
3. Campi A, Ramzi N, Molyneux AJ, et al. **Retreatment of ruptured cerebral aneurysms in patients randomized by coiling or clipping in the International Subarachnoid Aneurysm Trial (ISAT).** *Stroke* 2007; 38:1538–44 CrossRef Medline
4. Kotowski M, Naggara O, Darsaut TE, et al. **Safety and occlusion rates of surgical treatment of unruptured intracranial aneurysms: a systematic review and meta-analysis of the literature from 1990 to 2011.** *J Neurol Neurosurg Psychiatry* 2013;84:42–48 CrossRef Medline

D.M. Pelz
S.P. Lownie
Departments of Medical Imaging and Clinical Neurological Sciences
Schulich School of Medicine and Dentistry, Western University
London, Ontario, Canada

REPLY:

We have read with great interest the letter of Pelz and Lownie, and we are grateful for their interesting comments regarding our paper on the WEBCAST-2 study.[1] We wish to make the following comments in response.

1) Because Pelz and Lownie are only challenging the "high" efficacy of WEB treatment, it probably implies that they concur with the high safety profile of the WEB device reported in WEBCAST-2. This is the primary concern when dealing with aneurysm treatment, and all published results of good clinical practice studies evaluating WEB (WEBCAST, French Observatory, and WEB-IT) have indeed confirmed similar high safety results: low morbidity (between 0.7% and 3.2%) and no mortality at 1 month.[2-4] For reference, the meta-analysis cited by Pelz and Lownie reports mortality of 1.7% for surgical treatment of unruptured aneurysms, with the rate of unfavorable outcome at 6.7%.[5]

2) Pelz and Lownie are probably right when they write that "high" efficacy might not be the appropriate wording to qualify WEBCAST-2 anatomical results. Still, the rate of adequate occlusion at 1 year is 80.0%, consistent with observations from other WEB good clinical practice studies.[2,3] Although we know that neck remnant is rarely associated with rupture or rerupture, adequate occlusion is really what matters once safety is confirmed. It is also important to point out that patients with wide-neck bifurcation aneurysms—the target population of the WEBCAST-2 study—represent a challenging and difficult-to-treat population, regardless of the treatment technique. We actually agree that long-term follow-up is needed to properly evaluate the stability of aneurysm treatment and claim "high" efficacy. Long-term follow-up has been obtained in a small, retrospective European series, but the most important data will come from the good clinical practice studies where 5 years' follow-up is foreseen.[6]

3) Interestingly, Pelz and Lownie are comparing the efficacy of WEB treatment with surgical treatment. Kotowski et al[5] report 2 interesting facts in their meta-analysis: aneurysm occlusion data are missing for 82.2% of all clipped aneurysms in the analyzed series, and there was no long-term follow-up available. With that in mind, can we scientifically consider surgical treatment "effective" from a long-term anatomic standpoint?

http://dx.doi.org/10.3174/ajnr.A5416

REFERENCES

1. Pierot L, Gubucz I, Buhk JH, et al. **Safety and efficacy of aneurysm treatment with the WEB: results of the WEBCAST-2 study.** *AJNR Am J Neuroradiol* 2017;38:1151–55 CrossRef Medline
2. Pierot L, Costalat V, Moret J, et al. **Safety and efficacy of aneurysm treatment with WEB: results of the WEBCAST study.** *J Neurosurg* 2016;124:1250–56 CrossRef Medline
3. Pierot L, Moret J, Turjman F, et al. **WEB treatment of intracranial aneurysms: clinical and anatomical results in the French Observatory.** *AJNR Am J Neuroradiol* 2016;37:655–59 CrossRef Medline
4. Fiorella D, Molyneux A, Coon A, et al. **Demographic, procedural, and 30-day safety results from the WEB Intra-saccular Therapy Study (WEB-IT).** *J Neurointerv Surg* 2017 Jan 17. [Epub ahead of print] CrossRef Medline
5. Kotowski M, Naggara O, Darsaut TE, et al. **Safety and occlusion rates of surgical treatment of unruptured intracranial aneurysms: a systematic review and meta-analysis of the literature from 1990 to 2011.** *J Neurol Neurosurg Psychiatry* 2013;84:42–48 CrossRef Medline
6. Pierot L, Klisch J, Liebig T, et al. **WEB-DL endovascular treatment of wide-neck bifurcation aneurysms: long-term results in a European series.** *AJNR Am J Neuroradiol* 2015;36:2314–19 CrossRef Medline

L. Pierot
Department of Neuroradiology
Hôpital Maison-Blanche
CHU Reims
Université Reims-Champagne-Ardenne
Reims, France